ISSN en trámite

instituto de astronomía

unam

revista mexicana de astronomía y astrofísica

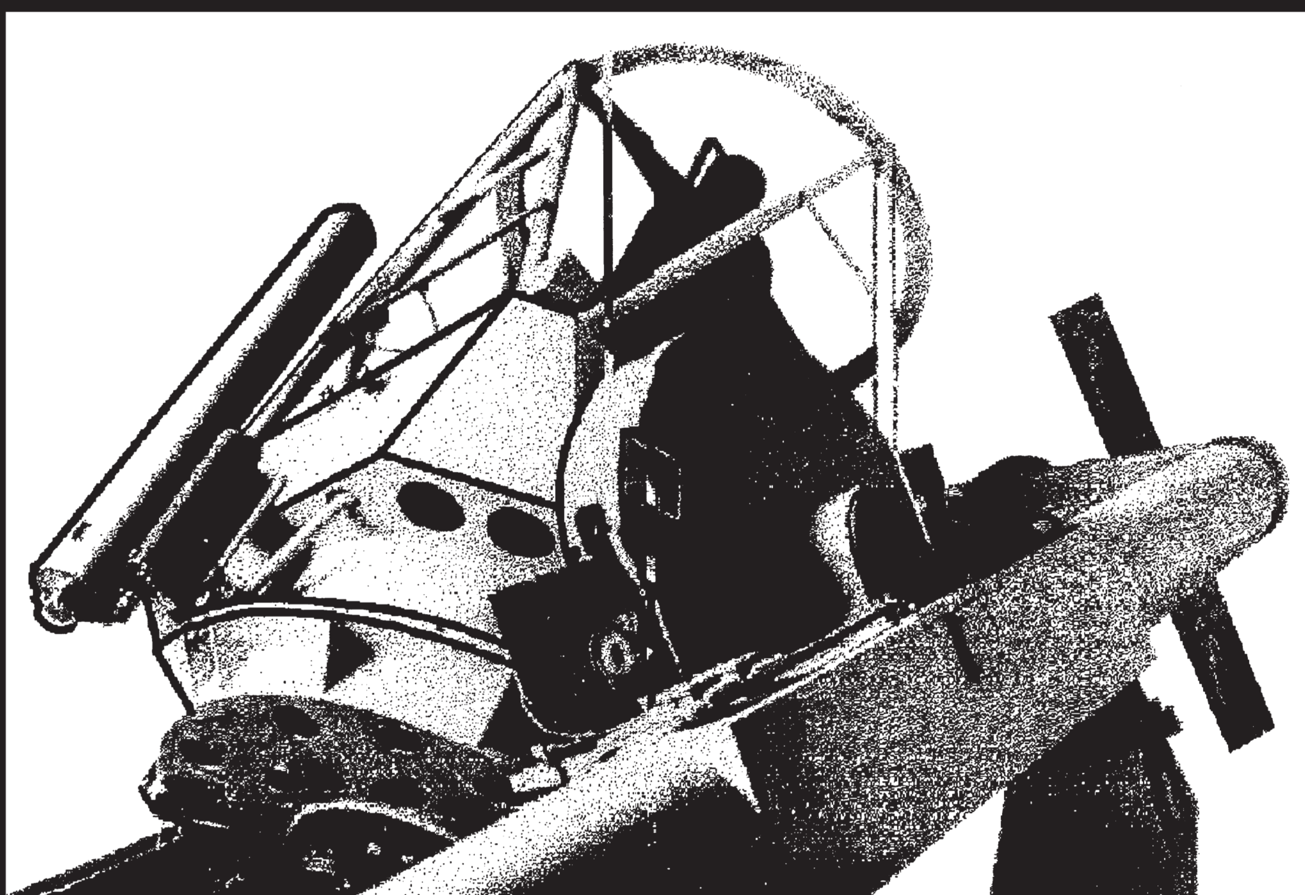

volumen 57
número 1
octubre 2021

volumen 57, número 1, abril 2021

revista mexicana de astronomía y astrofísica

Instituto de Astronomía
Universidad Nacional Autónoma de México

revista mexicana de astronomía y astrofísica

ISSN en trámite

URL de DOI: https://doi.org/10.22201/ia.01851101p.2021.57.01

rmaa@astro.unam.mx

http://www.astroscu.unam.mx/RMxAA/

La *RMxAA* aparece indexada en Current Contents, Science Citation Index, Astronomy and Astrophysics Abstracts, Physics Briefs, Publicaciones Científicas en América Latina, Astronomy and Astrophysics Monthly Index, PERIODICA, RedALyC, Latindex y SciELO.

Revista Mexicana de Astronomía y Astrofísica, volumen 57, número 1, abril 2021, es una publicación semestral, editada y distribuida por el Instituto de Astronomía, UNAM, Circuito Exterior, Ciudad Universitaria, 04510, Alcaldía Coyoacán, Ciudad de México, Teléfono: 5556223906, Correo Electrónico: rmaa@astro.unam.mx, ISSN en trámite. Editora responsable: Christine Patricia Allen Armiño. Distribución: Bienes y Servicios del Instituto de Astronomía, UNAM. Impresa por Grupo Edición, S.A. de C.V., Xochicalco 619, Colonia Letrán Valle, 03650, Alcaldía Benito Juárez, Ciudad de México. Fecha de impresión: 27 de marzo de 2021. Número de ejemplares impresos: 500 en papel Couché de 100 gramos los interiores y en cartulina Couché de 250 gramos los forros. Precio de la publicación: gratuito.

CONTENTS

Revista Mexicana de Astronomía y Astrofísica, **57**, 3–38 (2021)

https://doi.org/10.22201/ia.01851101p.2021.57.01.01

FROM GLOBAL TO SPATIALLY RESOLVED IN LOW-REDSHIFT GALAXIES

S. F. Sánchez[1], C. J. Walcher[2], C. Lopez-Cobá[1], J. K. Barrera-Ballesteros[1], A. Mejía-Narváez[1], C. Espinosa-Ponce[1], and A. Camps-Fariña[1]

Received July 6 2020; accepted September 9 2020

ABSTRACT

Our understanding of the structure, composition and evolution of galaxies has strongly improved in the last decades, mostly due to new results based on large spectroscopic and imaging surveys. In particular, the nature of ionized gas, its ionization mechanisms, its relation with the stellar properties and chemical composition, the existence of scaling relations that describe the cycle between stars and gas, and the corresponding evolution patterns have been widely explored and described. More recently, the introduction of additional techniques, in particular integral field spectroscopy, and their use in large galaxy surveys, have forced us to re-interpret most of those recent results from a spatially resolved perspective. This review is aimed to complement recent efforts to compile and summarize this change of paradigm in the interpretation of galaxy evolution. To this end we replicate published results, and present novel ones, based on the largest compilation of IFS data of galaxies in the nearby universe to date.

RESUMEN

Nuestro entendimiento de la estructura, composición y evolución de las galaxias se ha visto ampliamente modificado en las últimas décadas principalmente debido a la explosión de resultados basados en grandes muestreos en imagen y espectroscopía. En particular, la naturaleza de la ionización observada, su relación con las propiedades estelares y la composición química, la existencia de relaciones evolutivas o de escala que regulan el ciclo entre el gas y las estrellas, y los patrones evolutivos se han explorado y descrito en detalle. Más recientemente, la introducción de técnicas adicionales, en particular la espectroscopía de campo integral, ha forzado a una reinterpretación de estos resultados recientes desde una perspetiva espacialmente resuelta. Este artículo de revisión tiene como objetivo complementar esfuerzos recientes enfocados en la compilación y resumen de este cambio de paradigma en la interpretación de la evolución de las galaxias.

Key Words: galaxies: evolution — galaxies: fundamental parameters — galaxies: ISM — galaxies: star formation — galaxies: stellar content — techniques: imaging spectroscopy

1. INTRODUCTION

The evolution of galaxies during cosmic time is the story of the cycle of transformation of gas into stars, the production of metals inside these stars, the release of metals during stellar life and death, and the interaction between these processes and their environment, i.e their host galaxies' dynamics and overall structure. All this evolution leaves signatures in the observed properties of galaxies that we can analyse to reconstruct it. The analysis of this fossil record is a key tool to understand how galaxies in the nearby universe evolved. In combination with the massive acquisition of spectroscopic data, both integrated (e.g., Sloan Digital Sky Survey, SDSS, Galaxy and Mass Assembly Survey, GAMA, York et al. 2000; Driver et al. 2009, respectively), and spatially resolved (e.g., Calar Alto legacy Integral Field Spectroscopy Area, CALIFA, or Mapping Nearby Galaxies at APO, MaNGA Sánchez et al. 2012a; Bundy et al. 2015a, respectively) our understanding of the processes that govern galaxy evolution has increased considerably.

In a recent review, Sánchez (2020), the most recent results obtained by the analysis of Integral Field Spectroscopy (IFS) Galaxy Surveys (GS) were summarized. Among the results reviewed there were the following: (i) the sources of ionization across the optical extent of galaxies; (ii) the interplay among the global (i.e., in-

[1]Instituto de Astronomía, UNAM, México.
[2]Leibniz-Institut für Astrophysik Potsdam (AIP), Germany.

tegrated/characteristic) properties of galaxies, the local (i.e., spatially resolved) ones, and the link between these two kinds of relations; and (iii) the radial distributions of different properties of the stars and ionized gas. However, due to the narrow scope and space limitations of such reviews, some important aspects of those results were not fully addressed.

In particular, it was not possible to include a detailed description of the adopted dataset (a compilation of publicly accessible IFS data), and the description of the analysis performed to derive the results. We include those details in the current manuscript. Furthermore, we now (i) provide additional detail on the nature of the different ionizing sources and how the ionized gas is observed in galaxies; (ii) demonstrate analytically how local and global relations are connected and (iii) provide a quantitative statement on the gradients described in Sánchez (2020).

The main aim of the current article is to provide the details that were not covered in Sánchez (2020), presenting more quantitative results. Even though the two article are clearly complementary, the current one presents results not described in detail in that review and includes new ones. This review is organized as follows: (i) a description of the adopted dataset is provided in § 2; (ii) § 3 includes a summary of the performed analysis; (iii) the results of the analysis are presented in § 4, including a detailed description of the different sources of ionization within galaxies and the diagnostic diagrams widely used to disentangle them through observational signatures; (iv) the analytical description of the connection between local and global relations is included in § 5, showing that indeed both relations are essentially the same; (v) finally, a quantitative statement on the radial gradients and characteristic values of the different resolved properties explored in Sánchez (2020) is included in § 6; we summarize our results and the main conclusions in § 7.

2. DATA SAMPLE

We adopted the same dataset already presented in Sánchez (2020). This represents a compilation of the publicly accessible IFS data provided by the most recent IFS-GS and compilations, including: AMUSING++ (447 Galbany et al. 2016), eCALIFA (910 Sánchez et al. 2012a; Galbany et al. 2018), MaNGA (4,655 Bundy et al. 2015b) and SAMI (Croom et al. 2012, 2,222). Details of the particular characteristics of each survey and the differences between the provided data are discussed in detail in Appendix A of Sánchez (2020). They all provide spatially resolved spectroscopic information of large samples of galaxies mostly located at $z \approx$0.01-0.06. After removing a few cubes with low-S/N, or covering just a fraction of the optical extent of the target galaxies, the final compilation comprises 8203 galaxies, 5637 with morphological information. However, due to the strong differences among the surveys, not all galaxies are sampled with the same quality. Thus, we select what we consider *the best quality data*, in terms of the ability to explore the spatial variations of galaxy properties in an optimal way, by restricting the dataset to those galaxies/cubes that satisfy the following criteria:

(i) They should have a reliable morphological classification. This is extremely important since one of the main goals of the current exploration is to characterise the physical resolved properties of galaxies for different morphological types.

(ii) They should be sampled out to 2.5 effective radii (R_e). This requirement was included to explore only those galaxies with IFS data covering a significant fraction of their optical extension. This is particular important for disk-dominated late-type objects, whose bulge may cover a range up to 0.5-1.0 R_e (e.g. González Delgado et al. 2014), since the average properties of the disk would not be well covered if the FoV of the IFS data is limited to 1-1.5 R_e. Furthermore, it is known that beyond 2 R_e disk galaxies may present a different behavior than that of the main disk, showing truncations or upturns in their surface-brightness (e.g. van der Kruit 2001; Bakos et al. 2008; van der Kruit & Freeman 2011), and deviations from the global oxygen abundance trends (e.g. Marino et al. 2016). But is is also relevant in elliptical galaxies, in particular those that present some remnants of star-formation in the outskirts, but nowhere else (e.g. Gomes et al. 2016b). Thus, to cover up to 2.5 R_e guarantees that we sample the real radial distributions in galaxies, not being biased to either the properties of the very central regions or those of the outermost ones.

(iii) R_e should be at least two times the full-width-at-half-maximum (FWHM) of the point spread function (PSF) of the data. This is indeed a basic requirement to guarantee that galaxies are resolved by the data. If the PSF FWHM is of the order of or larger than R_e, the considered galaxy would be unresolved. Thus, even if it is sampled beyond its full optical extension no reliable gradient or variation across the FoV could or should be derived. Although this may sound obvious it is sometimes ignored, in particular since sometimes there is confusion between the size of sampling element (e.g., the pixel or spaxel in which the data are recorded or stored) and the resolution (given by the FWHM of the PSF or beam of the instrument or final dataset).

(iv) We limit the redshift range up to $z < 0.02$. This requirement was included to restrict ad maximum the range of cosmological distances sampled by the data

(D_L <90 Mpc, t <380 Myr), but without excluding a significant fraction of galaxies of a particular type (mostly morphology) or stellar mass. This way there is no space for a strong cosmological evolution of the properties between the galaxies sampled at higher and lower redshifts, and most of the galaxies would be sampled at a similar physical resolution. Some of the original samples from which our collection is drawn span through much larger cosmological times (up to z≈0.15), with strong correlations between galaxy properties and redshift (e.g. Wake et al. 2017). This creates a complication in the exploration of the dependence of the derived observables on either the properties of the galaxies and/or their cosmological evolution.

(v) Highly inclined galaxies are excluded (i.e. we require $i < 75^o$). It is known that when a galaxy is observed at high inclinations many of its global and spatial resolved properties are strongly biased (e.g., the molecular gas derived from the dust attenuation, Concas & Popesso 2019, that we explore later on). Although this is a general problem, it is obviously more evident in disk-dominated galaxies. There is a combined effect of (a) dust attenuation, that obscures more the inner than the outer regions of inclined galaxies, (b) the intrinsic differences between radial and vertical variations, and (c) the difficulty to deproject the observed properties. For instance, disk-galaxies with prominent bulges, bars or thick disks would present strong vertical variations that should not be assigned to radial differences (e.g. Levy et al. 2018). Although these galaxies are very important laboratories for the exploration of some particular and relevant galactic processes, like outflows (e.g. López-Cobá et al. 2019), they are not suitable to provide representative properties of galaxies in general (e.g. Ibarra-Medel et al. 2019).

(vi) The field-of-view (FoV) covered by the IFS data should have a diameter of at least 25″. This requirement is introduced to have a good sampling of the radial properties of the galaxies. Considering that the PSF FWHM of the collected data range between ≈1″ (AMUSING data), and 2.5″ (the rest of the IFS-GS), and that we have imposed that galaxies are sampled at least up to 2.5 R_e, with an R_e of at least 2 times the PSF FWHM, the current requirement guarantees that we have between 5 and 10 resolution elements to explore the radial distributions. Below this number we consider that the derived gradients would not be very reliable.

This *well resolved* sub-sample contains almost 1,500 galaxies. In this review we sometimes adopt the full dataset, sometimes the *well resolved* one, depending on which is more appropriate. We clearly indicate which sample is used to derive each result.

Figure 1 shows the main properties of the compiled sample of galaxies, including the morphological distribution against stellar mass, $B-R$ color, effective radius and the ratio between velocity and velocity dispersion (within one R_e). In general the compiled sample resembles, in the observed distribution of these properties, what would be observed for a volume complete sample in a similar redshift range. For comparison purposes we have included in Figure 1, when feasible, the locus of the galaxy sample by Nair & Abraham (2010) from SDSS DR4 (Abazajian et al. 2009) at a redshift range similar to ours. Our compilation is dominated by late-type galaxies (≈70%), with a clear peak at Sb/Sbc, and a decline towards earlier types, in particular concerning elliptical galaxies. As expected, there is an increase of the average stellar mass from late- to early-types, from $\approx 10^{8.5} M_\odot$ (Sd) to $\approx 10^{11.5} M_\odot$ (E). This mild trend is smooth, and for each particular morphological bin a considerable range of stellar masses is covered. The main difference with respect to the SDSS distribution is an under-representation of Sab galaxies and an over-representation of Sc/Sd galaxies.

However, despite these differences, the overall trend between morphology and stellar mass is very similar. Both in Sánchez (2020) and the current exploration we try to separate the effects of stellar mass and morphology dividing galaxies in mass/morphology bins. However, it is worth noticing that in this type of segregation there are intrinsic biases. In particular, groups of early-type galaxies (E/S0) and low stellar mass ($<10^{9.5} M_\odot$) and late-type galaxies (Sc/Sd) and high stellar mass ($>10^{11} M_\odot$) have so few galaxies that the results are not statistically robust. Although we have included (and discussed) these bins in the present publication, we advise the reader to treat the results obtained for these bins with due caution.

A trend similar to the one observed between morphology and mass is observed between $B-R$ color and mass (e.g. Balogh et al. 2004). Early-type galaxies are red, covering a very narrow range of colors (i.e., defining a clear red sequence at $B-R$ ≈1.2 mag). Later-type galaxies have bluer colors, covering a wider range of colors (i.e., a cloud rather than a sequence). The most relevant difference between the two groups is that there is a deficit of blue/early-type galaxies (E/S0, $B-R$ <0.5 mag) and a corresponding deficit of red/late-type galaxies (Sc/Sd, $B-R$ >0.8 mag). Again, this distribution resembles what would be observed in a volume limited sample at a similar cosmological distance.

Regarding the sizes of the galaxies, characterized by the effective radius (R_e), there is also a relation with morphology. However, this seems to be a secondary correlation arising because of the well known relation of R_e with stellar mass (e.g. Conselice 2006, 2012; Sánchez 2020, Figure 20). However, this trend is more shallow than the one with M_*. On average, early-type galaxies are slightly larger and cover a wider size range than late-

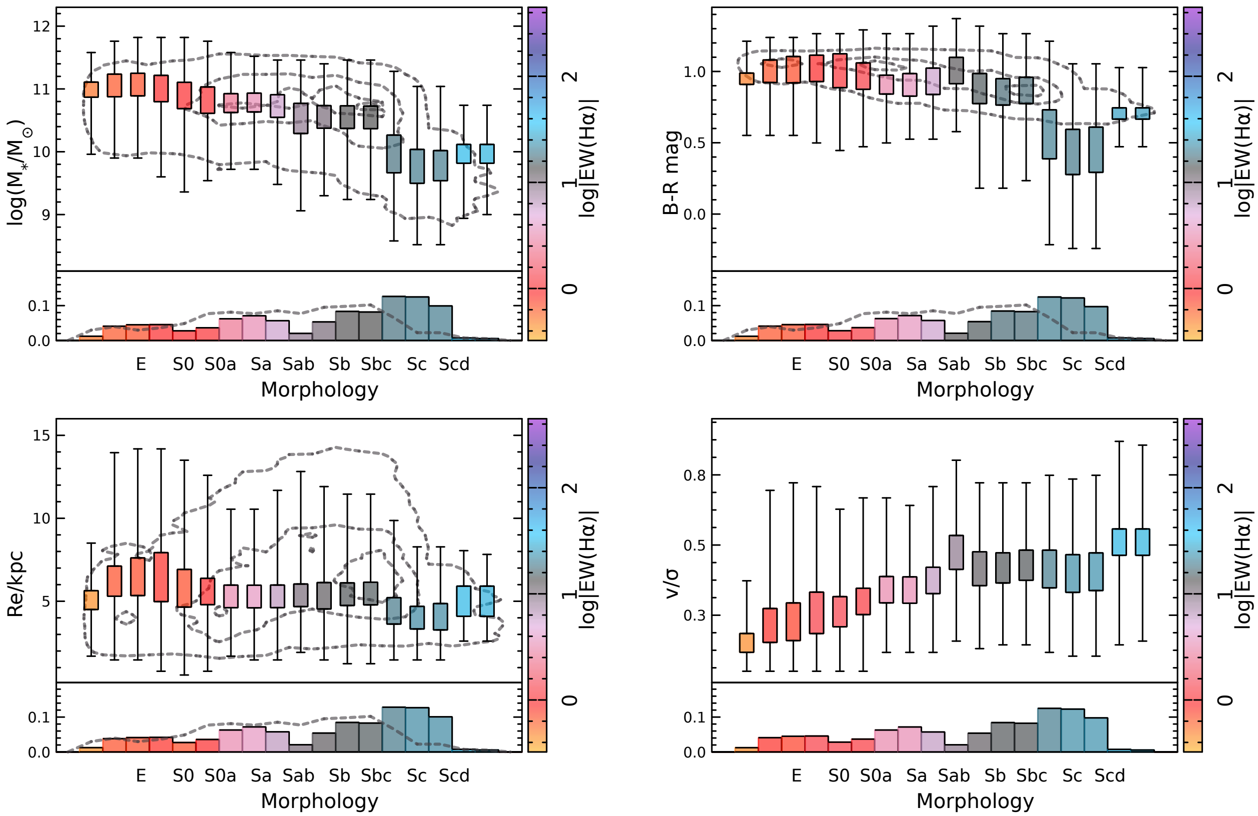

Fig. 1. Distribution of stellar masses (top-left panel), $B-R$ color (top-right panel), effective radius (bottom-left panel) and v/σ ratio within one effective radius (bottom-right panel) versus the morphological type for the full sample of galaxies. Symbols have the same meaning in each panel. Boxes are located at the average value for each morphology bin, with the size in the y-axis corresponding to the standard deviation around this value. Colors represent the mean value of the EW(Hα) of the galaxies, and error bars indicate the range of values covered by 98% of the sample, in each bin and for each of the explored parameters. In addition, for the first three panels, we include, as grey-dashed contours, the density distribution reported by Nair & Abraham (2010) for a sub-sample of the galaxies in the SDSS survey, located at a similar redshift range. The color figure can be viewed online.

type galaxis. This trend has a large dispersion and, for a given morphology, galaxies present a wide range of sizes, although in general there is a lack of spiral galaxies larger than R_e >10 kpc (for galaxies later than Sb). This figure shows that size is primarily dependent on galaxy mass, rather than morphology. When comparing with the literature results, there are clear differences. The data of Nair & Abraham (2010) show a sharper increase in size from Scd to Sab galaxies, with a drop for earlier type galaxies. This distribution is not expected naively, and could be related to a size bias in that sample rather than a real effect. In any case, the average values are not very different between the two samples.

Finally, we present the distribution of the ratio between stellar rotation velocity and velocity dispersion within one R_e over morphology. This ratio is a proxy for the fraction of ordered rotation in these galaxies (e.g. Cappellari 2016). Large values correspond to galaxies with stars following well ordered orbits distributed in a plane or disk, i.e., cold, rotationally supported orbits. On the contrary, low values correspond to galaxies with stars on hot/warm orbits (pressure supported), with a triaxial structure, including galaxies with strong bulges (e.g. Zhu et al. 2018). As expected, early-type galaxies present the lowest values for the v/σ ratio, with a mode ≈0.1 and a deficit of galaxies with v/σ >0.5 for pure ellipticals. On the other hand, late-type galaxies present the largest values, with a mode ≈0.5 (for Sc/Sd) galaxies. It is interesting to highlight that the range of values covered by this parameter for late-type galaxies is also wider, which is a consequence of projection effects. Like in the case of the previous figures, the observed distribution for the compiled sample agrees with the expected one for galaxies in the nearby Universe (e.g. Davies et al. 1983).

The symbols in the panels of Figure 1 are color-coded by the average distribution of the equivalent width (EW) of the Hα emission line. As extensively discussed in different studies (e.g. Stasińska et al. 2008; Cid Fernandes et al. 2010; Sánchez et al. 2018) and reviewed in Sánchez (2020), this parameter segregates well between star-forming and retired galaxies (SFGs/RGs). It separates equally well between star-forming and retired areas (SFAs/RAs) within galaxies (e.g. Cano-Díaz et al. 2019). The distributions shown in Figure 1 illustrate clearly the connection between the different global properties and the star-formation activity of galaxies. Early-type, massive, red, large and pressure supported galaxies are mostly RGs, with little or no star-formation. On the contrary, late-type, less massive, bluer, smaller and rotationally supported galaxies are mostly SFGs. Thus, those are the galaxies that contribute most to the star formation budget in the nearby universe. There are clear, continuous trends from SFGs to RGs, just as from late to early type galaxies, with most galaxies in the transition region between the two groups corresponding to early spirals (Sa/Sb), i.e. spirals with prominent bulges.

In summary, the compiled sample of galaxies covers the space of explored parameters just as well as a well-defined, statistically significant sample at the same cosmological distance. In general, the distributions are similar to those reported for this kind of samples (e.g. Blanton & Moustakas 2009). Therefore, although our sample was assembled in an ill-defined manner, the properties and results extracted from its analysis can be considered a good representation of the average population of galaxies in the nearby Universe (i.e. within a few hundred Mpc).

3. ANALYSIS

To provide a homogeneous analysis of this somewhat heterogeneous dataset we analysed all cubes using the same tool, the Pipe3D pipeline (Sánchez et al. 2016a). This pipeline was designed for IFS datacubes to (i) fit the stellar continuum with spectra from stellar population models and (ii) extract the information about the emission lines of ionized gas. Pipe3D uses FIT3D algorithms as basic fitting routines (Sánchez et al. 2016b)[3]. We include here a brief description of the fitting procedure (extensively described in Sánchez et al. 2016b,a), and a more detailed description of how the different parameters used in this review (and in Sánchez 2020) were derived.

3.1. *Stellar Population Analysis*

The fitting of the stellar continuum requires a minimum signal-to-noise ratio (S/N) to provide reliable results. Since it is not guaranteed that this S/N is reached throughout the entire FoV (or optical extent of the galaxy), as a first step, a spatial binning is performed in each datacube to increase the S/N above this limit by co-adding adjacent spectra. This limit was selected to be 50 for most of the compiled data (CALIFA, MaNGA and AMUSING++), and 20 for the SAMI data (which have slightly lower S/N in the continuum). The actual value of this S/N limit was derived based on simulations for the spectral resolutions and wavelength ranges covered by the data (Sánchez et al. 2016b).

Then, the stellar continuum of the co-added spectra corresponding to each spatial bin was fitted with a stellar population model, taking into account a model for the line-of-sight velocity distribution (LOSVD), and the dust attenuation. The stellar population model consists of a linear combination of a set of simple stellar populations (SSP) taken from a particular library. Therefore, the model spectrum is described by the following equation:

$$\begin{aligned} &S_{obs}(\lambda) \approx S_{mod}(\lambda) = \\ &\left[\Sigma_{ssp} w_{ssp} S_{ssp}(\lambda)\right] 10^{-0.4\ A_V\ E(\lambda)} * G(v,\sigma), \end{aligned} \quad (1)$$

where $S_{obs}(\lambda)$ is the observed intensity of the spectrum at the wavelength λ for a particular bin; $S_{mod}(\lambda)$ is the overall model, which is derived by minimizing the difference with respect to $S_{obs}(\lambda)$ (by means of χ^2 minimization); w_{ssp} is the normalization of each contributing model SSP spectrum $S_{ssp}(\lambda)$; A_V is the dust attenuation in the V-band (in magnitudes), and $E(\lambda)$ is the adopted extinction curve (in this particular case Cardelli et al. 1989). This unbroadened model spectrum is convolved with the LOSVD, $G(v,\sigma)$, modelled by a Gaussian function of two parameters (the velocity, v, and velocity dispersion, σ). Thus, the best fitting model comprises three non-linear parameters (A_v, v and σ), and a set of linear parameters, w_{ssp}, one for each SSP in the considered library. Note that equation 1 assumes that the kinematics of all stars is described with a single LOSVD, and that they are all affected by a single dust attenuation. These are simplifications of the problem. Young and old stars are known to follow different orbits within galaxies, and they may be affected by different dust attenuation. Experiments with more complex decomposition procedures are described in Vale Asari et al. (2016).

Each SSP in the library is represented by a single spectrum, which is the result of co-adding all the spectra of the surviving stars (i.e., considering the mass-loss with time, e.g. Courteau et al. 2014) created by a single burst that happened a certain time in the past (i.e. the age of the SSP) from gas with a certain chemical composition (i.e. a certain metallicity). SSPs are created by stellar population synthesis codes (e.g. Bruzual & Charlot 2003), using as basic ingredients: (i) an initial mass function (IMF) of stars (e.g. Salpeter 1955; Chabrier 2003); (ii) a model for the evolution of the stars, described by isochrones in the Hertzsprung-Russell diagram; and (iii) a synthetic (e.g. Coelho et al. 2007; Maraston et al. 2010)

[3] http://www.astroscu.unam.mx/~sfsanchez/FIT3D/.

or observational (Sánchez-Blázquez et al. 2006) stellar library of spectra for each star with a particular set of physical parameters (i.e. at each location within the HR diagram and for each metallicity). The different ingredients included in the generation of the SSP, and differences in the model algorithms, produce subtle differences in the synthetic stellar population spectra for the same physical parameters. Therefore, any inversion method/stellar decomposition like the one described before (equation 1) may produce different quantitative results depending on the adopted SSP library. The limitations of this method have been described in more detail elsewhere (Walcher et al. 2011; Conroy 2013).

The adopted implementation of Pipe3D uses the GSD156 SSP-library. This library, first described in Cid Fernandes et al. (2013), comprises 156 SSP templates, that sample 39 ages (1 Myr to 14 Gyr, on an almost logarithmic scale), and 4 different metallicities ($Z/Z_{\odot}$=0.2, 0.4, 1, and 1.5), adopting the Salpeter IMF (Salpeter 1955). It is assumed that the number of stars in each selected resolution element (typically $\approx$1 kpc) is large enough ($\gtrsim 10^4 M_{\odot}$) to have a complete statistical coverage of the IMF [4]. These templates have been extensively used in previous studies (e.g. Pérez et al. 2013a; González Delgado et al. 2014; Ibarra-Medel et al. 2016; Sánchez et al. 2018, 2019a).

We should stress that this particular library is not a priori better than others adopted to derive the properties of the stellar populations. Detailed comparisons and simulations presented in different studies (e.g. Cid Fernandes et al. 2014; González Delgado et al. 2014; Sánchez et al. 2016b,a; González Delgado et al. 2016), demonstrate that, as long as the space of parameters is fairly covered (mostly expected ages and metallicities), the explored quantities are well recovered and/or the values are consistent at least qualitatively when using different SSP templates. The main reason why the GSD156 library is best placed for the current study is because it is the only one used to explore in common the different datasets comprised in this study and, at the same time, has been confronted against mock IFS observations of galaxies created from hydrodynamical simulations (Ibarra-Medel et al. 2019). Therefore we understand better the systematics associated with the derivation of parameters than with other SSP templates.

Once the best model for the stellar population in each bin was derived, the model was adapted for each spaxel. This was done by re-scaling the model spectrum in each bin to the continuum flux intensity at the considered spaxel, as described in Cid Fernandes et al. (2013) and Sánchez et al. (2016b) (we say that the model is *"dezonified"*). Finally, based on the results of the fitting, it is possible to derive different physical quantities in each parameter P, both light-weighted (LW) and mass-weighted (MW), using the formulae:

$$\log P_{LW} = \frac{\Sigma_{ssp} w_{ssp} \log P_{ssp}}{\Sigma_{ssp} w_{ssp}}, \quad (2)$$

and

$$\log P_{MW} = \frac{\Sigma_{ssp} w_{ssp} M/L_{ssp} \log P_{ssp}}{\Sigma_{ssp} w_{ssp} M/L_{ssp}}, \quad (3)$$

where: (i) P is the considered parameter, (ii) w_{ssp} are the light weights (normalizations) described in equation 1, and (iii) M/L_{ssp} is the mass-to-light ratio of the SSP. The parameters can be derived both in a spatially resolved way (spaxel-by-spaxel or bin-by-bin) or integrated (on coadded spectra or averaged across the FoV). These equations are also used in Sánchez (2020) and the current review to obtain further quantities of interest. Among them the most relevant are: (i) the average light-weighted mass-to-light ratio (M/L), obtained by substituting P by M/L_{ssp} in equation 2; (ii) the stellar mass surface density (Σ_*), by multiplying the average M/L derived before by the surface brightness (μ), i.e.:

$$\Sigma_* = \mu M/L, \\ \mu = \frac{4\pi D_L^2 I_{obs,V}}{A_{spax}} 10^{0.4 A_{V,*}}, \quad (4)$$

where D_L is the luminosity distance and A_{spax} is the area of each spaxel (in the corresponding units, pc^2 in the present review). By integration over the FoV it is possible to derive the integrated stellar Mass (M$_*$); (iii) in a similar way, if instead of co-adding all the ages included in the SSP library, both quantities are added from the beginning of star formation in the universe up to a certain look-back time (and with additional corrections for the mass-loss), it is possible to derive $M_{*,t}$ and $\Sigma_{*,t}$ at a certain look-back time (t). $M_{*,t}$ and $\Sigma_{*,t}$ are the mass (density) assembly histories (MAH) of a galaxy (or a region in a galaxy: Pérez et al. 2013a; Ibarra-Medel et al. 2016); (iv) the derivative of this MAH over time is the star formation history (SFH), which is the star formation rate as a function of time (SFR(t)). $SFR(t)$ is indeed defined as

$$\mathrm{SFR}(t) = \frac{dM_{*,t}}{dt} \approx \frac{\Delta M_{*,t}}{\Delta t} \equiv \frac{M_{*,t_1} - M_{*,t_0}}{|t_1 - t_0|}, \quad (5)$$

where t_1 and t_0 are two look-back times (where $t_1 < t_0$ and $t_0 - t_l$ is relatively small). This way it is possible to estimate the most recent SFR from the stellar population analysis, usually defined as SFR$_{ssp}$ =SFR$_{32\mathrm{Myr}}$

[4] Note that for smaller apertures or very low surface brightness galaxies, this may not be the case.

(González Delgado et al. 2016) (although other time ranges, in general below 100 Myr, are considered too)[5]; (v) the LW and MW Age ($Age_{LW|MW}$) and metallicity ($[Z/H]_{LW|MW}$), derived substituting P by the age and metallicity of each SSP included in the library (i.e., Age_{ssp} and $[Z/H]_{ssp}$), either adding over all ages (i.e., the current LW and MW ages and metallicities) or up to an age corresponding to a certain look-back time, t ($Age_{LW|MW,t}$ and $[Z/H]_{LW|MW,t}$). In this way it is possible to derive the chemical enrichment history of a galaxy (or a region within a galaxy) by exploring $[Z/H]_{LW,MW,t}$ over time (e.g. Vale Asari et al. 2009; Walcher et al. 2015; González Delgado et al. 2016). Errors in the different parameters are derived based on the uncertainties in the individual analyzed spectra propagated through a Monte-Carlo procedure included in the FIT3D code.

3.2. *Analysis of the Ionized Gas*

In conjunction with the analysis of the stellar population we explore the properties of the ionized gas (both resolved and integrated) by deriving a set of emission line parameters, including the flux intensity, equivalent width and kinematic properties. To that end, we create a cube that contains just the information from these emission lines by subtracting the best fitting stellar population model, spaxel-by-spaxel, from the original cube. This *gas-pure* cube inherits a variance vector from the original cube which is made from two components: the original noise associated with the observations and the standard deviation of the residuals obtained from a Monte Carlo run of the continuum fitting with stellar population models. Finally, the parameters for each individual emission line within each spectrum at each spaxel of this cube are extracted using a weighted momentum analysis as described in Sánchez et al. (2016a). More than 50 emission lines are included in the analysis in the case of the CALIFA, MaNGA and SAMI datasets, and around 20 lines in the case of MUSE. Among them we include the strongest emission lines within the optical wavelength range: Hα, Hβ, [O II] λ3727[6], [O III] λ4959, [O III] λ5007, [N II] λ6548, [N II] λ6583, [S II]λ6717 and [S II]λ6731. The final product of this analysis is a set of maps showing the spatial distributions of the emission line flux intensities and equivalent widths. Integrated (or averaged) quantities across the optical extent of galaxies (or across the FoV of the instrument) are then easily derived.

Finally, as in the case of the stellar mass, we derive the spatial distribution of different physical quantities used in the present review (and throughout Sánchez 2020): (i) The attenuation of ionized gas emission (A_V), derived from the spatial distribution of the Hα/Hβ ratio. We adopt the canonical value of 2.86 (Osterbrock 1989) for the non-attenuated ratio and use a Milky Way-like extinction law (Cardelli et al. 1989) with R_V=3.1. (ii) The SFR, both resolved (i.e. the SFR surface density, Σ_{SFR}) and integrated, is derived from the Hα dust-corrected luminosity (and surface brightness), following a prescription described by Catalán-Torrecilla et al. (2015). To calculate the attenuation-corrected Hα luminosity $L_{H\alpha}$ we use a formula similar to equation 4, substituting the Hα intensity for I_{obs}, and the gas attenuation, i.e. A_V as defined before, for $A_{V,*}$. We then use the relation derived by Kennicutt et al. (1989), SFR= 8 10^{42} $L_{H\alpha}$, but apply it to each spaxel. Consistency tests of the SFR derived using Hα and the stellar population analysis can be found in the literature (e.g. González Delgado et al. 2016; Sánchez et al. 2019b). (iii) The molecular gas mass (M_{gas}), and its resolved version, the molecular gas mass surface density (Σ_{gas}), is derived from both the dust-to-gas calibrator described by Barrera-Ballesteros et al. (2020), defined as $\Sigma_{gas} = 23A_V$, and an updated calibration with the functional form $\Sigma_{gas} = a\ A_V^b$, presented in Barrera-Ballesteros et al. (2021). We will refer to the latter as Σ'_{gas} hereafter. (iv) The oxygen abundance, 12+log(O/H), is derived from strong emission line calibrators, using those spaxels compatible with ionization related to star-formation (i.e. young, massive OB stars). To select those spaxels we follow the prescriptions described in § 4.3. A list of possible calibrations was included in Sánchez et al. (2019b). However, for the present contribution, we limited ourselves to the O3N2 calibrator by Marino et al. (2013).

Based on these primary parameters, we can also derive some additional parameters discussed within this review: (i) Star-formation efficiency, defined as the ratio between the SFR and M_{gas} (or between Σ_{SFR} and Σ_{gas}, for their spatially resolved version). This parameter is just the inverse of the depletion time ($\tau_{dep} \equiv \frac{1}{SFE}$). (ii) The specific star-formation rate (sSFR), defined as the ratio between SFR and M_* (or between Σ_{SFR} and Σ_*, for their spatially resolved version).

All the physical parameters derived from emission lines are not directly calculated by Pipe3D, although they are part of a post-processing analysis that is performed by the same algorithms for the different datasets. Finally, we should strongly stress that Pipe3D is just one of several different pipelines/tools developed in the last years with the goal of analysing IFS data (e.g., PyCASSO, LZIFU, MaNGA DAP de Amorim et al. 2017; Ho et al. 2016; Belfiore et al. 2019). Most of the performed compar-

[5] A more recent one could be derived using the Hα dust corrected luminosity, that would correspond to <10 Myr.

[6] Not covered by MUSE data at the considered redshift.

isons demonstrate a remarkable agreement in the results (Sánchez et al. 2016a; Belfiore et al. 2019; Sánchez et al. 2019b).

4. IONIZING SOURCES IN GALAXIES

Star forming galaxies (SFGs) and star forming areas within galaxies (SFAs) are frequently identified based on the observational properties of the ionized gas. In our current understanding of the star-formation process when a molecular gas cloud reaches the conditions of the Jeans instability (Jeans 1902; Bonnor 1957) it fragments and collapses, eventually igniting star formation activity (Low & Lynden-Bell 1976; Truelove et al. 1997). This process creates thousands of stars at the typical scale of a molecular cloud, in general. These stars are not equally distributed in mass: as expected from a fragmented cloud (Bate & Bonnell 2005), there is a larger number of less massive stars than of more massive ones (Salpeter 1955; Chabrier 2003). These massive, short-lived, young stars (classified spectroscopically as O and B stars) have a blue spectrum, with a significant contribution of photons below the limit required to ionize not only hydrogen (E >13.6 eV, λ <912Å), but also other, heavier elements, in particular oxygen, nitrogen and sulfur. Therefore, they ionize the gas distributed around the recently formed stellar cluster, producing a large number of emission lines observed in the optical spectrum. These emission lines arise due to the recombination of ions with electrons, and the subsequent cascade of lines as the electron drops onto low energy levels, or by the radiative de-excitation of electrons on levels previously excited by collisions between ions and electrons (e.g. Osterbrock 1989). These ionized gas clouds are the classical H II regions (e.g. Sharpless 1959; Peimbert 1967).

The ratios between emission lines originating from ionized metals and those from hydrogen depend on the physical conditions inside the nebulae. In general, classical H II regions show typical values for certain line ratios (like [O II]/Hβ, [O III]/Hβ, [O I]/Hα, [N II]/Hα and [S II]/Hα): (i) <1 dex in the case of [O III]/Hb; (ii) < −0.1 dex, in the case of [N II]/Hb and [S II]/Hα; and (iii) < −1 dex, in the case of [O I]/Ha (e.g. Osterbrock 1989). The reason for these relatively low values is the shape of the ionizing spectra, that, although hard enough to cause some ionization, are not hard enough to provide enough high energy photons to strongly ionize heavy elements like oxygen or nitrogen. These ratios are then further modulated by the oxygen and nitrogen abundances, the ionization parameter (the ratio between the available ionizing photons and the hydrogen content), the electron density, dust content and even the geometry of the nebulae with respect to the ionizing source (e.g. Baldwin et al. 1981a; Evans & Dopita 1985; Dopita & Evans 1986; Veilleux & Osterbrock 1987; Veilleux et al. 1995; Dopita et al. 2000; Kewley et al. 2001; Kewley & Dopita 2002; Sánchez et al. 2015; Morisset et al. 2016).

However, young stars resulting from recent SF are not the only ionizing sources in galaxies (although they are in general the dominant one). Other sources, in order of importance (strength and frequency) are: (i) The hard and intense ionizing spectra associated with non-thermal and thermal emission of active galactic nuclei, which are observed in a limited fraction of galaxies. This ionization is particularly important in the central regions of galaxies, and for those galaxies in the AGN phase (≈10% of galaxies in the nearby Universe, or even less, e.g. Schawinski et al. 2010; Lacerda et al. 2020, although their relative importance increases at high-z). (ii) The hard but weak ionizing radiation from hot evolved stars (HOLMES, post-AGB stars Binette et al. 1994; Flores-Fajardo et al. 2011), that could significantly contribute to the excitation of the so-called diffuse ionized gas in galaxies (DIG, e.g. Singh et al. 2013a; Lacerda et al. 2018). (iii) Shocks associated with galactic winds, either induced by high-velocity galactic-scale winds due to the kinetic energy introduced by central starbursts (e.g. Heckman et al. 1990) or AGN, or low-velocity winds associated with gas cooling processes or internal movements in triaxial galaxies (Dopita et al. 1996). This ionization may also contribute significantly to the DIG. (iv) Supernova remnants, associated with past (but relatively recent, <100 Myr) SF processes, also present an expanding shock wave, but with very different geometry than the previous ones. Similar in shape to H II regions, and frequently misclassified or mixed with them, they could explain a fraction of the nitrogen enhanced regions described in the literature (Ho et al. 1997; Sánchez et al. 2012b, Cid Fernandes et al., submitted). In general, all those ionizing sources have harder ionizing spectra than the ones observed in H II regions. Therefore, they emit a relatively larger fraction of their flux in high energy photons and thus produce larger values for the line ratios described above.

When using emission lines as diagnostics of the ionized ISM, it is important to keep in mind a second concept, which we will call the "ionization conditions" in the remainder of this review. Indeed, it is customary to subsume all gas that does not reside in a spatial region clearly associated with star formation (i.e. H II regions) or clearly associated with AGN (narrow line regions NLR) into the diffuse ionized gas (DIG). The DIG is, in general, all emission that has no clear peaky structure, but has a rather smooth surface brightness distribution. DIG may still show structure (filaments, spiral arms), but to a lesser degree than is typical for H II regions.

A clear-cut case where the ionization source has to be distinguished from the ionization conditions is the leaking of ionizing photons from H II regions. Indeed, these photons may show a somewhat harder ionizing spectrum than the original source (hot, massive stars e.g. Weilbacher et al. 2018), and therefore show a much wider range of line ratios than the H II regions directly associated with the ionizing source. As we will see later, in galaxies that are primarily ionized by SF, leaked photons can contribute significantly to the DIG.

The physical differences between the possible ionizing sources listed before (mostly the hardness of their spectra), and the ionized gas (mostly their metal content) have been used to define demarcation lines in diagrams comparing pairs of metallic to hydrogen line ratios, with the intent of distinguishing between ionizing sources directly. These are the so-called diagnostic diagrams (e.g. Baldwin et al. 1981a; Osterbrock 1989; Veilleux et al. 2001). This concept is quite successful to identify gas ionized by star forming regions, which shows a nearly one-to-one correspondence between the location of the spatial regions within the diagnostic diagrams and the ionizing source (e.g. Kewley et al. 2001). Unfortunately, the distinction among the different physical processes in the second group is less clear (e.g. Cid Fernandes et al. 2010). Some of the complication arises because of the mixing between different ionizing sources. This is particularly important for those ionizing sources that contribute to the DIG, where shocks, the contribution of ionization by old stars, and even photons leaked from H II regions could be spatially co-existing (e.g. Della Bruna et al. 2020). We will try to shed some light on this complex problem in the next section.

4.1. *Complexity and Myths of Diagnostic Diagrams*

Figure 2 shows the distribution of galaxies in three of the most frequently adopted diagnostic diagrams (Veilleux et al. 1995). The left panels show the distributions for the central regions of galaxies, corresponding to $\approx$ 1 kpc at the average redshift of our compilation ($3'' \times 3''$ aperture). This region corresponds to the one most affected by any ionization associated with an AGN, a shock induced by a central outflow, or ionization due to hot evolved stars (more frequently present in the bulge of galaxies, the so-called cLIERs, e.g. Belfiore et al. 2017a). The right panels present similar distributions for a ring at one effective radius of each galaxy. This region is far enough from the center to be clearly less affected by central ionizing sources, and therefore the ionization is more related to H II regions in the case of SFGs. In all these plots each galaxy contributes as a single point in the considered distributions. The distributions are color-coded by the average value of EW(Hα) for all the galaxies at a particular locus within the diagram. As indicated before, several studies have demonstrated that the EW(Hα), in combination with the described line ratios, is a good discriminator between ionization conditions: (i) AGN and high-velocity shocks show in general high values of the EW(Hα), >6Å (e.g. Stasińska et al. 2008; Cid Fernandes et al. 2010). (ii) HOLMES/post-AGBs and low-velocity shocks show in general low values of the EW(Hα), <3Å (e.g. Binette et al. 1994; Sarzi et al. 2010; Lacerda et al. 2018; López-Cobá et al. 2020). (iii) Weak AGN could show EW values between 3-6Å (e.g. Cid Fernandes et al. 2010), and sometimes even lower (for very weak ones). It is important to note here that H II regions are expected to show a high value of the EW(Hα) too. In our sample they show values larger than 6Å (e.g., Sánchez et al. 2014; Lacerda et al. 2018; Espinosa-Ponce et al. 2020). However, they are located in a different region in the diagnostic diagrams, as indicated before.

The described trends can also be seen in the average distributions shown in the top panels of both right and left figures. Ionized regions with high EW are mostly located in the left part of the diagrams, i.e., at the classical location of H II regions. On the other hand, ionized regions with low EW are found in the right parts of the three diagrams. We will show in upcoming sections that indeed low EW is in general associated with DIG. Such regions are more numerous in the left panels (central regions of galaxies) than at one R_e.

There are a few galaxies with high EW regions in the upper right area of the diagram. They are clearly less numerous than the low EW ones and therefore do not show up well in our representation. Their influence can, however, be seen in the three diagrams in the last row on the left. A comparison with the three panels on the right in the same row also shows that they are more numerous in the center than at one R_e. Those correspond to either strong AGN ionization or the contribution of shocks created by high velocity galactic outflows (e.g. Bland-Hawthorn 1995; Veilleux et al. 2001; Ho et al. 2014; López-Cobá et al. 2019, 2020).

As mentioned before, based on the described average distributions, different demarcation lines have been proposed in these diagrams to separate between the different ionizing sources. The most popular ones are the Kauffmann et al. (2003) (K03) and Kewley et al. (2001) (K01) curves (included in Figure 2 as a dashed and a solid line). They are usually invoked to distinguish between star-forming regions (below the K03 curve) and AGN (above the K01 curve). The location between both curves is generally assigned to a mixture of different sources of ionization, being refereed to as the *composite* region (e.g. Cid Fernandes et al. 2010; Davies et al. 2016). However,

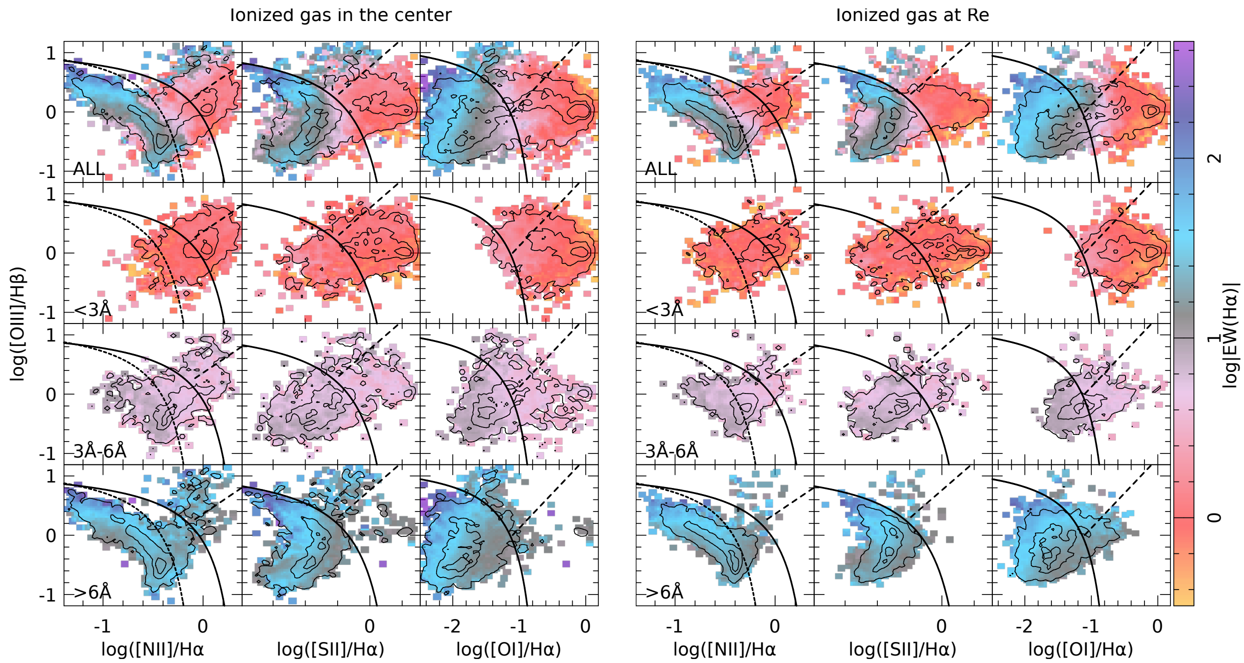

Fig. 2. *Left panels*: Diagnostic diagrams for ionized gas built from the central (≈ 3″ diameter) apertures of the galaxies in the sample, including the distributions of the [O III/Hβ] vs. [N II]/Hα line ratio (left panel), [O III/Hβ] vs. [S II]/Hα (central panel), and [O III/Hβ] vs. [O I]/Hα (right panel). Each galaxy contributes a single point in the distributions, which in turn are shown as contours representing the density of objects. Each contour encompasses 95%, 50% and 10% of the points, respectively. The color code shows the average EW(Hα), on a logarithmic scale, of all galaxies at each point in the diagrams. In all panels the solid line represents the locus of the Kewley et al. (2001) boundary lines, with the proposed separation between Seyferts and LINERs indicated with a dashed-line. Finally, in the left-most diagram the dotted-line represents the locus of the Kauffmann et al. (2003) demarcation line. The upper panels show the distributions for all galaxies, irrespective of their EW(Hα) values. Then, from top to bottom, galaxies are separated by EW(Hα), comprising low values (<3Å, panels in the 2nd row), intermediate values (3-6Å, panels in the 3rd row), and high values (>6Å, bottom-panels). *Right panels:* Similar plots for the average ionized gas at the effective radius in each galaxy. The color figure can be viewed online.

as we will discuss later, this is only one of multiple possibilities to populate that area of the diagnostic diagrams. The demarcations lines have a very different origin. The K03 line is a purely empirical boundary traced by hand as an envelope of the star-forming galaxies detected in the SDSS spectroscopic survey. The second demarcation line was derived based on a set of photo-ionization models, as the envelope of the largest values for the considered line ratios that can be produced by ionization due to young stars and a continuous star formation (similar curves were derived by Dopita et al. 2000; Stasińska et al. 2006, using other photoionization models and star-formation histories). In essence, only these latter demarcation lines are physically driven, indicating which region of the diagrams cannot be populated by ionization due to star-formation.

A first exploration of the distributions shown in Figure 2 seems to demonstrate that the proposed demarcation lines do a good job of segregating at least the harder (AGN, shocks, post-AGBs) from the softer (H II) ionization. When exploring the upper panels in both figures it seems that all H II regions (high-EW, left-size) are well constrained by the K03 demarcation line, while most of the hard ionized regions are above the K01 one. This seems to be particularly true for AGN, which correspond to the hard ionized regions (upper right in each diagram) in the bottom panels (i.e., with high EWs).

However, while it is certainly true that low spatial resolution or single aperture data may mix different spatial components of galaxies with different ionization mechanisms, and thus may populate the region between the two demarcation lines, it is not true that only mixed ionization can be found there. A detailed inspection of the distributions segregated by the EW(Hα) clearly demonstrates so. High EW regions with mixed ionization could only result from the mixing of H II and AGN/shock ionization. However, such a case could be present only in a very limited fraction of galaxies (<10% or so, at the considered redshift), and only in the central regions of galaxies (left panels). So, in general, mixed ionization resulting from a mixture of SF and DIG should be identifiable by intermediate EW values. This corresponds to the third row of panels in both figures. While a substantial fraction of spatial regions with intermediate EW are located in the intermediate region, a considerable fraction of these are well below and above the K03 and K01 curves. Thus, there are no features in the EW-augmented diagnostic diagrams that would allow to define a unique locus of mixed ionization.

Furthermore, exploring the diagrams corresponding to the high and low EWs (2nd and 4th rows), the complete continuity in the distributions over the K01 and K03 lines seems to indicate that this intermediate region is populated by a non-negligible fraction of both DIG and/or H II regions (the so-called nitrogen enhanced regions, Ho et al. 1997, that could be polluted by SNR). Thus, the region between both demarcations lines is not exclusively populated by spatial regions with a mixed ionization. Finally, an additional complication are the low EW regions well below both the K01 and the K03 demarcation line (in particular at one R_e and for K01). Some authors have even claimed that low-metallicity AGNs could also populate a region below the K01 (or the K03) line (e.g. Stasińska 2017). This indeed does not contradict the nature of the K01 line, that was defined as a maximum envelope for the H II/SF regions (which seems to be a valid interpretation), and not as a definitive boundary between soft and hard ionization (as frequently and wrongly interpreted).

In summary: (i) classifying the ionizing source based only on the distribution in the so-called diagnostic diagrams may be valid only in a statistical sense. Thus, for individual targets in boundary/intermediate regions, the use of these diagrams may lead to important mistakes; (ii) considering the additional information provided by the EW(Hα) may mitigate the mis-classifications induced by a selection based only on the loci within these diagrams; and (iii) interpreting the location in a diagram as a combination of mixing of ionizing sources may be largely misleading. However, as we will see in the next section, additional information provided by the morphology/shape of the ionized structures, the underlying stellar population, and even the kinematics of the gas may shed some further light on the ionization conditions.

4.2. *Spatial Distribution of the Ionized Gas*

In this section we explore the spatial distribution of the ionized gas and the line ratios in some prototype galaxies included in our galaxy sample. The main aim of this section is to reinforce the results highlighted in the previous section, and to demonstrate how the shape/morphology and general spatial distribution of the ionized gas may help to disentangle different ionizing sources, beyond the use of just diagnostic diagrams (and EWs). We adopted only data taken with the best spatial resolution (MUSE data), although similar conclusions could be extracted from other datasets (strongly affected by resolution effects, in some cases). Figures 3, 4 and 5 show, for each of the considered galaxies, in the top-left panel, a true color continuum image. This image is reconstructed from the datacubes by convolving the individual spectra at each spaxel with the response curve of the g, r and i-band filters. Then, the three images are combined into one, with each filter corresponding to the blue, green and red color respectively. In addition, the figure shows, in the top-middle panel, a color image created using the [O III] (blue), Hα (green) and [N II] (red) emission line maps extracted from the *gas-pure* datacube, as described in § 3.2. These two images (continuum and emission line) allow us to explore the distribution of the ionized gas structures across the optical extent of galaxies, and its association with the different morphological sub-structures (such as bulges, disks, arms, bars..). In addition to these two maps we show, for each galaxy, four different diagnostic diagrams, including the ones shown in Figure 2, and the WHAM diagram (Cid Fernandes et al. 2010), that compares the [N II] ratio with the EW(Hα). Thus, this figure takes into account the main conclusion of § 4.1 on the classification of the ionizing sources, mitigating the segregation problems by considering the EW(Hα) in addition to the classical diagnostic diagrams.

Each pixel shown in the top-middle image is mapped with the same color in the four diagnostic diagrams, clearly showing the association between the loci in those diagrams and the spatial distribution of the ionized gas. Figure 3 shows four examples of galaxies with a considerable number of H II regions, which dominate the ionization across the galaxy disk. They are seen as clumpy/peaked ionized structures, almost circular, at the spatial resolution of these data (≈0.1-0.5 kpc), as described by Sánchez-Menguiano et al. (2018). They are clearly distinguished in the emission-line maps, tracing the spiral arm structure. Furthermore, they are mostly located in the lower-left region of the diagnostic diagrams, forming an arc where the classical H II regions are found (e.g. Osterbrock 1989). They are easily identified in the four considered galaxies (MCG-01-04-025, UGC 1395, ESO 0298-28, and IC1657).

In the case of MCG-01-04-025 all the ionization seems to be produced directly by H II regions (clumpy structures), with a possible component of DIG (not clumpy, smooth distribution). In this galaxy DIG is most probably due to photon leaking from those regions, being the most frequent or dominant ionizing source for the diffuse gas in late-type spirals as reported in the literature (e.g. Zurita et al. 2000; Relaño et al. 2012). The color change in the ionized gas map for the H II regions from

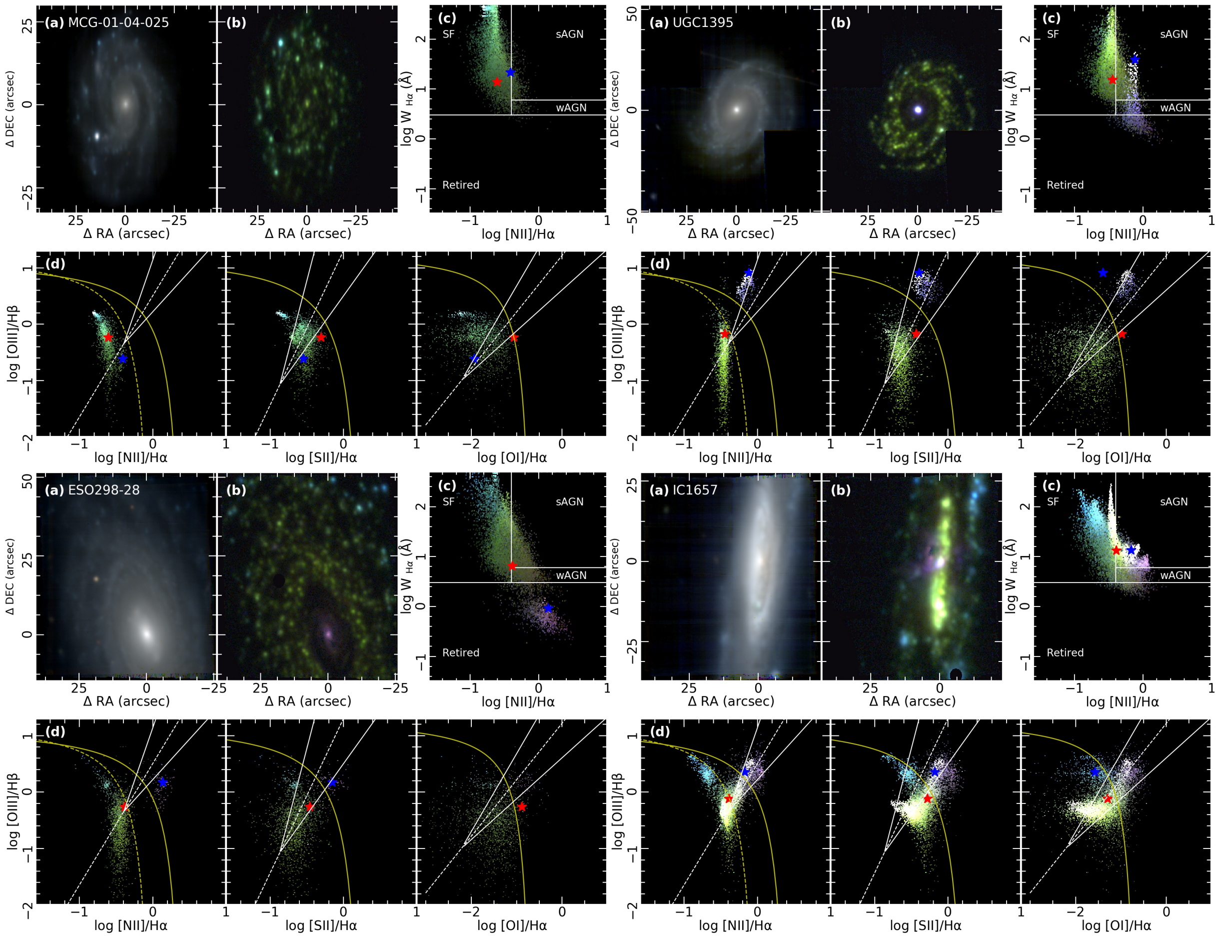

Fig. 3. Each panel shows, for different galaxies: (a) the continuum image created using g (blue),r (green) and i-band (red) images extracted from a MUSE datacube, by convolving the individual spectrum in each spaxel with the corresponding filter response curve (left-panel); (b) the emission line image created using the [O III] (blue), Hα (green) and [N II] (red) emission line maps extracted from the same datacube using the PIPE3D pipeline (central-panel); (c) the WHAN diagnostic diagram presented by Cid Fernandes et al. (2010), showing the distribution of EW(Hα) versus the [N II]/Hα line ration; and finally, (d) the classical diagnostic diagrams involving the [O III]/Hβ line ratios vs. [N II]/Hα (left), [S II]/Hα (middle) and [O I]/Hα (right), respectively (Baldwin et al. 1981b; Veilleux et al. 1995). The four diagnostic diagrams included in panels (c) and (d) are color-coded by the values shown in the emission line image shown in panel (b). The average value of the parameters shown in panels (c) and (d) across the entire FoV of the IFU data is shown as a red star in each diagnostic diagram, while the central value is marked with a blue star. The solid and dashed lines represent the location of the Kewley et al. (2001) and Kauffmann et al. (2003) demarcation lines, respectively. The name of each galaxy shown in each panel is included in the figures, comprising from top to bottom MCG-01-04-025, UGC1395, ESO0298-28 and IC1657. The color figure can be viewed online.

the center (more green) to the outer parts (blueish), reflects both the well known negative abundance gradient in these galaxies (e.g. Searle 1971; Vila-Costas & Edmunds 1992; Sánchez et al. 2014; Sánchez-Menguiano et al. 2018), and most probably a positive gradient in the ionization parameter (e.g. Sánchez et al. 2012b, 2015).

The other three galaxies show additional ionizing conditions in their central regions. In the case of UGC 1395, the almost point-like, strong and hard ionization, at the very center of the galaxy is a clear indication of the presence of an AGN. Indeed, the line ratios in this central region are located well above the K01 curve, with an EW(Hα) that in most of the cases is well above the 6Å cut proposed by Cid Fernandes et al. (2010) for strong AGN. Despite the clear presence of an AGN, we should notice that a strict cut in the EW is not fully valid for these resolved spectroscopic data. At the edge of the distribution dominated by the AGN the EW drops below 6Å and even 3Å, just because the PSF size and/or the strong radial decline expected for this kind of ionization (Singh et al. 2013b; Papaderos et al. 2013). Thus, the inclusion of the EW(Hα) helps to discriminate the nature

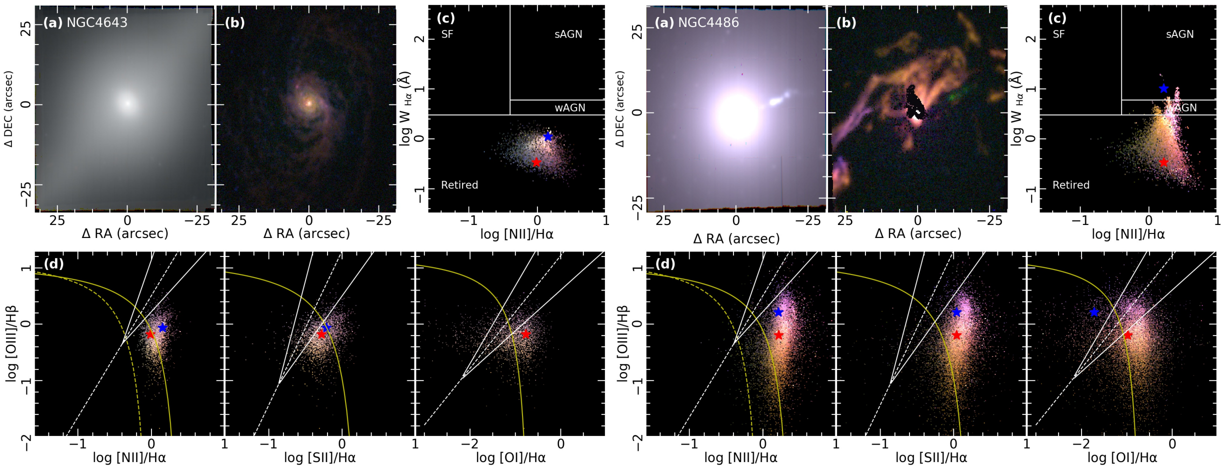

Fig. 4. Similar figure as Figure 3, for galaxies NGC4643 and NGC4486. The color figure can be viewed online.

of the ionization, but without spatial information it may provide an incomplete picture.

In the central region of the next example, ESO 0298-28, a hard ionization is clearly present as well. However, contrary to the previous case, although the line ratios are very similar, both the EW(Hα) (clearly below the 3Å cut proposed by Cid Fernandes et al. 2010, for retired galaxies) and the spatial distribution (smoother, following the stellar light distribution), indicate that the ionized gas has a completely different nature in the central regions of this galaxy. We suggest that this is a good example of diffuse ionized gas associated with ionization by hot evolved stars. Different theoretical explorations have demonstrated that those stars can produce the ionizing photons required to explain the observed ionized gas (e.g. Binette et al. 1994; Flores-Fajardo et al. 2011). The exploration of the properties of the underlying stellar population and their compatibility with the observed ionized gas properties (i.e., the fraction of young and old stars able to ionize the gas), is becoming an important tool to identify this ionizing source (Gomes et al. 2016b; Morisset et al. 2016; Espinosa-Ponce et al. 2020). Based on this kind of analysis, it is expected that these specific ionizing sources are ubiquitous in galaxies, albeit more evident in structures associated with old stellar populations (e.g. Singh et al. 2013a; Belfiore et al. 2017a). Indeed, stars in galaxies were formed mostly a long time ago (Panter et al. 2007; Pérez et al. 2013a), meaning that old stars, the progenitor population of hot evolved stars, are available everywhere. However, it is obvious that this ionization is observed most frequently in the absence of H ii regions, as its characteristic line ratios would otherwise be swamped by the more luminous ionizing sources.

Even photons leaked from H ii regions may blur the signature of ionization by hot evolved stars, that is in general very weak, with a typical EW(Hα)≈1Å (e.g. Binette et al. 1994, as indicated before). This ionization is also difficult to distinguish from a weak AGN, and in general it is not feasible to fully discard the presence of those faint central sources. However, the spatial association with the stellar continuum and the lack of a central peak (although weak) in both the flux intensity and EWs of Hα is a guidance to discard (or at least not confirm) the presence of an AGN. The selection of AGN candidates in optical spectroscopic surveys without considering the EW(Hα) is a general mistake, as discussed in detail in the literature (e.g. Cid Fernandes et al. 2010), but it is still not fully abandoned by the community.

The last galaxy shown in Figure 4, IC 1657, is a disk galaxy (Sab) that has been classified as a Seyfert-2 based on its emission line ratios (e.g. Gu et al. 2006). It shows strong X-ray emission, a hallmark of the presence of nuclear activity. However, its X-ray-to-IR properties are somewhat atypical, indicating a heavily obscured AGN (Lanz et al. 2019). The observed ionization throughout the FoV of the current data was explored in detail by López-Cobá et al. (2020). They demonstrated the presence of an outflow at galactic scales that produced shock ionization in a bi-conical structure emanating from the center of this galaxy. Figure 4 shows this structure, as a *pink* triangle (in projection), superposed on the ionization associated with H ii regions located in the heavily inclined disk of this galaxy (clumpy ionized regions, greenish and blueish). Contrary to previous claims, we consider that the presence of an AGN cannot be fully confirmed or discarded by the optical data. It is true that the central ionization is compatible with the presence of a nuclear source: it presents a hard ionization, with line ratios above the K01 curve and an EW(Hα) larger (but only marginally) than 6Å. If a single fiber observation were taken of this central region, this galaxy would be clearly classified as an AGN candidate. However, there is a lack of such ionization outside the very central region, and even this is clearly associated with the cone defining the shock ionization associated with the outflow. Elsewhere, the ionization is dominated by H II regions, as indicated before. Indeed, the line ratios in the very center are at the edge of the K01 curve (for two of the diagnostic diagrams) and below it for one of them (the one involving the [O I]/Hα ratio. Those line ratios could be a consequence of the mix between shock ionization and the underlying ionization due to young hot stars. As a matter of fact, the conclusion by López-Cobá et al. (2020) was that this galaxy hosts an outflow most probably due to strong star-formation activity in the central regions.

Independently of the final conclusion on the presence or not of an AGN, the observed line ratios across the central region are fully compatible with those usually considered as evidence of an AGN, and that would most probably be the conclusion from single aperture spectroscopic data. In reality, the ionization structure of this galaxy is far more complex, showing (i) clear evidence of strong SF activity across its entire disk and towards the very center, (ii) a conical outflow, and (iii) maybe the presence (or not) of an AGN. Lacking spatially resolved information, despite the combined use of diagnostic diagrams and EW(Hα), the description of the ionizing source would be limited and misleading.

Figure 4 presents similar plots for two more galaxies: NGC 4643 and the well known NGC 4486 (M87). The first galaxy, NGC 4643, lacks any trace of ionization associated with SF activity. No evident H II region is detected in the emission line maps, which show no greenish clumpy ionized structure as is evident in the four previously explored galaxies. NGC4643 is an S0 ring galaxy observed by MUSE as part of the TIMER survey (Gadotti et al. 2019); it was also observed within the Atlas3D survey (Cappellari et al. 2011). It has a strong bar, and there is no evidence of SF in the optical images (although there are known cases of SF in the outer regions of early-type galaxies, Gomes et al. 2016b). If there is remnant SF activity, the H II regions are not observed, implying that they would be less luminous and smaller than typical H II regions in spiral galaxies. This would imply a strong variability in the Hα luminosity function of H II regions, which so far is not observed (e.g. Bradley et al. 2006). Thus, all evidence indicates that there is no SF activity in this galaxy. Therefore, the observed ionization is most probably due to ionization by hot evolved stars: it is diffuse, following the stellar continuum, hard on average, and with low EW(Hα). However, low velocity shocks cannot be excluded (e.g., Dopita et al. 1996), although they would be more expected in the presence of weak AGN outflows or cooling flows in elliptical galaxies in cluster cores (e.g. Balmaverde et al. 2018; Roy et al. 2018b; Olivares et al. 2019; López-Cobá et al. 2020). Additionally, slow shocks are expected to show a filamentary structure and there is no reason their flux distributions should follow the stellar continuum emission (and kinematics, e.g. Kehrig et al. 2012; Lin et al. 2017; Cheung et al. 2016). Therefore, we consider this object as a clear candidate of DIG due to HOLMES or post-AGB stars. Nevertheless, not all spatial regions are located above the K01 curves in the diagnostic diagrams, although the ionization is on average clearly harder than for ionization associated with H II regions. Indeed, in the classical BPT diagram half of the observed regions are located in the so-called *intermediate* region between the K01 and K03 demarcation lines. This is a clear example of a possible misleading use of the diagnostic diagrams. Without considering the EW(Hα) this galaxy would be classified as an AGN (and in fact in the literature it has been reported as a weak AGN or LINER). Moreover, a considerable fraction of the region covered by the FoV of the IFU data would be classified as showing *mixed* ionization, suggesting the presence of clearly unobserved SF activity.

The diversity of ionization conditions observed in the previously explored galaxies can only be appropriately explored by using the diagnostic diagrams together with the spatial shape of the ionized structures. A similar situation is observed in NGC 4486 (M87). This extremely massive galaxy in the center of the Virgo-A cluster hosts a super-massive black hole without any doubt (as recently demonstrated by the Event Horizon Telescope Collaboration et al. 2019). Known to be a radio-galaxy for decades (e.g. Meisenheimer et al. 1996), it was one of the optically detected counterparts of a radio-jet (indeed, the optical emission was reported in the first decades of the 20th century, e.g. Curtis 1918). The counter-part is so strong that it is clearly seen in the continuum emission color-maps in the upper-left panel of Figure 4. It is also appreciated in the emission line maps as a series of greenish knots placed along the continuum counterpart, as already described in the literature (e.g. Jarvis 1990). More interesting to us is the filamentary emission structure observed across the north-eastern half of the MUSE FoV. This ionization was previously reported as a disky ionized gas structure based on narrow-band images by Ford et al. (1994). However, neither the shape of the ionization (filamentary, not clumpy) nor the spatial distribution (not following the shape of a disk), nor the distribution across the diagnostic diagrams, together with the distorted kinematics (López-Cobá et al. 2020), support this interpretation. The line ratios and the EW(Hα) indicate that the ionization is most probably due to either hot evolved stars or shocks of moderate velocity. However, considering the morphology, we are more inclined to suggest that this ionization is due to shocks. The nature of this gas is clearly under debate. However, recent results suggest that galaxies in the centers of clusters may present ionized gas originating from cooling flows that may be connected with cluster-wide flows (e.g., Balmaverde et al. 2018; Olivares et al. 2019). Remnants of past wet mergers may also be an alternative origin of that gas. In the particular case of M87 this inflow of gas could be the feeding mechanism of the AGN. Whatever is the ultimate origin of the gas, it is clear that the presence of the AGN is not easily uncovered by the optical line ratios, and that the properties of the ionized gas can easily lead to confusion with post-AGB ionization. Furthermore, a fraction of the line ratios are located below the K01 curve, and as in the case of NGC 4643, SF that may induce a *mixed* ionization is not observed. Like in the previous case, the complexity of the ionization would be impossible to uncover without a detailed exploration of the shape, distribution, and location in the different diagnostic diagrams, together with the use of the EW(Hα) and the comparison with the spatial distribution of the continuum emission (either stellar or the radio-jet). Additional information, as provided by the gas and stellar kinematics (and the comparison between them), and an analysis of the velocity dispersion and asymmetry of the lines helps to disentangle the real nature of such ionizing sources (D'Agostino et al. 2019; López-Cobá et al. 2020).

Figure 5 shows the last case of our illustration of the complexity of deriving the nature of the ionization in galaxies. NGC 4030 is a grand design Sbc galaxy observed almost face-on. Its disk shows hundreds of H ii regions easily identified in the emission-line image (middle-top panel in Figure 5) as green clumpy ionized regions. As expected, most of the ionization is located below the K01 demarcation line (with a large fraction below the K03). However, contrary to examples discussed before (MCG-01-04-025, UGC 1395 and ESO298-28), the distribution does not follow the classical location of H ii regions. Certainly, a substantial fraction of the line ratios are located in between the K03 and K01 region, and even above the K01 curve in the classical BPT diagram. Following the usual and broadly accepted interpretation of this diagram, this shift should be due to *mixing* of the ionization produced by the overlap of the H ii regions with other ionizing sources that pollute those line ratios (either by a central AGN or DIG due to hot evolved stars, e.g. Davies et al. 2016; Lacerda et al. 2018). However, a more detailed exploration indicates that the polluting sources correspond to clumpy ionized structures, morphologically similar to H ii regions, but with line ratios corresponding to the presence of a harder ionization. Those regions clearly correspond to those regions with higher [N ii]/Hα line ratios, previously detected in the central regions of galaxies (Kennicutt et al. 1989; Sánchez et al. 2012b), usually referred to as nitrogen enhanced regions (Ho et al. 1997; Sánchez et al. 2015). Recent explorations have shown that they are compatible with supernova remnants combined in some cases with ionization by young hot stars (Cid-Fernandes et al., submitted). Thus, again, the intermediate region can be populated without invoking an AGN to explain the mix of ionization.

In summary, gas in galaxies could be ionized by many different physical processes, as is the case of our own galaxy. Therefore, to associate a single ionization to the observed emission across an entire galaxy is a first order approximation that can lead to considerable errors, in particular in the derivation of the physical parameters of the ionized gas, like dust attenuation or oxygen abundance (due to the non linearity of the combination of line ratios). Furthermore, our ability to distinguish between the different ionization conditions should not rely on the classical diagnostic diagrams only. They should be combined with morphological and kinematic information about the emission line structures and complemented with the study of the properties of the underlying stellar populations to determine their potential ionizing sources. This highlights the fundamental importance of integral field spectroscopy in the study of the ionized gas in extragalactic sources. However, these data are also limited by their spectral and, in particular, their spatial resolution, which can produce a mix of ionization (e.g. Davies et al. 2016) and limit our understanding of the derived properties (e.g. Rupke et al. 2010; Mast et al. 2014).

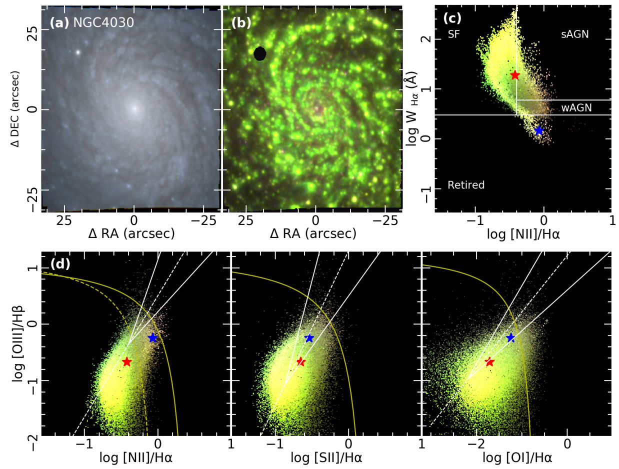

Fig. 5. Similar figure as Figure 3, for galaxy NGC4030. The color figure can be viewed online.

4.3. *Ionized Gas: A Practical Classification Scheme*

Based on the results outlined before, we propose a new procedure to classify the components of the ionized ISM. To illustrate it we present in Figure 6 a scheme of the distribution of the most dominant ionization conditions for different galaxy types. We consider that this classification procedure is valid for spatially resolved spectroscopic data between a few hundred pc to a few kpc scales. However, it may not be valid for smaller scales, where the ionization structure is resolved for the different conditions described in the explored data.

- **A star-forming region** is observed as (i) a clumpy/peaked region (clustered) in the ionized gas maps of a galaxy with (ii) line ratios below the (Kewley et al. 2001) demarcation line in at least one of the classical diagnostic diagrams shown in Figure 2 (and Figures 3, 4, and 5), with (iii) EW(Hα) above 6Å (see Figure 6, in particular Panels 1 and 2), and with (iv) a fraction of light assigned to young stars (Age < 100 Myr), in the $V-$band of at least 4-10%. This definition is valid for giant H II regions and H II region clusters at the indicated resolution. Small H II regions, like the Milky Way's Orion Nebula, would be spatially and spectroscopically diluted, and confused with the diffuse gas. In other words, this classification scheme guarantees that the selected regions are indeed ionized by young stars, but it cannot guarantee a complete selection of all regions with the presence of young ionizing stars. Higher spatial resolution data, covering bluer wavelength ranges (UV) would improve this selection process.

- **An AGN ionized region** is observed as (i) a central ionized region (almost unresolved to the considered resolution), well above the intensity of the diffuse ionized gas (Figure 6, Panel 2 and 3, and Figure 3, top-right panel). (ii) Its emission line ratios are above the K01 demarcation lines in the three diagrams discussed before, and (iii) its EW(Hα) is above 3Å (6Å for strong AGN Cid Fernandes et al. 2010). Below that limit it is not possible to determine if the ionization is due to an AGN or to other processes (post-AGBs/HOLMES, low-velocity shocks, photon leaked from H II regions). They (iv) present a decrease of the considered line ratios with respect to the central values in the galaxy, and (v) show a steep decay in the flux intensity, which is never shallower than an r^{-2} distribution (e.g., Singh et al. 2013a).

- **Diffuse gas ionized by hot, evolved stars** is seen as (i) a smooth (not clumpy or filamentary) ionized structure that follows the light distribution of the old stellar populations in galaxies. (ii) The EW(Hα) in these regions is clearly below 3Å, with (iii) the fraction of young stars never larger than 4%. (iv) The distributions in the diagnostic diagrams cover a wide range of values from the LINER-like area towards the range covered by metal-rich H II regions (see Figure 6, panel 3). (v) This component is observed in galaxies with old stellar populations (massive, early types, e.g., Figure 4, left panel) or regions in galaxies with the same characteristics (bulges, Figure 3, bottom-left panel). (vi) The kinematics of this ionized gas does not deviate significantly from that of the old stellar population in the galaxy. Two caveats: In high spatial resolution data (10-100 pc) this component may present, in some cases, clumpy structures associated with individual sources. This is not visible at the resolutions considered in this review. Also, as indicated before, the signal from small-size H II regions is diluted at these resolutions by the ubiquitous DIG emission, which could alter the observed line ratios.

- **Diffuse gas due to photon-leaking by H II regions** is observed as (i) a smooth ionized structure present in galaxies with young stellar populations (in general, low mass and late-type galaxies) or regions in galaxies with the same characteristics (disks, e.g. Figure 6, Panel 1 and Figure 3, greenish diffuse ionization shown in the emission line image located at the disk of the four galaxies). This component should (ii) have a fraction of young stars never larger than 4% within the same resolution element and at the considered resolution (e.g. Espinosa-Ponce et al. 2020). (iii) Its kinematics are not fundamentally different from those of the disk. In the diagnostic diagrams this component may present varying line ratios, from very similar to H II regions to significantly different from them (e.g. Weilbacher et al. 2018). It also covers a wide range of EW(Hα). Caveats: In high spatial resolution data (10-100 pc) it may present some shells or bubble-like structures, not visible at the considered resolutions. In late spirals (Sc/Sd), it may be the dominant or at least a large fraction of the DIG (e.g. Relaño et al. 2012). In this case, this component should be included in the photon budget to derive the SFR in galaxies (e.g. Zurita et al. 2000).

- **A high-velocity shock ionized region** is seen as (i) a filamentary or bi-conical ionized gas structure with fluxes (and EWs) well above those of the diffuse ionized gas. Its emission line ratios cover a wide range of values. In general, (ii) the line ra-

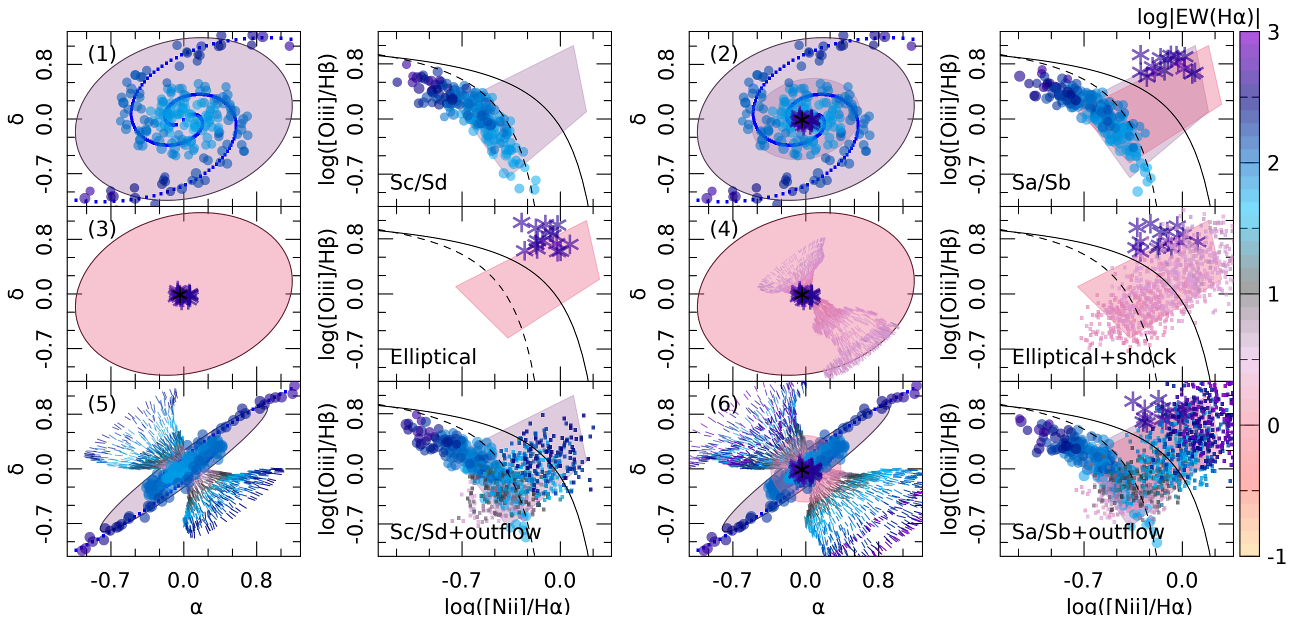

Fig. 6. Scheme of the main ionizing conditions typically observed in galaxies of different morphological types, including both the distribution across the optical extent (left) and the classical BPT diagram (right): (1) late-type spirals (Sc/Sd), without a prominent (or without) bulge. Their main morphological feature is a thin disk (ellipse) together with the spiral arms (dotted line). The main components of the ionized ISM are the H II regions distributed mostly in the disk and following more or less the spiral structure (blue solid-circles), together with some diffuse ionized gas that, in this case, is dominated by photons leaked from those regions (represented as a pale pink ellipse). (2) Early-type spirals (Sa/Sb), with a prominent and well defined bulge, in addition to the disk and spiral arms. They present H II regions and diffuse ionized gas in the disk too, like late spirals. However, the DIG is ionized by a mix of photon leaking and ionization by hot evolved stars, mostly associated with the presence of old stellar populations (i.e., more clearly observed in the bulge, shown as a pink central ellipse). Some also show ionization due to AGN, mostly located in the central regions (violet stars). (3) Early-type galaxies (E/S0), with very weak or no disk. Ionization across their optical extent is dominated by hot evolved stars (pink ellipse), that ionize the diffuse gas, with the possible presence of a central AGN. (4) Early-type galaxies may present shock-ionized gas, observed mostly in central galaxies in clusters, radio-galaxies, and weak AGN (e.g., like in the case of Geyser galaxies, Roy et al. 2018a). The structure of these relatively low-velocity shocks is filamentary, with a velocity dispersion slightly larger than the one observed in the diffuse ionized gas), and with kinematics largely decoupled from those of the stellar populations in these galaxies. (5) Late-type spirals may present galaxy scale shock ionization associated with galactic winds, which can usually be seen in edge-on or highly inclined galaxies. They show a patchy filamentary distribution, following a conical or biconical structure, emanating from the central regions and escaping to high altitudes with respect to the disk height in some cases. (6) Early-type spirals may show the same kind of galactic winds, but in this case they can be produced by the kinetic energy injected by an AGN too. When observed at high inclination the ionization in the vertical direction can be associated with old stellar populations either in the bulge or a thick disk (not shown in the figure). This latter ionization is less patchy, more diffuse. In all panels, colors represent the typical EW(Hα) associated with the different ionization conditions. The color figure can be viewed online.

tios are above the K01 demarcation line in the three diagrams, and (iii) in most cases, the lines are asymmetrical, with (iv) a clear increase of the line ratios (in particular [O I/Hα]) with the velocity dispersion and the distance from the source of the outflow. In addition (v) they have an EW(Hα) above 3Å. (vi) This component is usually located in the central regions (or emanating from this region), for both star-formation driven (Figure 6, Panel 5, and Figure 3, bottom right panel) and/or AGN driven outflows (Figure 6, panel 6). Caveats: The line ratios can spread from the area usually associated with AGN ionization (top-right region of the diagram), to the area covered by H II regions (i.e., below both demarcation lines, and spread through the so-called *mixed* region). A demarcation line has been proposed to separate between SF and AGN driven outflows (Sharp & Bland-Hawthorn 2010), although this should be tested using large/statistically significant samples (e.g. López-Cobá et al. 2020).

- **A low-velocity shock ionized region** shares many of the characteristics of the DIG by old, evolved stars, and indeed it is considered by different authors as part of this diffuse gas component (e.g. Dopita et al. 1996; Monreal-Ibero et al. 2010). However, these regions present (i) a clear filamentary structure (Figure 6, panel 4), and (ii) a velocity distribution not following the general rotational pattern of the galaxy. The recently named *Geyser-galaxies* (Cheung et al. 2016; Roy et al. 2018a) or the cooling flows observed in ellipticals (in clusters in general) show most probably shock ionization corresponding to this type (e.g., Figure 4, right panel).

- **Supernova remnants** are less frequent than in the previous types; they are observed (i) at this resolution as clumpy/ionized regions, similar in shape to the giant H II regions/star-forming areas discussed before. However, they (ii) are ionized by a harder ionization spectrum and therefore show higher values for the line ratios shown in the classical diagnostic diagrams. Caveats: At the current resolution this component is hard to see without considerable contamination by adjacent or superposed (through the line of sight) H II regions or photon leaking ionized DIG. For this reason they cover a wide range of line ratios, from the classical location of H II regions to the intermediate region between the K03 and K01 regime. In the emission line maps presented in this review this component may appear as reddish clumpy structures (e.g., Figure 5). In general it is required to explore other emission lines, frequently associated with SN and SNR (e.g. Fesen & Hurford 1996), to detect them (e.g., Cid-Fernandes et al. submitted).

We present this classification scheme as a practical tool, with the hope to improve on current classification methods. However, it is by construction incomplete and will require future revisions based on the improvement of our understanding of the ionization conditions observed in galaxies.

5. GLOBAL AND RESOLVED RELATIONS

One of the main results emerging from IFS-GS, as highlighted by Sánchez (2020), is that the global relations uncovered in the exploration of extensive properties of galaxies show local/resolved counterparts that are valid at kiloparsec scales. Among them, the most evident ones are:

- The star-formation main sequence (SFMS, e.g. Brinchmann et al. 2004; Renzini & Peng 2015), that relates the SFR and the M_* for SFGs, has a resolved version that relates the $\Sigma_{\rm SFR}$ and the Σ_* for SFAs (rSFMS, e.g. Ryder 1995; Sánchez et al. 2013; Cano-Díaz et al. 2016; Hsieh et al. 2017; Cano-Díaz et al. 2019).
- The mass-metallicity relation (MZR, Tremonti et al. 2004), that relates the central and/or characteristic gaseous oxygen abundance, 12+log(O/H), of a galaxy with its M_*, is reflected in the relation found between the local (spatially resolved) oxygen abundance and the mass surface density Σ_* in star-forming regions (rMZR, e.g. Rosales-Ortega et al. 2012a; Barrera-Ballesteros et al. 2016).
- The scaling relation between the molecular gas mass and the stellar one (e.g. Calette et al. 2018, and references therein), corresponds to the recently reported relation between $\Sigma_{\rm gas}$ and Σ_* (e.g. Lin et al. 2019; Barrera-Ballesteros et al. 2020). Because of its similitude with the SFMS, we will refer to this relation as the *mass gas main sequence*, or MGMS, and to its resolved version as rMGMS, following Lin et al. (2019).

In addition to all these extensive relations and their local/resolved intensive counterparts, recent IFS-GS have allowed to explore in detail well-known relations, like the Schmidt-Kennicutt relation (SK-law, Kennicutt 1998). The SK-law was formulated as a relation between intensive quantities, connecting the average $\Sigma_{\rm SFR}$ and the average $\Sigma_{\rm gas}$ across the optical extent of galaxies. However, in principle it was also a global relation, since it relates characteristic properties of individual galaxies. Much work has gone into investigating the true nature of the SK-law, in particular concerning the spatial scales over which it holds and the phases of the neutral ISM which provide the tightest relation. A consensus has emerged in which the SK-law is tightest when relating SFR to molecular hydrogen H_2 over scales of a few hundred parsec (e.g. Bigiel et al. 2008, 2011). The advent of IFS-GS, in combination with spatially resolved explorations of the gas content, has allowed to confirm that relation over statistically large samples at kiloparsec scales (e.g. Bolatto et al. 2017). For nomenclature consistency we refer to the resolved SK-law as rSK-law.

It is important to note here that these relations are valid either for SFGs (global) or star-forming areas (SFAs, local/resolved). Retired galaxies (and retired areas) do not follow those relations, showing in general much lower values of the SFR ($\Sigma_{\rm SFR}$) and $M_{\rm gas}$ ($\Sigma_{\rm gas}$) for a fixed M_* (Σ_*), and slightly lower values of SFR ($\Sigma_{\rm SFR}$) for a fixed $M_{\rm gas}$ ($\Sigma_{\rm gas}$). Whether those RGs (and RAs) follow well defined trends or are distributed over extended loci (clouds) in each diagram, is under debate (e.g. Hsieh et al. 2017). Regarding the MZR (rMZR), it is difficult to determine if they follow the same trends or not, since the gas-phase metallicity is very hard to obtain for RGs (RAs). In the few cases in which a globally retired galaxy presents a few SFAs (e.g., Gomes et al. 2016a), it seems that those regions have a slightly lower oxygen abundance than predicted from the relation (Sánchez 2020). However, more statistics are required in this regards.

There are two possible ways to look at the evidence connecting the resolved/local relations with their global counterparts. First, concerning the MZR, theoretical investigations seems to imply that chemical evolution is not dominated by local processes only, but that transport of gas and metals plays a significant role in the physical origin of the relation (e.g. Trayford & Schaye 2019). Similar arguments could be made invoking radial migration, accretion and merging when it comes to the rSFMS. However, the second way to look at the relations is purely empirical, to investigate whether they are at least interchangeable in terms of their intensive vs. extensive nature (e.g. Barrera-Ballesteros et al. 2016; Gao et al. 2018; Sánchez Almeida & Sánchez-Menguiano 2019). Indeed, we will show in the next section that the extensive/global relations are in general a natural consequence of the intensive/resolved ones, while the reverse is not true. While this does not yet make up a proof of which physical processes shape those relations, it becomes probable that most processes surrounding star formation and metal enrichment in galaxies are predominantly local, while global processes only perturb, but do not fundamentally alter, the resulting relations.

In the following we investigate two topics: (i) we transform the global extensive relations into intensive ones, by deriving the average surface densities of the involved quantities (following the exploration of the SK-law by Kennicutt 1998). Then we compare the intensive global relation with the local/resolved one; and (ii) we explain with simple calculations why a resolved relation directly leads to an intensive global one, following Sánchez Almeida & Sánchez-Menguiano (2019).

5.1. *The Intensive Global Relations*

As indicated above, the global scaling relations involve extensive quantities (in most cases), relating often the stellar mass (or gas mass) to other properties of galaxies, such as the SFR, oxygen abundance, of both properties between themselves. As described before, those relations could be a pure consequence of a scaling between galaxies, since they involve pure extensive quantities: the larger and more massive a galaxy is, the higher are the values of any other extensive property, such as the SFR or the gas mass (at least for SFGs). The MZR is slightly different in this regard, since it involves an extensive quantity (M_*) and an intensive one (the oxygen abundance). However, in many cases it is ill-defined, since it is well known that the oxygen abundance shows a radial gradient in galaxies (e.g. Sánchez et al. 2014, and references therein). Furthermore, the oxygen abundance is frequently estimated using variable physical apertures in galaxies, rather than a fixed aperture or a characteristic radius (see Sánchez et al. 2019b, for a recent discussion on the topic). Thus, although the MZR involves an intensive quantity, it is measured as an extensive one (i.e., not averaged across the extension of galaxies). However, it is true that in this particular case the simple scaling of the two parameters due to their extensive nature cannot explain this relation (see the discussion in the seminal article by Tremonti et al. 2004)

We attempt to explore the existence of intensive global relations (rather than extensive ones), by deriving the average surface densities of the considered extensive parameters (M_*, $M_{\rm gas}$ and SFR), and the characteristic value of the oxygen abundance (i.e., the value at the effective radius, following Sánchez et al. 2013). To that end we divide each extensive quantity by the effective area of each galaxy, defined as the area within $2r_e$, i.e., $A_e = \pi (2r_e)^2$. We choose this particular radius because most of the IFS data explored in this review sample the galaxies up to this galacto-centric distance. Therefore, most of the reported extensive properties are actually aperture-limited values corresponding to that radius. How the actual parameters were derived, both global and resolved, is described in detail in § 3.

We will demonstrate in the upcoming section that indeed the average intensive parameters derived as described before scale with the corresponding value at the effective radius. For this reason, the current results would be qualitatively similar to the ones found assuming a different scale-length for the galaxy. Finally, for the oxygen abundance we fit its radial gradient, normalized to the effective radius, within 0.5-2 r_e with a simple linear profile (following Sánchez-Menguiano et al. 2018). Then, we derive the value at the effective radius using the best fit profile for each galaxy.

Figure 7 shows the result of this experiment. In each panel we show, in color-code, number density distributions of the intensive global parameters defined before (and the characteristic one, in the case of the oxygen abundance), including: (i) $\langle\Sigma_{\rm SFR}\rangle$ versus $\langle\Sigma_*\rangle$; (ii) $\langle\Sigma_{\rm SFR}\rangle$ versus $\left\langle\Sigma_{\rm gas}\right\rangle$; (iii) $\left\langle\Sigma_{\rm gas}\right\rangle$ versus $\langle\Sigma_*\rangle$ and finally (iv) 12+log(O/H)$_e$ against $\langle\Sigma_*\rangle$. First, we note that the intensive global distributions expressed in extensive quantities (color-coded data) follow the same trends as the extensive local ones (contours) reported in the literature and, in more detail, the relations found for resolved quantities. The first panel ($\Sigma_{\rm SFR}$-Σ_* diagram) corresponds to the SFR-M_* diagram, and the distribution shows the two well known trends for SFGs (the SFMS) and the RGs (with a

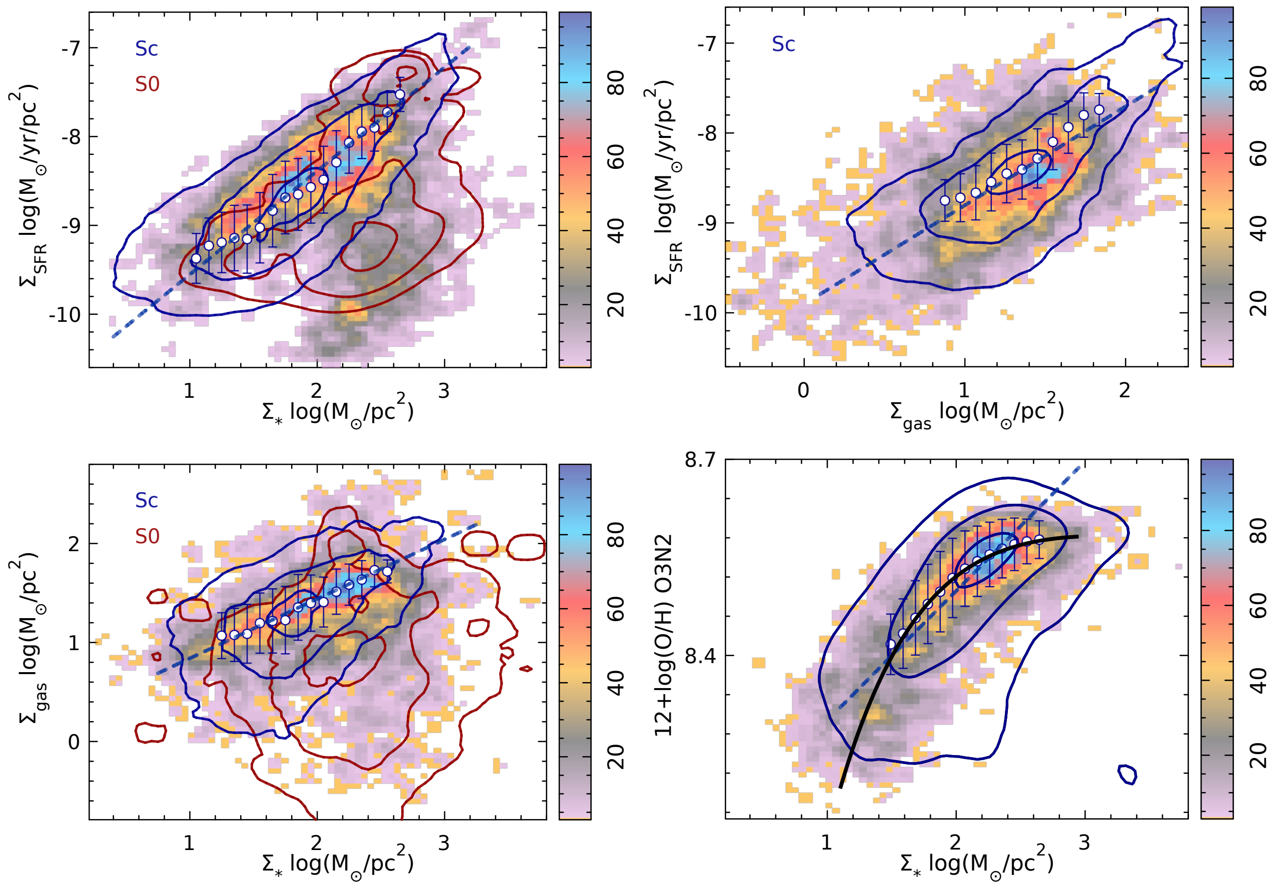

Fig. 7. Global and local (resolved) scaling relations compared. *Top-left panel:* number density distribution of galaxies in terms of mean Σ_{SFR} against mean Σ_* for entire galaxies within our compilation. The distributions are shown as color coded images, where the color bar indicates the cumulative distribution as a fraction of total. In addition, we show the number density distribution of Σ_{SFR} vs. the Σ_* for each individual spaxel of each individual galaxy as contour plots, for both the Sc (blue contours) and S0 (red contours) galaxies within the compilation. Each contour encircles 85%, 50% and 10% of the sample, from the outermost to the innermost one. Solid white circles represent the average value of Σ_{SFR} for bins of ≈0.1 dex in Σ_*, for galaxies of type Sc, and for those values encircled by the 85% distribution contour, with error bars corresponding to the standard deviation within each bin. The blue dashed line represents the best linear regression to these average points. *Top-right panel:* Similar plot for the galaxy averaged and spaxel-wise Σ_{SFR} against Σ_{gas} distribution. In this case, for the resolved properties we only show the contours corresponding to Sc galaxies. *Bottom-left panel:* Similar plot for the Σ_{gas}-Σ_* diagram. *Bottom-right panel:* Similar plot for the distribution of oxygen abundance vs. Σ_*. In the last case, the contours correspond to the number density distribution of all the spaxels with measured oxygen abundance for the full sample of compiled galaxies (black contours); although in practice, it contains mostly late-type, star-forming galaxies. In this panel a best fitting curve is included as a black solid-line, following the functional form usually adopted to describe the relation between these two parameters, first proposed by Sánchez et al. (2013). The color figure can be viewed online.

cloud of points well below the SFMS). The agreement between global and local relations was already explored in detail by Pan et al. (2018) and Cano-Díaz et al. (2019), being in general good.

The second panel ($\Sigma_{\rm SFR}$-$\Sigma_{\rm gas}$ diagram) shows the well known SK-law for the analysed sample. Like in the case of the SFMS, the well known trend between the two parameters is visible, despite the fact that we are using a proxy to estimate the gas content, based on the dust attenuation (Barrera-Ballesteros et al. 2020), as discussed in § 3.2. The third panel ($\Sigma_{\rm gas}$-Σ_* diagram) mimics the known relation between the gas and the stellar mass, for SFGs, with a tail towards lower values of M_{gas} (Σ_{gas} in this case) for retired galaxies (e.g. Saintonge et al. 2016; Calette et al. 2018; Sánchez et al. 2018; Lacerda et al. 2020). Finally, the fourth panel shows the intensive version of the MZR diagram, thus, the distribution of the characteristic oxygen abundance of each galaxy (i.e., the

TABLE 1

LOG-LOG FITTING TO RESOLVED RELATIONS

Relation	Reference	β	α	r_c	σ
rSFMS	This work	-10.35±0.03	0.98±0.02	0.96	0.17
	Sánchez et al. (2013)		0.66±0.18	0.66	
	Wuyts et al. (2013)	-8.4[1]	0.95		
	Cano-Díaz et al. (2016)	-10.19±0.33	0.72±0.04	0.63	0.16
	Lin et al. (2019)	-11.68±0.11	1.19±0.01		0.25
	Cano-Díaz et al. (2019)	-10.48±0.69	0.94±0.08	0.62	0.27
rMGMS	This work using Σ_{gas}	0.24±0.04	0.60±0.02	0.93	0.08
	This work using Σ'_{gas}	-1.10±0.07	1.22±0.03	0.95	0.14
	Lin et al. (2019)	-1.19±0.08	1.10±0.01		0.20
	Barrera-Ballesteros et al. (2020)	-0.95	0.93		0.20
rSK	This work	-9.85±0.02	1.19±0.02	0.96	0.11
	Using Σ'_{gas}	-10.72±0.04	1.17±0.02	0.97	0.15
	Bolatto et al. (2017)	-9.22	1.00		
	Lin et al. (2019)	-9.33±0.06	1.05±0.01		0.19
rMZR	This work	8.21±0.01	0.13±0.01	0.88	0.06

Results for the log-log regressions between the different parameters shown in Figure 7, with β being the zero-point of the relation, α the slope, r_c the correlation coefficient between the involved parameters and σ the standard deviation around the best fit relation. We include similar results extracted from the literature, shifted when needed to match the adopted units for the different quantities. We remind the reader that our surface density quantities are all expressed in units of pc^2 for the area. (1) We should note that the Wuyts et al. (2013) results are based on galaxies at $z \approx 1$. Thus, the offset in β reflects an evolution in the rSFMS similar to the one reported for the SFMS (e.g. Speagle et al. 2014; Sánchez et al. 2019a).

value at r_e) against the average Σ_*. This diagram replicates the well known MZR distribution with an almost linear regime, where the abundance increases with the stellar mass (here the stellar mass density) and a plateau at high Σ_* values ($\sim 2 M_\odot$ pc^{-2}), where oxygen abundances reach an asymptotic value.

The main goal of this exploration is not to discuss the physical origin of the reported relations. For that discussion we refer to Sánchez (2020), where the different relations are described in more detail. In this particularly case we are just interested in showing that the global relations, here expressed in their intensive form, do actually correspond to the local/resolved ones reported in the literature. For this reason we overplotted in the different diagrams the corresponding local/resolved distributions for the individual spaxels within our compilation of IFS data. When required, we plot the distributions segregated by morphology, since in many cases the reported relations depend on the morphology (as discussed before), being in general different for star-forming galaxies (dominated by late-type galaxies) than for retired galaxies (dominated by early-type ones) (e.g. Lacerda et al. 2020). Panel by panel we can see that the resolved distributions for SFGs (represented by Sc galaxies) follow exactly the same trends as the global intensive properties for the $\Sigma_{\rm SFR}$-Σ_*, $\Sigma_{\rm SFR}$-$\Sigma_{\rm gas}$ and $\Sigma_{\rm gas}$-Σ_* diagrams. Similar results are found when using a different estimator for the gas mass density, as the one described in § 3.2 (labeled as Σ_{gas}).

We perform a linear regression between the different parameters shown in Figure 7 to characterize the relation between them. For this analysis we derive the mode of the distribution along the y−axis in a set of bins of ≈0.1 dex along the x−axis for each diagram, for those values encircled by the 80% density contour in Figure 7. The points derived this way are represented as solid white circles in the figure. Then we perform a least-squares regression based on a Monte-Carlo procedure, with the best fit parameters and their errors derived as the mean and standard deviations of the reported parameters in each iteration. This procedure is very similar to the one adopted by similar recent explorations (Sánchez et al. 2019b; Barrera-Ballesteros et al. 2020). The result of this procedure is included in Table 5, together with values reported in the literature. In general, there is good agreement between the current reported trends and values in the literature. This is particularly true for the $\Sigma'_{\rm gas}$ estimation of the gas mass density (in the relation involving this parameter, i.e., rSK and rMgM*). The dispersion around the main trend, characterized by the standard deviation, is also of the same order or smaller than the one reported in the literature. In the case of the rMZR we included a linear regression for consistency with the other explored relations. However, it is well known and it is clear from inspection of Figure 7 that this functional form does not describe the distribution along the full range of explored parameters. Other functional forms, like a higher order polynomial function (Rosales-Ortega et al. 2012b) or a linear+exponential one (Sánchez et al. 2013), better describe this distribution. For this reason we include in the figure the best fit curve using this latter model, with the functional form:

$$y = 8.54 + 0.003\,(x - 2.25)\exp(5.75 - x), \qquad (6)$$

where x is $\log(\Sigma_*)$ and y is 12+log(O/H). Like in the case of the linear relations for the previous distributions, the trend described by this functional form is very similar to the one reported by recent explorations of the rMZR (e.g. Barrera-Ballesteros et al. 2016). Furthermore, similar functional forms have also been adopted to parameterize the extensive MZR (Barrera-Ballesteros et al. 2016, 2018; Sánchez et al. 2017, 2019b).

The distributions shown in Figure 7 clearly demonstrate that the rSFMS, rSK and rMGMS resolved relations are indeed the same relations as the *intensive* versions of the SFMS, SK and gas-stellar ones. Even more, the individual spaxels of the RGs (represented by S0 galaxies in here), are located off and below the reported relations for the SFGs in the Σ_{SFR}-Σ_* and Σ_{gas}-Σ_* diagrams, following exactly the same trends as those reported for the RGs. Finally, the rMZR distribution for the bulk sample of galaxies follows exactly the same distribution as the intensive version of the MZR. This distribution is always dominated by SFGs, since they are the only ones were the oxygen abundance is properly derived.

This exercise shows that the global and local/resolved relations are indeed the same relations, covering the same ranges, following the same distributions (and trends) and the same morphological segregation (in general). We should note, however, that selecting SFGs and RGs is not exactly the same as selecting star-forming areas (SFAs) and retired-areas (RAs), as recently discussed by Cano-Díaz et al. (2019). There are RAs located in (mostly the center) of SFGs, and also a few SFAs located in (mostly the outer part) of RGs (e.g., Singh et al. 2013a; Gomes et al. 2016b; Belfiore et al. 2017a). This should surely affect the global (intensive or extensive) relations, since they deal with average quantities, mixing SFAs and RAs within the considered apertures. Despite this caveat we stress the remarkable agreement between the explored global and resolved relations.

5.2. *Universality of the Local Relations*

One relevant question regarding the local relations explored in the present section is their universality. In other words, whether the resolved regions of different galaxies lie along the same reported relation, irrespective of the properties of the host galaxies (global or local), or, on the contrary, if part of the dispersion reported in those relations is the consequence of the existence of different relations for different families of galaxies (or possible secondary correlations). In global relations this exploration has led, for instance to the extensive search for a third parameter to explain (or reduce) the scatter in the SFMS (SFE or gas fraction, e.g. Saintonge et al. 2017) and the MZR relations (SFR, gas fraction, e.g. Mannucci et al. 2010; Bothwell et al. 2013). It has also led to a debate over the need for that third parameter (e.g. Sánchez et al. 2013; Barrera-Ballesteros et al. 2018). Regarding the local/resolved relations, similar explorations were recently performed by Barrera-Ballesteros et al. (2016), Cano-Díaz et al. (2019) and Ellison et al. (2020) in the case of the rMZR, rSFMS and rSK (resolved SK-law), respectively. They find that: (i) it is not clear that a secondary parameter is required to explain the dispersion in the rMZR (in particular the $\Sigma_{\rm SFR}$); (ii) galaxies of different morphologies and SFE segregate both the SFMS and the rSFMS (as already noticed by González Delgado et al. 2016; Catalán-Torrecilla et al. 2017); and (ii) stellar mass and SFE segregate the rSK (see also Bolatto et al. 2017; Colombo et al. 2018). This was already discussed in Sánchez (2020) in detail, describing the similarities and differences for different stellar masses and morphologies. The rMZR was not included here, since it clearly requires a more complex parametrization. In order to present a more quantitative evaluation of the variation of the different local relations with global properties of galaxies we repeat the linear regression to the rSFMS, rMGMS and rSK relations discussed in the previous section segregated in bins of mass and morphology. rMZR was not included here since it clearly requires a more complex parametrization

We adopted the same bins as those described in Sánchez (2020), including four ranges of stellar mass (M $=10^{7.5}$-$10^{9.5}$, $10^{9.5}$-$10^{10.5}$, $10^{10.5}$-10^{11} and 10^{11}-$10^{13.5} M_{\odot}$), seven morphological types (E, S0, Sa, Sb, Sbc, Sc and Sd), and an additional bin including all morphologies, and the same stellar mass bins (labelled as *ALL*). Figure 8 illustrates the result of this analysis, showing the variation of the zero-point (β) and slope (α) of the linear relations against morphology and stellar mass. The values shown in this figure are contained in different tables available to the community [7].

[7] http://ifs.astroscu.unam.mx/RMxAA/.

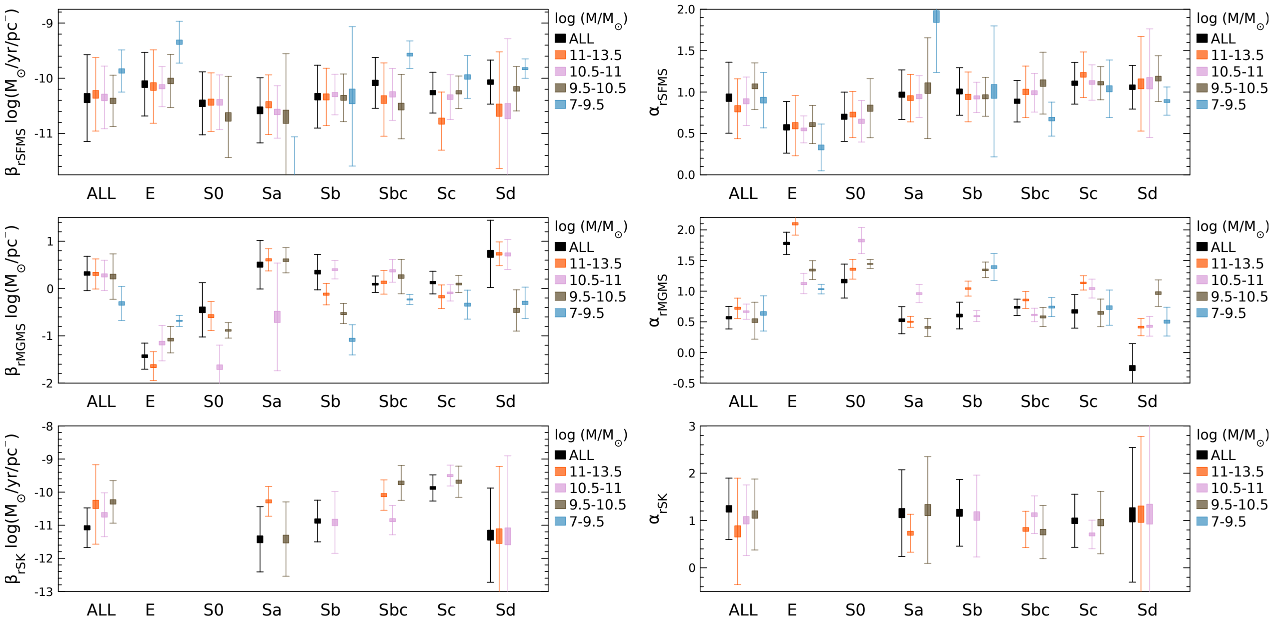

Fig. 8. *Top panel:* Zero-point of the rSFMS relation derived for different morphology (black symbols) and stellar mass (colors) bins. For each sub-sample the mean value of the considered zero-point is shown, together with the standard deviation (shown as a rectangle) and the minimum and maximum values within the distribution (shown as error-bars). *Middle panel:* Similar distribution for the slope of the rMGMS. *Bottom panel:* Similar distribution for the slope of the rSFMS. The color figure can be viewed online.

The distributions confirm the results reported in the literature: (i) the rSFMS presents a mild change with the stellar mass, and a stronger variation with morphology, with SFAs of more massive and earlier galaxies showing a shallower slope in the relation and lower values of the $\Sigma_{\rm SFR}$ for a given Σ_*; (ii) the rMGMS shows clear patterns with mass, but again, even stronger and clearer ones with morphology. SFAs in early-type galaxies have lower values of Σ_{gas} for a given Σ_* (i.e., a molecular gas deficit), an effect that is enhanced by the stellar mass (i.e., the gas deficit is stronger in more massive early-type galaxies). The relation between the two mass densities is steeper (larger value of α) than the one reported for their counterparts in SFGs, indicating that the central (more massive) regions of early/massive galaxies may still contain some molecular gas that is scarce in the outer regions (see Figure of 18 Sánchez 2020). On the contrary, the SFAs of more massive SFGs have an overall higher Σ_{gas} for given Σ_{SFR} than those of less massive SFGs, and a shallower relation between both parameters; (iii) the rSK, which has the noisiest distribution, shows a dependence with mass and morphology that is more evident in the zero-point (or scale) than in the slope (which seems rather constant, with $\alpha \approx 1$). This trend indicates that the SFE is lower in SFAs of earlier and more massive galaxies.

Thus, although there are local/resolved relations in galaxies suggesting that the SF processes are governed by physical processes that happen at kiloparsec scales, those relations are not fully universal. Indeed, most probably they are not fundamental, being the statistical effect of physical processes that happen at a much smaller scales($\approx$10 pc). They show dependencies with the global properties of galaxies that modulate them, indicating a clear interconnection between local and global processes, as also discussed in Sánchez (2020).

5.3. *Prevalence of Local Relations*

The experiments in previous sections show that local/resolved and global intensive relations are indeed the same relations. However, they do not indicate which of them is prevalent in their physical origin. In other words, they do not show that global relations are just an integrated (averaged) version of the resolved ones. To demonstrate that this is the case, at least mathematically, we should show that once there is a local/resolved relation it is inevitable to generate a global one, but not the contrary. We will now explore this.

It is well known that many of the physical properties in galaxies have a radial gradient at first order. In particular, all the properties described in the previous section do actually show a radial decline for all galaxy types and all stellar masses and morphologies, on average. This is particularly true for the radial distributions of Σ_* and Σ_{gas}. In some particular mass/morphological types and for some particular galaxies the radial distribution may be flat of even inverted. This may be the case for Σ_{SFR} and 12+log(O/H), although those are not the general/average trends. If the local relations have a physical prevalence, this means that all radial relations/trends are a consequence of the relations between the explored quantities and Σ_*, and the radial dependence of this parameter, i.e., $\Sigma_* = F(r)$. In general, the radial distribution of Σ_* is well represented by a log-linear dependence with the galactocentric distance (which we adopt normalized to the effective radius, following Sánchez 2020). At first order it shows an almost universal exponential decline that can be parametrized with the following functional form:

$$\Sigma_* = \Sigma_0 \exp\left[-b(r/r_e)\right], \quad (7)$$

where Σ_0 is the stellar mass density in the central regions, r_e is the effective radius, and b is a parameter that controls the slope of the log-linear relation (with that slope being $b' = b/\ln(10)$).

Therefore, if a parameter p (e.g., Σ_{SFR}), has a log-linear relation with Σ_*, of the form:

$$p = c\Sigma_*^d, \quad (8)$$

then:

$$p(r) = c\left(\Sigma_0 \exp\left[-b(r/r_e)\right]\right)^d = c\Sigma_0^d \exp\left[-db(r/r_e)\right]; \quad (9)$$

or, in another form:

$$p(r) = p_0 \exp\left[-b'(r/r_e)\right], \quad (10)$$

where $p_0 = c\Sigma_0^d$ and $b' = db$. In summary, if a parameter p has a log-linear relation with Σ_*, and this latter one shows an exponential decline with the radius, then p will have a similar dependence on the radius.

However, the existence of a radial dependence of Σ_* is an empirical result, the nature of which is most probably related to the shape of the gravitational potential, how the gas settles in that potential (i.e., the dynamics), and how gas is transformed into stars. But there is no global relation between extensive or intensive properties (such as the one explored in the previous sections) that predicts the existence of such a radial distribution. In other words, it could be that galaxies follow all the four relations explored before, without presenting a radial decline in the surface densities (or any of the explored properties). Thus, galaxies could equally well have flat radial distributions (which it is unphysical for dynamical reasons) and at the same time the global relations could still hold. Furthermore, it could be that one of the parameters shows a radial decline, and another does not, without affecting the shape of the global relations.

In more detail, let P be the global property corresponding to the resolved property p (e.g., like the SFR to the Σ_{SFR}). In this particular case, we will show that it is possible for P to follow a global dependence with M_*, with the same functional form as the local relation shown in equation 8:

$$P = c\mathrm{M}_*^d, \quad (11)$$

without fulfilling a local/resolved relation between p and Σ_*. Let us assume that Σ_* has a radial dependence described by equation 7, but that p is constant along the extension of a galaxy. Then, no local/resolved relation would be verified, since at different galactocentric distances Σ_* would have different values, while p would remain constant. However, if both quantities are integrated up to a particular radius (e.g., $r < 2\,r_e$), then:

$$P = \int_0^{2r_e} 2\pi r p\, dr = 4\pi r_e^2 p, \quad (12)$$

and:

$$\begin{aligned} M_* &= \int_0^{2r_e} 2\pi r \Sigma_0 \exp\left[-b(r/r_e)\right]\, dr, \\ &= 2\pi\Sigma_0 r_e^2 b^{-2}\left[1 - e^{-2b}(2b+1)\right]; \end{aligned} \quad (13)$$

then, even if all galaxies had universal Σ_0 and p values, both quantities would show a similar dependence with the effective radius, and they would show a global relation similar to the one indicated before.

It is true that this is a very particular case, and it is totally unrealistic. However, it illustrates that the presence of a global relation does not guarantee the existence of a local/resolved one. The converse, on the other hand, is not possible. If galaxies present a local relation between parameter p and Σ_* in the form described by equation 8, then galaxies would present a global relation as the one described by equation 11. To demonstrate this, we use the results of equations 13 and 10 to show that in this case P would be:

$$P = 2\pi p_0 r_e^2 (b')^{-2}\left[1 - e^{-2b'}(2b'+1)\right], \quad (14)$$

and recalling the definition of p_0, and b', and equation 13 then:

$$\begin{aligned} P &= 2\pi c\Sigma_0^d r_e^2 D \\ &= 2\pi c\left[\frac{M_*}{2\pi r_e^2 B}\right]^d r_e^2 D \\ &= (2\pi)^{1-d} r_e^{2-2d} B^{-d} c D M_*^d, \end{aligned} \quad (15)$$

where

$$D = (db)^{-2}\left[1 - e^{-2db}(2db+1)\right],$$

and

$$B = (b)^{-2}\left[1 - e^{-2b}(2b+1)\right].$$

Since the effective radius r_e has an almost log-linear scaling relation with M_* (e.g. Sánchez 2020, and references therein), following a similar functional form as equation 11:

$$r_e = \beta M_*^{\alpha}, \quad (16)$$

then:

$$P = (2\pi)^{1-d}\beta^{\alpha(2-2d)}B^{-d}cDM_*^{d+\alpha(2-2d)}, \quad (17)$$

and therefore the proposed extensive global relation is verified (i.e., we recover naturally equation 11).

Furthermore, even when the relation shown in equation 16 is not verified, an intensive global relation holds. If we define the intensive global quantities $\langle p\rangle = \frac{P}{4\pi r_e^2}$ and $\langle\Sigma_*\rangle = \frac{M_*}{4\pi r_e^2}$, as the respective extensive ones (P and M_*) divided by the area within $2r_e$ (as defined in § 5.1), then, based on equation 13 to 15 it is easy to demonstrate that:

$$\langle p\rangle = cB^{-d}D\langle\Sigma_*\rangle^d, \quad (18)$$

which it is indeed a global relation between intensive quantities that mimics the local one. In particular, it has the same slope as the local one, with a slightly different zero-point, when represented in a log-log form. We should highlight here that the zero-point of this relation is not a dimensionless quantity, and particular care should be taken when the surface densities are expressed in different areal units (e.g., when transforming between pc^{-2} or kpc^{-2}, if the value of d is not one). These are the relations that match the local/resolved ones, as shown in Figure 7. In principle, the scale/zero-point are different by a factor $B^{-d}D$ between local and global intensive relations. However, adopting the average values reported for those relations, shown in Table 5, we found that the expected offset is ≈0.05 dex, being compatible with zero in some cases (like the rSK and rSFMS relations).

Finally, we should stress that if local relations segregate by morphological type (or other properties of galaxies), then global ones should also segregate, depending on the particular effect in the scaling of the zero-point. This effect should be stronger for the extensive global relations, which depend on the relation between the effective radius and the stellar mass shown in equation 16. It is known that this relation is different for early- and late-type galaxies. Therefore, even if both families show the same local/resolved relations, their global extensive ones should segregate just due to this effect, without involving different physical processes. This stresses the need to explore the global relations in their intensive and not in their extensive form, as it is usually done.

5.4. *Characteristic Intensive Properties*

In the previous sections we studied the existence of global relations between galaxy parameters based on an intensive formulation, rather than an extensive one as customary in the literature. We used average surface densities within 2 r_e in galaxies. In the case of the oxygen abundance, we adopted the value at r_e as the characteristic oxygen abundance for a galaxy. Previous studies have indeed reported that the values of many different quantities at this particular radius are representative/characteristic of the average quantity across the optical extent in galaxies (e.g. oxygen abundance, stellar ages and metallicities, stellar mass density, Sánchez et al. 2013; González Delgado et al. 2014; García-Benito et al. 2017). This is indeed a corollary of the derivations in the previous section, as we will see here.

We assume again that P is a global extensive quantity, and that it results from the integral of the corresponding surface density p across the optical extent of a galaxy, as described in the previous section. A radial distribution described by equation 10 follows. Then, with equation 14 and the definition of $\langle p\rangle$, we find that:

$$\langle p\rangle = 0.5p_0(b')^{-2}\left[1 - e^{-2b'}(2b' + 1)\right]. \quad (19)$$

Then, defining $p_{\rm e}$ as the value of p at the effective radius, it is possible to derive the relation:

$$\langle p\rangle = p_e e^{b'}(b')^{-2}\left[1 - e^{-2b'}(2b' + 1)\right]. \quad (20)$$

Thus, the average value of the surface density across the optical extent ($r < 2r_e$) is related to the value at the effective radius by a multiplicative constant that depends only on the slope of the radial gradient. Indeed, in the case of $b' \approx 1$, i.e., an exponential profile, $\langle p\rangle \approx 0.8p_e$.

6. CHARACTERISTIC GRADIENTS OF RESOLVED PROPERTIES

So far, we have demonstrated that the existence of a local relation between an observed property and Σ_* implies that this property has a radial gradient (if Σ_* has that gradient originally, as shown by Barrera-Ballesteros et al. 2016). The radial gradients of all the properties explored in the previous sections do indeed exist and were extensively discussed in Sánchez (2020). It was shown that in general, most of those properties show indeed a radial decline. This decline is frequently characterised to first order with an exponential function (as indicated in the previous sections), i.e. a log-linear function. Fitting that function to the observed distributions it is possible to derive the corresponding value of each considered parameter at the effective radius (which is representative of the average value), plus the magnitude of the radial gradient/slope of the radial gradient, either galaxy by galaxy, or averaged by galaxy type.

This analysis has been frequently performed to explore whether the proposed radial distributions (and therefore the local and global relations, as demonstrated in the previous sections) are universal (i.e., essentially the same, not dependent on other galaxy properties) or if they depend on the properties of the galaxies (e.g. morphology, mass, star-formation rate, gas content). In this particular section we report on the log-linear fitting performed on the average radial profiles of the properties explored by Sánchez (2020) in different mass bins and morphological types. We use the same bins described in that article, including four ranges of stellar masses (M = $10^{7.5}$-$10^{9.5}$, $10^{9.5}$-$10^{10.5}$, $10^{10.5}$-10^{11} and 10^{11}-$10^{13.5} M_{\odot}$), and seven morphological types (E, S0, Sa, Sb, Sbc, Sc and Sc), and an additional bin including all morphologies and the same stellar mass bins (labelled as *ALL*). We fit each of the radial profiles with the functional form described in equation 10, which corresponds to the log-linear relation:

$$\log p(r) = \beta - \alpha(r/r_e), \tag{21}$$

where α is the slope of the gradient (related to the b' parameter of equation 10) and β is the zero-point. From this relation it is possible to derive the characteristic value (i.e., the value at r_e), which would be

$$\log\, p_e = \beta - \alpha. \tag{22}$$

In order to avoid possible resolution problems affecting the central regions of the galaxies and to truncate to a radius covered by all IFS data, we restricted the fitting to the radial range between 0.5 and 2.0 r_e. Like in the case of the local relations explored in § 5.2, we repeat the analysis for galaxy subgroups segregated by mass and morphology, following Sánchez (2020). The results of the analysis are included in the electronically distributed tables.[8] Figures 9 to 16 present the results of this analysis, showing the distribution of the characteristic value (e.g., $\Sigma_{*,e}$) and the gradient slope (e.g. $\nabla\Sigma_*$) for the different explored properties, in each bin of stellar mass and morphology. In this way, it is possible to explore the variations of both parameters along these galaxy properties in a more quantitative way than presented in Sánchez (2020), although the same conclusions are extracted from these figures. In summary we find:

Stellar mass density gradients: Figure 9 shows that the characteristic stellar mass density has a clear dependence with the integrated stellar mass (M_*), as a consequence of the relation shown in equation 13. In this way

[8] http://ifs.astroscu.unam.mx/RMxAA/.

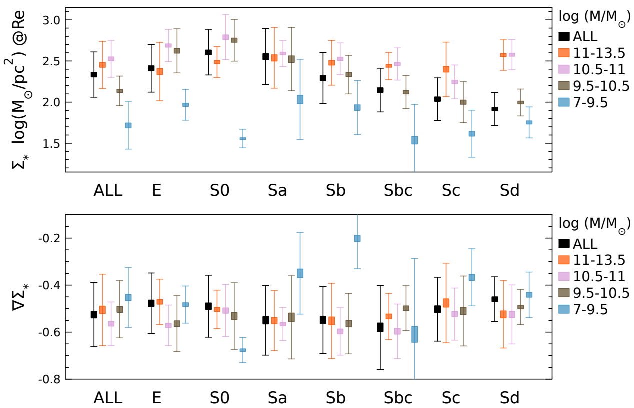

Fig. 9. *Top-panel:* Characteristic value of Σ_* at the effective radius for all galaxies in the sample (black symbols), and for different stellar masses (colors) and different morphologies. For each subsample we show the mean value of the considered parameter, together with the standard deviation (shown as a rectangle) and the minimum and maximum values within the distribution (shown as error-bars). *Bottom-panel:* Similar distribution for the characteristic slope of the radial gradient of the Σ_* parameter. The color figure can be viewed online.

$\Sigma_{*,e}$ increases with M_* in general, up to $\approx 10^{11} M_{\odot}$. However, this trend is modulated by the morphology of the galaxy, with later types showing lower values of $\Sigma_{*,e}$ than earlier types for the same stellar mass. This trend is particularly strong for the less massive galaxies. Based on the results in § 5, this indicates that the radial gradient of Σ_* should depend on the morphology. This is indeed appreciated in the bottom panel of Figure 9. All galaxies show a negative gradient of $\nabla\Sigma_* \sim -0.5$ dex. However, there are clear variations with the morphology, with shallower gradients for both the earliest (E/S0) and latest (Sc/Sd) morphological bins, but strongly modulated by the stellar mass. In general, the most massive Sb (and to a lesser extent Sbc) galaxies are those presenting the steeper gradients. Similar results were reported by González Delgado et al. (2014) and reviewed in Sánchez (2020).

It is worth noticing that the most massive E-type galaxies are not the ones with the largest $\Sigma_{*,e}$. This is a consequence of these galaxies not following a single exponential profile (or log-linear relation) such as the one shown here (i.e. they show cores). For them the parameterization adopted here is too simple. Finally, it is important to highlight that not all galaxy types are equally well represented in each mass bin, and therefore the results are not equally significant. In particular, the results for late-type galaxies in the more massive bins and for early-type ones in the less massive bins should be taken with care.

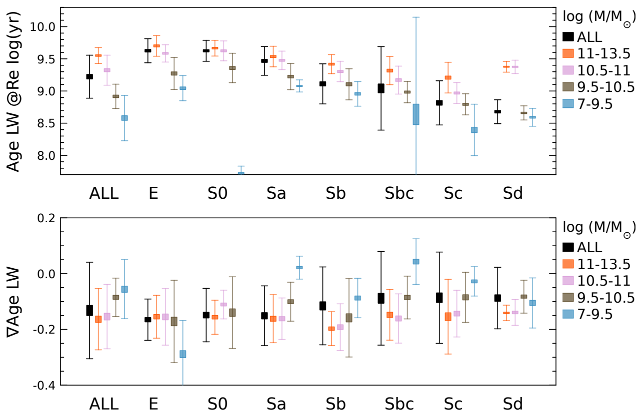

Fig. 10. Same as Figure 9, but for the luminosity-weighted ages of the stellar populations. The color figure can be viewed online.

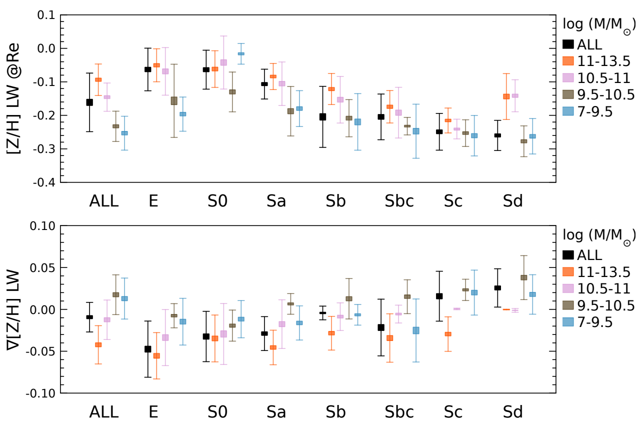

Fig. 11. Same as Figure 9, but for the luminosity-weighted stellar metallicity. The color figure can be viewed online.

Age and metallicity gradients: Figure 10 and 11 show the distributions of the luminosity weighted (LW) characteristic ages and metallicities of the stellar populations together with the slope of the radial gradients. For both parameters similar trends are found, with earlier and more massive galaxies showing older (Age_e ≈5 Gyr) and more metal rich ($[Z/H]_e \approx -0.05$ dex) stellar populations, with more pronounced negative gradients in both explored quantities: $\nabla_{Age} \approx -0.2$ dex/r and $\nabla_{[Z/H]} \approx -0.04$ dex/r. On the other hand, later and less massive galaxies have younger ($Age_e \approx 0.3$ Gyr) and more metal poor ($[Z/H]_e \approx -0.3$ dex) stellar populations, with shallower age gradients and even flat or positive metallicity gradients: $\nabla_{Age} \approx -0.1$ dex/r and $\nabla_{[Z/H]} \approx 0.02$ dex/r. As reviewed by Sánchez (2020) this has been interpreted as a clear evidence of (i) average inside-out growth of galaxies, which is more pronounced in more massive and earlier types, and (ii) a change in

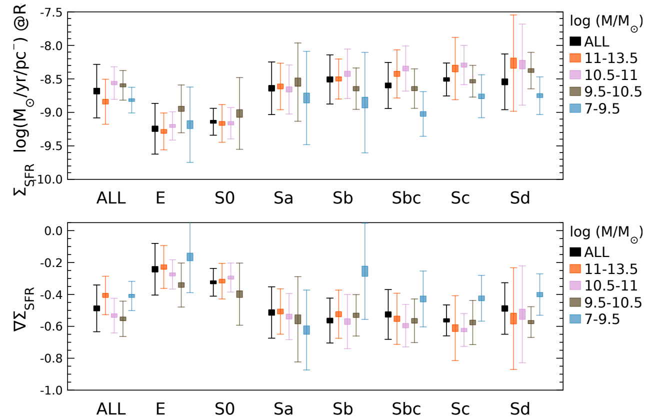

Fig. 12. Same as Figure 9, but for the star-formation rate surface density Σ_{SFR}. The color figure can be viewed online.

the SFHs and ChEHs from earlier to later types, with the first ones showing a sharper evolution with a stronger enrichment in earlier times and the latter ones having a smoother evolution with ongoing enrichment processes. Similar trends are found for the mass weighted ages and metallicities, although covering a narrower dynamical range in the described parameters. We do not reproduce here to avoid repetition, although we provide the corresponding measurements in the tables available for distribution.

Star-formation density gradients: Figure 12 shows the distribution of characteristic values and gradient slopes of the star-formation surface densities for the different morphological and stellar mass bins. As expected, early type galaxies (E/S0) show lower $\Sigma_{SFR,e}$ ($\approx 10^{-9.5} M_\odot \mathrm{yr}^{-1}$ pc^{-2}) at any stellar mass than late type ones ($\approx 10^{-8.3} M_\odot \mathrm{yr}^{-1}$ pc^{-2}). For SFGs there is a clear trend between Σ_{SFR} and stellar mass, which is a consequence of the existence of an rSFMS, as described in § 5, and the relation between $\Sigma_{*,Re}$ and M_* (e.g. García-Benito et al. 2017). On the other hand, earlier galaxies show shallower negative radial gradient in Σ_{SFR} ($\nabla_{\Sigma_{SFR}} \approx -0.2$ dex/r) than later ones ($\nabla_{\Sigma_{SFR}} \approx -0.5$ dex/r). This trend is also observed for the mass, from more massive to less massive galaxies, at least for E, S0 and Sa galaxies. This indicates that in these galaxies the SFR is not as uniformly distributed in the central regions as in the case of later and less massive galaxies. This is clearly a consequence of the presence of a bulge dominated by retired areas that do not form stars. The trend with the mass is inverted for later type galaxies (Sb to Sd), which indicates that in these galaxies there is a mild increase of the SFR in the outer regions (with $\nabla_{\Sigma_{SFR}}$ rising from -0.5 to -0.4 dex/r). This reinforces the idea that low-mass galax-

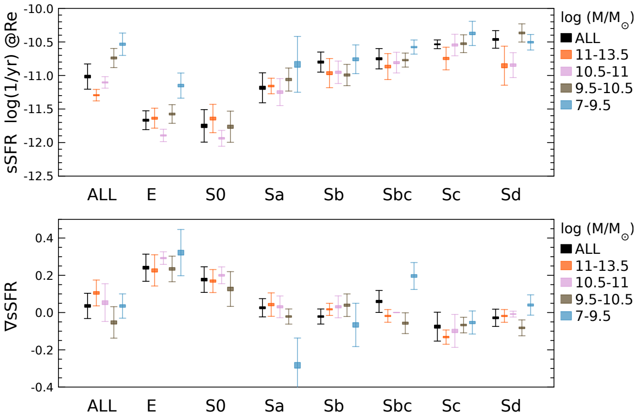

Fig. 13. Same as Figure 9, but for the specific star-formation rate. The color figure can be viewed online.

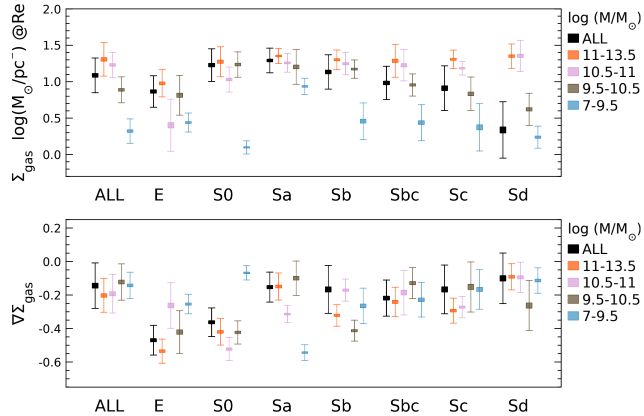

Fig. 14. Same as Figure 9, but for the molecular gas mass surface density Σ_{gas}. The color figure can be viewed online.

ies may show a less strong inside-out evolution (which was shown in the stellar metallicity gradients too).

Similar trends are reported for the radial distribution of the specific star-formation rate, as shown in Figure 13, with clearer and sharper distributions as a consequence of the combination of Σ_{SFR} with Σ_* (as sSFR is the ratio of both quantities). Due to that the sSFR presents a sharp segregation by morphology, with most massive early type galaxies showing the lowest characteristic values (sSFR$_e$ $\approx$$10^{-11.75}$ yr^{-1}), and a clear increase for later and less massive galaxies, rising up to sSFR$_e$ $\approx$$10^{-10.5}$yr^{-1} for the less massive Sd galaxies. The average radial gradient slope for the full sample is almost zero. However, there is a strong morphology and stellar mass segregation, with positive gradients for early-type galaxies ($\nabla_{\rm sSFR}$ $\approx$0.2 dex/r) and shallow and slightly negative gradients for the latest type ones ($\nabla_{\rm sSFR}$ $\approx$ -0.02 dex/r). These trends indicate that the SFR relative to the stellar mass (which measures the sSFR) is stronger in the outer regions of early-type galaxies than in their inner regions (e.g. González Delgado et al. 2016), as a consequence of both very low SFR in the inner regions and either an inside-out dimming or a rejuvenation due to the capture of gas rich galaxies in the outer regions of those galaxies (e.g. Gomes et al. 2016b). On the contrary, for late-type galaxies SF happens at a relatively similar rate with respect to the underlying stellar mass, which is again a direct consequence of the already discussed rSFMS relation (e.g. Cano-Díaz et al. 2016). The mild but significant differences with morphology in the gradients indicate that galaxies slightly deviate from the average rSFMS with a pattern showing that later type ones are located above the average and earlier spirals below, as discussed in González Delgado et al. (2016) and Cano-Díaz et al. (2019), and shown in the previous section.

Similar results are found when other estimators for the SFR are adopted. In particular, in the case of the SFR derived using the stellar population analysis described in § 3.1 the results are totally compatible with those described here. We provide the corresponding measurements in the distributed tables, although no figures are provided to avoid repetition.

Gas density gradients: Figure 14 includes the distributions of the characteristic values and the radial gradients for the molecular gas mass surface density for the considered sub-samples. We should stress out that this derivation was obtained based on the dust-to-gas calibrator presented in Barrera-Ballesteros et al. (2019) (as described in § 3.2). Like in the previous properties, there are clear trends, with more massive galaxies showing more gas (Σ_{gas} $\approx$ $1.2M_\odot$ pc^{-2}) than less massive ones (Σ_{gas} $\approx$ $0.2M_\odot$ pc^{-2}. Regarding morphology, elliptical galaxies have a clear gas deficit compared to other early type galaxies (S0) or early-spirals (Sa, Sb), for any mass, and for the more massive ones they show this deficit compared to any other galaxy of any later morphology. On average, gas density decreases from earlier to later type galaxies (besides the described trend for pure elliptical galaxies), from (Σ_{gas} $\approx$ $1.2M_\odot$ pc^{-2}) to (Σ_{gas} $\approx$ $0.5M_\odot$ pc^{-2}). This trend is enhanced by a similar one observed for mass, with more massive galaxies having larger amounts of gas than less massive ones. This trend is a clear consequence of the MGMS and rMGMS relations described for SFGs between M_{gas} (Σ_{gas}) and M_* (Σ_*) by different authors (e.g., Saintonge et al. 2016; Calette et al. 2018; Lin et al. 2019; Barrera-Ballesteros et al. 2019), and discussed in § 5. The clear morphological segregation reinforces the results, indicating that the rMGMS do not present a universal shape, as seen in Figure 8 and discussed in § 5.2.

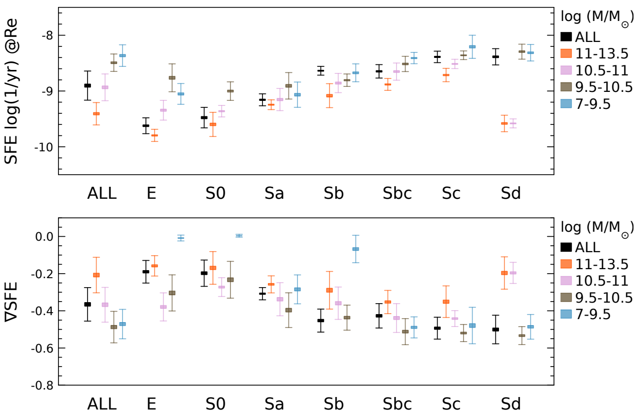

Fig. 15. Same as Figure 9, but for the star-formation efficiency. The color figure can be viewed online.

Regarding the slope of the radial gradient, the trends are more complicated than the ones described so far. On average, when all morphologies are included, the slope for late type galaxies is almost constant $\nabla_{\Sigma_{gas}} \approx -0.15$ dex/r, without a clear trend with stellar mass. However, early type galaxies show a sharp negative gradient ($\nabla_{\Sigma_{gas}} \approx -0.5$ dex/r. Furthermore, for each morphology the modulation is different: (i) less massive elliptical galaxies have less steep negative gradients than those with higher masses; (ii) S0 have shallow negative gradients for the lowest stellar mass ranges; (iii) Sa and Sb have the stronger negative gradients for the lower masses; and, finally, (iv) the latest spirals have almost the same gradient, independently of their stellar masses.

In general these results indicate that RGs have a global lack of molecular gas, as discussed by Saintonge et al. (2016) and Sánchez et al. (2018). Furthermore, they show a deficit that is stronger in the inner regions than in the outer ones, which suggests that the inside-out quenching process (e.g. González Delgado et al. 2016; Belfiore et al. 2017b), is driven also by a lack of gas. The fact that quenching seems to be connected with the presence of a central (active) massive black-hole has been frequently proposed in the literature (e.g. Hopkins et al. 2010). Recently explorations using spatially resolved IFS data support this scenario (e.g. Bluck et al. 2019), suggesting that AGN are related with inside-out quenching and the removal (or heating) of gas which is thus prevented from settling as molecular clouds. However, there is no general consensus in this regard, since other recent contributions (e.g. Ellison et al. 2020) indicate that star-formation efficiency could be the primary driver for halting of the SF rather than a real lack of gas. We should be cautious in this regards since most estimations of the spatially resolved molecular gas density, based on CO observations, are biased towards late-type galaxies (e.g., EDGE, ALMAQUEST, Bolatto et al. 2017; Lin et al. 2019), while the current estimations, although indirect, also cover early-types (in particular pure ellipticals), where the strongest drop in Σ_{gas} is reported. This unsettled result highlights the need for a large CO mapping survey over an unbiased sample already covered by an IFS-GS with a similar spatial resolution (and deep enough) to shed light on this fundamental question.

Star-formation efficiency gradients: Figure 15 shows similar plots as the ones described before for the star-formation efficiency (SFE=$\Sigma_{SFR}/\Sigma_{gas}$), i.e., the inverse of the depletion time τ_{dep}. The average value found for all galaxies is SFE$\approx 10^{-9}$ yr^{-1}, thus, $\tau_{dep} \approx 1$ Gyr), a value slightly lower than the typical value reported of $\approx$2 Gyr in other studies using *direct* gas estimations based on CO observations (e.g. Bolatto et al. 2017; Utomo et al. 2017; Colombo et al. 2018). This difference is most probably due to a zero-point effect in the adopted dust-to-gas calibration (see Table 5. Despite this offset, as reviewed in Sánchez (2020), the trends with mass and morphology are similar to the ones described in the literature (e.g. Colombo et al. 2018): earliest and most massive galaxies have lower values of SFE$\approx 10^{-9.8}$ yr^{-1} (larger $\tau_{dep} \approx 6$ Gyr) than later-type one, with values as high as SFE$\approx 10^{-8.25}$ yr^{-1} (i.e., lower $\tau_{dep} \approx 0.2$ Gyr).

In addition to this global dependence with galaxy mass and morphology, there are also evident radial differences. On average the SFE presents a gradient with a negative slope of $\nabla_{SFE} \approx$-0.4 dex/r. However, the gradient is shallower, the more massive and earlier is a galaxy (∇_{SFE}−0.2 dex/r), and steeper the less massive and later type it is (∇_{SFE}−0.5 dex/r). There are some significant outliers in this trend, which correspond to galaxy subgroups with a very small number of galaxies in our sample (such as low mass early-types). In summary, as indicated by different studies there is no single SFE (τ_{dep}) among galaxies and within galaxies. Different scenarios to explain this variation that affects in different way galaxies of different masses, morphologies and galactocentric distances have been proposed: (i) the effect of the orbital or dynamical time (τ_{dyn}), that relates the gravitational instability (e.g., spiral arms) with an increase in the SFE (Silk 1997; Elmegreen 1997); (ii) the self-regulation of the star-formation which increases the local velocity dispersion (e.g. the local pressure) and decreases the SFE (Silk 1997); (iii) the stabilization of molecular clouds which decreases the SFE (or even quenches the SF) due to the presence of warm/hot orbits associated with a bulge (Martig et al. 2009); (iv) the differential/local gravitational potential that may affect the SFE (e.g. Saintonge et al. 2011) ; (v) the metal content of the ISM that affects the cooling; or (vi) a combination of all of them (e.g. Dey et al. 2019).

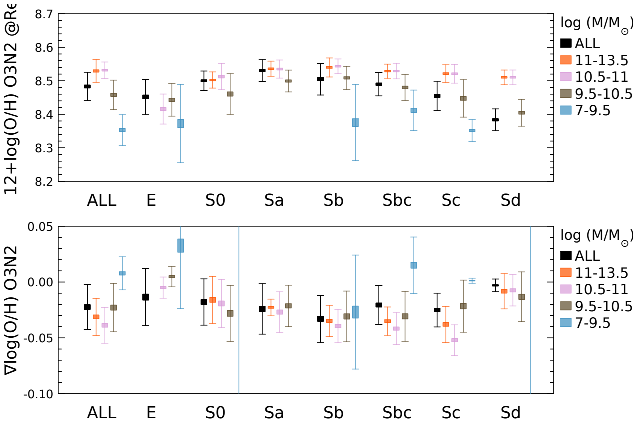

Fig. 16. Same as Figure 9, but for the gas phase oxygen abundance derived using the O3N2 calibrator. The color figure can be viewed online.

Oxygen abundance gradients: Figure 16 shows the distribution of the characteristic oxygen abundance and the slope of the corresponding radial gradient for the different stellar masses and morphologies explored in this section. We adopted the O3N2 calibrator proposed by Marino et al. (2013), which imposes certain restrictions/biases regarding the absolute values of the abundances and the range of values covered with each galaxy (see Kewley & Ellison 2008; Sánchez et al. 2019b). However most of the qualitative results are independent of the adopted calibrator (in particular regarding the abundance gradient, e.g. Sánchez-Menguiano et al. 2016, 2018). Another caveat to note is that oxygen abundance is only derived for those galaxies that have SF ionized regions populating the explored spatial range densely enough to derive a reliable gradient. Therefore, the numbers of galaxies in the earliest-type subgroups are really small.

On average, galaxies in the nearby Universe have an oxygen abundance of 12+log(O/H)≈8.5 dex. However, this is strongly modulated by the stellar mass due to the well known MZR (Tremonti et al. 2004), and the resolved version discussed in § 5. The most massive galaxies show a plateau in the oxygen abundance around ≈8.5 dex, while the less massive ones have values as low as ≈8.3 dex. We remind the reader that the actual absolute values may change from calibrator to calibrator. Furthermore, a trend with morphology is apparent. However, in most of the cases the abundance is very similar among galaxies of the same mass, despite their morphology. Thus, the morphology trend seems to be induced by the mass-morphology and MZR relations, rather than being a real secondary trend. Only for the less massive and latest type galaxies is there some appreciable difference induced by the morphology and not only by the stellar mass.

Regarding the abundance gradient, it was reported that late-type galaxies of mass $M_* > 10^{9.5} M_\odot$ have a very similar value for their slope (Sánchez et al. 2013), which for the explored calibrator in that study has a value of $\nabla_{\log(O/H)} \approx -0.1$ dex/r. This result was confirmed by more recent explorations based on different datasets (e.g. Sánchez-Menguiano et al. 2016, 2018). At lower stellar masses the abundance gradient becomes shallower (e.g. Belfiore et al. 2017b). In general these results are reproduced in Figure 16, although with a different characteristic abundance gradient, namely $\nabla_{\log(O/H)} \approx -0.03$ dex (due to the use of a different calibrator). Little to no morphology dependence is appreciated in the average slope (when all masses are considered), from E to Sc galaxies. A significantly shallower slope is detected only for Sd galaxies, with a slope near to zero. Curiously, the reported mass dependence seems to be present only when the latest type galaxies (Sc and Sd) are considered, and for elliptical galaxies (a very limited number of objects). Therefore, it is not clear if the reported mass dependency is actually due to the mass or to the morphology, an issue that should be explored in more detail in the future.

7. DISCUSSION AND CONCLUSIONS

In this manuscript we have reviewed the most recent results based on IFS extracted from recent galaxy surveys following Sánchez (2020), but including additional details that clarify some of the conclusions presented in that review. We made use of the large collection of galaxies observed with IFS selected for the previous study. All of them were analyzed using the same tool (Pipe3D, Sánchez et al. 2016b), in order to homogenize as much as possible the compiled data. Based on those parameters we explored different spatially resolved and integrated properties of galaxies.

First, we explore the local/resolved nature of the dominant ionization processes in galaxies. Based on this analysis we demonstrate that the use of integrated or aperture limited parameters of the emission lines (line flux intensities and ratios) may produce significant errors in the interpretation of the ionizing sources in galaxies. We show the main trends of the integrated and resolved line ratios with galaxy morphology and masses, illustrating them in detail with a few galaxies observed with the IFU which provides the best spatial resolution so far for a wide FoV (i.e. MUSE). Based on that analysis we update the practical scheme presented in Sánchez (2020) to classify the ionization sources at the spatial resolution considered in this review (∼1 kpc). Our main conclusion is that the location within the classical diagnostic diagrams is not enough to distinguish between the dominant ionizing sources in galaxies. The inclusion of a third parameter, like the EW(Hα), partially mitigates the intrinsic degeneracy in the observed line ratios. The additional use of (i) the knowledge of the composition of the underlying stellar population, (ii) the spatial distribution and shape of the ionized gas, and (iii) a knowledge of the gas kinematics, substantially improves our ability to distinguish between different ionizing sources. However, all this is hampered by the spatial and spectral resolution of the adopted data.

Then, we explore in a more quantitative way the global and local relations that seem to result from the star-formation processes in galaxies (and regions within galaxies) already reviewed in Sánchez (2020): the SFMS, MGMS, SK and MZR relations. We revisit the most recent results in this regard and re-evaluate them using our extensive dataset. The main conclusions of this exploration are that: (i) there are resolved/local versions of the global relations which are verified at kiloparsec scales for SFAs; (ii) those relations are similar in shape to global ones. This is particularly true for the intensive versions of those relations, which totally overlap the resolved/local ones; (iii) global and local relations are verified for star-forming galaxies (and areas/regions within galaxies), but not for retired galaxies (areas). Thus, these relations are tightly related to the star-formation activity. Retired galaxies (areas) follow different trends, which show more lose relations or clouds; (iv) global and local relations are not fully universal: i.e., they are similar but not exactly the same for different galaxy types and stellar masses; (iv) global relations can be derived from local ones with fewer assumptions than the other way around. Indeed, just considering that more massive galaxies are in general more extended (i.e. the existence of a M_*-R_e relation), the existence of a local relation implies the presence of a global one. The contrary is not true: i.e. it is possible to have global relations without the need for local ones.

All these results suggest that local relations have a physical prevalence over global ones, and that the star-formation is governed by processes that leave clear imprints at kiloparsec scales rather than galaxy- wide. In fact, these processes are likely originated at much smaller scales. They involve most probably the self-regulation introduced by the feedback that modulates the gravitationally driven trend of molecular clouds to collapse and form new stars. The rSFMS and rSK relations, and the dispersion around them, are most probably the result of the bouncing effect of those two processes working one against each other. In this way, the MGMS relation would highlight the ability of the local gravitational potential to hold both components bound to the system. Under this interpretation it is naturally explained that the rSFMS and rMGMS evolve along cosmic times: (i) galaxies (and regions within them) in the past have higher SFRs at a given M* (or Σ_*) and (ii) galaxies (and regions within them) have larger amounts of molecular gas. The expected evolution is demonstrated for the rSFMS just by comparing the relation reported at $z \approx 0$ (Sánchez et al. 2013) with the one reported at $z \approx 0.7$ (Wuyts et al. 2013), showing an evolution similar to the one found for the SFMS (e.g. Speagle et al. 2014). Under this scenario the rSK (SK) relation should show a weaker evolution along cosmological times. The same scenario would explain the morphological segregation of the rSFMS and MGMS relations, since later-type galaxies (and SFAs within them) would show a smoother evolution of the rSFMS as a consequence of a smoother star-formation history (e.g. López Fernández et al. 2018).

In this way the dependence (or modulation) of local/resolved relations on global properties of galaxies is naturally explained. The dynamical stage of a galaxy influences the way the star formation happens (or is halted) in different locations, modifying the local relations. The presence of a bulge seems to stabilize the molecular clouds (Martig et al. 2009) and it would be the reason behind the morphological segregation of the SFMS (Catalán-Torrecilla et al. 2017, e.g.) and rSFMS (e.g. González Delgado et al. 2016; Cano-Díaz et al. 2019). On the contrary, local effects, like the over-pressure produced by the passage of a spiral arm, may enhance the SFR locally, producing local fluctuations in the local relations (e.g. Sánchez-Menguiano et al. 2017, 2019). Another interpretation is that the SFMS (and the rSFMS) holds only for the disk (or regions within disks) of galaxies (regions with cold orbits), and the morphological segregation is a consequence of the increase of M_* (Σ_*) due to the inclusion of stars in warm/hot orbits. This is supported by the recent results by Méndez-Abreu et al. (2019), which show that SFMS holds for the disk component of galaxies once they are spatially decomposed.

Additional global processes, like galactic winds or the presence of an AGN can alter those relations. Physically, it is known that galaxy-wide winds are important for setting galaxy metallicities and even baryonic fractions. In particular, galactic winds are usually claimed to be responsible for the shape of the MZR. The linear rising phase of this relation, observed at $M_* < 10^{10} M_\odot$, is easily interpreted as a natural consequence of the internal enrichment processes in galaxies (e.g. Pilyugin et al. 2007). However, the flat regime at high mass requires a certain amount of gas inflow/outflow, or a dependence of the IMF on the metallicity (as reported by Martín-Navarro et al. 2015), with galaxies exhibiting an equilibrium between the inflow of pristine gas, the internal enrichment, and the outflow of metal rich material (e.g. Tremonti et al. 2004; Belfiore et al. 2016). The same scenario could explain the rMZR. Outflows and inflows may produce a differential effect between the central and the outer regions in galaxies. Recent explorations indicate that outflows are indeed needed to shape the rMZR (e.g. Barrera-Ballesteros et al. 2018), when considered as local effects, not as global ones. However, gas leaking has to be compensated by gas accretion (e.g. Sánchez Almeida & Sánchez-Menguiano 2019), which seems to have a much stronger influence on the flattening of the rMZR than outflows (Figure 11 Barrera-Ballesteros et al. 2018). Once the rMZR is shaped, the global MZR emerges as pure integral, as demonstrated in § 5.

On the other hand, it seems that AGN may be more relevant in the quenching of star-formation activity. The energy injection by these powerful sources is the primary candidate to explain the halt of star formation either by removal or heating of gas (e.g. Hopkins et al. 2010). The location of AGN hosts in the green valley region of galaxies in different diagrams (like the CMD or the SFR-M_*), reinforces this perception (e.g. Kauffmann et al. 2003; Sánchez et al. 2004; Schawinski et al. 2014; Lacerda et al. 2020). Nevertheless, quenching is not an instantaneous and coherent process galaxy-wide. It is a local process too, evolving from the inside out (González Delgado et al. 2016; Belfiore et al. 2017a), with AGN hosts being in transition between SFGs and RGs in this regard too (Sánchez et al. 2018). Recent explorations suggest that the presence of a central massive black hole is directly connected with the global and local quenching (Bluck et al. 2019). Thus, again, although the presence of an AGN could be considered as a global process, its effects in the processes and relations are local.

Finally, to be efficient, both processes, galactic winds and AGN, require that the injected kinetic energy equals or exceeds the local escape velocity. For this reason their effect was much stronger in earlier cosmological times, when galaxies were less massive, had larger SFRs, and hosted AGN more frequently. Maybe for this reason their effect seems less evident in the relations and patterns explored in this review, which correspond to those of nearby galaxies. For instance, the metal redistribution usually associated with galactic outflows should have a limited effect in todayÂ´s massive galaxies. It is known that massive galaxies exhibit a strong metal enrichment in their early cosmological times (e.g. Vale Asari et al. 2009; Walcher et al. 2015, Camps-Fariña in prep.), in agreement with their known SFHs (e.g. Panter et al. 2007; Thomas et al. 2010). At the same time, they show oxygen abundances (e.g. Sánchez et al. 2013) and stellar metallicity gradients (e.g. González Delgado et al. 2014) that agree with a local downsizing and inside-out growth (e.g. Pérez et al. 2013b). The gradients in their stellar and ionized gas properties, like the ones explored in § 6, are therefore a fossil record of the early evolutionary phases in galaxies. Thus, even in the period of more violent SFRs, and therefore stronger and more frequent outflows, the metal redistribution induced was not strong enough to blur the observed gradient. It is expected that nowadays, when outflows are more scarce and less energetic (Ho et al. 2018; López-Cobá et al. 2019, 2020), their effect is even less prevalent in this regard, at least for massive galaxies.

On the other hand, low mass and late-type galaxies could be more strongly affected by SF driven outflows. Their SFHs, global or resolved, show a smoother cosmological evolution, being still in the rising phase for the lowest mass and latest type galaxies (e.g. López Fernández et al. 2018), with smaller inside-out differences. As a consequence, in those galaxies the signatures of inside-out formation (e.g. radial gradients in the explored properties, § 6), are less evident. This is particularly true for the oxygen abundance and stellar metallicity distributions. As already discussed in Sánchez (2020) those galaxies exhibit a flat or even inverse gradient in these properties, even potentially implying an outside-in growth phase. In general, it can be considered that their overall evolution is delayed with respect to that of more massive galaxies with earlier morphological types.

The influence of galaxy environment on the evolution of galaxies and the observed global and local patterns has been very little discussed in this review (and in Sánchez 2020). The main reason is that galaxy samples currently observed by IFS-GS are still not large enough, or will require a more detailed reevaluation to distinguish the environmental effects. In this regard, the results of the SAMI project (which has by design a large sub-sample of cluster galaxies) and the GASP survey (Poggianti et al. 2017, which explores the gas stripping in galaxies entering into clusters), would be of a particular importance. The comparison between the properties of field and cluster members, or central and satellite galaxies, in large samples, like the one provided by MaNGA, would also provide more insight on this particular problem. However, the current number of these analyses is too limited and they are too recent to make firm conclusions in this regard.

In summary, we review here our current understanding of the interconnection between the local and global properties of the ionized gas and stellar populations in galaxies in the nearby universe. In particular, we discuss the ionization processes and the star formation and metal enrichment cycle in galaxies. The main conclusion, in the same line as the ones presented in Sánchez (2020), is that these processes are governed mostly by local physical processes which are modulated by global ones. Whether the influence of those global properties is through local ones or not would be a matter of exploration for the next years.

We acknowledge the anonymous referee for reading this manuscript and helping us to improve its content.

We thank the sharing of ideas with the IA-MaNGA team, in particular with Prof. V. Avila-Reese, and the help with the morphological analysis of the MaNGA dataset by Dr. H. Hernandez-Toledo. The enthusiasm and hard work of Dr. H. Ibarra-Medel and Dr. Mariana Cano Diaz is acknowledged.

We are grateful for the support of CONACYT grants CB-285080 and FC-2016-01-1916, and funding from the PAPIIT-DGAPA-IN100519 (UNAM) project.

J.K.B-B acknowledges support from grant IA-100420 (DGAPA-PAPIIT ,UNAM).

Part of this research was conducted by the Australian Research Council Centre of Excellence for All Sky Astrophysics in 3 Dimensions (ASTRO 3D), through project number CE170100013.

The SAMI Galaxy Survey is based on observations made at the Anglo-Australian Telescope. The Sydney-AAO Multi-object Integral field spectrograph (SAMI) was developed jointly by the University of Sydney and the Australian Astronomical Observatory. The SAMI input catalogue is based on data taken from the Sloan Digital Sky Survey, the GAMA Survey and the VST ATLAS Survey. The SAMI Galaxy Survey is supported by the Australian Research Council Centre of Excellence for All Sky Astrophysics in 3 Dimensions (ASTRO 3D), through project number CE170100013, the Australian Research Council Centre of Excellence for All-sky Astrophysics (CAASTRO), through project number CE110001020, and other participating institutions. The SAMI Galaxy Survey website is http://sami-survey.org/.

This project makes use of the MaNGA-Pipe3D dataproducts. We thank the IA-UNAM MaNGA team for creating this catalogue, and the Conacyt-180125 project for support.

Funding for the Sloan Digital Sky Survey IV has been provided by the Alfred P. Sloan Foundation, the U.S. Department of Energy Office of Science, and the Participating Institutions. SDSS-IV acknowledges support and resources from the Center for High-Performance Computing at the University of Utah. The SDSS web site is www.sdss.org.

SDSS-IV is managed by the Astrophysical Research Consortium for the Participating Institutions of the SDSS Collaboration including the Brazilian Participation Group, the Carnegie Institution for Science, Carnegie Mellon University, the Chilean Participation Group, the French Participation Group, Harvard-Smithsonian Center for Astrophysics, Instituto de Astrofísica de Canarias, The Johns Hopkins University, Kavli Institute for the Physics and Mathematics of the Universe (IPMU) / University of Tokyo, Lawrence Berkeley National Laboratory, Leibniz Institut für Astrophysik Potsdam (AIP), Max-Planck-Institut für Astronomie (MPIA Heidelberg), Max-Planck-Institut für Astrophysik (MPA Garching), Max-Planck-Institut für Extraterrestrische Physik (MPE), National Astronomical Observatories of China, New Mexico State University, New York University, University of Notre Dame, Observatário Nacional / MCTI, The Ohio State University, Pennsylvania State University, Shanghai Astronomical Observatory, United Kingdom Participation Group, Universidad Nacional Autónoma de México, University of Arizona, University of Colorado Boulder, University of Oxford, University of Portsmouth, University of Utah, University of Virginia, University of Washington, University of Wisconsin, Vanderbilt University, and Yale University.

This study uses data provided by the Calar Alto Legacy Integral Field Area (CALIFA) survey (http://califa.caha.es/).

Based on observations collected at the Centro Astronómico Hispano Alemán (CAHA) at Calar Alto, operated jointly by the Max-Planck-Institut fur Astronomie and the Instituto de Astrofísica de Andalucía (CSIC).

REFERENCES

Abazajian, K. N., Adelman-McCarthy, J. K., Agüeros, M. A., et al. 2009, ApJS, 182, 543

Bakos, J., Trujillo, I., & Pohlen, M. 2008, ApJ, 683, 103

Baldwin, J. A., Phillips, M. M., & Terlevich, R. 1981a, PASP, 93, 5

_________. 1981b, PASP, 93, 5

Balmaverde, B., Capetti, A., Marconi, A., & Venturi, G. 2018, A&A, 612, 19

Balogh, M. L., Baldry, I. K., Nichol, R., et al. 2004, ApJ, 615, 101

Barrera-Ballesteros, J. K., Heckman, T. M., Sánchez, S. F., et al. 2018, ApJ, 852, 74

Barrera-Ballesteros, J. K., Heckman, T. M., Zhu, G. B., et al. 2016, MNRAS, 463, 2513

Barrera-Ballesteros, J. K., Utomo, D., Bolatto, A. D., et al. 2019, arXiv e-prints, arXiv:1911.09677

_________. 2020, MNRAS, 492, 2651

Barrera-Ballesteros, J. K., Heckman, T., Sanchez, S. F., et al. 2021, arXiv eprint, arXiv:2101.02711

Bate, M. R. & Bonnell, I. A. 2005, MNRAS, 356, 1201

Belfiore, F., Maiolino, R., & Bothwell, M. 2016, MNRAS, 455, 1218

Belfiore, F., Maiolino, R., Maraston, C., et al. 2017a, MNRAS, 466, 2570

Belfiore, F., Maiolino, R., Tremonti, C., et al. 2017b, MNRAS, 469, 151

Belfiore, F., Westfall, K. B., Schaefer, A., et al. 2019, AJ, 158, 160

Bigiel, F., Leroy, A., & Walter, F. 2011, IAUS, Computational Star Formation, ed. J. Alves, B. G. Elmegreen, J. M. Girart, & V. Trimble, (Cambridge, MA: CUP), 327
Bigiel, F., Leroy, A., Walter, F., et al. 2008, AJ, 136, 2846
Binette, L., Magris, C. G., Stasińska, G., & Bruzual, A. G. 1994, A&A, 292, 13
Bland-Hawthorn, J. 1995, PASA, 12, 190
Blanton, M. R. & Moustakas, J. 2009, ARA&A, 47, 159
Bluck, A. F. L., Maiolino, R., Sanchez, S., et al. 2019, arXiv e-prints, arXiv:1911.08857
Bolatto, A. D., Wong, T., Utomo, D., et al. 2017, ApJ, 846, 159
Bonnor, W. B. 1957, MNRAS, 117, 104
Bothwell, M. S., Maiolino, R., Kennicutt, R., et al. 2013, MNRAS, 433, 1425
Bradley, T. R., Knapen, J. H., Beckman, J. E., & Folkes, S. L. 2006, A&A, 459, 13
Brinchmann, J., Charlot, S., White, S. D. M., et al. 2004, MNRAS, 351, 1151
Bruzual, G. & Charlot, S. 2003, MNRAS, 344, 1000
Bundy, K., Bershady, M. A., Law, D. R., et al. 2015a, ApJ, 798, 7
__________. 2015b, ApJ, 798, 7
Calette, A. R., Avila-Reese, V., Rodríguez-Puebla, A., Hernández-Toledo, H., & Papastergis, E. 2018, RMxAA, 54, 443
Cano-Díaz, M., Ávila-Reese, V., Sánchez, S. F., et al. 2019, MNRAS, 488, 3929
Cano-Díaz, M., Sánchez, S. F., Zibetti, S., et al. 2016, ApJ, 821, 26
Cappellari, M. 2016, ARA&A, 54, 597
Cappellari, M., Emsellem, E., Krajnović, D., et al. 2011, MNRAS, 413, 813
Cardelli, J. A., Clayton, G. C., & Mathis, J. S. 1989, ApJ, 345, 245
Catalán-Torrecilla, C., Gil de Paz, A., Castillo-Morales, A., et al. 2015, A&A, 584, 87
Catalán-Torrecilla, C., Gil de Paz, A., Castillo-Morales, A., et al. 2017, ApJ, 848, 87
Chabrier, G. 2003, PASP, 115, 763
Cheung, E., Bundy, K., Cappellari, M., et al. 2016, Natur, 533, 504
Cid Fernandes, R., González Delgado, R. M., García Benito, R., et al. 2014, A&A, 561, 130
Cid Fernandes, R., Pérez, E., García Benito, R., et al. 2013, A&A, 557, 86
Cid Fernandes, R., Stasińska, G., Schlickmann, M. S., et al. 2010, MNRAS, 403, 1036
Coelho, P., Bruzual, G., Charlot, S., et al. 2007, MNRAS, 382, 498
Colombo, D., Kalinova, V., Utomo, D., et al. 2018, MNRAS, 475, 1791
Concas, A. & Popesso, P. 2019, MNRAS, 486, 91
Conroy, Ch. 2013, ARA&A, 51, 393
Conselice, C. J. 2006, MNRAS, 373, 1389
__________. 2012, arXiv e-prints, arXiv:1212.5641
Courteau, S., Cappellari, M., de Jong, R. S., et al. 2014, RvMP, 86, 47
Croom, S. M., Lawrence, J. S., Bland-Hawthorn, J., et al. 2012, MNRAS, 421, 872
Curtis, H. D. 1918, PASP, 30, 159
D'Agostino, J. J., Kewley, L. J., Groves, B. A., et al. 2019, MNRAS, 485, 38
Davies, R. L., Efstathiou, G., Fall, S. M., Illingworth, G., & Schechter, P. L. 1983, ApJ, 266, 41
Davies, R. L., Groves, B., Kewley, L. J., et al. 2016, MNRAS, 462, 1616
de Amorim, A. L., García-Benito, R., Cid Fernandes, R., et al. 2017, MNRAS, 471, 3727
Della Bruna, L., Adamo, A., Bik, A., et al. 2020, A&A, 635, 134
Dey, B., Rosolowsky, E., Cao, Y., et al. 2019, MNRAS, 488, 1926
Dopita, M. A. & Evans, I. N. 1986, ApJ, 307, 431
Dopita, M. A., Kewley, L. J., Heisler, C. A., & Sutherland, R. S. 2000, ApJ, 542, 224
Dopita, M. A., Koratkar, A. P., Evans, I. N., et al. 1996, ASPC 103, The Physics of Liners in View of Recent Observations, ed. M. Eracleous, A. Koratkar, C. Leitherer, & L. Ho, 44
Driver, S. P., Norberg, P., Baldry, I. K., et al. 2009, A&G, 50, 12
Ellison, S. L., Thorp, M. D., Lin, L., et al. 2020, MNRAS, 493, 39
Elmegreen, B. G. 1997, RMxAC, 6, 165
Espinosa-Ponce, C., Sánchez, S. F., Morisset, C., et al. 2020, MNRAS, 494, 1622
Evans, I. N. & Dopita, M. A. 1985, ApJS, 58, 125
Event Horizon Telescope Collaboration, Akiyama, K., Alberdi, A., et al. 2019, ApJ, 875, 1
Fesen, R. A. & Hurford, A. P. 1996, ApJS, 106, 563
Flores-Fajardo, N., Morisset, C., Stasińska, G., & Binette, L. 2011, MNRAS, 415, 2182
Ford, H. C., Harms, R. J., Tsvetanov, Z. I., et al. 1994, ApJ, 435, 27
Gadotti, D. A., Sánchez-Blázquez, P., Falcón-Barroso, J., et al. 2019, MNRAS, 482, 506
Galbany, L., Anderson, J. P., Rosales-Ortega, F. F., et al. 2016, MNRAS, 455, 4087
Galbany, L., Anderson, J. P., Sánchez, S. F., et al. 2018, ApJ, 855, 107
Gao, Y., Wang, E., Kong, X., et al. 2018, ApJ, 868, 89
García-Benito, R., González Delgado, R. M., Pérez, E., et al. 2017, A&A, 608, 27
Gomes, J. M., Papaderos, P., Kehrig, C., et al. 2016a, A&A, 588, 68
Gomes, J. M., Papaderos, P., Vílchez, J. M., et al. 2016b, A&A, 585, 92
González Delgado, R. M., Cid Fernandes, R., Pérez, E., et al. 2016, A&A, 590, 44
González Delgado, R. M., Pérez, E., Cid Fernandes, R., & et al. 2014, A&A, 562, 47
Gu, Q., Melnick, J., Cid Fernandes, R., et al. 2006, MNRAS, 366, 480
Heckman, T. M., Armus, L., & Miley, G. K. 1990, ApJS, 74, 833

Ho, I.-T., Kewley, L. J., Dopita, M. A., et al. 2014, MNRAS, 444, 3894
Ho, I. T., Medling, A. M., Groves, B., et al. 2016, Ap&SS, 361, 280
Ho, I. T., Meidt, S. E., Kudritzki, R.-P., et al. 2018, A&A, 618, 64
Ho, L. C., Filippenko, A. V., & Sargent, W. L. W. 1997, ApJ, 487, 579
Hopkins, P. F., Bundy, K., Croton, D., et al. 2010, ApJ, 715, 202
Hsieh, B. C., Lin, L., Lin, J. H., et al. 2017, ApJ, 851, 24
Ibarra-Medel, H. J., Avila-Reese, V., Sánchez, S. F., González-Samaniego, A., & Rodríguez-Puebla, A. 2019, MNRAS, 483, 4525
Ibarra-Medel, H. J., Sánchez, S. F., Avila-Reese, V., et al. 2016, MNRAS, 463, 2799
Jarvis, B. J. 1990, A&A, 240, 8
Jeans, J. H. 1902, RSPTA, 199, 1
Kauffmann, G., Heckman, T. M., Tremonti, C., et al. 2003, MNRAS, 346, 1055
Kehrig, C., Monreal-Ibero, A., Papaderos, P., et al. 2012, A&A, 540, 11
Kennicutt, Jr. R. C. 1998, ARA&A, 36, 189
Kennicutt, Jr. R. C., Keel, W. C., & Blaha, C. A. 1989, AJ, 97, 1022
Kewley, L. J. & Dopita, M. A. 2002, ApJS, 142, 35
Kewley, L. J., Dopita, M. A., Sutherland, R. S., Heisler, C. A., & Trevena, J. 2001, ApJ, 556, 121
Kewley, L. J. & Ellison, S. L. 2008, ApJ, 681, 1183
Lacerda, E. A. D., Cid Fernandes, R., Couto, G. S., et al. 2018, MNRAS, 474, 3727
Lacerda, E. A. D., Sánchez, S. F., Cid Fernandes, R., et al. 2020, MNRAS, 492, 3073
Lanz, L., Hickox, R. C., Baloković, M., et al. 2019, ApJ, 870, 26
Levy, R. C., Bolatto, A. D., Teuben, P., et al. 2018, ApJ, 860, 92
Lin, L., Lin, J.-H., Hsu, C.-H., et al. 2017, ApJ, 837, 32
Lin, L., Pan, H.-A., Ellison, S. L., et al. 2019, arXiv e-prints, arXiv:1909.11243
López-Cobá, C., Sánchez, S. F., Anderson, J. P., et al. 2020, arXiv e-prints, arXiv:2002.09328
López-Cobá, C., Sánchez, S. F., Bland -Hawthorn, J., et al. 2019, MNRAS, 482, 4032
López Fernández, R., González Delgado, R. M., Pérez, E., et al. 2018, A&A, 615, 27
Low, C. & Lynden-Bell, D. 1976, MNRAS, 176, 367
Mannucci, F., Cresci, G., Maiolino, R., Marconi, A., & Gnerucci, A. 2010, MNRAS, 408, 2115
Maraston, C., Pforr, J., Renzini, A., et al. 2010, MNRAS, 407, 830
Marino, R. A., Gil de Paz, A., Sánchez, S. F., et al. 2016, A&A, 585, 47
Marino, R. A., Rosales-Ortega, F. F., Sánchez, S. F., et al. 2013, A&A, 559, 114
Martig, M., Bournaud, F., Teyssier, R., & Dekel, A. 2009, ApJ, 707, 250
Martín-Navarro, I., Vazdekis, A., La Barbera, F., et al. 2015, ApJ, 806, 31
Mast, D., Rosales-Ortega, F. F., Sánchez, S. F., et al. 2014, A&A, 561, 129
Meisenheimer, K., Roeser, H.-J., & Schloetelburg, M. 1996, A&A, 307, 61
Méndez-Abreu, J., Sánchez, S. F., & de Lorenzo-Cáceres, A. 2019, MNRAS, 488, 80
Monreal-Ibero, A., Vílchez, J. M., Walsh, J. R., & Muñoz-Tuñón, C. 2010, A&A, 517, 27
Morisset, C., Delgado-Inglada, G., Sánchez, S. F., et al. 2016, A&A, 594, 37
Nair, P. B. & Abraham, R. 2010, ApJS, 186, 427
Olivares, V., Salome, P., Combes, F., et al. 2019, A&A, 631, 22
Osterbrock, D. E. 1989, Astrophysics of gaseous nebulae and active galactic nuclei (University Science Books)
Pan, H.-A., Lin, L., Hsieh, B.-C., et al. 2018, ApJ, 854, 159
Panter, B., Jimenez, R., Heavens, A. F., & Charlot, S. 2007, MNRAS, 378, 1550
Papaderos, P., Gomes, J. M., Vílchez, J. M., et al. 2013, A&A, 555, 1
Peimbert, M. 1967, ApJ, 150, 825
Pérez, E., Cid Fernandes, R., González Delgado, R. M., et al. 2013a, ApJ, 764, 1
__________. 2013b, ApJ, 764, 1
Pilyugin, L. S., Thuan, T. X., & Vílchez, J. M. 2007, MNRAS, 376, 353
Poggianti, B. M., Moretti, A., Gullieuszik, M., et al. 2017, ApJ, 844, 48
Relaño, M., Kennicutt, Jr. R. C., Eldridge, J. J., Lee, J. C., & Verley, S. 2012, MNRAS, 423, 2933
Renzini, A. & Peng, Y.-j. 2015, ApJ, 801, 29
Rosales-Ortega, F. F., Sánchez, S. F., Iglesias-Páramo, J., et al. 2012a, ApJ, 756, 31
__________. 2012b, ApJ, 756, 31
Roy, N., Bundy, K., Cheung, E., & MaNGA Team. 2018a, AAS, 231, 250.46
Roy, N., Bundy, K., Cheung, E., et al. 2018b, ApJ, 869, 117
Rupke, D. S. N., Kewley, L. J., & Barnes, J. E. 2010, ApJ, 710, 156
Ryder, S. D. 1995, ApJ, 444, 610
Saintonge, A., Catinella, B., Cortese, L., et al. 2016, MNRAS, 462, 1749
Saintonge, A., Catinella, B., Tacconi, L. J., et al. 2017, ApJS, 233, 22
Saintonge, A., Kauffmann, G., Kramer, C., et al. 2011, MNRAS, 415, 32
Salpeter, E. E. 1955, ApJ, 121, 161
Sánchez, S. F. 2020, ARA&A, 58, 99S
Sánchez, S. F., Avila-Reese, V., Hernandez-Toledo, H., et al. 2018, RMxAA, 54, 217
Sánchez, S. F., Avila-Reese, V., Rodríguez-Puebla, A., et al. 2019a, MNRAS, 482, 1557
Sánchez, S. F., Barrera-Ballesteros, J. K., López-Cobá, C., et al. 2019b, MNRAS, 484, 3042
Sánchez, S. F., Barrera-Ballesteros, J. K., Sánchez-Menguiano, L., et al. 2017, MNRAS, 469, 2121

Sánchez, S. F., Jahnke, K., Wisotzki, L., et al. 2004, ApJ, 614, 586
Sánchez, S. F., Kennicutt, R. C., Gil de Paz, A., et al. 2012a, A&A, 538, 8
Sánchez, S. F., Pérez, E., Rosales-Ortega, F. F., et al. 2015, A&A, 574, 47
Sánchez, S. F., Pérez, E., Sánchez-Blázquez, P., et al. 2016a, RMxAA, 52, 171
Sánchez, S. F., Pérez, E., Sánchez-Blázquez, P., et al. 2016b, RMxAA, 52, 21
Sánchez, S. F., Rosales-Ortega, F. F., Iglesias-Páramo, J., et al. 2014, A&A, 563, 49
Sánchez, S. F., Rosales-Ortega, F. F., Jungwiert, B., et al. 2013, A&A, 554, 58
Sánchez, S. F., Rosales-Ortega, F. F., Marino, R. A., et al. 2012b, A&A, 546, 2
Sánchez Almeida, J. & Sánchez-Menguiano, L. 2019, ApJ, 878, 6
Sánchez-Blázquez, P., Peletier, R. F., Jiménez-Vicente, J., et al. 2006, MNRAS, 371, 703
Sánchez-Menguiano, L., Sánchez, S. F., Pérez, I., et al. 2016, A&A, 587, 70
Sánchez-Menguiano, L., Sánchez, S. F., Pérez, I., et al. 2017, arXiv e-prints, arXiv:1710.01188
__________. 2018, A&A, 609, 119
Sánchez-Menguiano, L., Sánchez Almeida, J., Muñoz-Tuñón, C., et al. 2019, ApJ, 882, 9
Sarzi, M., Shields, J. C., Schawinski, K., et al. 2010, MNRAS, 402, 2187
Schawinski, K., Urry, C. M., Simmons, B. D., et al. 2014, MNRAS, 440, 889
Schawinski, K., Urry, C. M., Virani, S., et al. 2010, ApJ, 711, 284
Searle, L. 1971, ApJ, 168, 327
Sharp, R. G. & Bland-Hawthorn, J. 2010, ApJ, 711, 818
Sharpless, S. 1959, ApJS, 4, 257
Silk, J. 1997, ApJ, 481, 703
Singh, R., van de Ven, G., Jahnke, K., et al. 2013a, A&A, 558, 43
__________. 2013b, A&A, 558, 43
Speagle, J. S., Steinhardt, C. L., Capak, P. L., & Silverman, J. D. 2014, ApJS, 214, 15
Stasińska, G. 2017, Cosmic Feast of the Elements, ed. C. Morisset, G. Delgado-Inglada, & J. García Rojas. Online at http:www.astroscu.unam.mx/CosmicFeast/presentaciones/proceedings, 37
Stasińska, G., Cid Fernandes, R., Mateus, A., Sodré, L., & Asari, N. V. 2006, MNRAS, 371, 972
Stasińska, G., Vale Asari, N., Cid Fernandes, R., et al. 2008, MNRAS, 391, 29
Thomas, D., Maraston, C., Schawinski, K., Sarzi, M., & Silk, J. 2010, MNRAS, 404, 1775
Trayford, J. W. & Schaye, J. 2019, MNRAS, 485, 5715
Tremonti, C. A., Heckman, T. M., Kauffmann, G., et al. 2004, ApJ, 613, 898
Truelove, J. K., Klein, R. I., McKee, C. F., et al. 1997, ApJ, 489, 179
Utomo, D., Bolatto, A. D., Wong, T., et al. 2017, ApJ, 849, 26
Vale Asari, N., Stasińska, G., Cid Fernandes, R., et al. 2009, MNRAS, 396, 71
Vale Asari, N., Stasińska, G., Morisset, C., & Cid Fernandes, R. 2016, MNRAS, 460, 1739
van der Kruit, P. C. 2001, ASPC 230, Galaxy Disks and Disk Galaxies, ed. J. G. Funes & E. M. Corsini (San Francisco, CA: ASPC), 119
van der Kruit, P. C. & Freeman, K. C. 2011, ARA&A, 49, 301
Veilleux, S., Kim, D.-C., Sanders, D. B., Mazzarella, J. M., & Soifer, B. T. 1995, ApJS, 98, 171
Veilleux, S. & Osterbrock, D. E. 1987, ApJS, 63, 295
Veilleux, S., Shopbell, P. L., & Miller, S. T. 2001, AJ, 121, 198
Vila-Costas, M. B. & Edmunds, M. G. 1992, MNRAS, 259, 121
Wake, D. A., Bundy, K., Diamond-Stanic, A. M., et al. 2017, AJ, 154, 86
Walcher, C. J., Coelho, P. R. T., Gallazzi, A., et al. 2015, A&A, 582, 46
Walcher, J., Groves, B., Budavári, T., & Dale, D. 2011, Ap&SS, 331, 1
Weilbacher, P. M., Monreal-Ibero, A., Verhamme, A., et al. 2018, A&A, 611, 95
Wuyts, S., Förster Schreiber, N. M., Nelson, E. J., et al. 2013, ApJ, 779, 135
York, D. G., Adelman, J., Anderson, J. E., Jr., et al. 2000, AJ, 120, 1579
Zhu, L., van den Bosch, R., van de Ven, G., et al. 2018, MNRAS, 473, 3000
Zurita, A., Rozas, M., & Beckman, J. E. 2000, A&A, 363, 9

J. K. Barrera-Ballesteros, A. Camps-Fariña, C. Espinosa-Ponce, C. Lopez-Cobá, A. Mejía-Narváez, & S. F. Sánchez: Instituto de Astronomía, Universidad Nacional Autonóma de México, A.P. 70-264, 04510, Ciudad de México, México (sfsanchez@astro.unam.mx).
C. J. Walcher: Leibniz-Institut für Astrophysik Potsdam (AIP), An der Sternwarte 16, D-14482 Potsdam, Germany.

Revista Mexicana de Astronomía y Astrofísica, **57**, 39–55 (2021)

https://doi.org/10.22201/ia.01851101p.2021.57.01.02

A PULSATING FLARE STAR IN THE NEW PLANETARY SYSTEM: KOI-258

E. Yoldaş and H. A. Dal

Department of Astronomy and Space Sciences, University of Ege, Bornova, 35100 İzmir, Turkey.

Received May 5 2020; accepted September 10 2020

ABSTRACT

We present findings about the nature of KOI-258. Its temperature was found to be 6500 ± 200 K from its spectrum, which also indicates that the target is a single main sequence star despite the existence of a radial velocity variation with a small amplitude. Ca II H, K lines indicate the existence of magnetic activity, though there is no remarkable excess or variation in the H_α line. We found 51 flares with a frequency of 0.00186 h^{-1}, whose plateau value is 0.659 s. Apart from the flares, we found 420 frequencies due to solar-like oscillations at out-of-eclipses. Removing these 420 frequencies, we demonstrated three different transits caused by three exo-planets. Their radii were found to be 2.33 $R_\oplus$ for the first planet, 0.53 $R_\oplus$ for the second one, and 1.15 $R_\oplus$ for the third planet. Consequently, KOI-258 is an oscillating, single, main sequence star, with in a planetary system and remarkable flare activity.

RESUMEN

Presentamos nuestros hallazgos sobre KOI-258. A partir de su espectro determinamos que su temperatura es 6500 ± 200 K. El espectro muestra que KOI-258 es una estrella sencilla de secuencia principal, pese a las pequeñas variaciones en su velocidad radial. Las líneas H y K del Ca II indican la existencia de actividad magnética, aunque no se observa un exceso o variaciones en la línea H_α. Encontramos 51 ráfagas con una frecuencia de 0.00186 h^{-1} y un valor plateau de 0.659 s. Además de las ráfagas, encontramos 420 frecuencias fuera de eclipses, debidas a oscilaciones tipo solar. Omitiendo estas 420 frecuencias, encontramos tres tránsitos distintos, debidos a tres exoplanetas. Sus radios son 2.33 $R_\oplus$, 0.53 $R_\oplus$, y 1.15 $R_\oplus$ para el primer, segundo y tercer exoplaneta, respectivamente.

Key Words: methods: statistical — planetary systems — stars: flare — techniques: photometric — techniques: spectroscopic

1. INTRODUCTION

In the last two decades, the space missions gave an incredible perspective to the astronomer desiring to understand the universe. One of the most efficient space missions is the Kepler Mission, which was originally aimed to find exo-planets (Borucki et al. 2010; Koch et al. 2010; Caldwell et al. 2010). The mission has reached the highest quality and sensitivity ever obtained in the photometry (Jenkins et al. 2010a,b). Consequently, the high quality data include many variable targets, such as new eclipsing binaries, discovered apart from the exo-planets (Slawson et al. 2011; Matijevič et al. 2012). Many of the newly discovered eclipsing binaries have chromospherically active components exhibiting frequent flares (Balona 2015), while some of them have pulsating components with several frequencies (Özdarcan & Dal 2017; Kamil & Dal 2017).

Although each system observed by the Kepler Mission is interesting, some, like KOI-258, are remarkable showing different characteristic features together, which make these targets difficult to interpret. As we list below in detail, there are some unresolved problems about KOI-258. It is still controversial whether KOI-258 is a binary system or not, as well as the reason for the sinusoidal variation seen at out-of-eclipses in its light curve. In the literature, it is established that the target exhibits clear flare activity. The flare activity makes KOI-258 an important target, but poses some problems. First of all, if the target is a single star, and if the sinusoidal variation is caused by a γ Doradus or δ Scuti type pulsation (Cunha et al. 2007; Aerts et al. 2010), the target should be located in the instability strip of the Hertzsprung-Russell diagram. In this case, the flare activity should come from another source in the same direction, according to the results of Dal & Evren (2011) and Dal (2012). This is because the observed flare activity level is higher for these stars. Secondly, if KOI-258 is a single star, the flare activity should be similar to that exhibited by UV Ceti type stars (Dal & Evren 2010, 2011). On the other hand, if KOI-258 is a binary system, the flare activity should be like those exhibited by the analogues of FL Lyr (Yoldaş & Dal 2016). According to these authors, although FL Lyr and its analogues exhibit flare activity, the activity behavior is clearly different from the UV Ceti type stars. In the literature there are many studies about these possibilities, but there is no absolute solution, which makes KOI-258 an important target to be studied.

In the literature, KOI-258 has been classified as an eclipsing binary system in several studies (Slawson et al. 2011; Coughlin et al. 2014; Armstrong et al. 2014). In these studies, the target is mentioned as KOI-258AB. However, KOI-258 has also been discussed as a single star in a planetary system by some authors (Borucki et al. 2011; Ford et al. 2012).

Originally, the target was listed as BD+48 2800 in the AGK3 Catalogue by Lacroute & Valbousquet (1975). KOI-258 was classified as a variable star with a period of 4.157476 day by Watson et al. (2006); Borucki et al. (2011). Considering the target as an eclipsing binary system, Armstrong et al. (2014) computed the temperature as 6549 K for the primary component, and as 5781 K for the secondary component. The $B-V$ colour index was listed as $0^{m}.42$ in the Hipparcos and Tycho Catalogues (Egret et al. 1992). The mass of the primary component was found to be 1.27 $M_{\odot}$, and its radius was found to be 1.53 $R_{\odot}$ by Burke et al. (2014), while the age was given as 0.61 Gyr by Walkowicz & Basri (2013). A semi-major axis was given as 0.054 AU by Borucki et al. (2011). In the latest studies the binarity nature of the target is still controversial. Depending on the Kepler data, Kirk et al. (2016) and Van Eylen et al. (2016) listed KOI-258 as an eclipsing binary, though the system is defined as a planetary candidate by Rowe et al. (2015); Baranec et al. (2016).

KOI-258 exhibits dominant flare activity (Balona 2015). The presence of flare activity makes the target an important object in this study. However, being a binary system is also important. This is because there are few eclipsing binaries with cool components which exhibit flare activity like UV Ceti stars.

Red dwarfs are very abundant in our Galaxy. They represent about 65% of the whole population of the galaxy, and 75% of them exhibit flare activity (Rodono 1986). Consequently, it appears that half of the galactic population exhibit frequent flare activity at different energy levels, which makes these targets important, because they affect the evolution of the galaxy due to their high rates of mass loss.

Flare events on a dMe star are generally explained by the classical theories for solar flares. Indeed, we know that the primary energy sources of the flare events are magnetic reconnection processes (Gershberg 2005; Hudson & Khan 1996). Unfortunately, there are still numerous problems waiting to be solved in the classical theory since the first flare was observed on the solar surface by R. C. Carrington and R. Hodgson (1859). For instance, nobody knows why the flare energy levels vary from one star to another of different spectral type. Like the flare energy, a similar variation is also observed for the mass loss rate for stars of different spectral types (Gershberg & Shakhovskaia 1983; Haisch et al. 1991; Gershberg 2005; Benz 2008).

In the case of KOI-258, there is another problem which has been discussed as much as the binary nature of the target. The light variation of KOI-258 indicates that there is an irregular sinusoidal variation out-of-eclipses. Considering the presence of the flare activity, it could be decided that this variation would be caused by stellar cool spots. An alternative explanation could be solar-like oscillations. However, Campante et al. (2014), listed KOI-258 in the table of solar type stars with no detected oscillations.

In this study, we analyze each variation seen in the light curve of KOI-258. We first determine the temperatures of the components and the radial velocity variation from the available spectral observations in § 3.1. Analyses of the variation out-of-eclipses are given in § 3.2. We examine the minima time variation in § 3.3. The eclipses in the light curve are analyzed under the planetary transit assumption in § 3.4. Finally, statistical models of the flare activity are derived in § 3.5, while all the results are discussed in § 4.

2. OBSERVATION AND DATA REDUCTION

We study the nature of the system by analyzing both photometric and spectroscopic observations as described in the following paragraphs.

2.1. *Spectral Observation*

Optical spectroscopic observations were obtained using the 1.5 m Russian-Turkish telescope at TUBITAK National Observatory. We carried out observations with Turkish Faint Object Spectrograph Camera (TFOSC[1]) attached on the telescope. The instrumental set-up provided medium resolution échelle spectra covering wavelengths between 3900Å and 9100Å in 11 échelle orders with a resolution of R≈2800 around 6500Å. The spectral observations were recorded with a back illuminated 2048×2048 pixels CCD camera with a pixel size of 15×15 μm^2. All the spectra were taken on HJD 2457964.36250, 2457964.45115, 2457997.51822 and 2457995.57256 in the observing season of 2017 with a signal-to-noise ratio (hereafter SNR) between 50 and 100, depending on atmospheric conditions and exposure times. We also observed three spectroscopic comparison stars, 54 Psc (K0V, Gray et al. 2003), HD 190404 (K1V, Frasca et al. 2009) and τ Cet (G8.5V, Gray et al. 2006) to determine the spectral type of the target star. Their spectra were also used as the radial velocity template.

Following classical échelle spectra reduction steps in the IRAF[2] environment, after removing instrumental noise from all observations by using nightly averaged bias frames, the average flat-field image was obtained using the bias corrected halogen lamp frames and it was normalized to unity. The science and Fe-Ar calibration lamp frames were divided by the normalized flat-field frame. Applying scattered light correction and removing cosmic rays from all flat-field corrected frames, we obtained reduced calibration lamp and science frames. After extracting the spectra from reduced science frames, we applied wavelength calibration to these spectra. In the last step, we normalized all science spectra to unity by using a cubic spline function.

2.2. *Photometric Data*

KOI-258's photometric data analyzed in this study were taken from the Kepler Mission Database. In order to reveal short term variations, such as flares, transits, as well as the sinusoidal variation, the detrended short-cadence (hereafter SC) data were used in the analyses and models (Slawson et al. 2011; Matijevič et al. 2012). The available SC data cover a wide time range from BJD 24 55064.383103 to 24 56204.331583 with some time gaps due to interrupted observations.

The light curve derived from the available SC data is shown in Figure 1. In the figure, the light variation is plotted versus time in three colors considering the observing time gaps in the upper panel, while it is plotted versus phase in the bottom panel. This light curve was derived phase by phase with intervals of 0.001 from the SC data, from which all flares were removed. Here, we computed the phase using the orbital period of 4.1574813 day given by Slawson et al. (2011). There are three different variations: flares, minima and also a sinusoidal variation. The sinusoidal variation and the flares are so dominant in the light variation that the minima could not be observed easily. Because of this, the light variations should be analyzed in a sequence. We tried to first reveal and model the sinusoidal variation. Then, we determined the flares. After removing all of them, we demonstrated the existence of transits, as described in § 3.4.

3. ANALYSES AND MODELS

3.1. *Spectral Type and Radial Velocity*

Before determining the temperatures and spectral types of the components, we checked whether the observed spectra are combined spectra of a binary system. For this aim, following the cross-correlation procedure (Simkin 1974; Tonry & Davis 1979) via the FXCOR task under the IRAF environment, we cross-correlated the spectra of KOI-258 with the spectra of 54 Psc (HD 3651, K0V), HD 190404 (K1V) and τ Cet (HD 10700, G8.5V). In this procedure, some absorption lines between 5000Å and 6500Å were used (except for broad or strongly blended lines) to calculate the cross-correlation function. Unfortunately, contrary to what is discussed in the literature, we detected just a sharp and symmetric cross-correlation function. Considering the target as a single source, we modelled the spectrum.

In the beginning, we attempted to use the spectra of 54 Psc, HD 190404 and τ Cet as comparison templates in order to find the spectral types of the target. However, we did not achieve good agreement. Because of this, following Özdarcan & Dal (2017) and Özdarcan et al. (2018) in order to achieve the best fit model for the observed spectrum, we used

[1] http://www.tug.tubitak.gov.tr/rtt150_tfosc.php.

[2] The Image Reduction and Analysis Facility is hosted by the National Optical Astronomy Observatories in Tucson, Arizona at iraf.noao.edu.

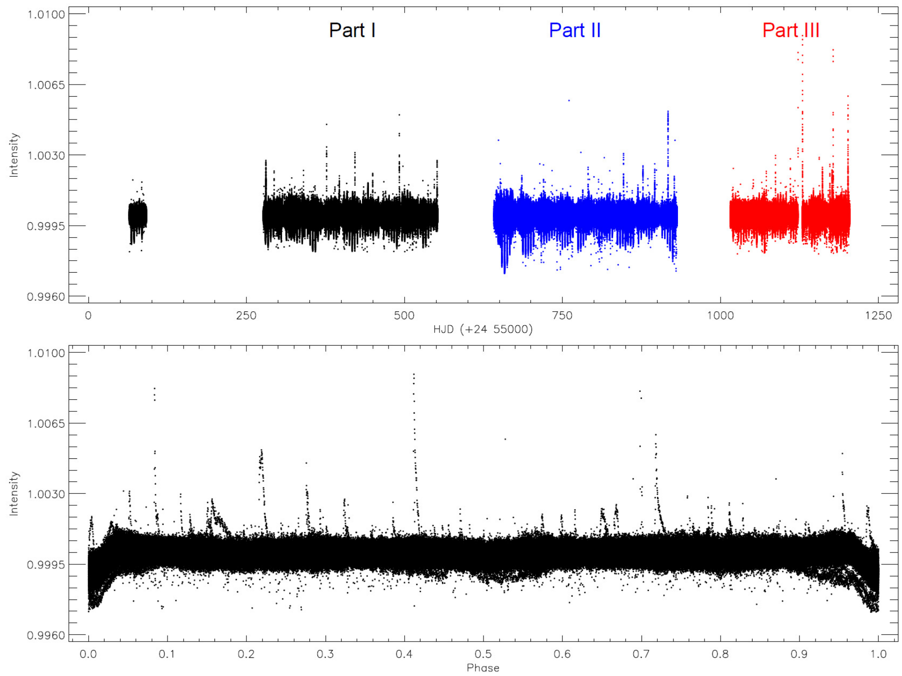

Fig. 1. KOI-258's light curve derived with data from the Kepler Database. In the upper panel, the light variation is plotted versus time, depending on available SC Data. In this panel, SC data are divided into three parts and plotted in three colors, according to observing time gaps. The light variation is plotted versus phase in the bottom panel. The color figure can be viewed online.

several synthetic templates derived for different effective temperatures and metallicity values to determine the spectral type of KOI-258. Taking the list of spectral lines between 300 and 1100 nm from the Vienna Atomic Line Database (VALD, Ryabchikova et al. 2015), the synthetic templates were derived with the iSpec software (Blanco-Cuaresma et al. 2014) using Spectrum code (Gray & Corbally 1994) depending on the ATLAS9 model atmospheres derived by Castelli & Kurucz (2004). Comparing each spectrum of the target to all the synthetic templates, we determined the spectral type of KOI-258.

The available spectra of KOI-258 are in agreement with the synthetic template derived for 6500±200 K with a metallicity of $[M/H] = 0.00$. According to these results, KOI-258 is a single star of spectral type F6 V (Cox & Pilachowski 2000) with solar metallicity. The spectra of KOI-258 are shown with the compatible synthetic template in Figure 2. In this figure, we plot all spectra observed at different times, over each other. To show the achieved consistency between the observations and the synthetic model, we overplot the synthetic template derived to fit the observed spectra.

Considering the remarkable flare activity, we checked whether there is any sign of magnetic activity in the spectrum. First, we compared four spectra among themselves depending on the synthetic template for the Ca II H, K and H_α lines, as shown in upper-left panel of Figure 3. There is a clear excess and some variation in Ca II H, K, while variation is hardly visible in the case of the H_α lines seen in the bottom-left panel.

We noticed that the spectrum regions of Mg I b (λ5167Å, λ5173Å, λ5184Å) triplets and Na I D1 (λ5896Å) and D2 (λ5890Å) are clearly incompatible with the synthetic template, while all the observed spectrum parts can be fitted very well with the synthetic templates. These lines match none of the templates derived by different parameters. The Mg I b triplets and Na I D1, D2 lines are plotted with the templates in the right panel of Figure 3. In the figure, as in Figure 2, each observed spectrum part is plotted with a thin line of different color, while the synthetic template spectrum is plotted with a thick line in black. Here it must be noted that the Mg I b triplets and Na I D1 and D2 lines are well known to be sensitive to magnetic activity.

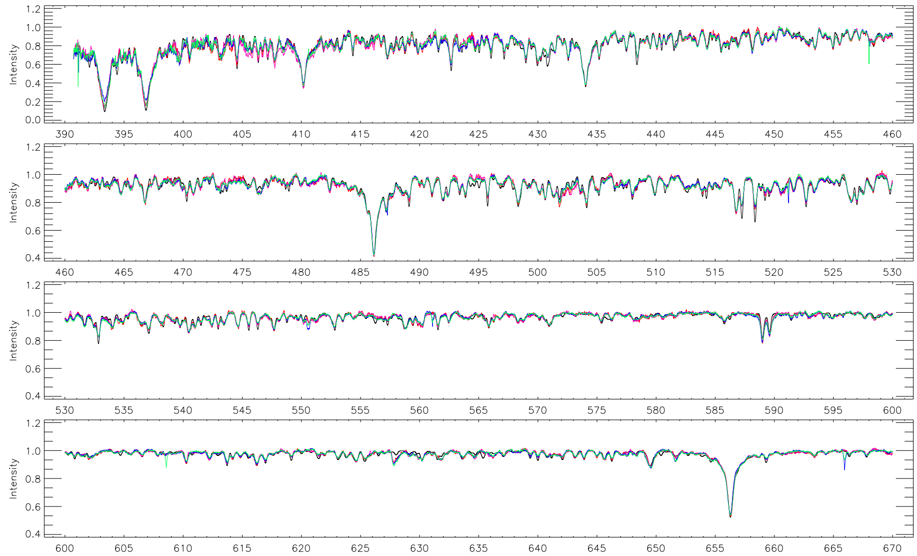

Fig. 2. Observed spectra of KOI-258 are plotted with the most compatible synthetic template derived for 6500±200 K with the metallicity of $[M/H] = 0.00$. In the figure, the observed spectrum is shown by thin lines in different color, while the synthetic template is shown by thick line in black. The color figure can be viewed online.

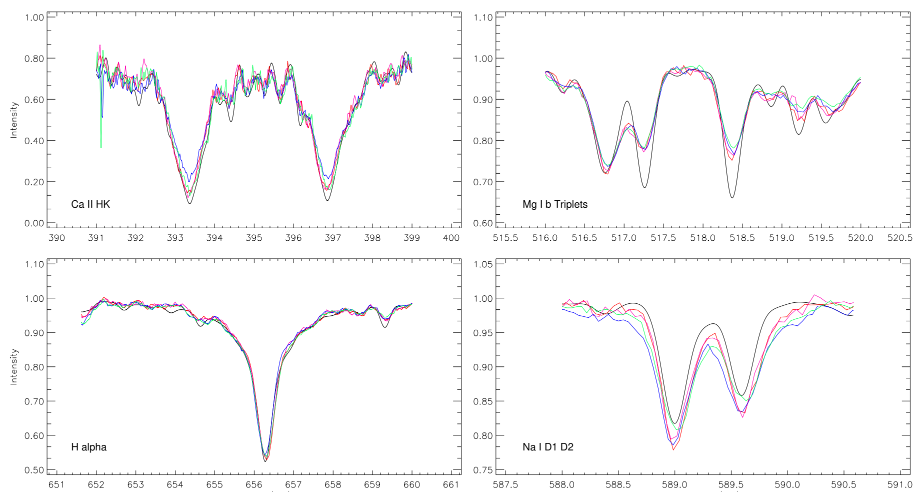

Fig. 3. Ca II H (λ3968Å), K (λ3934Å) and H_α (λ6563Å) in the observed spectra are plotted with the lines taken from the synthetic template in the left panels, while the variation of Mg I b (λ5167Å, λ5173Å, λ5184Å) triplets, Na I D1 (λ5890Å) and D2 (λ5896Å) lines are shown in the right panels. The symbols in each panel are the same as in Figure 2. The color figure can be viewed online.

The cross-correlation functions indicated that KOI-258 is a single source as explained above. However, examining the lines shown in Figures 3 and 4, it will be easily observed that the core wavelengths of the lines have some variations. We tried to determine whether there is any radial velocity variation of KOI-258.

To determine the radial velocity, we used the spectra of iot Psc (HD 222368, F7 V, Gray et al. 2006) as a radial velocity template. Using the FXCOR task, we cross-correlated it with each KOI-258 spectrum following the same procedure, in which the absorption lines between 5000Å and 6500Å were used (except for broad or strongly blended lines among them) for the cross-correlation function.

The cross-correlation functions indicate that the target has a single signal over the acceptable level of S/N ratio. A sample of the obtained cross-

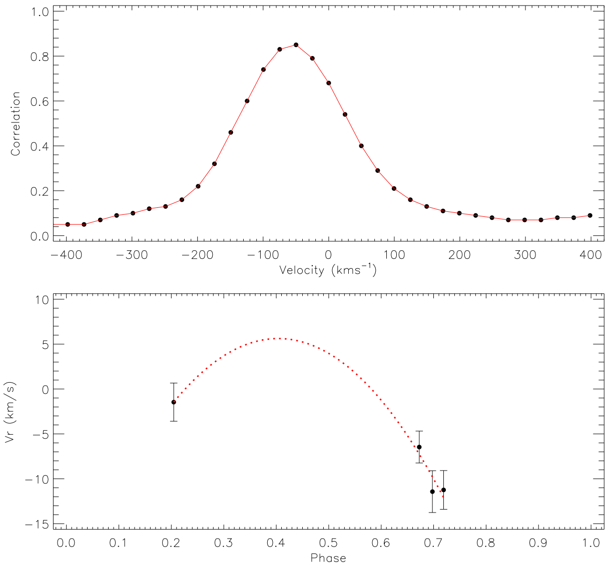

Fig. 4. A sample of the obtained cross-correlation functions and the radial velocities is plotted. In the upper panel, the cross-correlation function is shown. The observed radial velocities of KOI-258 are shown in the bottom panel. The filled circles represent observations, while the line represents the cross-correlation function, and the dotted line is a polynomial curve of second order to show one of the possible variations, as an example. The color figure can be viewed online.

correlation functions is plotted for a phase of 0.6972 in the upper panel of Figure 4. We list measured radial velocities in Table 1, together with brief information on the observed spectra as shown in the bottom panel of Figure 4.

3.2. *The Variation at Out-of-Minima*

The light variation shown in Figure 1 indicate an evident sinusoidal variation. Considering the presence of prominent flare activity clearly seen in the figure, one can think that this sinusoidal variation might be caused by a stellar cool spot. However, when the light variation is examined cycle by cycle, it is clearly observed that the shape of the light curve rapidly changes from one cycle to the next, sometimes in the same cycle. This variation cannot be caused by stellar spots. If the variation were caused by spots, the shape of the light curve would change, but not from one cycle to the next. Considering this situation and the temperature of the target, we searched the frequencies of the variation to see if it could be an effect of stellar pulsation.

We used the SC data to search for possible frequencies. First, all flares and minima were removed from the SC data. In the analysis, we used the PERIOD04 software (Lenz & Breger 2005) that is based on the Discrete Fourier Transform (hereafter DFT) method (Scargle 1982). We faced a problem initially because the software installed on the best computer system we have could not analyse whole SC data in one step. More than a few weeks were required to find just one frequency. To solve this problem, we divided the SC data into three parts, considering the time gaps in the data as shown in the upper panel of Figure 1.

We found the frequencies with this solution: 140 frequencies were acceptable according to their 3σ levels from each data part, as shown in Figure 5, for a total of 420 frequencies; they are tabulated in Table 2. The first five lines are given in this paper, the rest are given in the online archive of the journal. In the table, the data part number is listed in the first column; the number of frequencies in that part is listed in the second column; the found frequency, the amplitude of the signal and its phase are listed in the following columns. To determine which pulsation types the target exhibits, we plot the target on the plane $\log T - \log L$ in Figure 6. The frequencies found are able to model the variation seen out-of-minima. We derived the synthetic curve using equation (1) described by Scargle (1982) and Lenz & Breger (2005).

$$L(\theta) = A_0 + \sum_{\mathrm{i}=1}^{N} A_i \cos(i\theta) + \sum_{\mathrm{i}=1}^{N} B_i \sin(i\theta), \quad (1)$$

where A_0 is the zero point, θ is the phase, A_i and B_i are the amplitude parameters. In Figure 7, we plot the residual data without any flares for each data part. In the figures, the models derived with the frequency parameters listed in Table 2 via equation (1) are also plotted with a smooth red line. As shown in the figures, the frequency parameters perfectly fit

TABLE 1

MEASURED RADIAL VELOCITIES*

HJD (24 00000+)	Orbital Phase	Exposure Time (s)	V_r (kms^{-1})
57964.36250	0.698	3600	-11.428 ± 2.328
57964.45115	0.719	3600	-11.238 ± 2.158
57997.51822	0.673	3600	-6.463 ± 1.778
57995.57256	0.205	3600	-1.461 ± 2.125

*With their standard errors and brief information on the observed spectra.

TABLE 2

FREQUENCY LIST OF SOLAR-LIKE PULSATION FOUND

Part No	Frequency No	Frequency (d^{-1})	Amplitude (Intensity)	Fourier Phase
Part 1	F1	0.9749192 ± 0.0000200	0.0000298 ± 0.0000002	0.0638716 ± 0.0009652
Part 1	F2	0.9651721 ± 0.0000778	0.0000112 ± 0.0000003	0.5867471 ± 0.0044517
Part 1	F3	0.6888211 ± 0.0000307	0.0000346 ± 0.0000011	0.0723017 ± 0.0063921
Part 1	F4	0.6714099 ± 0.0000247	0.0000242 ± 0.0000002	0.0909970 ± 0.0012073
Part 1	F5	0.9880577 ± 0.0000039	0.0006001 ± 0.0000011	0.0784607 ± 0.0003106

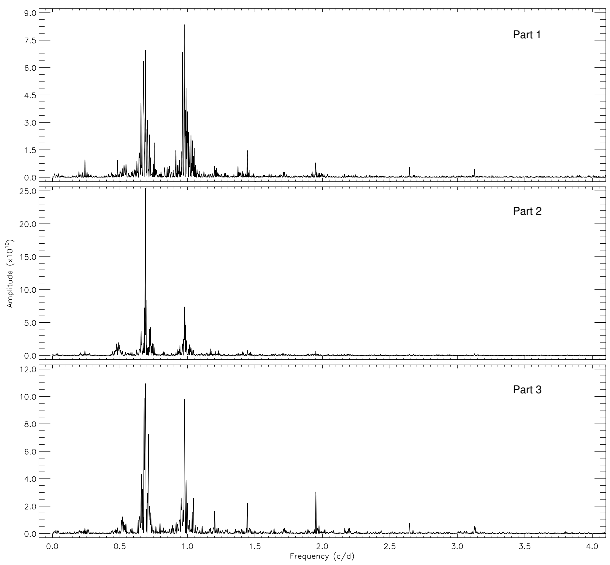

Fig. 5. The Fourier amplitude spectrum derived by using the DFT is plotted for three parts of the data.

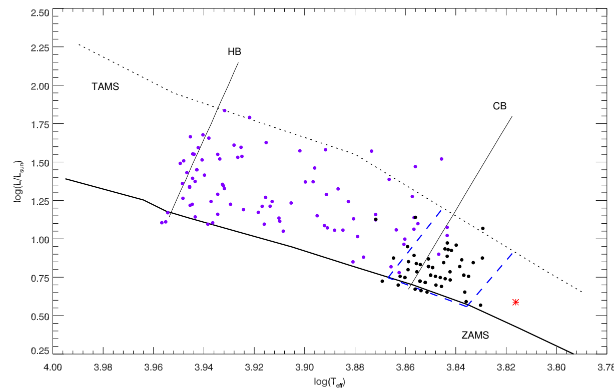

Fig. 6. Location of the target in the Hertzsprung Russell diagram. The small filled black circles represent γ Doradus type stars as listed in (Henry et al. 2005); the red asterisk represents the target. The dash dotted lines represent the borders of the area, in which γ Doradus type stars occur. Also plotted are the hot (HB) and cold (CB) borders of the δ Scuti stars for comparison. The small filled purple circles represent some semi- and un-detached binaries taken from Soydugan et al. (2006 and references therein). The ZAMS and TAMS were taken from Pols et al. (1998) for $Z = 0.02$; the borders of the instability strip were computed from Rolland et al. (2002). The color figure can be viewed online.

the residual data. It should be noted here that the data for the first panel are shown in this paper, while other two panels are derived for the two partial data given in the online archive of the journal.

3.3. *Orbital Period Variation*

According to the spectral analyses, KOI-258 is not a binary star despite the existence of a radial velocity variation. However, if the averaged light curve shown in the bottom panel of Figure 1 is carefully examined, it will be noticed that a minimum in phase 0.00 appears to be the primary minimum, but also that a second one in phase 0.50 seems to be the secondary minimum. The light curve appears to be that of an eclipsing binary system. Considering the system as a binary, we checked whether there is any variation in the minima times.

First, using the frequencies described in the previous section, we removed all the sinusoidal variation from the SC data as well as all the flares. Then, all the detectable times of minima were computed without any extra correction on the residual data. Because of the dominant flare activity, we cannot detect the minima times in some data parts. Especially, we cannot detect times of the secondary minima due to low S/N ratio. After determining minima times, we computed the differences between observations and calculations, which were calculated by using the light elements given in equation (2) Slawson et al. (2011), to obtain the residuals $(O-C)\ I$.

$$JD\ (Hel.) = 24\ 54993.02033 + 4^{d}.1574813 \times E. \quad (2)$$

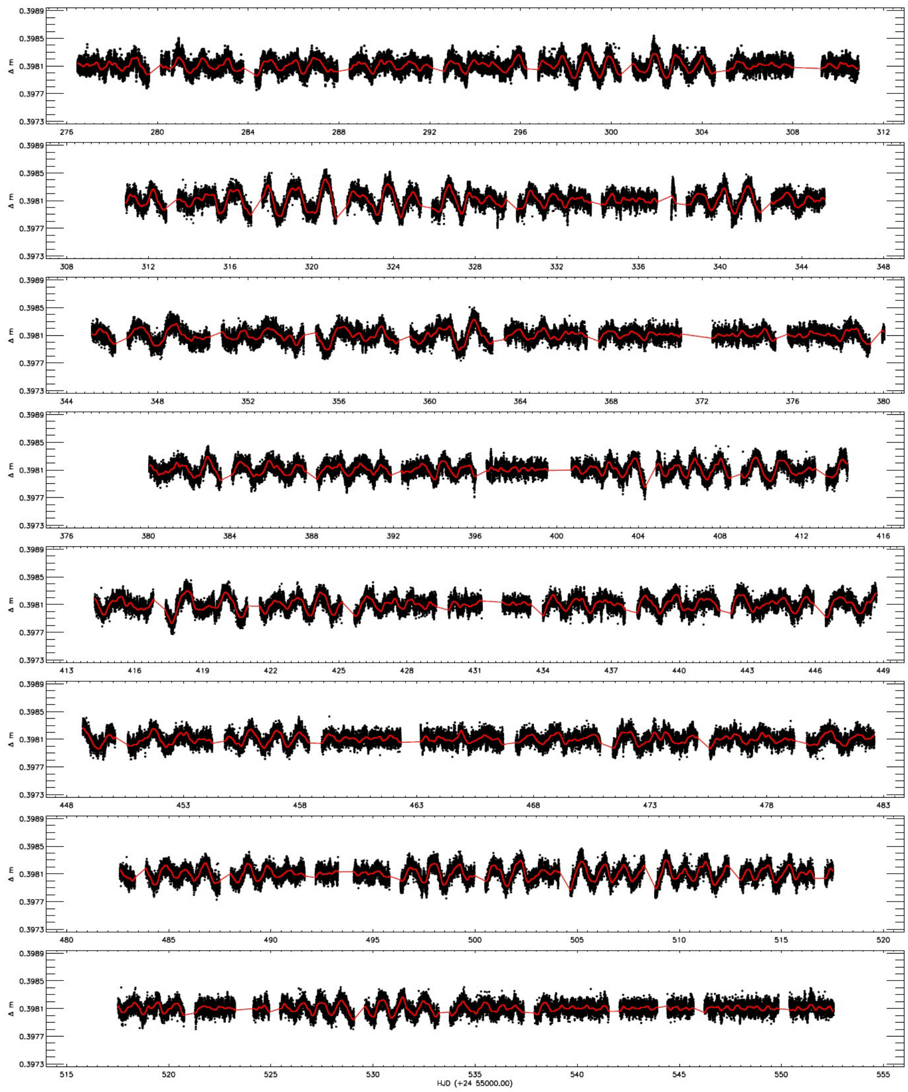

Fig. 7. The light variation out-of-minima are plotted for KOI-258 together with the synthetic model fit derived with Part 1's frequency parameters tabulated in Table 2. In the panels, filled circles in black represent the residual data, smooth lines represent the model fit. Similar synthetic model fits derived for the other two parts are given in the online archive of the journal. The color figure can be viewed online.

In total, we obtained 172 minima times from the primary minima with the largest amplitude, and we grouped them in one data set (Min I). In addition, 29 minima times were obtained from the secondary minima with small amplitude; we grouped these minima in the second data set (Min II). Using the regression calculations, a linear correction was applied to the differences separately for each data set, and the $(O-C)\ II$ residuals were obtained for each one. After the linear correction on $(O-C)\ I$, new ephemerides were calculated for both the primary and secondary minima as:

$$JD\ (Hel.) = 24\ 54993.02852 \pm 0.00344 + 4^d.1574436 \pm 0^d.0000182 \times E, \quad (3)$$

$$JD\ (Hel.) = 24\ 54993.23944 \pm 0.07592 + 4^d.1562511 \pm 0^d.0004139\ \times\ E. \quad (4)$$

The first five minima times are listed in Table 3, the full table is given in the online archive of the

TABLE 3

MINIMA TIMES AND $(O-C)\ I$ AND $(O-C)\ II$ RESIDUALS

Minima Time HJD(+2400000)	Epoch Number (E)	Minimum Type	$(O-C)\ I$ (day)	$(O-C)\ II$ (day)
55279.907292	69.0	I	0.020752	0.015164
55284.042145	70.0	I	−0.001876	−0.007427
55288.220071	71.0	I	0.018569	0.013055
55292.340623	72.0	I	−0.018361	−0.023836
55296.528439	73.0	I	0.011974	0.006536

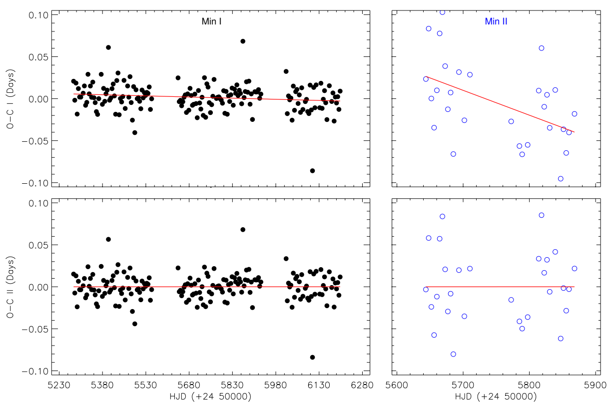

Fig. 8. The variations of the $(O-C)\ I$ and $(O-C)\ II$ residuals are shown separately for the data sets of Min I and II. The filled circles in black represent the minima times determined from the primary minima; the open circles in blue represent the minima times determined from the secondary minima. The lines in red represent linear fits applied for the correction. The color figure can be viewed online.

journal. We show the variations of both $(O-C)\ I$ and $(O-C)\ II$ residuals in Figure 8 for the data sets of Min I and II.

3.4. *Planetary Transit*

To find the cause of the minima seen in the general light variation, we tried to analyse the minima in two ways. Firstly, we assumed KOI-258 to be an eclipsing binary; secondly, we assumed the minima to be planetary transits.

As a first step, we tried to obtain the absolute light variation caused by the components for both cases. We first removed all detected flares from the SC data. Secondly, we removed the synthetic model fits derived with equation (1) by using the frequencies listed in Table 2. We used these residual data for both cases.

In first the case, we used the PHOEBE V.0.32 software (Prša & Zwitter 2005), which employs the 2003 version of the Wilson-Devinney Code (Wilson & Devinney 1971; Wilson 1990), to analyse the light curve under the eclipsing binary assumption. We analyzed the light curves obtained from the averages of SC data, which are shown in Figure 1. The temperature of the primary component was taken as 6500±200 K as found from the spectra. The temperature of the secondary component was assumed 5781 K as given by Armstrong et al. (2014). Considering the spectral type of the components, the albedos (A_1 and A_2) and the gravity-darkening coefficients (g_1 and g_1) were taken for the stars with convective envelopes (Lucy 1967; Ruciński 1969); the non-linear limb-darkening coefficients (x_1 and x_2) were taken from van Hamme (1993). The dimensionless potentials (Ω_1 and Ω_2), the luminosity (L_1) of the primary component, the inclination (i) of the system, the mass ratio of the system (q), and the semi-major axis (a) were taken as adjustable free parameters. We attempted to analyse the light curves in various modes, such as the detached system mode (Mod2), semi-detached system with the primary component filling its Roche-Lobe mode (Mod4), and semi-detached system with the secondary component filling its Roche-Lobe mode (Mod5). The initial tests demonstrated that an astrophysically acceptable solution was not obtainable in any mode when we consider both the obtained stellar absolute parameters and the stellar evolution models in the analysis.

For the second case we used JKTEBOP software (Southworth 2012) to analyse the minima assumed to be due to planetary transits. In these analyses, we used just the transit parts of the light variation instead of the whole light curve. According to the Data Validation Report[3] for Kepler ID 11231334 presented

[3]https://archive.stsci.edu/missions/kepler/dv_files/0112/011231334/.

TABLE 4

PARAMETERS OBTAINED FROM ANALYSES AND CALCULATIONS OF THE TRANSITS DETECTED IN THE LIGHT VARIATION OF KOI-258

Parameter	Planet 1	Planet 2	Planet 3
Fractional Radii Sum ($r_1 + r_2$)	0.22917±0.00011	0.12442±0.00014	0.00074±0.00016
Fractional Radii Ratio (r_1/r_2)	0.01695±0.00009	0.00384±0.00013	0.00838±0.00015
Orbit Inclination i (°)	82.20±0.23	84.42±0.27	89.99±0.43
Mass Ratio (q)	0.000010±0.000005	0.000010±0.000007	0.000005±0.000007
Orbital Period (day)	4.157444±0.000018	4.156251±0.000414	233.20
Semi Major Axis (a) (AU)	0.026	0.073	7.983
Planet Radius (R, $R_\oplus$)	2.330	0.528	1.153

by the Kepler Science Operations Center Pipeline at NASA Ames Research Center, KOI-258 has five candidate planets. However, we detected just three transits. It must be noted that we also detected the reported two other transits, but the amplitudes of these transits were so small that we could not obtain any statistically acceptable models for them.

Consequently, we modelled three different transits using the JKTEBOP software. We obtained the sum of the fractional radii, their ratio (r_1+r_2, r_1/r_2), the orbital inclination (i) and the mass ratio (q). To obtain the radii, we used the parameters of the host star. According to the spectra, the host star is a main sequence star, whose temperature is 6500 K corresponding to spectral type F6. Using the calibrations given by Cox & Pilachowski (2000), we computed the radius of the host star as 1.26 $R_\odot$; its mass was found to be 1.30 $M_\odot$. With these values, we tried to determine the radius for each planet. All the parameters obtained from both analyses and calculations are tabulated in Table 4, the model fits derived depending on these parameters are plotted in Figure 9. In the figure, the transit light curves are plotted versus phase; they were computed using the orbital period of each planet. In the case of Planets 1 and 2, the orbital periods were determined from the $(O-C)$ I analyses in this study, while the orbital period of Planet 3 was taken from the Data Validation Report for Kepler ID 11231334. We could not improve this period because of insufficient data.

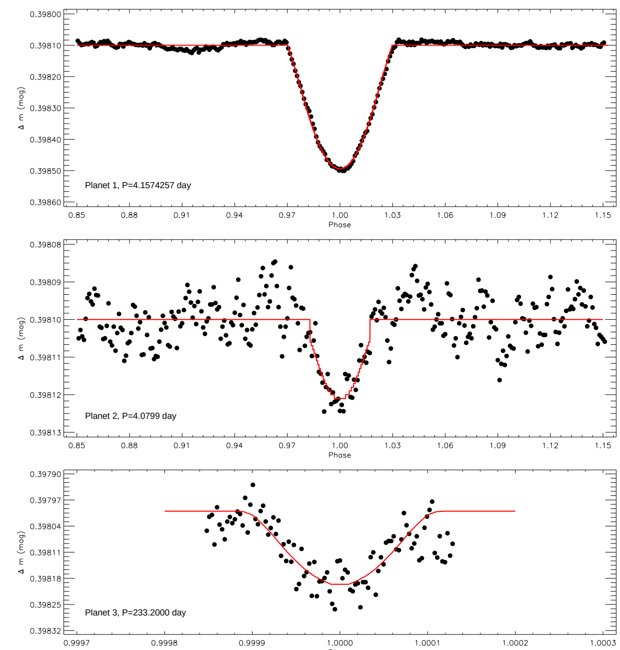

Fig. 9. The transits detected from the residual data and the model fits derived depending on transit parameters obtained by the JKTEBOP software. The color figure can be viewed online.

3.5. *Flare Activity and the OPEA Model*

Analyzing photometric data, a method was described by Dal & Evren (2010) and Dal (2012) depending on Gershberg (1972) to determine the light variation caused just by flare activity occurring on a star. Their method is useful only for smooth light curves without flaring events. However, KOI-258 exhibits remarkable sinusoidal variation out-of-minima due to solar-like oscillation together with transits of several planets, apart from flare activity. The situation led us to improve the method to obtain the flares of KOI-258.

As we did for determining the transits, we firstly removed all the sinusoidal variations. We used the synthetic light curve of sinusoidal variation described in § 3.2. Before determining flare light curve and computing their parameters, we removed the syn-

TABLE 5

CALCULATED PARAMETERS OF FLARES DETECTED IN THE OBSERVATIONS OF KOI-258

Flare Max (+24 00000)	Equivalent Durations P (s)	Rise Time T_r (s)	Decay Time T_d (s)	Total Time T_t (s)	Amplitude (Intensity)
55719.852734	0.036329	117.706176	235.394208	353.100384	0.000383
55541.086474	0.094022	176.535936	588.472128	765.008064	0.000370
56051.786437	0.201431	235.413216	588.505824	823.919040	0.000591
55469.977713	0.173162	647.325216	294.236064	941.561280	0.000409
55733.442779	0.202894	353.098656	588.500640	941.599296	0.000730

thetic light curve from all SC data. Secondly we removed all the minima from the light curve. Thus, we obtained a smooth light variation containing only flare variations. Considering also the standard deviation computed from the data without any flares, we determined the beginning and the end of each flare. An example of the flare light curves in magnitude and the quiescent levels derived from the synthetic light curve are shown in Figures 10. To compute the parameters of the flares, the synthetic light curve was also used as the quiescent level for each flare at the moment it occurred. In total, 51 flares were detected from the available SC data.

As discussed by Dal & Evren (2010, 2011), we used the flare-equivalent duration parameter in all the computations and analyses, instead of the flare energy. Considering both the beginning and the end of each flare, some flare parameters, such as flare rise times, decay times, amplitudes of flare maxima, and flare equivalent durations, were computed. The equivalent durations of the flares were computed using equation (5) taken from Gershberg (1972):

$$P = \int [(I_{flare} - I_0)/I_0] \, dt, \qquad (5)$$

where I_0 is the flux of the star in the quiet state. As described above, the synthetic light curve derived with the light curve analysis was taken as I_0. However, I_{flare} is the intensity observed at the moment of the flare. P is the flare-equivalent duration in the observing band. All the computed parameters are listed in Table 5, whose first five lines are given in this paper, while the rest are available in the online archive of the journal. Flare maximum time, equivalent duration (P), flare rise time (T_r), flare decay time (T_d), flare total time (T_t) from the beginning to the end, and flare amplitude at the moment of flare maximum are tabulated in succesive columns of the table.

The distributions of equivalent durations on a logarithmic scale versus flare total durations were

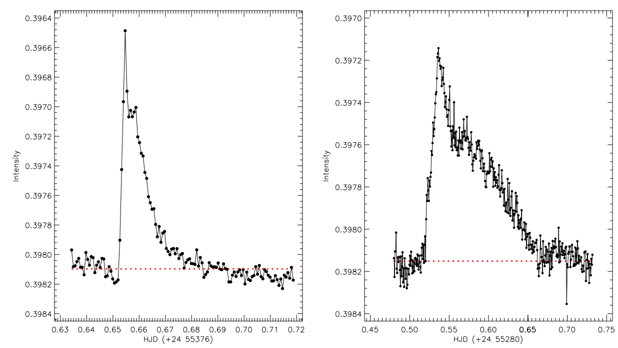

Fig. 10. A flare example detected in the observations of the system. Filled circles show observations, while the dashed line represents the level of the quiescent state of the star for the observing night. The color figure can be viewed online.

modelled by the One Phase Exponential Association (hereafter OPEA), using the SPSS V17.0 (Green et al. 1996) and GrahpPad Prism V5.02 (Dawson & Trapp 2004) programs.

According to Dal & Evren (2011), the OPEA function defined by equation (6) is a special function containing the $Plateau$ term:

$$y = y_0 + (Plateau - y_0) \times (1 - e^{-k \times x}), \qquad (6)$$

where y is the flare equivalent duration, x is the flare total duration as the free parameter. y_0 is the flare-equivalent duration on a logarithmic scale for the least total duration. The parameter $Plateau$ value is upper limit for the flare equivalent duration. The $half-life$ value is half of the first x value, at which the model reaches the $Plateau$ value. According to the definition of Dal & Evren (2010), the $Plateau$ value is an indicator of the saturation level for the white-light flares. The obtained model is shown in Figure 11 together with the observed flare equivalent durations, The parameters computed from the OPEA model are tabulated in Table 6.

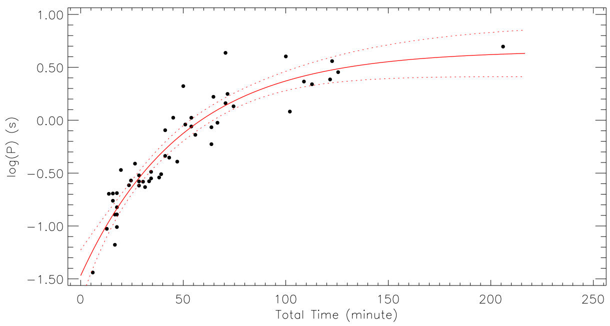

Fig. 11. The distributions of flare equivalent durations on the logarithmic scale versus flare total durations for 51 detected flares and the OPEA model derived for this distribution. Filled circles show observed flares, while the line represents the OPEA model. The color figure can be viewed online.

Although Dal & Evren (2011) show that the OPEA is the best function to model the equivalent duration distribution for each star, we statistically checked the model again. Using the D'Agostino-Pearson, the Shapiro-Wilk and also the Kolmogorov-Smirnov normality tests (D'Agostino & Stephens 1986), we calculated the probability value called as $p-value$ to test whether there is any other function to fit the distribution. The $p-value$ was found to be ≈ 0.1 and this means that there is no other function to model the distributions of flare equivalent durations (Motulsky 2007; Spanier & Oldham 1987).

Gershberg (1972) described the flare frequency distribution depending on the flare energy to reveal the flare activity behavior of a star and also compared the activity levels of different stars. However, as it was described by Dal & Evren (2011), there is a problem in the comparisons of these distributions among different stars due to the stellar luminosity term in the energy computation. This is why we derived the flare frequency distribution depending on the flare equivalent duration instead of the flare energy parameter. In this study, the flare frequencies were calculated for different flare equivalent duration limits for the 51 flares. If one wants to compare the cumulative flare frequency distributions of different targets together, the cumulative flare frequency distribution must be independent of the total observing durations. Because of this, in this study, we computed the flare cumulative frequency considering the flare frequencies, which are calculated as a flare number per an hour, in each equivalent duration level. This is why the x-axis of Figure 12 has units of h^{-1}. The obtained cumulative flare frequency distribution is shown in Figure 12. The flare cumulative frequencies exhibit a distribution in the form of an exponential function. However, in the literature, the linear part of the flare frequency distribution is generally used to compare stars among themselves. In this study, in order to determine the beginning of the linear part of the distribution, we modelled the entire distribution with an exponential function, and then we determined the turning point of the distribution, using this exponential function. The exponential function is shown by the red line in the upper panel of Figure 12. Considering the turning point, we fitted the linear part of the distribution with the correlation coefficient (R^2) of 0.89 by equation (7) following the linear regression calculations:

$$\log(P) = -0.981 \pm 0.063 \times \log(\nu) + 1.906 \pm 0.123. \quad (7)$$

In the literature, there are also two different flare frequency descriptions. Ishida et al. (1991) described the flare frequencies, N_1 as a flare number per hour and N_2 as a total flare-equivalent emitting duration per hour. In the SC data taken from the Kepler Database, there are 1139.94848 day observations for KOI-258, from which 51 flares were detected. The total flare equivalent durations were found to be 50.86556 s for all these flares. We computed the

TABLE 6

THE OPEA MODEL PARAMETERS BY USING THE LEAST-SQUARES METHOD

Best-fit Values	
y_0	-1.46859 ±0.12025
$Plateau$	0.65941 ±0.12880
K	0.000332898 ±0.0000570662
$Half-life$	2082.16
$Span$	2.12800 ±0.1152
95% Confidence Intervals	
y_0	-1.71060 to -1.22658
$Plateau$	0.400195 to 0.918618
K	0.000218047 to 0.000447749
$Half-life$	1548.07 to 3178.90
$Span$	1.89611 to 2.35988
Goodness of Fit	
R^2	0.88
Averaged $P-value$	0.10
Deviation from Model	Not Significant

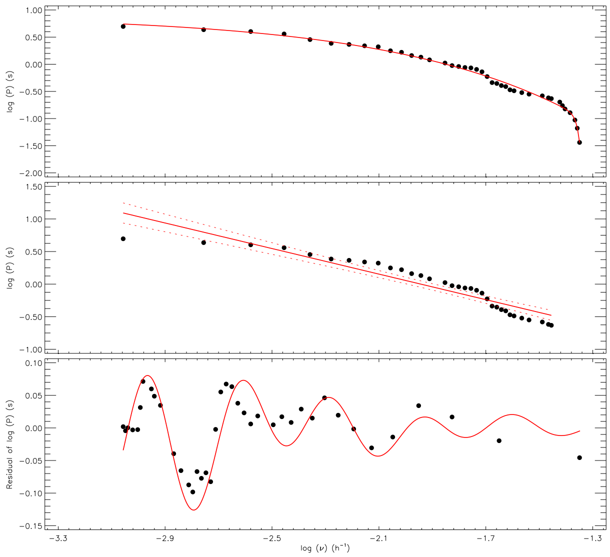

Fig. 12. Cumulative flare frequencies and model calculated for KOI-258 over 51 flares are shown in the upper panel, while its liner part is shown with a linear model in the middle panel. The residuals of the model are shown in the bottom panel. The color figure can be viewed online.

frequencies described by Ishida et al. (1991) in equations (8) and (9):

$$N_1 = \Sigma\, n_f \,/\, \Sigma T_t, \quad (8)$$

$$N_2 = \Sigma\, P \,/\, \Sigma T_t, \quad (9)$$

where Σn_f is the total flare number, and ΣT_t is the total observing duration, while ΣP is the total equivalent duration. We found that the N_1 frequency is 0.00186 h^{-1}, and the N_2 frequency is 0.000052 for KOI-258.

It is well known that the flare events are generally random phenomena in the case of UV Ceti type flare stars. To test this situation for KOI-258, we calculated the phase distribution of the flares, depending on the orbital period of the target. The phase distribution is shown in Figure 13. In the figure, the distribution of the total number of flares computed in phase intervals of 0.05, for all 51 flares is shown.

4. RESULTS AND DISCUSSION

KOI-258 is one of the controversial systems discovered in the Kepler Mission. According to some authors such as Slawson et al. (2011); Coughlin et al. (2014); Armstrong et al. (2014), KOI-258 is an eclipsing binary. They tried to estimate the physical parameters of the system. On the other hand, KOI-258

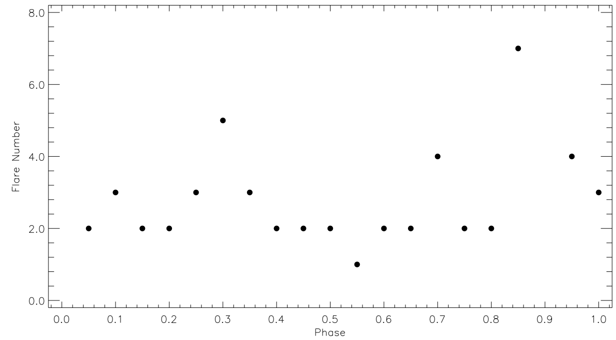

Fig. 13. The distribution of flare total number in each phase interval of 0.05, plotted versus phase for 51 flares.

is listed as a candidate for a planetary system in several studies, such as Borucki et al. (2011); Ford et al. (2012). The target's spectrum can give a clue. If the minima amplitudes in the light curve are considered, it can be clearly noticed that the ratio of the minima amplitudes is almost equal to 1.0. If KOI-258 were a binary system, it would be expected that the temperatures of the components be almost equal, and then, the existence of signs for the secondary component in the cross-correlation derived for KOI-258's spectra would also be expected. However, the spectrum taken seems to be that of a single star.

Analyzing four spectra corresponding to different phases demonstrated that KOI-258 is a single star. We could not find any sign for the lines belonging to the secondary component in the cross-correlation, using the spectra of 54 Psc, HD 190404 and τ Cet with high SNR as a radial velocity templates. However, if the cores of the lines shown in Figures 3 are carefully examined, it will be easily noticed that the wavelengths of the line cores vary from one spectrum to the next. Considering this variation, we tried to determine the radial velocity of the target from each spectrum by using the spectra of the same stars as a radial velocity templates. We obtained four radial velocities corresponding to different phases, which were computed depending on the light elements given by Slawson et al. (2011). As also seen from Figure 4, there is a variation in the radial velocity of the target, and its amplitude is remarkably larger than the error bars. Considering the trend observed in Figure 4, it appears to us that KOI-258 has one or more companions, but there is no object as massive as a companion star.

Then, we tried to determine the temperature of the star by using the same comparison template stars. Because of the mismatches between the target spectra and comparison templates, we used synthetic templates to find the spectral type of KOI-258. Comparisons indicated that target spectra match the synthetic template derived for 6500±200 K with a metallicity of $[M/H] = 0.00$. Thus, we decided that KOI-258 is a F6V star with solar metallicity. This result is in agreement with those given in the literature. For example, both Borucki et al. (2011) and Batalha et al. (2013) gave the temperature of the target as 6278 K with $\log g = 4.17$. However, according to Campante et al. (2014); Pinsonneault et al. (2012); Rowe et al. (2015); Huber et al. (2014), the temperature of KOI-258 is between 6528 K and 6535 K, and the $\log g$ value is between 4.161 and 4.35.

Before analyzing the whole light curve and determining the short term flares, we tried to find the cause of the sinusoidal variation at out-of-eclipses. For this aim, we considered the temperature and $\log g$ parameters determined from the KOI-258's spectra. Then, we compared the consecutive cycles of the light curve to see whether the variation at out-of-eclipses is like that expected for stellar spot activity. We firstly considered that it is a rotational modulation effect due to cool spots, because of the presence of flare activity clearly seen in Figure 1. Examination of the light variation cycle by cycle indicated that the sinusoidal variation absolutely changes its shape in very short times, as shown in Figure 7. However, if the sinusoidal variation were caused by cool stellar spots, the frequency analysis would reveal a few dominant frequencies corresponding to the stellar period. Indeed, if the sinusoidal variation were caused by a cool stellar spot, it would be expected also that the minima phases of the sinusoidal variation should migrate, as shown for spotted stars by Yoldaş & Dal (2017b, 2019). It could be thought that the variation is caused by the stellar spots, and new spots occur in each cycle. On the other hand, it is well known that cool stellar spots can be alive for a few months. However, the active regions, where the spots occur, can be alive for several years. Therefore, if the variation were caused by the stellar spot, a regular phase migration should be observed. According to the results obtained from the spectral analyses, KOI-258 is a main sequence star of spectral type F6, which provides another possibility for this variability. The sinusoidal variation could be caused by pulsation, instead of cool spots. However, KOI-258 is located out of the instability strip in the Hertzsprung-Russell diagram. Because of this, even if KOI-258 is not a γ Doradus or δ Scuti type pulsating star, it could be a solar-like oscillating star.

Indeed, we found 420 frequencies between 0.240536±0.000014 d^{-1} and 6.827660±0.000003 d^{-1} with different amplitudes by the PERIOD04 search based on the DFT method (Scargle 1982; Lenz & Breger 2005). Using equation (1), we derived the synthetic model curve for the data with these frequencies. The concordance between observations and the synthetic curves is shown in Figure 7. According to these results, the sinusoidal variation exhibited by KOI-258 seems to be caused by solar-like oscillations. As described in § 3.2, the analyzed datasets are so large that the software cannot model the whole dataset to find frequencies.Therefore, we divided the data into three parts as shown in Figure 1. Although it appears that splitting can cause some trouble to achieve reliable results, it provides some clues to reveal the nature of the target. For instance, we did not find exactly the same frequencies from each data part, though there are a few similar frequencies found from all three parts. This indicates that the sinusoidal variation is not caused by any stable process like the rotational modulation caused by cool spots. If it were caused by a stable, semi-regular phenomenon like stellar spot activity, we would expect to find some similar frequencies and their harmonics. Therefore, KOI-258 appears to be a pulsating star. Indeed, as shown in Figure 6, the location of the target is outside the instability strip in the Hertzsprung Russell diagram. This means that the observed sinusoidal variation should be neither a γ Doradus nor a δ Scuti type pulsation. It is more likely that KOI-258 is a solar-like oscillating star, which also indicates that KOI-258 is a main sequence star, not an evolved one as mentioned by Frasca et al. (2016).

According to the spectra, KOI-258 is a single star where the minima could be caused by some orbiting planets. Despite this thought, we tried to analyse the light curve as an eclipsing binary, using the PHOEBE V.0.32 software (Prša & Zwitter 2005), which depends on the 2003 version of the Wilson-Devinney Code (Wilson & Devinney 1971; Wilson 1990). We could not reach any astrophysically acceptable solution.

There is the Data Validation Report for Kepler ID 11231334 prepared by the Kepler Science Operations Center Pipeline at NASA Ames Research Center. According to this report, KOI-258 has possibly five planets. After removing the flares and the sinusoidal variation using the derived synthetic fit, we detected several transits caused by five different planets. Two transit light curves could not be modelled due to the very low SNR, but we were able to model three of them. According to the Data Validation Report, the Planet candidates 1 and 2 have the same orbital periods of 4.2 day with the same semi-major axis of 0.1 AU. The radius of candidate Planet 1 is given as 20.2 $R_\oplus$, and it is given as 6.1 $R_\oplus$ for Planet 2. Here is an astrophysically very interesting situation where two planets with different radii orbit the host star with the same period at the same distance. In addition, another three candidate planets with different radii orbit the star with somewhat different periods also at nearly the same distance.

Using the JKTEBOP software (Southworth 2012) in this study, we found the sum of the fractional radii ($r_1 + r_2$), their ratio (r_1/r_2), the orbital inclination (i) and the mass ratio (q) as tabulated in Table 4. Depending on the temperature found from the spectra for the host star, we computed the radius of the host star as 1.26 $R_\odot$ using the calibration given by Cox & Pilachowski (2000). In this case, considering both the sum and the ratio of the fractional radii, we estimated the possible radii of the first three candidate planets as 2.330 $R_\oplus$ for Planet 1, 0.528 $R_\oplus$ for Planet 2 and 1.153 $R_\oplus$ for Planet 3. In addition, using Kepler's third law, we also estimated the semi-major axes as 0.026 AU, 0.073 AU and 7.983 AU for each planet, respectively.

The orbital periods of Planets 1 and 2 are so short that their transits were observed several times by the Kepler Satellite. In this case, using the orbital period given by Slawson et al. (2011) as an initial ephemeris, we adjusted their orbital periods as 4.157444±0.000018 day and 4.156251±0.000414 day for Planets 1 and 2. However, there are few observed transits for Planet 3, due to its long orbital period. Because of this, we could not adjust its period, and we used the orbital period of 233.20 day as given in the Data Validation Report for Kepler ID 11231334. In our opinion, the appearance of KOI-258's planet system is much more acceptable than stated in the Data Validation Report.

Apart from the sinusoidal variation and transits, the most noticeable variations observed in the light curve of KOI-258 are the instant short term flares, which are mentioned by Balona (2015) for the first time. Indeed, we found signs of magnetic activity in the spectra apart from the photometric data. For instance, the Ca II lines exhibit some excess as well as a noticeable variation, as shown in the upper panel of Figure 3. However, the H_α line reveals neither any excess nor any variation. Unexpectedly, some other lines such as Mg I b triplets and Na I D1,D2, which are indicators of the presence of magnetic instability in the stellar chromosphere, especially in the middle and upper chromosphere, exhibit both a remarkable excess and an evident variation, as seen in Figure 3.

As well as its spectra, we analyzed KOI-258's photometric data. The target was observed by the Kepler Satellite over 1139.94848 days from HJD 24 55064.383103 to HJD 24 56204.331583, which means that the photometric data of KOI-258 cover more than 27358 hours of observing time in total. Although there are numerous data available to analyse, we could detect only 51 flares, following the method described in the § 3.5. We computed the total flare equivalent duration as 50.86556 s from 51 flares. As a result, the flare frequency N_1, an averaged flare number per an hour, is 0.001864 h^{-1}, while the flare frequency N_2 is about 0.00005. In the case of the flare timescales, we found that the maximum flare total time is 4472.5 s for KOI-258, and we obtained the maximum flare rise time as 1765.46 s. Moreover, the *Plateau* value was found to be 0.659406±0.128795 s, and the half-life is 2082.16 s.

If we compare the target with the eclipsing binaries observed by the Kepler Satellite, KOI-258 has obviously a lower activity level, since the flare frequencies were found to be N_1 =0.0174 h^{-1} and N_2 =0.00027 for FL Lyr, N_1 =0.01351 h^{-1} and N_2 =0.00006 for KIC 9761199, N_1 =0.05087 h^{-1} and N_2 =0.00050 for KIC 11548140 (Yoldaş & Dal 2016, 2017b,a). The flare frequencies of KOI-258 are smaller than those of its analogues. The half-life is 2291.7 s for KIC 9641031, 1014 s for KIC 9761199 and 2233.6 s for KIC 11548140 (Yoldaş & Dal 2016, 2017b,a). The longest flares lasted 5178.9 s for KIC 9641031, 1118.1 s for KIC 9761199 and 22185.4 s for KIC 11548140 (Yoldaş & Dal 2016, 2017b,a). In the case of the flare timescales, KOI-258 has a behavior similar to the Kepler eclipsing binaries. According to the OPEA models, the *Plateau* values were found to be 1.232 s for KIC 9641031, 1.951 s for KIC 9761199, 2.312 s for KIC 11548140 (Yoldaş & Dal 2016, 2017b,a). Consequently, KOI-258 is similar to the Kepler eclipsing binaries according to the flare timescales, which means that the flares detected from KOI-258 last as long as those obtained from the Kepler eclipsing binaries. However, KOI-258's *Plateau* value and the flare frequencies are smaller than in those binaries.

In the case of UV Ceti-type single stars, the N_1 flare frequency was found to be N_1 =1.331 h^{-1} for AD Leo ($B - V = 1^m.498$), N_1 =1.056 h^{-1} for EV Lac ($B - V = 1^m.554$). The N_2 flare frequencies were found to be N_2 =0.088 for EQ Peg ($B - V = 1^m.574$) and N_2 =0.086 for AD Leo (Dal & Evren 2011). Solving the OPEA models, the half-life parameters were fount to be 433.10 s for DO Cep ($B-V=1^m.604$), 334.30 s for EQ Peg and 226.30 s for V1005 Ori ($B-V=1^m.307$) (Dal & Evren 2011). Moreover, the maximum flare rise times are 2062 s for V1005 Ori and 1967 s for CR Dra ($B-V=1^m.370$) (Dal & Evren 2011), while the maximum flare total times are 5236 s for V1005 Ori and 4955 s for CR Dra (Dal & Evren 2011). According to Dal & Evren (2011), the *Plateau* values are 3.014 for EV Lac and 2.935 for EQ Peg, and 2.637 for V1005 Ori. If the target is compared with UV Ceti type single stars, KOI-258 has obviously a lower activity level. The observed flares have very low energies, and the target's flare frequencies are also much lower.

In order to reveal where KOI-258 is located among similar targets regarding flare activity, we derived the cumulative flare frequency distribution depending on the flare equivalent duration instead of the flare energy. In the literature, a similar model was derived recently for KIC 12418816 (one of the most interesting systems) by Dal & Özdarcan (2018). If their flare cumulative frequency distributions are compared, it will be seen that the interval of flare cumulative frequencies is spread from $\log(\nu)$ of $-1.50\,h^{-1}$ to $0.00\,h^{-1}$ for Group 1 and from $-1.50\,h^{-1}$ to $+0.30\,h^{-1}$ for Group 2 in the case of KIC 12418816, while it is spread from $\log(\nu)$ of $-3.1\,h^{-1}$ to $-1.3\,h^{-1}$ for KOI-258. In addition, the $\log(P)$ values vary from -1.00 s to 2.50 s for Group 1 and from -1.00 s to 1.50 s for Group 2 of KIC 12418816; the $\log(P)$ values vary from -1.50 s to 0.70 s for KOI-258. Considering the variation intervals of both $\log(\nu)$ and $\log(P)$, it seems that KIC 12418816 is able to exhibit more frequent flares with higher energy than those KOI-258 exhibits. According to some authors such as Gershberg (1972); Gershberg & Shakhovskaia (1983); Haisch et al. (1991); Gershberg (2005), the occurrence of more frequent flares with higher energy is an indicator of high level magnetic activity as well as fast rotation due to binarity or a younger age, as estimated for KOI-258 by Walkowicz & Basri (2013).

UV Ceti type flare stars exhibit a random flare distribution in time. However, recent studies such as Yoldaş & Dal (2017b), Dal & Özdarcan (2018) and Yoldaş & Dal (2019), indicate that flares tend to aggregate around certain phases. The flare number distribution shown in Figure 13 indicates two important cases, which indicates that KOI-258's flares occur in each phase, and occur randomly as well, as do those on UV Ceti type single stars.

According to these results, KOI-258 is a single star with three planets. The target exhibits magnetic activity, though its level is very low, which indicates that KOI-258 should be a star older than that estimated by Walkowicz & Basri (2013). If the target were a younger star, the activity level would be similar to that observed in the case of UV Ceti type stars. On the other hand, if the target were a binary system, it is expected that the activity level would be higher than it is. Finally, analyses of both photometric and spectroscopic observations reveal an interesting system. It appears that KOI-258 exhibits pulsation (solar-like oscillations) as well as flares. According to the spectroscopic observations, the target should be a single star hosting a planetary system consisting of three planets.

We thank the referee for useful comments that contributed to the improvement of the paper. We wish to thank the Turkish Scientific and Technical Research Council (TÜBİTAK) for supporting this work through grant No. 116F213 and for partial support in using RTT-150 (Russian-Turkish 1.5-m telescope in Antalya) with project number 14BRTT150-667. The authors also acknowledge generous allotments of observing time at the Ege University Observatory under project number 116F213.

REFERENCES

Aerts, C., Christensen-Dalsgaard, J., & Kurtz, D. W. 2010, Asteroseismology, Astronomy and Astrophysics Library (Dordrecht Heidelberg: Springer)

Armstrong, D. J., Gómez Maqueo Chew, Y., Faedi, F., & Pollacco, D. 2014, MNRAS, 437, 3473

Balona, L. A. 2015, MNRAS, 447, 2714

Baranec, Ch., Ziegler, C., Law, N. M., et al. 2016, AJ, 152, 18

Batalha, N. M., Rowe, J. F., Bryson, S. T., et al. 2013, ApJS, 204, 24

Benz, A. O. 2008, LRSP, 5, 1

Blanco-Cuaresma, S., Soubiran, C., Heiter, U., & Jofré, P. 2014, A&A, 569, 111

Borucki, W. J., Koch, D., Basri, G., et al. 2010, Sci, 327, 977

Borucki, W. J., Koch, D. G., Basri, G., et al. 2011, ApJ, 736, 19

Burke, Ch., Bryson, S. T., Mullally, F., et al. 2014, ApJS, 210, 19

Caldwell, D. A., Kolodziejczak, J. J., Van Cleve, J. E., et al. 2010, ApJ, 713, 92

Campante, T. L., Chaplin, W. J., Lund, M. N., et al. 2014, ApJ, 783, 123

Carrington, R. C. 1859, MNRAS, 20, 13

Castelli, F. & Kurucz, R. L. 2004, arXiv:astro-ph/0405087

Coughlin, J. L., Thompson, S. E., Bryson, S. T., et al. 2014, AJ, 147, 119
Cox, A. N. & Pilachowski, C. A. 2000, PhT, 53, 77
Cunha, M. S., Aerts, C., Christensen-Dalsgaard, J., et al. 2007, A&ARv, 14, 217
D'Agostino, R. B. & Stephens, M. A. 1986, Goodness-of-fit techniques (New York, NY: Marcel Dekker Inc.)
Dal, H. A. 2012, PASJ, 64, 82
Dal, H. A. & Evren, S. 2010, AJ, 140, 483
_________. 2011, AJ, 141, 33
Dal, H. A. & Özdarcan, O. 2018, MNRAS, 474, 326
Dawson, B. & Trapp, R. 2004, Basic & Clinical Biostatistics (4th ed.; New York, NY: McGraw-Hill)
Egret, D., Didelon, P., McLean, B. J., Russell, J. L., & Turon, C. 1992, A&A, 258, 217
Ford, E. B., Ragozzine, D., Rowe, J. F., et al. 2012, ApJ, 756, 185
Frasca, A., Covino, E., Spezzi, L., et al. 2009, A&A, 508, 1313
Frasca, A., Molenda-Żakowicz, J., De Cat, P., et al. 2016, A&A, 594, 39
Gershberg, R. E. 1972, Ap&SS, 19, 75
_________. 2005, Solar-Type Activity in Main-Sequence Stars (Berlin: Springer)
Gershberg, R. E. & Shakhovskaia, N. I. 1983, Ap&SS, 95, 235
Gray, R. O. & Corbally, C. J. 1994, AJ, 107, 742
Gray, R. O., Corbally, C. J., Garrison, R. F., et al. 2006, AJ, 132, 161
Gray, R. O., Corbally, C. J., Garrison, R. F., McFadden, M. T., & Robinson, P. E. 2003, AJ, 126, 2048
Green, S. B., Salkind, N. J., & Jones, T. M. 1996, Using SPSS for Windows; Analyzing and Understanding Data, 1st ed. (Upper Saddle River, NJ: Prentice Hall)
Haisch, B., Strong, K. T., & Rodono, M. 1991, ARA&A, 29, 275
Henry, G. W., Fekel, F. C., & Henry, S. M. 2005, AJ, 129, 2815
Hodgson, R. 1859, MNRAS, 20, 15
Huber, D., Silva Aguirre, V., Matthews, J. M., et al. 2014, ApJS, 211, 2
Hudson, H. S. & Khan, J. I. in , ASPC 111, Magnetic Reconnection in the Solar Atmosphere, ed. R. D. Bentley & J. T. Mariska (San Francisco, CA: ASPC) 135
Ishida, K., Ichimura, K., Shimizu, Y., & Mahasenaputra. 1991, Ap&SS, 182, 227
Jenkins, J. M., Caldwell, D. A., Chandrasekaran, H., et al. 2010a, ApJ, 713, 87
Jenkins, J. M., Chandrasekaran, H., McCauliff, S. D., et al. 2010b, SPIE, 7740, 77400
Kamil, C. & Dal, H. A. 2017, PASA, 34, 29
Kirk, B., Conroy, K., Prša, A., et al. 2016, AJ, 151, 68
Koch, D. G., Borucki, W. J., Basri, G., et al. 2010, ApJ, 713, 79
Lacroute, P. & Valbousquet, A. 1975, BICDS, 9, 2
Lenz, P. & Breger, M. 2005, CoAst, 146, 53
Lucy, L. B. 1967, ZA, 65, 89
Matijevič, G., Prša, A., Orosz, J. A., et al. 2012, AJ, 143, 123
Motulsky, H. 2007, GraphPad Software, 31, 39
Özdarcan, O. & Dal, H. A. 2017, PASA, 34, 17
Özdarcan, O., Yoldaş, E., & Dal, H. A. 2018, RMxAA, 54, 37
Pinsonneault, M. H., An, D., Molenda-Żakowicz, J., et al. 2012, ApJS, 199, 30
Pols, O. R., Schröder, K.-P., Hurley, J. R., Tout, C. A., & Eggleton, P. P. 1998, MNRAS, 298, 525
Prša, A. & Zwitter, T. 2005, ApJ, 628, 426
Rodono, M. 1986, NASSP, 492, 409
Rolland, A., Costa, V., Rodriguez, E., et al. 2002, CoAst, 142, 57
Rowe, J. F., Coughlin, J. L., Antoci, V., et al. 2015, ApJS, 217, 16
Ruciński, S. M. 1969, AcA, 19, 245
Ryabchikova, T., Piskunov, N., Kurucz, R. L., et al. 2015, PhyS, 90, 4005
Scargle, J. D. 1982, ApJ, 263, 835
Simkin, S. M. 1974, A&A, 31, 129
Slawson, R. W., Prša, A., Welsh, W. F., et al. 2011, AJ, 142, 160
Southworth, J. 2012, JKTEBOP: Analyzing light curves of detached eclipsing binaries, ascl soft 07013
Soydugan, E., Soydugan, F., Demircan, O., & İbanoğlu, C. 2006, MNRAS, 370, 2013
Spanier, J. & Oldham, K. B. 1987, An Atlas of Functions (Bristol, PA: Taylor & Francis/Hemisphere)
Tonry, J. & Davis, M. 1979, AJ, 84, 1511
Van Eylen, V., Winn, J. N., & Albrecht, S. 2016, ApJ, 824, 15
van Hamme, W. 1993, AJ, 106, 2096
Walkowicz, L. M. & Basri, G. S. 2013, MNRAS, 436, 1883
Watson, C. L., Henden, A. A., & Price, A. 2006, SASS, 25, 47
Wilson, R. E. 1990, ApJ, 356, 613
Wilson, R. E. & Devinney, E. J. 1971, ApJ, 166, 605
Yoldaş, E. & Dal, H. A. 2016, PASA, 33, 16
_________. 2017a, PASA, 34, 60
_________. 2017b, RMxAA, 53, 67
_________. 2019, RMxAA, 55, 73

H. A. Dal and E. Yoldaş: Department of Astronomy and Space Sciences, University of Ege, Bornova, 35100 İzmir, Turkey (ali.dal@ege.edu.tr).

Revista Mexicana de Astronomía y Astrofísica, **57**, 57–66 (2021)

https://doi.org/10.22201/ia.01851101p.2021.57.01.03

COMPARATIVE ANALYSIS OF SKY QUALITY AND METEOROLOGICAL VARIABLES DURING THE TOTAL LUNAR ECLIPSE ON 14-15 APRIL 2014 AND THEIR EFFECT ON QUALITATIVE MEASUREMENTS OF THE BORTLE SCALE

C. Góez Therán[1,2,3] and S. Vargas Domínguez[4]

Received November 25 2019; accepted September 11 2020

ABSTRACT

A total lunar eclipse plausibly has an influence on the variation of some environmental physical parameters, specifically on the conditions of the sky brightness, humidity and temperature. During the eclipse on 14^{th}-15^{th} April 2014, these parameters were measured with a photometer and a weather station. The obtained results allow the comparison, practically, of the optimal conditions for observational astronomy work in the Tatacoa desert and, therefore, to certify it as suitable place to develop night sky astronomical observations. This investigation determined, to some extent, the suitability of this place to carry out astronomical work and research within the optical range. Thus, the changes recorded during the astronomical phenomenon allowed the classification of the sky based on the Bortle Scale.

RESUMEN

Es factible que un eclipse total de Luna tenga influencia en la variación de parámetros físicos en una zona ambiental, específicamente en el brillo del cielo, humedad y temperatura. Durante el eclipse del 14 y 15 de abril de 2014, estos parámetros se midieron por medio de un fotómetro y de una estación meteorológica. Los resultados obtenidos permiten hacer comparaciones de manera práctica sobre las condiciones óptimas para el trabajo de astronomía observacional en el desierto de la Tatacoa (Colombia) y así catalogarlo como un lugar apto para realizar observaciones astronómicas nocturnas. Esta investigación permite determinar, hasta cierto punto, la idoneidad de este lugar para llevar a cabo trabajos astronómicos e investigaciones dentro del rango óptico. De esta manera, los cambios registrados durante el fenómeno astronómico permitieron la clasificación del cielo con base en la escala de Bortle.

Key Words: atmospheric effects — eclipses — methods: observational — site testing

1. INTRODUCTION AND MOTIVATION

Through the history of our species, the universe populated with stars, galaxies and other celestial objects has been visible in the darkness of the night sky, inspiring questions about the cosmos and our relationship to it, and therefore star gazing has been crucial not only for astronomy but also for literature, arts, philosophy and multiple human activities. Nevertheless, the technological advances of our society, added to world population growth, resulted in light pollution in most living areas where people do not have the opportunity to enjoy the night sky. Furthermore issues on human health caused by artificial lighting and impacts on the behavior of plants and animals have been demonstrated. For years now, astronomers have highlighted the negative consequences of the current situation and are promoting the conservation of the dark sky through multiple initiatives (Dark Skies Annual Report 2019). Millions of astronomy enthusiasts will benefit from these efforts which were not an issue for our ancestors.

[1]CINDES Research Group, Department of Engineering, Universidad Libre.
[2]Research Group CENIT, Universidad Nacional de Colombia.
[3]Olympiades Office, Astronomy and Astrophysics, Universidad Antonio Nariño.
[4]Universidad Nacional de Colombia - Sede Bogotá - Facultad de Ciencias - Observatorio Astronómico Nacional.

In Colombia, the interest in astronomy dates back to the end of the 17th century according to recent evidence found in a historical manuscript describing some ideas about the universe by Antonio Sánchez de Cozar, a humble priest whose work, drafted between 1676 and 1696, can be considered as the first original study of astronomy written in Colombia (Portilla & Moreno 2019). Some time later, José Celestino Mutis, a pioneer of science and knowledge, led a botanic expedition and founded an astronomical observatory as part of his initiative to spread science in the region. Erected in 1803, the National Astronomical Observatory of Colombia is the first astronomical observatory that was built in the Americas. The work by Arias De Greiff (1987) details the different historical and cultural aspects related to the development of astronomy in Colombia until the 20th century.

Even though the sky conditions for astronomical observations in the optical range are not very suitable in Colombia, there is a great interest from amateur astronomers, and still quite a few places in which people can enjoy the wonders of the night sky. Many careers of professional astronomers are the result of their early interest in astronomy while being part of amateur groups. This was the case of the geographer, meteorologist and astrometry specialist, William Cepeda Peña, an important disseminator of astronomy since 1965. In the 70s he began astronomical studies in Colombia, such as a star occultations by the Moon (1988-1995), the movement of the Sun using the Hipparcos catalog (2002) and, in particular, related to eclipse observations, e.g., annular solar eclipse (1995), annular eclipse (1980), total solar eclipse (1998), works grouped in Cepeda (2006).

With a valuable legacy behind, we continue investigating eclipses observed from Colombia. In this work, we report on information collected, analyzed and interpreted during the total lunar eclipse on April 14^{th} and 15^{th} in 2014, one of the four total lunar eclipses visible during 2014 and 2015 from Colombia. Particularly, we complement the work by Góez Therán & Vargas Domínguez (2016) doing a deeper analysis of the data acquired from the Tatacoa Desert, a valuable natural location in the country, by measuring meteorological variables and the sly brightness to study the variation of these parameters during the occurrence of the eclipse. This work presents a statistical study and a comparative analysis of sky quality to establish qualitative measurements of the Bortle scale.

2. METHODOLOGY

An eclipse takes place when three celestial bodies, i.e. the Earth, the Sun and the Moon, line up or get close to an alignment. A total lunar eclipse is a well-known astronomic event that occurs when planet Earth stands in the way between the Sun and the Moon, allowing our natural satellite to enter into the cone of shadow of the Earth, thus getting darker and turning into a characteristic russet color during the total occultation. At totality, the Earth obstructs most of the solar rays that arrive at the Moon, which has to happen during full-moon phase; some portion (mainly the red part of the visible light spectrum) is deflected by the Earth's atmosphere and hits the lunar surface making the moon a brownish-red color different from the typical yellow light. The effect depends also on the atmospheric conditions of our planet (clouds, dust particles, clouds of gas due to volcanic eruptions, fires and other gas emissions close to the location where the eclipse observation is carried out), and on the distance between the Moon and the center of the umbra. Figure 1 shows the visibility map for the total lunar eclipse of 14^{th}-15^{th} April 2014 and the different phases of this total eclipse, which is far more common than a total solar eclipse. The total lunar eclipse was followed from the astronomical observatory of Tatacoa and other places in Colombia, with monitoring that depended on the local meteorological conditions of the observing points.

In this work we aim at measuring the variations of sky quality (Cinzano 2005) and the main meteorological variables during the total lunar eclipse on April 14^{th} and 15^{th} of 2014 and their effect on qualitative measurements of the Bortle scale. Tracking changes in the environmental parameters and sky brightness prior to and during the eclipse are used to classify the sky according to the official global scales.

3. OBSERVATION AND MEASUREMENTS

3.1. *Location*

The observation of the total lunar eclipse on 14^{th}-15^{th} April, 2014 was carried out from the astronomical observatory of the Tatacoa, near the town of Villavieja in the Department of Huila, as shown in Figure 2. The geographic coordinates of this location are $3°14'$ North and $75°10'$ West.

The Tatacoa Desert is one of the most exotic places in Colombia. It has an area of 370 km^2. This dry tropical forest is the second largest arid zone in the country after the Guajira Peninsula, with geomorphic principally of *estoraques* and *cavarcas*,

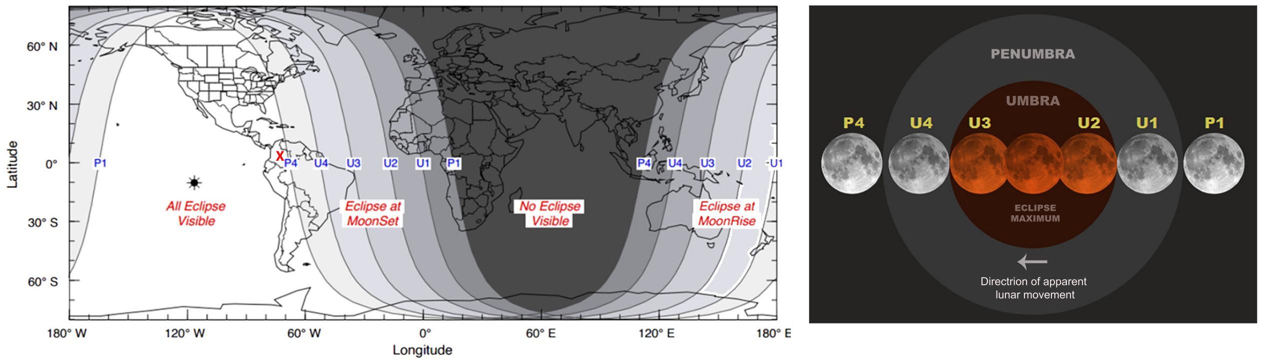

Fig. 1. Visibility map of the total lunar eclipse on 14^{th}-15^{th} April 2014 (left panel). The red X marks the location in Colombia where the eclipse was observed to carry out this research work. All different stages of a total lunar eclipse are also shown in the figure (right panel). Modified from NASA Reference Publication 1178. The color figure can be viewed online.

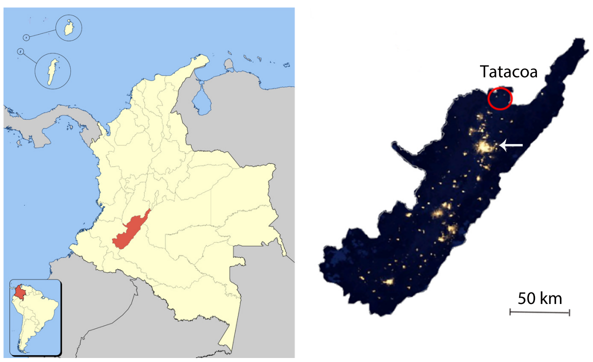

Fig. 2. Map of Colombia with a colored reddish area highlighting the Department of Huila (left panel) and a night sky satellite image (right panel) showing some illuminated areas in the same Department, corresponding to small towns and to the city of Neiva (white arrow). The location of Tatacoa Desert is encircled in red. The color figure can be viewed online.

among others. We decided to select this place for the follow-up of the eclipse, motivated by the success of previous visits pursuing astronomical observations of the Milky Way, globular clusters, nebulae and meteor showers, in addition to the reasonably good average conditions of the location in terms of clear nights, low clouds and water vapor (Góez Therán 2015; Góez Therán & Vargas Domínguez 2016; Pinzon 2016).

3.2. *Calibration*

Before the acquisition of scientific data, the equipment was tested and prepared. The installation, assembly and calibration process of the different devices and sensors began at 00:40 UTC, i.e., photometers, weather stations, telescopes, computers and CCD cameras, in order to ensure an optimal and reliable data collection before the eclipse began. Figure 3 displays the main components of the equipment.

TABLE 1

STAGES OF THE TOTAL LUNAR ECLIPSE

STAGE	Time (UTC)
P1	04:53:37
U1	05:58:19
U2	07:06:47 (Beginning of Totality Phase)
MAX	07:45:40 (Totality)
U3	08:24:35 (Completion of Totality Phase)
U4	09:33:04
P4	10:37:37

3.3. *Data*

Data acquisition for scientific measurements started right after the first contact, P1, at 4:53:37 UTC. Contact times and all different phases of the eclipse are listed in Table 1. Measurements of sky brightness were taken pointing the SQM to the zenith in all cases.

We used a photometer called SQM-LE to measure the brightness of the sky[5], a weather station, WMR200 Davis Instruments Pro with wireless sensors, as shown in Figure 3. Furthermore, three CCD cameras for Celestron astrophotography were employed in order to record all stages of the eclipse (P1, U1, U2, U3 and U4) by using a calibrated Meade ETX-90 telescope (two-star method) and with a per-

[5] www.unihedron.com/projects/darksky/.

Fig. 3. Main equipment and sensors that were used to measure sky quality and meteorological variables. See the text for details.

manent monitoring of the Moon to obtain the alt-azimuth values during the data collection period.

The photometer acquires data on a scale of mag.arsec^{-2}. Figure 4 exemplifies the use of this instrument and the way we refer to the magnitude as describing the brightness of an object, i.e. the amount of light striking the sensor. Sky brightness, humidity, pressure and horizontal coordinates of the Moon were registered every 5 minutes and tabulated for the subsequent statistical analysis using the software package SPSS (Argyrous 2005).

Table 2 presents all the collected data during the observing session.

4. ANALYSIS AND RESULTS

Figure 5 displays the temporal variation of sky brightness as plotted from all acquired data. The multiple total lunar eclipse stages are identified at the corresponding times (see Table 1). The plot shows clear periods of stability, increase and decrease in the sky brightness, as follows: from P1 to U1 there are not many variations, but starting from U1 there is a continuous increase ending at U2. This moment marks the beginning of the totality phase, in which the sky brightness remains steady for the entire period, that extended until U3 is reached. Soon after, the trend of the plot reveals, for the first time, a decrease of sky brightness.

Detailed analysis of Figure 5 allows us to establish an average SQM value of 21.15 mag.arcsec^{-2} during the totality phase of the eclipse, which can be associated to a Bortle Class 4 of sky quality, as itemized in Table 3 on the international measurement scale. Up to this moment, and from the beginning of the eclipse, SQM values increased and therefore the sky quality improved (Rabaza et al. 2010), meaning that during this period, the sky can be classified in a Bortle class ranging from 1 to 8.9.

Figure 6 plots the temporal evolution of different physical parameters. The values of Moon height and sky brightness measurements are also included. In particular we are interested in the variation of pressure, humidity and temperature during the occurrence of the eclipse. As expected, there are no significant or abnormal changes in these variables for about 5 hours (from 00:40 to 05:40 UTC) before phase U1 of the eclipse. There is a slight decrease in the sky quality (SQM) associated with the rising of the Moon in the sky (from ≈25° to ≈77°). From phase U1 until U2 is reached (07:10 UTC), the temperature and humidity exhibit substantial changes, that remain up to phase U3 (08:35 UTC), corresponding to the finishing time for totality.The humidity evidences a peak value soon after, while a maximum temperature of 32.2° is reached closer to U2. On the other hand, the minimum temperature occurs at U3, about 40 minutes after the maximum (MAX) was observed. After totality, from U3 to U4, changes of these variables are still present, with an overall decrease of both.

The relative humidity shows a clear decrease after U1, when the eclipse is on its way to totality, but once it is reached, it starts to increase up to a maximum value soon after U3. The maximum humidity value registered is 47% and the minimum value is 39%. Regarding pressure values, shown in the bottom panel in Figure 6, there is a tiny variation of pressure with extreme values of 1002 and 1004 millibars. During the totality phase (U2 to U3) the average value registered is 1002 millibars. Finally, during the maximum of the total lunar eclipse (07:45:40 UT) the Moon height was 46° and the azimuth was 251° from the observation point.

A statistical analysis was carried out in order to study the behavior of all different measurements before and during the eclipse, as shown in Figure 7 from the values listed in Table 4. It also includes statistics for all the acquired data.

5. CONCLUSIONS

The expedition to the Tatacoa Desert, in Colombia, to observe the total lunar eclipse on 14^{th}-15^{th} April 2014, was successfully accomplished. The team managed to complete 9 hours of continuous observation and registration of meteorological variables and sky brightness. The month of April is characterized by the occurrence of intense rainfalls in Colombia. Fortunately the conditions present during the total lu-

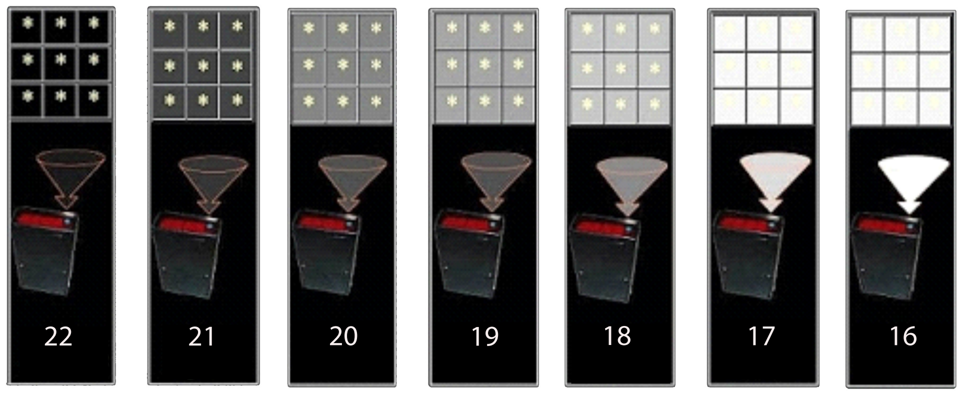

Fig. 4. Sketch showing the use of a sky quality meter (SQM) to measure the amount of light striking the sensor. Numbers in every panel correspond to the value of sky brightness (measured in units of mag. arcsec^{-2}) characterizing the quality of the sky. Taken from www.nightwise.org. The color figure can be viewed online.

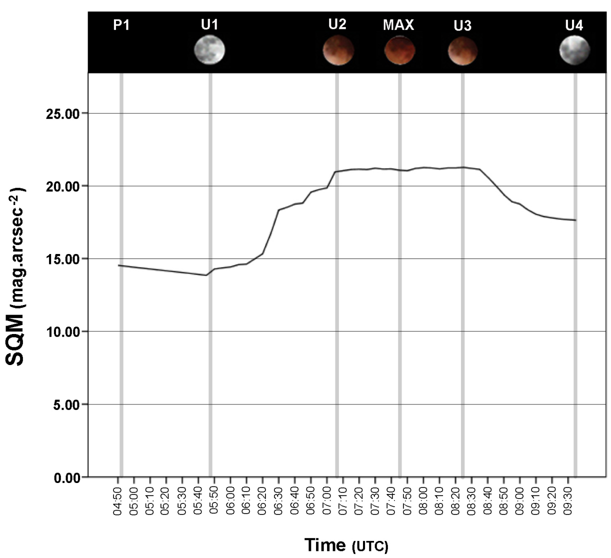

Fig. 5. Plot displaying the time evolution of the sky brightness during the total lunar eclipse observed in Colombia on 14-15 April 2014. The upper image shows the different stages as listed in Table 1. Note that times are shown in UTC. The color figure can be viewed online.

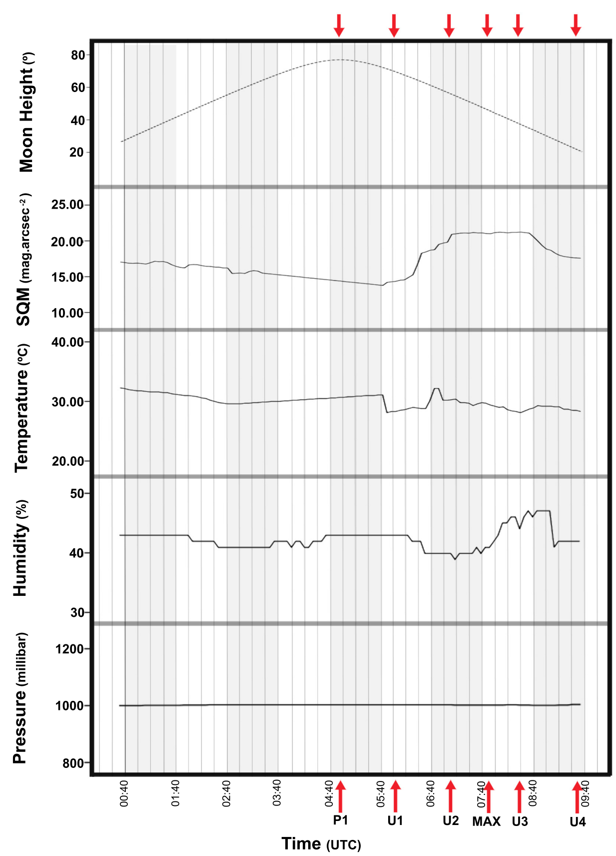

Fig. 6. Temporal evolution of physical parameters (Moon height, SQM, temperature, humidity, pressure) during the total lunar eclipse observed in Colombia on 14^{th}-15^{th} April 2014. The red arrows on top stand as a reference of the times pointed by the bottom arrows, for stages P1, U1, U2, MAX, U3 and U4, respectively. Note that times are shown in UTC. The color figure can be viewed online.

nar eclipse in the selected location allowed the expedition team to observe and to record, which was not the case for some other observing locations where attempts failed. Nevertheless, from 09:35 UTC onwards, cloudiness at the observation area in the Tatacoa did not allow us to take measurements during the last part of the astronomical event, in the final penumbral phase. These conditions might have influenced the humidity and temperature values acquired close to the ending phase of the partiality, and future

TABLE 2

DATA

DATA	LOCAL TIME	UTC	SQM ($mag.arcsec^{-2}$)	TEMPERATURE (°C)	PRESSURE (mbar)	MOON HEIGHT (°)	HUMIDITY (%)	STAGE
1	19:40	0:40	17.11	32.3	1000	26.6	43	C*
2	19:45	0:45	17.04	32.2	1000	27.8	43	C*
3	19:50	0:50	16.94	32	1000	28.9	43	C*
4	19:55	0:55	16.92	31.9	1000	30.1	43	C*
5	20:00	1:00	16.95	31.8	1000	31.3	43	C*
6	20:05	1:05	16.9	31.8	1000	32.3	43	C*
7	20:10	1:10	16.82	31.7	1001	33.7	43	C*
8	20:15	1:15	17	31.6	1001	34.9	43	C*
9	20:20	1:20	17.2	31.6	1001	36	43	C*
10	20:25	1:25	17.15	31.6	1001	37.2	43	C*
11	20:30	1:30	17.18	31.5	1001	38.4	43	C*
12	20:35	1:35	17.03	31.5	1001	39.6	43	C*
13	20:40	1:40	16.72	31.3	1001	40.8	43	C*
14	20:45	1:45	16.5	31.2	1001	41.9	43	C*
15	20:50	1:50	16.35	31.1	1001	43.1	43	C*
16	20:55	1:55	16.29	31	1002	44.3	43	C*
17	21:00	2:00	16.71	31	1002	45.4	43	C*
18	21:05	2:05	16.76	30.9	1002	46.6	42	C*
19	21:10	2:10	16.73	30.8	1002	47.8	42	C*
20	21:15	2:15	16.6	30.6	1002	48.9	42	C*
21	21:20	2:20	16.51	30.5	1002	50.1	42	C*
22	21:25	2:25	16.49	30.2	1003	51.2	42	C*
23	21:30	2:30	16.39	30	1003	52.4	42	C*
24	21:35	2:35	16.39	29.8	1003	53.5	41	C*
25	21:40	2:40	16.27	29.7	1003	54.7	41	C*
26	21:45	2:45	16.27	29.6	1003	55.8	41	C*
27	21:50	2:50	15.52	29.6	1003	56.9	41	C*
28	21:55	2:55	15.55	29.6	1003	58	41	C*
29	22:00	3:00	15.57	29.6	1003	59.2	41	C*
30	22:05	3:05	15.52	29.7	1003	60.3	41	C*
31	22:10	3:10	15.79	29.7	1003	61.4	41	C*
32	22:15	3:15	15.91	29.8	1003	62.4	41	C*
33	22:20	3:20	15.84	29.8	1003	63.5	41	C*
34	22:25	3:25	15.57	29.9	1003	64.6	41	C*
35	22:30	3:30	15.50	29.9	1003	65.6	41	C*
36	22:35	3:35	15.44	30.0	1003	66.6	41	C*
37	22:40	3:40	15.38	30.0	1003	67.6	42	C*
38	22:45	3:45	15.32	30.0	1003	68.6	42	C*
39	22:50	3:50	15.26	30.1	1003	69.6	42	C*
40	22:55	3:55	15.20	30.1	1003	70.5	42	C*
41	23:00	4:00	15.14	30.2	1003	71.4	41	C*
42	23:05	4:05	15.08	30.2	1003	72.2	42	C*
43	23:10	4:10	15.02	30.3	1003	73.1	42	C*
44	23:15	4:15	14.95	30.3	1003	73.8	41	C*
45	23:20	4:20	14.89	30.4	1003	74.5	41	C*
46	23:25	4:25	14.83	30.4	1003	75.1	42	C*
47	23:30	4:30	14.77	30.5	1003	75.7	42	C*
48	23:35	4:35	14.71	30.5	1003	76.1	42	C*
49	23:40	4:40	14.65	30.5	1003	76.5	43	C*
50	23:45	4:45	14.59	30.6	1003	76.8	43	C*
51	23:50	4:50	14.53	30.6	1003	76.9	43	P1
52	23:55	4:55	14.47	30.7	1003	76.9	43	P1
53	0:00	5:00	14.40	30.7	1003	76.9	43	P1
54	0:05	5:05	14.34	30.8	1003	76.7	43	P1
55	0:10	5:10	14.28	30.8	1003	76.4	43	P1
56	0:15	5:15	14.22	30.9	1003	76	43	P1
57	0:20	5:20	14.16	30.9	1003	75.5	43	P1
58	0:25	5:25	14.10	31.0	1003	74.9	43	P1
59	0:30	5:30	14.04	31.0	1003	74.3	43	P1

C*: CALIBRATION OF EQUIPMENT AND SENSORS

TABLE 2. CONTINUED

DATA	LOCAL TIME	UTC	SQM (mag.arcsec^{-2})	TEMPERATURE (°C)	PRESSURE (mbar)	MOON HEIGHT (°)	HUMIDITY (%)	STAGE
60	0:35	5:35	13.98	31.0	1003	73.6	43	P1
61	0:40	5:40	13.91	31.1	1003	72.8	43	P1
62	0:45	5:45	13.85	31.1	1003	72	43	P1
63	0:50	5:50	14.28	28.1	1003	71.1	43	U1
64	0:55	5:55	14.36	28.3	1003	70.2	43	U1
65	1:00	6:00	14.42	28.3	1003	69.3	43	U1
66	1:05	6:05	14.58	28.5	1003	68.3	43	U1
67	1:10	6:10	14.62	28.6	1003	67.3	43	U1
68	1:15	6:15	14.97	28.8	1003	66.3	43	U1
69	1:20	6:20	15.33	29	1003	65.3	42	U1
70	1:25	6:25	16.69	28.9	1003	64.2	42	U1
71	1:30	6:30	18.33	28.8	1003	63.2	42	U1
72	1:35	6:35	18.51	28.8	1003	62.1	40	U1
73	1:40	6:40	18.74	30.2	1003	61	40	U1
74	1:45	6:45	18.81	32.2	1003	59.9	40	U1
75	1:50	6:50	19.56	32.2	1003	58.8	40	U1
76	1:55	6:55	19.73	30.2	1003	57.7	40	U1
77	2:00	7:00	19.85	30.2	1003	56.6	40	U1
78	2:05	7:05	20.95	30.3	1003	55.4	40	U1
79	2:10	7:10	21.03	30.4	1002	54.3	39	U2
80	2:15	7:15	21.11	29.8	1002	53.2	40	U2
81	2:20	7:20	21.13	29.8	1002	52	40	U2
82	2:25	7:25	21.11	29.7	1002	50.9	40	U2
83	2:30	7:30	21.2	29.3	1002	49.7	40	U2
84	2:35	7:35	21.14	29.6	1002	48.6	41	U2
85	2:40	7:40	21.15	29.8	1002	47.4	40	U2
86	2:45	7:45	21.06	29.7	1002	46.2	41	MAX
87	2:50	7:50	21.03	29.4	1002	45.1	41	U3
88	2:55	7:55	21.19	29.2	1002	43.9	42	U3
89	3:00	8:00	21.24	29	1002	42.7	43	U3
90	3:05	8:05	21.22	29.1	1002	41.6	45	U3
91	3:10	8:10	21.15	28.6	1003	40.4	45	U3
92	3:15	8:15	21.22	28.4	1003	39.2	46	U3
93	3:20	8:20	21.22	28.3	1003	38.1	46	U3
94	3:25	8:25	21.26	28.1	1002	36.9	44	U3
95	3:30	8:30	21.19	28.4	1002	35.7	46	U4
96	3:35	8:35	21.12	28.7	1002	34.5	47	U4
97	3:40	8:40	20.59	28.9	1001	33.3	46	U4
98	3:45	8:45	20.01	29.3	1001	32.2	47	U4
99	3:50	8:50	19.39	29.2	1001	31	47	U4
100	3:55	8:55	18.9	29.2	1001	29.8	47	U4
101	4:00	9:00	18.74	29.2	1001	28.6	47	U4
102	4:05	9:05	18.34	29.1	1001	27.4	41	U4
103	4:10	9:10	18.04	29.1	1002	26.2	42	U4
104	4:15	9:15	17.88	28.7	1002	25.1	42	U4
105	4:20	9:20	17.79	28.7	1002	23.9	42	U4
106	4:25	9:25	17.71	28.5	1004	22.7	42	U4
107	4:30	9:30	17.67	28.5	1004	21.5	42	U4
108	4:35	9:35	17.63	28.3	1004	20.3	42	U4

work will have to manage to register these data for the whole duration of the eclipse after P4 is reached.

As explained in § 4, it was possible to detect changes in these variables during the occurrence of the eclipse, except for pressure measurements, which were very stable for all recorded data. Particularly during the totality phase, the temperature and humidity show significant variations, as seen in Figure 6. The corresponding average of sky brightness during totality gives an SQM value of 21.15 mag.arcsec^{-2} and conditions are such as to classify the sky of the Tatacoa Desert according to the Bortle scale as 4. The maximum total lunar eclipse took place at 07:45:40 UTC on 15th of April, 2014, the moment where the measured temperature was 29.7°. At the initial phase of the lunar eclipse, from P1 to U1, the brightness of the sky slightly increased, reaching a minimum SQM value of 13.85 mag.arcsec^{-2}. Once entering the umbral phase, the brightness of the sky began to decrease considerably, as expected from a reduction in the illumination of the lunar disc. A clear trend is shown

TABLE 3

SCALE MEASUREMENTS OF THE SKY QUALITY

Sky brightness (mag.arcsec^{-2})	Bortle Class
>21.90	1
21.90 - 21.50	2
21.50 - 21.30	3
21.30 - 20.80	4
20.80 - 20.10	4.5
20.10 - 19.10	5
19.10 - 18.00	6.7
<18.00	8.9

in Figure 5. At the precise moment when the eclipse sequence surpassed the umbral phase, the SQM values start to increase. From U2 to U3 the values reached a *plateau* that remained stable for almost 1.5 hours. Note that the lowest value recorded by the SQM during the entire eclipse (13.85 mag.arcsec^{-2}) corresponds to 8.9 according to the Bortle scale, whereas the highest value was 4. Sources of error in the sky brightness come from the error introduced by the SQM measurements, with a typical value of 0.2302, indicating that the samples were taken as accurately as possible based on the previous calibration of the equipment. Other external factors that can influence the local measurements and that should be borne in mind, are cloudiness, latitude from where it is observed, the environment, vegetation, and the time of year.

Close to the moment of maximum altitude of the Moon (77°), the humidity and pressure do not vary significantly. Humidity is about 43% with a pressure of 1003 mbar. Pressure values keep very stable throughout the whole observing session and ≈75% of the data collected for atmospheric pressure have variations of only 1 mbar. The pressure was the variable that registered the least variation compared to other variables. There was no noticeable variation of the pressure with the height of the Moon, and the humidity value at that time did not change significantly.

When the Moon enters the umbra, the twilight zone generated by Earth, it does not reflect the same amount of light from the Sun, and therefore a decrease in temperature is plausible. In our records, the ambient temperature varies depending on the transition zone the Moon reaches. In P1 the temperature is higher, compared to averages for the penumbra (U1) and umbra (U2), for which lower temperatures are registered. Nevertheless, in this period of time we noticed some clouds approaching to the location, and therefore the temperature decrease can not be directly associated to the totality phase of the eclipse. Further studies should be made to clarify if the actual dependence of the radiation from the Sun reflected by the Moon diminished during the totality phase and if the ambient temperature decreased. We can only determine that the maximum humidity coincides with a minimum temperature value.

Regarding the quality of the sky, depending on the levels of sky brightness, it was observed that SQM values start increasing when the eclipse is in phase U1 with a maximum value of 21.26 mag.arcsec^{-2}. This means that the quality of the sky improves considerably, because there is less brightness of the sky, and therefore the sensor captures fewer photons. It is also discernible from the Moon height and SQM plots in Figure 5 that the sky brightness at the beginning (00:40 UTC) and the end (09:35 UTC) of the observing run are very similar

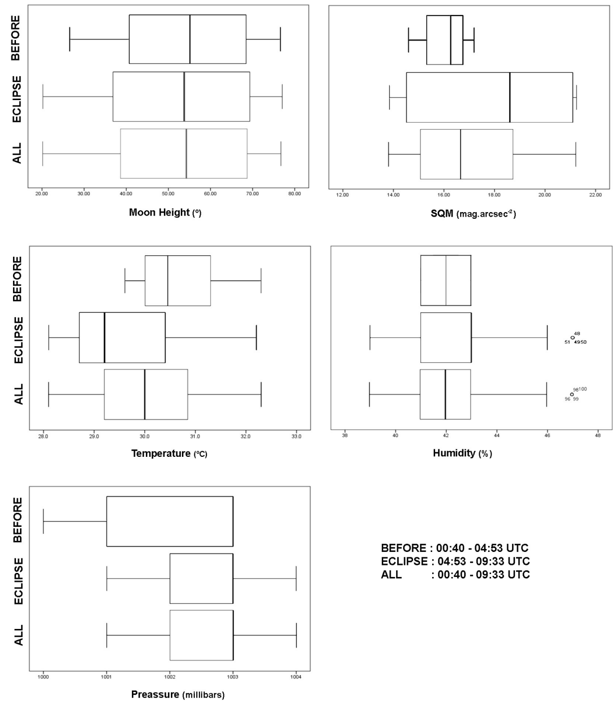

Fig. 7. Statistical box plots for several physical parameters **before** the occurrence of the eclipse (BEFORE), during the eclipse (ECLIPSE) and for all the acquired data (ALL) on 14^{th}-15^{th} April 2014. Every plot shows the median value (vertical solid line), $\pm 1\sigma$, and total range. Atypical values for humidity are marked by small circles. The mean values and standard deviations are listed in Table 4.

TABLE 4

DESCRIPTIVE STATISTICS

	N	MINIMUM	MAXIMUM	MEAN		STANDARD DEVIATION
				Value	Standard error	
ALL DATA (00:40 - 09:35 UT)						
SQM	58	13.85	21.26	18.0598	0.37640	2.86654
Temperature	58	28.1	32.2	29.552	0.1383	1.0532
Pressure	58	1001	1004	1002.53	0.099	0.754
Humidity	58	39	47	42.64	0.284	2.166
Height	58	20.37	76.92	52.4621	2.36154	17.98499
BEFORE THE ECLIPSE (00:40 - 04:45 UT)						
SQM	50	14.59	17.20	16.0244	0.11687	0.82636
Temperature	50	29.5	32.3	30.618	0.1132	0.8004
Pressure	50	1000	1003	1002.16	0.157	1.113
Humidity	50	41	43	42.06	0.119	0.843
Height	50	26.55	76.73	54.2426	2.21850	15.68714
DURING THE ECLIPSE (04:50 - 09:35 UT)						
SQM	108	13.85	21.26	17.1175	0.23033	2.39368
Temperature	108	28.1	32.3	30.045	0.1041	1.0815
Pressure	108	1000	1004	1002.36	0.092	0.952
Humidity	108	39	47	42.37	0.164	1.705
Height	108	20.37	76.92	53.2864	1.62674	16.90561

with SQM values of 17.11 and 17.63 mag.arcsec^{-2}, respectively, with also a rather similar Moon height values of 26.6° and 20.3° for every case. This confirms that the effect of sky quality variation depends almost entirely on the eclipse occurrence and not on the altitude of the Moon over the horizon and the way it affects the scattered light. Unfortunately, as mentioned before, the weather conditions were not favorable after U4 to continue acquiring data and measuring the conditions after P4 was reached. Nevertheless, it can be established without further inspection, that the sky quality of that night at the Tatacoa Desert corresponded to a Bortle Class value of 8.9 when the eclipse was not occurring.

Figure 7 displays statistical box plots for all the different parameters separated in three different intervals: before the occurrence of the eclipse (BEFORE), during the eclipse (ECLIPSE) and for all the acquired data (ALL), in order to quantify the influence of the eclipse on the normal conditions of at the beginning of the night, and how the median values are affected.

Our results were compared with recent studies based on comparative data, reports, and measurements associated with the extension project of the National Astronomical Observatory of Colombia entitled "Monitoring the quality of the sky in the Tatacoa Desert to obtain the Starlight certification as an astrotourism destination"[6]. The study included measurements obtained during the new moons over a year, from January to December 2018, and their respective analysis, confirming that the quality of the Tatacoa sky is compatible with the requirements as a Starlight astronomical destination[7] This comparative study aims at monitoring the quality of the sky in three locations to characterize this destination; the authors recorded their data at the beginning, in the middle, and at the end of the night, in units of mag.arcsec^{-2} verifying that, according to their results, the required values are close to, or greater than, 21 mag.arcsec^{-2}, in agreement with the the result for sky quality presented in our work during the totality phase of a lunar eclipse.

REFERENCES

Argyrous, G. 2005, Statistics for Research: With a Guide to SPSS (3rd. ed.; London: SAGE Publications)

Arias de Greiff, J. 1987, Cienc. Tec. Des. Bogotá (Colombia), 11 (1-2), 1

Cepeda Peña, W. E. 2006, Eclipses, ed: Panamericana v.11(1), 1

Cinzano, P. 2005, Night Sky Photometry with Sky Quality Meter, 9

[6]Visit the information about this project: http://168.176.14.11/index.php?id=6181.

[7]Website: https://www.fundacionstarlight.org/contenido/49-listado-destinos-turisticos-starlight.html.

Góez Therán, C. 2015, Master Thesis, Estudio astrometeorológico para el diagnóstico y emplazamiento de observatorios astronómicos ópticos en Colombia, Universidad Nacional de Colombia

Góez Therán C. & Vargas Domínguez, S. 2016, Iranian Journal of Astronomy and Astrophysics, 3, 15

Nightscape Annual Report. 2019, Int. Dark Sky Association, 101

Pinzón, G., González, D., & Ramírez, A. 2016, Rev. Acad. Colomb. Cienc. Ex. Fis. Nat., 40(154), 53

Portilla, J. G. & Moreno, F. 2019, Rev. Acad. Colomb. Cienc. Ex. Fis. Nat., 43(167), 255

Rabaza, O., Galadí-Enríquez, D., Espín Estrella, A., & Aznar Dols, F. 2010, Journal of Environmental Management, 91, 1278

Cristian Góez Therán: CINDES Research Group, Department of Engineering, Universidad Libre, Bogotá, Colombia (cristian.goezt@unilibre.edu.co).

Cristian Góez Therán: Research Group CENIT, Universidad Nacional de Colombia, Colombia.

Cristian Góez Therán: Olympiades Office, Astronomy and Astrophysics, Universidad Antonio Nariño, Colombia.

Santiago Vargas Domínguez: Universidad Nacional de Colombia - Sede Bogotá - Facultad de Ciencias - Observatorio Astronómico Nacional - Carrera 45 # 26-85, Bogotá - Colombia (svargasd@unal.edu.co).

Revista Mexicana de Astronomía y Astrofísica, **57**, 67–80 (2021)

https://doi.org/10.22201/ia.01851101p.2021.57.01.04

SPECKLE INTERFEROMETRY AT THE OBSERVATORIO ASTRONÓMICO NACIONAL. VII

V. G. Orlov

Instituto de Astronomía, Universidad Nacional Autónoma de México, Ciudad de México, México.

Received August 25 2020; accepted September 22 2020

ABSTRACT

The results of speckle interferometric measurements of binary stars performed during June, 2016 with the 2.1 m telescope at the Observatorio Astronómico Nacional at SPM (México) are given. We report 480 astrometric measurements of 468 double stars systems. The measured angular separations ρ range from $0''.091$ to $5''.93$. Most of the observed pairs (414 out of 468) are close double stars having separations of $\rho \leq 1''$. We confirm as double stars 59 targets and we found 3 new pairs with separation of less than $1''$. Finally, we show that the high resolution autocorrelation function in polar coordinates allows to easily recover astrometric parameters even in the presence of strong telescope aberrations.

RESUMEN

Se presentan las mediciones de interferometría de motas de estrellas binarias, realizadas durante el mes de junio de 2016 con el telescopio de 2.1 m del Observatorio Astronómico Nacional en SPM (México). Reportamos 480 mediciones astrométricas de 468 sistemas de estrellas dobles. Las separaciones angulares medidas ρ van desde $0''.091$ a $5''.93$. La mayoría de los pares observados (414 de 468) son estrellas dobles cercanas con una separación $\rho \leq 1''$. Confirmamos 59 objetos como estrellas dobles e identificamos 3 nuevos pares con una separación de menos de $1''$. Finalmente, mostramos que la función de autocorrelación de alta resolución en coordenadas polares permite recuperar fácilmente los parámetros astrométricos, incluso en presencia de fuertes aberraciones del telescopio.

Key Words: binaries: close — techniques:high angular resolution — techniques: interferometric

1. INTRODUCTION

In this paper we report astrometric results for double stars obtained by speckle interferometric observations carried out with the 2.1 m telescope of Sierra San Pedro Mártir National Astronomical Observatory (OAN-SPM) in June of 2016. This is the seventh in a series of publications that started with speckle interferometric measurements performed with the OAN telescopes in 2008 (Orlov et al. 2009). As in our previous publications, we focus on double stars from the Washington Double Star (WDS) catalog (Worley & Douglass 1997).

The Speckle Interferometry (SI) (Labeyrie 1970) is one of the most used high resolution techniques. This method allows the observer to obtain information about relative positions in close binary stars systems with diffraction-limited accuracy. This technique was most widely used in the study of binary and multiple stars (Tokovinin et al. 2020; Guerrero et al. 2020; Mitrofanova et al. 2020). The observation methodology and data processing of SI is very well studied and described by Tokovinin et al. (2010).

The 2.1 m telescope of OAN-SPM has a thin primary mirror; its shape is corrected by air bags. The process of correction takes about one hour and is performed only once before observations. During the night, the temperature of the primary mirror and of the telescope mount change, which leads to thermal deformations. Also, corrections introduced by the airbags depend on the hour angle and the zenith distance of the target. As a result, we have different aberrations for each object (Figure 1). Because of this, it is unfeasible to construct a universal synthetic speckle interferometric transfer function or even to

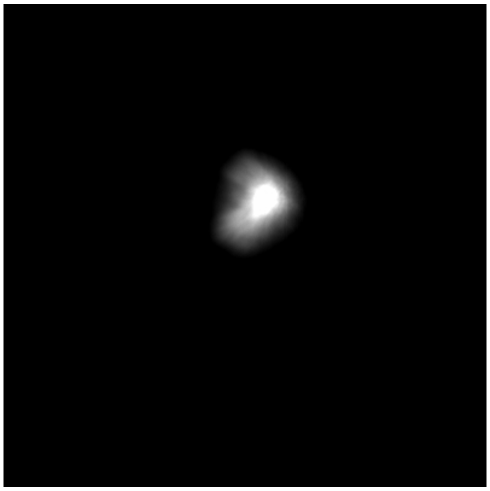

(a)

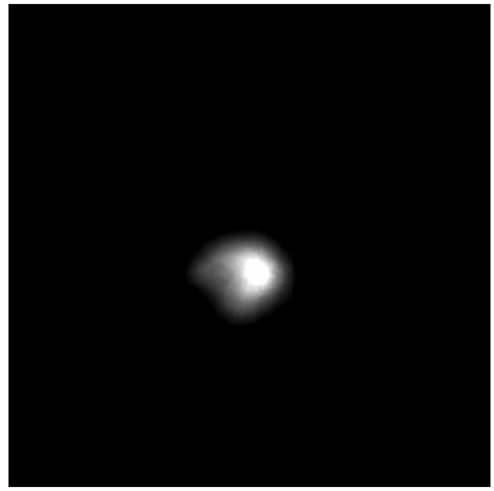

(b)

Fig. 1. Long exposure image of WDS 20480+3917 (a). Long exposure image of WDS 18003+2154 (b). Both images show very strong coma aberration with different angles.

use a reference star. This fact limits the possibility of finding both astrometric and photometric parameters of double stars. In addition, the telescope's vibration distorts the specklegrams. All these factors have a greater impact on the ability to recover photometric parameters than on the recovery of astrometric parameters. Therefore, in this study we focus on improving the recovery of astrometric parameters.

In order to estimate astrometric parameters, we designed an algorithm which allows one to recover each measurement from the distorted power spectrum. In section 3.2 we describe the calculation of the high resolution autocorrelation function in polar coordinates. This algorithm allows for blind searching of the astrometric parameters ρ and θ of double stars, since it finds the coordinates of the absolute maximum of a two-dimensional discrete function.

2. OBSERVATIONS

Speckle interferograms were taken during four nights in the summer of 2016, from June 28 to July 1 at the 2.1 m telescope of the Observatorio Astronómico Nacional (OAN), which is located at the astronomical site Sierra San Pedro Mártir, México.

The observations were performed using the EMCCD iXon Ultra 888 from Andor Technology. This is a low-noise, high-sensitivity EMCCD camera that can be cooled thermoelectrically down to $-95°C$ which provides excellent elimination of dark noise, even for the short time exposures. The detector has quantum efficiency higher than 80% in the range of $450-750$ nm, with a maximum of 95% at 550 nm (V-band). This camera allows a fast frame rate so it can be used for speckle interferometry. The detector has 1024×1024 square pixels of 13 μm per side.

The observations were carried out using broadband filters $V(538/98$ nm), $R(630/118$ nm) and $I(894/330$ nm) from the Johnson-Cousins set. The size of the diffraction-limited speckle (λ/D) for the 2.1m telescope is approximately 70 mas at this filter wavelength. Given these parameters, we need an angular pixel scale of about 35 mas to obtain a Nyquist sampling of specklegrams. To provide a suitable sampling, we used the $f/7.5$ secondary mirror combined with a microscope objective lens $\times 4$.

We recorded 500 speckle frames of 400×400 pixel per object, taken with exposure times of 29.5 ms. We use EM gain of 1/300 photons/e^- for all observations.

The seeing was better than $1''$over all the observing nights. However, aberrations introduced by the telescope have a larger effect (Figure 1). As a result, long exposure images have a resolution of about $1.5''$.

3. DATA PROCESSING

The first step of the data processing is the dark field correction of detected images $I'_n(\mathbf{x})$:

$$I_n(\mathbf{x}) = I'_n(\mathbf{x}) - Dark(\mathbf{x}), \qquad (1)$$

where $\mathbf{x}$ is a 2D spatial coordinate, $I_n(\mathbf{x})$ is the corrected image, $Dark(\mathbf{x})$ is the average dark image captured with a closed shutter (Figure 2 left). In order to remove the reading noise, we also set to zero all values less than 4σ of dark (Figure 2 right).

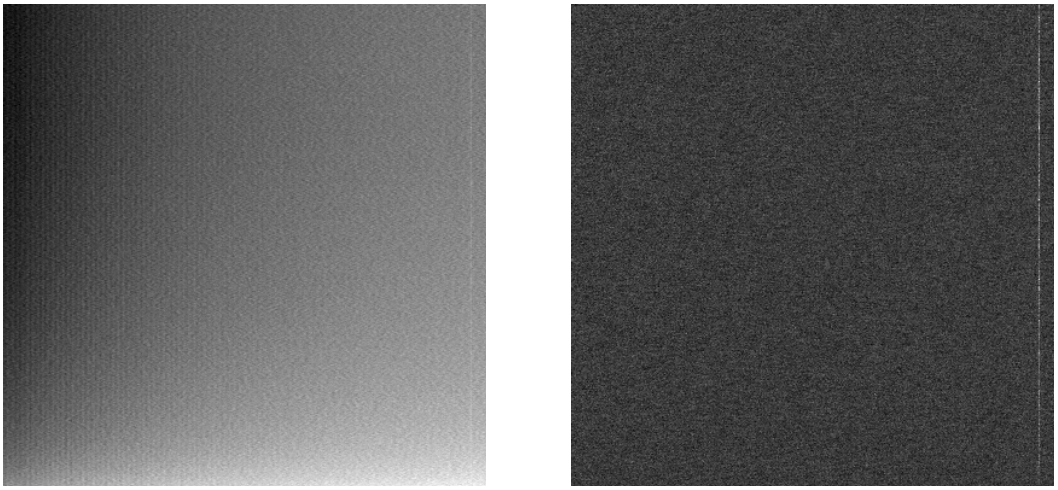

Fig. 2. The average Dark image (left) and σ of Dark image (right).

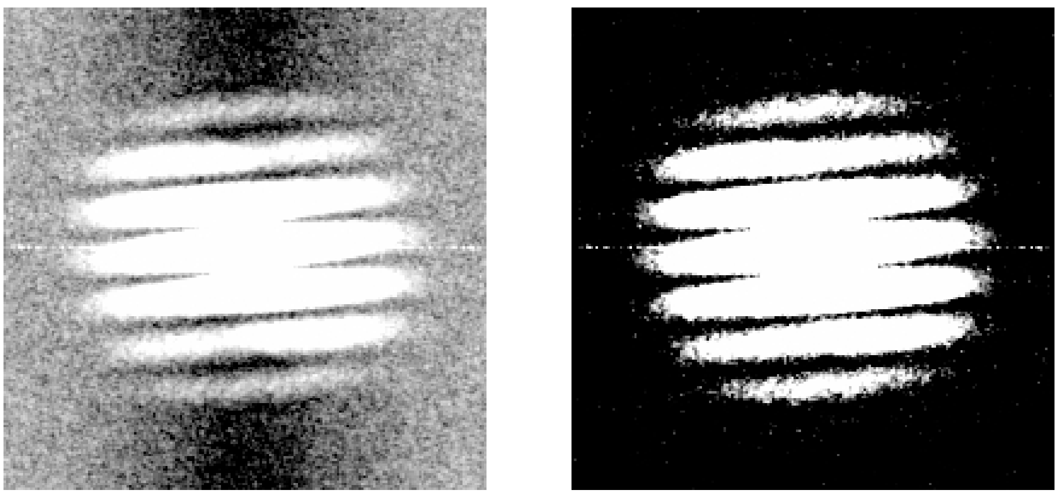

Fig. 3. Power spectrum of WDS 20312+1116 before photon bias correction (left) and after correction (right). The separation is $0.''3$.

3.1. *Unshifted Power Spectrum*

The next step is to calculate the averaged power spectrum (PS) for each star:

$$PS(\mathbf{f}) = \left\langle \left| FT\left\{ I_n(\mathbf{x}) \right\} \right|^2 \right\rangle, \tag{2}$$

where $\mathbf{f}$ is a spatial frequency, $FT\{...\}$ is the Fourier transform and $\langle ... \rangle$ denotes averaging over all images.

In the case of low light images, the averaged power spectrum can be expressed as (Kerp et al. 1992):

$$PS(\mathbf{f}) = P(\mathbf{f}) \cdot |G(\mathbf{f})|^2 + q\,|G(\mathbf{f})|^2, \tag{3}$$

where $P(\mathbf{f})$ is the unshifted estimation of the power spectrum, q is some constant, $|G(\mathbf{f})|^2$ is the power spectrum of the photon event shape function, also known as photon bias. The photon bias $|G(\mathbf{f})|^2$ can be determined as the normalized power spectrum of the night sky. $|G(\mathbf{f})|^2$ is constant in the Y direction for this camera. Thus, it can be determined directly from $PS(\mathbf{f})$ (Figure 3, left) by analysis of its part beyond the cut-off frequency of telescope. The unshifted power spectrum of specklegrams $P(\mathbf{f})$ is shown in Figure 3 (right). Therefore, it can be presented as:

$$P(\mathbf{f}) = |O(\mathbf{f})|^2 \left\langle |S_n(\mathbf{f})|^2 \right\rangle, \tag{4}$$

where $|O(\mathbf{f})|^2$ is the power spectrum of the object, and $\left\langle |S_n(\mathbf{f})|^2 \right\rangle$ is the speckle interferometric transfer

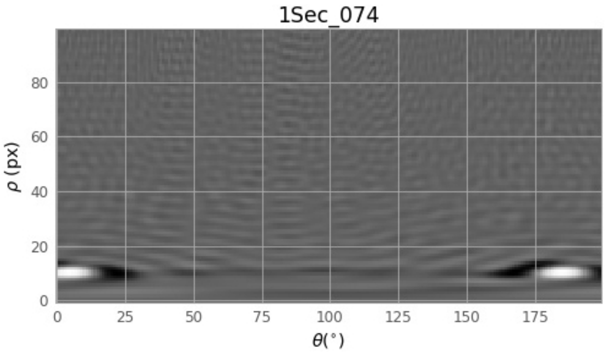

Fig. 4. The ACF in polar coordinates for WDS 20312+1116. The separation is 0.″3.

function. The speckle interferometric transfer function can be obtained by observing a reference star, or one can construct a universal synthetic speckle interferometric transfer function (Tokovinin et al. 2010). If one needs only astrometric parameters, they can be obtained without the speckle interferometric transfer function, directly from P(**f**).

3.2. *Autocorrelation Function in Polar Coordinates*

In order to find astrometric parameters from the unshifted power spectrum we calculated the high resolution autocorrelation function in polar coordinates ACF_p:

$$ACF_p(\rho,\theta) = const \int_0^\infty \int_0^{2\pi} \cos(2\pi r\rho\cos(\theta-\phi))\times \times P(r,\phi)W(r,\phi)rdrd\phi, \quad (5)$$

where $W(r,\phi)$ is the window which excludes part of $P(r,\phi)$ beyond the cut-off frequency of the telescope f_T and for frequencies lower than the atmospheric cutoff f_A. Also, taking in to account central symmetry of $P(r,\phi)$ equation 5 can be rewritten as:

$$ACF_p(\rho,\theta) = const \int_{f_A}^{f_T} \int_0^{\pi} \cos(2\pi r\rho\cos(\theta-\phi))\times \times P(r,\phi)rdrd\phi. \quad (6)$$

One example of ACF_p is shown in Figure 4. The position of the maximum gives us ρ and θ which determine the position of the component in the coordinates of the detector.

Now let us see if ACF_p allows us to find astrometric parameters when the power spectrum is distorted by vibrations and strong aberrations of the telescope. As shown in Figure 5 (left) the power spectrum loses the high frequencies in the vertical direction. However, the high resolution ACF_p has a strong maximum (Figure 5, right). The precision of determining astrometric parameters of the binary system depends on the accuracy with which we can determine the coordinates of the maximum of the discrete function ACF_p. Thus, we can recover the astrometric parameters from the distorted power spectrum. Although measurements can be carried out without the speckle interferometric transfer function correction, its use improves their accuracy.

3.3. *180 Degree Ambiguity*

The power spectrum has a 180° ambiguity. To deal with this issue, we used the self-calibrating shift-and-add technique (Christou et al. 1986). The technique allows us to get diffraction-limited images without using any reference star. When the components have similar magnitudes, the result of this technique is similar to the diffraction-limited autocorrelation, as in Figure 6 (left), contrary to the case in which there is a clear difference between the components, as shown in Figure 6 (right). This double star has a difference of one magnitude between components. This technique allows us to overcome the common 180 degree ambiguity, thus obtaining a reconstruction of the close double star system. Then we can obtain the real θ (position angle) and ρ (separation) by calibration.

3.4. *Calibration*

To perform the calibration, we need to find the pixel scale and the position angle offset. There are two common ways to do this. The first one is by observing some binary stars which have known orbits of grade 1 and calculating ephemerides from the orbital elements. The second way is by observing double stars with very slow relative motion of the components. In this case, ephemerides are calculated by linear approximation of the component motion, or by using the last known value of ρ and θ if there is no evidence of motion over more than 20 years. Most suitable for this method are optical doubles with slow proper motion. This method is preferable to the first one, because the accuracy of speckle interferometric measurements with 2-meter telescopes exceeds the accuracy of even the best orbits (Tokovinin et al. 2015).

For the astrometric calibration, we selected 21 systems with a separation ranging from 4″to 6″ which had more than one reliable observation from the Fourth Catalog of Interferometric Measurements

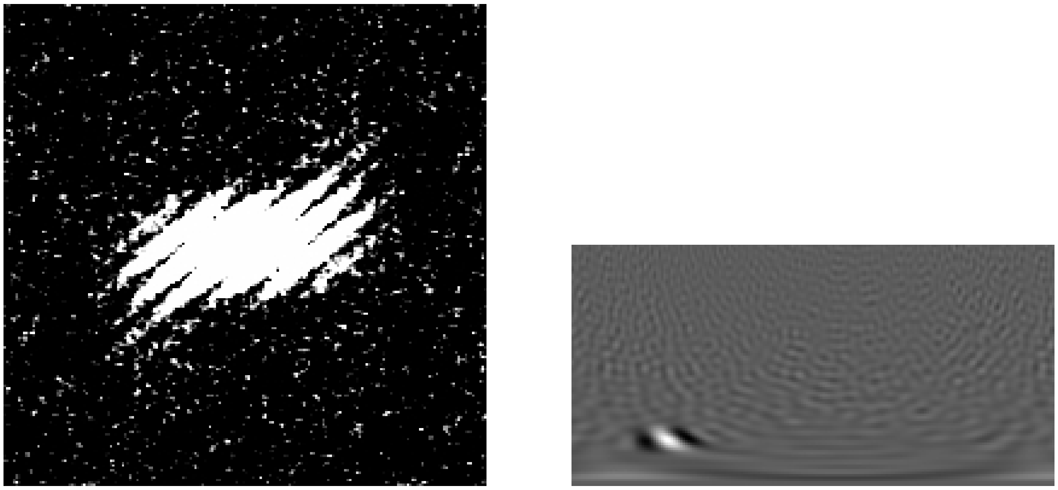

Fig. 5. Power spectrum $P(\mathbf{f})$ of WDS 14394-0733 distorted by vibrations and aberrations of the telescope (left). ACF_p of WDS 14394-0733 obtained from its $P(\mathbf{f})$ (right). The separation is $0.''55$.

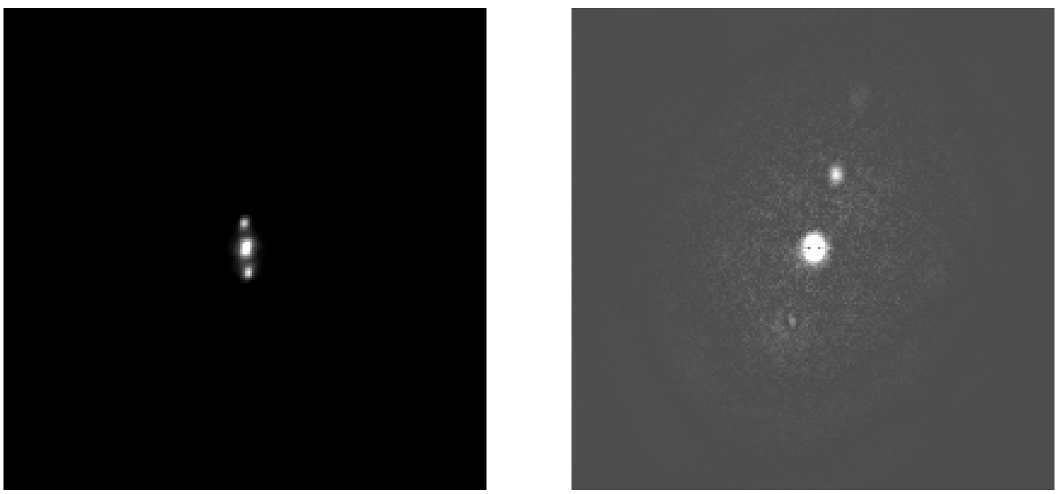

Fig. 6. Example of the reconstruction of WDS 20312+1116 (left) and WDS 19326+0435, $\Delta m = 1$(right).

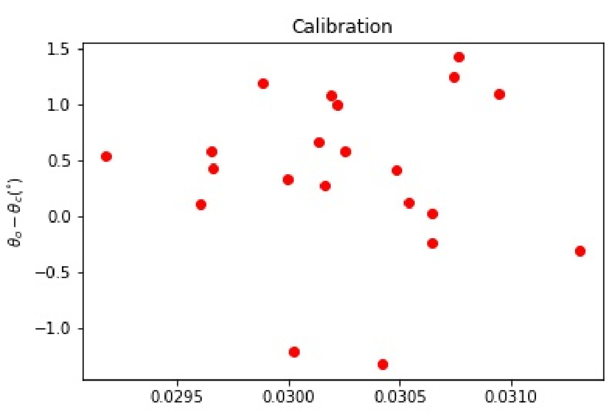

Fig. 7. Calibration.

of Binary Stars (Hartkopf et al. 2001) and from the WDS catalog. These 21 systems also have very slow movements and a long time base of observations. A comparison with our data (Figure 7) gives us the following offset for the position angle $\theta_0 = -0.42^\circ \pm 0.14^\circ$ and a pixel scale $s = 0''.03026 \pm 0''.00009$ per pixel.

4. ASTROMETRIC MEASUREMENTS

The astrometric measurements we obtained for double stars are displayed in four tables (Tables 1-4). Table 1 presents astrometric measurements of 21 double stars used for calibration. All these systems show slow motions of components. The first column contains the epoch-2000 coordinates in the

TABLE 1

WIDE DOUBLE STARS WITH VERY SLOW RELATIVE MOTION

WDS (2000)	Discoverer designation	Epoch Julian year	Fil.	θ ($^\circ$)	ρ ($''$)
$14083+2112$	STF1804	2016.4882	I	14.01 ± 0.14	4.796 ± 0.014
$14100+0401$	STF1805	2016.4882	I	33.60 ± 0.14	4.837 ± 0.014
$14134+0524$	STF1813	2016.4882	I	193.54 ± 0.14	4.703 ± 0.014
$14165+2007$	STF1825	2016.4882	I	153.51 ± 0.14	4.369 ± 0.013
$14279+2123$	HO 543	2016.4882	I	237.37 ± 0.14	4.631 ± 0.014
$14506-0001$	STF1885	2016.4882	I	145.70 ± 0.14	4.100 ± 0.012
$15276+0522$	STF1943	2016.4883	I	148.27 ± 0.14	5.094 ± 0.015
$15589+2147$	STF1990 BC	2016.4883	I	26.34 ± 0.14	4.048 ± 0.012
$16003+1140$	STF1992 AB,C	2016.4883	I	326.35 ± 0.14	5.946 ± 0.018
$17178+0733$	J 450	2016.4896	R	60.99 ± 0.14	4.651 ± 0.014
$17268+2240$	J 1032	2016.4896	R	350.78 ± 0.14	4.057 ± 0.012
$17324+2352$	STF2182 AB	2016.4896	R	0.86 ± 0.14	5.418 ± 0.016
$17362+0637$	STF2188	2016.4896	R	203.71 ± 0.14	5.516 ± 0.016
$17590+0202$	STF2252 AB	2016.4896	R	24.26 ± 0.14	3.948 ± 0.012
$18106+0349$	FOX 220	2016.4896	R	75.37 ± 0.14	5.977 ± 0.018
$18148+1153$	ROE 143	2016.4896	R	90.40 ± 0.14	4.207 ± 0.013
$18154+1946$	STT 346	2016.4896	R	329.58 ± 0.14	5.208 ± 0.015
$18206+2248$	STF2310	2016.4896	R	237.96 ± 0.14	5.052 ± 0.015
$18247-0636$	STF2313	2016.4896	R	196.00 ± 0.14	5.857 ± 0.017
$18258+0359$	J 462	2016.4896	R	348.32 ± 0.14	4.180 ± 0.012
$18266+0627$	GCB 31	2016.4896	R	75.87 ± 0.14	4.501 ± 0.013

TABLE 2

ASTROMETRIC MEASUREMENTS OF THE OBSERVED DOUBLE STARS WITH NO CALCULATED ORBITS

WDS (2000)	Discoverer designation	Epoch 2016+	Fil.	θ ($^\circ$)	$\delta\theta$ ($^\circ$)	ρ ($''$)	$\delta\rho$ ($''$)
$14216+1315$	HEI 531	0.4919	R	260.5	0.3	1.367	0.011
$14222+0513$	HDS2023	0.4919	R	129.5	0.3	0.455	0.006
$14222+1350$ *	HDS2022	0.4919	R	54.3	0.3	0.338	0.005
$14227+0216$	HDS2025	0.4919	R	14.4	0.2	0.689	0.004
$14236+2009$	COU 184	0.4919	R	113.8	0.2	0.950	0.009
$14242+0001$	RST5385	0.4919	R	357.3	0.6	0.397	0.006
$14249-0912$	RST3876	0.4919	R	23.4	0.4	0.699	0.007
$14252-0546$	RST4527	0.4919	R	108.4	0.6	0.428	0.006
$14262-0950$	RST3878	0.4919	R	67.4	1.5	0.457	0.006
$14263+0152$	HDS2033	0.4919	R	234.4	0.4	0.582	0.007
$14276+2037$	HO 542	0.4919	R	33.2	0.2	1.007	0.009
$14286-0856$	RST3880	0.4919	R	176.4	0.6	0.731	0.008
$14286+1818$	COU2508	0.4919	R	67.3	0.3	0.486	0.006
$14293+0018$	HDS2043 Aa,Ab	0.4919	R	47.3	0.5	0.699	0.007
$14293+1318$	HDS2042	0.4919	R	118.5	0.4	0.310	0.005
$14305+2055$	COU 97	0.4919	R	254.4	0.4	0.276	0.005
$14325+0308$	A 2226 AB	0.4919	R	80.5	0.2	0.461	0.006
$14330+0656$	YSC 6	0.4919	R	105.9	0.2	0.183	0.004
$14333+2725$	A 688	0.4919	R	16.4	0.2	0.764	0.008
$14339+2949$	AGC 6	0.4919	R	134.3	0.2	0.767	0.008
$14340-0507$	A 2589	0.4920	R	203.5	0.2	1.036	0.009
$14354+1915$	HU 574	0.4920	R	112.4	0.2	0.150	0.004
$14356+1554$	HEI 233	0.4920	R	5.2	0.2	1.129	0.010
$14359+1200$	HU 1269	0.4920	R	203.4	0.2	0.368	0.005
$14367+2014$	COU 98	0.4920	R	173.4	0.6	0.187	0.004
$14369-0417$	HDS2061	0.4920	R	148.7	0.2	0.701	0.007
$14376+2809$	COU 405	0.4920	R	105.6	0.7	1.496	0.012
$14376+3137$	HDS2062	0.4920	R	121.4	0.2	0.123	0.004
$14394-0733$	RST3889	0.4920	R	220.3	0.4	0.548	0.007
$14401+0246$	HDS2069	0.4920	R	80.5	0.4	0.481	0.006
$14401+0504$	A 1107	0.4920	R	89.5	0.2	0.333	0.005
$14416+2747$	COU 407	0.4920	R	113.5	0.2	0.428	0.006

TABLE 2. CONTINUED

14417 + 0932	STF1866	0.4920	R	205.2	0.2	0.761	0.008
14419 + 1847	COU 185	0.4920	R	305.9	0.3	0.899	0.009
15261 + 1810	STF1940	0.4974	R	332.4	0.2	0.370	0.005
15262 + 1418	HEI 236	0.4974	R	107.5	0.3	0.523	0.006
15268 + 2840	COU 484	0.4975	R	263.4	0.2	0.333	0.005
16013 − 0658	BU 623	0.4920	R	225.6	0.2	0.733	0.008
16043 − 0313	RST4558	0.4921	R	170.3	0.3	0.580	0.007
16049 + 0213	HEI 793	0.4921	R	196.1	0.2	1.523	0.012
16062 + 1809	COU2389	0.4921	R	238.5	0.2	1.126	0.010
16071 + 1654	BU 812	0.4921	R	97.4	0.2	0.731	0.007
16072 + 1848 *	COU 196	0.4921	R	349.6	1.9	1.584	0.013
16080 + 0559	TDS9770	0.4921	R	256.3	0.3	0.582	0.007
16087 + 0524	HDS2278	0.4921	R	112.4	0.2	0.281	0.005
16092 − 0549	RST4559	0.4921	R	296.4	0.4	0.975	0.009
16092 − 1057 *	HDS2279	0.4921	R	325.5	0.4	0.335	0.005
16097 − 0633	RST3932	0.4921	R	137.4	0.8	0.212	0.005
16139 + 0123	RST5407	0.4921	R	223.3	0.2	0.972	0.009
16152 − 0709	RST3938	0.4921	R	209.5	0.3	1.249	0.011
16168 + 1447	HDS2301	0.4921	R	55.4	0.2	1.007	0.009
16169 + 1948	COU 107	0.4921	R	114.4	0.2	0.637	0.007
16173 + 1626	YSC 153	0.4921	R	131.4	0.3	0.338	0.005
16174 + 0643 *	TDS9822	0.4921	R	349.6	0.4	0.546	0.007
16177 + 1342	YSC 154	0.4921	R	44.9	0.4	0.682	0.007
16186 + 1247	HEI 241	0.4921	R	59.5	0.3	0.763	0.008
16581 + 0902	HDS2401	0.4922	R	17.5	0.2	0.332	0.005
16581 + 1509	STT 319	0.4922	R	65.8	0.1	0.858	0.008
16584 + 1358	YSC 61	0.4922	R	260.4	1.0	0.608	0.007
16594 + 1419	STT 321	0.4922	R	15.3	0.2	0.581	0.007
16595 + 0942	BU 1298 AB	0.4922	R	133.3	0.2	0.429	0.006
17003 + 0106	A 2235	0.4922	R	269.4	0.3	0.827	0.008
17012 + 0627 *	HDS2409	0.4922	R	37.4	0.7	0.274	0.005
17042 + 1834 *	TDT 197	0.4922	R	91.4	0.4	0.396	0.006
17046 − 0339	RST4565	0.4922	R	164.6	0.3	0.823	0.008
17050 + 0724	TDT 204	0.4922	R	152.3	0.3	0.638	0.007
17080 − 0957	RST3966	0.4922	R	111.0	1.2	0.487	0.006
17086 + 0951	HU 167	0.4922	R	272.6	0.5	0.820	0.008
17088 + 0002	A 2237	0.4922	R	69.9	0.3	0.918	0.009
17107 + 1651	HEI 167	0.4922	R	98.4	0.3	0.394	0.006
17107 + 2104 *	TDT 251	0.4922	R	122.4	0.4	0.544	0.007
17107 + 2312 *	TDT 250	0.4922	R	11.0	0.3	0.795	0.008
17110 + 0302	HDS2426	0.4922	R	195.4	0.3	0.883	0.009
17110 + 1622	HEI 168	0.4922	R	65.7	0.2	0.763	0.008
17136 + 0405	HEI 895	0.4922	R	15.5	1.7	0.854	0.009
17140 + 2119	COU 111	0.4923	R	249.5	0.3	0.613	0.007
17142 + 2731	COU 495	0.4923	R	100.6	0.4	0.819	0.008
17150 + 1238 *	HDS2439	0.4923	R	168.9	0.5	0.518	0.006
17155 + 2007	HU 489	0.4923	R	35.8	0.2	1.035	0.009
17160 + 1702 *	TDT 294	0.4923	R	77.6	0.5	0.582	0.007
17174 + 1939	COU 496 AB	0.4923	R	172.0	0.9	0.823	0.008
17182 + 1559	HEI 246	0.4923	R	45.3	0.3	1.160	0.010
17247 + 3802	COU1142 AB	0.4977	R	222.4	0.2	1.858	0.014
17272 + 3235 *	TDT 362	0.4977	R	156.4	0.4	0.310	0.005
17285 + 3657	COU1143	0.4977	R	244.4	0.3	0.370	0.005
17290 + 3845	COU1297	0.4977	R	99.4	0.3	0.276	0.005
17293 + 3758	HO 417	0.4977	R	306.4	0.2	0.310	0.005
17345 + 3935	COU1298	0.4977	R	251.5	0.2	0.302	0.005
17354 + 3443	COU 995	0.4977	R	335.3	0.2	0.421	0.006
17359 + 3205	COU 807	0.4977	R	143.4	0.3	0.670	0.007
17455 + 3554	HDS2509	0.4977	R	74.9	0.2	0.548	0.006
17462 + 3853	COU1300	0.4977	R	125.7	0.2	0.765	0.008
17464 + 3553 *	TDT 497	0.4977	R	263.8	0.3	0.761	0.008
17470 + 3750	COU1144	0.4977	R	283.9	0.2	0.941	0.009
17471 + 3235	COU 634	0.4977	R	79.4	0.3	0.246	0.005
17504 + 3526	ORL 1 Aa,Ab	0.4977	R	29.4	0.2	0.304	0.005
17512 + 3821	HU 1183	0.4977	R	191.4	0.2	0.489	0.006

TABLE 2. (CONTINUED)

17528 + 3408 *	TDT 553	0.4977	R	62.4	0.3	0.702	0.007
17553 + 3532	A 2987 AC	0.4977	R	60.9	0.2	1.402	0.012
17569 + 3236	HU 1184	0.4977	R	204.6	0.2	0.916	0.009
17583 + 3329	HO 74 AB	0.4977	R	124.8	0.2	3.287	0.023
17583 + 3329	COU1001 Aa,Ab	0.4977	R	220.5	0.2	0.483	0.006
17584 + 2233 *	TDS 893	0.4923	R	279.8	0.5	0.766	0.008
17584 + 3524	COU1000	0.4977	R	154.4	0.2	0.944	0.009
17587 + 3538	COU1002	0.4977	R	163.7	0.2	0.853	0.008
17592 + 3926	COU1458	0.4977	R	78.4	0.4	0.364	0.005
18000 + 2449	COU 115	0.4950	R	118.5	0.2	0.278	0.005
18007 + 1736	COU 810	0.4950	R	99.4	0.4	0.157	0.004
18009 + 2432 *	TDT 636	0.4950	R	185.4	0.7	0.167	0.004
18036 + 3731	COU1147	0.4950	R	178.2	0.2	0.737	0.008
18036 + 3731	COU1147	0.4978	R	178.2	0.2	0.737	0.008
18047 + 4650 *	COU2115	0.4950	R	41.9	0.8	0.274	0.005
18048 + 5344 *	HDS2546	0.4950	R	235.5	0.4	0.578	0.007
18054 + 4306	COU1787	0.4951	R	325.4	0.3	0.395	0.006
18054 + 5155	COU2513	0.4951	R	57.6	0.2	0.915	0.009
18058 + 3512	TDT 678	0.4978	R	236.4	0.4	0.669	0.007
18062 + 3326	HO 79	0.4978	R	61.4	0.9	0.216	0.005
18070 + 3323 *	TDT 689	0.4978	R	242.4	1.0	0.366	0.006
18104 + 5104	COU2392	0.4951	R	147.3	0.3	0.641	0.007
18109 + 3321	COU1005 AB,C	0.4978	R	25.4	0.4	1.889	0.015
18109 + 3321	COU1005 AB	0.4978	R	333.4	0.4	0.211	0.005
18110 + 5038	HDS2564	0.4951	R	306.4	0.3	0.364	0.005
18112 + 3906	HDS2565	0.4978	R	340.1	0.2	0.670	0.007
18114 + 2519	A 238	0.4924	R	71.6	0.2	0.636	0.007
18118 + 3327	HO 82 AB,C	0.4978	R	220.7	0.2	0.701	0.007
18119 + 4733	COU2117	0.4951	R	298.5	0.3	0.426	0.006
18121 + 2739	STF2292	0.4924	R	276.9	0.2	0.885	0.008
18127 + 5446	MLR 585	0.4951	R	335.4	0.3	0.428	0.006
18132 + 5749 *	HDS2571	0.4951	R	310.4	0.4	0.274	0.005
18133 + 0906	HDS2573	0.4924	R	165.4	0.2	0.853	0.008
18133 + 2118	TDT 743	0.4924	R	67.8	1.0	1.004	0.010
18133 + 5242	A 1376	0.4951	R	203.4	0.3	0.338	0.005
18134 + 1643	HEI 170	0.4924	R	313.4	0.4	0.337	0.005
18139 + 3212 *	TDT 749	0.4978	R	15.4	0.7	0.167	0.004
18144 + 1953	HDS2576	0.4924	R	68.1	0.3	0.966	0.009
18145 + 3249	HU 927	0.4978	R	102.4	0.2	0.369	0.005
18145 + 3313	COU1007	0.4978	R	38.4	0.3	0.274	0.005
18177 + 3932 *	TDT 778	0.4978	R	177.4	0.5	0.914	0.009
18182 + 5337	MLR 586	0.4951	R	194.4	0.2	0.636	0.007
18208 + 3639	COU1306	0.4978	R	42.4	0.3	0.454	0.006
18212 + 3917	COU1460	0.4978	R	341.5	0.2	0.452	0.006
18217 + 5740	MLR 536	0.4951	R	194.7	0.3	0.851	0.008
18222 + 3417 *	TDT 818	0.4978	R	205.4	0.4	0.273	0.005
18238 + 5318 *	YSC 66	0.4951	R	42.7	0.2	0.914	0.009
18243 + 3609	HDS2603	0.4978	R	353.7	0.3	0.853	0.008
18250 − 0517	RST4587	0.4895	R	332.3	0.3	0.395	0.006
18252 + 5659	MLR 537	0.4951	R	56.5	0.2	0.579	0.007
18253 + 2805	HDS2604 Aa,Ab	0.4924	R	212.1	0.3	0.729	0.008
18256 + 3945	COU1461	0.4978	R	245.1	0.3	0.790	0.008
18266 + 0633	HDS2607	0.4896	R	243.4	0.5	0.151	0.004
18272 + 0012	STF2316 AB	0.4896	R	321.7	0.2	3.749	0.026
18279 + 0124	HDS2614	0.4896	R	333.3	0.3	0.704	0.007
18283 + 0537 *	TDT 897	0.4896	R	169.4	0.4	0.489	0.006
18285 + 2010	COU 203	0.4896	R	60.5	0.3	0.488	0.006
18285 + 2010	COU 203	0.4924	R	60.5	1.1	0.486	0.006
18289 + 1815	COU 507	0.4896	R	154.0	0.4	0.947	0.009
18291 + 0408	A 581 AB	0.4896	R	139.5	0.3	0.392	0.006
18297 + 3929	TDT 910	0.4978	R	195.6	0.2	0.821	0.008
18298 + 5314	TDT 911	0.4951	R	196.4	0.3	0.734	0.008
18301 + 5805	MLR 357	0.4951	R	204.3	0.4	0.582	0.007
18303 + 1907	COU 508	0.4896	R	253.7	0.3	0.910	0.009
18304 + 1348	HU 583	0.4896	R	307.3	0.2	0.759	0.008

TABLE 2. (CONTINUED)

18305 + 0416	A 583	0.4896	R	265.4	0.4	0.177	0.004
18309 + 3417	COU1150 Aa,Ab	0.4978	R	265.4	0.2	0.214	0.004
18310 + 0712 *	TDT 924	0.4897	R	318.3	0.6	0.611	0.007
18310 + 2424	TDT 923	0.4897	R	328.6	0.2	0.823	0.008
18312 + 2516	A 248	0.4897	R	34.5	0.3	0.490	0.006
18314 + 0802	HDS2627	0.4897	R	211.4	0.2	0.457	0.006
18316 + 2030	COU 119	0.4897	R	229.2	0.3	0.673	0.007
18319 + 3538	COU1151	0.4978	R	280.0	0.2	1.310	0.011
18321 + 1359	J 1133	0.4897	R	125.4	1.9	2.254	0.017
18324 + 3231 *	TDT 932	0.4978	R	320.3	0.2	0.512	0.006
18325 + 0036	RST5450	0.4897	R	254.4	0.4	0.703	0.007
18327 + 1741	TDT 934	0.4897	R	128.2	0.3	0.820	0.008
18332 + 3420 *	TDT 935	0.4978	R	174.9	0.5	0.868	0.009
18335 + 3510	HO 86	0.4978	R	199.5	0.2	0.307	0.005
18385 + 3503	COU1308	0.4978	R	28.5	0.2	0.422	0.006
18402 + 3822	HDS2644	0.4978	R	76.4	0.2	0.095	0.004
18402 + 5048	COU2515	0.4951	V	276.4	0.7	0.334	0.005
18405 + 3139	HO 437 AB	0.4978	R	140.4	0.2	0.270	0.005
18423 + 3616	A 1381	0.4978	R	94.4	0.2	0.367	0.005
18432 + 3822	HDS2651	0.4978	R	52.2	0.3	0.481	0.006
18448 + 5201	HU 755	0.4951	V	125.4	0.3	0.579	0.007
18453 + 3856	COU1608	0.4979	R	230.0	0.3	1.070	0.010
18459 + 3657	COU1309	0.4979	R	180.4	0.4	0.482	0.006
18461 + 5212	MLR 637	0.4951	V	102.1	0.5	0.763	0.008
18465 + 3414	COU1153	0.4979	R	115.5	0.3	0.393	0.006
18466 + 5142	HU 756	0.4952	V	262.8	0.3	1.036	0.009
18476 + 3248	COU1154	0.4979	R	56.5	0.3	0.578	0.007
18481 + 3929	COU1609	0.4979	R	201.7	0.4	0.822	0.008
18490 + 3432	YSC 11	0.4979	R	54.9	0.2	0.359	0.005
18490 + 3914	COU1610	0.4979	R	144.5	0.4	0.399	0.006
18499 + 5516	MLR 574	0.4952	V	54.7	0.3	1.093	0.010
18521 + 2431	COU 510	0.4924	R	181.4	0.9	0.185	0.005
18525 + 2632	HDS2677 Aa,Ab	0.4924	R	80.2	0.5	1.030	0.010
18527 + 5842	HDS2678	0.4952	V	33.7	0.9	0.659	0.007
18528 + 3125	A 257 CD	0.4924	R	262.8	0.9	0.759	0.008
18528 + 3125	A 257 CD	0.4979	R	262.7	0.3	0.758	0.008
18528 + 3125	A 257 AB	0.4924	R	95.1	0.3	0.914	0.009
18552 + 3941	TDT1126	0.4979	R	190.5	0.5	0.362	0.005
18554 + 3556	A 1385 AB	0.4979	R	295.4	0.3	0.454	0.006
18555 + 3215	COU1013	0.4979	R	147.4	0.3	0.643	0.007
18557 + 5714	TDT1129	0.4952	V	14.3	1.7	0.549	0.007
18563 + 5432 *	HDS2682 Aa,Ab	0.4952	V	327.4	0.6	0.366	0.006
18563 + 5432 *	HDS2682 Aa,Ab	0.4952	V	326.5	0.6	0.366	0.006
18564 + 5854	TDS 955	0.4952	V	149.3	0.4	0.914	0.009
18571 + 3451	HDS2685	0.4979	R	200.3	0.2	0.515	0.006
18572 + 3845	COU1611	0.4979	R	111.5	0.4	0.643	0.007
18576 + 3209	A 260	0.4979	R	246.3	0.2	0.911	0.009
18586 + 5210	MLR 638	0.4952	V	131.5	0.3	0.278	0.005
18589 + 3229	BU 649	0.4979	R	1.0	0.2	1.832	0.014
18593 + 5450	A 1387 AB	0.4952	V	351.4	0.3	0.331	0.005
19006 + 3300	COU1156	0.4979	R	110.8	0.2	0.793	0.008
19006 + 3951	COU1933	0.4979	R	197.3	0.2	0.552	0.006
19006 + 3952	HDS2696	0.4979	R	138.4	0.2	0.302	0.005
19016 + 3253	HU 1295	0.4979	R	223.4	0.4	0.272	0.005
19018 + 3448	COU1612	0.4979	R	322.4	0.3	0.883	0.009
19020 + 3210	HU 1296	0.4979	R	195.4	0.8	0.119	0.004
19023 + 3328	COU1312	0.4979	R	235.4	0.4	0.270	0.005
19024 + 3608	COU1613	0.4979	R	318.5	0.4	0.545	0.007
19028 + 2208 *	TDS 961	0.4925	R	215.0	0.3	0.885	0.009
19034 + 2511	A 2991	0.4925	R	84.1	0.3	0.734	0.008
19036 + 3705	HDS2702	0.4979	R	266.4	0.5	0.168	0.004
19050 + 5553	A 1389	0.4952	R	231.4	0.3	0.249	0.005
19056 + 2724	HDS2709	0.4925	R	43.4	0.4	0.331	0.005
19057 + 2717	HO 95	0.4925	R	143.4	0.3	0.208	0.004
19061 + 3549	COU1614	0.4979	R	121.4	0.2	0.577	0.007
19064 + 3144	HO 97 AB	0.4925	R	196.6	0.2	0.762	0.008

TABLE 2. (CONTINUED)

19066 + 2646	COU 722	0.4925	R	336.3	0.2	1.063	0.010
19074 + 3601	COU1615	0.4979	R	96.4	0.4	0.426	0.006
19081 + 3031	HO 99	0.4925	R	167.4	0.3	0.396	0.006
19082 + 3829	COU1936 AB	0.4979	R	124.3	0.4	0.550	0.007
19086 + 5208	MLR 639	0.4952	R	37.4	0.3	0.392	0.006
19086 + 5531 *	TDS 967	0.4952	R	153.3	0.3	0.973	0.009
19087 + 5630	MLR 577	0.4952	R	277.2	0.3	0.762	0.008
19103 + 3044	COU1020	0.4925	R	100.7	0.3	1.035	0.009
19150 + 5528	TDT1319	0.4952	R	65.6	0.3	0.855	0.008
19158 + 5458	A 1392	0.4952	R	277.4	0.2	0.151	0.004
19165 + 5003	COU2627	0.4952	R	22.4	0.6	0.186	0.004
19178 + 5950	HDS2729	0.4952	R	161.4	0.3	0.093	0.004
19186 + 5358	A 1393	0.4952	R	256.4	0.2	0.704	0.007
19195 + 5729	MLR 539	0.4952	R	192.4	0.3	0.248	0.005
19207 + 5811 *	TDT1387	0.4952	R	300.3	0.3	0.819	0.008
19213 + 5817	TDT1395	0.4952	R	168.7	0.2	0.857	0.008
19221 + 5347 *	TDT1403	0.4952	R	125.4	0.3	0.515	0.006
19228 + 5637	A 708	0.4952	R	170.6	0.2	1.007	0.009
19251 + 2213	COU 513	0.4925	R	6.4	0.3	0.271	0.005
19266 + 2619	HDS2763	0.4925	R	208.9	0.3	0.792	0.008
19290 + 1515	A 1651	0.4897	R	253.4	0.3	0.184	0.004
19301 − 0735	RST4630	0.4897	R	290.4	1.0	0.362	0.006
19303 + 0333	TDT1506	0.4897	R	16.8	0.5	0.729	0.008
19305 + 1151	HEI 573	0.4897	R	226.7	0.4	0.885	0.009
19307 + 1439 *	TDT1512	0.4897	R	324.5	0.5	0.552	0.007
19310 + 0429	A 366	0.4897	R	304.4	0.3	0.489	0.006
19311 + 0824	A 1184	0.4897	R	114.2	0.2	0.879	0.008
19311 + 0829 *	TDT1516	0.4897	R	358.1	0.4	0.822	0.008
19321 + 0858 *	TDT1527	0.4898	R	159.4	0.6	0.457	0.006
19321 + 1206	TDT1526	0.4898	R	132.3	0.4	0.548	0.007
19326 + 0435 *	TDS 999	0.4898	R	343.8	0.4	0.972	0.009
19326 + 1203	HEI 574	0.4898	R	150.5	0.2	0.455	0.006
19334 − 0602	RST4632	0.4898	R	53.7	0.9	0.731	0.008
19342 + 0747 *	HDS2777	0.4898	R	252.4	0.2	0.186	0.004
19343 + 0021	HDS2779	0.4898	R	214.4	0.3	0.273	0.005
19383 + 5535	TDT1597	0.4953	R	125.4	0.3	0.667	0.007
19395 + 5748 *	TDT1608	0.4953	R	121.4	0.3	1.097	0.010
19400 + 5545	A 1403	0.4953	R	166.4	0.4	0.209	0.004
19411 + 5811	A 716	0.4953	R	284.5	0.3	0.454	0.006
20087 + 5320	A 1417	0.4953	R	173.4	0.2	0.621	0.007
20096 + 5034	TDT2035	0.4953	R	91.7	0.3	0.788	0.008
20176 + 5113 *	TDS1056	0.4953	R	256.2	0.3	1.436	0.012
20183 + 5152	HDS2900	0.4953	R	286.4	0.2	0.149	0.004
20185 + 5542	BU 1260	0.4953	R	135.4	0.3	0.340	0.005
20187 + 5823	TDT2157	0.4953	R	37.3	0.3	0.788	0.008
20196 + 5132	TDT2169	0.4953	R	52.9	0.2	0.914	0.009
20232 + 5946	MLR 432	0.4953	R	216.4	0.3	0.184	0.004
20239 + 5232	A 1428	0.4953	R	205.4	0.2	0.333	0.005
20239 + 5420	HDS2914	0.4953	R	213.4	0.6	0.211	0.005
20246 + 5527	MLR 588	0.4953	R	245.4	0.2	0.242	0.005
20257 + 5508	A 1429	0.4953	R	187.4	0.2	0.641	0.007
20278 + 5456	TDT2293	0.4953	R	81.4	0.3	0.762	0.008
20298 + 5654 *	TDT2322	0.4953	R	19.5	1.6	1.676	0.014
20310 + 5953	HDS2933	0.4953	R	8.6	0.3	0.427	0.006
20312 + 5714	A 872	0.4953	R	178.4	0.4	0.214	0.005
20315 + 5520	TDS1079	0.4953	R	125.5	0.2	0.880	0.008
20316 + 0530	A 395	0.4898	R	161.6	0.5	0.642	0.007
20318 + 5128	TDT2339	0.4953	R	338.4	0.3	0.976	0.009
20329 + 1357	BU 670 AB	0.4898	R	6.4	0.2	0.851	0.008
20329 + 1906	COU2644	0.4898	R	290.4	0.3	0.822	0.008
20331 + 2324	A 2792	0.4898	R	305.4	0.6	0.214	0.005
20334 − 0321	HDS2936	0.4898	R	156.4	0.5	0.244	0.005
20335 + 0527	STF2696 AB	0.4899	R	299.4	0.2	0.520	0.006
20339 + 1106 *	TDT2376	0.4899	R	76.1	0.4	0.761	0.008
20342 + 1333	HEI 277	0.4899	R	247.4	0.3	0.697	0.007
20348 + 1726	COU 223	0.4899	R	161.4	0.5	0.393	0.006

TABLE 2. (CONTINUED)

20349 + 1120	TDT2394	0.4899	R	1.5	0.2	0.455	0.006
20351 − 0436	RST4671	0.4899	R	227.5	0.2	0.730	0.008
20354 + 1121	YR 16	0.4899	R	278.4	0.4	0.701	0.008
20381 + 2953	A 744	0.4925	R	274.3	0.2	0.732	0.008
20383 + 2106 *	TDT2441	0.4925	R	269.2	0.3	0.608	0.007
20384 + 2455	TDT2446	0.4925	R	99.5	0.4	0.459	0.006
20385 + 2945	COU1172	0.4925	R	279.5	0.4	0.336	0.005
20386 + 2007	COU 225	0.4925	R	286.4	0.8	0.277	0.005
20390 + 3702	COU2219	0.4981	R	45.2	0.3	0.941	0.009
20393 + 2714	TDT2454 Ba,Bb	0.4926	R	46.3	0.3	0.916	0.009
20397 + 3658	A 1432	0.4981	R	117.4	0.3	0.432	0.006
20401 + 3044	TDT2457 Aa,Ab	0.4926	R	138.5	0.4	0.888	0.009
20406 + 2156	A 2795	0.4926	R	240.4	0.2	0.246	0.005
20410 + 3218	STF2716 AB	0.4981	R	46.4	0.1	2.772	0.020
20411 + 2751 *	TDT2471	0.4926	R	2.4	0.8	0.240	0.005
20411 + 3516	COU1963 AB,C	0.4981	R	48.4	0.2	1.645	0.013
20411 + 3516	COU1963 AB	0.4981	R	180.4	0.2	0.213	0.004
20412 + 2023	COU 423	0.4926	R	162.4	0.4	0.401	0.006
20416 + 3000	COU1174	0.4926	R	32.4	0.4	0.339	0.005
20416 + 3950	COU2290	0.4981	R	43.3	0.2	0.545	0.006
20424 + 3455	COU1965	0.4981	R	277.5	0.2	0.365	0.005
20432 + 3350	HDS2949	0.4981	R	166.4	0.2	0.944	0.009
20433 + 2616	COU1039	0.4926	R	237.1	0.4	1.035	0.009
20440 + 3839	COU2292	0.4981	R	240.4	0.2	0.309	0.005
20445 + 3409	HU 690	0.4981	R	281.5	0.2	0.490	0.006
20447 + 2703 *	TDT2515	0.4926	R	277.5	0.6	0.400	0.006
20451 + 3529	COU1809	0.4981	R	101.4	0.3	0.731	0.008
20459 + 3852 *	COU2294	0.4982	R	124.9	0.3	0.857	0.008
20460 + 3554 *	TDT2525	0.4982	R	70.3	0.3	0.579	0.007
20463 + 2853 *	TDT2530	0.4926	R	207.3	0.3	0.606	0.007
20464 + 3511	COU1810	0.4982	R	183.4	0.5	0.187	0.004
20475 + 3016	COU1176	0.4926	R	225.4	0.4	0.366	0.005
20477 + 3258	COU1634	0.4982	R	61.4	0.4	0.395	0.006
20480 + 3917	A 1434 AB,C	0.4982	R	255.9	0.2	2.513	0.018
20482 + 2622	COU 827 Aa,Ab	0.4926	R	329.4	0.3	0.574	0.007
20487 + 2943 *	TDT2556	0.4926	R	280.4	0.2	0.790	0.008
20490 + 2540 *	HDS2966	0.4926	R	229.4	0.2	0.518	0.006
20490 + 2637	COU 828 AB	0.4927	R	188.5	0.2	0.913	0.009
20490 + 3619	COU1811	0.4982	R	255.4	0.3	0.759	0.008
20503 + 5937	MLR 239	0.4954	R	286.3	0.3	0.888	0.009
20531 + 2909	STT 417 AB	0.4927	R	28.5	0.2	0.917	0.009
20535 + 2630	COU1177	0.4927	R	14.4	0.4	0.248	0.005
20547 + 2516	COU 830	0.4927	R	168.8	0.3	1.039	0.009
20573 + 2345 *	TDT2656	0.4927	R	349.4	0.2	0.735	0.008
21009 + 5929	MLR 241	0.4954	R	174.6	0.2	0.948	0.009
21012 + 5953 *	TDT2696	0.4954	R	67.3	0.3	0.519	0.006
21035 + 5925	MLR 243	0.4954	R	224.4	0.6	0.211	0.005
21036 + 5358	HDS2999 Aa,Ab	0.4954	R	351.5	0.2	0.337	0.005
21055 + 5340	BU 680 AB	0.4954	R	284.5	0.2	0.635	0.007
21067 + 5556	TDT2753	0.4954	R	211.4	0.3	0.704	0.007
21096 + 0550 *	TDT2793	0.4899	R	173.4	0.5	0.336	0.005
21106 + 1650	HU 367	0.4899	R	339.4	0.2	0.331	0.005
21118 + 5959	STF2780 AB	0.4954	R	214.1	0.1	1.037	0.009
21119 + 2758 *	TDT2814	0.4927	R	290.4	0.4	2.254	0.017
21142 + 1231	HEI 406	0.4899	R	180.2	0.3	0.704	0.007
21152 + 2753	COU 531	0.4927	R	144.2	0.2	0.943	0.009
21152 + 5531	A 1692	0.4954	R	167.4	0.2	0.272	0.005
21160 + 5914 *	TDT2869	0.4954	R	113.3	0.5	0.674	0.007
21196 + 5552	MLR 582	0.4954	R	347.5	0.3	0.948	0.009
21197 + 5455	A 1694	0.4954	R	94.6	0.2	0.850	0.008
21199 + 5319	A 1695	0.4954	R	193.5	0.2	0.483	0.006
21200 + 5436	TDT2908 Aa,Ab	0.4954	R	115.4	0.5	0.306	0.005
21202 + 5411	HDS3036	0.4954	R	165.4	0.2	0.392	0.005
21203 + 5354	TDT2910	0.4954	R	286.6	0.2	0.675	0.007
21227 + 5214	HU 591	0.4954	R	129.5	0.2	0.761	0.008

TABLE 2. (CONTINUED)

21237 + 5518	A 1892	0.4954	R	350.1	0.2	0.766	0.008
21249 + 5734	A 766	0.4954	R	228.3	0.3	0.486	0.006
21251 + 5229	HU 592	0.4954	R	325.4	0.2	0.823	0.008
21252 + 5618	TDS1127	0.4954	R	235.7	0.2	1.097	0.010
21263 + 5951	MLR 361	0.4954	R	268.4	0.3	0.606	0.007
21273 + 5953	MLR 362	0.4954	R	55.5	0.3	0.338	0.005
21274 + 5835	MLR 435	0.4954	R	236.4	0.5	0.181	0.004
21287 + 5710	BU 1142	0.4954	R	5.5	0.4	0.369	0.005
21327 + 5459 *	HDS3063	0.4954	R	2.4	0.2	0.339	0.005
21346 + 5633	A 1893 AB	0.4954	R	28.3	0.2	0.641	0.007
21362 + 5139	HDS3075	0.4954	R	15.9	0.2	0.609	0.007
21372 + 5346	MLR 609	0.4954	R	40.5	0.2	1.035	0.009
21376 + 5546	BU 686 AB	0.4954	R	311.2	0.2	1.004	0.009
21377 + 5659	MLR 583	0.4954	R	15.2	0.3	0.789	0.008
21377 + 5734	D 25 AB	0.4955	R	163.6	0.2	0.974	0.009
21378 + 5333 *	TDT3067	0.4955	R	33.6	0.2	0.821	0.008
21398 + 5403	TDT3093	0.4955	R	332.5	0.4	0.398	0.006
21399 + 5533	TDT3096	0.4955	R	36.3	0.4	1.032	0.009
22016 + 5654 *	TDT3295	0.4955	R	42.4	1.1	0.179	0.005
22033 + 5403 *	TDT3313	0.4955	R	133.3	0.4	0.886	0.009
22045 + 5239	HU 776	0.4955	R	357.4	0.8	0.164	0.004
22056 + 5711	BAR 57 AB	0.4955	R	274.5	0.4	0.976	0.009
22075 + 5631	HDS3141	0.4955	R	330.5	0.2	0.514	0.006
22077 + 5020	COU2550	0.4955	R	114.2	0.2	0.673	0.007
22078 + 5333	MLR 592	0.4955	R	22.4	0.3	0.488	0.006
22080 + 5635	HDS3144	0.4955	R	33.4	0.2	0.166	0.004
22093 + 5804	MLR 557	0.4955	R	304.6	0.3	0.970	0.009
22107 + 5830	A 624	0.4955	R	14.4	0.2	0.763	0.008
22115 + 5110	COU2660	0.4955	R	250.2	0.3	0.670	0.007
22115 + 5232	COU2659	0.4955	R	161.9	0.3	1.253	0.011
22117 + 5743	A 625 AB	0.4955	R	81.5	0.2	0.551	0.006
22122 + 5909	MLR 439	0.4955	R	253.6	0.2	0.791	0.008

TABLE 3

ASTROMETRIC MEASUREMENTS AND RESIDUALS FOR OBSERVED BINARY STARS WITH CALCULATED ORBITS

WDS (2000)	Discoverer designation	Epoch 2016+	Fil.	θ (°)	$\delta\theta$ (°)	ρ ($''$)	$\delta\rho$ ($''$)	$\theta_O - \theta_C$ (°)	$\rho_O - \rho_C$ ($''$)	Orbit Ref.
14190 − 0636	HDS2016 AB	0.4919	R	325.9	0.3	0.198	0.004	1.5	0.011	Tok2015c
14231 + 0729	A 1104	0.4919	R	244.4	0.2	0.423	0.006	1.3	-0.058	Izm2019
14267 + 1625	A 2069	0.4919	R	102.4	0.3	0.159	0.004	24.8	0.034	Sca2001g
14426 + 1929	HU 575 AB	0.4920	R	115.4	0.2	0.368	0.005	0.5	0.003	Sod1999
16038 + 1406	HDS2265	0.4921	R	9.4	0.3	0.276	0.005	0.1	0.000	Tok2018e
16059 + 1041	HDS2273 Aa,Ab	0.4921	R	253.5	0.2	0.364	0.005	0.4	0.009	Tok2019h
16079 + 1425	A 1798	0.4921	R	344.4	0.2	0.211	0.004	11.2	0.064	USN2002
16115 + 1507	A 1799	0.4921	R	296.6	0.2	0.817	0.008	1.4	0.024	Zir2014a
16169 + 0113	A 2181	0.4921	R	86.5	0.3	0.518	0.006	-18.8	0.101	Pop1995d
17066 + 0039	TOK 52 Ba,Bb	0.4922	R	18.4	0.2	0.091	0.004	-4.8	-0.008	Izm2019
17066 + 0039	BU 823 AB	0.4922	R	172.0	0.2	1.037	0.009	0.7	-0.004	Izm2019
17136 + 1716	A 2087	0.4923	R	133.4	0.3	0.488	0.006	-1.8	0.016	Mnt2001a
17155 + 1052	HDS2440	0.4923	R	113.4	0.5	0.160	0.004	-7.5	0.021	Cve2014
17176 + 1025	HDS2445	0.4923	R	261.4	0.3	0.215	0.004	1.5	-0.002	Tok2017b
17240 + 3835	HU 1179	0.4977	R	272.4	0.1	0.303	0.005	3.1	0.039	Hrt2000b
17247 + 3802	HSL 1 Aa,Ac	0.4977	R	61.7	0.2	0.254	0.005	3.9	-0.045	Rbr2018
17251 + 3444	HU 922 Aa,Ab	0.4977	R	30.4	0.3	0.275	0.005	0.4	-0.009	FMR2016b
17487 + 3536	HU 1182	0.4977	R	298.5	0.2	0.426	0.006	-0.8	0.021	USN2002
17490 + 3704	COU1145	0.4977	R	103.4	0.2	0.164	0.004	1.0	0.017	Hrt1996a
17591 + 3228	HU 1185	0.4977	R	145.5	0.2	0.394	0.006	1.2	-0.005	Doc2012i
18003 + 2154	A 1374 AB	0.4950	R	215.4	0.2	0.485	0.006	2.2	-0.012	Msn2017a
18017 + 4011	STF2267	0.4950	R	277.5	0.2	0.521	0.006	1.9	0.000	Zir2014a
18025 + 4414	BU 1127 AB	0.4950	R	46.3	0.2	0.701	0.007	0.7	0.000	Cve2016c
18033 + 3921	STF2275	0.4977	R	303.5	0.2	0.336	0.005	-1.5	0.023	Pop2000a

TABLE 3. (CONTINUED)

18033 + 3921	STF2275	0.4950	R	303.5	0.2	0.335	0.005	-1.4	0.022	Pop2000a
18035 + 4032	COU1785	0.4950	R	30.4	0.2	0.166	0.004	-5.0	0.000	Doc2008a
18043 + 4206	COU1786 Aa,Ab	0.4950	R	11.4	0.2	0.152	0.004	12.0	-0.030	Hrt2009
18063 + 3824	HU 1186	0.4978	R	134.4	0.2	0.176	0.004	-29.7	0.104	USN2006b
18092 + 3129	COU 812	0.4923	R	265.6	0.3	0.672	0.007	-21.0	-0.006	Cou1999b
18097 + 5024	HU 674	0.4951	R	214.4	0.2	0.765	0.008	0.6	0.024	Msn2017e
18126 + 3836	BU 1091	0.4978	R	320.3	0.2	0.765	0.008	1.5	0.004	Zir2012b
18130 + 3318	COU1006	0.4978	R	337.4	0.2	0.514	0.006	81.6	0.220	Cou1999b
18154 + 5720	HDS2577	0.4951	R	330.4	0.2	0.186	0.004	10.9	-0.038	RAO2015
18163 + 3625	HU 1291	0.4978	R	52.4	0.2	0.304	0.005	3.0	0.017	Hrt2014b
18250 − 0135	AC 11	0.4895	R	355.7	0.1	0.914	0.009	0.8	0.005	Tok2017c
18261 + 0047	BU 1203	0.4896	R	158.3	0.2	0.518	0.006	0.4	0.021	Pop1996b
18320 + 0647	STT 354	0.4897	R	217.3	0.2	0.549	0.006	2.5	-0.026	Zir2013a
18339 + 5221	A 1377 AB	0.4951	V	134.4	0.1	0.244	0.005	-6.3	0.109	Mut2010e
18421 + 3445	B 2546 Aa,Ab	0.4978	R	24.4	0.2	0.124	0.004	-2.5	0.018	USN2002
18437 + 3141	A 253	0.4979	R	134.2	0.2	0.702	0.007	-2.2	0.094	Baz1987d
18466 + 3821	HU 1191	0.4979	R	338.4	0.2	0.218	0.004	-2.2	-0.009	Doc2009g
18534 + 2553	A 2989	0.4925	R	199.4	0.4	0.309	0.005	-2.0	0.022	USN2002
19039 + 2642	A 2992	0.4925	R	224.4	0.4	0.167	0.004	-3.7	-0.018	Doc2009g
19055 + 3352	HU 940	0.4979	R	191.4	0.2	0.458	0.006	2.0	-0.004	Doc2009g
19073 + 2432	A 262	0.4925	R	269.4	0.3	0.167	0.004	-3.2	-0.034	Zir2012b
19083 + 2706	HO 98 AB	0.4925	R	61.4	0.2	0.209	0.004	5.3	0.030	Lin2012a
19083 + 5520	D 19 AB	0.4952	R	344.5	0.2	0.458	0.006	1.6	-0.034	Hrt2013c
19106 + 5429	A 1391	0.4952	R	22.4	0.3	0.246	0.005	-2.7	0.013	Pru2014
19216 + 5223	BU 1129	0.4952	R	343.4	0.2	0.304	0.005	2.9	-0.014	Baz1984a
19296 + 1224	A 1653	0.4897	R	142.4	0.2	0.210	0.004	7.1	0.013	Pru2014
19330 + 0546	A 367	0.4898	R	306.3	0.2	1.037	0.009	2.2	0.078	Izm2019
19351 + 5038	HU 679	0.4953	R	272.5	0.2	0.397	0.005	3.3	0.001	Ana2005
20306 + 1349	HDS2932	0.4898	R	309.4	0.4	0.122	0.004	-10.1	-0.017	Hor2011b
20311 + 1548	A 1675	0.4898	R	304.4	0.2	0.165	0.004	0.8	0.004	Hrt2001b
20312 + 1116	CHR 99 Aa,Ab	0.4898	R	185.3	0.2	0.307	0.005	-2.8	-0.030	Hrt2014b
20329 + 1357	L 35 CD	0.4898	R	143.5	0.3	0.515	0.006	-0.1	0.032	Hrt2014b
20410 + 3905	MCA 62 Aa,Ab	0.4981	R	276.4	0.2	0.122	0.004	-1.6	0.034	Ole2003c
20444 + 1945	CAR 2	0.4926	R	320.4	0.8	0.218	0.005	13.1	0.008	Cve2017b
20471 + 2525	BU 364	0.4926	R	75.3	0.2	0.731	0.007	2.0	0.005	Izm2019
20474 + 3629	STT 413 AB	0.4982	R	2.6	0.1	0.942	0.009	0.8	0.042	Izm2019
21109 + 2925	BAG 29	0.4927	R	174.4	0.7	0.188	0.004	1.2	0.000	Bag2010
21125 + 2821	HO 152	0.4927	R	158.4	0.3	0.167	0.004	6.2	0.026	Doc2016g
21135 + 0713	BU 270 AB	0.4899	R	345.4	0.2	0.490	0.006	0.7	0.008	Msn2017a
21147 − 0050	A 883 AB	0.4899	R	287.4	0.3	0.160	0.004	0.5	0.013	Hrt2009
22086 + 5917	STF2872 BC	0.4955	R	298.2	0.2	0.848	0.008	1.3	0.046	USN2002

TABLE 4

NEW CLOSE DOUBLE STARS

Identifier	Coordinates RA & DEC (2000)	Flux m_V	Epoch 2016+	Fil.	θ (°)	ρ (″)
TYC 416 − 564 − 1	17 45 54.92 +01 34 56.60	10.96	0.4893	I	349.4 ± 0.3	0.490 ± 0.008
TYC 420 − 1003 − 1	17 46 16.60 +01 56 45.87	11.35	0.4893	I	265.4 ± 0.4	0.276 ± 0.009
TYC 416 − 174 − 1	17 46 21.64 +01 22 08.59	10.07	0.4893	I	11.6 ± 0.2	0.613 ± 0.007

format used in the WDS Catalog (Worley & Douglass 1997). The second column gives the official binary star discoverer designation. The third column gives the epoch of the observation in fractional Julian years. The fourth column indicates the filter used. The two following columns contain the measured position angles given in degrees, with the errors of their determination, and the angular separation in arcseconds, with the errors of its determination.

The astrometric measurements of close double stars without known orbits are displayed in Table 2. The symbol (*) indicates that this system was previously discovered but never confirmed. We confirm these systems as double stars. However, for many of them, the current position of the component is far away from the one reported previously. Therefore, it is uncertain to determine whether it is a confirmation or a new pair. The second column gives the official binary star discoverer designation. The last four columns give the position angle θ (Column 5) with its error $\sigma\theta$ (Column 6) in degrees, and the angular separation ρ (Column 7) with its error $\sigma\rho$ (Column 8) in arcseconds.

Furthermore, we have observed 65 close binary stars with known orbits from the Sixth Catalog of Orbits of Visual Binary Stars (OC6) (Hartkopf et al. 2001). The astrometric measurements are displayed in Table 3. The first 8 columns are the same as in Table 2. The last three columns give the difference between our measurements and the ephemeris calculated for the date of observation, as well as references in the format of OC6. The orbital elements and the complete list of references may be found in the current electronic version of OC6: http://ad.usno.navy.mil/wds/orb6.html.

The last Table 4 displays the astrometric parameters of three new close double stars with separation less than one arcsecond.

The astrometric results include errors arising in the process of recovering the component positions from the power spectrum. In addition, the position angle measure (θ) can have a systematic error of 0.14° and the separation measure (ρ) has an additional error pertaining to the pixel scale.

5. CONCLUSIONS

We present results of double star speckle interferometric observations focused on close binaries from the WDS catalog. We present the astrometric results for 468 resolved stars. We confirm 59 stars as doubles.

For astrometric measurements, we calculate the high resolution autocorrelation function in polar coordinates. It allows one to perform astrometric measurements even for a distorted power spectrum. The coordinates of the global maximum of ACF_p corresponds to the ρ and θ of the component. The measurements can be carried out without a speckle interferometric transfer function correction, because we exclude atmospheric distortion by using the window $W(r, \phi)$. Finally, the self-calibrating shift-and-add technique solves the 180 degree ambiguity.

This research is supported by the Dirección General de Asuntos del Personal Académico (UNAM, México) under project IN107818. Based upon observations acquired at the Observatorio Astronómico Nacional in the Sierra San Pedro Mártir (OAN-SPM), Baja California, México. We thank the daytime and night support staff at the OAN-SPM for facilitating and helping us to obtain our observations. We have made an extensive use of the SIMBAD and ADS services, for which we are thankful. Also, we would like to thank the reviewers for the time they spent on our manuscript and for their comments which helped us to improve it.

REFERENCES

Christou, J. C., Hege, E. K., Freeman, J. D., & Ribak, E. 1986, JOSAA, 3, 204

Guerrero, C. A., Rosales-Ortega, F. F., Escobedo, G., et al. 2020, MNRAS, 495, 806

Hartkopf, W. I., Mason, B. D., & Worley, C. E. 2001, AJ, 122, 3472

Hartkopf, W. I., McAlister, H. A., & Mason, B. D. 2001, AJ, 122, 3480

Kerp, J., Barth, W., Hofmann, K., Reinheimer, T., & Weigelt, G. 1992, ESO Conference on High-Resolution Imaging by Interferometry II. Part 1: ground interferometry and infrared wavelengths, ed. J. M. Beckers & F. Merkle , 1, 269

Labeyrie, A. 1970, A&A, 6, 85

Mitrofanova, A., Dyachenko, V., Beskakotov, A., et al. 2020, AJ, 159, 266

Orlov, V. G., Voitsekhovich, V. V., Mendoza-Valencia, G. A., et al. 2009, RMxAA, 45, 155

Tokovinin, A., Mason, B. D., & Hartkopf, W. I. 2010, AJ, 139, 743

Tokovinin, A., Mason, B. D., Hartkopf, W. I., Mendez, R. A., & Horch, E. P. 2015, AJ, 150, 50

Tokovinin, A., Mason, B. D., Mendez, R. A., Costa, E., & Horch, E. P. 2020, AJ, 160, 7

Worley, C. E. & Douglass, G. G. 1997, A&AS, 125, 523

V. G. Orlov: Instituto de Astronomía, Universidad Nacional Autónoma de México, Apdo. Postal 70-264, Cd. Universitaria, 04510 Ciudad de México, México (orlov@astro.unam.mx).

Revista Mexicana de Astronomía y Astrofísica, **57**, 81–89 (2021)

https://doi.org/10.22201/ia.01851101p.2021.57.01.05

EXPLORING THE NATURE OF COMPACT RADIO SOURCES ASSOCIATED TO UCHII REGIONS

Josep M. Masqué[1], Luis F. Rodríguez[2,3], Sergio A. Dzib[4], S.-N. X. Medina[4], Laurent Loinard[2], Miguel A. Trinidad[1], Stan Kurtz[2], and Carlos A. Rodríguez-Rico[1]

Received August 25 2020; accepted October 7 2020

ABSTRACT

We present Very Large Array 7 mm continuum observations of four ultra-compact (UC) HII regions, observed previously at 1.3 cm, in order to investigate the nature of the compact radio sources associated with these regions. We detect a total of seven compact radio sources, four of them with thermal emission, and two compact radio sources with clear non-thermal emission. The thermal emission is consistent with the presence of an ionized envelope, either static (i.e., trapped in the gravitational radius of an associated massive star) or flowing away (i.e., a photo-evaporative flow). The nature of the non-thermal sources remains unclear and several possibilities are proposed. The possibility that most of these compact radio sources are photo-evaporating objects, and the remaining ones more evolved objects, is consistent with previous studies on UCHII regions.

RESUMEN

Presentamos observaciones del continuo a 7 mm con el Very Large Array de cuatro regiones HII ultra-compactas (UCHII), observadas previamente a 1.3 cm, con el fin de investigar la naturaleza de las fuentes de radio compactas asociadas con estas regiones. Detectamos un total de siete radio fuentes compactas, cuatro de ellas con emisión térmica, y dos radio fuentes compactas claramente con emisión no térmica. La emisión térmica es congruente con la presencia de una envolvente ionizada estática (i.e., atrapada en el pozo de potencial de la estrella masiva asociada a la región) o fluyendo (i.e., un flujo foto evaporándose). La naturaleza de las fuentes no térmicas no es clara y se proponen algunas posibilidades. La posibilidad de que la mayoría de estas fuentes de radio compactas sean objetos foto evaporándose y las fuentes restantes objetos más evolucionados concuerda con estudios previos sobre regiones UCHII.

Key Words: HII regions — stars: formation

1. INTRODUCTION

The advent of a new generation of upgraded instruments (e.g. the Karl G. Jansky Very Large Array) enables radio astronomers to detect and systematically study the weakest and most compact sources emitting at radio wavelengths in star forming regions. As an outcome, extremely rich populations of compact emitting sources, most of them a few hundreds of AU in size (when resolved), are unveiled in these regions (e.g., Forbrich et al. 2016; Medina et al. 2018). The nature of these Compact Radio Sources (CRS) is not unique, as shown by the variety of spectral indices that they exhibit, among other properties. Furthermore, special attention has been recently paid to the particular case of CRS associated with UCHII regions (i.e., very close to the massive star). Good examples can be found in W3(OH) (Kawamura & Masson 1998; Dzib et al. 2013a) and NGC6334A (Carral et al. 2002; Rodríguez et al. 2014). The detection of these sources, associated with the probably densest part of the cloud, is challenging because they are usually weak compared to the extended free-free emission of the UCHII region where they are possibly embedded. In a recent systematic study

[1]Departamento de Astronomía, Universidad de Guanajuato, México.

[2]Instituto de Radioastronomía y Astrofísica, Universidad Nacional Autónoma de México, México.

[3]Mesoamerican Center for Theoretical Physics, Universidad Autónoma de Chiapas, México.

[4]Max Planck Institut für Radioastronomie, Germany.

(Masqué et al. 2017, hereafter MRT2017), 12 UCHII regions were observed to obtain an unbiased census of CRS associated with them. They reported 13 CRS, showing that the above-mentioned association is common. The significant number of CRS found allowed MRT2017 to classify them into two main types depending on the position of the compact sources with respect to the peak emission of the UCHII region. The CRS that appear projected close to the peak (i.e., possibly embedded in the dense ionized gas of the region) were called Type I sources, whereas the CRS scattered around the UCHII region were called Type II sources. The authors argued that Type I sources probably correspond to photo-evaporating objects with high mass depletion rates as a consequence of the harsh irradiation from the nearby massive star. The large amount of expanding plasma emanating from these objects, either associated or not with the exciting star, maintains large emission measures in a compact volume around it, and an UCHII region is observed (lasting $\approx 10^5$ yr according to Hollenbach et al. 1994). On the other hand, Type II sources could be photo-evaporating objects with lower depletion rates because the massive star is not so nearby. Their low mass depletion rates would prevent producing an observable UCHII region around them, and the CRS appears 'naked'. As they are probably long-lived, Type II objects are expected to be on average more evolved than Type I objects, and some of them could be pre-main sequence stars.

In this paper we present a follow-up study of MRT2017 to explore further the nature of the CRS. The interpretation of the nature of CRS given in MRT2017 was tentative, but sufficient to provide a possible schematic evolution and elucidate the role of CRS in star forming regions. We will constrain observational properties of the CRS, particularly the spectral index, supported by new Q-band observations of 4 UCHII regions containing both types of CRS. The results presented here are important to probe the scheme proposed in MRT2107 and shed light on the evolution of young objects embedded in giant clouds. The 7 mm observations are described in § 2. In § 3 we give our observational results and their discussion is presented in § 4. Finally, in § 5 we list our conclusions.

2. OBSERVATIONS AND DATA REDUCTION

2.1. *Source Selection*

We observed the UCHII regions G28.29-0.36, G35.20-1.74, G60.88-0.13 and G61.48+0.09A. All these regions are excited by late O or early B type stars and are part of the original selection of MRT2017. These authors found that G28.29-0.36 and G35.20-1.74 contain CRS of Type I, whereas G60.88-0.13 and G61.48+0.09A have Type II CRS. Our UCHII regions are located at fairly high declinations, since at 7 mm the quality of the observations strongly depends on source elevation. At the same time, we excluded the most compact UCHII regions because the CRS can be difficult to isolate in their corresponding maps.

G28.29-0.36, located at 3.1 kpc, is associated with IRAS 18416-0420. The maps of Kurtz et al. (1994) show that this UCHII region is composed of two peaks aligned north-south, with the CRS associated with the northern one. The G35.20-1.74 UCHII region is part of the W48 complex (Zeilik & Lada 1978) located at 3.3 kpc (Zhang et al. 2009). The cm emission at subarcsec scales shows a cometary shape with the tip oriented to the NE (Wood & Churchwell 1989; Kurtz et al. 1994). The CRS is found less than 1″ away from the peak of the UCHII region and very close to its geometric center. The G60.88-0.13 region, or Sh 87, is located at 2.1 kpc. Several IR sources were found in the field (Campbell et al. 1989), suggesting that a cluster of YSO surrounding the UCHII region is present. Within uncertainties, the CRS is coincident with one of these IR sources. Finally, G61.48+0.09A is embedded in the emission nebula Sh 2-88B, for which we adopted a distance of 2.0 kpc (Crampton et al. 1978). This UCHII region shows compact northern emission and some southern extended emission. We found two CRSs embedded in the southern part, which is filtered out by our observations, and we consider that these CRS are detached from the densest part of the UCHII region. One of them is resolved, and has an arc-shaped morphology.

2.2. *7 mm Continuum Observations and Mapping Procedures*

On 2016 May 22 and 24, we observed four UCHII regions of the sample of 12 regions observed at 1.3 cm by MRT2017 (program VLA/16A-003). The observations were performed in the 7 mm band with the VLA in the B configuration. We tuned the frequency range of 40.0-47.9 GHz arranged in 64 spectral windows of 64 channels each. Each channel had a width of 2 MHz. We used the 3 bit samplers with full polarization and 3 seconds as the integration time. The flux and bandpass calibrator was 3C286. Pointing corrections were applied for telescope slews larger

TABLE 1

OBSERVED UCHII REGIONS AND SUMMARY OF THE VLA OBSERVATIONS

UCHII name	Distance[a] (kpc)	Pointing Center α (J2000)	Pointing Center δ (J2000)	Gain Calibrator	Positional Accuracy[b] (mas)	$S_\nu^{\mathrm{cal,c}}$ (Jy)	Spectral Index[d]
G28.29-0.36	3.1	$18^{\mathrm{h}}44^{\mathrm{m}}15^{\mathrm{s}}097$	$-04°17'55''.29$	J1851-0035	150	0.68	-0.54
G35.20-1.74	3.3	$19^{\mathrm{h}}01^{\mathrm{m}}46^{\mathrm{s}}490$	$01°13'24''.65$	J1851-0035	150	0.68	-0.54
G60.88+0.13	2.1	$19^{\mathrm{h}}46^{\mathrm{m}}20^{\mathrm{s}}130$	$24°35'29''.39$	J1931+2243	2	0.36	-0.41
G61.48+0.09	2.0	$19^{\mathrm{h}}46^{\mathrm{m}}49^{\mathrm{s}}202$	$25°12'48''.05$	J1931+2243	2	0.36	-0.41

[a]See references in the text.
[b]Obtained from the NRAO database.
[c]Bootstrapped flux density of gain calibrator at 41.128 GHz.
[d]Spectral index of gain calibrator derived from the outcome of CASA tasks.

TABLE 2

PARAMETERS OF THE VLA MAPS

	Maps with all the visibilities[a]		Maps without short spacings[b]		
UCHII name	Beamsize ($'' \times ''$; °)	map *rms* noise (μJy bm^{-1})	Beamsize ($'' \times ''$; °)	map *rms* noise (μJy bm^{-1})	$N^{\mathrm{c}}_{\mathrm{sources}}$
G28.29-0.36	0.160 × 0.119; -19.2	120	0.138 × 0.099; -19.7	70	1
G35.20-1.74	0.148 × 0.124; -33.2	300	0.127 × 0.106; -35.2	90	2
G60.88+0.13	0.130 × 0.116; -84.3	45	0.113 × 0.100; 89.4	60	1
G61.48+0.09	0.130 × 0.117; -89.4	80	0.113 × 0.100; -89.7	50	3

[a]Maps weighted with robust 0.
[b]Maps constructed with uniform weighting. We removed structures larger than 0''.5 (see text).
[c]Number of CRS associated with the region. We included the newly discovered sources.

than 10 degrees on the sky. We employed integrations of 1 to 1.5 minutes on-source, preceded and followed by integrations of 25 to 40 sec on the gain calibrator to obtain a total on-source time of about 6 minutes. This sequence permits calibration solutions in intervals below the typical time scale of atmospheric phase fluctuations (which can be highly variable at the high frequency bands of the VLA) due to turbulence in the troposphere. The observational parameters are listed in Table 1.

The data were calibrated with the Common Astronomical Software Applications (CASA) package through the pipeline provided by NRAO. The CLEAN task of CASA with the *nterms* parameter set to 2 was used to construct the maps. We obtained a first set of maps setting the robust parameter to 0 to search for all the emission components. In order to remove extended emission from the maps, we re-imaged the fields using only uv-distances larger than 515 kλ, equivalent to mapping only structures smaller than 0''.5 in size, and with uniform weighting. This cut was chosen to employ the same uv-range as that used in the synthesis of the 1.3 cm maps of MRT2017. This is a requirement for a proper comparison between the maps at both wavelengths in the forthcoming analysis. The parameters of the 7 mm maps are shown in Table 2.

3. RESULTS

In Figure 1 we show our VLA 7 mm maps. The color scale corresponds to the maps obtained including all the visibilities; the contours show only the longer baseline data. The G28.29-0.36 and G35.20-1.74 regions are more extended than the nominal largest angular scale structure visible to the array (4'', observing at the 7 mm band in the B configuration); hence, we only recover the brightest emission of these regions. On the other hand, the maps without extended structures shown as contours appear cleaner and the compact structures of the regions are clearly seen. In these maps, all the CRS reported in MRT2017 for these four UCHII regions are detected at 7 mm, confirming that they are real structures and not artifacts of the maps. Using the nomenclature of MRT2017, they are G28-VLA1, G35-VLA1, G60-VLA1, G61-VLA1 and G61-VLA2; they are shown in Figure 2.

We found two additional CRS not reported in MRT2017 (we name them G35-VLA2 and

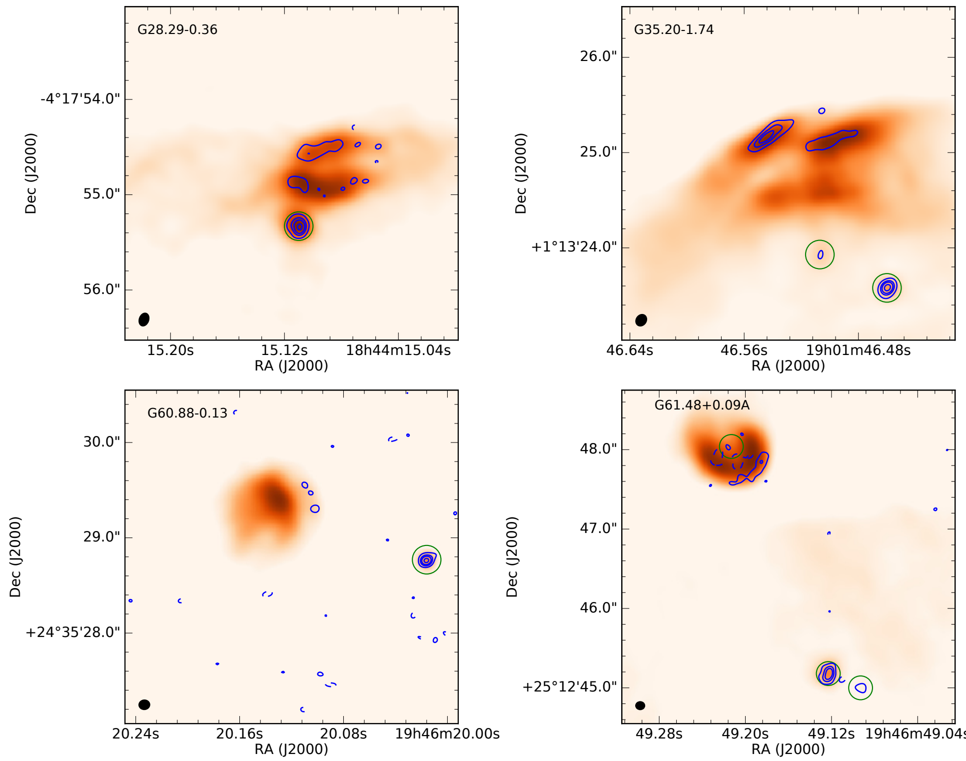

Fig. 1. Continuum 7 mm emission maps of the observed regions listed in Table 1 constructed with all the visibilities (color scale) with the maps constructed with baselines longer than 515 kλ superimposed (contours). For the contours, levels are -3, 3, 7, 10, and 15 times the rms noise level shown in Column 6 of Table 2. The color-scale maps are smoothed to an angular resolution of 0.2$''$ to improve the appearance. The green circles indicate the location of the CRS reported in Table 3. The synthesized beam of the maps without short spacings is shown in the bottom right corner. The color figure can be viewed online.

TABLE 3

OBSERVED FLUXES AND SPECTRAL INDICES FOR THE CRSS

Source	Coordinates[a] α (J2000)	δ (J2000)	$S_{7\mathrm{mm}}$ (mJy)	$I_{7\mathrm{mm}}^{Peak}$ (mJy bm^{-1})	$S_{1.3\mathrm{cm}}$[b] (mJy)	$I_{1.3\mathrm{cm}}^{Peak}$[b] (mJy bm^{-1})	α_S[c]	α_I[d]
G28-VLA1	18:44:15.110	-4.17.55.33	3.0 ± 0.2	1.79 ± 0.08	3.41 ± 0.22	1.79 ± 0.08	-0.18 ± 0.13	0.00 ± 0.09
G35-VLA1	19:01:46.460	01.13.23.58	5.7 ± 0.2	4.8 ± 0.1	5.88 ± 0.23	4.53 ± 0.11	-0.05 ± 0.07	0.09 ± 0.05
G35-VLA2	19:01:46.507	01.13.23.93	1.0 ± 0.4	1.09 ± 0.21	1.0 ± 0.3	0.89 ± 0.16	-0.1 ± 0.7	0.3 ± 0.4
G60-VLA1	19:46:20.016	24.35.28.77	1.01 ± 0.07	1.04 ± 0.04	0.31 ± 0.02	0.34 ± 0.01	1.69 ± 0.13	1.62 ± 0.07
G61-VLA1	19:46:49.123	25.12.45.18	2.4 ± 0.3	1.1 ± 0.1	3.5 ± 0.3	1.39 ± 0.09	-0.56 ± 0.21	-0.28 ± 0.15
G61-VLA2	19:46:49.093	25.12.45.00	0.6 ± 0.1	0.54 ± 0.06	0.40 ± 0.06	0.35 ± 0.03	0.5 ± 0.3	0.61 ± 0.20
G61-VLA3	19:46:49.216	25.12.48.03	0.28 ± 0.07	0.28 ± 0.07	0.73 ± 0.16	0.56 ± 0.08	-1.4 ± 0.5	-1.0 ± 0.4

[a]Typical positional uncertainties are $\approx$ 150 mas for the CRSs associated with G28.29-0.36 and G35.20-1.74 (due to the poor positional accuracy of the J1851-0035 calibrator); and $\leq$ 30 mas for the CRSs associated with G60.88+0.13 and G61.48+0.09.
[b]Obtained from the 1.3 cm maps of Masqué et al. (2017) convolved to the 7 mm beam size of the maps shown in Figures 1 and 2 (contour maps).
[c]Spectral index derived using integrated flux.
[d]Spectral index derived using peak intensity.

G61-VLA3, and they are also shown in Figure 2). To confirm these new detections, we inspected the 1.3 cm maps of the corresponding UCHII regions and found that these new sources were marginally detected in the MRT2017 maps. They both share the characteristic of being centered on the UCHII

TABLE 4

PHYSICAL PARAMETERS OF THE MARGINALLY RESOLVED CRSS

Source	$\theta_M \times \theta_m$; P.A [a] ($mas \times mas$; °)	Size (AU × AU)	$T_{\rm B}^{\rm b}$ (K)	$\tau^{\rm b}$	$EM^{\rm b}$ (10^8 cm^{-6} pc)
G28-VLA1	$114 \pm 15 \times 70 \pm 30; 48 \pm 20$	$340 \pm 50 \times 200 \pm 80$	360 ± 160	0.036 ± 0.016	3.0 ± 1.3
G35-VLA1	$61 \pm 8 \times 37 \pm 9; 136 \pm 20$	$200 \pm 30 \times 120 \pm 30$	2300 ± 600	0.26 ± 0.08	22 ± 7
G61-VLA1	$155 \pm 23 \times 60 \pm 30; 160 \pm 8$	$310 \pm 50 \times 120 \pm 50$	240 ± 120	–	–

[a]Size is deconvolved from the beam of each map (see Column 4 of Table 2).
[b]Brightness temperature (fourth column), optical depth (fifth column) and emission measure (sixth column) obtained in the same fashion as MRT2107, but with the expressions adapted for the frequency of 43.94 GHz (i.e. the central frequency of the observed 7 mm band), and assuming an electron temperature of 10^4 K.

region and they could be associated with the exciting source. The detection of additional CRSs agrees with the scenario of these sources being common in the surroundings of the UCHII regions, most of them being extremely weak and hard to detect.

As a comparison, the contours of the 1.3 cm continuum maps convolved to the larger 7 mm beam are also displayed in Figure 2. As a general trend, the compact sources are unresolved or marginally resolved at both wavelengths and, thus, they appear very similar in the maps. Only G35-VLA2 shows an offset of $\approx 0.''07$ between the two frequencies. This displacement is smaller than our estimated positional error and so it is unlikely to be real.

Table 3 shows the measured flux densities at 7 mm (and 1.3 cm using the MRT2017 data) and the spectral indices for the seven CRS. Flux densities and peak intensities were derived by fitting two dimensional Gaussians to each CRS in the same manner for both bands (with the 1.3 cm maps convolved to the 7 mm beam size). From these parameters we derived spectral indices for the integrated flux densities of the CRSs (α_S) and for their peak intensities (α_I). If the source is resolved, these two indices might differ if inhomogeneities in the source structure are present. Table 4 shows the deconvolved sizes (angular and linear) of the three CRSs that were resolved, at least marginally, in the fit. Despite the large errors, an assessment of the true physical size of the source can be obtained. Moreover, in Table 4 we show physical parameters derived from the flux density and size of the CRS, namely, brightness temperature, optical depth and emission measure. As can be seen in Table 4, G35-VLA1 appears to be smaller and denser than the other sources. These physical parameters are consistent with those derived in MRT2017. Thus, the 1.3 cm and 7 mm continuum emission arises from the same region, at least in the resolved sources.

4. ANALYSIS OF SELECTED SOURCES

In this section we analyze the nature of the 7 CRS detected in our 7 mm observations. A close examination of the properties of these CRSs, listed in Tables 3 and 4, shows that their properties are varied, suggesting a different physical nature for these sources. Thus, in the following we analyze them individually:

G28-VLA1: The possibility that this source is a very small HCHII region was discarded by MRT2017 because they showed that G28-VLA1 is unlikely to host the massive star exciting the region. The remaining possibilities are externally photo-evaporated disk/clump winds and thermal radio jets associated with young low-mass objects. Despite the different launching mechanism and structure of the outflowing gas, their observational signposts are often very similar. Unfortunately, our angular resolution yields a deconvolved size too uncertain for an accurate morphological inspection (either at 1.3 cm or 7 mm). Furthermore, our observing frequency is well above the turn-over frequency ($\approx$10 GHz for G28-VLA1) as indicated by the low values of the optical depth ($\approx 4 \times 10^{-2}$). This results in spectral indices α_I (≈ 0) and α_S (≈ -0.2), consistent with optically thin thermal emission of ionized gas. Flat spectral indices are expected for jets and disk winds when observed at frequencies high enough for essentially the whole object to become optically thin (Reynolds 1986; Hollenbach et al. 1994; Anglada et al. 2018).

On the other hand, the emission measure of G28-VLA1 (3×10^8 cm^{-2} pc) is in excellent agreement with the typical values obtained by Hollenbach et al. (1994) for their photo-evaporating disk wind models, but is significantly higher than that expected for a jet (e.g, see Rodríguez et al. 1990; Curiel et al. 1993). Furthermore, jets usually show additional structures, such as knots resulting from previous ejecta (e.g. Martí et al. 1993), which are not seen in our maps. Therefore, we favor the possi-

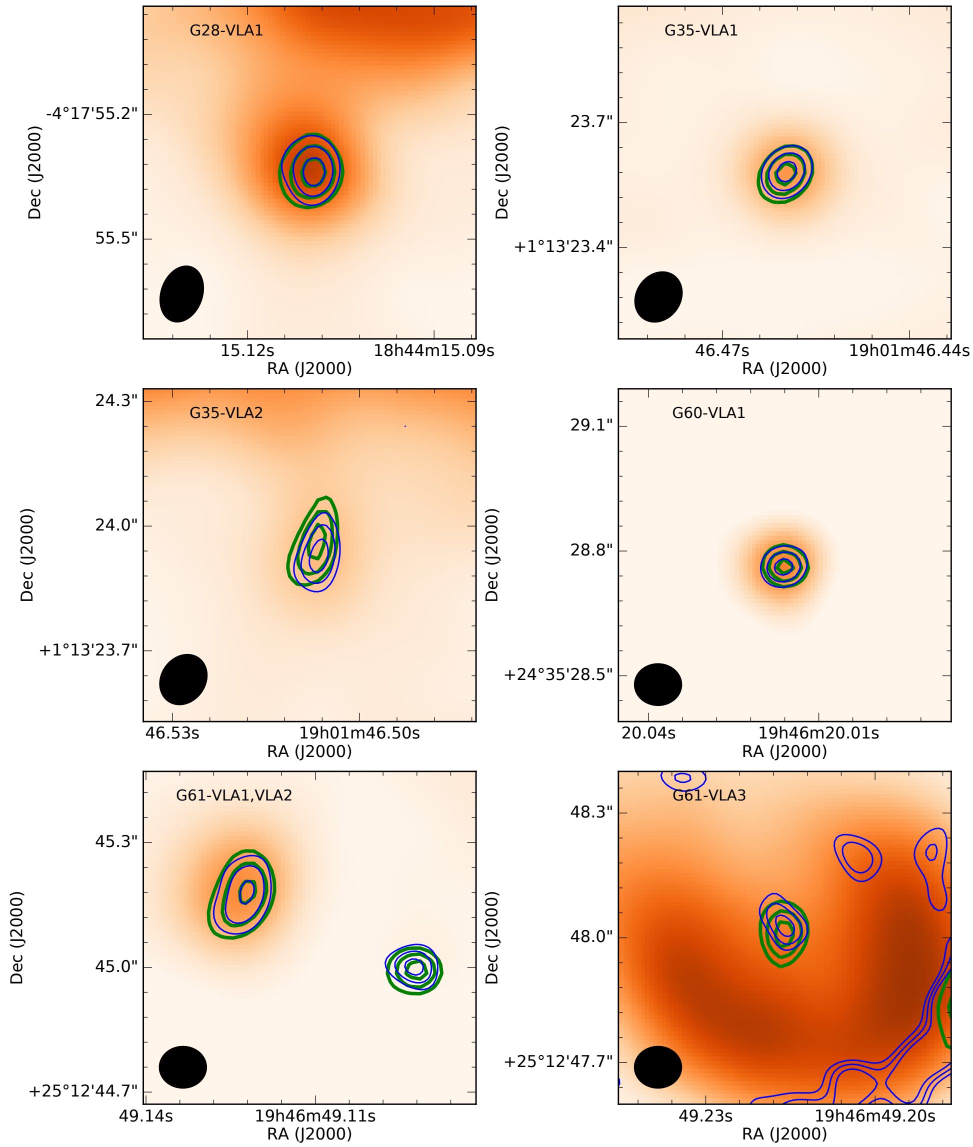

Fig. 2. Zooms on the CRS indicated by green circles in Figure 1. The color scale represents the 7 mm maps constructed with all the visibilities; the blue contours represent the levels corresponding to 50%, 70% and 90% of the brightness peak of the CRS, and the green contours represent the same, but for the 1.3 cm continuum emission. The maps shown with a color scale are the same as those shown in Figure 1 (i.e. smoothed to an angular resolution of 0.2″) but with a modified range. Both maps shown with contours have been convolved to the same synthesized beam, which is shown in the bottom left corner. The color figure can be viewed online.

bility that the optically thin emission of G28-VLA1 is produced by a photo-evaporated disk/clump wind.

G35-VLA1: This CRS has the largest derived EM ($\approx 10^9$ cm^{-6} pc) and a relatively compact size (< 100 AU) compared to other resolved CRSs (G28-VLA1 and G61-VLA1). Based upon size and density, MRT2017 proposed that G35-VLA1 is associated with the exciting star of the UCHII region, as its size is smaller than twice the gravitational radius. The large emission measure of G35-VLA1 rules out a jet as a possibility for this CRS. The turnover frequency for an emission measure of 2.2×10^9 cm^{-6} pc is ≈25 GHz. At our observing frequency of 45 GHz the gas should be completely transparent. This seems consistent with the flat values for the spectral indexes. However, within the uncertainties, we cannot discard a slight step in these indices, and the optical depth (≈ 0.3) is too large to consider optically thin emission.

By comparing α_S and α_I of Table 3, we see that $\alpha_S < \alpha_I$. The same result was found for some of the radio sources of Cepheus A by Garay et al. (1996). These authors conclude that a larger spectral index of the peak emission suggests the presence of an optically thick compact region at the center of the source. Considering G35-VLA1 as a trapped HCHII region, its optically thick part must be < 70 AU in radius (see Table 5 of Keto 2003, where an O6 star is assumed, more massive than the star exciting G35.20-1.74). On the other hand, following the prescription of Hollenbach et al. (1994) for photo-evaporating disk winds (see their equation 7.1) this radius varies between 36-168 AU, observing at 7 mm and for mass loss rates typical for Type I objects ($10^{-5} - 10^{-6}$ $M_\odot$ yr^{-1}). These values are consistent with the deconvolved size of G35-VLA1 of Table 4. Because this size is well below our angular resolution, only a slight rise in α_I is observed. Therefore, the observational properties of G35-VLA1 suggest a density gradient in the CRS that could be the result of outflowing ionized material, or of a trapped HCHII region.

G35-VLA2: This CRS lies near the geometrical center of the G35.20-1.74 UCHII region and is clearly a Type I object according to MRT2017. The detection of G35-VLA2 is too marginal to reach any strong conclusion about its nature; additional observational constraints are required.

G60-VLA1: MRT2017 propose that this source is composed of ionized gas trapped in the potential well of a B-type star, forming a small HCHII region. This is consistent with the lower limit of EM of 7×10^7 cm^{-6} pc for this CRS. Moreover, our derived spectral index is ≈ 1.7, which indicates an optically thick gas, usually found at centimeter wavelengths in HCHII regions.

G61-VLA1: This CRS is the best-resolved of our sample and shows hints of an arc-like shape. The tip of the arc points towards G61-VLA2 suggesting that the latter is responsible for photo-evaporating the former. Both α_S and α_I for G61-VLA1 are clearly negative, showing unambiguously that the emission is mainly non-thermal. Other cases of negative spectral indices around proplyds have been previously reported (Mücke et al. 2002; Masqué et al. 2014), and are attributed to the presence of a relativistic electron population in a magnetized medium. Regardless of the mechanism that produces high-energy electrons, an estimation of the magnetic field can be obtained by assuming equipartition of energy between the magnetic field and relativistic particles. Following Pacholczyk (1970), the magnetic field estimated under these conditions is given by:

$$B[\mathrm{Gauss}] = [4.5(1+\chi)c_{12}L]^{2/7}\, R^{-6/7}, \qquad (1)$$

where L and R are the radio luminosity and radius of the source (assuming spherical symmetry) given in *cgs* units, and χ is the energy ratio of the heavy particles to electrons. L is obtained by integrating the area below the spectra derived from the 1.3 cm and 7 mm fluxes and extrapolated to the limits of 0.01 to 100 GHz (e.g., Miley 1980). Thus, this parameter implicitly includes the dependence on the spectral index α. The total luminosity in the radio domain is 1.6×10^{30} erg s^{-1}. The parameter c_{12} is a function of the spectral index and frequency; tabulated values were given by Pacholczyk (1970). In our particular case its value is 2×10^7 Gauss$^{3/2}$s. For R we calculated an equivalent source size $\theta_{\rm eq} = (\theta_{\rm M}\theta_{\rm m})^{1/2}$ (see Column 2 of Table 4), which corresponds to a linear size of $R = 1.4 \times 10^{15}$ cm. The value of χ is very uncertain and varies from 1 to 2000 depending on the mixture of relativistic particles considered (e.g. electrons, positrons and/or protons). However, the exponent 2/7 makes the magnetic field weakly dependent on χ and we do not expect changes beyond an order of magnitude. For this parameter, we adopted 40 as measured by Simpson et al. (1983) near the Earth.

We obtained a value of $B \approx 25$ mG which, despite being a rough number (it has about 50% uncertainty), it is well above other values found in a variety of radio sources showing thermal emission, such as Cepheus A (≈ 0.3 mG, Garay et al. 1996) or in proplyds like those found in the NGC 3603 region (≈ 1 mG, Mücke et al. 2002). The high value of B depends on the compact size of G61-VLA1 and suggests that the magnetic field increased its strength as a consequence of a prior contraction (either gravitational or driven by external pressure) suffered by these sources (Mouschovias & Spitzer 1976). Consistently, the proplyds discussed in Mücke et al. (2002) are much larger than G61-VLA1 (10^4 vs. 200 AU). The tendency of $\alpha_S < \alpha_I$ can be interpreted as an increase of electron density in the central part of the source, similar to the G5.59-VLA1 proplyd (Masqué et al. 2014): given a mixture of thermal and non-thermal emission, the former will tend to dominate in the densest part of the source because it depends on n_e^2, where n_e is the electron density, contrary to non-thermal emission, which depends on other parameters, like magnetic field or shock energetics.

Alternatively, a wind collision region (WCR) of two massive stars, where the most massive member is G61-VLA2, could explain the non-thermal nature of the emission and the morphology of G61-VLA1. Examples of WCR between two massive stars have been reported previously, such as in Cyg OB #5 (Contreras et al. 1996, 1997; Dzib et al. 2013b). This scenario is favored by our value for the magnetic field, which matches well with that found in other WCR (20 mG in HD 93129A, del Palacio et al. 2016). The only caveat in this scenario is the lack of a point IR counterpart indicating the presence of a massive ionizing star in G61-VLA2, unless its IR emission is obscured by a small disk located edge on. A possible candidate is a 2MASS point source located $10''$ (20,000 AU at 2 kpc) to the west. With the present data, we cannot discriminate between a magnetized neutral object (i.e., a clump or protostellar disk) that is being photo-evaporated or a WCR between massive stars present in the region to explain the nature of G61-VLA1.

G61-VLA2: The spectral index of G61-VLA2 is similar to that of collimated winds (i.e., jets) or isotropic winds with a density gradient (0.6, Panagia & Felli 1975). The lower limit of EM for this CRS (4×10^7 cm^{-6} pc) rules out the protostellar jet possibility, as they have lower expected values (Rodríguez et al. 1990; Curiel et al. 1993). On the other hand, an expanding ionized disk wind with a radial density gradient is an excellent match (in terms of spectral index) to the Hollenbach et al. (1994) model. Therefore, G61-VLA2 could be a photo-evaporating object, possibly a disk around a YSO. However, instead of having a photo-evaporated flow with a resolved volume (sizes $>$ 200 AU) such as other CRS, the volume of the ionized flow of G61-VLA2 is so small that its optically thick region fills a significant fraction of the total volume. The nearby cometary-shaped G61-VLA1 supports the existence of a stellar/disk wind.

G61-VLA3: Despite its large uncertainty, the spectral index of G61-VLA3 is clearly negative (≈ -1). This suggests gyro-synchrotron radiation produced in the magnetically-active corona of a young solar type star. This emission mechanism is commonly observed in star-forming regions containing low-mass YSO (e.g., Dzib et al. 2013b). Since they can show dramatic flux variations over days or hours, we obtained fluxes separately for the two observing days and compared their values to search for rapid flux variability. We observed differences of 40%, which is slightly above the relative errors of our flux determination and consistent with a non-thermal nature of G61-VLA3. Nevertheless, future flux monitoring of this source is needed to assess flux variability. Also, we mapped the Stokes V parameter to look for circular polarization at 1.3 cm and 7 mm. The weak brightness of this CRS hinders a clear detection of polarized emission, but we obtained an upper limit of 10%, from which we cannot discard the presence of circularly polarized emission and the possibility that G61-VLA2 is a magnetic star.

5. DISCUSSION AND CONCLUSIONS

We detected seven CRS located in four UCHII regions previously studied by MRT2017. The analysis of their properties yields that four of them have thermal and two non-thermal emission. One remaining source (G35-VLA2) is detected too marginally to elucidate its emission nature.

The four thermal sources have free-free emission arising from ionized gas in the CRS. According to the MRT2017 scenario, G28-VLA1 and G35-VLA1 are Type I sources and, hence, the ionized gas corresponds to a photo-evaporated flowing material with high mass depletion rates ($\dot{M}>10^{-6}$ $M_\odot$ yr^{-1}). On the other hand, G60-VLA1 and G61-VLA2 are Type II sources and have significantly lower, or even no, depletion rates. This scenario is in excellent agreement with our interpretation of the nature of G28-VLA1 as it appears well-centered on G28.29-0.36 and, at least partially, is feeding the UCHII region with its photo-evaporated outflowing material. The scenario is consistent with the isolated locations of CRSs G60-VLA1 and G61-VLA2, as they are unable to produce a sufficiently extended ionized region around them. It is worth noting that the possibility that G60-VLA1 is a trapped HII region is also consistent with the scenario discussed by Keto (2002, 2003), where instead of outflowing gas, the accretion proceeds through the HII region and the star is still growing in mass.

There is some ambiguity in the interpretation of the nature of G35-VLA1 as either being a trapped HII region or a photo-evaporated wind. Depending on each possibility, the material within the UCHII region could be expanding or infalling from/onto the CRS. Interestingly, these scenarios are not mutually exclusive if rotation is included (Keto & Wood 2006; Keto 2007). In the resulting configuration, the gas is outflowing except for a given range of equatorial angles with respect to the rotation axis, where the gas is infalling. This possibility implies bipolar morphologies, which are not observed for G35-VLA1 because its compact size prevents us from determining its morphology with these observations. Additional observations with higher angular resolution (i.e., the A configuration) to explore the kinematics of the G35.20 UCHII region (e.g., through recombination lines) are crucial to shed light on this last possibility.

The non-thermal CRSs possibly have natures different than the photo-evaporating objects. G61-VLA1 is a Type II source and, hence, consistent with the MRT2017 scenario. On the other hand, the location of G61-VLA3 centered on G61.48+0.09 and the nature of its radio emission mechanism are puzzling: it is difficult to explain the presence of a low mass YSO embedded in an UCHII region (i.e., Type I source). A possible scenario can be that G61-VLA3 is unrelated to the dense gas of the UCHII region but projected in its direction on the sky. Such an arrangement is unlikely, but not impossible (e.g. Trejo & Rodríguez 2010; Dzib et al. 2016). Future investigations to constrain the nature of these CRS are required to conclusively confirm or reject the scenario proposed by MRT2017.

JMM acknowledges the support of DAIP-UG (CIIC2020 project 068/2020). L.L. acknowledges the support of DGAPA-UNAM (PAPIIT project IN112820) and CONACyT (Ciencia de frontera project 263356).

REFERENCES

Anglada, G., Rodríguez, L. F., & Carrasco-González, C. 2018, A&ARv, 26, 3
Campbell, B., Persson, S. E., & Matthews, K. 1989, AJ, 98, 643
Carral, P., Kurtz, S. E., Rodríguez, L. F., et al. 2002, AJ, 123, 2574
Contreras, M. E., Rodriguez, L. F., Gomez, Y., & Velazquez, A. 1996, ApJ, 469, 329
Contreras, M. E., Rodriguez, L. F., Tapia, M., et al. 1997, ESASP 402, 'Hipparcos - Venice '97', 401
Crampton, D., Hutchings, J. B., & Cowley, A. P. 1978, ApJ, 223, 79
Curiel, S., Rodriguez, L. F., Moran, J. M., & Canto, J. 1993, ApJ, 415, 191
del Palacio, S., Bosch-Ramon, V., Romero, G. E., & Benaglia, P. 2016, A&A, 591, 139
Dzib, S. A., Ortiz-León, G. N., Loinard, L., et al. 2016, ApJ, 826, 201
Dzib, S. A., Rodríguez, L. F., Loinard, L., et al. 2013a, ApJ, 763, 139
Dzib, S. A., Rodríguez-Garza, C. B., Rodríguez, L. F., et al. 2013b, ApJ, 772, 151
Forbrich, J., Rivilla, V. M., Menten, K. M., et al. 2016, ApJ, 822, 93
Garay, G., Ramírez, S., Rodríguez, L. F., Curiel, S., & Torrelles, J. M. 1996, ApJ, 459, 193
Hollenbach, D., Johnstone, D., Lizano, S., & Shu, F. 1994, ApJ, 428, 654
Kawamura, J. H. & Masson, C. R. 1998, ApJ, 509, 270
Keto, E. 2002, ApJ, 580, 980
———. 2003, ApJ, 599, 1196
———. 2007, ApJ, 666, 976
Keto, E. & Wood, K. 2006, ApJ, 637, 850
Kurtz, S., Churchwell, E., & Wood, D. O. S. 1994, ApJS, 91, 659
Martí, J., Rodríguez, L. F., & Reipurth, B. 1993, ApJ, 416, 208
Masqué, J. M., Dzib, S., & Rodríguez, L. F. 2014, ApJ, 797, 60
Masqué, J. M., Rodríguez, L. F., Trinidad, M. A., et al. 2017, ApJ, 836, 96
Medina, S.-N. X., Dzib, S. A., Tapia, M., Rodríguez, L. F., & Loinard, L. 2018, A&A, 610, 27
Miley, G. 1980, ARA&A, 18, 165
Mouschovias, T. Ch. & Spitzer, L. Jr. 1976, ApJ, 210, 326
Mücke, A., Koribalski, B. S., Moffat, A. F. J., Corcoran, M. F., & Stevens, I. R. 2002, ApJ, 571, 366
Pacholczyk, A. G. 1970, Radio astrophysics. Nonthermal processes in galactic and extragalactic sources (San Francisco, CA: Freeman)
Panagia, N. & Felli, M. 1975, A&A, 39, 1
Reynolds, S. P. 1986, ApJ, 304, 713
Rodríguez, L. F., Ho, P. T. P., Torrelles, J. M., Curiel, S., & Canto, J. 1990, ApJ, 352, 645
Rodríguez, L. F., Masqué, J. M., Dzib, S. A., Loinard, L., & Kurtz, S. E. 2014, RMxAA, 50, 3
Simpson, J. A., Wefel, J. P., & Zamow, R. 1983, ICRC, 10, 322
Trejo, A. & Rodríguez, L. F. 2010, RMxAA, 46, 357
Wood, D. O. S. & Churchwell, E. 1989, ApJ, 340, 265
Zeilik, M. I. & Lada, C. J. 1978, ApJ, 222, 896
Zhang, Q., Wang, Y., Pillai, T., & Rathborne, J. 2009, ApJ, 696, 268

Josep M. Masqué, Miguel A. Trinidad, and Carlos A. Rodríguez-Rico: Departamento de Astronomía, Universidad de Guanajuato, Apdo. Postal 144, 36000 Guanajuato, México.
Luis F. Rodríguez, Laurent Loinard, and Stan Kurtz: Instituto de Radioastronomía y Astrofísica, Universidad Nacional Autónoma de México, Morelia 58089, México.
Luis F. Rodríguez: Mesoamerican Center for Theoretical Physics, Universidad Autónoma de Chiapas, Carretera Emiliano Zapata Km. 4, Real del Bosque (Terán), 29050 Tuxtla Gutiérrez, Chiapas, México.
Sergio A. Dzib and Sac N. Medina: Max Planck Institut für Radioastronomie, Auf dem Hügel 69, D-53121 Bonn, Germany.

Revista Mexicana de Astronomía y Astrofísica, **57**, 91–105 (2021)

https://doi.org/10.22201/ia.01851101p.2021.57.01.06

A STUDY OF THE TIME VARIABILITY AND LINE PROFILE VARIATIONS OF κ DRA

S. M. Saad[1,2], M. I. Nouh[1], A. Shokry[1,2], and I. Zead[1,2]

Received November 25 2019; accepted October 14 2020

ABSTRACT

We present a spectroscopic analysis of the bright Be star κ Dra. Two independent sets of radial velocity (RV) measurements were obtained by direct measurement and using a line profile disentangling technique. By combining solutions from codes FOTEL and KOREL, we derived improved orbital elements. From the RVs of the Balmer lines and also from some strong metallic lines we found that all RV variations are phase-locked with the orbital period. V/R variations were obtained for $H\alpha$, $H\beta$, $H\gamma$ and some other photospheric lines. A moving absorption bump superposed over the emission line profiles was detected. The orbital solutions for κ Dra were derived assuming a circular orbit with a period $P = 61^d.5549$ and $K = 6.81$ km s^{-1}. We failed to find absorption or emission lines for the unresolved secondary component.

RESUMEN

Presentamos un análisis espectroscópico de la estrella Be κ Dra. Obtuvimos dos conjuntos de mediciones independientes de velocidades radiales, de manera directa y usando una técnica de separación de líneas. Con la combinación de las soluciones de los códigos FOTEL y KOREL obtuvimos elementos orbitales mejorados. A partir de las mediciones de las líneas de Balmer y de algunas líneas metálicas intensas encontramos que todas las variaciones de la velocidad radial estan acopladas en fase al movimiento orbital. Se obtuvieron estas variaciones para las líneas $H\alpha$, $H\beta$, $H\gamma$ y otras líneas fotosféricas, que también resultaron acopladas al movimiento orbital. Detectamos una protuberancia móvil en absorción sobrepuesta a los perfiles en emisión. Las soluciones orbitales para κ Dra se obtuvieron asumiendo una órbita circular con un período de $P = 61^d.5549$ y con $K = 6.81$ km s^{-1}. No fue posible detectar las líneas en absorción o emisión de la secundaria no resuelta.

Key Words: stars: individual: $\boldsymbol{\kappa}$ Dra — stars: binaries: general — line: profiles

1. INTRODUCTION

The system κ Dra (5 Dra, HD 109387, HR 4787, BD+70 703, MWC 222, HIP 61281, Gaia R2 1683102889080253312) is a bright variable ($m_{\rm v} = 3.75 - 3.95$), Be star known as a single-lined spectroscopic binary. The binary nature of κ Dra has been reported a long time ago by Hill (1926), Miczaika (1950) based on radial velocity (RV) variations. The first orbital solution was obtained by Juza et al. (1991). Based on an analysis of RV measurements, they derived an orbital period of and found phase-locked V/R (violet / red) variations of the double peak Balmer emission lines. In addition, information about eccentricity, semi-amplitude, and mass functions was obtained. However, some mystery about the candidate of the secondary star remains. Saad et al. (2004) suggest that κ Dra is a circular binary with $H\alpha$ and $H\beta$ emission locked with the orbl period. Juza et al. (1994) show that the maximum of the emission strength is preceeded by the long-term cycle maximum brightness and coincides with the maximum of the continuum polarization (Arsitaenijevic et al. 1994). Hirata (1995) investigated the brightening of the object and concluded that the extended photosphere may be modeled by rotating model photospheres. Hill et al. (1991) investigated available spectra and

[1]National Research Institute of Astronomy and Geophysics, 11421 Helwan, Cairo, Egypt.

[2]Kottamia Center of Scientific Excellence for Astronomy and Space Research KCScE STDF 5217.

TABLE 1

OBSERVATIONAL JOURNAL OF κ DRA AT THE ONDŘEJOV OBSERVATORY*

Epoch (HJD-2400000)	No. of Spectra	Spectrograph	Detector	Resolving Power	Spectral Range [Å]
48000-51714	93	coudé slit	Reticon RL-1872F/30	10000	6300−6740
49021-49026	3	coudé slit	Reticon RL-1872F/30	10000	4310−4520
49079-49116	6	coudé slit	Reticon RL-1872F/30	10000	4750−4960
52321-52321	1	coudé slit	CCD SITe005 800×2000	10000	4300−4554
52323-52323	2	coudé slit	CCD SITe005 800×2000	10000	6256−6769
51900-52727	15	HEROS	CCD EEV 2000×800	20000	3450−5650
51900-52727	15	HEROS	CCD EEV 1152×770	20000	5850−8620
52742-52754	6	coudé slit	CCD SITe005 800×2000	10000	4753−5005
52734-52754	22	coudé slit	CCD SITe005 800×2000	10000	6256−6769

*Saad et al. 2004.

showed that a period of $0.^d545$ interprets the rapid variation better than the period of $0.^d89$ period computed by Juza et al. (1991). Saad et al. (2004) derived the stellar mass $M = 4.8 \pm 0.8 M_\odot$ and radius $R = 6.4 \pm 0.5 R_\odot$ for the primary.

In the present paper, we analyze the spectroscopic data of the bright Be star κ Dra obtained in the period (1994-2003). We use KOREL and FOTEL codes to compute the orbit of the system. Time variability, line profile variations, and the V/R variations are analyzed.

2. OBSERVATIONS AND DATA REDUCTION

Our data consist of three sets of electronic spectra obtained between June 1992 and April 2003 in both the coudé and Cassegrain foci of the Ondřejov Perek 2-m telescope between HJD 48813.4316 and 52754.8733.

- The main set consists of 102 spectra, which mainly cover the region in a spectral range 6300-6700 Å and were obtained using the **Reticon** detector in the coudé focus.
- The second set is a series of simultaneous red (5850-7850 Å) and blue (3450-5650 Å) spectra secured with the **HEROS** echelle spectrograph in the Cassegrain focus.
- Several CCD spectrograms in both red (6300-6740 Å) and blue (4753-5005 Å) regions were obtained in the coudé focus.

The main features of the spectrograms and a description of the detectors used are summarized in Saad et al. (2004), where the details about the main reduction procedures are also discussed. Table 1 lists the journal of the spectroscopic observations of the system.

2.1. *Radial Velocity Measurements*

The RV measurements were performed interactively using the computer program **SPEFO** (developed by the late Dr. Jiří Horn) by matching the original and mirrored line profiles. The RV analysis is based mainly on the $H\alpha$ line, where RVs are measured in several parts of the line (namely in the steep parts of the line wings, the central absorption, the absorption bump, and the violet and red peaks displacements) and in strong lines of other elements in its vicinity such as He I 6678 Å and Si II 6347, 6371 Å. In addition, for **HEROS** (i.e. the wide range) spectra, RVs for Balmer lines up to H7, and other metallic lines such as Mg II 4481 Å and He I 4471 Å were determined. In the latter cases, RVs for these lines were measured for the outermost parts of the absorption wings, neglecting the details in the line core. Measurement of RVs in κ Dra was not an easy task due to the low amplitude of the variations (only a few km/s) and the line-profile distortion.

The measured RVs for different lines are listed in Table 2, where the file ID, Heliocentric Julian Date of observations (HJD), and the RVs in km/s for each line are listed.

2.2. *V/R Measurements*

As we have already discussed in detail in Saad et al. (2004), the optical and near infrared spectra of κ Dra in the region 3450-7850 Å are characterized by the presence of emission in lower Balmer lines ($H\alpha$, $H\beta$, $H\gamma$), in some Fe II lines, and in the oxygen triplet line OI 7772, 7774, 7775 Å. All the above mentioned lines display double-peaked profiles. The V/R ratio is obtained for these lines whenever it is measurable. The violet (V) and red (R) peak intensities of $H\alpha$ are variable on a long-timescale (see Figure 4a, b in Saad et al. 2004). The intensity ratio V/R (concerning the normalized continuum) was found to be

TABLE 2

RADIAL VELOCITY MEASUREMENTS IN THE $H\alpha$ REGION

File ID	HJD	$H\alpha$					SiII	SiII	HeI
	−2400000	Wing	Abs. Cent.	V-Peak	R-Peak	Abs. Bump	6347	6371	6678
311	48813.4316	1.5	36.6	-50.6	71.7	-120.2	14.18	10.85	-7.88
685	48883.5011	-2.3	7	-39.8	44.5	-101.8	-2.64	-5.89	-18.3
743	48893.2295	-2.8	-12.7	-53.7	40	—	-10.48	-11.43	-14.81
939	49018.5005	-0.46	-13.93	-61.96	48.15	—	—	—	—
940	49018.5748	-0.5	-16.6	-64.3	48.7	—	-12.82	-7.29	-2.39
1270	49045.4876	2.59	—	—	—	—	3.04	-0.1	1.59
1303	49066.4515	2.75	—	—	—	—	2.84	4.63	1.44
1381	49079.5351	2.5	-14	-61.4	51.7	—	-3.5	1.32	-1.28
1407	49080.3336	—	—	—	—	—	-4.06	—	-6.19
1442	49081.4162	—	—	—	—	—	-8.38	-9.24	-10.24
1448	49081.4524	-1.7	-14	-65.6	45.7	—	-10.03	-4.31	-10.85
1465	49088.3751	1.7	-10	-56.9	58	-127.7	-8.87	6.36	-0.72
1515	49092.4615	1.9	—	—	—	—	-4.83	-10.58	-7.8
1565	49102.3385	7.72	—	—	—	—	0.73	2.04	-1.81
1566	49102.3636	5	-12.6	-54.2	56.5	—	0.72	0.83	-0.09
1568	49102.3819	3.7	-10.9	-57.2	53.5	—	-1.53	5.3	-3.55
1697	49116.4731	-1.00	25	-50.01	60.83	-127.13	11.48	-0.88	-2.34
1740	49119.5658	0.7	24.2	-54.3	68.7	-119.3	8.98	-1.35	-1.24
1849	49133.4032	-4.5	10.7	-60.2	62.3	—	-9.34	-20.15	-11.36
3466	49310.5844	—	—	—	—	—	-1.67	10.93	-5.29
3467	49310.6279	-2.5	14.5	-52.9	57.8	-111.5	-1.08	-1.15	2.75
3601	49350.6331	-4	-9.9	-57.9	42.3	—	-9.66	-11.72	-10.06
3848	49403.6115	—	—	—	—	—	-8.06	0.46	-5.74
4243	49463.3294	-7.2	-6	-63.5	57.8	-129.7	-12.23	-16.24	-9.07
4249	49463.3564	-6.5	-6.2	-65.4	58	-130.4	-9.89	-16.32	-4.97
4261	49463.4929	-5	-7.9	-60	58.3	-129.2	-6.3	-4.9	-10.14
4274	49463.5259	-6	-3	-62.8	58.5	-128.4	-10.95	-11.29	-10.16
4406	49466.3311	-5.6	-3.9	-66	59.4	-116.4	-9.1	-8.34	-5.44
4407	49466.3459	—	—	—	—	—	-9.71	-7.74	-14.08
4427	49466.3994	-6.5	-6.5	-65.6	58.6	—	-7.41	-9.08	-9.07
4433	49466.4142	-9.1	-10.3	-68.3	54.8	-126.9	-14.94	-13.45	-13.37
4445	49466.5338	-8	-8.5	-68.3	57.1	-125.2	-15.47	-16.51	-9.42
4446	49466.5492	-7.3	-7.6	-66.5	57.1	-118.7	-14.96	-12.3	-15.11
4462	49466.6149	-6.4	-7	-66.1	60.4	-115.4	-14.6	-7.07	-10.35
4469	49467.3034	-6.9	-10.4	-63.2	58.7	-122.31	-5.62	-11.49	-8.49
4484	49467.3497	-9.5	-11.8	-65.7	56.8	-124.9	-9.83	-3.58	-10.14
4496	49467.4651	-8.6	-11.5	-64.8	50	—	-10.93	-3.49	-11.41
4515	49467.5566	-6	-9.5	-62.2	60.8	—	-9.24	-10.83	-11.41
7348	49702.655	-6.54	-15.33	-62	37	—	-4.7	-9.21	-13.25
8124	49853.4086	—	—	—	—	—	-3.01	-0.19	2.38
8126	49853.4793	—	—	—	—	—	-1.55	-0.56	2.68
8190	49862.3759	-3.6	25.8	-61	67.9	-115.5	-3.78	-1.71	-0.87
8191	49862.3842	-6.4	25.2	-60.9	67.4	-117.8	5.31	-6.54	0.86
8551	49918.3372	0.2	37.7	-56.1	72.8	-125.8	-2.03	-10.58	-2.99
8739	49930.3387	-3.1	28	-55.3	73.7	-112.1	0.27	-3.73	-0.21
9690	50080.6261	-5.4	-10.7	-57.5	53.8	—	-7.33	-12.9	-5.58
9798	50097.6859	-0.67	—	—	—	—	—	—	—
9862	50104.7034	-1.7	19.4	-57.9	68.6	-112.4	2.15	-6.38	-1.17
10089	50140.59	-3.2	-6.8	-59.5	57.1	-111.6	-7.13	-15.41	-9.87
10245	50158.5779	-2.2	27.1	-57.2	58.1	—	12.9	2.41	7.12
10268	50159.4882	-1	24.7	-59.5	61.6	—	7.89	2.99	-0.39
10285	50160.4201	-3.1	21.4	-64	64.7	—	-2.49	3.45	1.05
10562	50193.4706	-7.4	-25.6	-77.1	52.3	-123.3	-18.45	-24.42	-11.36
10972	50249.4667	-1.4	-13.7	-71.6	57.7	—	-11.66	-13.96	-10.7
10995	50251.383	-4.8	-20.6	-75	50.8	—	-16.16	1.52	-0.48
11509	50316.3418	-3.1	-23.6	-68.1	43.1	-117.2	-1.38	-21.16	-14.34
12257	50448.6371	-4.8	-14.2	-66.3	56.1	—	-7.81	-16.21	-7.85
12528	50497.4534	-6.0	-17.25	-70.5	47.11	-122	22.2	—	0.33
12576	50506.5231	-7	-8.7	-70.2	58.6	—	-9.7	-14.04	0.35
12619	50509.529	-6.6	-9.5	-69.8	60.1	-130.6	-14.86	-16.93	-6.8
12743	50518.464	-5.3	-8.2	-69.7	64.3	—	-7.35	-0.23	-1.39
13044	50583.4009	-1.4	12.1	-64.6	74.1	—	0.93	-0.3	2.42
13401	51081.3122	—	—	—	—	—	—	—	—

TABLE 2. CONTINUED

13544	51238.5568	-5.45	-15.98	-66.92	56.03	—	—	-24.21	1.47
13622	51250.4931	-4.8	-15.9	—	—	—	0.15	-3.89	-5.41
13741	51304.5682	—	—	—	—	—	-15.44	—	—
13795	51316.368	-2.75	-10.94	-69.49	65.17	—	—	8.01	-7.46
13799	51316.4734	-1.26	-14.14	-67.42	67.24	—	-3.75	—	15.85
13842	51322.4657	—	—	—	—	—	-4.56	—	3.11
13849	51323.3312	-1.3	11.6	-61	74.2	—	-2.23	-13.11	-2.52
13851	51323.3469	-0.4	12.5	-61.8	72.2	—	-8.57	-17.03	-0.39
13853	51323.3652	-0.5	10.6	-62	73.2	—	-7.68	-12.52	-1.91
13855	51323.3851	0.9	10.3	-60.5	73.5	—	-1.38	—	3.72
13857	51323.4095	1.5	9.1	-61.7	72.9	—	-13.26	-26.47	-0.73
13859	51323.4402	-0.1	9.3	-61.6	73.6	—	-6.74	-26.62	-4.28
13868	51325.3803	-2.1	23.6	-58.3	71.6	—	-1.27	-11.64	10.26
13920	51328.4117	-0.2	43.7	-59.9	79.4	—	-7.14	16.15	3.05
13922	51328.4401	-0.5	44	-61.4	77.9	—	-1.92	-5.21	3.3
14118	51378.5441	0.4	12.1	-62.2	81.8	-112.5	-0.97	-18.53	-8.52
14137	51379.4291	-2.5	14.5	-62.2	77.6	—	7.58	-14.94	-3.97
14276	51391.4448	-0.8	51.2	-58.8	70	-116.7	0.51	-0.75	-1.69
14438	51401.3442	2.5	60.2	-50.5	84.2	-113.8	—	—	9.37
14477	51410.3629	-1.5	27.7	-58.9	63.4	-112.2	-9.37	-20.37	-4.52
14787	51433.3458	-5.2	-8.1	-59	45.1	—	-26.19	-5.62	-9.43
15597	51580.6094	-0.1	56.7	-55.1	74.8	—	4.71	-2	7.94
15740	51602.4666	-1	-19.2	-61.9	45.8	—	-10.27	-23.28	0.77
15898	51643.4587	-1.1	35.8	-52	66.2	—	3.48	—	8.4
15973	51656.3361	-2.2	15.4	-53.7	66.9	—	-1.3	-14.39	-2.8
16003	51661.4248	-4	-21.6	-62.6	45.1	—	-16.32	-25.03	-1.15
16079	51669.3847	-3.3	-17.3	-67.1	46.5	—	-10.09	—	-1.61
16137	51678.3676	-4.2	-4.2	-54.5	55.5	-123.6	-21.83	—	3.75
16148	51679.3875	-4.1	-4.1	-57.3	62.6	-124.6	-5.28	-15.89	-0.34
16150	51679.4007	-4.5	-0.4	-57.8	62.8	-124.5	-3.6	—	0.1
16153	51679.4206	-4.9	2.1	-56.4	61.8	-122	-9.99	-17.56	-4.21
16154	51679.4386	-4.6	-1.7	-56.7	62.7	-125.2	-16.04	-27.21	-1.92
16167	51680.3669	-8.2	-3.8	-57.6	53.6	-129	-1.52	-28.23	-1.41
16195	51681.4058	-7.3	4.4	-59.9	58.3	-127.8	-9.01	-19.65	-14.84
16505	51714.3661	-4.2	28	-52.2	67.2	-110.1	-11.34	—	-3.78
17134	51924.5382	-7.6	—	-53.3	46.7	-114.5	-4.97	—	0.21
17139	51936.5112	-5	-10.1	-50.7	33.3	—	-2.61	-9.98	2.24
17141	51938.4974	-2.5	-0.2	-46.3	44.6	—	-0.01	—	-0.91
17161	51959.5478	-4.9	17.5	-36.9	50.4	-91.7	9.44	-14.69	-1.58
17185	52005.3348	-2.6	6.1	-36	47.6	—	-0.48	-24.1	4.7
17195	52027.4354	-7.3	-10.7	-50.5	41.8	—	-0.25	-19.4	-7.19
17196	52029.3592	-5.6	-9.2	-49.4	—	—	-9.22	-23.87	6.05
17205	52038.5591	-4.9	-1.2	-69.7	50.9	—	-17.01	-19.4	-2.03
17003	52322.6262	-7.1	—	-45.2	60.3	-113.2	9.57	1.27	4.25
17004	52322.6737	-4.9	—	-46.5	59	-113.9	7.72	-2.98	0.19
17333	52343.4844	5.17	—	—	—	—	-0.42	-24.51	—
17346	52352.5487	-6	—	—	—	—	-12.53	-3.87	-3.6
17349	52362.3617	-7	—	-43.1	—	-108.5	-9.69	-14.69	-7.42
17356	52366.3776	-5.5	—	—	—	-101.9	0.94	-12.34	2.46
17365	52373.4292	-1.5	4.9	-35.8	32.3	—	4.3	-2.87	-0.62
17397	52417.4381	-6.8	—	-39.3	44.3	-124.7	-11.99	-19.8	-13.87
17533	52657.5959	-7.9	—	—	25.5	—	-16.01	-5.69	-6.91
18411	52683.5671	-4.6	7.2	-24.8	29.6	—	8.79	1.13	6.33
18431	52684.4712	-6	9.1	-19.2	—	—	6.66	1.6	4.54
18434	52684.5418	-5.6	4.5	-20.2	21	—	1.94	-2.63	4.99
18481	52687.4981	-8.54	—	—	—	—	-1.37	-0.04	-1.3
18484	52687.5881	-8.08	—	—	—	—	4.77	-17.45	0.05
18495	52688.4042	-5.4	—	-47	—	-118.7	5.72	-0.28	2.18
18524	52692.4424	-8.9	—	-31.3	55	-103	6.66	0.9	5.21
18537	52693.4215	-7.8	—	-37	—	-102.8	0.05	1.6	2.07
19757	52720.317	-6.1	1.9	-51.1	39.8	—	-5.62	-15.1	2.07
19793	52721.4777	-4.5	8.3	-47.9	—	—	-14.59	-14.63	-9.6
19816	52722.5142	-3	4.8	-47.7	35	-117.6	-14.35	-15.1	-5.34
19836	52723.4036	-5.3	8.5	-47.3	34.5	-120.4	-10.1	-21.92	-13.87
19837	52723.4325	-5.5	4.1	-45.7	36.5	-116.1	-20.02	-12.98	-5.79
19864	52724.4549	-5.5	19.2	-42	31.1	-117.4	-12.23	-19.8	-10.28
19926	52727.4657	-7.6	14.4	-40.4	36.8	-122.2	-0.42	-15.1	-10.05

TABLE 2. CONTINUED

20412	52734.7316	-6.4	—	-38.6	30	-107.2	-2.98	-5.14	-4.2
21118	52741.9524	-1.9	9.8	-31.8	28	-77.5	0.62	-8.18	-5.18
21221	52742.6241	-2.6	8	-33.6	25	—	2.42	-4.63	-3.53
21222	52742.6307	-2.6	6.2	-33.1	26.1	—	-4.25	10.47	3.38
21421	52744.8203	-3.5	16.5	-25.7	27.6	—	1.06	-17.44	-7.55
21422	52744.8238	-2.8	11.5	-27.5	26.2	—	7.12	-1.74	-1.21
21426	52744.8590	-2.2	13.1	-26.2	27.1	-78.4	8.31	0.05	1.65
22111	52751.7782	-7	—	-47.4	58.7	-120.7	2.18	3.02	2.45
22112	52751.7863	-6.9	—	-49.1	62.3	-119.4	-2.06	3.62	11.08
22114	52751.7979	-3.1	—	-44.1	62.6	—	5.21	5.43	19.14
22115	52751.8014	-5.5	—	-47.1	68.4	—	8.84	-8.46	15.11
22229	52752.5113	-2.8	—	-46.8	64	-122.4	12.03	3.14	-1.3
22429	52754.8454	-5.2	45.2	-38.1	67.5	-102.6	8.38	-2.3	4.46
22430	52754.8493	-6.1	44.3	-38.9	66.6	-108.7	2.93	1.92	6.19
22431	52754.8534	-7.1	43.9	-43.5	67.9	-103.8	0.5	-12.57	-0.15
22432	52754.8576	-6.4	40	-43.3	66.3	-109.5	-1.32	1.31	8.49
22433	52754.8600	-6.6	40.9	-41.1	65.6	-103.9	2.92	5.54	2.73
22434	52754.8624	-8.6	41.8	-44.9	66.4	-114.7	13.23	0.11	2.15
22435	52754.8644	-6.1	41.4	-40.6	64.9	-110.4	7.77	9.16	-3.04
22436	52754.8680	-5.3	40.4	-44.6	65.6	-113.2	7.77	-8.35	5.6
22437	52754.8699	-7.1	39.8	-42.3	64.4	-111.5	9.59	-5.33	12.52
22438	52754.8733	-10.3	38.9	-43.2	63.5	-110	4.13	2.52	11.36

variable with time. However, the first inspection of its time plot reveals that it varies independently of other line parameters (strength and intensity), which show cyclic long-term variations on a time scale of decades. In some phases, it was quite difficult to identify the double-peak structure of the $H\alpha$ line or one of its peaks. For both $H\beta$ and $H\gamma$ lines, V/R variations were obtained over the last three years of the observations, since older Reticon spectra do not cover corresponding spectral regions. Their V/R variations generally behave similarly to those of $H\alpha$. V/R variations of $H\beta$ show stronger R phases than V for the same epochs and its value is longer below unity ($V/R > 1$), in addition to its lower amplitude scale. Due to the weak emission feature of the $H\gamma$ line, V/R variations are not significant and the values are distributed almost around unity. Figure 1 illustrates temporal V/R variations for the $H\alpha, H\beta$ and $H\gamma$ lines. Moreover, V/R variations were found for some other photospheric lines affected by emission, namely for the iron lines Fe II 7462, 7712 Å, and for the triplet O I 7772-5 Å. Their relative V and R intensities are very weak, 4-6 % of the continuum level for the Fe II 7712 Å and O I 7772-5 Å lines, and 1-3 % for the Fe II 7462 Å line. During our observations, the Fe II 7462 Å line has phases dominated by relatively strong R peaks, in contradiction to the FeII 7712 Å line, where the ratio V/R is almost around unity. For the O I 7772-5 Å line, V/R displays consequent slight changes from values > 1 to < 1.

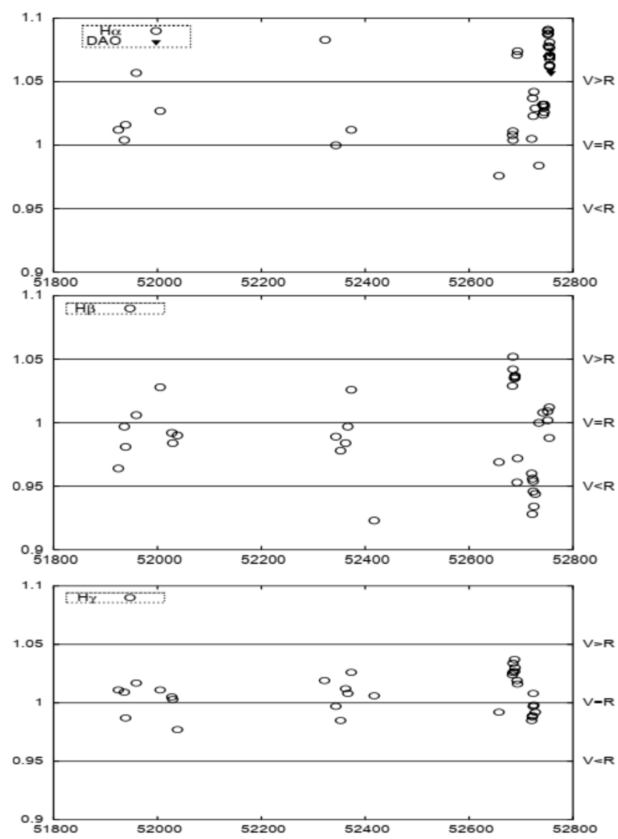

Fig. 1. Simultaneous time distribution of the V/R ratio for $H\alpha$, $H\beta$, and $H\gamma$ lines.

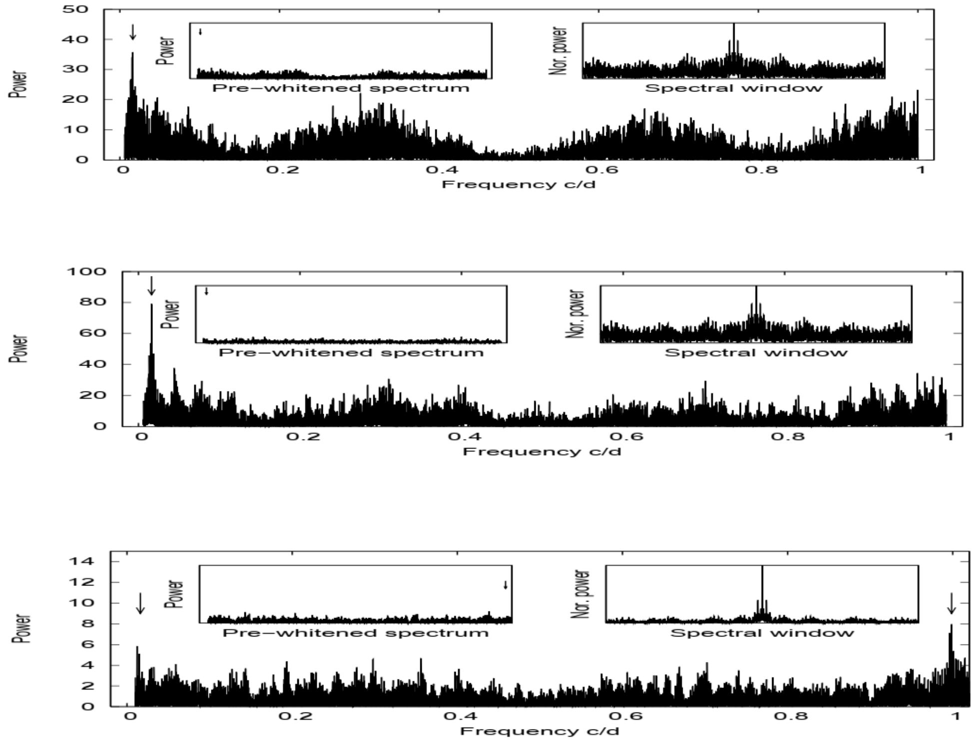

Fig. 2. Each main panel displays the periodogram of the orginal data, the other left and right panels represent the spectral window for the detected frequency and the residual after prewhitening with the detected frequency, respectively. The arrows refer to the peak of the predicted frequency. The panels represent period search results. *Upper panel:* for He I 6678 Å, *Middle panel:* for Si II 6347 Å and *Lower panel:* for $H\alpha$ line.

2.3. *Period Analysis*

Preliminary analysis of the RV variations was important to select a suitable set of lines for further evaluation of the orbital elements. The period search was carried out separately for several line data sets (basically those which cover a long time interval of observations), where two independent numerical period searching routines were used. One is based on the phase dispersion minimization (PDM) technique (Stellingwerf 1978), the other is a computer program PERIOD04 (Breger 1990). For PERIOD, starting values for the frequencies need to be determined by some other technique such as Fourier (which is available in the program itself) or using PDM. Within limits given by the alias structure of the observations, PERIOD can improve the frequency values by minimizing the residuals of a sinusoidal fit to the data. A search for periodicity in the interval 1-160 d has been performed for three sets of RVs, namely RVs of the $H\alpha$ emission wings, of the metallic lines Si II 6347, 6371 Å, and of the He I 6678 Å line. The analysis confirmed the $61^d.5549$ period for two sets of lines: He I 6678 Å and Si II 6347 Å (which Juza et al. 1991 reported for the orbital period) with amplitudes of 5.9 km/s and 8.9 km/s, respectively. For the $H\alpha$ data set, we detected two frequencies, at $0.9987cd^{-1}$ and $0.0162cd^{-1}$ (the orbital one). The upper and middle panels of Figure 2 represent a periodogram (frequency vs. power) of the original data; the right insets in each panel illustrate the spectral window function around the detected frequency, while the left insets represent the residuals pre-whitened for the detected frequency for the He II 6678 Å and Si II 6347 Å lines, respectively.

In Figure 2, the lower panel is similar to the upper and middle ones, but for the $H\alpha$ data set. The pre-whitened spectra for a higher frequency of $0.9987cd^{-1}$ show the disappearance of the frequencies and that of the orbital period as well. Figure 3 displays the corresponding phase diagrams for both data sets. We adopted a similar procedure for searching the period of the V/R ratio of $H\alpha$. The frequency of $0.0162cd^{-1}$ (P= $61^d.64$) was detected for the V/R variations (which is close to the orbital frequency), the corresponding phase variations for this frequency are illustrated in Figure 4. Phase diagrams of the V/R variations for $H\alpha, H\beta$ and $H\gamma$ lines display consistent behavior with each other.

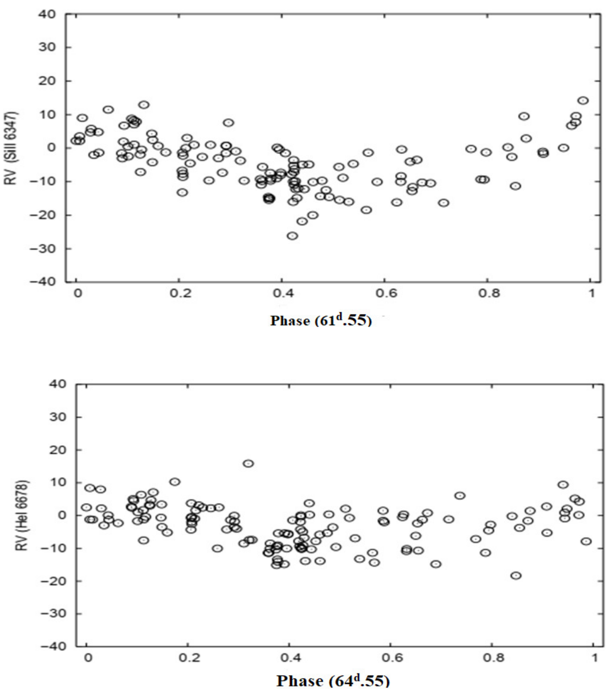

Fig. 3. Corresponding phase diagrams for RVs of Si II 6347 Å and He I 6678 Å lines folded with the period $61^{d}.5549$.

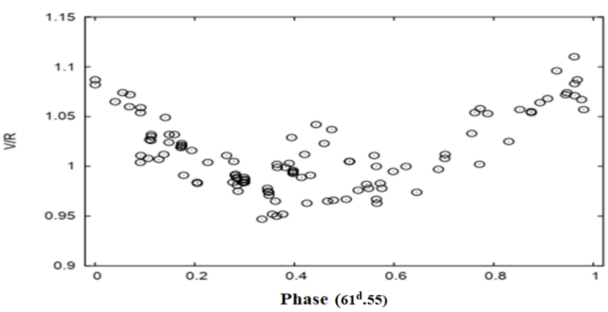

Fig. 4. V/R variations of $H\alpha$ folded with the $61^{d}.64$ period.

Figure 5 represents the phase diagrams folded with $P = 61^{d}.64$ for the $H\alpha$ emission wings (upper panels) and $H\alpha$ absorption center (lower panels).

3. RVS ANALYSIS AND ORBITAL ELEMENTS

Orbital elements were computed from the RVs obtained by the method described in § 2.1 and using the codes FOTEL (Hadrava 1990) and SPEL (developed by the late Dr. Horn). FOTEL is a FORTRAN code for separate or simultaneous solving of light curves, radial-velocity curves, visual (interferometric) measurements, and eclipse timing of binary and/or triple stellar systems.

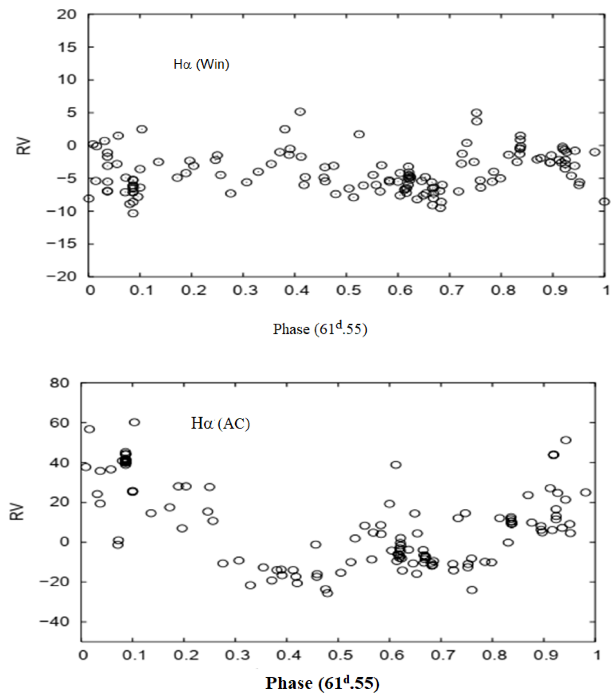

Fig. 5. Phase diagrams folded for ($P = 61^{d}.5549$) Upper panel: $H\alpha$ emission wings, Lower panel: $H\alpha$ absorption center.

Given the results of the period analysis (§ 3), we excluded the data set of the $H\alpha$ from the final solution, since it was dominated by a higher frequency, $0.9987 cd^{-1}$.

The values of the eccentricity e and the periastron longitude ω have been examined through different runs of both codes for RVs in different lines. The test of Lucy and Sweeney (1971) built into the code SPEL indicated that the orbit is circular and small values of the eccentricity are spurious. We thus fixed $e = 0$ and $\omega = 0$ and allowed the code to converge for the period P, the time of the periastron passage $T_{\rm peri.}$ and the semiamplitude K only.

The RV-curves measured for eight different lines (in addition to $H\alpha$) have been solved to check for the constancy of the solution. Five formal solutions were obtained and are given in Table 3. The first three (I to III) were obtained individually for the Si II 6347 Å, Si II 6371 Å, and He II 6678 Å lines. Let us note that solution II (obtained for Si II 6371 Å) shows a higher rms than the other solutions. The line Si II 6371 Å is very weak in the spectrum of κ Dra and, in addition, it is blended with an iron line, and therefore it has a complicated structure. As a result, the phase distribution of its RVs has a larger scatter. The solution IV was obtained from

TABLE 3

FOTEL SOLUTIONS FOR κ DRA

Element	Solution I SiII 6371	Solution II SiII 6371	Solution III HeI 6678	Solution IV (I-III) $H\beta$,$H\gamma$,$H\delta$	Solution V (I-IV) MgII,HeI ,OI 7772, H7
P[d]	61.52±0.03	61.60±0.06	61.54±0.06	61.59±0.03	61.55±0.02
Tperiast	49979.95±1	49977.51±1.7	49980.05±1.6	49978.95±0.90	49980.22±0.59
K[km s^{-1}]	8.10±0.38	6.79±0.68	5.17±0.82	6.84±0.25	6.81±0.24
γ(mean)	-4.5	-8.7	-2.8	–	–
γ(SiII6347)[km s^{-1}]	–	–	–	-4.21	-4.11
γ(SiII6371)[km s^{-1}]	–	–	–	-8.55	-8.51
γ (HeI6678)[km s^{-1}]	–	–	–	-2.9	-2.84
γ ($H\beta$)[km s^{-1}]	–	–	–	-2.5	-2.47
γ ($H\gamma$)[km s^{-1}]	–	–	–	-0.32	-0.31
γ ($H\delta$)[km s^{-1}]	–	–	–	0.41	0.39
γ (MgII+HeI)[km s^{-1}]	–	–	–	–	4.26
γ (OI 7772)[km s^{-1}]	–	–	–	–	-0.81
γ (H7)[km s^{-1}]	–	–	–	–	-0.3
f(m)($M_\odot$)	.0033	0.002	0.0009	0.002	0.002
A sin i($R_\odot$)	5.54	63.4	48.27	64.05	63.49
No. of RVs	151	147	159	325	354
rms [km s^{-1}]	5.55	7.92	5.57	4.83	4.75

the previous sets in addition to the three sets of RVs measurements in the Balmer lines ($H\alpha, H\beta$ and $H\gamma$). FOTEL also allows us to derive individual systemic RV γ for each data set. Finally, we performed another solution V using all data sets involved in solutions IV and three other regions He I 4471 Å + Mg II 4481 Å (as one region), O I 7772-5 Å and H_γ. We fixed the period at the value $61^d.5549$ obtained by an alternative KOREL solution (cf. § 7) and solved with the following ephemeris (similar to Juza et al. 1991)

$$T_{\rm max.RV} = (\rm HJD\,2449980.22 \pm 0.59) + 61\overset{d}{.}5549E.$$

Solution V has the smallest scatter, the smallest errors of the orbital elements, and agrees with other solutions I and III within their errors. It is thus accepted as the final solution.

4. ORBITAL AND PHASE-LOCKED VARIATIONS

4.1. *RVs Variations*

RVs of the red and violet emission peaks show long-term variations in terms of years. Figure 6a displays its time-distribution. These long-term variations were found for the strength and intensity of the whole line (more details in Saad et al. 2004). A signature of the $61^d.5549$ orbital period has been detected after pre-whitening it for the long-term variations period. Figure 6b and Figure 6c illustrate the periodograms of their RVs after pre-whitening for long-term variations, with that (8044 d) cycle obtained by Saad et al. (2004) from brightness, line intensity, and equivalent width variations. The arrow indicates the peaks of the detected frequencies, which are very close to that of the orbital period. Therefore we can say that the violet and red peaks in their displacement follow two different movements of the systems, one of them is related to the circumstellar matter surrounding the system (which is the dominant one as it is clear from a time-distribution diagram), while the other expresses the orbital motion of the binary system. In this respect, we have to note that we failed to find similar behavior in other parameters with dominant long-term variations (intensity of red and violet peaks, and the line strength).

4.2. *V/R Variations*

Violet-to-red peak intensity ratio (V/R) variations are one of the most striking features of the emission lines, which give a measure of the line asymmetry. Usually, the V/R ratio behaves quasi-periodic on a timescale of years. Be stars may change from a stable V/R=1 ratio to V/R variability and back (Porter & Rivinius 2003). Hanuschik et al. (1996) supposed that the majority of Be stars have emission lines with stable and equal V and R peaks, although one-third of them show a cyclic variation of V/R.

On average, periods of V/R variations are usually about seven years (Mennickent & Vogt 1991) and

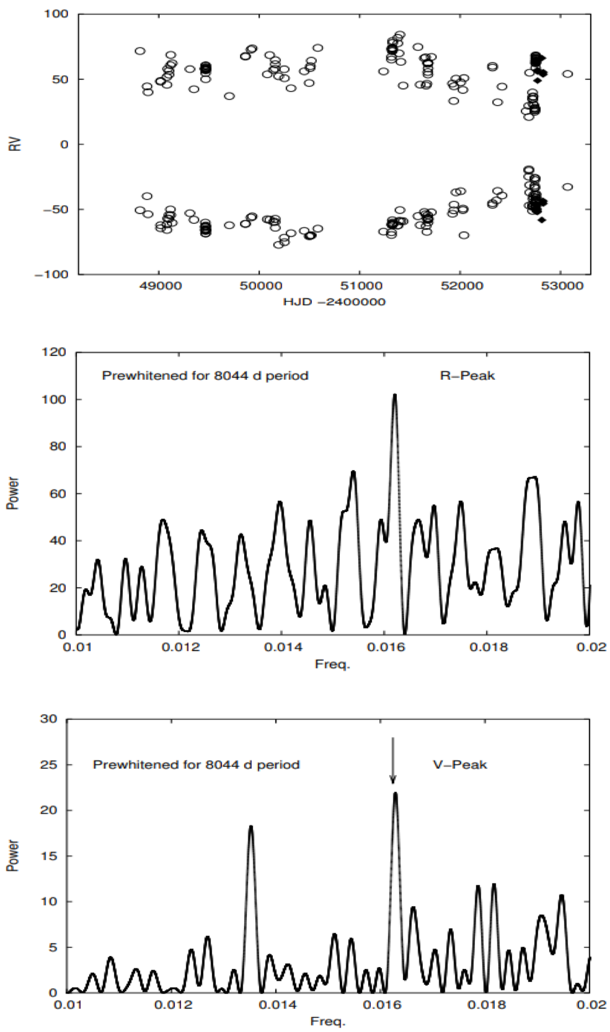

Fig. 6. Violet and red peaks variations of $H\alpha$. **(a):** the long-term distribution of the RVs of V and R peaks, **(b):** the periodogram of the RVs residuals of the V peak after prewhitening for long term variations, **(c):** similar to **(b)** but for the R peak.The arrow indicates the peaks of the predicted frequencies.

connected with long-term variations. In some particular cases, they display different successive phases of activity, as reported for 59 Cyg (Harmanec et al. 2002) or ζ Tau (Hubert et al. 1982). For several other stars, V/R variations are quasi-periodic on a long-timescale, e.g., γ Cas with a period of 9150 d, and κ CMa with a period of 8052 d (Mennickent & Vogt 1991). We found erratic or quasi-periodic variations, as reported also for β CMi (Mennickent & Vogt 1991). In most cases with V/R variations, long-term variations are found to be superimposed on short-term ones, which are sometimes misinterpreted as irregular variations. In the particular case of 59 Cyg, two significant periods have been obtained. A short one, of 28.1971 d, which follows the orbital period of the binary system, and a long one of 722 d, which is connected with the formation of the new Be envelope (for more details see Harmanec et al. 2002).

κ Dra is one of a few Be stars, which are known for the synchronization of the V/R variations with that of the orbital motion and its behavior independent of its long-term variations. Other similar systems include 4 Her, where the V/R variations follow its orbital period of $46^d.1921$ period (Koubský et al. 1997), 88 Her, which varies with a $86^d.7221$ period (Doazan et al. 1985), and Per with a period of $126^d.696$ (Poeckert 1981). They are known as systems with V/R phase-locked with their orbital period. Concerning $H\alpha$, the V/R asymmetry of κ Dra, Arsenijevic et al. (1994) noted that, according to the polarization results, the internal layers of the envelope have axial symmetry, but the outer $H\alpha$ emitting region, affected by the presence of the companion, is probably associated with nonaxisymmetric external layers. In different panels of Figure 7 we give a series of simultaneous profiles of $H\alpha$, $H\beta$, and $H\gamma$ showing variations of the V/R at different phases. Various hypotheses and models have been devoted to explain long-term V/R variations. Struve (1931) suggested an elliptical-ring model (a geometrical one), which was elaborated by McLaughlin (1961). Further modifications were done by Huang (1973, 1975), who attributed the V/R variations to the apsidal motion of an elliptical ring, in which emitting atoms revolve around the star according to Kepler's law. A binary model proposed by Kriz & Harmanec (1975) is another view, where the companion star deforms the disk into an elliptical one through tidal interactions.

Kato (1983) and Okazaki (1991) explained the long-term V/R variations by one-armed global oscillations, where a thin non-self gravitating Keplerian disk is distorted by a density wave. Let us apply this model to κ Dra. The emission structure originates in the envelope, while the binary star is sitting somewhere inside. Therefore, it affects the innermost parts of the surrounding structure. This part of the disk rotates most rapidly. Due to the Roche lobe geometry, there is a high asymmetry in the outer parts of the disk, which therefore reflects in an asymmetry between the red and blue components (i.e V/R variations), alternating around the orbit. In κ Dra, binarity seems to play the most important role in the line asymmetry (Panoglou et al. 2018), which explains the V/R phase-locked variations with the $61^d.5549$ period.

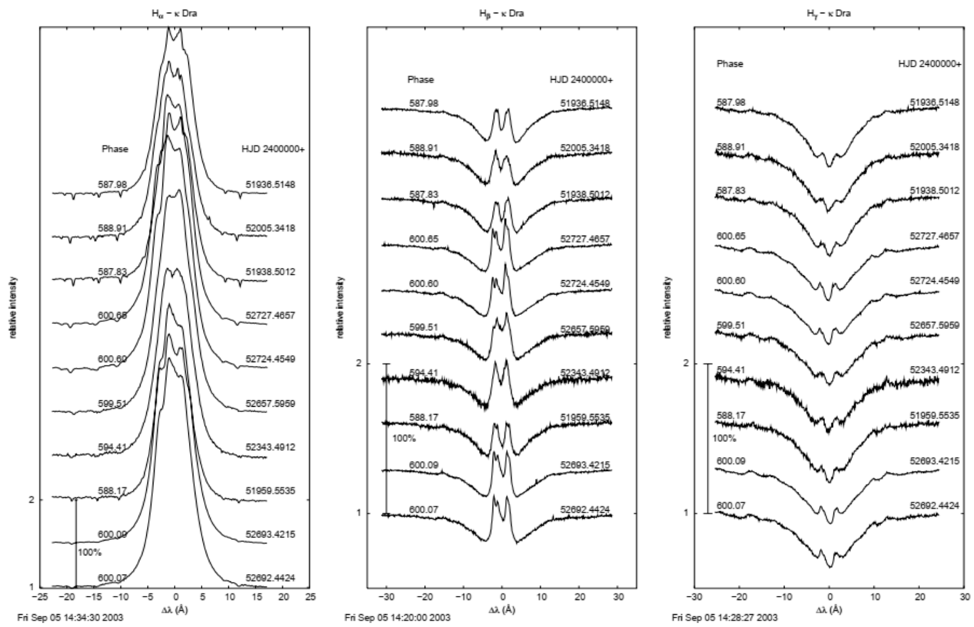

Fig. 7. Variations of the double-emission peaks for different phases during one period. *Left panel:* for $H\alpha$, *Middle panel:* for $H\beta$, and *Right panel:* for $H\gamma$.

5. MOVING ABSORPTION BUMPS

A traveling sub-feature from the blue to the red part of the profiles of some absorption lines on a time scale of hours has been reported by Hill et al. (1991) for κ Dra. This feature has been already detected in the spectra of some Be stars. For 4 Her, it was discovered by Koubský et al. (1997). These authors detected this feature in the violet wing of the line and folded it with the corresponding orbital period.

For κ Dra moving absorption bumps (MAB) were found simultaneously in the violet peaks of both $H\alpha$ and $H\beta$ over their observing run. They are moving through the violet peak redward, and their RV varies from -130 to -80 for $H\alpha$ and from -100 to -20 for $H\beta$. Their strength is variable, from a deep absorption to a faint one. The feature completely disappears in some particular phases.

Its velocity-time distribution does not show long-term variations comparable to those found in brightness, equivalent width, and line intensity. We also found no sign of short-term variability of the MAB. In Figure 8 we illustrate this feature in $H\alpha$ and $H\beta$ with different intensity and velocities at the same epoch.

With a notable scatter its variability is more probably related to the orbital period, Figure 9 shows the phase diagram of the MAB velocities folded with the orbital period for $H\alpha$ and $H\beta$. Although these absorption features have been a subject of many studies, no one clear theory can account for this variation. The new result found here is the simultaneous appearance in both $H\alpha$ and $H\beta$. Taking into account the fact that the characteristic time variation of this MAB is close to that of the orbital variation, its nature may be due to the binary interaction.

6. SPECTRAL DISENTANGLING

In addition to the RV analysis, we used the method of spectral disentangling for a more detailed analysis of the κ Dra spectra. The application of this method is not straightforward for this star and it thus needs a special discussion. In its original form (cf. Simon & Sturm 1994) disentangling requires that the line-profiles of the component stars are not subject to any intrinsic variability, and all variations observed in the spectra are solely due to blending of the Doppler-shifted lines from the stellar components. The long-term variations in the strengths of the $H\alpha$ line together with the V/R variations are most obvious in the case of κ Dra. We thus took the assumptions of the code KOREL for Fourier disentangling (i.e. simultaneous decomposition of component spectra and solution of orbital elements) and "line-photometry" of binary and multiple stars with variable line strengths (Hadrava 1997) model to fit the observed profiles.

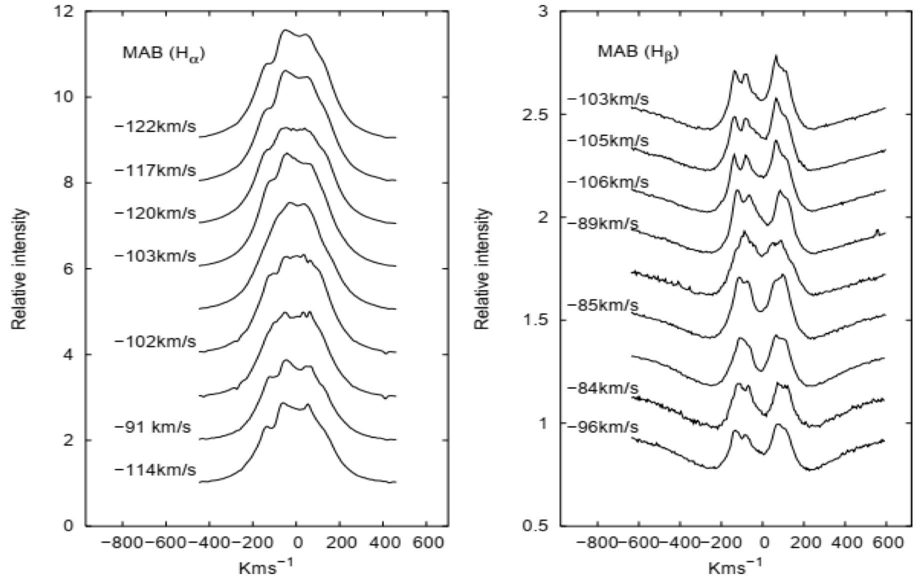

Fig. 8. Simultaneous plots of the absorption bump in the $H\alpha$ and $H\beta$ lines.

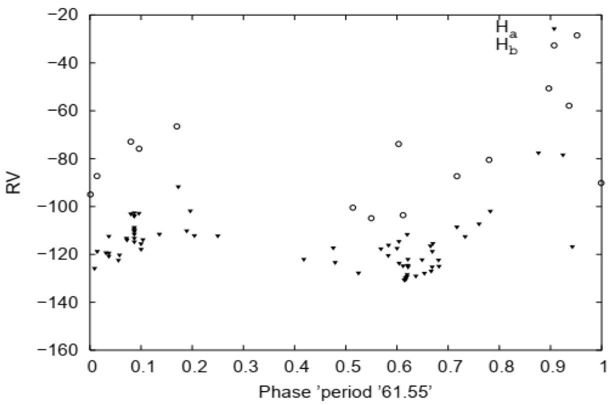

Fig. 9. Phase diagram of the RVs of the absorption feature folded with the orbital period for $H\alpha$ and $H\beta$.

TABLE 4

KOREL SOLUTIONS FOR κ DRA
$P = 61.5549$, $E = 0$, AND $\omega = 0$ ARE FIXED

Region	$T_{\rm peri.}$ HJD	K km s^{-1}
$H\alpha$	49963.6107	1.20
He I 6678	49980.6272	5.83
Si II 6347&6371	49983.0273	4.90
OI 7772-5 A	49982.7098	6.66
$H\beta$	49987.3446	4.20
$H\gamma$	49984.4458	5.13
He I 4471+Mg II 4481	49983.3012	5.09
$H\delta$	49976.7465	7.14
Si II+He I+O I	49982.1262	5.08

As a first step, we ran KOREL for one-component solutions (plus telluric lines when necessary) with variable line-strengths in different spectral regions (see Table 4). For each region, we obtained a decomposed profile. Figure 10 illustrates the comparison of the disentangled spectra of selected photospheric lines with that of the theoretical model for the following parameters ($T_{\rm eff} = 14000$ K, $\log g = 3.5$, and $v \sin i = 170$ km/s), determined for κ Dra in Saad et al. (2004).

7. RAPID VARIABILITY AND LINE PROFILE VARIATIONS

Rapid variability and line profile variations (lpv) are common features in early-type stars. Be stars show various features with different scales of variations from star to star, which increase the mystery of the Be phenomenon since we can not generally accept one model for all stars.

7.1. *Rapid Variability*

For κ Dra, rapid variability was reported by Hubert & Hubert (1979) and Andrillat & Fehrenbach (1982). Three decades ago lpv of κ Dra was studied by Hill et al. (1991). They detected rapid variations (on a timescale of hours) with a period of 0.545 days in the width and asymmetry of the absorption lines He I 4471 Å, Mg II 4481 Å, and He I 4388 Å, and attributed these variations to nonradial pulsations. However, Juza et al. (1991) showed that the de-

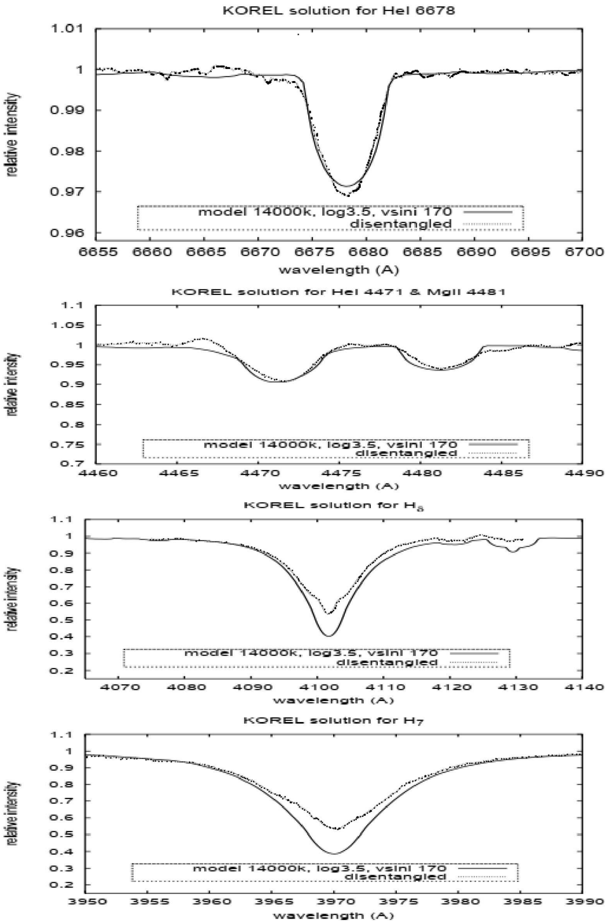

Fig. 10. Comparison of disentangled spectra of some photospheric lines (dashed line) with that of a synthetic theoretical model (solid line) for parameters $T_{\rm eff} = 14000$ K, $\log g = 3.5$, and $v \sin i = 170\,{\rm km/s}$

tected periods of rapid variations are all aliases of one physical period and that they are related to the rotation of the star.

In this respect, we derived more constrained limits of the rotational period of the primary ($0^d.95 - 1^d.91$) in comparison to ($0^d.5 - 2^d.0$) reported by Juza et al. (1991), based on the revised values of the Be star radius $6.4 \pm 0.5 R_e$ and projected rotational velocity $v \sin i = 170$ km/s (Saad et al. 2004) for different inclination angles, from 30° to 90°, and using explicitly the relation

$$P_{rot} = 50.633\ (R/R_{\odot})\ (v \sin i)^{-1} \sin i.$$

For the orbital inclination $i = 30°$, the rotational period is 0.953 ± 0.07 days. The error accounts only for the uncertainty in the determined radius. An ultra-rapid variation on a time ≈2min in the $H\alpha$ profile structure detected on 14/15 Feb. 1993 (from 36 co-added and averaged profiles) is reported by Anandarao et al. (1993). The lpv manifest themselves mainly through the line profile asymmetry, line width, and sometimes give rise to the moving (absorption or emission) sub-features.

For different regions of the spectra, our RV measurements were examined for rapid variability. We searched periodicity using the two above mentioned independent numerical period searching routines. As mentioned earlier (in § 2.3) for $H\alpha$, the periodogram for the RV measurements of the outermost parts of the line (wings), the lower panel of Figure 2 gives a higher frequency at $0.9987\,{\rm cd}^{-1}$, while the other frequency is centered at the orbital period.

After the pre-whitening process other frequencies peaks completely disappear, which supports the suggestion that this rapid variation in the RV (around one day) is not a real one, and it is probably associated with the orbital frequency. For some absorption lines (mainly for He I 6678 Å and Si II 6347Å) we searched for short period variations. After removing the orbital variation from the data (pre-whitened) of RV measurements of the mentioned two lines, the residuals were searched for short term variations. Two different short periods with lower powers are found for each set of data, $0^d.171198$ (at an amplitude 3.775 km/s) and $0^d.416805$ (at amplitude 2.9956 km/s) for HeI 6678 Å and Si II 6347 Å respectively.

The various sets of RVs available from all lines (366 points which were previously used to obtain the final solution with FOTEL), after pre-whitening for the orbital period, were searched for short term variations. The detected period of $0.^d39526$ with low power ($3.321\,{\rm km\,s}^{-1}$) may belong to the noise level.

Finally, we have used the measurements of equivalent width (EW) and line central intensity (I_c) of $H\alpha$ to search for the short term variability. We searched for a period in both data sets in the range between 0.1 - 2 d first using the program PERIOD. Figure 11 represents a periodogram of the original data, a spectral window, and a periodogram of the pre-whitened spectra. Two main frequencies (ordered by power) at: $1.00020\,{\rm cd}^{-1}$ and at $2.00343\,{\rm cd}^{-1}$ have 75% and 65% of confidence level (as shown in the spectral window), respectively. Using the PDM technique for the same data sets and the range of periods gave the highest peak at $f = 1.00020\,{\rm cd}^{-1}$, similar to that obtained using PERIOD. Pre-whitening the original spectra with an f of $1.00020\,{\rm cd}^{-1}$, removed the one at $2.00343\,{\rm cd}^{-1}$; however, an f of $2.0025\,{\rm cd}^{-1}$ at lower amplitude is still found (third panel of Figure 11).

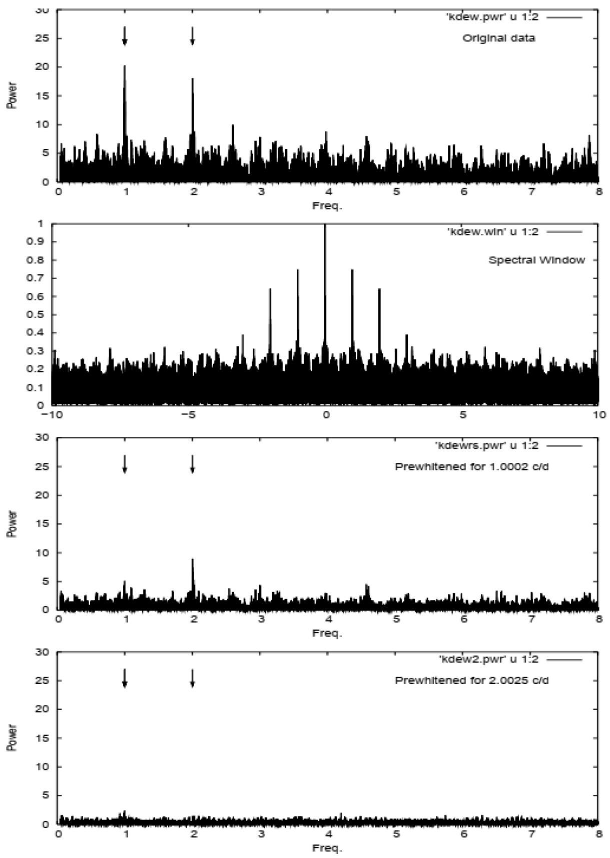

Fig. 11. Periodogram of the original data for the EW of $H\alpha$, spectral window, and the periodograms through the process of successive prewhitening for the detected short-term period..

Since the obtained frequency is around 1 day, this raises the question of whether a one-day periodicity may be caused by the cadence of the observations. To solve this problem we applied the randomizing technique suggested by Eaton et al. (1995). We created the randomizing sample for our data, then we calculated the power again for the periodicity in the same frequency range; the same results were obtained. Comparable highest peaks are found in the normalized power of the original data and those obtained from a randomized data set.

7.2. *Line Profile Variation*

The profile variations (lbv) of the He I 6678 Å absorption line were investigated by inspection of the residuals (subtraction of the individual spectra from the average one). Two sets of closely time-spaced observations of this line were obtained. Eleven spectra were obtained in the course of two successive nights, on 23/24 April 1994, between epochs 49466.3311 − 49467.5566 (≈29h) using a Reticon detector in the coudé spectrograph. Another ten spectra were obtained during a 40-min period of the night of April 24 (at JD 52754.8454 -52754.8733) using the coudé spectrograph and the CCD detector. The lower panel of Figure 12 displays the residuals of the individual spectra obtained by subtraction from the average one, and the time evolution of the corresponding profiles of individual lines, respectively. Each set of observations related to different phases of line strength (the first set obtained in 1994 corresponds to phases of higher line strength in comparison to that obtained in 2003) as was already known from the study of long-term variations of the line. The deviation from the mean profile is clear in some spectra. The upper panel of Figure 12 shows the line wings affected by the emission. The residuals of the individual spectra from the averaged one show fluctuations from one exposure to the other. However, no clear sequence of variation can be detected. No night-to-night changes similar to those found in the Be star FX Lib (as reported by Guo, 1994) were found in the $H\alpha$ line profile of κ Dra.

8. CONCLUSIONS

We reanalyzed the spectroscopic data of the bright Be star κ Dra obtained from June 1992 to April 2003. We used the generally accepted orbital parameters derived with two codes FOTEL and KOREL. A circular orbit with a period of $61\overset{\text{d}}{.}55$ and semi-amplitude of RV variations of the primary component of the binary system (K= 6.81 km s^{-1}) was suggested. Based on the FOTEL solution, the estimated values of the projected separation of the system components A = 126.9 $R_\odot$ and the mass function were derived.

V/R variations were measured for $H\alpha, H\beta, H\gamma$ and some other photospheric lines. They were found to be phase-locked with the orbital motion. Rapid variability was investigated and for different line parameters, it is related to the rotational velocity of the star. No night-to-night variations were found in the line profiles of κ Dra. The presence of an absorption bump traveling in phase with high negative RVs may be explained by some cold clumps in a distant outflowing gas. It is noted that from the KOREL disentangling of different regions of the spectra, no direct evidence of the secondary spectrum was found for Balmer and other metallic lines in both optical and near-infrared spectra.

Taking into account the spectroscopic mass of κ Dra ($M_1 = 4.8 M_\odot$) determined by Saad et al. (2004) and the results of the FOTEL solution, we

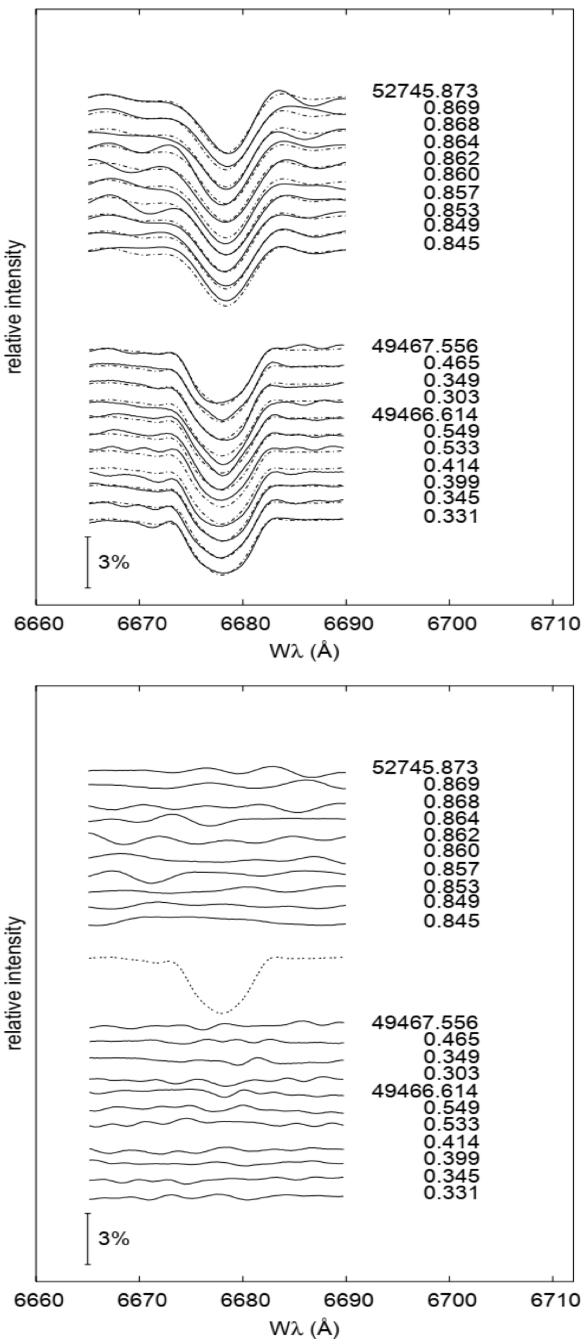

Fig. 12. *Upper panel:* Line profiles of He I 6678 Å observed on 24 April 2003 and 23/24 April 1994. Each profile is fitted with the average one (dashed lines). The number at the right hand side is the midexposure HJD. *Lower panel:* The residuals of individual spectra subtracted from the averaged one.

calculated several possible values of the secondary mass M_2 for different inclination angles. If the rotation axis of the primary and the orbital axis are parallel, then for the stellar radius $R = 6.4 R_\odot$ and rotation velocity 170 $\mathrm{km\,s^{-1}}$ (Saad et al. 2004) the minimum inclination angle $i \approx 27$. Thus if κ Dra rotates near its break-up velocity, the most appropriate inclination angle is about 30°. A corresponding mass of the secondary is then $M_2 = 0.8 M_\odot$.

The research is supported by the National Research Institute of Astronomy and Geophysics (NRIAG) and the Science and Technology Development Fund (STDF No. 5217). This paper used spectroscopic data from the archive of the Perek 2-meter Telescope and has made use of NASA's Astrophysics Data System Abstract Service. The criticism of the first version of this article by the anonymous referee and the revision of the text done by Dr. J. Kubát, greatly helped us to improve the article and the arguments, and the authors gratefully appreciate this effort. S. Saad would like to thank Prof. Dr. P. Hadrava, (the author of the KOREL and FOTEL codes) for his helpful discussions when using the codes, and to express her great thanks to the system administrators at Czech Astronomical Institute, Ondřejov.

REFERENCES

Anandarao, B. G., Chakraborty, A., Swaminathan, R., & Lokanadham, B. 1994, IAUS 162, Pulsation, Rotation and Mass Loss in Early-Type Stars, ed. L. A. Balona, H. Henrichs, & J. M. LeContel (Dordrecht: Kluwer Academic Publishers), 234

Andrillat, Y. & Fehrenbach, Ch. 1982, A&AS, 48, 93

Arsenijevic, J., Jankov, S., Krsljanin, S., et al. 1994, IAUS 162, Pulsation, Rotation and Mass Loss in Early-Type Stars, ed. L. A. Balona, H. Henrichs, & J. M. LeContel (Dordrecht: Kluwer Academic Publishers), 234

Breger, M. 1990, A&A 240, 308

Doazan, V., Grady, C. A., Snow, T. P., et al. 1985, A&A 152, 182

Eaton, N. L., Herbst, W., & Hillenbrand, L. A. 1995, AJ, 110, 1735

Guo, Y. 1994, IBVS, 4113

Hadrava, P. 1990, CoSka, 20, 23

_________. 1995, A&AS, 114, 393

_________. 1997, A&AS, 122, 581

Hanuschik, R. W., Hummel, W., Sutorius, E., Dietle, O., & Thimm, G. 1996, A&AS, 116, 309

Harmanec, P., Bozić, H., Percy, J. R., et al. 2002, A&A, 387, 580

Hill, S. N. 1926, PDAO, 3, 349

Hill, G. M., Walker, G. A. H., & Yang, S. 1991, A&A 246, 146

Hirata, R. 1995, PASJ, 47, 195

Horn, J., Kubat, J., Harmanec, P., et al. 1996, A&A, 309, 521

Huang, S. S. 1973, ApJ, 183, 541
_________. 1975, S&T, 49, 359
Hubert-Delplace, A. M. & Hubert, H. 1979, An atlas of Be Stars (Paris-Meudon: Observatory)
Hubert-Delplace, A. M., Hubert, H., Chambon, M. T., & Jaschek, M. 1982, IAUS 98, Be Stars, (Dordrecht: Reidel Publishing)
Juza, K., Harmanec, P., Hill, G. M., et al. 1991, BAICz, 42, 39
Juza, K., Harmanec, P., Bozic, H., et al. 1994, A&AS, 107, 403
Kato, S. 1983, PASJ, 35, 249
Koubský, P., Harmanec, P., Kubat, J., et al. 1997, A&A, 328, 551
Koubský, P., Harmanec, P., Hubert, A. M., et al. 2000, A&A, 356, 913
Kriz, S. & Harmanec, P. 1975, BAICz, 26, 65
Lucy, L., B. & Sweeney, M. A. 1971, AJ, 76, 544
McLaughlin, D. B. 1961, JRASC, 55, 73
Mennickent, R. E. & Vogt, N. 1991, A&A, 241, 159
Miczaika, G., R. 1950, ZA, 28, 203
Okazaki, A. T. 1991, PASJ, 43, 75
Panoglou, D., Faes, D. M., Carciofi, A. C., et al. 2018, MNRAS, 473, 3039
Poeckert R. 1981, PASP, 93, 535
Pogodin, M. A. 1997, A&A, 317, 185
Porter, J. M. & Rivinius, T. 2003, PASP, 115, 1153
Simon, K. P. & Sturm, E. 1994, A&A, 281, 286
Saad, S. M., Kubát, J., Koubský, P., et al. 2004, A&A, 419, 607
Saad, S. M., Kubát, J., Hadrava, P., et al. 2005, Ap&SS, 296, 173
Stellingwerf, R. F. 1978, ApJ, 224, 953
Struve, O. 1931, ApJ, 73, 94

M. I. Nouh, S. M. Saad, A. Shokry, and I. Zead: National Research Institute of Astronomy and Geophysics, 11421 Helwan, Cairo, Egypt (abdo_nouh@hotmail.com).
S. M. Saad, A. Shokry, and I. Zead: Kottamia Center of Scientific Excellence for Astronomy and Space Research KCScE STDF 5217.

Revista Mexicana de Astronomía y Astrofísica, **57**, 107–122 (2021)

https://doi.org/10.22201/ia.01851101p.2021.57.01.07

PERIODICITY DETECTION IN AGN WITH THE BOOSTED TREE METHOD

S. B. Soltau[1,2] and L. C. L. Botti[2,3]

Received August 3 2020; accepted October 15 2020

ABSTRACT

We apply a machine learning algorithm called XGBoost to explore the periodicity of two radio sources: PKS 1921-293 (OV 236) and PKS 2200+420 (BL Lac), both radio frequency datasets obtained from University of Michigan Radio Astronomy Observatory (UMRAO), at 4.8 GHz, 8.0 GHz, and 14.5 GHz, between 1969 to 2012. From this methods, we find that the XGBoost provides the opportunity to use a machine learning based methodology on radio datasets and to extract information with strategies quite different from those traditionally used to treat time series, as well as to obtain periodicity through the classification of recurrent events. The results were compared with other methods that examined the same datasets and exhibit a good agreement with them.

RESUMEN

Aplicamos un algoritmo de aprendizaje automático llamado XGBoost para explorar la periodicidad de dos fuentes de radio: PKS 1921-293 (OV 236) y PKS 2200+420 (BL Lac), ambos conjuntos de datos de radiofrecuencia obtenidos del Observatorio de Radio Astronomía de la Universidad de Michigan (UMRAO), a 4.8 GHz, 8.0 GHz, y 14.5 GHz, entre 1969 y 2012. A partir de estos métodos, encontramos que XGBoost brinda la oportunidad de utilizar una metodología basada en aprendizaje automático en el conjunto de datos de radio y extraer información con estrategias bastante diferentes de las utilizadas tradicionalmente para tratar series temporales y obtener periodicidad a través de la clasificación de eventos recurrentes. Los resultados se compararon con los obtenidos en otros trabajos que examinaron el mismo conjunto de datos y muestraron resultados compatibles.

Key Words: galaxies: active — galaxies: BL Lacertae objects: general — galaxies: quasars: general — methods: data analysis — methods: numerical

1. INTRODUCTION

Ever since the discovery of first radio sources (Matthews & Sandage 1963; Schmidt 1963) in 1963, a considerable amount of work and computing resources have been invested in exploring the observable Universe to detect radio sources. Quasar and *BL* Lacertae objects are supermassive rotating black holes, with jet ejection and rotation axes, which emit in radio, X-rays and gamma rays. Their radio signals are observable when the axis of their emission cone is directed along the line of sight to the instrument. Subsequently, they have also been observed throughout the electromagnetic spectrum. A review of the various observational properties of quasars and other kinds of active galaxy nuclei (AGN) can be found in Véron-Cetty & Véron (2010).

AGNs, particularly quasars, have been studied at many radio frequencies to understand the mechanisms and regimes of energies involved in the phenomenon. As a result, a unified model was elaborated in which the different denominations given to the AGN are derived from the orientation of the jets in relation to the viewing angle of the observer (Antonucci 1993; Urry & Padovani 1995; Beckmann & Shrader 2012).

The variability is the aspect of AGN that attracts the most attention. Some radio sources have pe-

[1]Federal University of Alfenas, Brazil.
[2]Center for Radio Astronomy and Astrophysics Mackenzie, São Paulo, Brazil.
[3]Brazilian National Institute for Space Research, São José dos Campos, Brazil.

riodicities measured in a scale of years, but due to the delay between the measurements made in several frequencies, it is difficult to accurately specify the periodicity. Delays make it difficult to study time series when comparing light curves at different frequencies. In addition, the data set comprises a time series of irregular sampling due to various factors influencing the acquisition of astronomical data from ground stations, such as weather conditions, system maintenance, receivers, etc. These sampling difficulties produce unequally spaced time series, which impose limitations on more conventional methods of analysis.

Multifrequency studies explore distinct aspects of compact radio sources, in particular, flux density variations, to determine periodicities in light curves (Abraham et al. 1982; Botti & Abraham 1987, 1988; Botti 1990, 1994; Aller et al. 2009; Aller & Aller 2010, 2011). Methods for determining periodicities in the radio range include Fourier Transform, Lomb-Scargle Periodogram, Wavelet Transform and Cross Entropy, among others (Cincotta et al. 1995; Tornikoski et al. 1996; Santos 2007; Soldi et al. 2008; Vitoriano & Botti 2018). A combination of methods, like decision trees, random forests and autoregressive models is usual for the specific goal of exoplanets detection in stellar light curves (Caceres et at. 2019).

Advances in artificial intelligence have provided machine learning algorithms, such as neural networks, ensemble and deep learning (LeCun et al. 2015), that aid astrophysical studies and provide computational approaches dissimilar to previous methods, including potential applications for radio source analyses (Witten et al. 2016).

Motivated by the successful performance of XGBoost (Chen & Guestrin 2016) in International Challenges on Machine Learning (Xu 2018), and animated by the many different kinds of results presented by Pashchenko et al. (2017), Smirnov & Markov (2017), Bethapudi & Desai (2018), Abay et al. (2018), van Roestel et al. (2018), Saha et al. (2018), Lam & Kipping (2018), Shu et al. (2019), Liu et al. (2019), Askar et al. (2019), Calderon & Berlind (2019), Chong & Yang (2019), Jin et al. (2019), Menou (2019), Plavin et al. (2019), Wang et al. (2019), Yi et al. (2019), Li et al. (2020), Lin et al. (2020), Hinkel et al. (2020), Tamayo et al. (2020) and Tsizh et al. (2020), we decided to test how this kind of algorithm would perform specific tasks related to the treatment of time series in radio datasets of AGNs, such as light curves of quasars and BL Lacs. For this reason we selected two well-studied objects, the PKS 1921-293 (OV 236) quasar and PKS 2200+420 (BL Lac) for a case study.

TABLE 1

IRREGULARLY SPACED TIME SERIES*

Frequency (GHz)	**PKS 2200+420**	**PKS 1921-293**
4.8	1977–2012	1979–2011
8.0	1968–2012	1974–2011
14.5	1974–2012	1975–2011

*The UMRAO datasets were acquired in frequencies of 4.8 GHz, 8.0 GHz and 14.5 GHz from radio sources PKS 1921-293 (OV 236) and PKS 2200+420 (BL Lacertae).

The outline of this paper is as follows. In § 2, the AGNs datasets from the UMRAO survey, along with the features used for training and tests, are described. In § 3, we show the machine learning algorithms applied to the AGNs datasets. The implementation of XGBoost is described in detail. We discuss the feature selection procedure methods in § 4. We report and discuss the results of machine learning algorithms for the selected tasks in § 5. We present a summary and conclusions in § 6.

2. INSTRUMENT AND DATASETS

The Michigan Radio Astronomy Observatory (UMRAO), has a parabolic reflector antenna of about 26 meters in diameter. This radio telescope has been used extensively since 1965 to monitor continuous full-flux density and linear polarization of variable extragalactic radio source in the frequencies of 4.8 GHz (6.24 cm), 8.0 GHz (3.75 cm) and 14.5 GHz (2.07 cm). More details about UMRAO characteristics and their astrophysics applications are reviewed and can be found in Aller (1992); Aller et al. (2017).

In our study, we used UMRAO datasets for PKS 1921-293 (OV 236) and PKS 2200+420 (BL Lac), in the time intervals presented in Table 1.

It is worth mentioning that these are irregularly spaced time series, so the years indicated in Table 1 refer to the range of years covered in this study. The differences in the years of radio datasets start for each frequency, for both objects of study, are due to the fact that the UMRAO began to operate in each one of the frequencies in different epochs.

For all objects in the dataset collection and at all operating frequencies, UMRAO provides daily time

TABLE 2

OBSERVATIONS IN TIME SERIES*

Frequency (GHz)	**PKS 2200+420**	**PKS 1921-293**
4.8	692	618
8.0	843	910
14.5	962	1 035

*The UMRAO datasets acquired at frequencies of 4.8 GHz, 8.0GHz and 14.5GHz from radio sources PKS 1921-293 (OV 236) and PKS 2200+420 (BL Lac).

series[4]. Due to several inherent aspects of observations, such as weather and instrumental maintenance, the data sets are irregularly spaced, requiring treatment before being used in the research. The procedures adopted during processing for this purpose will be described later, in § 4.

The Figures 9 and 10 in Appendix A, show the light curves for the objects PKS 2200+420 (BL Lac) and PKS 1921-293 (OV 236), respectively, arranged in graphs according to the same time interval, for comparison purposes.

The characteristics of the radio source PKS 2200+420 (BL Lac)[5] used in this study are galactic coordinates 92.5896 -10.4412, equatorial coordinates (J2000) RA 22h02m43, 291s DE $+42^o16'39, 98$, constellation *Lacerta*, apparent magnitude $V = 14.72$, absolute magnitude $MV = -22.4$ and redshift $z \approx 0.069$.

The characteristics of the radio source PKS 1921-293 (OV 236)[6] are equatorial coordinates (J2000) RA 19h24m51.056s DE $-29^o14'30, 11$, galactic coordinates 9.3441 -19.6068, constelation *Sagittarius*, apparent magnitude $V = 17.5$, absolute magnitude $MV = -24.6$ and redshift $z \approx 0.353$.

The UMRAO datasets are provided in digital files in the American Standard Code for Information Interchange (ASCII) coding standard and contain, listed in daily sequences, the acquisition date in modified Julian date format, the flux density and the associated measurement error, both in jansky. Table 2 shows the number of observations per frequency for each radio source addressed in this study.

[4]Publicly available in https://dept.astro.lsa.umich.edu/datasets/umrao.php with permission.

[5]Available data http://simbad.u-strasbg.fr/simbad/sim-id?Ident=NAME%20BL%20Lac.

[6]Available data http://simbad.u-strasbg.fr/simbad/sim-id?Ident=PKS%201921-293.

3. XGBOOST

XGBoost, an acronym for eXtreme Gradient Boosting, is a set of machine learning methods boosted tree based, packaged in a library designed and optimized for the creation of high performance algorithms (Chen & Guestrin 2016). Its popularity in the machine learning community has grown since its inception in 2016. This model was also the winner of High Energy Physics Meets Machine Learning Kaggle Challenge (Xu 2018). In astrophysics, XGBoost was recently used for the classification of pulsar signals from noise (Bethapudi & Desai 2018) and also to search for exoplanets extracted from the PHL-EC (Exoplanet Catalog hosted by the Planetary Habitability Laboratory)[7] using physically motivated features with the help of supervised learning (Saha et al. 2018).

Gradient boosting is a technique for building models in machine learning. The idea of boosting originated in a branch of machine learning research known as computational learning theory. There are many variants on the idea of boosting (Witten et al. 2016). The central idea of boosting came out of the question of whether a “weak learner” can be modified to become better. The first realization of boosting that saw a great success in its application was Adaptive Boosting or AdaBoost and was designed specifically for classification. The weak learners in AdaBoost are decision trees with a single split, called decision stumps for their shortness (Witten et al. 2016).

AdaBoost and related algorithms were recast in a statistical framework and became known as Gradient Boosting Machines. The statistical framework cast boosting as a numerical optimization problem, where the objective is to minimize the loss function of the model by adding weak learners using a gradient descent like procedure. The Gradient Boosting algorithm involves three elements. (i) A loss function to be optimized, such as cross entropy for classification or mean squared error for regression problems. (ii) A weak learner to make decisions, integrating a decision tree. (iii) An additive model, used to add weak learners to minimize the loss function. New weak learners are added to the model in an effort to correct the residual errors of all previous trees. The result is a powerful modeling algorithm.

XGBoost works in the same way as Gradient Boosting, but with the addition of an Adaboost-like feature of assigning weights to each sample. In ad-

[7]The latest updated (July 2, 2018) dataset can be downloaded from the PHL website: http://phl.upr.edu/projects/habitable-exoplanets-catalog/data/database.

dition to supporting all key variations of the technique, the real interest is the speed provided by the implementation, including: (i) parallelization of tree construction using all computer CPU cores during training; (ii) distributed computing for training very large models using a cluster of computers; (iii) out-of-core computing for very large datasets that do not fit into memory; (iv) cache optimization of data structures and algorithms to make best use of hardware (Mitchell & Frank 2017).

The XGBoost core engine can parallelize all members of the ensemble (tree), giving substantial speed boost and reducing computational time. On the other hand, the statistical machine-learning classification method is used for supervised learning problems, where the training data with multiple features are used to forecast a target variable, and the regularization techniques are used to control over-fitting. The XGBoost method uses a non-metric classifier, and is a fairly recent addition to the suite of machine learning algorithms (Chen & Guestrin 2016). Non-metric classifiers are applied in scenarios where there are no definitive notions of similarity between feature vectors.

Traditionally, gradient boosting implementations are slow because of the sequential nature in which each tree must be constructed and added to the model. XGBoost solves the slowness problem putting trees to work together, and creating the concept of forest. This approach improves the performance in the development of XGBoost and has resulted in one of the best modeling algorithms that can now harness the full capability of very large hardware platforms (cf. benchmark tests in (Zhang et al. 2018; Huang, Yu-Pei, Yen, Meng-Feng 2019)).

In a typical machine-learning problem, the processed input data try to combine a large number of regression trees with a small learning rate to produce a model as output. In this case, learning means recognizing complex patterns and making intelligent decisions based on input dataset features provided by the human supervisor.

The algorithm comes up with its own prediction rule, based on which a previously unobserved sample will be classified as of a certain type, e. g. high and low activity period, to give a pertinent example, with a reasonable accuracy. In order to appropriately apply a method (including preprocessing and classification), a thorough study of the nature of the data should be done; this includes understanding the number of samples in each class, the separability of the data, etc. Depending on the nature of the data, appropriate preprocessing and post processing methods should be determined along with the right kind of classifier for the task (e.g. binary classification or multiclass classification, LeCun et al. 2015).

XGBoost has only two distinct machine learning capabilities: regression and classification trees. All tasks and problems to be solved need be reduced to these two categories. Regression trees are used for continuous dependent variables. Classification trees for categorical dependent variables. In regression trees, the value obtained by the terminal nodes in the training data is the mean response of the observation falling in that region. In classification trees, the value obtained by the terminal node in the training data is the mode of observations falling in that region. In this research, the developed method uses both of capabilities, as will be shown in § 4.

XGBoost is readily available as a Python API (Application Program Interface), which is used in this work.[8]

To the best of our knowledge, XGBoost algorithms have never been used before in AGN research for regularization of time series or during the post-processing of outbursts selection candidates.

4. METHOD

We prepare the machine to learn the features associated with the training and test data to fill irregularly spaced time series and to identify the occurrence of outbursts in radio sources datasets from UMRAO through the machine classification algorithm XGBoost. The goal, as stated earlier, is to test the ability of the algorithm to be used in astrophysics studies of AGN-like radio sources with a reasonably high accuracy, thereby establishing the utility of this method where different approaches are useless. The classification of outbursts was done with classification tree, whilst the regularization of time series was done with regression tree.

The entire method can be summarized in the following steps: (i) obtaining and preparing the data (preprocessing); (ii) regularizing the time series; (iii) detection of outbursts; and, (iv) calculation of periodicity within defined limits of accuracy. Here we will highlight the regularization of time series and the detection of outbursts, mainly.

4.1. *Preprocessing*

Preprocessing is an essential preliminary step in any machine learning technique, as the quality and effectiveness of the following steps depend on it (Brighton

[8] The source code was available at https://github.com/sbs-PhD/astroph.

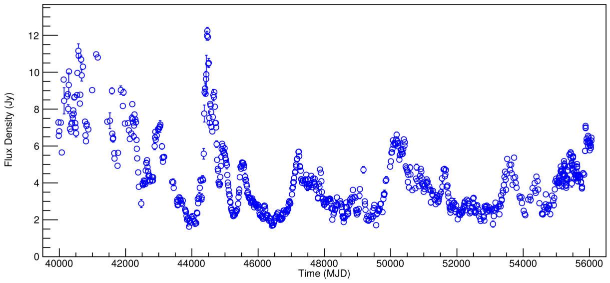

Fig. 1. Light curve of PKS 2200+420 radio source, at 8.0 GHz. The raw dataset is shown. The color figure can be viewed online.

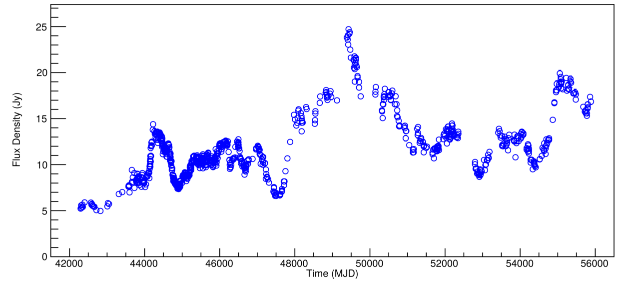

Fig. 2. Light curve of PKS 1921-293 radio source at 8.0 GHz The raw dataset is shown. The color figure can be viewed online.

& Mellish 2002). This covers from obtaining the original UMRAO files, in ASCII digital format, to preparing the data with the application of algorithms whose purpose is to check data consistency, eliminate incomplete lines or other inconsistencies typical of experimental datasets stored in formatted files such as spurious characters, formatting, etc. All the procedures applied in this phase act directly and only on the original data, but without altering them in their fundamental characteristics. The procedure also has the purpose of removing the beginning or end of the data in the case of a big time lag to the next data, reducing the error propagation and the computational time.

The original data files of the UMRAO contain all three frequencies acquired, 4.8 GHz, 8.0 GHz and 14.5 GHz unsorted in the file lines. Each line corresponds to a daily measurement in a given frequency. During preprocessing, rows of the same frequency were collected and stored together in a separate file. In this way, each frequency can be treated independently for each object studied.

At the end of this step, the graphs of the original daily flux density data were plotted. For simplicity, only the 8.0 GHz data are shown in Figure 1 for the PKS 2200+420 (BL Lac) radio source. All other frequencies, 4.8 GHz and 14.5 GHz are shown in Figures 11 and 12, Appendix B.

Likewise, the same preprocessing step give the result shown in Figure 2 for the PKS 1921-293 (OV 236) radio source. In this way, it was possible to visualize the segments of light curves that had most discontinuities. As before, Figures 13 and 14 for frequencies 4.8 GHz and 14.5 GHz are shown in Appendix B.

Notice that the time intervals for each radio source shown in Table 1 and in Figures 9 in Appendix A, differ from those shown in Figure 1 and Figures 11 and 12. Also, the curves in Figure 10 in Appendix A, differ from those show in Figure 2 and Figures 13 and 14. Such discrepancy is due to the head and tail elimination of the dataset effected during the preprocessing procedure.

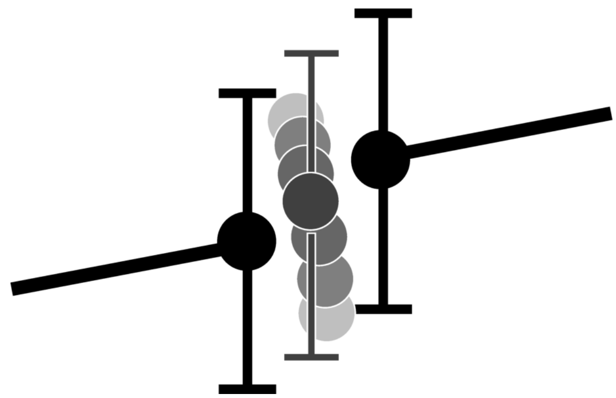

Fig. 3. Schematic representation of how the algorithm using XGBoost finds a missing point to fill and complete the irregularly spaced time series. The error bars can limit the search space.

4.2. *Regularizing Time Series*

The UMRAO datasets containing the individual frequencies have several time gaps configuring an irregularly spaced time series. In this method step, XGBoost was used to fill the intervals by applying machine learning regression techniques, rather than conventional techniques or methods of usual statistic adjusting. The strategy employed with XGBoost is shown in Figure 3.

In Figure 3, the black point represents the best point found, i.e., flux density value, to fill the series at that missing point. Gradually darker gray points represent the successive efforts does by the new weak learners added to the model to correct the residual errors of all previous trees to choose the point to be

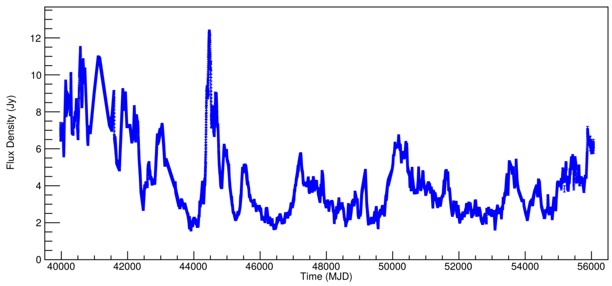

Fig. 4. Light curve of PKS 2200+420 (BL Lac) at 8.0 GHz. The regularized space-time series is shown. The color figure can be viewed online.

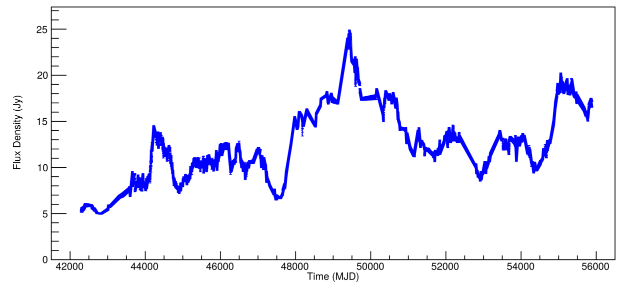

Fig. 5. Light curve of PKS 1921-293 (OV 236) at 8.0 GHz. The regularized space-time series is shown. The color figure can be viewed online.

tested in the scenario. In this schematic representation, the darker the point, the greater its assigned weight to minimize the loss function.

The term "regression" here refers to the logistic regression or soft-max for the classification task. XGBoost uses a set of decision trees as described the working principle detailed in § 3.

In the interval defined by each error value, ϵ_o, features were prepared using weighted moving averages, recursively, that is, mean of average, etc., providing the XGBoost training phase over several intervals of time below, ε_{o-n}, and above, ε_{o+n}, the point considered. Since

$$\varepsilon_{o-n}, \ldots, \varepsilon_{o-2}, \varepsilon_{o-1}, \varepsilon_o, \varepsilon_{o+1}, \varepsilon_{o+2}, \ldots, \varepsilon_{o+n}\,, \quad (1)$$

the algorithm search for the best value that can be set at the missing point ε_o.

The method of classification was to select known points, hide them from the algorithm as the training set and use the remaining samples in the dataset as the test set (subject to artificial balancing by undersampling the known flux density values). The points chosen by the algorithm fully match the previously hidden points for the same position in the time series. By this process, applied for all UMRAO radio sources datasets, the irregularly spaced time series, becomes a regularly spaced one.

Figure 4 shows the time series regularized for PKS 2200+420 (BL Lac) at 8.0 GHz frequency, by the process described. Appendix C contains Figures 15 and 16 for the frequencies 4.8 GHz and 14.5 GHz.

Likewise, Figure 5 shows the regularized time series for the PKS 1921-293 (OV 236) radio source. The frequencies 4.8 GHz and 14.5 GHz are shown in Figures 17 and 18 in Appendix C.

The accuracy of the regularization of the time series procedure was tested in three steps as follows. In the first step, approximately one quarter of points, constituted of flux density versus time from the original raw dataset of each frequency, are randomly chosen and put separately in different datasets for the next step. The files that contain one quarter of the points randomly extracted from the raw dataset are reserved for future comparisons. Three quarters of the raw data are put in another file to be processed by the algorithm of regularization of time series, generating another file with the regularized time series.

The file with one quarter of the randomly selected points in the first step and the file with the regularized time series generated in the second step are compared. The agreement between the separate and the new points produced by the regularization algorithm is checked through the Kolmogorov-Smirnov test (K-S Test) (Marsaglia et al. 2003; Bakoyannis 2020; Sadhanala et al. 2019; del Barrio et al. 2020).

After dataset regularization by the strategy implemented using XGBoost, any well-established statistical autoregressive model could be conveniently applied to the time series. However, we wanted to experiment and extend the use of XGBoost as much as possible and to investigate the possibilities of using machine learning also as a tool for time series regularization.

4.3. *Finding Outbursts in Light Curves*

In this method, XGBoost was used to classify light curve segments as probably representative of an outburst. Therefore, it is a binary classification. First, a data segment of the light curve containing a known outburst was used during the training session. Second, in the test session, the light curve of each frequency dataset was modified by the synthetic minority over-sampling technique, SMOTE (Chawla et al. 2002; Bethapudi & Desai 2018; Hosenie et al. 2020), producing a new artificial dataset, basically by introduction of noise.

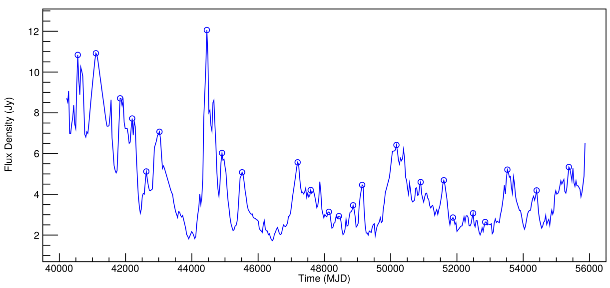

Fig. 6. Light curve of PKS 2200+420 (BL Lac) at 8.0 GHz, showing the detected outbursts to periodicities found. The color figure can be viewed online.

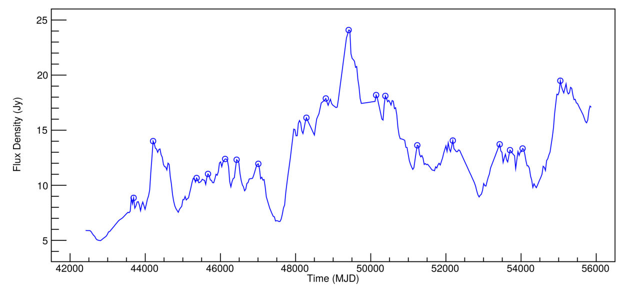

Fig. 7. Light curve of PKS 1921-293 (OV 236) at 8.0 GHz, showing the detected outbursts to periodicities found. The color figure can be viewed online.

By generating a known amount of the simulated noise signal and hiding it among a dataset as if being background noise, one can test if the analysis works, showing that the physics signal of the radio source is indeed detectable among the many unknown effects. It is is possible also to take note of how many false positives and negatives are introduced in each filtering step and to use those data to (a) optimize the XGBoost features and (b) evaluate the systematic uncertainly of the analysis.

The XGBoost algorithm detected peaks in the light curves at all frequencies during the training and testing processes, using the series artificially created by SMOTE. This procedure assigns a high degree of confidence to the algorithm, since it was able to identify the same peaks in the artificial and in the original light curve.

The method steps can be described as follows:

1. In the training and testing processes, the light curve of each frequency is already regularized by the previous step (§ 4.2). The peak of largest value was taken, assuming that it characterizes an outburst.

2. Preparation steps follow, including selecting samples samples covering a range of flux density with several time intervals, in days, before and after the occurrence of the largest peak in each light curve.

3. In the testing process, the algorithm is applied for outburst detection on the synthetic datasets created with SMOTE.

4. Finally, the algorithm is applied on real data sets, looking for segments of the light curve at each frequency containing, or not, an outburst; this is a binary classification.

At the end of this step, the outburst candidates detected by the algorithm for PKS 2200+420 (BL Lac) at 8.0 GHz were plotted as a graph, shown in Figure 6. All other frequencies for this object are shown in Figures 19 and 20, Appendix D. Also shown are graphs for PKS 1921-293 (OV 236) in Figure 7 and Figures 21 and 22, Appendix D.

4.4. *Periodicity*

The calculation to determine the periodicity takes the combination of the differences of time among all the outburst candidates identified in the classification by the XGBoost algorithm in the previous step (§ 4.3). The goal was to determine all possible combinations between the occurrences of outbursts by collecting the corresponding time intervals.

Each outburst candidate corresponds to an ordered pair of flux density with an occurrence date. The difference between all possible occurrence date combinations of all outburst candidates provides a set of time intervals, which may contain the periodicity of the phenomenon within the appropriate boundary conditions. This boundary conditions were proposed by Rasheed et al. (2011).

At this point, it is necessary to define what we considered 'periodicity' within the scope of this research.

Rasheed et al. (2011) distinguish between seven different definitions of periodicity. The one that interests in our context is the Periodicity with Time Tolerance. This postulates that, given a time series T which is not necessarily noise-free, a pattern X is periodic in an interval $[\mathrm{startPos}, endPos]$ of T with period p and time tolerance $tt \geq 0$, if X is found at positions

$$\mathrm{startPos}{+}p{\pm}tt, \mathrm{startPos}{+}2p{\pm}tt, \ldots, endPos{+}p{\pm}tt\,. \quad (2)$$

Because it is not always possible to achieve perfect periodicity we need to specify the confidence in the reported result. Rasheed et al. (2011) define the periodicity confidence, as follows.

The confidence of a periodic pattern X occurring in time series T is the ratio of its actual periodicity to its expected perfect periodicity.

Formally, the confidence of pattern X with periodicity p starting at position startPos is defined as:

$$\texttt{conf}\,(p, \mathrm{startPos}, X) = \frac{P_{\texttt{Actual}}\,(p, \mathrm{startPos}, X)}{P_{\mathrm{Perfect}}\,(p, \mathrm{startPos}, X)}, \tag{3}$$

where the perfect periodicity is,

$$P_{\mathrm{Perfect}}\,(p, \mathrm{startPos}, X) = \left[\frac{|T| - \mathrm{starPos} + 1}{p}\right], \tag{4}$$

and the actual periodicity $P_{\texttt{Actual}}$ is calculated by counting the number of occurrences of X in T, starting at startPos and repeatedly jumping by p positions.

Thus, for example, in $T = abbcaabcdbaccdbabbca$, the pattern ab is periodic with startPos $= 0$, $p = 5$, and $\texttt{conf}(5, 0, ab) = 3/4$. Note that the confidence is $4/4 = 1$ when perfect periodicity is achieved.

The correspondence between the time series, T, and the chain of binary digits, in which the '1's mark the position of the periodic pattern X occurrence in the series, helps to clarify the definition.

```
abbcaabcdba ccdbabbca
10000100000000010000
```

Applying the confidence definition (equation 3) in Periodicity with Time Tolerance like $T = abce\ dabc\ cabc\ aabc\ babc\ c$, the frequency is $\texttt{freq}(ab, 4, 0, 18, tt = 1) = 5$ and the confidence is $\texttt{conf}(ab, 4, 0, 18, tt = 1) = 5/5 = 1$ (Rasheed et al. 2011).

The concepts as defined here were used to compute and validate the periodicities found in the datasets, T, of the radio sources examined.

The outbursts represent the periodic pattern, X. The time tolerance, tt, assumed was that of the arithmetic mean difference in days between the arrival times, to the observer, of the main outbursts at each frequency (equation 5).

$$tt = \frac{\Delta t_{|f1-f2|} + \Delta t_{|f1-f3|} + \Delta t_{|f2-f3|}}{3}. \tag{5}$$

This way of stipulating the time tolerance tt is based on the *ansatz* that any real comparison or correlation between two or more radio sources frequencies examined must take into account the temporal separation between the incoming of the characteristic peaks of the outbursts to the observer point of view.

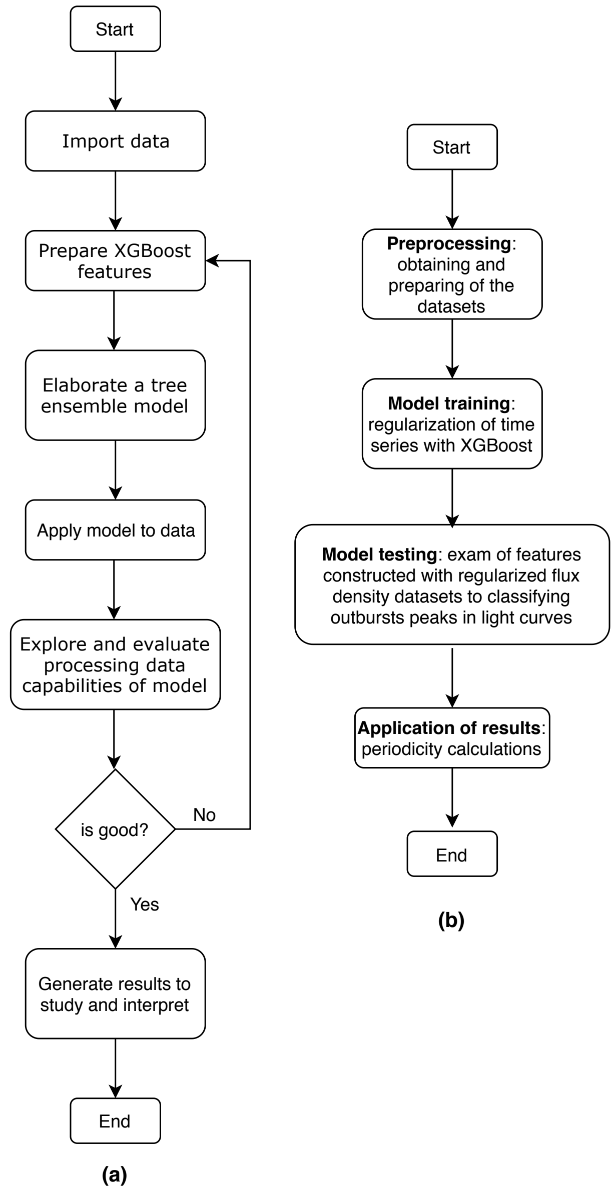

Fig. 8. In **(a)** the typical algorithm of machine learning to which, whatever the purpose, any task ends up being reduced. In **(b)** Sequences of the general method employed. Each box in diagram **(b)** may have one or more steps as described in **(a)**.

This way of stipulating tt is as expressed in equation (2) to a temporal interval.

Figure 8 shows a synthesis diagram of the steps of the applied method, emphasizing how the aspects inherent to the use of the XGBoost and those referring to the data and to the phenomenon studied were contemplated in the design of the method.

As in the case of the methodological option assumed in the regularization of time series in § 4.2,

TABLE 3

RESULT OF THE K-S TEST APPLIED ON TWO SAMPLES*

	PKS 2200+420 (BL Lac)		PKS 1921-293 (OV 236)	
Frequency (GHz)	statistic	p value	statistic	p value
4.8	0.03571429	0.99989572	0.03246753	0.99999660
8.0	0.03349282	0.99974697	0.03097345	0.99988705
14.5	0.03361345	0.99913286	0.02734375	0.99997300

*One with the raw empirical data of flux density and another calculated, for the same point, with the algorithm of regularization based on tree boosting.

here, too, we have chosen to explore the limits of possibilities, without making use of traditional methods of calculating periodicity. For this reason, we have adopted the postulates proposed by Rasheed et al. (2011) to compute and validate the periodicities.

5. RESULTS AND DISCUSSION

The initial methodological step, presented in § 4.1, eliminated flux density data temporally very far from each other only in the head and tail of the datasets. This process was necessary to reduce computational time of the next steps; otherwise, the time series regularization would be harder for the algorithm. As result, the time series was shortened by a few days in the head and tail. This did not bring perceptible losses to the accuracy of the method since the time series datasets were very extensive. At the head of the time series, the dates eliminated were in November of one year and in February of the following year. In the tail of the time series, the days of the following year were eliminated. Eliminating these days from the heads and tails of the time series allowed us to balance the computational time/accuracy ratio.

After refining and tuning the datasets as described above, separating frequencies into distinct files to prepare the XGBoost features was the next process.

The strategy used in the next step of the method is to have the XGBoost-based algorithm consider past and future events of flux density, to weigh and predict which flux density value within the same frequency examined is most suitable to be placed at a point missing between the past and future points of the time series.

The features delivered to XGBoost for processing in this step were prepared as a "sliding window" that traverses the points that make up the light curves of each frequency one by one, and repeating the process with each increment.

Some known points (originally existing in the time series) were hidden and the algorithm was asked to compute its value without knowing it previously as described before. The results for the p values can vary slightly due to the fact that the selected random points change with each execution of the algorithm which calculates the K-S test. Even so, the p values variation does not deviate from aproximately 99% as summarized in Table 3.

The empirical data versus values calculated by the time series regularization algorithm have a very high statistical adherence of about 0.99. Thus, the K-S Test rejects the the null hypothesis that the samples are drawn from the same distribution in the two-sample case. This means that there is no evidence to say that the set of values does not adhere, so it is understood that the calculated values come from the same probability distribution, since the correlation is high in all cases. In other words, the probability of these two samples not coming from same distribution is very low. But, statistically speaking, one cannot be 100% sure.

For this reason the method of regularization based on tree boosting is used instead of conventional techniques. This process offers more convincing results than the use of more conventional techniques such as spline, that smooth too much the curves from experimental data.

The curves shown in Figure 4 (§ 4.2) and Figures 15 and 16 (Appendix C) of PKS 2200+420 (BL Lac) and Figure 5 and Figures 17 and 18 of PKS 1921-293 (OV 236), are actually plots of daily points, merging previously obtained points from UMRAO and points forecast by the XGBoost algorithm. This is not a line in fact. The tessellated aspect results from the fact that some values of the flux density (real or forecast) are much higher or lower than their predecessors or successors.

TABLE 4

HYPER PARAMETERS OF XGBOOST MODELS*

Number of estimators	1000
Learning rate	0.001
Maximum depth	4
Regularization alpha	0.01
Gamma	0.1
Sub sample	0.8

*Used for the method applied for time series regularization discussed here.

Table 4 summarizes the hyper parameters values with which XGBoost was configured in this step of the method.

XGBoost Python API[9] provides a method to assess the incremental performance by the number of trees. It uses arguments to train, test and to measure errors on these evaluation sets. This allows us to adjust the model performance until best results in terms computational time/accuracy ratio are reached.

In Table 4, as in Table 5, the XGBoost hyper parameters are (Aarshay 2016):

Number of estimators : sets the number of trees in the model to be generated.

Learning rate : affects the computation time performance which decreases incrementally the learning rate, while increasing the number of trees.

Maximum depth : represents the depth of each tree, which is the maximum number of different features used in each tree.

Regularization alpha : is the linear booster term on weight; it controls the complexity of the model which prevents overfitting,

Gamma : specifies the minimum loss reduction required to make a node splitting in the tree. This occurs only when the resulting split gives a positive reduction in the loss function.

Sub sample : is the percentage of rows obtained to build each tree. Decreasing it, reduces performance.

[9]All information needed to properly install and use XGBoost Python API is available at: https://xgboost.readthedocs.io/en/latest/python/python_intro.html.

TABLE 5

HYPER PARAMETERS OF XGBOOST MODELS*

Number of estimators	200
Learning rate	0.001
Maximum depth	10
Regularization alpha	0.0001
Gamma	0.1
Sub sample	0.6

*Used for the method for outburst detection. We used the same set of hyper parameters for both the non-SMOTE and SMOTE datasets.

Good performance of XGBoost-based algorithms depends on the ability to adjust the hyper parameters of the model. It took time of processing in the training and testing processes, after preparing the models features, to achieve the results shown in Figure 4 and Figures 15 and 16 for the PKS 2200+420 (BL Lac) datasets, Figure 5 and Figures 17 and 18 for the PKS 1921-293 (OV 236) datasets.

The XGBoost-based algorithms exhibited a potential ability for detection of outbursts in the light curves of radio sources. Even when the datasets were disturbed with artificial noise introduced by SMOTE, the XGBoost algorithm retained the ability to identify outbursts, matching previous findings in all frequencies, without noise. The robustness of the method and the solid boosted tree implementation behind the algorithms are validated by the proximity of the scores computed for different datasets of both radio sources.

Figure 6 and Figures 19 and 20 of PKS 2200+420 (BL Lac) and Figure 7 and Figures 21 and 22 of PKS 1921-293 (OV 236), show the peaks identified by the XGBoost-based algorithm, according to the methodological strategy described in § 4.4.

Table 5 summarizes the hyper parameter values with which XGBoost was configured. The hyper parameters were the same in both SMOTE simulated and non-simulated, with acquired UMRAO data. This strategy was inspired by Bethapudi & Desai (2018).

As in the previous methodological step, at this stage also it was essential to adjust the hyper parameters to obtain the results discussed here.

The use of previously adjusted datasets contributed to gain precision in the accuracity of detection of the outbursts, since it enlarged the sample space and the temporal resolution.

XGBoost, as well as other implementations of tree optimization algorithms, is a good choice for

TABLE 6

PERIODICITY OBTAINED FOR
PKS 2200+420 (BL LAC)*

Frequency (GHz)	**Time interval**	**Periodicity (year)**
4.8	1978–2011	1.7, 3.4, 5.7
8.0	1969–2011	1.7, 3.8, 5.2
14.5	1975–2011	1.7, 2.9, 4.7

*After computational procedure to classify flux density segments as potential outbursts. Values with a precision of 88.95%.

both classification and prediction. But decision tree ensemble models are not directly applicable for variability or periodicity studies. A smart strategy was required to be able to extract periodicity from the light curves using tree boosting.

In fact, the XGBoost contribution to the periodicity calculation ended with the identification of outburst candidates from the light curves. Thereafter, the method is reduced to calculate differences, subtracting all pairs of peaks found from each other, and verifying if the values found fall within a time tolerance.

The algorithm based on XGBoost was subjected to two tests. In the first, artificial datasets SMOTE were used to verify if the algorithm would find the candidate peaks of outburst, despite the introduced random combination of artificial noises by the SMOTE technique. In the second, the light curves were inverted in such a way that the first point of the curve became the last and vice versa. After retraining the algorithm, all points were identified in both cases.

Finally. after the training and test procedures, the algorithm was applied to the UMRAO datasets of both object, obtaining good results.

The results were compared with those of previous works obtained using the same datasets, but with different statistical methods. In addition to the difference in method and size of the time series (which were smaller than the time series used in this work, since they were from years ago, when the datasets used here were not available) a characteristic of the works consulted is that they employed conventional ways to treat irregular time series.

The results for PKS 2200+420, shown in Table 6, are compared with the results found in several works, collected in Table 7 for the methods: Discrete Fourier Transform, Discrete AutoCorrelation Function (DFT/ACF) Villata et al. (2004), Simultaneous Threshold Interaction Modeling Algorithm (STIMA) Ciaramella et al. (2004), Power Spectral Analysis Method (PSA) Yuan (2011), Date-Compensated Discrete Fourier Transform (DCDFT) Fan et al. (2007) and Continuous Wavelet Transform, Cross-Wavelet Transform (WT) Kelly et al. (2003).

The results for PKS 1921-293, shown in Table 8, are compared with the results found in the Gastaldi (2016) work, collected in Table 9, unlike the various works collected to compare with the result of PKS 2200+420 (BL Lac). Gastaldi (2016) made a full review in his PhD thesis about other methods to find periodicities to compare with his own method to calculate periodicities in PKS 1921-293.

When comparing the results of Table 6 with Table 7 and of Table 8 with Table 9, it is noted that they are similar. It is recommended to keep in mind that the time series intervals are different and smaller than those used in this paper. In spite of this, and of the methods used in the manner in which the data are processed, it is seen that the periods are similar, in particular those of the frequency 14.5 GHz of the PKS 2200+420 radio source.

These results can only be considered compatible if a time tolerance limit is assumed, estimated through the arrival delay of the maximum peaks of the several frequencies at the observer. The value of this delay for PKS 1921-293, is, on average, approximately 42 days, and circa 21 days for PKS 2200+420.

6. SUMMARY AND CONCLUSIONS

In order to implement, test and improve a method that incorporates the tree boosting-based machine learning algorithm (XGBoost) for the analysis and study of characteristics of radio sources, and to figure out the potential capabilities that this specific tool has for astrophysics purposes, two typical datasets of radio sources are explored in the form of time series. The objects chosen were PKS 1921-293 (OV 236) and PKS 2200+420 (BL-Lac), because they were the most studied in the radio range and for which several attempts to discover the periodicity were performed by different methods. The datasets from University of Michigan Radio Astronomy Observatory (UMRAO), which operates at frequencies of 4.8 GHz, 8.0 GHz and 14.5 GHz were chosen.

A boost-based algorithm was tested. The method consists of using XGBoost in two different steps. In the first this machine learning library was exploited in its potential to act as a regression tool and thus to regularize non-spaced temporal series, making them regular. In the second, the potential of XGBoost

TABLE 7

COMPARISON OF THE PERIODICITY OBTAINED FOR PKS 2200+420 WITH PERIODICITIES ESTIMATED BY DIFFERENT METHODS

Time interval	**Method**	4.8 GHz	8.0GHz	14.5GHz
1968–2003	DFT/ACF	1.4 yr	3.7 yr	7.5; 1.6; 0.7 yr
1977–2003	STIMA	7.8 yr	6.3 yr	7.8 yr
1968–1999	PSA	5.4; 9.6; 2.1 yr	4.9; 9.6; 2.8 yr	2.4; 4.3.14.1 yr
1977–2005	DCDFT	3.9; 7.8 yr	3.8; 6.8 yr	3.9; 7.8 yr
1984–2003	WT	1.4 yr	3.7 yr	3.5; 1.6; 0.7 yr

TABLE 8

PERIODICITY OBTAINED FOR PKS 1921-293 (OV 236)*

Frequency (GHz)	**Time interval** **Time interval**	**Periodicity** **(year)**
4.8	1980–2011	1.2, 3.6, 5.0
8.0	1975–2011	1.3, 2.8, 5.2
14.5	1976–2011	1.6, 3.2, 6.3

*After computational procedure to classify flux density segments as potential outburst. Values with a precision of 89.83%.

TABLE 9

PERIODICITY OBTAINED FOR PKS 1921-293 (OV 236) AND PERIODICITIES ESTIMATED BY THE LOMB PERIODOGRAM AND WAVELET METHODS

Frequency) (GHz)	**Time interval**	**Method**	**Periodicity** **(year)**
4.8	1980–2006	Lomb	1.8, 3.3, 9.5
		Wavelet	1.2–1.9, 2.7–2.8, 5.2–5.3
8.0	1981–2006	Lomb	1.3, 2.8, 3.0, 5.0, 8.5u
		Wavelet	1.2–1.4, 2.3–2.6, 3.2, 4.3–5.1
14.5	1982–2006	Lomb	1.3, 2.5, 4.3, 6.5
		Wavelet	1.3–2.3, 3.6, 5.0–5.5

as a classification tool was emphasized to select regions in the light curves that mark outbursts. In both cases the researcher expertise is an indispensable component of the success of the methodological process.

XGBoost shows precise probabilistic results, as long as the researcher has a good understanding of the problem and clearly specifies the characteristics of the phenomenon to be studied through well-defined boundary conditions and a validity and tolerance interval of well-established values in the features.

The success or failure of using XGBoost-based algorithms depends on the researcher's skills to adjust the hyperparameters of the model. It should be noted that XGBoost cannot be used by itself for periodicity detection or calculation, such as some statistical methods or other Fourier derivative methods. The method uses the strategy of classifying outbursts in the light curve, a task viable for XGBoost, and later calculating the temporal difference between the candidates to an outburst identified by XGBoost, using a confidence interval that establishes the precision and thus, in spite of discrepancies falling within the interval, finding periodic values.

The results found were quite close to those found by other, more orthodox, methods. They have the advantage of low computational time, and the potential to be applied to big datasets.

In this first approximation of XGBoost to astrophysics through the study of radio sources, the great potential of this algorithm, and of machine learning in general, was perceived. The present results, by themselves, justify investigating other potential uses for this tool.

Future perspectives involve the extension of the study for other energy ranges, such as X-rays and gamma rays, and the exploration of the use of methods based on tree boosting and other machine learning techniques that allow for application in multifrequency analysis .

It is also expected to associate the tree boosting with XGBoost with the Monte Carlo technique to evaluate how well the available models are able to describe energy regimes, variability, and other aspects of radio sources.

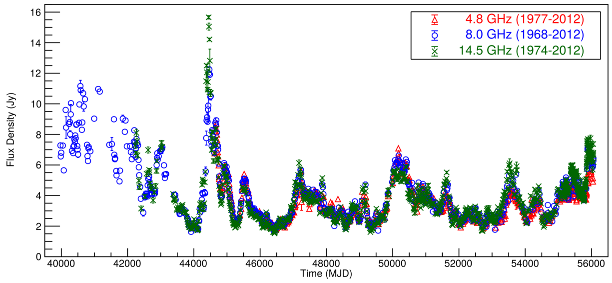

Fig. 9. Raw dataset of PKS 2200+420 (BL Lac), made available by UMRAO, before adjustments. Note that several point segments in the time series are missing at all available frequencies. The color figure can be viewed online.

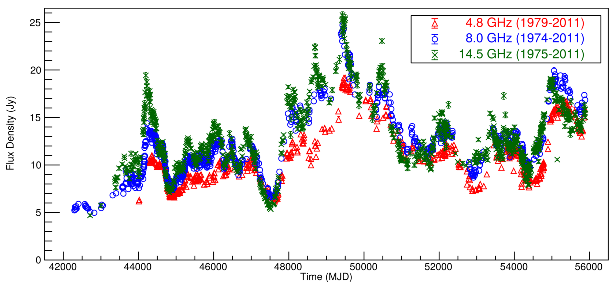

Fig. 10. Raw dataset of PKS 1921-293 (OV 236), made available by UMRAO, before adjustments. Note that several point segments in the time series are missing at all available frequencies. The color figure can be viewed online.

We are grateful for financial support from Mackenzie Presbyterian University. This research has made use of data from the University of Michigan Radio Astronomy Observatory which has been supported by the University of Michigan and by a series of grants from the National Science Foundation, most recently AST-0607523. Special thanks to Margo F. Aller and Hugh D. Aller for the datasets that made possible this work.

APPENDICES

This appendices contain supplementary material which is an important part of the research itself, and therefore may be useful in providing a more comprehensive understanding of the work, but is too cumbersome to include in the body of the paper.

A. RAW DATASET OF OBJECTS PKS 2200+420 AND PKS 1921-293

Figures 9 and 10 show the datasets of the two objects, PKS 2200+420 (BL Lac) and PKS 1921-293 (OV 236) respectively, as made available by UMRAO before adjustments of preprocessing. For clarity, the original colors used by UMRAO were maintained in this Appendix, as in the whole paper, according to the frequencies: red for 4.8 GHz, blue for 8.0 GHz and green for 14.5 GHz.

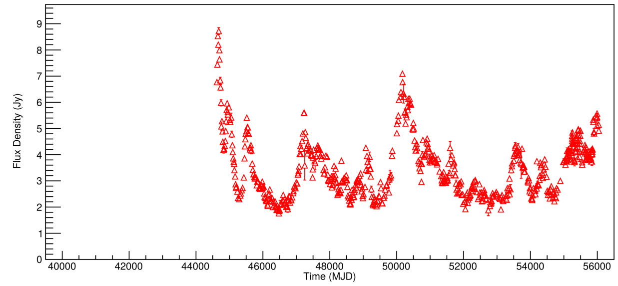

Fig. 11. Light curve of PKS 2200+420 at 4.8 GHz. The raw dataset is shown. The color figure can be viewed online.

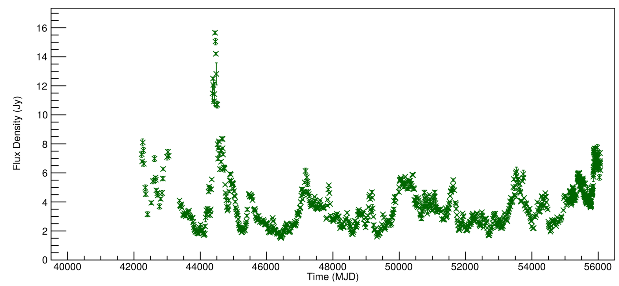

Fig. 12. Light curve of PKS 2200+420 at 14.5 GHz. The raw dataset is shown. The color figure can be viewed online.

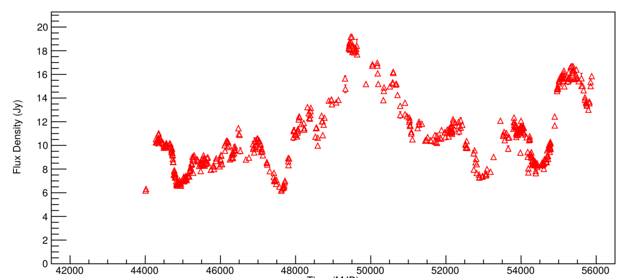

Fig. 13. Light curve of PKS 1921-293 at 4.8 GHz. The raw dataset is shown. The color figure can be viewed online.

B. RAW DATASET OF OBJECTS PKS 2200+420 AND PKS 1921-293 AFTER PREPROCESSING

Figures 11 and 12 show the light curves of PKS 2200+420 at 4.8 GHz and 14.5 GHz separately, after preprocessing.

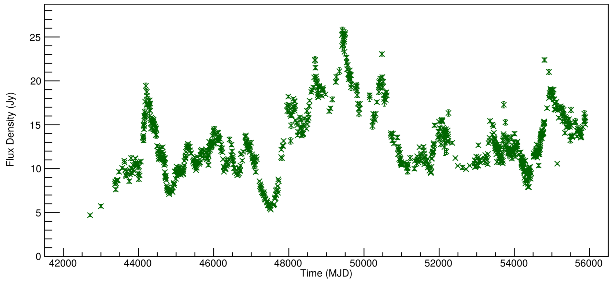

Fig. 14. Light curve of PKS 1921-293 at 14.5 GHz. The raw dataset is shown. The color figure can be viewed online.

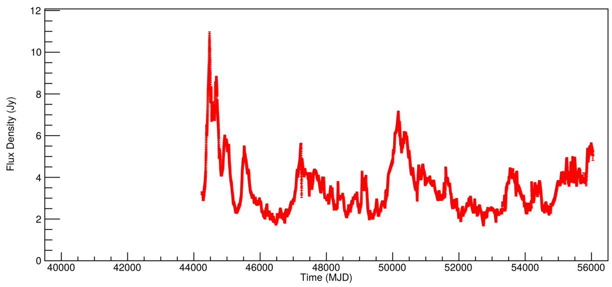

Fig. 15. Light curve of PKS 2200+420 (BL Lac) at 4.8 GHz. The regularized space-time series is shown. The color figure can be viewed online.

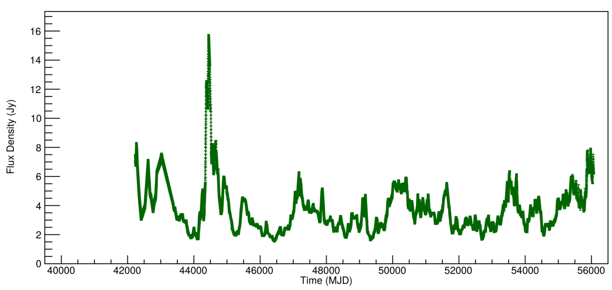

Fig. 16. Light curve of PKS 2200+420 (BL Lac) at 14.5 GHz. The regularized space-time series is shown. The color figure can be viewed online.

Figures 13 and 14 show the light curve of PKS 1921-293 at 4.8 GHz and 14.5 GHz separately after preprocessing.

C. TIME SERIES REGULARIZED FOR OBJECTS PKS 2200+420 AND PKS 1921-293

Figures 15 and 16 show the light curves of PKS 2200+420 at 4.8 GHz and 14.5 GHz, after regularization of the time series step.

Figures 17 and 18 show the light curves of PKS 1921-293 at 4.8 GHz and 14.5 GHz after regularization of the time series step.

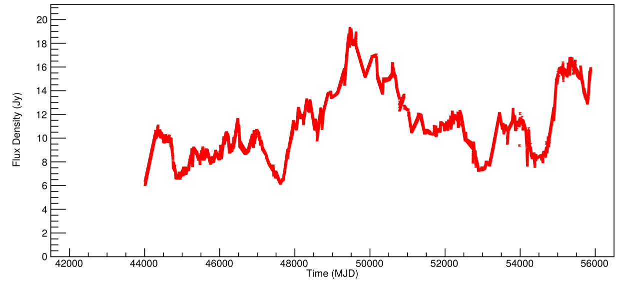

Fig. 17. Light curve of PKS 1921-293 (OV 236) at 4.8 GHz. The regularized space-time series is shown. The color figure can be viewed online.

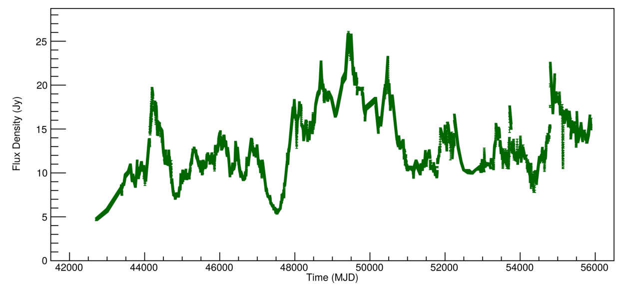

Fig. 18. Light curve of PKS 1921-293 (OV 236) at 14.5 GHz. The regularized space-time series is shown. The color figure can be viewed online.

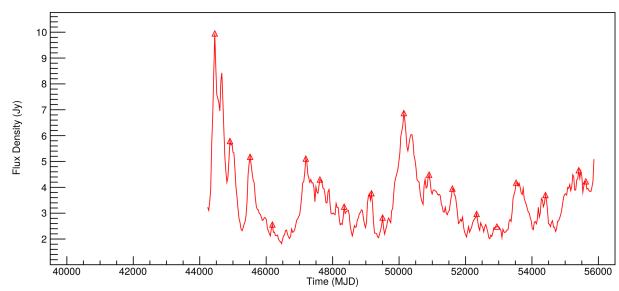

Fig. 19. Light curve of PKS 2200+420 (BL Lac) at 4.8 GHz. The detected outbursts to the periodicities found are shown. The color figure can be viewed online.

D. FINDING OUTBURSTS IN THE LIGHT CURVES OF PKS 2200+420 AND PKS 1921-293

At the end of the process of looking for explosions, the outburst candidates detected by the algorithm for PKS 2200+420 (BL Lac) at frequencies 4.8 GHz and 14.5 GHz, were plotted in a graph, as shown in Figures 19 and 20.

The same procedure was done for PKS 1921-293 (OV 236) at frequencies 4.8 GHz and 14.5 GHz, as shown in Figures 21 and 22.

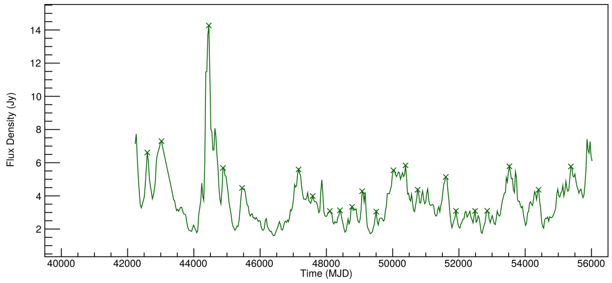

Fig. 20. Light curve of PKS 2200+420 (BL Lac) at 14.5 GHz. The detected outbursts to the periodicities found are shown. The color figure can be viewed online.

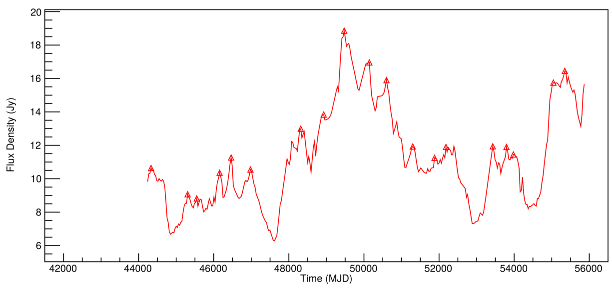

Fig. 21. Light curve of PKS 1921-293 (OV 236) at 4.8 GHz. The detected outbursts to the periodicities found are shown. The color figure can be viewed online.

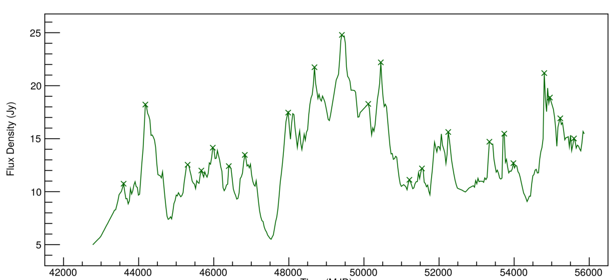

Fig. 22. Light curve of PKS 1921-293 (OV 236) source at 14.5 GHz. The detected outbursts to the periodicities found are shown. The color figure can be viewed online.

REFERENCES

Aarshay, J. 2016, Complete guide to parameter tuning in XGBoost, access date: 6 March 2019

Abay, R., Boyce, R., Brown, M., & Gehly, S. 2018, 42nd COSPAR Scientific Assembly, (Pasadena: CA), 42, 2

Abraham, Z., Kaufmann, P., & Botti, L. C. L. 1982, AJ, 87, 532

Aller, H. D. 1993, Observing At A Distance Proceedings Of A Workshop On Remote Observing, ed. D. T. Emerson & R. G. Clowes (Singapore: World Scientific Publishing Company), 31

Aller, H. D. & Aller, M. 2011, BAAS, 43, 142.47

Aller, H. D. & Aller, M. F. 2010, in BAAS, 42, 378

Aller, M. F., Aller, H. D., & Hughes, P. A. 2009, BAAS, 41, 331

Aller, M., Aller, H. & Hughes, P. 2017, Galax, 5, 75

Antonucci, R. R. J. 1993, ARA&A, 31, 473

Askar, A., Askar, A., Pasquato, M., & Giersz, M. 2019, MNRAS, 485, 5345

Bakoyannis, G. 2020, Journal of Nonparametric Statistics, 32, 131

Beckmann, V. & Shrader, C. 2012, Active Galactic Nuclei (Wiley-VCH Verlag)

Bethapudi, S. & Desai, S. 2018, A&C, 23, 15

Botti, L. C. L. 1990, Spectrum variability study of radio sources in the 22 to 43 Ghz range, Ph. D., Thesis, Instituto de Pesquisas Espaciais, SÃ£o José dos Campos (Brazil)

Botti, L. C. L. 1994, ASPC 59, Astronomy and Submillimeter Wave Interferometry, ed. M. Ishiguro and J. Welch, 50

Botti, L. C. L. & Abraham, Z. 1987, RMxAA, 14, 97

_________. 1988, AJ, 96, 465

Brighton, H. & Mellish, C. 2002, Data Mining and Knowledge Discovery, 6, 153

Caceres, G. A., Feigelson, E. D., Jogesh, B. G., et al. 2019, AJ, 158, 57

Calderon, V. F. & Berlind, A. A. 2019, MNRAS, 490, 2367

Carruba, V., Aljbaae, S., Domingos, R. C., Lucchini, A., & Furlaneto, P. 2020, MNRAS, 496, 540

Chawla, N. V., Bowyer, K. W., Hall, L. O., & Kegelmeyer, W. P. 2002, Journal Of Artificial Intelligence Research, 16, 321

Chen, T. & Guestrin, C. 2016, in Proceedings of the 22Nd ACM SIGKDD International Conference on Knowledge Discovery and Data Mining, KDD -16 (New York, NY: ACM Press), 785

Chong, K. & Yang, A. 2019, EPJ Web of Conferences, 206, 9006

Ciaramella, A., Bongardo, C., Aller, H. D., et al. 2004, A&A, 419, 485

Cincotta, P. M., Méndez, M., & Nunez, J. A. 1995, ApJ, 449, 231

del Barrio, E., Inouzhe, H., & Matrán, C. 2020, TEST: An Official Journal of the Spanish Society of Statistics and Operations Research, 29, 8, 938

Fan, J. H., Liu, Y., Yuan, Y. H., et al. 2007, A&A, 462, 547

Gastaldi, M. R. 2016, PhD thesis, Programa de Pós-Graduação em Ciências e Aplicações Geoespaciais da Universidade Presbiteriana Mackenzie, São Paulo (Brazil)

Hinkel, N., Unterborn, C., Kane, S., & Somers, G. 2020, AAS, 235, 52

Hosenie, Z., Lyon, R., Stappers, B., Mootoovaloo, A., & McBride, V. 2020, MNRAS, 493, 6050

Huang, Y.-P. & Yen, M.-F. 2019, Applied Soft Computing, 83, 105663

Jin, X., Zhang, Y., Zhang, J., et al. 2019, MNRAS, 485, 4539

Kelly, B. C., Hughes, P. A., Aller, H. D., & Aller, M. F. 2003, ApJ, 591, 695
Lam, Ch. & Kipping, D. 2018, MNRAS, 476, 5692
LeCun, Y., Bengio, Y., & Hinton, G. E. 2015, Natur, 521, 436
Li, C., Zhang, W. H., Li, R., Wang, J. Y., & Lin, J. M. 2020, AcASn, 61, 21
Lin, H., Li, X., & Luo, Z. 2020, MNRAS, 493, 1842
Liu, R. H., Hill, R., Scott, D., et al. 2019, MNRAS, 489, 1770
Marsaglia, G., Tsang, W. W., & Wang, J. 2003, Journal of Statistical Software, Articles, 8, 1
Matthews, T. A. & Sandage, A. R. 1963, ApJ, 138, 30
Menou, K. 2019, MNRAS, 489, 4802
Mitchell, R. & Frank, E. 2017, PeerJ Computer Science, 3, 127
Pashchenko, I. N., Sokolovsky, K. V., & Gavras, P. 2017, MNRAS, 475, 2326
Plavin, A. V., Kovalev, Y. Y., Pushkarev, A. B., & Lobanov, A. P. 2019, MNRAS, 485, 1822
Rasheed, F., Alshalalfa, M., & Alhajj, R. 2011, IEEE Transactions on Knowledge and Data Engineering, 23, 79
Sadhanala, V., Wang, Y.-X., Ramdas, A., & Tibshirani, R. J. 2019, Proceedings of Machine Learning Research, 89, 2621
Saha, S., Basak, S., Safonova, M., et al. A&C, 23, 141
Santos, M. A. d. 2007, Master Thesis, Mackenzie Presbyterian University, São Paulo
Schmidt, M. 1963, Natur, 197, 1040
Shu, Y., Koposov, S. E., Evans, N. W., et al. 2019, MNRAS, 489, 4741
Smirnov, E. A. & Markov, A. B. 2017, MNRAS, 469, 2024
Soldi, S., Türler, M., Paltani, S., et al. 2008, A&A, 486, 411
Tamayo, D., Cranmer, M., Hadden, S., et al. 2020, PNAS, 117, 18194
Tornikoski, M., Valtaoja, E., Teraesranta, H., et al. 1996, A&AS, 116, 157
Tsizh, M., Novosyadlyj, B., Holovatch, Y., & Libeskind, N. I. 2020, MNRAS, 495, 1311
Urry, C. M. & Padovani, P. 1995, PASP, 107, 803
van Roestel, J., Kupfer, T., Ruiz-Carmona, R., et al. 2018, MNRAS, 475, 2560
Véron-Cetty, M.-P. & Véron, P. 2010, A&A, 518, 10
Villata, M., Raiteri, C. M., Aller, H. D., et al. 2004, A&A, 424, 497
Vitoriano, R. P. & Botti, L. C. L. 2018, ApJ, 854, 59
Wang, Y., Pan, Z., Zheng, J., Qian, L., & Li, M. 2019, Ap&SS, 364, 139
Witten, I. H., Frank, E., Hall, M. A., & Pal, C. J. 2016, Data Mining: Practical Machine Learning Tools and Techniques, The Morgan Kaufmann Series in Data Management Systems (Cambridge, MA: Elsevier Science)
Xu, B. 2018, Higgs Boson Machine Learning Challenge, access date: 28 August, 2018
Yi, Z., Chen, Z., Pan, J., et al. 2019, ApJ, 887, 241
Yuan, Y. 2011, JApA, 32, 43
Zhang, D., Qian, L., Mao, B., et al. 2018, IEEE Access, 6, 21020

Samuel Bueno Soltau: Department of Physics, Institute of Exact Sciences. Federal University of Alfenas, Minas Gerais, Brazil. (samuel.soltau@unifal-mg.edu.br), https://orcid.org/0000-0002-7211-2533.

Luiz Claudio Lima Botti: Center for Radio Astronomy and Astrophysics Mackenzie, Engineering School, Mackenzie Presbyterian University, São Paulo, Brazil. and Astrophysics Division, Brazilian National Institute for Space Research, São José dos Campos, São Paulo, Brazil (luizquas@yahoo.com.br), https://orcid.org/0000-0003-1424-0796.

Revista Mexicana de Astronomía y Astrofísica, **57**, 123–132 (2021)

https://doi.org/10.22201/ia.01851101p.2021.57.01.08

KEPLER PLANETARY SYSTEMS: DOPPLER BEAMING EFFECT SIGNIFICANCE

H. Barbier[1] and E. López[1,2]

Received January 1 2020; accepted October 22 2020

ABSTRACT

In the present work, in order to estimate the semi-amplitude of the radial velocity, we evaluate the contribution of the Doppler beaming effect to the phase curves of the all confirmed extrasolar planets (2776, September 2019), observed so far by the Kepler telescope. By modeling the tiny photometric variations (reflection, ellipsoidal and Doppler beaming effects) of the light curves, we found that the best observational data are in close agreement with the theoretical and published values of the amplitudes only for exoplanets: KOI-13b and TrES-2b. The derived values for the radial velocity also are in good agreement with those published by some authors. Furthermore, we found it necessary to introduce a third harmonic (3ϕ) contribution into the KOI-13b and HAT-P7b light curve models, in order to decrease the residuals.

RESUMEN

En el presente trabajo, con el fin de estimar la semi-amplitud de la velocidad radial, evaluamos la contribución del efecto Doppler beaming a las curvas de fase de todos los planetas extrasolares confirmados (2776, septiembre de 2019), observados hasta ahora por el telescopio Kepler. Modelando las pequeñas variaciones fotométricas (reflexión, efectos elipsoidales y de enfoque Doppler) de las curvas de luz, encontramos que los mejores datos observacionales están en acuerdo con los valores teóricos y publicados de las amplitudes solo para los exoplanetas: KOI-13b y TrES-2b. Los valores derivados para la velocidad radial también concuerdan con los publicados por algunos autores. Además, encontramos que es necesario introducir una tercera contribución armónica (3ϕ) en los modelos de curva de luz para KOI-13b y HAT-P7b, con el fin de reducir los residuos.

Key Words: methods: data analysis — planets and satellites: detection — relativistic processes — techniques: radial velocities

1. INTRODUCTION

Wolszczan and Frail studying the radio pulsar PSR1257+12 deduced the presence of two orbiting Earth-mass bodies (Wolszczan & Frail 1992): this was the first widely-accepted discovery of an exoplanet. Later, in 1995, Mayor and Queloz, using the radial velocity method, discovered the first exoplanet orbiting a solar type star, 51 Peg (Mayor & Queloz 1995). With this latter discovery began an entirely new field of astronomy: the study of exoplanets. So far, applying different observational methods the number of confirmed exoplanets has reached 4276 (https://exoplanetarchive.ipac.caltech.edu, september 2020). These observations have given us new insight on the extraordinary diversity of exoplanetary systems in our Milky Way (planets are found with very different masses, sizes and spatial distributions).

Among the available methods used to detect and characterize exoplanets, two techniques appear to be most effective: the transit photometry and the radial velocity. First, the transit photometric method, which is especially efficient, is used to detect tiny decreases (1 to 100 ppm) of the luminosity in the light curve of the central star. These correspond to the primary (transit) and secondary (occultation) star-planet eclipses. It allows us, in particular, to obtain

[1]Departamento de Física, Facultad de Ciencias, Escuela Politécnica Nacional, Quito, Ecuador.

[2]Observatorio Astrónomico de Quito, Escuela Politécnica Nacional, Quito, Ecuador.

an estimation of the planet's radius. Second, also when the star´s orbit is inclined, the star exhibits a periodic Doppler shift, so that in the stellar spectrum we are able to measure the blue and red shifted lines and, therefore, to estimate the star radial velocity curve. This is the so-called radial velocity method that allows us to obtain an estimation of the planet's mass. Combining these two methods provides a better characterization of an exoplanet.

Also, high-precision photometry from the Kepler mission has enabled us to study small-scale variable photometric effects that arise from the exoplanet motion around its host star; for example, stellar brightness also varies between eclipses due to three photometric effects that are: reflected light (as planetary contribution to the system light curve), the ellipsoidal variations (tidal ellipsoidal distortion) and the Doppler beaming (arising from modulation of the stellar flux by interactions with the orbiting planet). The magnitude of these effects is very weak, commonly, less than 100 ppm (Loeb & Gaudi 2003). Until the launch of CoRot and Kepler telescopes, the precision required to study these small-scale interactions was not available.

The photometric variation of the light curve due to these three effects, without considering the eclipses, is referred hereafter as the planetary phase curve. An important advantage of phase curve analysis is that it permits a full characterization of the physical and orbital parameters of an exoplanet. Several groups have been working in this way, characterizing individual exoplanets from their phase curves, e.g., planets discovered by the CoRot telescope, like CoRot-1b (Snellen et al. 2009) and planets discovered by the Kepler telescope like KOI-13b (Shporer et al. 2011; Mazeh et al. 2012), TrEs-2 (Barclay et al. 2012; Kipping & Spiegel 2011), Kepler-41b (Quintana et al. 2013), HAT-P-7b (Mislis et al. 2012; Welsh et al. 2010; Van Eylen et al. 2012) and Kepler-5b, Kepler-6b, Kepler-8b studied by Esteves et al. (2013), who also studied the phase curves for some of the above mentioned planets focusing on those planets with a ratio $\frac{a}{R_*} < 10$, where a is the semi-major axis of the orbit and R_* is the stellar radius.

Regarding the Doppler beaming effect, it is the result from the reflection movement of a host star due to the interaction with an orbiting companion. In the composite phase curve, considering all photometric effects, the introduction of the beaming effect yields asymmetries in the whole pattern due to the sinusoidal variation.

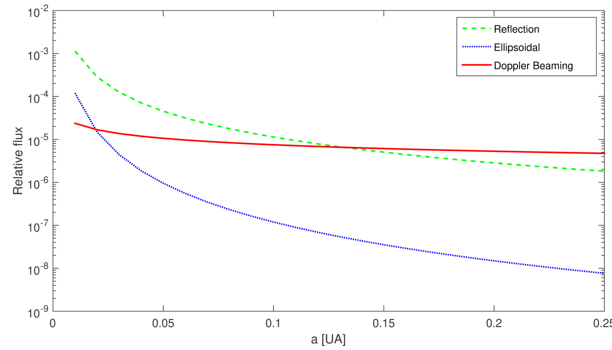

Fig. 1. Small scale photometric variations of a phase curve as a function of the radial semi-mayor axis of the planet orbit. The color figure can be viewed online.

In this contribution, we do not estimate the mass of the planet, although it could be done in a simple way. Instead, we focus on evaluating the Doppler beaming effect over each of all confirmed exoplanets, discovered so far by the Kepler telescope. In this way, we derive the planet radial velocity only for those planets which exhibit Doppler luminosity variations greater than 1 *ppm*. The Doppler beaming effect and the radial velocity for the selected planetary systems were theoretically evaluated using the parameters given in Table 1. In addition, they were also estimated from the observational data (experimental phase curve) using a fitting model. Finally, the obtained radial velocity values were compared with those found in the literature.

2. PHASE CURVE MODELING

Loeb & Gaudi (2003) have demonstrated that the small photometric variations of the phase curve arise from three different effects: the reflection and/or emission, the ellipsoidal and the Doppler beaming effect. Since the reflection and the planet thermal emission are degenerate at low eccentricities, these two planetary effects are difficult to distinguish. For this reason, both effects are added and considered hereafter together as only one planetary effect; the reflection effect, sometimes called the phase function. The first two effects vary as a^{-2} and a^{-3}, respectively and the third as $a^{-1/2}$, where a is the radial semi-major axis of the planet orbit (see Figure 1).

In what follows, we describe these three effects denoting the mass and radius of the star, Sun, planet and Jupiter as: M_*, R_*, M_{sun}, R_{sun}, M_P, R_P, M_J, R_J, respectively. The period of a planetary orbit is denoted by P_{orb}, a and i are the semi-major axis of the planet orbit and its inclination with respect

TABLE 1

EXOPLANET PARAMETERS[a]

Kepler Exoplanet	Orbit period P (days)	Orbit inclination i $\circ$	Planet mass M_p (M_J)	Stellar temperature (K)	Stellar mass (M_{sun})
HAT-P7	2.204	83.14	1.78	6350	1.47
Kepler-423b	2.68	87.828	0.595	5560	0.85
Kepler-5b	3.55	89.14	2.11	6297	1.37
Kepler-75b	8.88	89.12	10.1	5200	0.91
Kepler-8b	3.522	83.978	0.59	6213	1.21
KOI-13b	1.763	83.77	9.28	7650	1.72
Tr-ES-2b	2.470	83.87	1.19	5850	0.98

[a]Published values (http://exoplanetarchive.ipac.caltech.edu).

to the observation plane. V_r and K are the radial velocity and the semi-amplitude of the radial velocity and G and c are the gravitational constant and the speed of light.

2.1. *Reflection Effect*

This photometric effect, in essence, is an atmospheric phenomenon rather than a gravitational one. It mainly depends on the planet reflective capability. When a planet has a large albedo and is orbiting around a luminous star, its light variations are easier to detect in the visible range. Although the effect is small, it is significant for short-period planets in close orbits around their host stars. This is directly related to the fact that the stellar flux received by the planet decreases with distance as $\frac{1}{r^2}$. Planets in close orbits are also heated by their stars, making their thermal radiation detectable. Thus, giant planets like Jupiter, with an orbital period of few days, are easier to detect by space telescopes like Kepler, since these planets collect more light from their host stars. As mentioned above, the reflection of incident stellar radiation off the planetary surface and/or atmosphere and the planet thermal emission are not easy to distinguish between them. For this reason, they are considered here as just one effect; the reflection effect. As the reflection picks up at superior conjunction (occultation) and reaches a minimum at inferior conjunction (transit), it is reasonable to modulate it by a cosinusoidal function of the phase angle ϕ, which describes well the planet position. The amplitude of the reflected light alone is given by: $A_{Refl} = A_{geo}\, (\frac{R_p}{a}^2)$, where R_p is the planetary radius, and A_{geo} is the geometrical albedo.

Following the model described in Mazeh et al. (2012), Sudarsky et al. (2005) and Burrows & Orton (2009), the normalized photometric flux variation due to reflection is given by:

$$\frac{\Delta F}{F_o} = A_{Refl}\left[\frac{\sin\theta + (\pi-\theta)\cos\theta}{\pi}\right], \tag{1}$$

where the amplitude for the reflection effect, including the planetary thermal emission, is expressed as (Mazeh et al. 2012; Mazeh & Faigler 2010; Shporer et al. 2011):

$$A_{Refl} = \alpha_{Refl} 0.1 \left(\frac{R_p}{a}\right)^2 \sin i, \tag{2}$$

or in ppm units:

$$A_{Refl} = 57\alpha_{Refl}\sin i\left(\frac{M_*}{M_{sun}}\right)^{-2/3}\left(\frac{P_{orb}}{day}\right)^{-4/3}\times \times\left(\frac{R_p}{R_J}\right)^2 [ppm]. \tag{3}$$

Here, α_{Refl} is the reflection coefficient which depends on the albedo (α_{Refl} is of order unity), θ defined by $\theta = |\phi - \pi|$, is the complementary angle of ϕ, being ϕ the orbital phase angle.

The amount of reflected light does not change during their orbit for planets with circular face-on orbits from Earth's point of view; therefore, their reflected radiation is not detected.

In summary, planets in close orbits around their host star, larger planets, and planets with higher albedo, are easier to detect as they reflect more light.

2.2. *Ellipsoidal Effect*

The ellipsoidal effect has its origin in the gravitational deformation of the host star by an orbiting planet (tidal distortion). Planetary gravitational tidal forces produce stellar distortions that cause photometric variations of the light curve of exoplanetary systems. This effect was presented by Loeb &

Gaudi (2003) and Drake (2003). Pfahl et al. (2008) provide a detailed theoretical investigation of the ellipsoidal deformation of the host star.

Following Morris (1985), we describe the flux variation of the light curve due to the ellipsoidal effect. He proposed a model for the normalized flux variation that includes the first three cosinusoidal harmonics of the phase angle $\phi(t)$, as follows: $\frac{\Delta F}{F_o} = f_2 \cos(2\phi) + f_1 \cos(\phi) + f_3 \cos(3\phi)$; here, f_1, f_2 and f_3 are the cosinusoidal amplitudes. From the results obtained by Esteves et al. (2013), we note that the last two terms contribute less than 10% to the total ellipsoidal variations; so they are not considered in our calculations (Mazeh & Faigler 2010).

The ellipsoidal variations are a gravitational effect which produces a double peak of equal height at the quarter phases of the orbit, contributing to an overall bi-modal feature in the light curve. Then, the tidal ellipsoidal normalized flux variation can be modulated in a cosinusoidal manner as:

$$\frac{\Delta F}{F_o} = A_{Ellip} \cos(2\phi), \tag{4}$$

where the ellipsoidal amplitude is given by Shporer et al. (2011):

$$A_{Ellip} = \alpha_{Ellip} \frac{M_p \sin i}{M_*} \left(\frac{a}{R_*}\right)^{-3} \sin i, \tag{5}$$

or, in ppm units:

$$A_{Ellip} = 13 \alpha_{Ellip} \sin i \left(\frac{R_*}{R_{sun}}\right)^3 \left(\frac{M_*}{M_{sun}}\right)^{-2} \times \times \left(\frac{P_{orb}}{day}\right)^{-2} \left(\frac{M_p \sin i}{M_J}\right) [ppm]. \tag{6}$$

M_p, M_* are the planetary and stellar masses, a, P_{orb} and i are the semi-major axis, period and inclination of the planetary orbit, respectively. $\alpha_{Ellip} = = 0.15 \frac{(15+u)(1+g)}{(3-u)}$ is a coefficient which depends on the linear gravitational g and on u, the limb darkening coefficients of the host star (see Mazeh & Faigler (2010) for further details).

The effect of the stellar ellipsoidal distortions on the light curve can be larger than the relativistic beaming effect, which is often small, but the variation of the phase curve component is twice as fast. Furthermore, as seen in the relationships for calculating the ellipsoidal amplitude, the gravitational distortion of the star by the planet is larger if it has a low semi-major axis to stellar radius ratio and the density of the star is low. So, this ellipsoidal method can be used efficiently to find planets in evolved stars outside the main sequence. In contrast, the ellipsoidal effect is negligible for low mass planets far from the host stars.

2.3. *Doppler Beaming Effect and Radial Velocity Estimation*

The first theoretical contribution was presented by Hills & Dale (1974) and the first observational contribution by Maxted et al. (2000). Loeb & Gaudi (2003) were first to present the photometric effect in the context of exoplanet characterization. As the star and planets are orbiting around the system's barycenter, the host star will periodically advance toward, and recede from, an observer. Thus, the brightness of the host star will vary sinusoidally at the orbital frequency of the planet (a stellar wobble is induced by the planet). Then, as the star moves toward an observer, there is an increase in the observed flux, and as it recedes the observed flux decreases. It varies with the period of the orbit, but is off by a phase from the reflected light, since the maximum boosting occurs when the planet is in its first quarter phase and the star is moving toward the observer. The relativistic Doppler beaming (boosting), now is a detectable photometric variation effect, thanks to the high-precision photometry of space telescopes like Kepler (down to ≈ 10 parts per million). It is not an ideal method for discovering new planets, since the effect is small, even smaller than the emitted and reflected starlight from the planet. However, with the light variations due to relativistic beaming, it is easier to detect massive planets near their host stars, since these factors increase with the movement of the star (due to the motion around the center of mass of an exoplanet system). Like the radial velocity method, this can be used to determine the orbital eccentricity and the minimum mass of the planet (which is impossible to do from reflected light alone); but the Doppler beaming effect does not require a spectrum of the star, so it can be used to study more distant stars.

The Doppler beaming effect (DBE) itself has two contributions: the first one is actually the same Doppler beaming effect which increases the luminosity toward the direction of the radial velocity of the star. The second one is the Doppler shift of the star spectrum in the Kepler observation band. These two effects could be described by the following equations (Rybicki & Lightman 1979). First, considering a spherical star that radiates isotropically (or nearly isotropically) in the particle rest frame, the relativistic transformation of the received bolometric flux is given by:

$$\frac{F}{F_o} = \frac{1}{\gamma^4(1-\beta\cos\theta(t))^4}, \quad (7)$$

where $\gamma = \frac{1}{\sqrt{(1-\beta^2)}}$ and $\beta = \frac{v}{c}$ is the velocity of star in units of c, being c the speed of light. The angle $\theta(t)$ is the angle between the stellar velocity and the line of sight. From here, as the planet moves slowly compared with the speed of light, in the non-relativistic limit, the stellar normalized boosted flux is given by (Ben Placek and Kevin H. Knuth, 2015):

$$\frac{\Delta F}{F_o} = (3 - \alpha_{Beam})\,\frac{v_r}{c}, \quad (8)$$

where α_{Beam} is the photon-weighted integrated bandpass beaming factor, v_r the radial velocity of the host star which varies in a sinusoidal manner as $v_r = K\sin(\phi)$, with K the semi-amplitude of the radial velocity given by (Cumming et al. 1999):

$$K = \left(\frac{2\pi G}{P_{orb}}\right)^{1/3} \frac{M_p\sin(i)}{(M_* + M_p)^{-2/3}} \left(1-e^2\right)^{-1/2}. \quad (9)$$

Or, considering that $M_P << M_*$ and the eccentricity $e = 0$ for a circular orbit, in a first approximation, we can rewrite the previous expression as:

$$K = 28.4\left(\frac{M_*}{M_{sun}}\right)^{-2/3}\left(\frac{P_{orb}}{yr}\right)^{-1/3}\frac{M_p\sin(i)}{M_J}\left[m\ s^{-1}\right]. \quad (10)$$

This relation, in this work, is evaluated using the well-known physical parameters, to make an analytical estimation of the radial velocity.

From here, the normalized flux variation for the Doppler beaming effect can be written as (Loeb & Gaudi 2003; Shporer et al. 2011):

$$\frac{\Delta F}{F_o} = A_{Beam}\ \sin(\phi), \quad (11)$$

where the beaming amplitude is found to be (Shporer et al. 2011):

$$A_{Beam} = (3-\alpha_{Beam})\,\frac{K}{c}, \quad (12)$$

$$A_{Beam} = 2.7\ \alpha_{Beam}\left(\frac{M_*}{M_{sun}}\right)^{-2/3}\left(\frac{P_{orb}}{day}\right)^{-1/3}\times$$
$$\times\frac{M_p\sin(i)}{M_J}[ppm]. \quad (13)$$

Therefore, the amplitude of the effect can be used to estimate the mass of the planet if the host star mass is known. The amplitude of the observed Doppler beaming photometric variation depends on the bandpass through which the planetary system is observed. The actual value of α_{Beam} (the average spectral index) depends on the telescope band pass as well as on the type of the observed star. It can be written as $\alpha_{Beam} \propto \frac{d\ ln(F_\nu)}{d\ ln(\nu)}$. Considering a black-body effective temperature T_{eff}, we can compute α_{Beam} by $\alpha_{Beam} = \frac{e^x*(3-x)-3}{e^x-1}$ (Loeb & Gaudi 2003), where $x = \frac{h\nu}{k\ T_{eff}}$ and h and k are, respectively, the Planck and Boltzmann constants.

It is worth noting that the radial velocity can be estimated from the Doppler beaming amplitude. Therefore, the mass of the planet also can be estimated from the amplitude of the Doppler boosting, as this effect is proportional to the radial velocity. Finally, it is also important to keep in mind that the Doppler variations for short period ($P \lesssim 0.2\ yr$) and massive ($M\sin i \gtrsim M_J$) planets should be a significant contributor to the variability of the exoplanetary phase curve signal (Loeb & Gaudi 2003).

3. KEPLER PLANETARY SYSTEMS

We analyze all the quarters of the Kepler short and long cadence data for all the planets which exhibit a phase curve.

We start by computing the Doppler beaming effect, explained in § 2.3, for all confirmed exoplanets observed by the Kepler telescope (2776 objects). For that, we use the published data available at https://exoplanetarchive.ipac.caltech.edu. We found just 60 objects in which a Doppler beaming amplitude is detectable. Currently, the Kepler photometric instrument is sensitive enough to detect Doppler variations equal or greater than 1 ppm; this was not possible in past space missions.

During the mission, Kepler took 30 seconds short cadence (SC) integrations with its 42-CCD photometer (Borucki et al. 2010). For each exoplanet system, 10 to 50 photometric measurement files are available, corresponding to observations from 2009 to 2019. Details of the process of data reduction are explained below.

3.1. *Removal of Systematics*

First, in order to improve the signal to noise ratio, we treat the photometric data eliminating the jumps between the quarters and correcting for systematics. Since photometric variations are normally small for the primary and secondary eclipses, and even less between eclipses (due to the above mentioned photometric effects), we do not expect to have abrupt signal changes in the observed data. Then, in each data file a central moving median and a central moving average have been applied to eliminate bad points and to smooth the curve. We tested different combinations of these two steps, using 3 to 101 points, looking for the most suitable combination to smooth the curve without affecting the particularities of the signal (primary eclipse). A central moving median of 40 orders with a central moving average of 10 orders produced the best results. This procedure provided a light curve that had between 3 to 20 eclipses, depending on the planetary period and the available Kepler files. Finally, the phase curve for each planetary system was obtained by adding the light curve over parts of a period, applying the folding phase method. The phases $\phi = 0$ in the primary eclipse and $\phi = \pi$ in the secondary, are taken as the starting points. The last step consists of removing the primary and secondary eclipses to obtain only the light variation curve between eclipses, which is the phase curve to be modeled.

Finally, we apply small-scale photometric variation models to find the best fitting curves to our observational data.

3.2. *The Data Analysis: Phase Curve Fitting*

The fitting model for a given light curve, essentially involves tuning the amplitude values for each of the three effects mentioned earlier, i.e., A_{Refl}, A_{Ellip}, and A_{Beam}, in order to find the best fit to the corresponding photometric data of our selected planetary systems.

As was shown in the previous section, the small-scale photometric variations of these planets are proportional to trigonometric functions of the phase ϕ which ranges from 0 to 2π; 0 corresponds to the transit and π to the occultation.

For the normalized phase curve, adding the contribution of all phase effects, the following expression describes the pattern for the relative flux variation:

$$F = A_0 + A_{Refl}\cos(\phi) + A_{Ellip}\cos(2\phi) + A_{Beam}\sin(\phi). \quad (14)$$

A_0 is expected to be of the order of unity, A_{Beam} positive, A_{Refl} and A_{Ellip} negative.

Only the planets with the correct amplitude effect (7 planets out of the original 60), have been presented in this work. The theoretical values for the amplitude A_{Beam} have been obtained from the evaluation of the relations exhibited in the Phase Curve Modeling § 2, using the parameters (mass, radius, and inclination) given in Table 1.

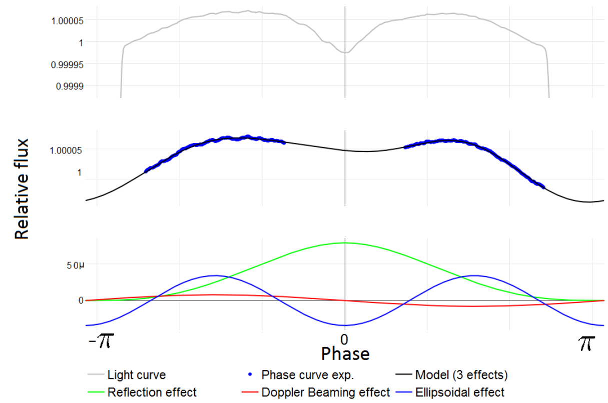

Fig. 2. KOI-13b phase curve fitting. The color figure can be viewed online.

In Figure 2, we present the composite phase curve for KOI-13b. For this planetary system the reflection contribution is dominant, but it is modulated by the bimodal ellipsoidal effect.

The Doppler beaming effect is also appreciable by the asymmetries in the total phase curve. However, the residual was not small enough to be considered as a good fit.

A result with a smaller residual (see Table 2) is obtained by incorporating, a priori, additional harmonics in 2ϕ and 3ϕ. Harmonics of higher order also have been considered, but no appreciable contributions was found.

Therefore, the models described below have been applied to KOI-13 and the other planets of our selected sample (Figure 3):

Model 1: Reflection effect + DBE + Ellipsoidal effect

Model 2: Reflection effect + DBE + Ellipsoidal effect + $\sin(2\phi)$

Model 3: Reflection effect + DBE + Ellipsoidal effect + $\sin(2\phi) + \cos(3\phi) + \sin(3\phi)$

In Figure 4 the phase curves with their best fitting models are presented for each of the six planetary systems that were analyzed in this contribution.

In Table 3 we show, together with the published values, the theoretical and estimated Doppler amplitudes A_{Beam}, along with the values deduced for the radial velocity K.

4. RESULTS AND DISCUSSION

Unlike other works in the literature, in this contribution we have compared the radial velocity values

TABLE 2

STANDARD RESIDUAL ERRORS FOR DIFFERENT MODELS

Kepler Exoplanet	Model 1: Three effects	Model 2: Model 1 + $\sin(2\phi)$	Model 3: Model 2 + 3ϕ term
HAT-P-7b	2.227e-06	1.953e-06	1.731e-06
Kepler-423b	2.075e-05	2.032e-05	1.99e-05
Kepler-5b	1.613e-05	1.602e-05	1.588e-05
Kepler-75b	0.0001155	0.0001146	0.0001141
Kepler-8b	2.663e-05	2.663e-05	2.662e-05
KOI-13b	4.458e-06	2.531e-06	1.116e-06
TrES-2b	3.28e-06	3.249e-06	3.229e-06

TABLE 3

DOPPLER BEAMING AMPLITUDE AND RADIAL VELOCITY

Kepler Exoplanet (ppm)	Theoretical A_{Beam} [a] $(m.s^{-1})$	Theoretical K [a] (ppm)	Calculated A_{Beam} [b] $(m.s^{-1})$	Calculated K [b] (ppm)	Published A_{Beam} $(m.s^{-1})$	Published K
HAT-P-7b	2.75	213.33	5.19 ± 1.99	402.43 ± 155.43	5.8 ± 0.19 [3]	211.8 ± 2.6 [8]
Kepler-423b	1.41	98.88	12.74 ± 2.36	873.36 ± 159.49	NA	96.7 ± 11.8 [11]
Kepler-5b	2.96	227.77	4.74 ± 3.22	366.84 ± 247.08	NA	227.5 ± 2.8 [10]
Kepler-75b	19.94	1283.04	384.4 ± 290	24731 ± 18575.44	NA	1288 ± 24 [12]
Kepler-8b	0.90	68.94	0.29 ± 26	–	2.5 ± 1.2 [3]	NA
KOI-13b	11.85	1084.47	11.70 ± 4.2	1100.73 ± 376.02	7.14 ± 0.24 [3]	≤ 1000[9]
						8.6 ± 1.1 [1]
					10.4 ± 1.1 [1]	
					5.28 ± 0.44 [4]	
TrES-2b	2.51	181.14	2.33 ± 4.39	167.51 ± 31.29	2.4 ± 0.3 [3]	181.3 ± 2.6 [6]
					0.22 ± 0.88 [2]	
					0.23 ± 0.89 [2]	
					0.31 ± 0.88 [2]	
					0.78 ± 0.85 [2]	
					0.79 ± 0.86 [2]	
					3.44 ± 0.35 [5]	

[a]Theoretical Doppler beaming values.
[b]Doppler beaming values derived from a fitting model; observational data.
[1]Mazeh et al. (2012), [2]Kipping & Spiegel (2011), [3]Esteves et al. (2013), [4]Shporer et al. (2011), [5]Barclay et al. (2012), [6]O'Donovan et al. (2006), [7]Quintana et al. (2013), [8]Winn et al. (2009), [9]Santerne et al. (2012), [10]Koch et al. (2010), [11]Endl et al. (2014), [12]Hébrard et al. (2013).

obtained from the theory of the Doppler beaming effect with the experimental ones, and also with experimental results reported by other authors. We note that our theoretical values for K (radial velocity) are in good agreement with those calculated via the radial velocity (RV) method. We found that, in most of the cases, our estimations for the Doppler Beaming effect are better than those previously published.

In Table 3 are shown the Doppler amplitudes (theoretical, calculated and published), as well as the calculated radial velocities, for the planetary systems: HAT-P-7b, Kepler-423b, Kepler-5b, Kepler-75b, KOI-13b, TrES-2 (exoplanet with coherent phase curves and coherent amplitude signs, for each of the three photometric effects). Kepler-8b, with an incorrect amplitude sign for the reflection effect, but not for the beaming effect, has also been included in the list because it is a very well-studied planetary system. All these exoplanets exhibit a transit depth, but not necessarily an occultation. We also note that for the other planets, like Kepler-41b, Kepler-43b, Kepler-44b and Kepler-6b, there are transit and occultation depths, but the signs of the amplitudes for at least one of the three effects are incorrect.

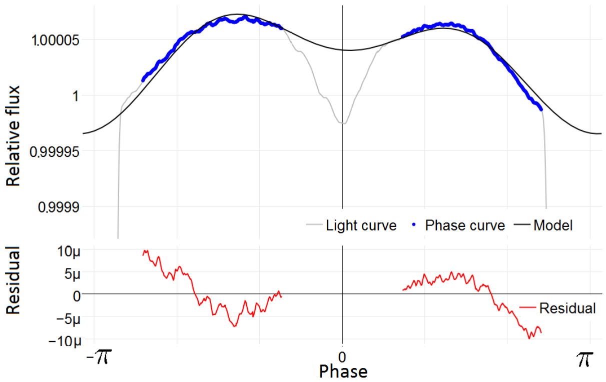

(a) KOI-13b: Model 1

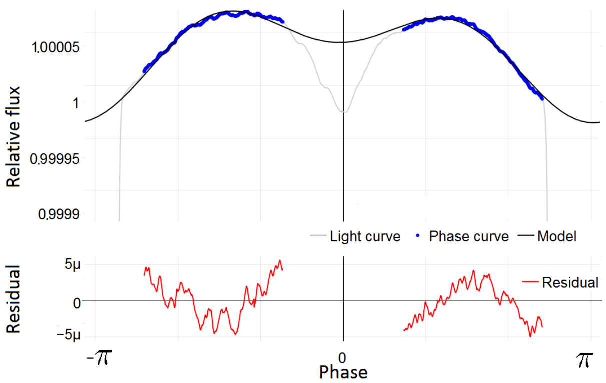

(b) KOI-13b: Model 2

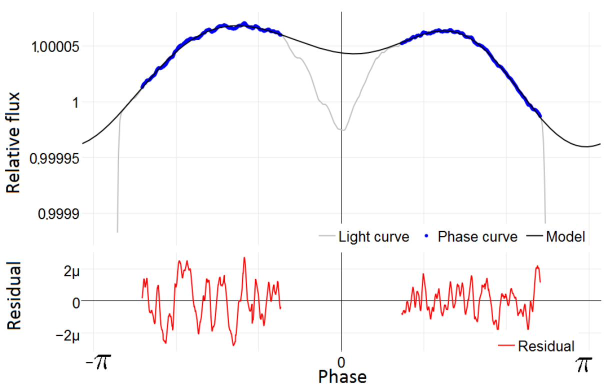

(c) KOI-13b: Model 3

Fig. 3. KOI-13b planetary light curve, phase curve, fitting model, and residuals for each of the three models indicated in the text. The color figure can be viewed online.

Our results reveal that for the KOI-13 planetary system, the fit becomes much better by adding into the fitting model the $\sin(2\phi)$ term and the cosine and sine of 3ϕ, (see Figure 3); the model-curve fits relatively well, and the experimental points and the distribution of the residuals decrease (Table 2). The physical reason for including additional harmonics in the fitting model could be related to the so-called dilution effect (Szabo et al. 2011), which takes place in a planetary system with a binary host star, as in the case of KOI-13. From the residual plot for KOI-13, it is clear that there is a signal at 3ϕ. Thus, it is reasonable to include in the fitting model the 3ϕ harmonics in order to get a better fit. On the other hand, adding the 4ϕ harmonics to the model does not result in further improvements. The residual standard error value remains close to that previously obtained (1.082×10^{-6}), so it is not necessary to consider additional harmonics corrections into the fitting model.

We note that the theoretical, calculated and published values for the beaming amplitude and radial velocity are always in disagreement, the only exceptions being the planetary systems KOI-13b and TrEs-2b, whose values are in agreement within 10 percent (O'Donovan et al. 2006; Santerne et al. 2012). For KOI-13b, taking into consideration the dilution effect (binary host star), its phase curve is quite well modeled, giving a value for the Doppler amplitude close to that expected. Consequently, the radial velocity that we have obtained is also close to values already published by other authors using the radial velocity method. In the case of the TrES-2b exoplanet, adding the 3ϕ harmonic, our results are in agreement with those published by Esteves et al. (2013) for the Doppler beaming estimation and according to the theory.

On the other hand, we see that for the exoplanet HAT-P-7b (with well defined transits and occultations) the amplitude and the radial velocity are double the values found in the literature, which were obtained using the radial velocity method (see Table 3). Moreover, for the planets Kepler-423b, Kepler-5b and Kepler-75b, our results are far from the theoretical predictions but they are quite similar to the values obtained by other authors, who also have used the planetary light curves. There is no publication in the literature concerning Doppler beaming for these objects.

Finally, with Kepler-8b the sign of the reflection effect is wrong, but the experimental value of the beaming amplitude is closer to its theoretical prediction, much better than the estimations given by other authors. This planet, with a weak Doppler beaming effect (less than that of the other planets) has been studied by other authors, who have obtained a tiny value for the amplitude A_{Beam} of about 10^{-7}.

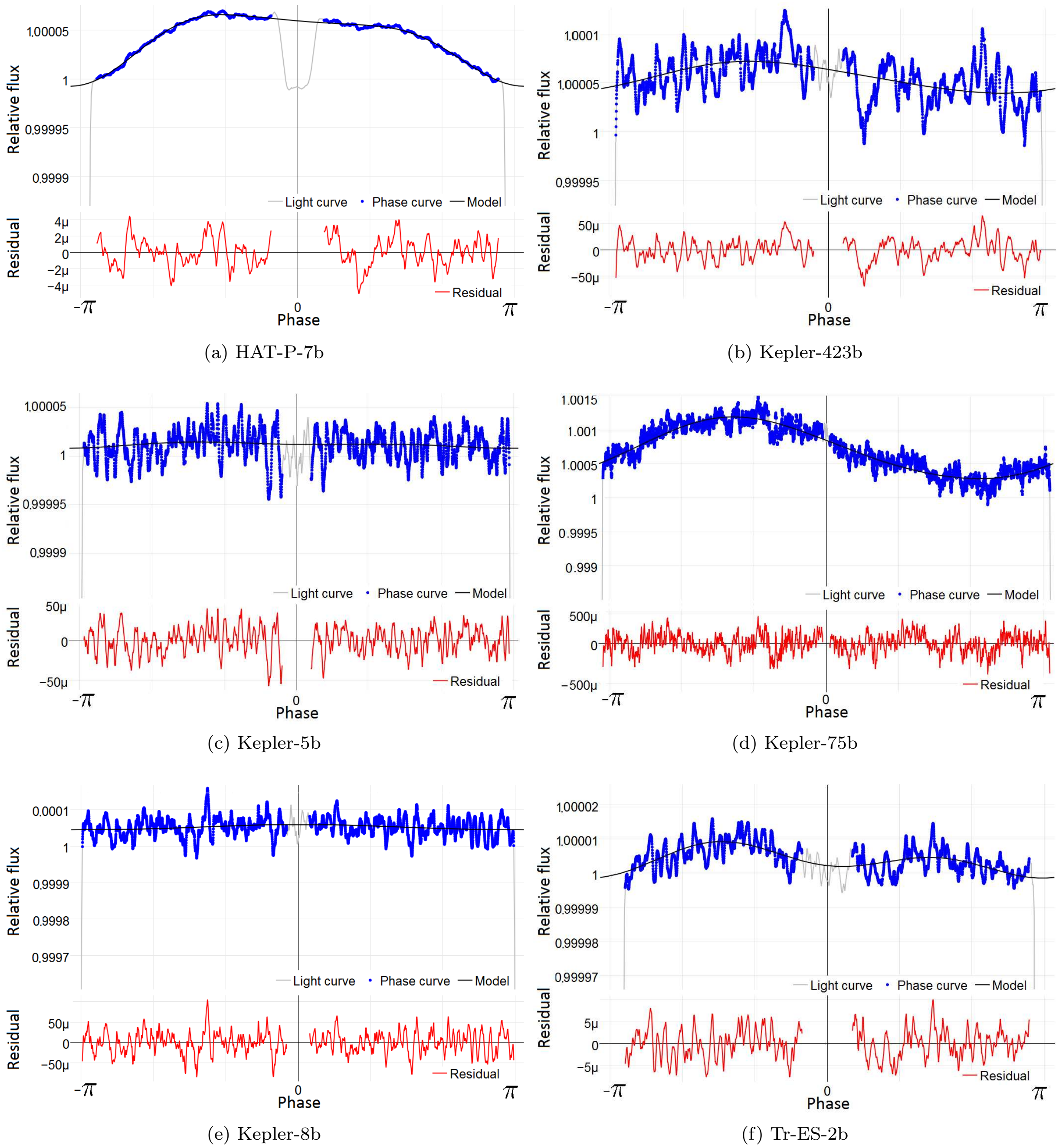

(a) HAT-P-7b (b) Kepler-423b

(c) Kepler-5b (d) Kepler-75b

(e) Kepler-8b (f) Tr-ES-2b

Fig. 4. Light curve, phase curve, fit model, and residual for the different planets we found with coherent effect sign. The color figure can be viewed online.

We do not understand the reasons for these disagreements in determining the beaming amplitude and consequent radial velocity. They could be a consequence of the different approaches proposed, linked to the intrinsic development of the study methods of exoplanets, which give rise to different results as theory and experimental methods become more precise. A second reason could be that we use the full Kepler data, while other teams conducted their research a few years ago and with fewer data available.

Alternatively, they may be related to the different instruments used in the observations, with different sensitivity and precision.

The method for the estimation of the radial velocity via the Doppler beaming effect proposed in the current contribution yields good results exclusively for KOI-13b and TrES-2b. This fact is closely related to the sensitivity of the current instrumentation and to the strong variability of the stars, which limit our ability to obtain well-defined light curves. The suggestion to add an offset, as described by Esteves et al. (2015), does not improve the results. The current and emerging exoplanet science depends on the capability and photometric sensitivity of the next generation of space-based instruments. New instruments and missions, including the TESS (recently launched), CHEOPS, JWST and PLATO missions, are expected to provide brighter and more nearby planet samples, opening up exciting new opportunities for developments in their characterization.

REFERENCES

Barclay, T., Huber, D., Rowe, J., et al. 2012, ApJ, 761, 53

Borucki, W., Koch, D., Basri, G., et al. 2010, Sci, 327, 977

Burrows, A. & Orton, G. 2009, arXiv0910.0248

Cumming, A., Marcy, G. W., & Butler, R. P. 1999, ApJ, 526, 890

Drake, A. J. 2003, ApJ, 589, 1020

Endl, M., Caldwell, D. A., Barclay, T., et al. 2014, ApJ, 795, 151

Esteves, L. J., De Mooij, E. J. W., & Jayawardhana, R. 2013, ApJ, 772, 51

_________. 2015, ApJ, 804, 150

Hébrard, G., Almenara, J.-M., Santerne, A. et al. 2013, A&A, 554, 114

Hills, J. G. & Dale, T. M. 1974, A&A, 30, 135

Kipping, D. M. & Spiegel, D. S. 2011, MNRAS, 417, 88

Koch, D. G., Borucki, W. J., Rowe, J. F., et al. 2010, ApJ, 713, 131

Loeb, A. & Gaudi, B. S. 2003, ApJ, 588, 117

Maxted, P. F., Marsh, T. R., & North, R. C. 2000, MNRAS, 317, 41

Mayor, M. & Queloz, D. 1995, Natur, 378, 355

Mazeh, T. & Faigler, S. 2010, A&A, 521, 59

Mazeh, T., Nachmani, G., Sokol, G., Faigler, S., & Zucker, S. 2012, A&A, 541, 56

Mislis, D., Heller, R., Schmitt, J. H. M. M., & Hodgkin, S. 2012, A&A, 538, 4

Morris, S. L. 1985, ApJ, 295, 143

O'Donovan, F. T., Charbonneau, D., Mandushev, G., et al. 2006, ApJ, 651, 61

Pfahl, E., Arras, P., & Paxton, B. 2008, ApJ, 679, 783

Quintana, E. V., Rowe, J. F., Barclay, T., et al. 2013, ApJ, 767, 137

Rybicki, G. B. & Lightman, A. P. 1979, Radiative Processes in Astrophysics, (New York, NY: Wiley-Interscience Publication)

Santerne, A., Moutou, C., Barros, S. C. C., et al. 2012, A&A, 544, 12

Shporer, A., Jenkins, J. M., Rowe, J. F., et al. 2011, AJ, 142, 195

Snellen, I. A. G., de Mooij, E. J. W., & Albrecht, S. 2009, Natur, 459, 543

Sudarsky, D., Burrows, A., Hubeny, I., & Li, A. 2005, ApJ, 627, 520

Szabó, G. M., Szabó, R., Benko, J. M., et al. 2011, ApJ, 736, 4

Van Eylen, V., Kjeldsen, H., Christensen-Dalsgaard, J., & Aerts, C. 2012, AN, 333, 1088

Welsh, W. F., Seager, S., Fortney, J. J., et al. 2010, BAAS, 42, 318

Winn, J. N., Johnson, J. A., Albrecht, S., et al. 2009, ApJ, 703, 99

Wolszczan, A. & Frail, D. A. 1992, Natur, 355, 145

Hugo Barbier: Departamento de Física, Facultad de Ciencias, Escuela Politécnica Nacional, Quito, Ecuador (hugo.barbier@epn.edu.ec).

Ericson D. López: Observatorio Astronómico de Quito, Escuela Politecnica Nacional and Departamento de Física, Facultad de Ciencias, Escuela Politécnica Nacional, Quito, Ecuador (ericsson.lopez@epn.edu.ec).

Revista Mexicana de Astronomía y Astrofísica, **57**, 133–145 (2021)

https://doi.org/10.22201/ia.01851101p.2021.57.01.09

X-RAY FLUX AND SPECTRAL VARIABILITY OF BL LACERTAE OBJECTS MRK 421, MRK 501, AND 1ES1426+428 WITH SUZAKU SATELLITE

Saad, A. Ata[1], Nasser, M. Ahmed[1], Ahmed M. Abdelbar[2], and Beheary, M. M[2]

Received July 13 2020; accepted October 23 2020

ABSTRACT

We present a detailed spectral study of Suzaku observations of three blazars (Mrk 421, Mrk 501, and 1ES1426+428). The X-ray properties of our sample are derived by extracting the BL Lacertae sample spectra, and fitted by five models. The fit was in the soft X-ray band (0.8 - 10.0 keV). These models give similar results. By comparing the fits from the different models, we find that the (zbremss+zpowerlw) model is the best one to represent the data. An F-test is applied to compare the (zbremss+zpowerlw) model with the simple one zpower law. To test the X-ray variability of our BL Lacertae sample, we fit their spectra extracted from the same instrument with the same procedure by the same model to estimate their X-ray flux and luminosity. The estimated fluxes are compared to check their variability. We find that the flux variability ranges are 3.06, 0.12, $0.37 \times 10^{-10}\,\mathrm{erg\,s^{-1}\,cm^{-2}}$ for Mrk 421, Mrk 501, and 1ES1426+428, respectively.

RESUMEN

Presentamos un estudio espectroscópico de tres blazares (Mrk 421, Mrk 501, y 1ES1426+428) a partir de observaciones con el Susaku. Derivamos las propiedades en rayos X extrayendo espectros muestra de los BL Lacertae, y ajustamos cinco modelos en la banda de rayos X suaves (0.8 - 10.0 keV). Los modelos dan resultados similares; al compararlos, encontramos que el modelo (zbremss+zpowerlw) es el que mejor representa los datos. Aplicamos una prueba F para comparar el modelo (zbremss+zpowerlw) con una ley de potencias sencilla. Para estudiar la variabilidad en rayos X de nuestra muestra de BL Lacertae, ajustamos espectros extraídos con el mismo instrumento e iguales procedimientos y modelo para estimar el flujo en rayos X y la luminosidad. Comparamos los flujos para verificar su variabilidad. Encontramos una variación de los flujos de 3.06, 0.12, $0.37 \times 10^{-10}\,\mathrm{erg\,s^{-1}\,cm^{-2}}$ para Mrk 421, Mrk 501, y 1ES1426+428, respectivamente.

Key Words: BL Lacertae objects: general — BL Lacertae objects: individual: Mrk 421, Mrk 501, 1ES1426+428 — galaxies: active — galaxies: nuclei — X-rays: galaxies

1. INTRODUCTION

Blazars are a subcategory of the radio-loud active galactic nuclei (AGNs) characterized by a relativistic jet aligned close to the observer's line of sight (Urry & Padovani 1995). Most of the γ-ray emitting AGNs are blazars with more than 1500 objects known at GeV energies and more than 60 systems known at TeV energies. These galaxies are called AGNs, the most luminous objects in the universe across all wavebands of electromagnetic radiation from radio to γ-rays. The emitted radiation does not originate from the normal stars or thermal interstellar gas. This extreme energy is of non-thermal origin and comes mainly from the central few parsecs of the galaxies (accretion disc around a black hole). This non-thermal emission from AGNs is distinguished by relativistic electrons ($v \approx$ c) resulting from physical processes such as inverse Compton and synchrotron radiation.

Blazars, on the other hand, are defined as strongly polarized and highly variable compact radio

[1]Astronomy Department, National Research Institute of Astronomy and Geophysics (NRIAG), Helwan, Cairo, Egypt.
[2]Department of Astronomy and Meteorology, Faculty of Science, Al-Azhar University, Cairo, Egypt.

sources, and are separated into (i) BL Lacertae objects (from the name of one of its members, BL Lacertae) and (ii) flat-spectrum radio quasars (FSRQ) based on the strengths of their emission lines. Both of them show very different optical spectra even if, at other wavebands, they are similar. Flat-spectrum radio quasars have strong, broad emission lines at optical wavelengths, while BL Lacs show at most weak emission lines, occasionally display absorption features, and can also be completely featureless. Compact radio cores, flat radio spectra, strong rapid variability, superluminal motion, high-polarization (> 3 percent), and high brightness temperatures, are commonly found in both BL Lacs and FSRQs.

Astronomers initially thought that BL Lacs were stars whose brightness varied, variable stars, and so were given variable star designations. Later, astronomers discovered that BL Lacertae objects were AGNs, and they were a subclass of blazars, hosted by massive elliptical galaxies, the emission of which was controlled by a relativistic jet closely aligned with the line of sight. This successfully interprets their prominent features, like a non-thermal continuum emission across the whole spectrum and strong flux variability in all spectral bands (Massaro et al. 2011). One thing that roughly all AGNs have in common is a strong X-ray component (Elvis et al. 1978).

These objects are characterized by the absence of spectral lines. In general, the most distinctive characteristic of the BL Lacs is the weakness or absence of spectral lines that historically hindered the identification of their nature and thereafter proved to be a hurdle in the determination of their distance. We think the reason for this is a combination of spectral models and insufficiently precise calibration of the instruments. The cause of the lack of emission lines in BL Lacs has been the subject of much debate for the past thirty to forty years. The most commonly used explanation (Blandford & Rees 1978) is that BL Lacs are viewed close to the axis of a relativistic jet. The synchrotron radiation from this jet is Doppler boosted, increasing its intensity so that it swamps the continuum and line emission that would otherwise be visible.

The spectral energy distributions (SED) of BL Lacertae objects appear to be dominated by synchrotron emission at radio to ultraviolet energies (up to X-ray energies for X-ray selected objects) and by inverse-Compton emission at higher energies, and are characterized by two distinct components or humps in the $\nu F_\nu - \nu$ representation: (1) the low-energy component, which is commonly interpreted as being due to synchrotron emission of ultra-relativistic jet electrons and peaks in the infrared to X-ray range (The low-energy peak is well understood to be caused by the synchrotron emission from relativistic electrons in the jet); (2) the high-energy component, which peaks in the γ-ray range, most widely believed to be due to inverse-Compton scattering of low-energy photons by the synchrotron-emitting electrons (SEE).

The study of X-ray variability is useful for understanding the physical mechanisms. Worrall & Wilkes (1990) found that a single power law model with spectral index ≈ 1.0 provided acceptable fits to the X-ray spectra of more than 20 BL Lac objects observed by the Einstein Observatory. The X-ray spectra of many BL Lac objects in the BeppoSAX satellite were well described either by a single power law or by a broken power law (Beckmann et al. 2002).

In recent studies, X-ray spectra of blazars were found at high energies and were better fitted with a log-parabola (LP) model e.g., (Giommi et al. 2002; Donato et al. 2005; Tramacere et al. 2007). The log-par (LP) model was first used by Landau et al. (1986) to describe BL Lac objects' synchrotron emission best, but they did not provide any physical explanation of the model. Later, Massaro et al. (2004a,b, 2006) described the X-ray spectra of BL Lac objects Mrk 421 and Mrk 501 in terms of the curved logpar (LP) model and also expressed this model in terms of statistical particle acceleration by assuming that the probability of an increase in the energy of an emitting particle is a decreasing function of its energy. Through a recent study with the Swift satellite, Wierzcholska & Wagner (2016) found that the log-par model well describes most of the X-ray spectra of TeV-emitting blazars.

In these objects, X-ray and gamma-ray luminosities result from synchrotron radiation and inverse Compton scattering of photons on ultra-relativistic electrons, respectively. Analysis of their variability at high energies is an important method for studying the jet plasma and particle acceleration processes' dynamics e.g., (Kataoka et al. 2001). Blazar variability is one of the most puzzling cases in the field, because it requires large energy outputs within small physical scales, and these emission regions are very close to the supermassive black hole (SMBH). This paper studies the X-ray properties and spectral variability of three BL Lacertae objects, Mrk 421, Mrk 501, and 1ES1426+428. We use all available Suzaku observations for our samples. We investigate the shapes of the soft X-ray spectra of these objects using five models. The X-ray properties and variability are investigated in the energy range of 0.8 - 10.0 keV.

This paper is organised as follows. In § 2, we describe the blazars sample (MRK 421, MRK 501, and 1ES1426+428). In § 3, we describe the X-ray data reduction and analysis of the archival Suzaku observations. In § 4, we focus on results and discussion. Finally, in § 5, we present a summary of this work.

2. BLAZARS SAMPLE

In this paper, we study the objects Mrk 421, Mrk 501, and 1ES1426+428, hosted by elliptical galaxies at a redshift of $z = 0.031$, $z = 0.033$, and $z = 0.129$, respectively, with apparent magnitudes(v) 14.4, 13.7, 16.95 magnitudes. Mrk 421 and Mrk 501 are brightest high frequency-peaked BL Lac hosts known so far, and they were classified within the high-energy peaked BL Lacertae objects (HBLs) scheme (Rector et al. 2003; Giommi et al. 1995). Also, Mrk 421 and Mrk 501 are massive, luminous, and close elliptical galaxies (Ulrich et al. 1975). Most of the extragalactic sources from which X-ray and gamma-ray fluxes have been detected belong to the category of HBLs. These sources have higher X-ray luminosities than the very high energy (VHE) γ ray energy output, making them the most valuable objects for studying the characteristic spectral and temporal variations in the region of the synchrotron peak of the spectral energy distribution. The object 1ES 1426+428 belongs to this category (HBLs)(Costamante & Ghisellini 2002; Falcone et al. 2004).

Various X-ray instruments have detected these objects: Fermi, ASCA, Chandra, ROSAT, Swift, XMM-Newton, NuSTAR, Suzaku (this paper), BeppoSAX, and EXOSAT, to name just a few. The BL Lacertae objects Mrk 421, Mrk 501, and 1ES1426+428 are strong X-ray sources but confined mainly in the soft part of its X-ray spectrum (Einstein, ROSAT, RXTE, BeppoSAX, Suzaku, and XMM-Newton). These objects are similar to each other in that their lower energy component is in the X-ray band, while the higher energy peaks are in the TeV bands.

2.1. *Mrk 421*

The Mrk 421 object (RA = $11^h04^m27.3^s$; Dec = $+38°12'31.8''$), was detected in an ultra-violet survey (Markaryan & Lipovetskii 1972). It is about 397 million light-years (redshift: $z = 0.031$ corresponds to 122 Mpc) to 434 million light-years (133 Mpc) from the Earth. It was discovered as the first extragalactic object at VHE (Punch et al. 1992). Mrk 421 is one of the blazars closest to Earth, making it one of the brightest BL Lacs in the night sky. Mrk 421 is the brightest blazar at X-ray and UV wavelengths (Brinkmann et al. 2001). It is classified as the high-energy-peaked BLLac object (HBL) because of the synchrotron hump peaks at soft X-rays. Mrk 421 also had an outburst in 2001 and is monitored by the Whole Earth Blazar Telescope project. Due to its brightness (around 13.3, max. $\approx$ 11.6, and min. $\approx$ 16 magnitudes), the object can also be viewed by amateurs with smaller telescopes. The broadband emission observed from blazars spans all wavebands from radio to VHE ($E > 100$ GeV) γ-rays. Powerful flux variations on different time-scales were observed from many AGNs.

2.2. *Mrk 501*

Mrk 501 is a BL Lacertae object (RA = $16^h53^m52.2^s$; Dec = $+\,39°45'36.6''$); at $z = 0.033$, it was first cataloged in an ultraviolet survey (Markaryan & Lipovetskii 1972). It is one of the brightest X-ray sources in the sky and has been observed by RXTE to display significant X-ray variability up to 20 keV (Gliozzi et al. 2006). As previously observed in the X-ray band (Kataoka et al. 1999), it showed a more difficult trend when it was brighter during this campaign.

Mrk 501 emits bright X-rays and very-high-energies; it is the second most observed blazar after Mrk 421. In 2012, nearly 25 instruments took part in a three-month multiwavelength campaign to observe Mrk 501, and this included the FACT, MAGIC, and VERITAS Cherenkov telescopes. Mrk 501 is the third TeV blazar with a known GeV component. Previous multiwavelength observations of Mrk 501 showed well-correlated bursts at X-ray and TeV energies, with no significant activity at GeV energies. The flux of Mrk 501 showed, occasionally, ultrafast variability, and yet we do observe broad emission lines, indicating that it has a massive black hole and a very weak disc. The BL Lacertae object Mrk 501 is an excellent object to study blazar phenomena because it is bright and nearby, which permits significant detections in relatively short observing times at essentially all energy bands.

2.3. *1ES1426+428*

1ES1426+428 is a BL Lacertae object (RA = $14^h28^m32.6^s$; Dec = $+42°40'21.05''$), at a comparatively high-redshift ($z = 0.129$), regarding the other two sources for the study of the absorption of the TeV photon flux, it was first discovered by the high energy astronomy observatories (Wood et al. 1984), in the medium X-ray band (2.0 - 6.0 KeV).

TABLE 1

THE SUZAKU OBSERVATIONS OF MRK 421, MRK 501, AND 1ES1426+428

Object	RA	Dec	z	Obs. ID	Obs. Date yy mm dd	MJD	Exposure time (s)
Mrk 421	$11^h04^m27.3^s$	$+ 38°12'31.8''$	0.031	701024010	2006-04-28	53853	30008
				703043010	2008-05-05	54591	136003
				703020010	2008-12-03	54803	87943
Mrk 501	$16^h53^m52.2^s$	$+ 39°45'36.6''$	0.033	701027010	2006-07-18	53934	35842
				703046010	2009-03-23	54913	57258
1ES1426+428	$14^h28^m32.6^s$	$+ 42°40'21.05''$	0.1292	701026010	2006-06-16	53902	43069
				703063010	2008-06-05	54622	85058

X-ray observations are especially significant for observations of high-peaked BL Lac objects since the synchrotron component's peak lies in the band covered by X-ray detectors (e.g., Suzaku observations of 1ES1426+428 is an X-ray-selected, high-peaked, BL Lac object with an intense X-ray flux (Remillard et al. 1989). The object 1ES1426+428 is a classical X-ray-selected BL Lac object (Giommi et al. 1995), and one of the six BL Lac objects (out of 26 extragalactic objects) detected in the extreme ultraviolet band with the Extreme UV Explorer (EUV E) (Marshall et al. 1995; Fruscione 1996).

3. DATA REDUCTION AND ANALYSIS

3.1. *Data Reduction*

Our BL Lacertae sample has been targeted by many X-ray satellites. We preferred to use the archival data made by the Suzaku observatory. We used data from Suzaku-XIS due to its excellent detector sensitivity, a wide field of view that allows for good background subtraction, and the ability to continuously track the source. The Suzaku satellite orbit is circular, with a height of 568-km from the Earth, an inclination angle of 31.9°, and an orbital period of about 96 minutes. The Suzaku satellite carries four X-ray telescopes sensitive in the $0.2 - 12.0$ keV band (Mitsuda et al. 2007), including CCD cameras in the focal plane, in addition to a nonimaging instrument HXD; (Takahashi et al. 2007), sensitive in the $10.0 - 600.0$ keV band, composed of a Si-PIN photodiode detector (probing the $10.0 - 60.0$ keV band) and a GSO scintillator detector (sensitive above 30 keV). The hard X-ray Detector (HXD) includes a broad energy band of $10.0-700.0$ keV. Also, the HXD has such a low background that its sensitivity is higher than any past missions in the hard X-ray band. The XIS is an X-ray CCD camera which covers an energy range of 0.2-12.0 keV with typical energy resolution (Koyama et al. 2007). XIS has a high energy resolution, a large effective area, and a low and stable background (Yamaguchi et al. 2006). Simultaneous observations with the XIS CCD are very effective to constrain the time variability of the broad-band spectrum, which is especially important for active galaxies (Fukazawa et al. 2009).

Objects Mrk 421, Mrk 501, and 1ES1426+428, have been observed with the Suzaku X-ray satellite (Mitsuda et al. 2007), where the object Mrk 421 has three observations and the objects Mrk 501, 1ES1426+428 have two observations; see Table 1. The observations started with Suzaku's X-ray imaging spectrometer (XIS); XIS has CCD devices with three front-illuminated and one back-illuminated CCD cameras at the focal plane of the four X-ray telescopes XRTs; (Serlemitsos et al. 2007), and is sensitive in the energy range $0.2 - 12.0$ keV. We downloaded these observations from the Suzaku data archive center. During these observations of the keV blazar, XIS was operated in the 3×3 and 5×5 observation modes. The high throughput of the X-ray telescopes and the instrument's spectral capabilities allow an uninterrupted temporal and spectral study of the source with unprecedented time resolution. The Suzaku observations of our samples are listed in Table 1. The columns list the object name, in addition to the right ascension, declination, redshift, Obs.ID, observation date, modified Julian date(MJD), and total exposure time.

3.2. *X-ray Spectra Extraction*

Extraction of the data has been done by using FTOOLS (General Package of Software to Manipulate FITS Files), with the latest version of FTOOLS, 6.26.1, and using version of HEAsoft 6.26.1; the spec-

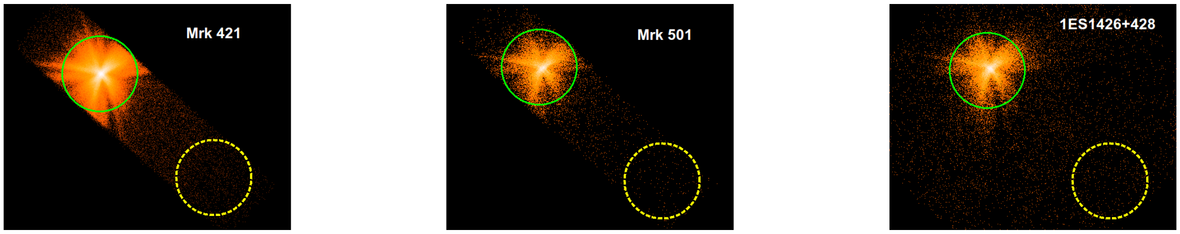

Fig. 1. The source and background regions are marked by solid and dotted circles, respectively. The size of both circles is 140 arcsec. North is up, and east is to the left. The color figure can be viewed online.

tral analysis is performed in XSPEC (X-ray spectra analysis package) version 12.10.1p. We also used the HEASOFT software package and Suzaku calibration database (CALDB). The subsequent data reduction includes cleaning hot and flickering pixels, filtering out the high-background periods, which was performed using the tool XSELECT. We also selected good time intervals, except for periods of high background (when the satellite crosses the South Atlantic Anomaly, or when the object is too close to the rim of the Earth). However, we extracted source events in a circle around the source with a radius of ≈ 140 arcsec. We also performed the extraction of background events within a radius of ≈ 140 arcsec from a region devoid of any obvious X-ray sources (see Figure 1).

Here we have taken the background from the distributed blank sky images in a region corresponding to the one used to extract source counts. The background has been preferably overestimated from the same image in a different location (see Figure 1). Since the background flux is never higher than 10 percent of the source$'s$ flux, the secular modulation has a negligible effect on the spectral results. As the sources were well centered in the Suzaku observing region, we used corresponding standard response (RMF) matrices by utilizing the tool xisrmfgen, picking the one closest in time to each observation. The auxiliary response files (ARFs) were generated using the tool xissimarfgen. We used the GRPPHA tool for grouping the data to get enough S/N or a suitable number of counts (minimum 50 counts) in each channel.

BL Lacertae objects are very strong variable emitters at all wavebands, especially in the X-ray band. Generaly, the continuum of these systems can be fitted well by a power law ($N(E) = kE^{-\Gamma}$), where Γ is the index. We used more than one model to determine any calibration problems or instrument-specific problems that might have occurred during the observations. In our work, all observations were reduced and analysed separately in the same way. The best spectral model for each source was determined in a procedure explained in § 4. During our investigation of the Suzaku data, we performed a spectral analysis to check for the presence of spectral variability. In our analysis, we ignored bad channels in the observations. We used χ^2 statistics, and we quote the errors of the best-fitting parameters. We present a detailed study of the X-ray spectrum of the three objects (and their parameters) in this work. We extracted spectra from event data of each observation using the XSELECT package and analysed them with the XSPEC package (Arnaud 1996).

3.3. *X-Ray Spectral Analysis*

In this section, we perform a spectral fitting of our BL Lacertae in the 0.8 - 10.0 keV band using the XSPEC package. We use χ^2 statistics for all model fitting and error estimation. The Suzaku-XIS0, XIS1, XIS2 (if available), and XIS3 image of Mrk 421, Mrk 501, and 1ES1426+428 are used in all models. To find the best fitting model, we fitted five different models or combinations. Then, we compared the output of χ^2 to determine the best. In each fitting process, we determine the X-ray properties of the sample that are provided by the fitting models. The spectral models used in our analysis are described below.

3.3.1. *zpower Law Model*

Power law (PL) is a simple photon power law. For zpowerlw the formula and corresponding parameters are shown in equation (1).

$$A(E) = K[E(1+z)]^{-\Gamma}, \tag{1}$$

where the parameters E, Γ, z, and K are the photon energy, index of power law (dimensionless), redshift, and normalization (photons/keV/cm^2/s at 1 keV), respectively. We performed a simultaneous spectral fitting of XIS0, XIS2 (if available), XIS3, and XIS1 data for each observation. We found that the zpowerlw model is flexible to adjust the parameters

TABLE 2

FIT RESULTS FOR A zpowerlw MODEL

Blazer name	Obs.ID	Index (Γ)	Normalization (K)	χ^2/dof (χ^2_{red})
Mrk 421	701024010	2.08±8.38E-04	0.25±2.80E-04	10778.92/9298 (1.35)
	703043010	2.40±5.01E-04	0.31±1.74E-04	14265.05/9845 (1.54)
	703020010	2.41±7.07E-04	0.24±1.94E-04	14390.64/10528 (1.46)
Mrk 501	701027010	2.30±2.12E-03	3.94E-02±1.05E-04	6549.9/6438 (1.02)
	703046010	2.20±1.96E-03	3.95E-02±9.33E-05	6259.36/5896 (1.06)
1ES1426+428	701026010	2.04±2.40E-03	1.97E-02±6.36E-04	6524.86/6298 (1.04)
	703063010	2.37±2.90E-03	1.38±4.54E-05	7769.39/7769 (1.005)

for a spectrum as in Table 2. The Suzaku spectrum was fitted with a simple absorbed power law model (constant*phabs*zpowerlaw in XSPEC). This model has been used to fit an X-ray spectrum of various BL Lacertae objects (Landt et al. 2002; Perri et al. 2003). We found that the spectra can be well fit with a simple power law model (zpowerlaw). Figure 2 shows the fitted spectra extracted from different observations of the three BL Lacertae objects.

3.3.2. *zbroken Power Law Model*

Bknpower(BPL) is a broken power law and zbknpower, a redshifted variant. The Suzaku spectrum was fitted with a simple broken power law (zbknpower) model, which is represented as constant*phabs*zbknpower and whose photon spectrum A(E) is expressed in equation (2).

$$A(E)=\begin{cases} K[E(1+z)^{-\Gamma_1}, \\ \qquad \text{if } [E(1+z)] \le E_{break}. \\ \\ K[E(1+z)^{\Gamma_2-\Gamma_1}_{break}([E(1+z)]/1keV)^{-\Gamma_2}, \\ \qquad \text{if } [E(1+z)] > E_{break}, \end{cases} \quad (2)$$

where the parameters E, Γ_1, E_{break}, Γ_2, z, and K are the photon energy in the rest frame, power law index for $E < E_{break}$, break point for the energy in keV, power law index for $E > E_{break}$, redshift, and normalization (photons/keV/cm^2/s at 1 keV), respectively. The Suzaku spectrum was fitted with a broken power law model (constant*phabs*zbknpower in XSPEC).

3.3.3. *zcutoff Power Law Model*

The zcutoffpl is a variant which computes a redshifted spectrum using the formula and parameters for the redshifted variant in equation (3).

$$A(E) = K[E(1+z)]^{-\Gamma}\exp(-E(1+z)/\beta), \quad (3)$$

where E is the photon energy, Γ is the power law photon index, β is the e-folding energy of exponential roll-off (in keV), z is the redshift, and K is the normalization in the unit of photons/keV/cm^2/s at 1 keV in the source frame. We used a zcutoff power law model to fit the spectra in the 0.8 - 10.0 keV energy range. We therefore substituted the power law component with a cutoff power law (constant*phabs*zcutoffpl in XSPEC). The spectrum was well fitted by a single power law model with an exponential cutoff (zcutoffpl model).

3.3.4. *zlogparabolic Model*

The logpar (log-parabolic blazar model) is a power law with an index that varies with energy as a log parabola. The zlogpar variant computes a redshifted spectrum (see, for instance, Lloyd-Jones et al. 2004). It is known that the X-ray spectra of many keV HBLs are described well by the zlogpar(logpar) model defined in equation (4). (Massaro et al. 2004a,b; Tramacere et al. 2007).

$$A(E) = K([E(1+z)]/E_0)^{(-a-blog([E(1+z)]/E_0))}, \quad (4)$$

where the parameters a, b, E_0, z, and K are the spectral slope (given by the log-derivative) at the pivot energy $E_0 = 10.0$ keV, curvature term, fixed pivot energy (best near low end of energy range), redshift and normalization, respectively. The zlogpar model has a description of X-ray spectral shapes in HBL-type AGNs (e.g., (Perlman et al. 2005)). An χ^2 test to the shape $\mathrm{d}N/\mathrm{d}E \propto E^{[-a-b\log(E)]}$ of the XIS spectrum revealed a statistically comparable goodness of fit compared to other models representing up to the highest reported energy point for the sources.

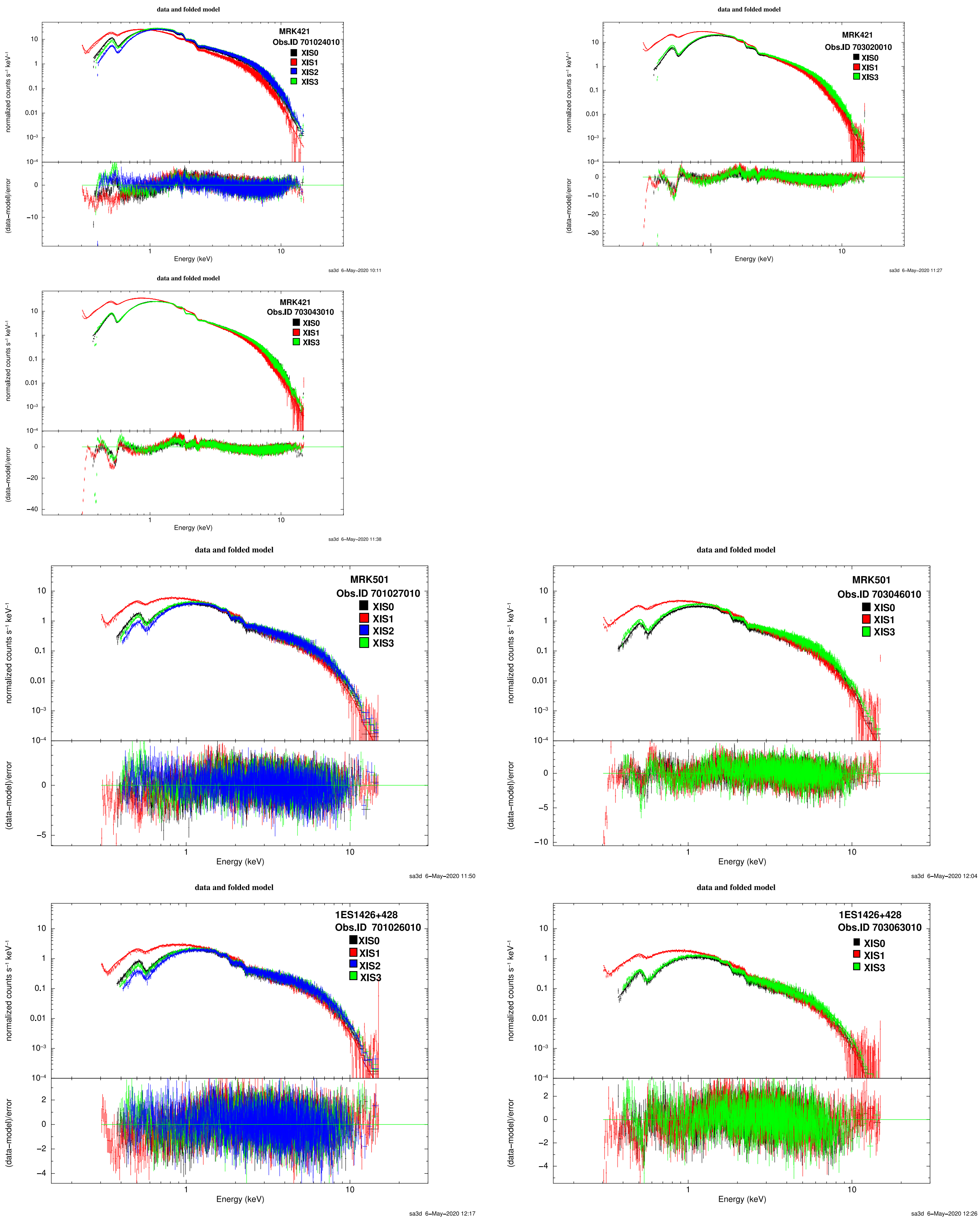

Fig. 2. X-ray spectra fitted with the power law model are shown in each figure, in the energy range 0.8 - 10.0 keV of the three sources. The name, instrument, and ID of each object's observation are also provided in each figure's upper right corner. The color figure can be viewed online.

TABLE 3

FIT RESULTS FOR A zbknpower MODEL

Blazer name	Obs.ID	Index Γ_1	Index Γ_2	E_{break} (keV)	Normalization	χ^2/dof (χ^2_{red})
Mrk 421	701024010	1.99±1.80E-03	2.25±3.59E-03	2.81±2.54E-02	0.25±2.97E-04	9432.552/8296 (1.137)
	703043010	2.32±9.43E-04	2.62±2.36E-03	2.92±1.35E-02	0.30±1.84E-04	11807.35/8143 (1.45)
	703020010	2.32±1.29E-03	2.66±3.54E-03	3.007±1.85E-02	0.23±2.03E-04	9489.396/7266 (1.306)
Mrk 501	701027010	2.25±4.32E-03	2.40±8.73E-03	2.63±8.67E-02	3.88±1.11E-04	6248.472/6236 (1.002)
	703046010	2.14±3.56E-03	2.37±1.02E-02	3.20±7.87E-02	3.87E-02±9.85E-05	5566.608/5394 (1.032)
1ES1426+428	701026010	1.91±1.13E-03	2.08±4.31E-03	1.60±4.96E-02	1.92±7.14E-05	6236.208/6096 (1.023)
	703063010	2.29±5.46E-03	2.55±1.36E-02	2.87±9.06E-02	1.34E-02±4.77E-05	4093.958/4169 (0.982)

3.3.5. *(zbremsstrahlung+zpower Law) Model*

In this section, we explore the behavior of this model. A (zbremss+zpowerlw) model has been proposed to provide a better description of the parameters of the spectrum at higher energies, better than the power law) with a local index (0.8 - 10.0 keV) $\Gamma \approx 2.25$ and a plasma temperature KT ≈ 2.44. A (zbremss+zpowerlw) spectrum based on a polynomial fits the numerical values, and includes a choice of redshift. In the regions with higher temperatures, we use (constant*phabs(zbremss + zpowerlw) in XSPEC.

4. RESULTS AND DISCUSSION

4.1. *X-ray Properties*

To determine the X-ray properties of our BL Lacertae sample, we fit the extracted spectral described in the previous section by five models that describe the BL Lacertae spectra. We also compare the quality of the fit using the F-test method. The three objects that we have studied are characterized by having intrinsic spectra, which is in favor of the robustness of the model selection, and these objects are common BL Lacertae objects. The X-ray properties of each model are described as follows.

First, using our BL Lacertae objects, we applied the power-law model, and we found photon indices between 2.04 and 2.41, where in the Mrk 421 object, the photon indices change from 2.08 to 2.41 while in Garson III et al. (2010) they change from 2.2 to 2.5. Compared to the results found with Garson III et al. (2010), we found that our parameters are the best-fit parameters for this model(see Table 2), and the χ^2 value in our sample is better than that of Ushio et al. (2010)(χ^2 = 3.47). In the Mrk 501 object, the photon indices change from 2.30 to 2.20, while in Sambruna et al. (2000), they change from 2.30 to 1.8, and in 1ES1426+428 they change from 2.04 to 2.37. However, we found that a single power law cannot represent a typical X-ray spectrum of these objects, but consists of multiple components, which are a power law (zpowerlw) component, a broken power law (zbknpower), an exponential cutoff power law (zcutoffpl), a log-parabolic blazar model (zlogpar), and a zbremss+zpowerlw model. Therefore, among the several models that describe the X-ray spectra, the one best fitting our data is achieved by five models we selected in XSPEC. We extracted recent results of the parameters and reduced the error rates. After we found that the X-ray spectrum of the sources was well suited to the simple energy law model in the data, we found that the χ^2 values were greater than the values for the other models, and the model was rejected. However, large values of χ^2 are partially caused by the XIS's insufficient calibration rather than by the inappropriate modeling of the spectra.

Second, we used a broken power law (constant*phabs*zbknpower in XSPEC) model for our data. We performed a spectral fit for the sources and the excellent spectrum from 0.8 - 10.0 keV allowed us to make predictions of the X-ray flux. A broken power-law model provides a better representation of the data: χ^2/dof = 1.1, 1.4,1.3 for Mrk 421 and 1.002, 1.032 for Mrk 501, and 1.023,0.982 for 1ES1426+428, with the photon indices between 1.99 - 2.66, 2.14 - 2.40, and 1.91 - 2.55 respectively, and the break photon energy as in Table 3. Compared to the previous results, as in Garson III et al. (2010), Ushio et al. (2010), Acciari et al. (2011), Anderhub et al. (2009), we found the best-fit parameters. The start and the end of the observations for the three sources are as detailed in Table 3. We found that the break energy (E break) ranges from 1.6 to 3 for the observations, which is consistent with previous studies of BL Lacertae objects (e.g. Reimer

TABLE 4

FIT RESULTS FOR A zcutoffpl MODEL

Blazer name	Obs.ID	Index Γ	High-E-Cut (keV)	Normalization	χ^2/dof (χ^2_{red})
Mrk 421	701024010	1.91±2.89E-03	14.82±0.23	0.27±3.41E-04	9699.193/8297 (1.169)
	703043010	2.20±1.69E-03	12.20±9.72	0.33±2.39E-04	11751.792/8144 (1.443)
	703020010	2.21±2.42E-03	10.98±0.113	0.26±2.77E-04	9396.231/7267 (1.293)
Mrk 501	701027010	2.20±7.09E-03	24.27±1.58	4.09E-02±1.32E-04	6255.711/6237 (1.003)
	703046010	2.06±6.67E-03	17.56±0.76	4.13E-02±1.16E-04	5573.035/5395 (1.033)
1ES1426+428	701026010	1.95±8.17E-03	26.15±2.02	2.03±7.51E-05	6273.813/6097 (1.029)
	703063010	2.19±9.88E-03	13.62±0.71	1.46E-02±6.19E-05	6976.41/7170 (0.973)

TABLE 5

FIT RESULTS FOR A zlogpar MODEL

Blazer name	Obs.ID	α	β	Normalization	χ^2/dof (χ^2_{red})
Mrk 421	701024010	2.09±8.72E-04	0.21±3.29E-03	4.35±4.86E-05	9541.55/8297 (1.15)
	703043010	2.43±5.42E-04	0.24±1.95E-03	4.06E-02±2.29E-05	11890.24/8144 (1.46)
	703020010	2.44±7.72E-04	0.26±2.77E-03	3.12±2.53E-05	9883.12/7267 (1.36)
Mrk 501	701027010	2.32±2.23E-03	0.13±8.19E-03	5.42E-3±1.51E-05	6230.763/6237 (0.999)
	703046010	2.21±2.05E-03	0.17±7.66E-03	5.96E-03±1.40E-05	5578.43/5395 (1.034)
1ES1426+428	701026010	2.05±2.47E-04	0.13±9.35E-03	3.40±1.11E-05	6243.328/6097 (1.024)
	703063010	2.39±3.16E-03	0.22±1.14E-02	1.80±6.09E-06	6990.75/7170 (0.975)

et al. 2008; Ushio et al. 2010, 2009; Anderhub et al. 2009). We noted that the data could be fitted satisfactorily by a broken power law model.

Third, we fitted the spectrum of the three objects between 0.8 keV and 10.0 keV and found that the spectrum, modeled with a cutoff power law (constant*phabs*zcutoffpl in XSPEC) model, provided the statistically most favored description of the data in the examined datasets. The high-energy cutoff (High-E-Cut) for our observations = 10.98 - 26.15 keV and the photon index = 1.91 - 2.21. For cutoff power law fits the average reduced χ^2 is 1.3 for Mrk 421, 1.018 for Mrk 501, and 1.001 for 1ES1426+428, while broken power law fits produced average reduced χ^2 of 1.29, 1.01, and 1.01 respectively. We note that these values are very close to the best-fit parameters of the broken power law model (see Table 4).

Fourth, besides both broken power law and cutoff power law, we attempted to fit the Suzaku spectra with a log-parabola model, as this model allows the spectral index to vary as a function of energy according to equation 4 The log-parabolic model is characterized only by the parameter β; a good estimate of β can be obtained when its value is small. In several studies, the X-ray spectra are described well with the curved log-parabola model; As in Massaro et al. (2004a), Massaro et al. (2004b) analysed the X-ray spectra for Mrk 421 and Mrk501 and found that the log-parabola model was the best model for characterizing their spectra for different activity states, where the β values varied from 0.341 to 0.48 while in our data they vary from 0.13 to 0.26. In Table 5 all parameters were appropriate simultaneously. Compared to the parameters in Furniss et al. (2015), we find that good fits were produced with the log-parabola model. In BL Lacs the X-ray radiation is due to synchrotron radiation and inverse Compton scattering (Maraschi et al. 1999; Tavecchio et al. 2001; Massaro et al. 2004a,b; Lichti et al. 2008; Giommi et al. 2012). Here, the non-thermal emissions from our data can be described by synchrotron radiation (relativistic electrons + magnetic field $\rightarrow$ weak photons in the radio waveband).

Fifth, the (zbremss+zpowerlw) model was found to fit the data better in each observation and was therefore used to compute fluxes in various subbands (as in § 4.2). In previous models, we found

TABLE 6

FIT RESULTS FOR A zbremss+zpowerlw MODEL

Blazer name	Obs.ID	Index Γ	KT	Normalization	χ^2/dof (χ^2_{red})
Mrk 421	701024010	2.05±5.16E-03	2.87±6.98E-02	0.19±1.11E-03	9291.52/8296 (1.12)
	703043010	2.42±2.61E-03	2.33±2.52E-02	0.25±5.58E-04	11255.91/8143 (1.37)
	703020010	2.45±4.13E-03	2.49±3.57E-02	0.19±5.81E-04	9327.82/7266 (1.27)
Mrk 501	701027010	2.28±9.66E-02	2.03±0.16	3.46E-02±4.05E-04	6211.056/6236 (0.996)
	703046010	2.22±1.20E-02	3.03±0.21	3.27E-02±3.14E-04	5555.82/5394 (1.030)
1ES1426+428	701026010	1.98±1.48E-02	2.07±0.14E-02	1.59E-02±3.95E-04	6224.016/6096 (1.021)
	703063010	2.37±1.50E-02	2.28±0.17E-02	1.12±1.49E-04	6968.268/7169 (0.972)

TABLE 7

F-TEST RESULTS OF COMPARING zbremss+zpowerlw AND zpower law FOR DIFFERENT OBSERVATIONS IN OUR SAMPLES

Blazer name	Obs.ID	χ^2_2 Bremss+PL	DOF_2 Bremss+PL	χ^2_1 PL	DOF_1 PL	F-test	P_{null}*
Mrk 421	701024010	9291.52	8296	10778.92	9298	1.32	2.98×10^{-10}
	703043010	11255.91	8143	14265.05	9845	1.27	9.58×10^{-12}
	703020010	9327.82	7266	14390.64	10528	1.20	5.80×10^{-11}
Mrk 501	701027010	6211.056	6236	6549.9	6438	1.68	8.64×10^{-9}
	703046010	5555.82	5394	6259.36	5896	1.36	5.08×10^{-7}
1ES1426+428	701026010	6224.016	6096	6524.86	6298	1.45	3.23×10^{-5}
	703063010	6968.268	7169	7769.39	7769	1.34	1.49×10^{-8}

*Notes. P_{null} is the null hypothesis probability.

the parameters and the spectra extracted from our observations well fit with a t model. The values of the photon index (Γ), normalization (K), and KT are listed in Table 6. We found a significantly improved χ^2 value for these sources when fitting to a (zbremss+zpowerlw) model compared to other models. The spectrum is well represented by a (zbremss+zpowerlw) model (reduced $\chi^2 = 1.12$, 0.996, 0.972) with photon index $\Gamma = 2.05$, 2.28, 2.37.

For all Suzaku observations, the three sources' X-ray spectra are best represented with a (zbremess+zpowerlw) model. All of the models tested are consistent with the fitting parameters; still, the compared models must be nested, and the null values of the additional parameters should not be on the boundary of the set of possible parameter values, according to Protassov et al. (2002). Therefore, in order to assess the significance of the parameter values, we compared the zpower law model with the (zbremess+zpowerlw) one using an F-test. The F-test gives the probability that the (zbremess+zpowerlw) model that has the smallest reduced χ^2 is a chance improvement compared to the zpower law model. A statistical F-test using the χ^2 and degrees of freedom (dof) of the zpower law versus (zbremess+zpowerlw) fit results in F-statistics of the observations corresponding to probabilities of being consistent with the null zpower law hypothesis; see Table 7. The general limit is 10^{-4}. If the F-test gives a value much lower than this limit, then the second model is statistically better than the first (Egron & Jeanne 2013); therefore, in our work, we found F-test values much smaller than this limit as in Table 7.

In this section, we successfully fitted the X-ray spectrum with five models, and we found photon indices between 2.08 - 2.41, 2.2 - 2.3, and 2.04 - 2.37 for Mrk 421, Mrk 501, and 1ES1426+428 respectively. From these models, the change in photon indices appears to be the factor responsible for the spectral change. One of the results in this Section is that the low and high photon indices suggest that electrons form a power-law distribution of energy index ≈ 2, which is expected from the standard shock ac-

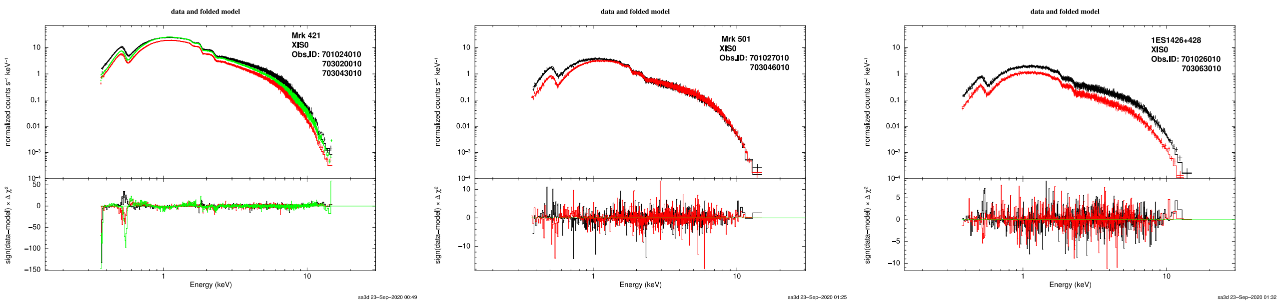

Fig. 3. XIS0 spectra of our BL Lacertae sample in the energy range 0.8-10.0 keV with the best-fit model zbremss+zpowerlw. The color figure can be viewed online.

celeration theory for both the relativistic and non-relativistic cases (Kirk et al. 2000). By comparing the χ^2 resulting from the different models, we found that the (zbremss+zpowerlw) has the best values. Therefore, we used this model combination to estimate the flux variability of our sample.

4.2. *X-ray Variability*

For the three sources of this study we used XIS0 because they are available in all observations. We created the spectrum with the same previous method (§ 3.1), using only XIS0. In the last section, we performed a spectral analysis of keV blazars obtained by Suzaku (see Table 1), where the object Mrk 421 has three observations, and the objects Mrk 501, 1ES1426+428 have two observations each. Since the X-ray spectra of blazars are often fitted to a spectral model involving a power law, a (zbremss+zpowerlw) model was proposed to better describe the blazars spectrum. In § 4.1, we successfully fitted the X-ray spectrum by the five models, and we found that the best model is (zbremss+zpowerlw). In order to show the spectral variability we perform the spectral fitting for each observation with this model. We found that the (zbremss+zpowerlw) model well fits all spectra. We derive the X-ray flux and luminosity in the energy range of 0.8 10.0 keV from the fitted spectra and their corresponding errors. The flux values estimated from different observations for each source are compared to check the X-ray variability in our BL Lacertae samples.

The spectral fluxes of the (zbremss+zpowerlw) model significantly change in the three observations of the source Mrk 421 (from 12.11 ± 0.74 to 10.95 ± 0.94, and then to $14.01 \pm 1.19 \times 10^{-10}$ erg s^{-1} cm^{-2}) and in the source Mrk 501 (from 1.85 $\pm$ 0.14 to 1.97 $\pm$ 0.14 $\times$ 10^{-10} erg s^{-1} cm^{-2}) for the two observations, and also in the source 1ES1426+428 (from 1.02 $\pm$ 0.06 to 0.65 $\pm$ 0.05 $\times$ 10^{-10} erg s^{-1} cm^{-2} for both observations) see Table 8. The flux variability is obvious in Mrk 421 and 1ES1426+428, where the variation ranges are 3.06 and 0.37 $\times 10^{-10}$ erg s^{-1} cm^{-2}, respectively. The fluxes of Mrk 501 derived from the two available observations are comparable within their error ranges. It is apparent that the spectrum changes with each observation; in Figure 3, we plot the spectra for all the observations; perhaps most striking is the fact that the spectral shapes of the objects do not vary significantly, but the photon index and flux change as listed in Table 8, where we summarize the fitting results of each observation. In Mrk 421, compared to previous literature, we found that the ranges are $3.06\times$ erg s^{-1} cm^{-2}, while in Ushio et al. (2009, 2010) they are $2.91\times$ erg s^{-1} cm^{-2}.

5. SUMMARY

In this paper we study the X-ray properties and spectral variability of three BL Lacertae objects, Mrk 421, Mrk 501, and 1ES1426+428. To achieve this work, we used all available Suzaku observations for our samples. We investigate the shapes of the soft X-ray spectra of these objects using five models. The X-ray properties and variability are investigated in the energy range of 0.8 - 10.0 keV. We use five spectral models for all available data (for the three objects), and we obtain that the absorbed single power law (constant*phabs*zpowerlaw) model fits our observations well, but the χ^2 values are greater than in the other of results. During the fitting, events with energy of 0.2 - 0.8 keV and 10.0 - 12.0 keV were excluded from the XIS data set because these channels were ignored in the spectra. The resulting spectrum was fitted with a (galactic absorption $\times$ zpowerlw). The galactic absorption parameter, N_H (hydrogen column density), was kept constant at average values of 1.94×10^{20} cm^{-2} (Mrk 421), 1.41×10^{20} cm^{-2} (Mrk 501), and 1.14×10^{20} cm^{-2} (1ES1426+428),

TABLE 8

FIT RESULTS OF DIFFERENT OBSERVATIONS FOR OUR BLAZAR SAMPLES*

Object	Obs. ID	Obs. Date yy mm dd	Index Γ	Flux erg s^{-1} cm^{-2} (10^{-10})	X-ray lumin erg s^{-1} (10^{45})	χ^2/dof
Mrk 421	701024010	2006-04-28	$2.07^{+0.01}_{-0.01}$	$12.11^{+0.001}_{-0.002}$	$2.66^{+0.003}_{-0.004}$	1.12 / 8296
	703043010	2008-05-05	$2.48^{+0.01}_{-0.01}$	$10.95^{+0.001}_{-0.002}$	$2.41^{+0.002}_{-0.004}$	1.37 / 8143
	703020010	2008-12-03	$2.45^{+0.01}_{-0.01}$	$14.01^{+0.001}_{-0.001}$	$3.08^{+0.002}_{-0.003}$	1.27 / 7266
Mrk 501	701027010	2006-07-18	$2.27^{+0.02}_{-0.02}$	$1.85^{+0.007}_{-0.006}$	$0.46^{+0.023}_{-0.017}$	0.996 / 6236
	703046010	2009-03-23	$2.22^{+0.02}_{-0.02}$	$1.98^{+0.007}_{-0.007}$	$0.49^{+0.015}_{-0.018}$	1.030 / 5394
1ES1426+428	701026010	2006-06-16	$1.96^{+0.02}_{-0.02}$	$1.02^{+0.004}_{-0.003}$	$0.22^{+0.011}_{-0.006}$	1.021 / 6096
	703063010	2008-06-05	$2.35^{+0.02}_{-0.02}$	$0.65^{+0.026}_{-0.042}$	$0.14^{+0.007}_{-0.008}$	0.972 / 7169

*These results were obtained from the zbremss+zpowerlw model.

acquired from the HI4PI map in the FTOOL. The redshifts of the systems are also fixed at the values in the literature, as listed in Table 1.

As a result of our fitting process, the X-ray properties of our sample were determined from five models, which fit well the BL Lacertae spectra. Comparing the fitting quality resulting from different models applied in our work, we found that the (zbremss+zpowerlw) model is the best one to represent the data. An F-test was applied to compare the adductive (zbremss+zpowerlw) model with the simple one, log-parabola. We also checked the variability of the soft X-ray (0.8 - 10.0 keV) flux in our BL Lacertae sample based on all avilable Suzaku observations. We extracted the spectra in the same way from the same instrument (XIS0) in the same energy band (0.8 - 10.0 keV) for each source. All available X-ray spectra were fitted simultanuosly by the same model to determine the X-ray fluxes and their errors. The estimated fluxes were compared to check their variability. We found that the flux variability ranges are $(3.06, 0.12, 0.37) \times 10^{-10}$ erg s^{-1} cm^{-2} for Mrk 421, Mrk 501, and 1ES1426+428, respectively. This yields that the most significant variation was found for Mrk 421.

We would like to thank Suzaku's team for providing their publicly available feedback and for their efforts in spacecraft operation, instrument calibration, and data processing. We would like to thank Dr. Gamal El Din Hamed for helpful suggestions that improved the paper's reading. Finally, we would also like to extend our sincere thanks to the reviewer for his/her very useful suggestions and comments, which helped to improve the paper's quality.

REFERENCES

Acciari, V. A., Arlen, T., Aune, T., et al. 2011, ApJ, 729, 2

Anderhub, H., Antonelli, L. A., Antoranz, P., et al. 2009, ApJ, 705, 1624

Arnaud, K. A. 1996, ASPC, 101, 17

Beckmann, V., Wolter, A., Celotti, A., et al. 2002, A&A, 383, 410

Blandford, R. D. & Rees, M. J. 1978, PhyS, 17, 265

Brinkmann, W., Sembay, S., Griffiths, R. G., et al. 2001, A&A, 365, 162

Costamante, L. & Ghisellini, G. 2002, A&A, 384, 56

Donato, D., Sambruna, R. M., & Gliozzi, M. 2005, A&A, 433, 1163

Egron, E. J. M. 2013, Spectral Comparisons of Neutron Star Low-Mass X-Ray Binaries with Black Hole X-Ray Binaries, Università degli Studi di Cagliari

Elvis, M., Maccacaro, T., Wilson, A., et al. 1978, MNRAS, 183, 129

Falcone, A. D., Cui, W., & Finley, J. P. 2004, ApJ, 601, 165

Fruscione, A. 1996, ApJ, 459, 509

Fukazawa, Y., Mizuno, T., Watanabe, S., et al. 2009, PASJ, 61, 17

Furniss, A., Noda, K., Boggs, S., et al. 2015, ApJ, 812, 65

Garson III, A. B., Baring, M. G., & Krawczynski, H. 2010, ApJ, 722, 358

Giommi, P., Ansari, S. G., & Micol, A. 1995, A&AS, 109, 267

Giommi, P., Massaro, E., & Palumbo, G. 2002, Blazar astrophysics with BeppoSAX ond other observatories, ASI Science Data Center, ESA-ESRIN, ed. P. Giommi, E. Massaro, & G. Palumbo, 2002babs conf.

Giommi, P., Polenta, G., Lähteenmäki, A., et al. 2012, A&A, 541, 160

Gliozzi, M., Sambruna, R. M., Jung, I., et al. 2006, ApJ, 646, 61

Kataoka, J., Mattox, J. R., Quinn, J., et al. 1999, ApJ, 514, 138

Kataoka, J., Takahashi, T., Wagner, S. J., et al. 2001, ApJ, 560, 659
Kirk, J. G., Guthmann, A. W., Gallant, Y. A., & Achterberg, A. 2000, ApJ, 542, 235
Koyama, K., Tsunemi, H., Dotani, T., et al. 2007, PASJ, 59, 23
Landau, R., Golisch, B., Jones, T. J., et al. 1986, ApJ, 308, 78
Landt, H., Padovani, P., & Giommi, P. 2002, MNRAS, 336, 945
Lichti, G. G., Bottacini, E., Ajello, M., et al. 2008, A&A, 486, 721
Lloyd-Jones, D. M., Wang, T. J., Leip, E. P., et al. 2004, Circulation, 110, 1042
Maraschi, L., Fossati, G., Tavecchio, F., et al. 1999, ApJ, 526, 81
Markaryan, B. E. & Lipovetskii, V. A. 1972, Ap, 8, 89
Marshall, H. L., Fruscione, A., & Carone, T. E. 1995, ApJ, 439, 90
Massaro, E., Perri, M., Giommi, P., & Nesci, R. 2004a, A&A, 413, 489
Massaro, E., Perri, M., Giommi, P., Nesci, R., & Verrecchia, F. 2004b, A&A, 422, 103
Massaro, E., Tramacere, A., Perri, M., Giommi, P., & Tosti, G. 2006, A&A, 448, 861
Massaro, F., Paggi, A., Elvis, M., & Cavaliere, A. 2011, ApJ, 739, 73
Mitsuda, K., Bautz, M., Inoue, H., et al. 2007, PASJ, 59, 1
Perlman, E. S., Madejski, G., Georganopoulos, M., et al. 2005, ApJ, 625, 727
Perri, M., Massaro, E., Giommi, P., et al. 2003, A&A, 407, 453
Protassov, R., Van Dyk, D. A., Connors, A., Kashyap, V. L., & Siemiginowska, A. 2002, ApJ, 571, 545
Punch, M., Akerlof, C. W., Cawley, M. F., et al. 1992, Natur, 358, 477
Rector, T. A., Gabuzda, D. C., & Stocke, J. T. 2003, AJ,125, 1060
Reimer, A., Costamante, L., Madejski, G., Reimer, O., & Dorner, D. 2008, ApJ, 682, 775
Remillard, R. A., Tuohy, I. R., Brissenden, R. J. V., et al. 1989, ApJ, 345, 140
Sambruna, R. M., Aharonian, F. A., Krawczynski, H., et al. 2000, ApJ, 538, 127
Serlemitsos, P., Soong, Y., Chan, K.-W., et al. 2007, PASJ, 59, 9
Takahashi, T., Abe, K., Endo, M., et al. 2007, PASJ, 59, 35
Tavecchio, F., Maraschi, L., Pian, E., et al. 2001, ApJ, 554, 725
Tramacere, A., Massaro, F., & Cavaliere, A. 2007, A&A, 466, 521
Ulrich, M.-H., Kinman, T. D., Lynds, C. R., Rieke, G. M., & Ekers, R. D. 1975, ApJ, 198, 261
Urry, C. M. & Padovani, P. 1995, PASP, 107, 803
Ushio, M., Stawarz, L., Takahashi, T., et al. 2010, ApJ, 724, 1509
Ushio, M., Tanaka, T., Madejski, G., et al. 2009, ApJ, 699, 1964
Wierzcholska, A. & Wagner, S. J. 2016, MNRAS, 458, 56
Wood, K. S., Meekins, J. F., Yentis, D. J., et al. 1984, ApJS, 56, 507
Worrall, D. M. & Wilkes, B. J. 1990, ApJ, 360, 396
Yamaguchi, H., Nakajima, H., Koyama, K., et al. 2006, SPIE 6266, Space Telescopes and Instrumentation II: Ultraviolet to Gamma Ray, ed. J. L. Martin Turner & G. Hasinger, 626642

Abdelbar, Ahmed M. and Beheary, M. M: Department of Astronomy and Meteorology, Faculty of Science, Al-Azhar University, Cairo, Egypt.
Nasser, M. Ahmed and Saad, A. Ata: Astronomy Department, National Research Institute of Astronomy and Geophysics (NRIAG), Helwan, Cairo, Egypt (nasser_ahnmed@yahoo.com, saad.ata0100@gmail.com).

Revista Mexicana de Astronomía y Astrofísica, **57**, 147–155 (2021)

https://doi.org/10.22201/ia.01851101p.2021.57.01.10

ASYMPTOTIC INTERNAL WORKING SURFACES OF PERIODICALLY VARIABLE JETS

A. C. Raga[1,2], J. Cantó[3], and A. Castellanos-Ramírez[3]

Received July 11 2020; accepted November 6 2020

ABSTRACT

We present a derivation based on the "center of mass formalism" of the asymptotic behaviour of internal working surfaces produced in a variable Herbig-Haro (HH) jet. We obtain the general solution for an arbitrary periodic ejection time-variability, and then show examples for a limited set of functional forms for the velocity and density time-evolutions. Finally, we derive a prescription for obtaining the time-averaged mass loss rate from observations of knots along an HH jet (based on the asymptotic solution), and apply it to derive the mass loss rate of the HH 1 jet.

RESUMEN

Presentamos una derivación basada en el "formalismo de centro de masa" del comportamiento asintótico de superficies de trabajo internas producidas en un yet Herbig-Haro (HH) variable. Obtenemos la solución general para una eyección periódica arbitraria, y después mostramos ejemplos para un conjunto limitado de formas funcionales para la evolución temporal de la velocidad y la densidad. Finalmente, derivamos una prescripción para calcular la tasa de pérdida de masa promedio de observaciones de los nudos a lo largo de un yet HH (basada en la solución asintótica), y la aplicamos para derivar la pérdida de masa del yet de HH 1.

Key Words: Herbig-Haro objects — ISM: individual objects: HH 1 — ISM: jets and outflows — ISM: kinematics and dynamics — stars: formation — stars: winds, outflows

1. INTRODUCTION

The suggestion that the knotty structures in astrophysical jets could be the result of a time-dependent ejection was first made in the context of extragalactic jets (see, e.g., Rees 1978; Wilson 1984; Roberts 1986). However, the theory of variable jets has been mostly developed and applied in the context of Herbig-Haro (HH) jets from young stars.

Raga et al. (1990) apparently first pointed out in an explicit way that the structures observed in HH jets could be easily modeled as "internal working surfaces" produced by an ejection velocity variability with a hypersonic amplitude (though the general idea that HH knots are the result of a variability of the ejection hovers around in the literature of the late 1980's). Since then, a relatively large number of papers has been written on numerical simulations and analytic models of variable ejection HH jets, as well as comparisons with observations (three relatively recent examples are Teşileanu et al. 2014; Hansen et al. 2017; Castellanos-Ramírez et al. 2018).

Kofman & Raga (1992) and Raga & Kofman (1992) studied analytically the asymptotic regime reached by internal working surfaces at large distances from the outflow source. They noted that the internal working surface shocks (see Figure 1) asymptotically have shock velocities that scale as $1/x$ and pre-shock densities with the same dependence on distance x from the source. Approximating the emission from these shocks with the predictions from plane-parallel shocks, Raga & Kofman (1992) showed that the asymptotic working surface model predicts a [S II] line intensity vs. x decay that agrees surprisingly well with observations of the HH 34 jet. More recently, Raga et al. (2017) showed that the

[1]Instituto de Ciencias Nucleares, UNAM, México.
[2]Inst. de Investigación en Ciencias Físicas y Matemáticas, USAC, Guatemala.
[3]Instituto de Astronomía, UNAM, México.

successive knots along the HH 1 jet have the predicted [S II] intensity vs. position dependence, and also that individual knots follow the predicted behaviour as a function of time, following the increase in x that results from their motion away from the outflow source.

Kofman & Raga (1992) and Raga & Kofman (1992) found the asymptotic regime by considering a "ram-pressure balance" equation of motion for the internal working surfaces. This equation of motion is valid for the case in which the gas that goes through the working surface shocks is ejected laterally in an efficient way, and does not remain within the working surface. Though these authors determined the form of the position dependence of the shock velocities and pre-shock densities of the internal working surfaces, they were unable to relate the proportionality constants of these dependencies to the functional form of the ejection velocity and density.

In this paper, we study the asymptotic regime (of internal working surfaces at large distances from the outflow source) using the "center of mass" equation of motion of Cantó et al. (2000). This equation of motion is valid for internal working surfaces in which a large part of the gas passing through the shocks stays within the working surface. The theoretical attraction of this formalism is that it generally leads to full (though possibly quite complex) analytic solutions (see, e.g., Cantó & Raga 2003).

The paper is organized as follows. In § 2 we provide a summary of the "center of mass formalism" of Cantó et al. (2000), giving the equation of motion for the internal working surfaces and the free-flow (velocity and density) solution for the continuous jet beam segments between the working surfaces. In § 3, we derive the full asymptotic solution for large distances from the outflow source. In § 4, we derive the properties of the working surfaces for a limited set of chosen ejection velocity and density variabilities. In § 5, we calculate the Hα and red [S II] position-dependent luminosities of the asymptotic working surfaces. In § 6, we discuss the "inverse problem" of taking the observed properties of a knot (in particular, the spatial velocity and line luminosity of a given knot, and the knot position and knot spacing) and deducing the mean mass loss rate of the outflow. In § 7, we use this inverse problem to deduce the mass loss rate of the HH 1 jet. Finally, the results are summarized in § 8.

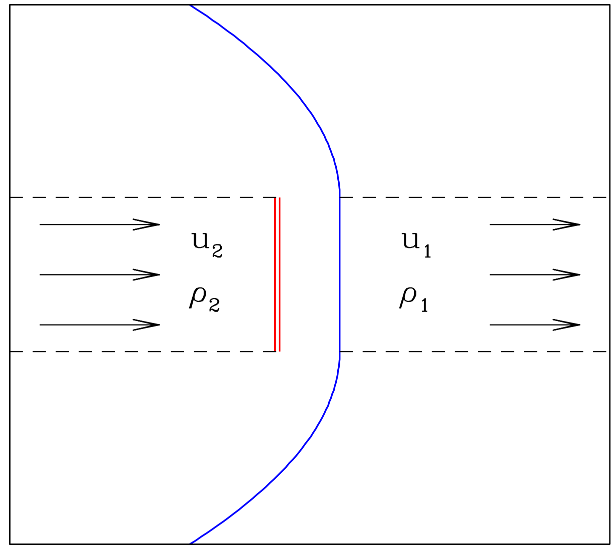

Fig. 1. Schematic diagram of an internal working surface produced by the interaction of slower material (of velocity u_1 and density ρ_1) with faster material (of velocity u_2 and density ρ_2) ejected at later times. The working surface has two shocks. the bow shock (blue, solid line) and the "jet shock" (double, solid red line). The dashed lines represent the outer boundary of the jet beam. The color figure can be viewed online.

2. EQUATION OF MOTION FOR AN INTERNAL WORKING SURFACE

This section is a short summary of the "center of mass equation of motion" for working surfaces derived by Cantó et al. (2000). The idea embodied by this formalism is as follows:

- in a hypersonic jet (or wind), in the absence of shocks the fluid parcels are free-streaming, preserving their initial ejection velocity u_0,
- when shocks form due to "catching up" of faster parcels ejected at later times with slower parcels ejected at earlier times, "internal working surfaces" are formed (see Figure 1). These working surfaces are assumed to be compact (with extents along the outflow direction which can be neglected), so that each of them has a single, time-dependent distance from the source x_{ws},
- if one assumes that all of the mass entering through the two working surface shocks stays in a region close to the working surface (an assumption that is correct for a spherical wind, and might also be appropriate for radiative jets), then:

- with this "mass conservation" condition, a working surface can be seen as a particle formed by the coalescence of fluid parcels, with the mass and momentum of the coalesced parcels. Then, the position x_{ws} of the working surface will be equal to the position x_{cm} of the center of mass of the fluid parcels *if they had continued free-streaming without coalescing.*

Cantó et al. (2000) showed that this center of mass can be calculated as a function of the ejection velocity and density history in a direct way, leading to analytic solutions for the time-dependent positions and velocities of the successive internal working surfaces. Here, we summarize their results.

Let us assume an arbitrary, periodic variation $u_0(\tau)$, $\rho_0(\tau)$ of the ejection velocity and density. This periodic ejection variability produces a chain of internal working surfaces, and we consider the time-dependent position

$$x_{cm}(t) = \frac{\int_{\tau_1}^{\tau_2} x(t,\tau)\rho_0(\tau)u_0(\tau)d\tau}{\int_{\tau_1}^{\tau_2} \rho_0(\tau)u_0(\tau)d\tau}\,, \tag{1}$$

of the centre of mass of the material within one of the working surfaces. In this equation, t is the present time, and $\tau \leq t$ is the "ejection time" at which the fluid parcels were ejected. The position $x(t,\tau)$ of the free-streaming fluid parcels is given by the free-streaming flow condition

$$x(t,\tau) = (t-\tau)u_0(\tau)\,. \tag{2}$$

The τ_1 and τ_2 values in equation (1) are the ejection times of the fluid parcels which are now entering the working surface from the downstream and upstream directions (respectively), and correspond to two successive roots of the equation:

$$x_{cm} = (t-\tau_{1,2})\,u_0(\tau_{1,2})\,. \tag{3}$$

We also note that the density of a free-streaming jet with a position-dependent cross section $\sigma(x)$ is given by:

$$\sigma(x)\rho(x,t) = \frac{\sigma_0\rho_0(\tau)u_0(\tau)}{u_0(\tau)-(t-\tau)\dot{u}_0(\tau)}\,, \tag{4}$$

where σ_0 and $\rho_0(\tau)$ are the ejection cross section and density, respectively, and $\dot{u}_0(\tau) = du_0/d\tau$. This solution for the density can be straightforwardly obtained by inserting the free flow condition (2) into the appropriate continuity equation.

3. THE ASYMPTOTIC REGIME

For large distances from the source, most of the ejected material has already entered the working surfaces, so that the ejection time-interval of the material entering the working surface from the upstream and downstream directions becomes $\tau_2 - \tau_1 \approx \tau_p$, where τ_p is the period of the ejection variability. In this regime, the $\tau_1 \to \tau_2$ interval of the integrals can therefore be replaced by the $-\tau_p/2 \to \tau_p/2$ interval. Equation (1) then becomes:

$$x_{cm} = (t-\tau_a)v_a\,, \tag{5}$$

where

$$v_a = \frac{\int_{-\tau_p/2}^{\tau_p/2} \rho_0(\tau)u_0^2(\tau)d\tau}{\int_{-\tau_p/2}^{\tau_p/2} \rho_0(\tau)u_0(\tau)d\tau}\,, \tag{6}$$

is the (constant) asymptotic velocity of the working surface and

$$\tau_a = \frac{\int_{-\tau_p/2}^{\tau_p/2} \tau\rho_0(\tau)u_0^2(\tau)d\tau}{v_a\int_{-\tau_p/2}^{\tau_p/2} \rho_0(\tau)u_0(\tau)d\tau}\,, \tag{7}$$

is an average ejection time of the material that lies within a given internal working surface. Clearly, by choosing to carry out the integrals over the $-\tau_p/2 \to \tau_p/2$ range we are choosing the internal working surface formed by the material ejected in this ejection time interval.

Therefore, regardless of the form of the periodic ejection velocity and density variability, at large distances from the source the working surfaces travel at a constant velocity, which is given by equation (6). It is also possible to obtain the shock velocities of the working surface shocks in the following way.

At large distances from the source, the material in the continuous segments of the jet corresponds to a small range of ejection times around τ_n, where the index n numbers the successive continuous segments. The ejection time τ_n is determined by the condition

$$u_0(\tau_n) = v_a\,, \tag{8}$$

where one has to choose the root with $\dot{u}_0(\tau_n) < 0$, and v_a is given by equation (6). Clearly,

$$\tau_{n+1} = \tau_n + \tau_p\,, \tag{9}$$

and the free-streaming flows on the two sides of the working surface have linear velocity vs. position relationships, giving velocities

$$u_1 = \frac{x_{cm}}{t-\tau_n}\,,\quad u_2 = \frac{x_{cm}}{t-\tau_{n+1}}\,, \tag{10}$$

immediately down- and up-stream of the working surface.

Using equation (9), we have

$$t - \tau_{n+1} = (t - \tau_n)(1 - \epsilon) \ , \ \text{with } \epsilon = \frac{\tau_p}{t - \tau_n} \ , \quad (11)$$

with $\epsilon \ll 1$ in the asymptotic regime.

We can then use equations (5), (10) and (11) to calculate the velocity jump accross the working surface:

$$\Delta u = u_2 - u_1 = \frac{v_a^2 \tau_p}{x_{cm}} \, , \quad (12)$$

where we have carried out a first order expansion in ϵ (see equation 11).

Also, the free-streaming flow density integral (4), when evaluated in τ_n gives:

$$\rho_{1,2} \approx \frac{\rho_0(\tau_n)\sigma_0}{\sigma(x_{cm})\left[1 - (t - \tau_n)\frac{d\ln u_0}{d\tau}(\tau_n)\right]} \, , \quad (13)$$

where we can calculate both upstream and downstream densities using τ_n, given that in the asymptotic regime we have $\epsilon \ll 1$ (see equation 11). In this equation, σ_0 is the ejection cross section and $\sigma(x_{cm})$ the cross section at the position of the working surface. Equation (13) can be further simplified by noting that

$$-(t - \tau_n)\frac{d\ln u_0}{d\tau}(\tau_n) \approx \frac{t - \tau_n}{\tau_p} = \epsilon^{-1} \, , \quad (14)$$

and therefore, in the asymptotic, $\epsilon \ll 1$ regime the first term in the denominator of equation (13) can be neglected. In this way, we obtain

$$\rho_{1,2} \approx -\frac{\rho_0(\tau_n)\sigma_0 u_0(\tau_n)}{\sigma(x_{cm})\dot{u}_0(\tau_n)(t - \tau_n)} \, , \quad (15)$$

with equal densities on both sides of the internal working surface. The fact that the densities on both sides of the working surface asymptotically approach each other, and that the velocity of the working surface becomes constant, implies that the shock velocities of the two working surface shocks also have the same value. Therefore, the velocity jump Δu across the working surface (see equation 12) is divided into two shocks of velocities $\Delta u/2$. In this way, we see that as the working surface travels away from the outflow source at the asymptotic velocity v_a, the shocks have velocities that decrease as $1/x_{cm}$ (see equation 12).

Combining equations (5), (15) and (8) we obtain:

$$\rho_{1,2} = \frac{\Sigma}{x_{cm}\sigma(x_{cm})} \, , \quad (16)$$

where

$$\Sigma \equiv -\rho_0(\tau_n)\sigma_0 \frac{v_a^2}{\dot{u}_0(\tau_n)} \, , \quad (17)$$

is a (positive) constant, $\sigma(x_{cm})$ is the cross section of the jet (at the position of the working surface) and ρ_0 and $\dot{u}_0$ are calculated at the time τ_n at which the material of the asymptotic segments of continuous jet beam were ejected, which is given by equation (8).

4. EXAMPLES FOR A SINUSOIDAL $U_0(\tau)$ AND TWO SIMPLE FORMS OF $\rho_0(\tau)$

4.1. *Ejection Velocity Variability*

For the ejection velocity, we choose a sinusoidal variability:

$$u_0(\tau) = v_0 + \Delta v_0 \sin \omega\tau \, , \quad (18)$$

with mean velocity v_0, half-amplitude Δv_0, frequency ω and period $\tau_p = 2\pi/\omega$. The half amplitude Δv_0 lies in the $0 \to v_0$ interval.

4.2. *Constant $\dot{M}$*

We first choose a density variability such that the jet has a time-independent $\dot{M}$. The ejection density then is:

$$\rho_0(\tau) = \frac{\dot{M}}{\sigma_0 u_0(\tau)} = \frac{\dot{M}}{\sigma_0\left(v_0 + \Delta v_0 \sin \omega\tau\right)} \, , \quad (19)$$

where σ_0 is the ejection cross section, and where we have used equation (18) for the second equality.

With the chosen $u_0(\tau)$ and $\rho_0(\tau)$ (equations 18 and 19, respectively), from equation (6) we obtain

$$v_a = v_0 \, , \quad (20)$$

from equation (8) we obtain

$$\tau_n = \tau_p/2 + n\tau_p \, , \quad (21)$$

and from equation (17) we obtain

$$\Sigma = \frac{\dot{M} v_0 \tau_p}{2\pi \Delta v_0} \, . \quad (22)$$

In this way, we can calculate the shock velocities $\Delta u/2$ (see equation 12) and pre-shock densities $\rho_1 = \rho_2$ (see equation 16) of the asymptotic working surfaces as a function of their position x_{cm}, the jet cross-section $\sigma(x_{cm})$, the (time-independent) mass loss rate $\dot{M}$, and the period τ_p, mean velocity v_0 and half-amplitude Δv_0 of the ejection velocity variability.

4.3. *Constant* ρ_0

We now consider the case of a time-independent ejection density ρ_0. Then, the time-averaged mass loss rate of the ejected jet is $\dot{M} = \sigma_0 \rho_0 v_0$, where σ_0 is the ejection cross section and v_0 is the mean velocity of the jet (see equation 18).

Using equation (18) and setting a time-independent ρ_0, from equation (6) we obtain

$$v_a = v_0 \left[1 + \frac{1}{2} \left(\frac{\Delta v_0}{v_0} \right)^2 \right] , \tag{23}$$

from equation (8) we obtain

$$\tau_n = \frac{\tau_p}{2} - \frac{\tau_p}{2\pi} \sin^{-1} \left(\frac{\Delta v_0}{2 v_0} \right) + n \tau_p , \tag{24}$$

and from equation (17) we obtain

$$\Sigma = \frac{\dot{M} v_0 \tau_p}{2\pi \Delta v_0} g \left(\frac{\Delta v_0}{v_0} \right) , \tag{25}$$

with

$$g \left(\frac{\Delta v_0}{v_0} \right) = \frac{\left[1 + \frac{1}{2} \left(\frac{\Delta v_0}{v_0} \right)^2 \right]^2}{\sqrt{1 - \frac{1}{4} \left(\frac{\Delta v_0}{v_0} \right)^2}} . \tag{26}$$

If we consider the $\Delta v_0 / v_0 \to 0$ lower limit of the velocity amplitude, we regain the results obtained for the constant mass loss rate case (see § 4.2). If we consider the $\Delta v_0 / v_0 \to 1$ upper limit, we obtain:

$$v_a = \frac{3 v_0}{2} , \tag{27}$$

$$\tau_n = \frac{5 \tau_p}{12} + n \tau_p , \tag{28}$$

and

$$\Sigma = \frac{3\sqrt{3} \dot{M} v_0 \tau_p}{4\pi \Delta v_0} . \tag{29}$$

Therefore, in the $\Delta v_0 / v_0 \to 1$ large amplitude limit the constant ρ_0 case gives an asymptotic velocity v_a for the working surfaces which is a factor 3/2 larger than the one of the constant mass loss case, and a "density constant" Σ larger by a factor $3\sqrt{3}/2$.

5. THE EMISSION OF ASYMPTOTIC WORKING SURFACES

We now estimate the Hα and red [S II] luminosities of the asymptotic working surfaces as:

$$L_{line} = 8\pi \sigma I_{line}(n_{pre}, v_s) , \tag{30}$$

where σ is the cross section of the jet at the position of the working surface, $n_{pre} = \rho_{1,2}/(1.3 m_H)$ (where $\rho_{1,2}$ is the pre-working surface shock density, see equation 16), $v_s = \Delta u / 2$ is the shock velocity (see equation 12), and I_{line} is the line flux emerging from one of the two shocks (the factor 8π accounting for the fact that we have 2 shocks radiating into 4π sterad).

As described in Appendix A, we use the plane-parallel, steady shock models of Hartigan et al. (1987) to determine the functional form:

$$I_{line} = n_{pre} f_{line}(v_s) , \tag{31}$$

with $f_{line} = f_{H\alpha}$ or $f_{[SII]}$ determined from fits to the predictions of the plane-parallel shock models (see equations A38 and A39 of Appendix A).

Combining equations (30), (31), (16) and (25), we obtain:

$$L_{line} = \frac{4 \dot{M} v_0 \tau_p}{1.3 m_H \Delta v_0} g \left(\frac{\Delta v_0}{v_0} \right) \frac{f_{line}(v_s)}{x_{cm}} , \tag{32}$$

where $\dot{M}$ is the time-averaged mass loss rate (see equation 25) and $v_s = \Delta u / 2$ is given by equation (12). Equation (32) is equivalent to equation (34) of Raga & Kofman (1992), but includes a more general form for the shock velocity dependence of the emission and a full determination of the constants.

For a sinusoidal ejection velocity variability and a density variability such that the mass loss rate is time-independent (see § 4.2), the position-dependent luminosity of the working surface in the Hα and [S II] lines can be obtained by setting $f = f_{H\alpha}$ or $f = f_{SII}$ (see equations A38 and A39 in Appendix A, respectively) and $g(\Delta v_0 / v_0) = 1$ (see equation 22).

For the case of a constant density ejection, the Hα and [S II] luminosities can be obtained using the $g(\Delta v_0 / v_0)$ function of equation (26). For $\Delta v_0 / v_0 \ll 1$, this function has a value $g(\Delta v_0 / v_0) \approx 1$.

6. THE INVERSE PROBLEM

Several HH outflow systems show chains of quasi-periodic, aligned knots within $\approx 10^{17}$ cm ($\approx 10^4$ AU) of the outflow source. These knots generally have spatial velocities in excess of ≈ 150 km s^{-1} (determined from radial velocity and proper motion studies), and have very low excitation emission line spectrum, with high red [S II]/Hα and [O I] 6300/Hα line ratios. These line ratios imply relatively slow shock velocities (of $\approx$ 20-30 km s^{-1}).

In the case of the HH 1 jet, this very low excitation is present in all of the observed knots along the HH 1 jet, including the knots that lie closer to the outflow source (observed in the IR, see, e.g., Table 2 of Nisini et al. 2005). The knots formed by a velocity variability with a half-amplitude Δv_0 produce internal working surfaces that rapidly reach peak shock velocities $v_s \approx \Delta v_0$ (before reaching the asymptotic regime described in § 3), as shown, e.g., by Raga & Cantó (1998) and Cantó et al. (2000). Therefore, the low excitation of all knots along the HH 1 jet (and in particular, the ones closer to the outflow source) indicates that the ejection time variability in HH 34 has a small $\Delta v_0/v_0$ (where v_0 is the mean ejection velocity, and Δv_0 is the half-amplitude of the variability, see, e.g., equation 18). A similar situation is found for the HH 1 jet, and for other jets in which all of the knots along the chains close to the outflow source have a very low excitation spectrum (e.g., HH 34, see Podio et al. 2006.

In this section we show how observational determinations of the knot spacing Δx, and the luminosity L_{line} of a given emission line and spatial velocity v_a of a knot at position x_{ws} can be used to constrain the average mass loss rate of the ejection. We will identify the observed position x_{ws} of the knot with the x_{cm} center of mass position that comes out of our model, so that in the following we will set $x_{cm} = x_{ws}$.

For a low-amplitude sinusoidal ejection velocity variability, both the constant mass loss rate and constant ejection density cases (see § 4.2 and § 4.3) give:

$$v_a \approx v_0\,;\;\; \rho_{pre} \approx \frac{\dot{M} v_0 \tau_p}{2\pi \Delta v_0 x_{ws} \sigma(x_{ws})}\,, \qquad (33)$$

where v_a is the asymptotic working surface velocity, and x_{ws} is the position of a given working surface. The line emission of the working surface is then given by equation (32) with $g(\Delta v_0/v_0) = 1$.

For a periodic ejection velocity, all of the working surfaces in the asymptotic regime move with the constant velocity v_a. Therefore, if we observe the spatial velocity v_a (determined from proper motion and radial velocity measurements) and knot spacing Δx, we can obtain the variability period as

$$\tau_p = \frac{\Delta x}{v_a}\,. \qquad (34)$$

We now observe the flux of a given emission line, and using the distance to the object and the extinction (which we assume has also been determined) we can calculate the luminosity L_{line} of the line. If the observed knot lies at a distance x_{ws} from the outflow source, we first use equation (12) to calculate the shock velocity of the two working surface shocks:

$$v_s = \frac{\Delta u}{2} = \frac{v_a^2 \tau_p}{2 x_{ws}} = \frac{v_a \Delta x}{2\, x_{ws}}\,. \qquad (35)$$

With our empirical determinations of L_{line}, τ_p and v_s, we then invert equation (32) (setting $g = 1$, see above) to calculate the average mass loss rate

$$\dot{M} = \frac{1.3 m_H L_{line} \Delta v_0\, x_{ws}}{4 v_0 \tau_p f_{line}(v_s)}\,, \qquad (36)$$

where in Appendix A we give analytic forms for the $f_{line}(v_s)$ functions for the Hα and red [S II] emission. Clearly, in order to calculate the mass loss rate, we need to know the value of the half-amplitude Δv_0 of the ejection velocity variability. If we cannot determine this parameter from other observations, we can set $\Delta v_0 \approx v_s$.

7. AN APPLICATION TO THE HH 1 JET

As an example we consider the "HH 1 jet", which points from near the source of the HH 1/2 outflow system towards HH 1. Raga et al. (2017) and Castellanos-Ramírez et al. (2018) argue that the intensity vs. position dependence of the knots at distances $> 5''$ from the source can be modelled as coming from working surfaces in the "asymptotic regime".

We calculate the mass loss rate of the HH 1 jet using the calibrated line fluxes of knot G by Nisini et al. (2005). At the time of their observations, the G knot was at $x_G = 6.5'' = 3.9\times10^{16}$ cm from the outflow source. From the HST images shown in Raga et al. (2017), we see that the separation between successive knots is $\Delta x_G \approx 2'' = 1.2\times10^{16}$ cm. Also, the proper motion velocity of knot G is $v_G = 287$ km s^{-1}, which is very close to its full spatial velocity because the outflow lies at a very small angle with respect to the plane of the sky.

First, with the x_G, Δx_G and v_G values, we use equations (34) and (35) to obtain a period $\tau_p = 13.3$ yr and a shock velocity $v_s = 44.2$ km s^{-1}.

Then, taking the knot G line fluxes from Nisini et al. (2005), applying a reddening correction with their $A_v = 2.0$ extinction (taking a standard, $E(B-V)/A_v = 3.1$ extinction curve) and assuming a distance of 400 pc to HH 1, we obtain $L_{H\alpha} = 1.77\times10^{-4} L_\odot$ and $L_{[SII]} = 5.19\times10^{-4} L_\odot$. Using equation (36) with $\Delta v_0 = v_s$, we obtain $\dot{M}_{H\alpha} = 7.76\times10^{-8} M_\odot \mathrm{yr}^{-1}$ and $\dot{M}_{[SII]} = 8.07\times10^{-7} M_\odot \mathrm{yr}^{-1}$ from the observed Hα and [S II] emission of knot G, respectively.

These two mass loss rate estimates can be compared with the estimates of Nisini et al. (2005). who (using different methods) find $\dot{M} \approx 6.9 \times 10^{-8} \to 2.4 \times 10^{-7} M_\odot\,\mathrm{yr}^{-1}$ for knot G of the HH 1 jet. Of our two estimates, we favour the $8.07\times10^{-7} M_\odot\,\mathrm{yr}^{-1}$ estimate obtained from the [S II] luminosity. This is because the [S II] emission is produced closer to the shock than Hα, and the [S II] prediction from stationary, 1D shock models is therefore more likely to be applicable to the time-dependent, multidimensional jet flow.

8. SUMMARY

We have applied the "center of mass equation of motion" to find the asymptotic behaviour (at large distances from the outflow source) of the internal working surfaces produced by an arbitrary, periodic outflow variability with an ejection velocity $u_0(\tau)$ and a density $\rho_0(\tau)$. We find the complete asymptotic solution, giving the constant, asymptotic velocity v_a and the position-dependent shock velocities and preshock densities of the working surfaces.

We obtain the same position-dependencies that have been found by Raga & Kofman (1992) using the "ram-presure balance" equation of motion for the working surfaces. However, Raga & Kofman (1992) were unable to find the relation between the proportionality constants (for the density and shock velocity vs. position) and the ejection variability.

With our full asymptotic solution, we compute the knot properties for two chosen combinations of $u_0(\tau)$ and $\rho_0(\tau)$ (see § 4). We also discuss the "inverse problem" of finding the properties of the ejection from the observational characteristics of the jet knots (see § 5). In particular, we derive a very simple expression for estimating the time-averaged mass loss rate of the ejection as a function of the position x, the separation Δx between successive knots, the spatial velocity v_a and the luminosity L_{line} (in Hα or in the red [S II] lines) of a given knot.

We apply this "inverse problem" to observations of the HH 1 jet (line intensities and extinctions of Nisini et al. 2005 and proper motions of Raga et al. 2017), and find mass loss rates which are similar to the ones of Nisini et al. (2005). This result is nothing short of surprising, given the fact that our mass loss rate determination is completely model-dependent, and comes from a rather eclectic collection of observational characteristics (e.g., including the knot spacing).

This success of obtaining the previously determined mass loss rate is interesting in two different ways:

- it shows in a quite definite way that the interpretation of the chain of knots of the HH 1 jet as internal working surfaces formed by a quasiperiodic outflow variablity is apparently correct,
- it gives us a new method for determing mass loss rates of outflows from young stars, using the spatial velocity, knot spacings and the intensity in a single emission line of the knots along the HH jet.

Less optimistically, we note that we have determined (through the use of the asymptotic working surface model) the mass loss rate of the HH 1 jet from the Hα and [S II] luminosities, obtaining $\dot{M} = 7.8 \times 10^{-8}$ and $8.1\times10^{-7} M_\odot\mathrm{yr}^{-1}$, respectively, which differ by one order of magnitude. This result is in agreement with the results of Nisini et al. (2005) partly because they also obtain a range of mass loss rate determinations which also differ (from each other) by an order of magnitude. This is clearly not a very good situation.

In our "asymptotic working surface model" mass loss rate determinations, the obvious possible reason for the discrepancy between the Hα and [S II] results is the modelling of the emission with steady, plane-parallel shock models. As has been already noted in the early literature on modelling HH objects (see Dopita et al. 1982), the cool tail of the recombination region does not have time to develop fully in HH shock waves. The resulting "truncation" of the cooling region has a stronger effect on the predicted Hα emission than on the forbidden lines (Raga & Binette 1991), so that the mass loss rate deduced from the [S II] luminosity (i.e., $\dot{M} = 8.1 \times 10^{-7} M_\odot\mathrm{yr}^{-1}$) is likely to be more reliable.

Also, not only the shocks in working surfaces have non-steady state recombination regions, but also they are not likely to be plane. This is seen in numerical simulations of variable jets (see, e.g., Raga et al. 2007) as well as in high angular resolution observations of HH jets (see, e.g., Reipurth et al. 2002). It is therefore to be expected that analyses with the assumption of the emission being produced by plane, steady, shocks will not give fully consistent mass loss rate determinations using different emission lines.

We end by noting that there is a lot of indirect evidence that the knot structures along HH jets are the result of a variable ejection. This evidence is provided by the surprising success of variable jet models at reproducing the observed morphologies, the proper motions and the time-evolution of HH jets (see, e.g., Castellanos-Ramírez et al. 2018). However, convincing observations of a variable ejection from the outflow sources (i,e., in the spectra of the young stars or the protostars ejecting the HH jets) that can be directly linked to structures along the jets have been elusive. Some observations of the so-called "HH microjets" (with distance scales of $\approx 10^{16}$ cm and timescales of $\approx$ a few years) might be showing such a connection (see, e.g., Agra-Amboage et al. 2011). However, for obvious reasons such observations have not been made for the larger scale "normal" HH jets (with distance scales $\approx 10^{17}$ cm and timescales from several decades to $\approx$ 1000 yr).

Because of this general lack of direct link to the time-dependence of the outflow source, the details of the ejection variability cannot be determined directly and have to be chosen in a way that results in the production of a jet with the observed characteristics. In particular, while the mean velocity and characteristic period of the variability producing a chain of knots can be satisfactorily constrained by observations of the spatial motion (radial velocities+proper motions) and knot spacing, estimates of the amplitude of the ejection velocity variability depend on less convincing arguments about the excitation of the emission line spectrum of the knots closer to the outflow sources (see § 7).

This work was supported by the DGAPA (UNAM) grant IG100218. AC was supported by a DGAPA (UNAM) postdoctoral fellowhip. We thank Pierre Lesaffre (the referee) for helpful comments.

APPENDIX

A. FITS TO THE LINE EMISSION OF PLANE-PARALLEL SHOCKS

We approximate the Hα and [S II] 6716+30 (which we will call "[S II]") line emission of the working surface shocks with the plane-parallel, steady shock models of Hartigan et al. (1987). These lines show the well known scaling:

$$I_{line} = n_{pre} f_{line}(v_s)\,, \tag{A37}$$

where I_{line} is the intensity in a given line emerging from the front of the shock, n_{pre} is the pre-shock ion+atom number density (which in the following we assume is in units of cm^{-3}), and $f_{line}(v_s)$ is a function of the shock velocity v_s which is obtained from the detailed 1D, stationary shock models. For a gas with 90% H and 10% He, $n_{pre} = \rho_{pre}/(1.3 m_H H)$ (with m_H being the hydrogen mass), where ρ_{pre} is the pre-shock density.

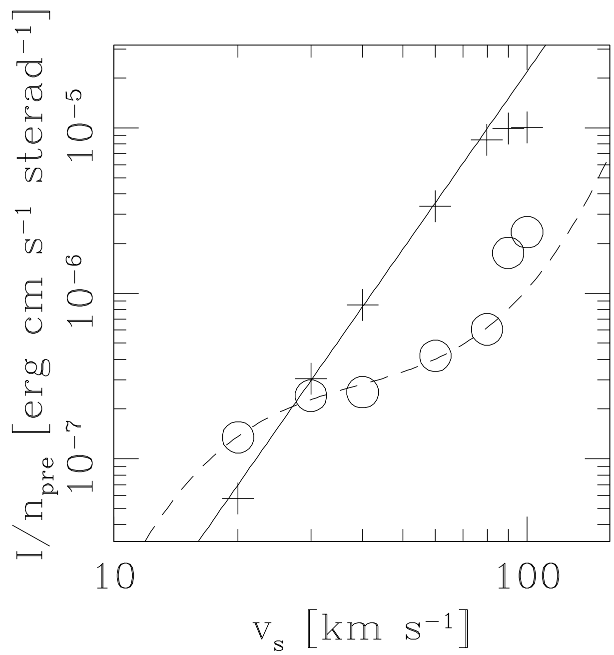

Fig. 2. Predictions of the Hα (crosses) and red [S II] intensities (open circles) as a function of shock velocity v_s from the models of Hartigan et al. (1987). The solid and dashed lines show the analytic fits of equations (A38) and (A39), respectively.

In Figure 2, we show the values of $f_{H\alpha} = F_{H\alpha}/n_{pre}$ and $f_{[SII]} = F_{[SII]}/n_{pre}$ for the $v_s = 20 \to 100$ km S^{-1} models of Hartigan et al. (1987). For the shocks in the $v_s = 20 \to 80$ km s^{-1} range, the Hα flux closely follows the power law:

$$\log_{10} f_{H\alpha} = 3.57 \log_{10} v_s - 11.84\,, \tag{A38}$$

with v_s in km s^{-1} and $f_{H\alpha}$ in erg cm s^{-1}.

The red [S II] emission has a more complicated dependence with v_s, and in order to fit it with power laws one has to specify limited shock velocity ranges. We fit a cubic polynomial to the "log-log" relation in the $v_s = 20 \to 80$ km s^{-1} range, obtaining:

$$\log_{10} f_{[SII]} = 4.28\,(\log_{10} v_s - 1.59)^3 + 0.70 \log_{10} v_s - 7.67\,, \tag{A39}$$

with v_s in km s^{-1} and $f_{[SII]}$ in erg cm s^{-1}. This relation provides a smooth interpolation between the predictions of the $20 \to 80$ km s^{-1} shock models (see Figure 2).

REFERENCES

Agra-Amboage, V., Dougados, C., Cabrit, S., & Reunanen, J. 2011, A&A, 532, A59

Cantó, J., Raga, A. C., & D'Alessio, P. 2000, MNRAS, 313, 656
Cantó, J. & Raga, A. C. 2003, RMxAA, 39, 261
Castellanos-Ramírez, A., Raga, A. C., & Rodríguez-González, A. 2018, ApJ, 867, 29
Dopita, M. A., Binette, L., & Schwartz, R. D. 1982, ApJ, 261, 183
Hansen, E. C., Frank, A., Hartigan, P., & Lebedev, S. V. 2017, ApJ, 837, 143
Hartigan, P., Raymond, J., & Hartmann, L. 1987, ApJ, 316, 323
Kofman, L. & Raga, A. C. 1992, ApJ, 390, 359
Nisini, B., Bacciotti, F., Giannini, T., et al. 2005, A&A, 441, 159
Podio, L., Bacciotti, F., Nisini, B., et al. 2006, A&A, 456, 189
Raga, A. C., Cantó, J., Binette, L., & Calvet, N. 1990, ApJ, 364, 601
Raga, A. C. & Binette, L. 1991, RMxAA, 22, 265
Raga, A. C. & Kofman, L. 1992, ApJ, 386, 222
Raga, A. C. & Cantó, J. 1998, RMxAA, 34, 73
Raga, A. C., de Colle, F., Kajdiĉ, P., Esquivel, A., & Cantó, J. 2007, A&A, 465, 879
Raga, A. C., Reipurth, B., Esquivel, A., et al. 2017, RMxAA, 53, 485
Rees, M. J. 1978, MNRAS, 184, 61
Reipurth, B., Heathcote, S., Morse, J., Hartigan, P., & Bally, J. 2002, AJ, 123, 362
Roberts, D. A. 1986, ApJ, 300, 568
Teşileanu, O., Matsakos, T., Massaglia, S., et al. 2014, A&A, 562, 117
Wilson, M. J. 1984, MNRAS, 209, 923

J. Cantó and A. Castellanos-Ramírez: Instituto de Astronomía, Ap. 70-468, 04510 Cd. Mx., México.
A. C. Raga: Instituto de Ciencias Nucleares, Universidad Nacional Autónoma de México, Ap. 70-543, 04510 CDMX, México, (raga@nucleares.unam.mx).
A. C. Raga: Instituto de Investigación en Ciencias Físicas y Matemáticas, USAC, Ciudad Universitaria, Zona 12, Guatemala, (raga@nucleares.unam.mx).

Revista Mexicana de Astronomía y Astrofísica, **57**, 157–166 (2021)

https://doi.org/10.22201/ia.01851101p.2021.57.01.11

ENVIRONMENTAL DEPENDENCE OF AGE, STELLAR MASS, STAR FORMATION RATE AND STELLAR VELOCITY DISPERSION OF ACTIVE GALACTIC NUCLEUS HOST GALAXIES

Xin-Fa Deng and Xiao-Qing Wen

School of Science, Nanchang University, Jiangxi, China, 330031.

Received July 19 2020; accepted November 9 2020

ABSTRACT

Using the apparent-magnitude limited active galactic nucleus (AGN) host galaxy sample of the Sloan Digital Sky Survey Data Release 12 (SDSS DR12), we investigate the environmental dependence of age, stellar mass, the star formation rate (SFR) and stellar velocity dispersion of AGN host galaxies. We divide the whole apparent-magnitude limited AGN sample into many subsamples with a redshift binning size of $\Delta z = 0.01$, and analyse the environmental dependence of these galaxy properties of subsamples in each redshift bin. It turns out that these parameters of AGN host galaxies seemingly only have a weak environmental dependence.

RESUMEN

Mediante la muestra limitada por magnitud aparente de las galaxias anfitrionas de núcleos activos (AGNs) contenida en la entrega 12 de datos del Sloan Digital Sky Survey (SDSS DR12) investigamos la dependencia ambiental de la edad, la masa estelar, la tasa de formación estelar y la dispersión de velocidades de las galaxias anfitrionas de AGNs. Dividimos la muestra limitada por magnitud aparente de AGNs en muchas submuestras, separándolas en grupos de corrimiento al rojo de $\Delta z = 0.01$, y analizamos la dependencia ambiental de las propiedades de las galaxias en cada grupo. El resultado es que aparentemente la dependencia ambiental de estos parámetros es débil.

Key Words: galaxies: fundamental parameters — galaxies: statistics

1. INTRODUCTION

For a long time, the study of active galactic nuclei (AGNs) has been an important subject in the galaxy field (Dressler et al. 1985; Miller et al. 2003; Hwang et al. 2012; Worpel et al. 2013; Capelo et al. 2017; Chen et al. 2018; Koulouridis & Bartalucci 2019; Zou et al. 2019). Dressler et al. (1985) and Miller et al. (2003) investigated the local environmental dependence of the presence of active galactic nuclei (AGNs). Hwang et al. (2012) explored the environmental effects on the activity in galactic nuclei by comparing galaxies in clusters and in the field. Worpel et al. (2013) examined the hypothesis that mergers and close encounters between galaxies can fuel AGNs by increasing the rate at which gas accretes toward the central black hole. Capelo et al. (2017) investigated the simultaneous triggering of AGN in merging galaxies, using a large suite of high-resolution hydrodynamical simulations. Chen et al. (2018) studied how to quantify the systematic differences resulting from using different stellar population models (SPM) in the optical spectroscopic identification of Type II AGNs. Zou et al. (2019) confirmed the prediction of the unified model of AGNs. Koulouridis & Bartalucci (2019) studied the distribution of X-ray detected AGNs in the five most massive and distant galaxy clusters in the Planck and South Pole Telescope (SPT) surveys.

Some studies demonstrated that galaxies in low-density environments are generally younger than galaxies in high-density environments (e.g., Proctor et al. 2004; Mendes de Oliveira et al. 2005; Thomas et al. 2005; Gallazzi et al. 2006; Rakos et al. 2007; Reed et al. 2007; Wegner & Grogin 2008; Smith et al. 2012; Deng 2014). For example, Proctor et al. (2004) and Mendes de Oliveira et al. (2005) reported that the member galaxies of compact groups are generally older than field galaxies. Smith et al. (2012) explored the variation in stellar population ages for Coma cluster galaxies as a function of projected cluster-centric distance, and found that the average age of dwarfs at the 2.5 Mpc limit of their sample is approximately half that of dwarfs near the cluster centre. Using two volume-limited Main galaxy (Strauss et al. 2002) samples of the SDSS, Deng (2014) examined the environmental dependence of galaxy age, and concluded that old galaxies exist preferentially in the densest regions of the universe, while young galaxies are located preferentially in low density regions. The above-mentioned conclusion is consistent with the current hierarchical assembly paradigm, which predicts a younger age of galaxies in lower density environments (e.g., Lanzoni et al. 2005; De Lucia et al. 2006).

The stellar mass of galaxies also strongly depends on environments. Kauffmann et al. (2004) observed that the stellar mass distribution of galaxies shifts by almost a factor of two towards higher masses between low and high density regions. Li et al. (2006) reported that more-massive galaxies cluster more strongly than less-massive galaxies. Deng et al. (2011, 2012) demonstrated that high mass galaxies exist preferentially in the densest regions of the universe, while low mass galaxies are located preferentially in low density regions. Poudel et al. (2016) showed that the elliptical satellite galaxies are generally more massive in high-density environments. Etherington et al. (2017) examined the environment components of the galaxy stellar mass function for the redshift range $0.15 < z < 1.05$. For $z < 0.75$, Etherington et al. (2017) found that the fraction of massive galaxies is larger in high-density environment than in low-density environments.

As is well-known, galaxies in a dense environment have suppressed star formation rates (SFRs) (e.g., Balogh et al. 1998; Hashimoto et al. 1998; Lewis et al. 2002; Gómez et al. 2003; Tanaka et al. 2004; Patel et al. 2009). Some authors compared star formation in cluster galaxies with that in field galaxies (e.g., Balogh et al. 1997, 1998; Hashimoto et al. 1998; Lewis et al. 2002), and found that the mean SFR in cluster galaxies is always less than the one in field galaxies. Gómez et al. (2003) also showed that the SFR of galaxies strongly depends on the local (projected) galaxy density. Lewis et al.(2002) believed that the low star formation rates well beyond the virialised cluster can rule out severe physical processes, such as ram pressure stripping of disk gas (Gunn & Gott 1972). In the apparent-magnitude limited Main galaxy sample (Strauss et al. 2002) of the SDSS, Deng et al. (2012) demonstrated a strong environmental dependence of the SFR of galaxies in nearly all subsamples with a redshift binning size of $\Delta z = 0.01$. Patel et al.(2009) even observed that the SFR of galaxies at $z \simeq 0.8$ shows a strong decrease with increasing local density, similar to the relation at $z \simeq 0$.

There is a close correlation between stellar velocity dispersion and masses of supermassive black holes (BHs) at galaxy centers (Botte et al. 2005; Greene & Ho 2006a-b; Hu 2008), which showed that stellar velocity dispersion also is a fairly important galaxy parameter. In the Main galaxy sample (Strauss et al. 2002) of the SDSS, Deng (2015) found that the stellar velocity dispersion of galaxies strongly depends on their local environments: galaxies with large stellar velocity dispersion tend to reside in the dense regions of the universe, whereas galaxies with small stellar velocity dispersion tend to reside in low-density regions.

The primary goal of this study is to explore the environmental dependence of age, stellar mass, SFR and stellar velocity dispersion of active galactic nucleus (AGN) host galaxies. The outline of this paper is as follows. In § 2, we describe the AGN host galaxy sample. We present statistical results in § 3. Our main results and conclusions are summarized in § 4.

To calculate the distance, we used a cosmological model with a matter density of $\Omega_0 = 0.3$, a cosmological constant of $\Omega_\Lambda = 0.7$, and a Hubble's constant of H_0=70 km·s^{-1}· Mpc^{-1}.

2. DATA

Data Release 12 (DR12) (Alam et al. 2015) of the SDSS is the final public release of spectroscopic data from the SDSS-III BOSS. In this work, the data of the Main galaxy sample (Strauss et al. 2002) were downloaded from the Catalog Archive Server of SDSS Data Release 12 (Alam et al. 2015) by the SDSS SQL Search (with SDSS flag: LEGACY_TARGET1 & $(64 \mid 128 \mid 256) > 0$). We extracted 631968 Main galaxies with the spectroscopic redshift $0.02 \leq z \leq 0.2$. In this study, the MEDIAN estimate is used. The data set of the SFR measurements was downloaded from the galSpecExtra table.

The galSpecExtra table contains estimated parameters for all galaxies in the MPA-JHU spectroscopic catalogue. BPT classification in this table is based on the methodology of Brinchmann et al. (2004):

All. The set of all galaxies in the sample regardless of the S/N of their emission lines.

TABLE 1

K-S PROBABILITIES FOR AGE, STELLAR MASS, SFR, AND STELLAR VELOCITY DISPERSION*

Redshift Bins	Galaxy Number	P(age)	P(mass)	P(SFR)	P(stellar velocity dispersion)
0.02-0.03	3433	0.183	0.693	0.231	0.0638
0.03-0.04	5105	0.000283	0.00823	0.00169	0.0329
0.04-0.05	6281	0.156	0.00491	0.00491	0.00370
0.05-0.06	7757	0.0300	0.000115	0.385	0.00126
0.06-0.07	10503	0.0559	0.0002	0.0398	1.546e-05
0.07-0.08	13062	0.0108	5.636e-10	0.238	5.840e-05
0.08-0.09	12860	0.0331	0.00313	0.000881	0.00313
0.09-0.10	9824	0.0303	0.0139	0.273	0.0617
0.10-0.11	8186	0.0373	3.914e-05	0.865	0.0201
0.11-0.12	9109	0.389	0.0938	0.304	0.389
0.12-0.13	8136	0.863	0.580	0.131	0.0126
0.13-0.14	7650	0.000857	0.00917	0.213	0.00198
0.14-0.15	6412	0.319	0.138	0.0627	0.0627
0.15-0.16	4787	0.0326	0.0423	0.00776	0.00567
0.16-0.17	3445	0.991	0.693	0.287	0.231
0.17-0.18	2710	0.0959	0.918	0.129	0.446
0.18-0.19	2190	0.840	0.996	0.0313	0.840
0.19-0.20	1473	0.961	0.994	0.961	0.994

*K-S probabilities that two samples at both extremes of the density are drawn from the same distribution.

SF. The star-forming galaxies. These are the galaxies with S/N >3 in all four BPT lines that lie below the lower line in Figure 1 of Brinchmann et al. (2004). This lower line is taken from equation (1) of Kauffmann et al. (2003).

C. The composite galaxies. They are the objects with S/N >3 in all four BPT lines that are between the upper and lower lines in Figure 1 of Brinchmann et al. (2004). The upper line has been taken from equation (5) of Kewley et al. (2001).

AGN. The AGN population consists of the galaxies above the upper line in Figure 1 of Brinchmann et al. (2004). This line corresponds to the theoretical upper limit for pure starburst models.

Low S/N AGNs. They have [NII]6584/Hα >0.6 (and S/N >3 in both lines) (e.g. Kauffmann et al. 2003), and still are classified as an AGN even if their [O III]5007 and/or Hβ have too low S/N. Miller et al. (2003) called such AGNs the "two-line AGNs".

Low S/N SF. The remaining galaxies with S/N>2 in Hα are considered low S/N star formers.

Unclassifiable. Those remaining galaxies that are impossible to classify using the BPT diagram. This class is mostly made up of galaxies with no or very weak emission lines.

Deng & Wen (2020) selected C, AGN and Low S/N AGN populations and constructed an apparent magnitude-limited AGN sample which contains 122923 AGN host galaxies. In this work, we use this AGN sample.

3. STATISTICAL RESULTS

Following Deng (2012), we measure the projected local density $\Sigma_5 = N/\pi d_5^2$ (galaxies Mpc^{-2}), where d_5 is the distance to the 5th nearest neighbor within a redshift slice ±1000 km s^{-1} of each galaxy (e.g., Goto et al. 2003; Balogh et al. 2004a, 2004b) and divide this AGN sample into subsamples with a redshift binning size of $\Delta z = 0.01$. In each subsample, we arrange galaxies in a density order from smallest to largest, select approximately 5% of the galaxies, construct two samples at both extremes of the density, and compare the distribution of age, stellar mass, SFR and stellar velocity dispersion of AGN host galaxies in the lowest density regime with those in the densest regime.

Figures 1-4 show age, stellar mass, SFR and stellar velocity dispersion distribution at both extremes of the density in different redshift bins for the apparent magnitude-limited AGN sample. As shown by Figures 1-4, these parameters of AGN host galaxies seemingly only have a weak environmental dependence.

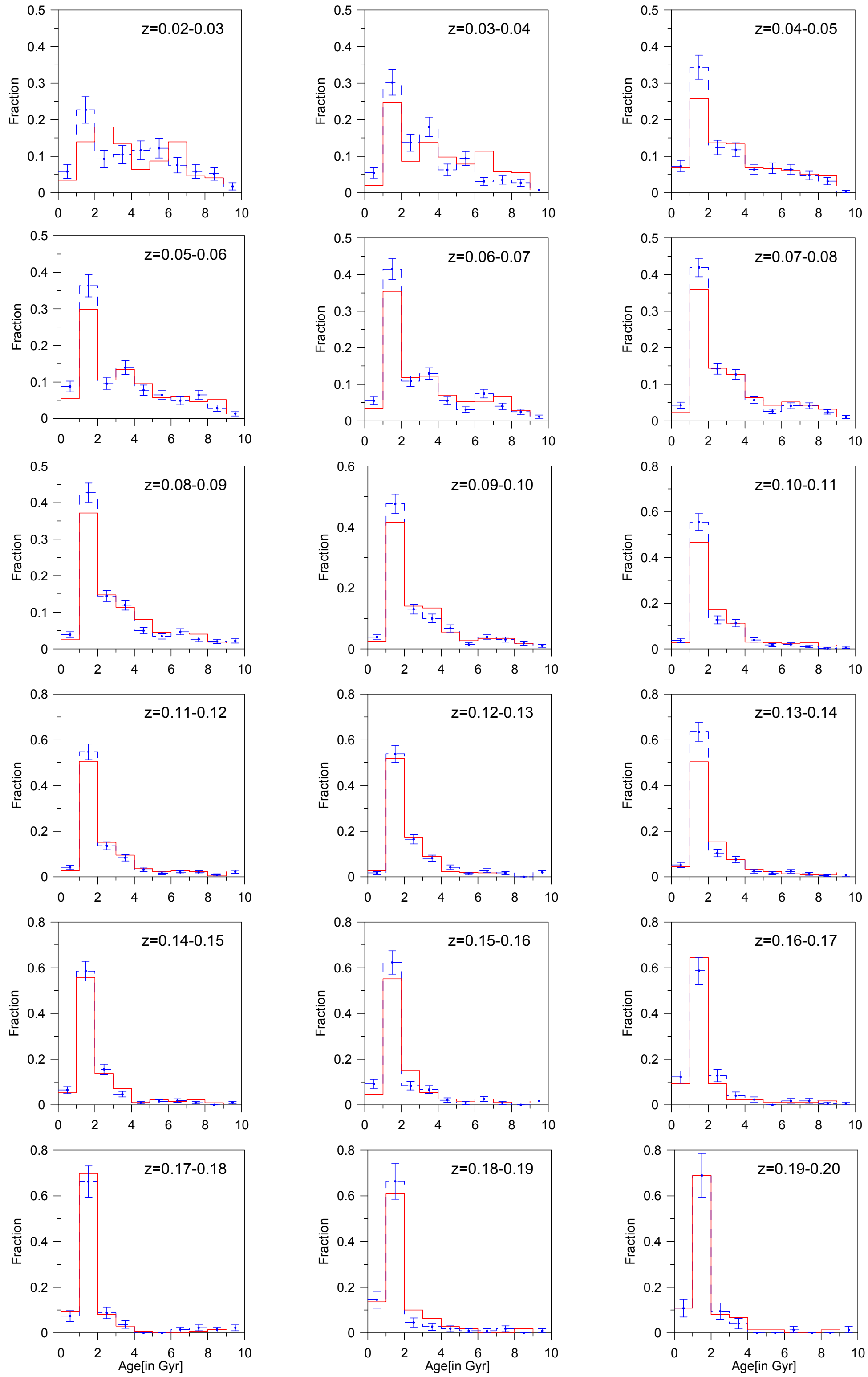

Fig. 1. Age distribution at both extremes of the density in different redshift bins: red solid line for the sample at high density, blue dashed line for the sample at low density. The error bars of blue lines are 1 σ Poissonian errors. Error-bars of red lines are omitted for clarity. The color figure can be viewed online.

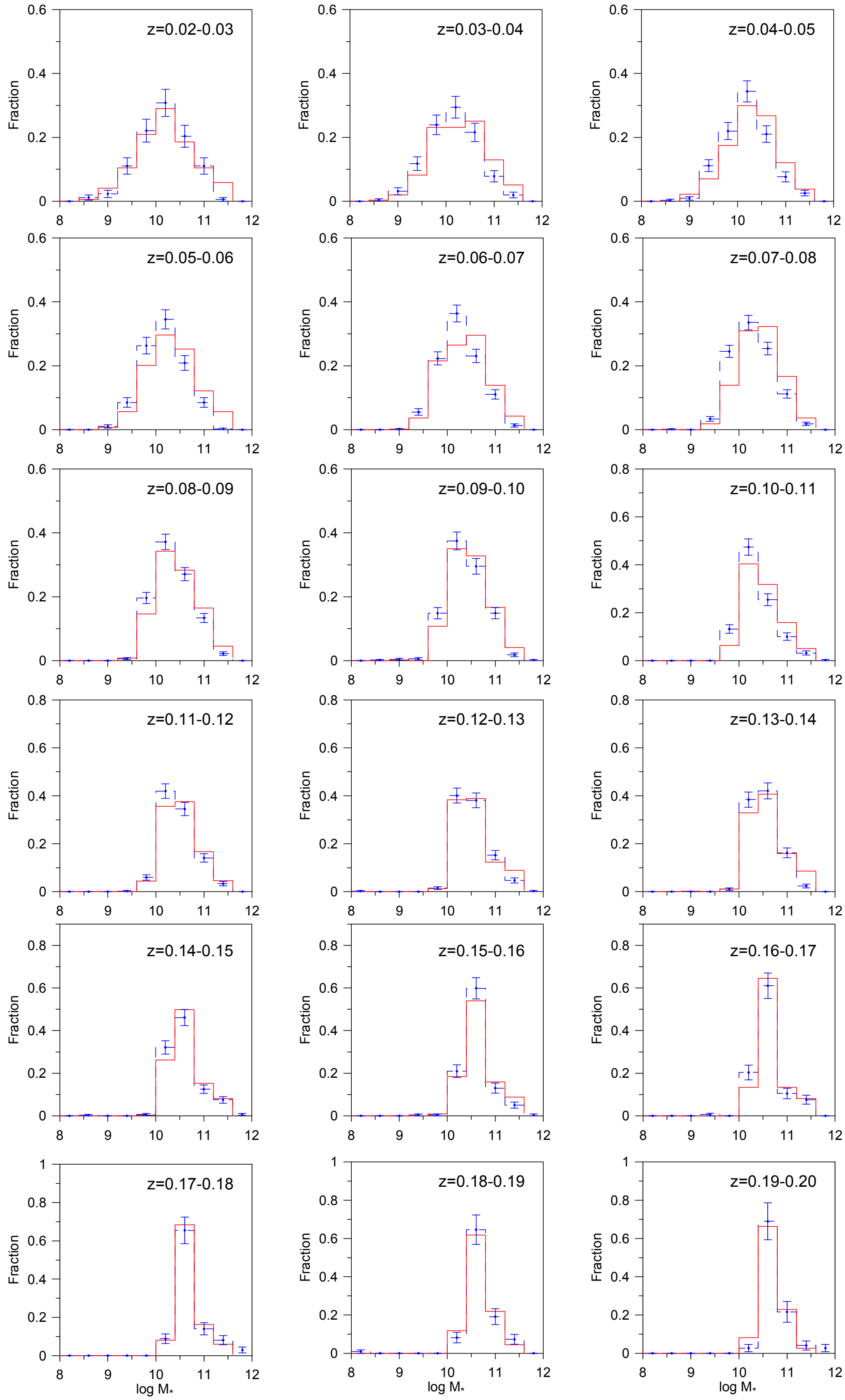

Fig. 2. Same as Figure 1 but for the stellar mass distribution at both extremes of the density in different redshift bins. The color figure can be viewed online.

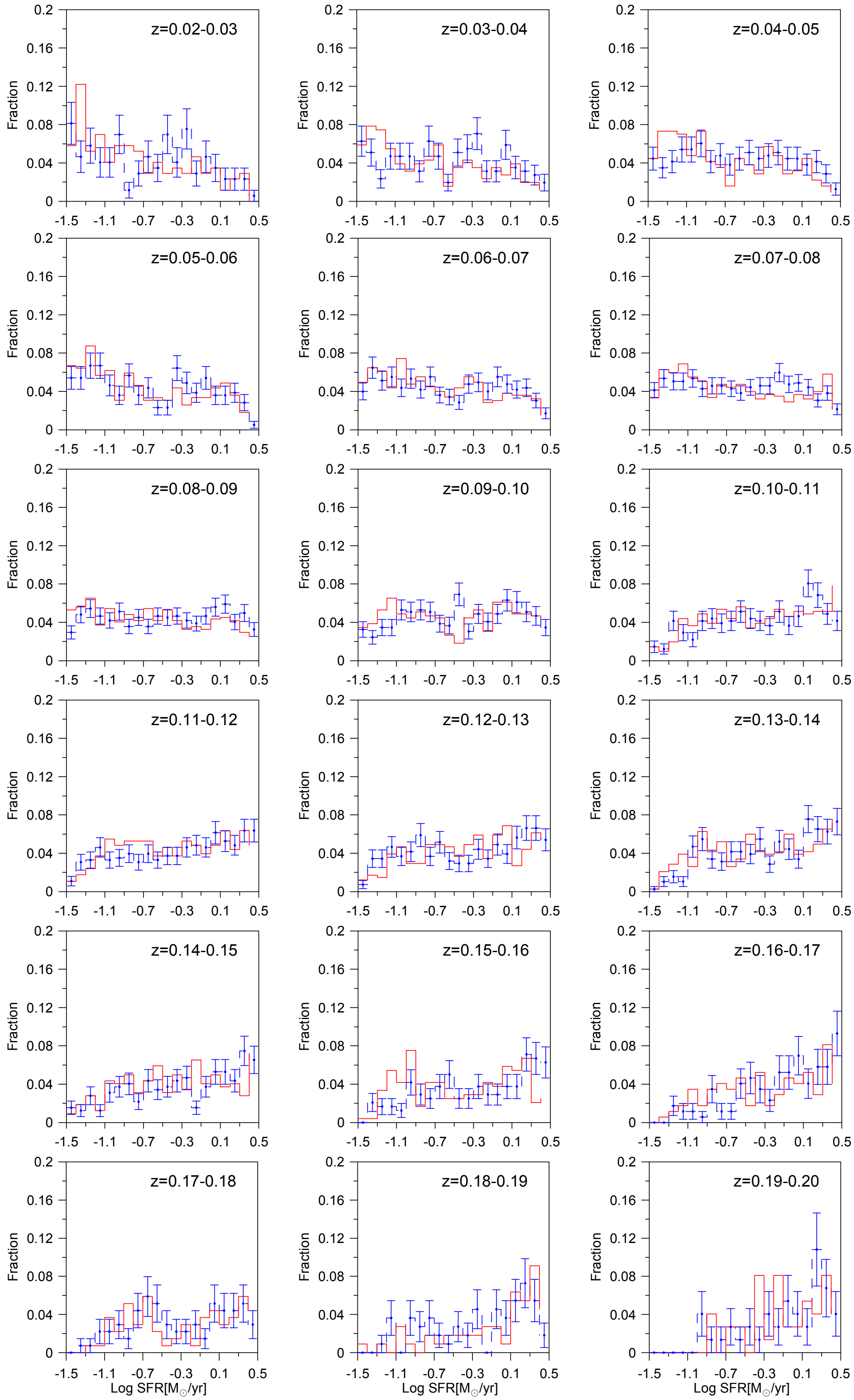

Fig. 3. Same as Figure 1 but for the SFR distribution at both extremes of the density in different redshift bins. The color figure can be viewed online.

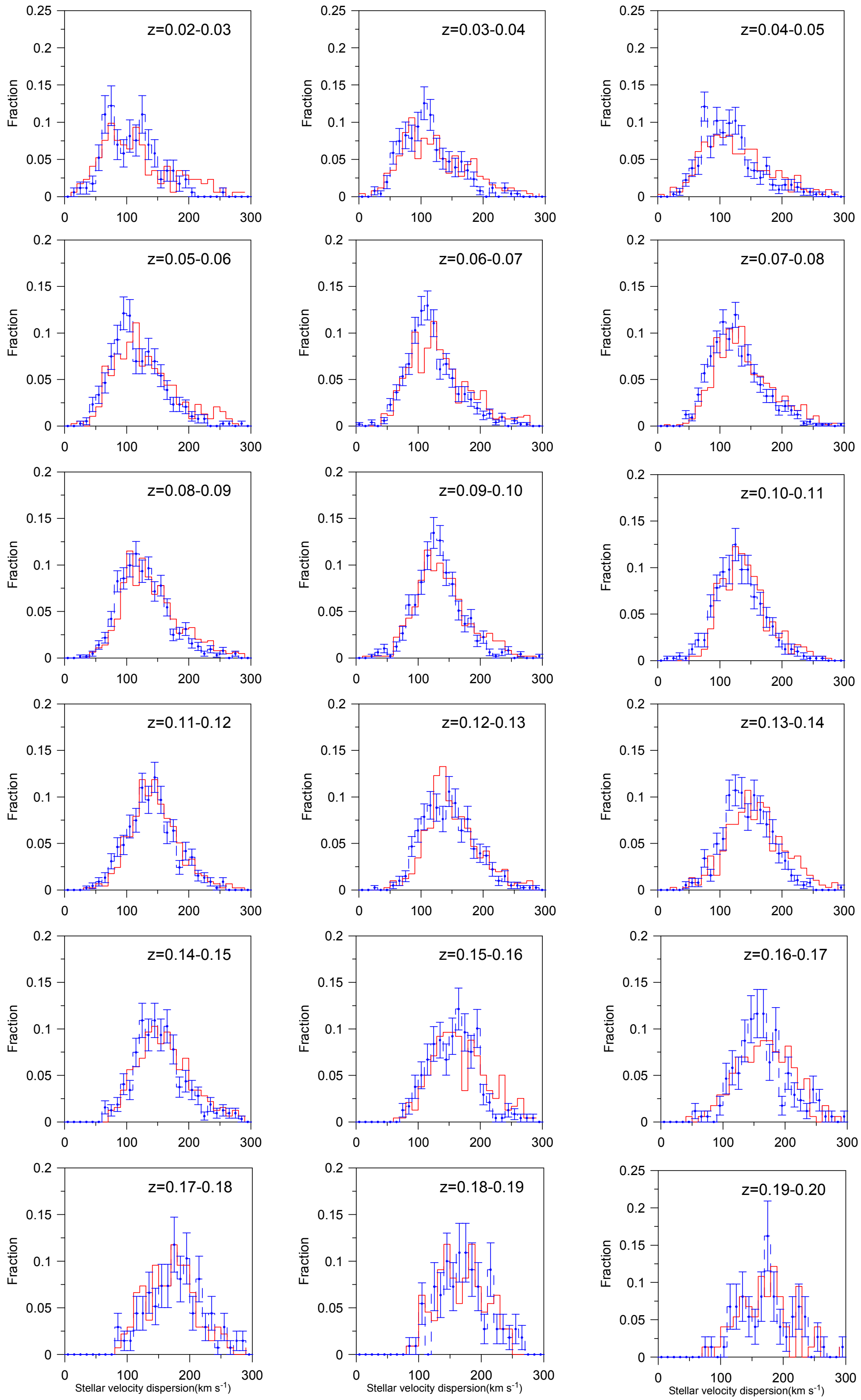

Fig. 4. Same as Figure 1 but for the stellar velocity dispersion distribution at both extremes of the density in different redshift bins. The color figure can be viewed online.

The Kolmogorov-Smirnov (KS) test can serve for a quantitative comparison, which demonstrates the degree of similarity or difference between two independent distributions in a figure by calculating a probability value. A large probability implies that it is very likely that the two distributions are derived from the same parent distribution. Conversely, a low probability implies that the two distributions are different. The probability of the two distributions coming from the same parent distribution is listed in Table 1, which is much larger than that obtained by Deng (2012) (see Table 1 of Deng 2012) and even much larger than 0.05 (5%, is the standard in a statistical analysis). Such a result shows that two independent distributions in these two figures are very similar. This is in good agreement with the conclusion obtained by the histogram figures.

The redshift range of the AGN sample in this work is the same as one of the apparent-magnitude limited Main galaxy sample of the SDSS used by Deng et al. (2012) and Deng (2015). Using the same method, Deng et al. (2012) demonstrated that there is a strong environmental dependence of the stellar mass, the star formation rate (SFR), the specific star formation rate (SSFR, the star formation rate per unit stellar mass) in nearly all redshift bins of the apparent-magnitude limited Main galaxy sample. Deng et al. (2012) also noted that in the high redshift region, the KS probability of the stellar mass, SFR and SSFR distributions increases considerably with increasing redshift, which means that the environmental dependence of stellar mass, SFR and SSFR becomes weak with increasing redshift.

In order to examine the environmental dependence of the stellar velocity dispersion in local galaxies, Deng (2015) constructed two volume-limited samples with the luminosity $-20.5 \leq M_r \leq -18.5$ and $-22.5 \leq M_r \leq -20.5$, respectively. Considering some drawbacks of volume-limited samples, Deng (2015) also used the apparent-magnitude limited Main galaxy sample. Statistical analyses in these different galaxy samples can reach the same conclusion: galaxies with large stellar velocity dispersions exist preferentially in high density regimes, while galaxies with small stellar velocity dispersions are located preferentially in low density regions.

Deng (2014) demonstrated a strong environmental dependence of galaxy age in two volume-limited Main galaxy samples, but Deng & Wen (2020) reported that in the faint volume-limited AGN host galaxy sample, the environmental dependence of the age is fairly weak. Zheng et al. (2017) presented the stellar age and metallicity distributions for 1105 galaxies on the SDSS-IV MaNGA (Mapping Nearby Galaxies at APO) (Bundy et al. 2015) integral field spectra, and also found that the galaxy age depends on local density. Thus, Deng & Wen (2020) believed that the environmental dependence of the age of AGN host galaxies is likely different from the one of genenal galaxies, which merits further studies.

When exploring an issue, one often used different samples or statistical methods to obtain information about it. Due to the Malmquist bias (Malmquist 1920; Teerikorpi 1997) in the apparent-magnitude limited sample, the averaged luminosity of galaxies dramatically increases with increasing redshift. Following Deng (2012) in order to decrease the effect of the Malmquist bias on statistical results, we divide the apparent-magnitude limited AGN sample into many subsamples with a redshift binning size of $\Delta z = 0.01$, and focus on a statistical analysis of the subsamples in each redshift bin. Such a method can also explore the variation of the environmental dependence of galaxy properties with redshift. Apparently, each subsample with a redshift binning size of $\Delta z = 0.01$ likely is limited to a narrow luminosity region. As is well-known, many other parameters of galaxies are closely correlated with the galaxy luminosity (e.g. de Vaucouleurs 1961; Kormendy 1977; Bower et al. 1992; Blanton et al. 2003; Shen et al. 2003; Baldry et al. 2004; Balogh et al. 2004a; Kelm et al. 2005). Thus, many other parameters of these subsamples are also limited, which leads to a decrease of the environmental dependence of these galaxy parameters in these subsamples. However, some works demonstrated that in the redshift bin $\Delta z = 0.01$, the environmental dependence of galaxy properties can still be observed if it exists (e.g., Deng 2012; Deng et al. 2012). In general, one often constructs the volume-limited galaxy samples in a luminosity region and a redshift limit Z_{max}, to decrease the Malmquist bias. In such volume-limited galaxy samples, the redshift range is much wider than our redshift bin; the range of other galaxy properties also is fairly large. Thus, one likely sees more apparent environmental dependence of galaxy properties in the volume-limited galaxy samples. If the environmental dependence of these galaxy properties in these subsamples can be apparently observed, it should be stronger in the volume-limited samples constructed by many authors in a luminosity region and a redshift limit Z_{max}.

4. SUMMARY

In this study, we use the apparent-magnitude limited AGN sample of the SDSS DR12 (Alam et al.

2015) which contains 122923 AGN host galaxies and investigate the environmental dependence of age, stellar mass, SFR and stellar velocity dispersion of active galactic nucleus (AGN) host galaxies. Following Deng (2012), we divide the whole apparent-magnitude limited AGN sample into many subsamples with a redshift binning size of $\Delta z = 0.01$, and analyse the environmental dependence of galaxy properties of subsamples in each redshift bin. As shown by Figures 1-4, these parameters of AGN host galaxies seemingly have only a weak environmental dependence. We also perform the Kolmogorov-Smirnov (KS) test. The statistical result is in good agreement with the conclusion obtained by the histogram figures.

We thank the anonymous referee for many useful comments and suggestions. This study was supported by the National Natural Science Foundation of China (NSFC, Grant 11533004, 11563005).

Funding for SDSS-III has been provided by the Alfred P. Sloan Foundation, the Participating Institutions, the National Science Foundation, and the U.S. Department of Energy. The SDSS-III web site is http://www.sdss3.org/.

SDSS-III is managed by the Astrophysical Research Consortium for the Participating Institutions of the SDSS-III Collaboration including the University of Arizona, the Brazilian Participation Group, Brookhaven National Laboratory, University of Cambridge, University of Florida, the French Participation Group, the German Participation Group, the Instituto de Astrofisica de Canarias, the Michigan State/Notre Dame/JINA Participation Group, Johns Hopkins University, Lawrence Berkeley National Laboratory, Max Planck Institute for Astrophysics, New Mexico State University, New York University, Ohio State University, Pennsylvania State University, University of Portsmouth, Princeton University, the Spanish Participation Group, University of Tokyo, University of Utah, Vanderbilt University, University of Virginia, University of Washington, and Yale University.

REFERENCES

Alam, S., Albareti, F. D., Allende Prieto, C., et al. 2015, ApJS, 219, 12

Baldry, I. K., Glazebrook, K., Brinkmann, J., et al. 2004, ApJ, 600, 681

Balogh, M. L., Baldry, I. K., Nichol, R., et al. 2004a, ApJ, 615, 101

Balogh, M., Eke, V., Miller, Ch., et al. 2004b, MNRAS, 348, 1355

Balogh, M. L., Morris, S. L., Yee, H. K. C., Carlberg, R. G., & Ellingson, E. 1997, ApJ, 488, 75

Balogh, M. L., Schade, D., Morris, S. L., et al. 1998, ApJ, 504, 75

Blanton, M. R., Hogg, D. W., Bahcall, N. A., et al. 2003, ApJ, 594,186

Botte, V., Ciroi, S., di Mille, F., Rafanelli, P., & Romano, A. 2005, MNRAS, 356, 789

Bower, R. G., Lucey, J. R., & Ellis, R. S. 1992, MNRAS, 254, 601

Brinchmann, J., Charlot, S., White, S. D. M., et al. 2004, MNRAS, 351, 1151

Bundy, K., Bershady, M. A., Law, D. R., et al. 2015, ApJ, 798, 7

Capelo, P. R., Dotti, M., Volonteri, M., et al. 2017, MNRAS, 469, 4437

Chen, Y. P., Zaw, I., Farrar, G. R. 2018, ApJ, 861, 67

De Lucia, G., Springel, V., White, S. D. M., Croton, D. & Kauffmann, G. 2006, MNRAS, 366, 499

de Vaucouleurs, G. 1961, ApJS, 5, 233

Deng, X. F., Chen, Y. Q., & Jiang, P. 2011, Chinese Journal of Physics, 49, 1137

Deng, X. F. 2012, AJ, 143, 15

Deng, X. F., Wu, P., Qian, X. X., & Luo, Ch. H. 2012, PASJ, 64, 93

Deng, X. F. 2014, BASI, 42, 59

________. 2015, OPhy, 13, 123

Deng, X. F. & Wen, X. Q. 2020, RMxAA, 56, 87

Dressler, A., Thompson, I. B., & Shectman, S. A. 1985, ApJ, 288, 481

Etherington, J., Thomas, D., Maraston, C., et al. 2017, MNRAS, 466 228

Gallazzi, A., Charlot, S., Brinchmann, J., & White, S. D. M. 2006, MNRAS, 370, 1106

Gómez, P. L., Nichol, R. C., Miller, C. J., et al. 2003, ApJ, 584, 210

Goto, T., Yamauchi, Ch., Fujita, Y., et al. 2003, MNRAS, 346, 601

Greene, J. E. & Ho, L. C. 2006a, ApJ, 641, 117

________. 2006b, ApJ, 641, 21

Gunn, J. E. & Gott, J. R. I. 1972, ApJ, 176,1

Hashimoto, Y., Oemler, A. Jr., Lin, H., & Tucker, D. L. 1998, ApJ, 499, 589

Hu, J. 2008, MNRAS, 386, 2242

Hwang, H. S., Park, C., Elbaz, D., & Choi, Y.-Y. 2012, A&A, 538, 15

Kauffmann, G., Heckman, T. M., Tremonti, Ch., et al. 2003, MNRAS, 346, 1055

Kauffmann, G., White, S. D. M., Heckman, T. M., et al. 2004, MNRAS, 353, 713

Kelm, B., Focardi, P., & Sorrentino, G. 2005, A&A, 442, 117

Kewley, L. J., Heisler, C. A., Dopita, M. A., & Lumsden, S. 2001, ApJS, 132, 37

Kormendy, J. 1977, ApJ, 217, 406

Koulouridis, E. & Bartalucci, I. 2019, A&A, 623, 10

Lanzoni, B., Guiderdoni, B., Mamon, G. A., Devriendt, J., & Hatton, S. 2005, MNRAS, 361, 369

Lewis, I., Balogh, M., Propris, R., et al. 2002, MNRAS, 334, 673
Li, Ch., Kauffmann, G., Jing, Y. P., et al. 2006, MNRAS, 368, 21
Malmquist, G. K. 1920, MeLuS, 22, 3
Mendes de Oliveira, C., Coelho, P., González, J. J., & Barbuy, B. 2005, ApJ, 130, 55
Miller, C. J., Nichol, R. C., Gómez, P. L., Hopkins, A. M., & Bernardi, M. 2003, ApJ, 597, 142
Patel, S. G., Holden, B. P., Kelson, D. D., Illingworth, G. D., Franx, M. 2009, ApJ, 705, 67
Poudel, A., Heinämäki, P., Nurmi, P., et al. 2016 A&A, 590, 29
Proctor, R. N., Forbes, D. A., Hau, G. K. T., et al. 2004, MNRAS, 349, 1381
Rakos, K., Schombert, J., & Odell, A. 2007, ApJ, 658, 929
Reed, D. S., Governato, F., Quinn, T., Stadel, J., & Lake, G. 2007, MNRAS, 378, 777
Shen, S., Mo, H. J., White, S. D. M., et al. 2003, MNRAS, 343, 978
Smith, R. J., Lucey, J. R., Price, J., Hudson, M. J., & Phillipps, S. 2012, MNRAS, 419, 3167
Strauss, M. A., Weinberg, D. H., Lupton, R. H., et al. 2002, AJ, 124, 1810
Tanaka, M., Goto, T., Okamura, S., Shimasaku, K., & Brinkmann, J. 2004, AJ, 128, 2677
Teerikorpi, P. 1997, ARA&A, 35, 101
Thomas, D., Maraston, C., Bender, R., & Mendes de Oliveira, C. 2005, ApJ, 621, 673
Wegner, G. & Grogin, N. A. 2008, AJ, 136, 1
Worpel, H., Brown, M. J. I., Jones, D. H., Floyd, D. J. E., & Beutler, F. 2013, ApJ, 772, 94
Zheng, Z., Wang, H., Ge, J., et al. 2017, MNRAS, 465, 4572
Zou, F., Yang, G., Brandt, W. N., & Xue, Y. 2019, ApJ, 878, 11

Xin-Fa Deng and Xiao-Qing Wen: School of Science, Nanchang University, Jiangxi, China, 330031, (xinfadeng@163.com).

Revista Mexicana de Astronomía y Astrofísica, **57**, 167–179 (2021)

https://doi.org/10.22201/ia.01851101p.2021.57.01.12

NEW SPECTRAL ANALYSIS RESULTS WITHIN THE SCOPE OF EXTENDED MATTER RESEARCH IN THE AR LACERTAE ACTIVE BINARY SYSTEM

O. Karakuş and F. Ekmekçi

Ankara University, Faculty of Science, Department of Astronomy and Space Sciences, 06100 Tandoğan, Ankara, Turkey.

Received July 23 2020; accepted November 16 2020

ABSTRACT

Within the scope of extended matter research, we present new spectral analysis results of an active binary system, AR Lac. The low and high resolution spectra of this system, were taken during the period 2013-2016. The evaluation of low dispersion spectra together with the B, V, R_c, I_c and `WISE` photometric data showed that AR Lac has an excess radiation in the `W2` band. In addition, the spectral energy distribution and the minima depth ratios of the light curves of this active binary system were studied to examine the flux contributions of the components of the system depending on wavelengths and on orbital phase. Furthermore, high resolution spectral analysis showed evidence of prominence-like structures and a possible extended matter around the cooler component of AR Lac.

RESUMEN

Presentamos los resultados de un nuevo análisis espectral de la binaria activa AR Lac. Obtuvimos espectros de baja y alta resolución de este sistema durante los años 2013-2016. La evaluación de los espectros de baja dispersión, junto con los datos fotométricos B, V, R_c, I_c y del `WISE`, mostró que AR Lac tiene un exceso de radiación en la banda `W2`. También estudiamos la distribución espectral de energía y los cocientes de los mínimos de las curvas de luz de esta binaria activa para determinar las contribuciones al flujo de las componentes, en función de la longitud de onda y de la fase orbital. Los espectros de alta resolución mostraron evidencia de estructuras tipo prominencia, y de la posible existencia de material extendido alrededor de la componente más fría de AR Lac.

Key Words: binaries: eclipsing — circumstellar matter — stars: activity — stars: chromospheres — stars: individual: AR Lac

1. INTRODUCTION

AR Lac (HD 210334, $Vmax = 6.09$, $P = 1.98$ days) is one of the bright chromospherically active and totally eclipsing binary systems (CABs). This RS CVn type binary system has components of spectral type `G2 IV + K0 IV`. Lu et al. (2012) summarized the previous studies that had been presented by numerous investigators, including photometric and spectroscopic observations. This active binary system is well known to have orbital period changes, magnetic and spot activity, which affect the cooler component, together with strong emission features in the Ca II H and K lines (see Lu et al. 2012). A long-term secular period decrease was estimated at a rate of $\mathrm{d}P/\mathrm{d}t = -(2.128 \pm 0.060) \times 10^{-9} d/\mathrm{d}$ by Lu et al. (2012), which may be caused by the magnetic activity of this active binary system. Based on this result, they also gave an estimation on the mass-loss rate for this binary system as $\mathrm{d}M/\mathrm{d}t = -2.8 \times 10^{-10} M_{\odot}\ \mathrm{yr}^{-1}$.

The spectral Hα and Ca II H and K emission lines are very important indicators of chromospheric or magnetic activity of the component(s) of CABs (see Rodono 1980). Thus, the activity level of a star can also be inferred by determining the presence of an Hα emission line or by the presence of Hα with a filled-in core (see Fernandez-Figueroa et al. 1994;

Barden 1985; Fekel et al. 1986; Bopp et al. 1988; Strassmeier et al. 1990).

In the studies of some CABs, it was found that there were evidences indicating that extended/circumstellar matter in that binary system may exist (see Scaltriti et al. 1993). In these studies the measurements of the excess radiation, especially in the spectral region of long wavelengths, were used to find excess radiation which may be caused by mass loss due to stellar winds, and which may be related to extended/circumstellar matter.

Assessments of some important observational data of disk structure around chromospherically active binary stars began with the infrared astronomical satellite (IRAS) in 1983. IRAS was the first mission to put a telescope in space to survey the entire sky in the 12, 25, 60, and 100 micron bands (Scaltriti et al. 1993). Based on IRAS observations, Busso et al. (1988) found that an IR excess is definitely present in CF Tuc, while the spectral distributions of the λ And, UX Ari and AR Lac can be accounted for by combinations of normal stellar components. They also concluded that the excess is not correlated with the activity level, nor with the evolutionary status, but may be correlated with the mass loss phenomena near the main sequence. Possible interpretations of the excess emission based on the evolutionary status of the binary components are also discussed by Busso et al. (1990). They discuss possible explanations in terms of mass loss phenomena(triggered by the binary nature) during the evolution of the sources near the main sequence. The behaviour of excess Ca II H and K and Hϵ emission in a sample of 73 CABs, including AR Lac, was examined by Montes et al. (1996), and they found that there was a good correlation between excess Ca II K and Hϵ chromospheric emission fluxes.

In their Hα line study of the system, Frasca et al. (2000) found that there are chromospheric emissions from both components in most spectra and the rotational modulation of Hα line emission is not obvious. They gave an interpretation of the excess absorption observed in 1997 during and near the primary minima as a comment for the effect of a prominence-like structure anchored between the leading and trailing hemisphere of the cool component. This interpretation was fully compatible with the radial velocities of Hα peaks in the extracted spectra. Zboril et al. (2004) reported that the central depth of Hα profiles of AR Lac at eclipses (at $0.041P$ and $0.043P$) were deeper than synthetic profiles and similar to the profiles of stars with the same spectral types (e.g. δ Eri).

Lanza et al. (1998) gave a detailed analysis of the long-term and seasonal light curves of AR Lac. Based on their main results concerning the magnetic activity of AR Lac binary system, they concluded that the large active region around the substellar point on the secondary showed itself not only at photospheric levels but also in the chromosphere and corona, with an extended structure which might well be an interconnecting loop between the two stars.

The results of Very Large Array (VLA) observations of AR Lac during optical eclipses in 1977 were reported by Owen & Spangler (1977). They found a small increase in radio flux density during $0.5P$, although the radio source had variation on time scales $\geq$ a few hours, but they did not detect a strong eclipse-like feature that occurs near $0.0P$ or $0.5P$ orbital phases. Together with their spectral evaluations and taking into account the synchrotron self-absorption, they suggested that the radiation is likely to be produced in a volume much larger than the stars in the system due to the lack of a clearly defined eclipse in the AR Lac binary system.

Simultaneous observations of AR Lac at radio and ultraviolet wavelengths during two consecutive secondary eclipses, made in 1979 May, were reported by Brown et al. (1979). During one of the eclipses they saw a quiescent radio source without evidence of an eclipse at radio wavelengths. On the second one, they found that the radio source was brighter by a factor of 3, together with an evident radio eclipse. And, in the latter case, the radio source was circularly polarized by 5-10% during eclipse. They also stated that:

- the sense of circular polarization changed abruptly at first contact, and
- the radio eclipse was twice as deep in one sense of circular polarization as it was in the other.

They identified the following features from their simultaneous ultraviolet observations: The ultraviolet coronal lines also showed the eclipse. But, the eclipse on the day in which the radio source was quiescent became much more prominent than the eclipse on the day in which the radio source was active. In other words, the effect of eclipse on the coronal ultraviolet lines increases while the radio source is in quiescent state, but while the radio source is in an active state the effect of eclipse decreases, and the eclipse becomes more uncertain. Thus, this result is evidence that coronal activity in the radio region increases the brightness, and this increase will not only be caused by stellar activity because the brightness effect of the radiation in the ultraviolet region was not seen at the same time.

By using the `Einstein` Imaging Proportional Counter `(IPC)` observations of the X-ray eclipse together with the cotemporal `International Ultraviolet Explorer (IUE)` and radio observations, Walter et al. (1983) found an extended corona with a scale of about $1R_*$, to be associated with the `K0 IV` component of AR Lac. They obtained X-ray, radio, and ultraviolet observations of the system over one orbital cycle. The primary minimum of the X-ray light curve they obtained for AR Lac was deep and the secondary minimum was broad and shallow. They found that the quiescent corona of the `G2 IV` component is small and asymmetric, extending to some $0.02R_*$ above the photosphere and is related with stellar spots. On the other hand, the `K0 IV` component was found to have two coronal components: (1) an outer, extended coronal component, which is presumably a hotter component that extends to $1R_*$ above the photosphere and exhibits a bright hemisphere; (2) an inner coronal component, which is small relative to the stellar radius.

Using their `VLA` observations at 1.5 and 4.9 GHz on 13 and 15 October 1982, Doiron & Mutel (1984) did not detect a clear eclipse signature in the light curve of AR Lac. On both observing days, a significant circular polarization of 2%-8% was observed with a helicity reversal between 1.5 and 4.9 GHz; they attributed this result to a gyro-synchrotron mechanism.

Using the `IUE LWR` and `SWP` spectra of AR Lac, obtained on 3-5 October 1983, and their `VLA` observation on 4-5 October 1983 at 2, 6, and 20 cm, Walter et al. (1987) determined the atmospheric structure within the plage regions together with the properties of the extended coronal component around the `K0 IV` star. They identified three discrete regions of emissions in the outer atmosphere of the `K0 IV` star in which there are two plages and a chromospheric brightening that was related to a radio flare.

Based on their results of the multifrequency `VLA` and Very Long Baseline Array (VLBA) observations, made in 1997, Trigilio et al. (2001) inferred the following:

- the spectral and spatial information of the corona of AR Lac indicate a structured morphology, which can be modeled with a core-halo source;
- the physical parameters, as derived from the fit of the observed spectra with the core-halo model, are consistent with the hypothesis of a co-spatial X-ray and radio source;
- the observed radio emission cannot be attributed to the same thermal electron population responsible for the observed X-ray emission.

Koch (2007) detected a variable polarization in the AR Lac. He reported that the seat of the polarization could provisionally be located in the assorted active clouds that populate the outer envelope of the `K0 IV` component. Also, he reported that the plasma must be poor in metals compared to the Sun and must not have a simple polarization spectrum. In this regard, he also gave the following explanation: “Since Z is about $0.6Z_{\odot}$, there is a possibility that the metal depletion is only apparent and not real, because of the grain condensation in the cool envelope, and that grains alone are the seats of the polarization.”

Recently, research on the extended/circumstellar matter in CABs was presented by Karakuş & Ekmekçi (2020). Based on their photometric `CCD` data of 13 CABs, including AR Lac, and together with the `2MASS` and `WISE` data, they found that AR Lac had some fluctuations in colour excess `(CE)` values around primary minimum. They also found that the system showed some characteristic variations in the `CE` values towards longer wavelengths, both around secondary minimum and outside eclipse, but with lower detectable `CE` values in all bands outside eclipses. They concluded that the main source of excess radiation in AR Lac is stellar activity. This stellar activity is expected to contribute to the formation of extended/circumstellar matter in AR Lac, but significant evidence on how much it contributes could not be presented by Karakuş & Ekmekçi (2020), based solely on their results of photometric `CE` measurements.

In this study, the spectra of AR Lac taken during the observing period 2013-2016 at different orbital phases by using the Coudé Echelle and `TFOSC (Faint Object Spectrograph and Camera)` instruments were analysed to investigate and to reveal the relationship between its stellar activity and a possible extended/circumstellar matter of the system. In addition, together with the results of this spectral analysis of the AR Lac system, an evaluation was made by including the results given by Karakuş & Ekmekçi (2020) based on their photometric `CCD, 2MASS` and `WISE` data taken during minima and outside eclipses. Within the scope of this evaluation, the B, V, R_c, I_c, and W1, W2, W3, W4 of WISE band light curves of AR Lac were also taken into consideration.

2. OBSERVATIONS AND DATA REDUCTIONS

Spectral observations of AR Lac were carried out at times to cover the external and internal contact parts of the light curve of the system during eclipses, together with descending and ascending parts. The choice of these observation times corresponding to these orbital phases was made to see the relationship of the system's activity events with the characteristics of the component stars on the disc edges and a possible extended/circumstellar matter. For this purpose, both low and high resolution spectral data were used to investigate the presence of a possible extended/circumstellar matter together with the properties and evolutionary states of the components of AR Lac.

For all low and high resolution spectra of this study, Image Reduction and Analysis Facility (IRAF)[1] was used to reduce the combined data with standard procedures, including the corrections for flat and bias, and the determination of aperture, wavelength calibration, velocity correction, and interstellar extinction/cosmic radiation. But, the atmospheric and interstellar extinction effects have only been corrected for the low resolution spectra. The standard stars selected and observed within the conditions of observability for flux calibration are as follows: Vega (HR 7001, A0 V, $V = 0.03$) and HR 8634 (B8 V, $V = 3.41$). Standard flux values for the stars are taken from the website "https://snfactory.lbl.gov/snf/spstds/" and the references therein. In addition, the TFOSC spectra of HR 5510 (M1 III, $V = 6.28$), a reference star, were taken to evaluate the effect of telluric line absorptions on the spectra of the AR Lac binary system. For the Hα profile analysis, the high resolution spectra of two reference stars of the same spectral types as the components of AR Lac, were also taken. These two stars are: HD 195405 (G2 IV) and HR 6256 (K0 IV).

In addition, photometric data, from Karakuş & Ekmekçi (2020), of AR Lac in the Johnson-Cousins BVR_cI_c and medium WISE bands were used to make a comparison with our spectroscopic results. In all these bands, the photometric light curves of AR Lac were also constructed and evaluated using the photometric colour excess measurements of Karakuş & Ekmekçi (2020). Some details about these photometric observational data are presented below in § 2.3.

[1] http://iraf.noao.edu/.

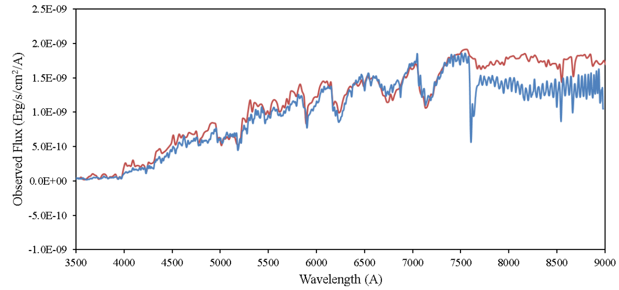

Fig. 1. A comparison synthetic spectrum(as a red line) and observational TFOSC spectrum(as a blue line) of the HR 5510 reference star. A drop in the continuum fluxes due to telluric lines is seen clearly. The synthetic spectrum is constructed by taking $\log g = 1.5$, $T(K) = 3500$, and $Z = 0$. The colour figure can be viewed online.

2.1. *Low Dispersion Spectra*

The optical low resolution spectral observations of AR Lac, a reference star (HR5510) and two standard stars (Vega and HR 8634) took place during the observing period 2015-2016, by using the TUG (TÜBİTAK National Observatory) Faint Object Spectrograph and Camera (TFOSC) mounted on the 1.5 m Russian Turkish Telescope RTT150[2] in Antalya, Turkey. The log of TFOSC observations is given in Table 1. Grism 15 was used with a 100 micron slit. The wavelength range in this configuration is 3230−9120 Å, and the resolving power (R)≈749. Ar, Ne, He and Halogen lamp spectra taken in the same night as the star were used for wavelength calibration and flat-fielding. A total of 65 slit spectra were obtained: 30 of the spectra were taken for AR Lac, and the rest were spectra for other standard stars (see Table 1).

As can be seen from Figure 1, the low resolution TFOSC spectra show the effect on the continuum level of telluric lines caused by water vapor, oxygen and carbon dioxide molecules in the Earth's atmosphere in the spectral range 6000 − 9000 Å. This effect is larger in cold stars than in hotter stars, especially in the photometric "Ic" band spectral region.

In order to compare the obtained TFOSC spectra with a synthetic spectrum, the synthetic spectra were constructed by using the appropriate temperature, surface acceleration and metal abundance values, taken from website "http://svo2.cab.intacsic.es/theory/newov2/index.php". Theoretical spectra were obtained using the ATLAS9 Kurucz ODFNEW/NOVER (Castelli et al. 1997) data in a model with zero metal abundance. To construct a model

[2] Specifications of RTT150 and TFSOC are available at www.tug.tubitak.gov.tr.

TABLE 1

LOG OF TUG TFOSC SPECTRAL OBSERVATIONS OF THREE STANDARD STARS AND AR LAC

Stellar Object	Type	Date of obs.	HJD	Start time of obs.(UT)	Exposure time (sec.)	Airmass (mag.)	Orbital phase	Number of images
Vega	*Standard*	Oct. 12, 2015	2457308.278	18:40:02	0.8	1.316	-	5
AR Lac	*Variable*	Oct. 12, 2015	2457308.428	22:11:28	30	1.295	0.995	10
HR 5510	*Reference*	June 04, 2016	2457544.282	18:42:21	5	1.033	-	5
Vega	*Standard*	June 04, 2016	2457544.351	20:21:48	5	1.286	-	5
Vega	*Standard*	June 05, 2016	2457545.404	21:39:36	0.03	1.089	-	10
AR Lac	*Variable*	June 05, 2016	2457545.422	22:08:49	20	1.739	0.496	10
HR 8634	*Standard*	Sept. 05, 2016	2457637.322	19:35:20	2	1.271	-	10
AR Lac	*Variable*	Sept. 05, 2016	2457637.438	22:25:47	7	1.048	0.894	10

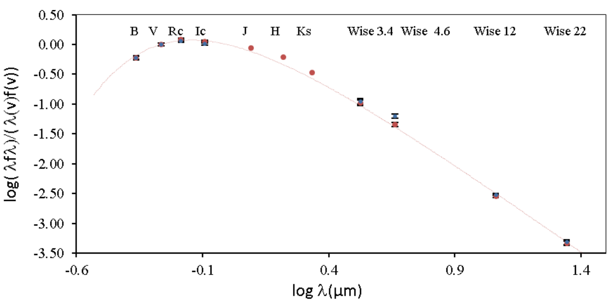

Fig. 2. Comparison of the SEDs of AR Lac and the reference star HD 56168. The photometric values of HD 56168 [$(B-V)_{\circ}$=0.90 ± 0.01] are indicated as red points, while the values of AR Lac [$(B-V)_{\circ}$=0.87±0.04], during 0.0P, are indicated as blue points. The straight line shows the black body energy distribution of T(K)=5100. The colour figure can be viewed online.

spectrum of AR Lac, by using the ATLAS9 Kurucz ODFNEW/NOVER model atmosphere, the related parameters were taken as:
For the G0 IV component; $T(K) = 5750$, $\log g = 4.0$, and $Z = 0$.
For the K0 IV component; $T(K) = 5000$, $\log g = 3.5$, and $Z = 0$.

The flux contributions from both components of AR Lac were computed using the physical parameters (masses; $M_{1,2}$, radii; $R_{1,2}$, Planck functions; $B_{1,2}$, fractional projected area depending on orbital phase; $A_{1,2}(\phi)$, orbital inclination; i) as done by Şenavcı et al. (2018) for SV Cam.

In Figure 2, the spectral energy distribution (SED) modeled for 0.0P orbital phase of AR Lac (i.e. the stellar configuration in which the hotter component of the system is totally eclipsed by the cooler component) was compared with the SED modeled for the HD 56168 reference star, of the same spectral type as the cooler component of AR Lac. In this figure, the SED of a black body radiation with the temperature of the cooler component of AR Lac (K0 IV, 5100 K) was also included. As shown in Figure 2, the flux values of the SED obtained from photometric CCD data are well compatible with the spectral model results. However, this compatibility appears to be seen in the B, V, R_c bands for the TFOSC spectral data, while there is a significant decrease in the continuum level of the TFOSC spectrum due to telluric line absorption effects in the I_c band spectral range (see Figure 3).

2.2. *High Dispersion Spectra*

In order to determine the activity level of a star depending on the spectral Hα profile, the photospheric effect must be removed from the Hα line profile. In the case of binary system, the flux contributions to photospheric Hα absorption from both components were also taken into consideration in this method of determination of the activity level. This method, which eliminates the photospheric absorption effect from the Hα line profile, is called *"Spectral Extraction Method"*. In this study, we tried to analyse the behaviour of Hα excess emission in the chromospherically active binary system AR Lac, by using this *Spectral Extraction Method*. For this purpose, high resolution spectra of AR Lac, at different orbital phases, in the wavelength range of $6500 - 6700$ Å with resolution power $R \approx 40000$ were taken on July 13-14, 2013 using the Coude Echelle Spectrograph on the RTT150 telescope of TUG. The logs of high resolution spectral observations are given in Tables 2 and 3.

The chromospheric contribution to the Hα line profile has been determined using the spectral subtraction technique. This technique was applied to high resolution spectra of AR Lac with the following steps:

(i) The high resolution spectra of reference stars (HD 195405 and HR 6256) taken with TUG

TABLE 2

LOG OF TUG ECHELLE SPECTRAL OBSERVATIONS OF AR LAC

HJD	Date of obs.	Start time of obs. (UT)	Exposure time (sec.)	Airmass (mag.)	Phase[a]	G2 IV Contribution rate	K0 IV Contribution rate	S/N
2456487.407	13.07.2013	21:29:29	1800	1.242	0.012	0.00	1.00	41
2456487.437	13.07.2013	22:04:36	2700	1.157	0.026	0.08	0.92	54
2456487.475	13.07.2013	22:59:53	2700	1.069	0.046	0.25	0.75	84
2456487.509	13.07.2013	23:48:50	2700	1.027	0.063	0.34	0.66	83
2456487.542	14.07.2013	00:36:32	2700	1.012	0.080	0.36	0.64	92
2456487.576	14.07.2013	01:24:42	2700	1.023	0.097	0.36	0.64	94
2456488.401	14.07.2013	21:12:38	2700	1.279	0.513	0.46	0.54	90
2456488.434	14.07.2013	22:00:09	2700	1.158	0.529	0.45	0.55	90
2456488.467	14.07.2013	23:01:02	2700	1.040	0.546	0.44	0.56	94
2456488.501	14.07.2013	23:36:17	2700	1.032	0.563	0.37	0.63	70
2456488.534	15.07.2013	00:23:47	2700	1.013	0.579	0.36	0.64	94
2456488.567	15.07.2013	01:11:18	2700	1.019	0.596	0.36	0.64	80

[a]Orbital phases are computed by using the light elements taken from TIDAK (TIming DAtabase in Krakow) http://www.as.up.krakow.pl/ephem/old-ephem/EPHEM-2012xi.TXT.

TABLE 3

LOG OF TUG ECHELLE SPECTRAL OBSERVATIONS OF REFERENCE STARS

Star	HJD	Date of obs.	Start time of obs.(UT)	Exposure time (sn)	Airmass (mag.)	S/N
HR 6256	2456488.287	14.07.2013	18:36:28	1800	1.016	89
HR 6256	2456488.310	14.07.2013	19:08:57	1800	1.007	61
HD 195405	2456487.333	13.07.2013	19:39:31	2000	1.280	30
HD 195405	2456487.366	13.07.2013	20:18:08	3000	1.174	31

were compared with the high resolution ELODIE spectra[3] of HD 12235 (G2 V) and HD 23249 (K0 IV), which were selected from the catalogue of Montes et al. (1997). This comparison showed that the Hα profiles of TUG and ELODIE spectra were compatible (see Figure 4).

(ii) From the catalogue of Montes et al. (1997), the equatorial rotational velocities were obtained as $15\,\mathrm{km\,s^{-1}}$ and $2\,\mathrm{km\,s^{-1}}$ for HD 12235 (G2 IV) and HD 23249 (K0 IV), respectively. Based on our compatible results, in accordance with their spectral type, we attributed these velocities to our reference stars (HD 195405 and HR 6256).

(iii) Rotational velocities for the components of AR Lac (G2 IV + K0 IV), were found by Frasca et al. (2001) as $46\,\mathrm{km\,s^{-1}}$ and $73\,\mathrm{km\,s^{-1}}$, respectively (see Table 4). Depending on the orbital phase, the observed Hα line profiles of the double-lined spectroscopic and active binary system, AR Lac, are shown in the left panel of Figure 6. Taking into account the rotational velocities of Frasca et al. (2001), given above, the following rotational velocities were applied to the observed spectra of reference stars in modelling the synthetic spectrum of AR Lac by using STARMOD program (see Barden 1985; Montes et al. 2000):
V(rot) $\approx 30\,\mathrm{km\,s^{-1}}$ $(= 46 - 15)$, for HD 195405 (G2 IV).
V(rot) $\approx 70\,\mathrm{km\,s^{-1}}$ $(= 73 - 2)$, for HR 6256 (K0 IV).
The input parameters for the STARMOD program were derived by using the parameters of the AR Lac as given in Table 4. The obtained synthetic spectra are shown in Figures 5 and 6 for the reference stars and AR Lac, respectively.

[3]Obtained from http://atlas.obs-hp.fr/elodie/index.html.

Since most of the high resolution spectra were taken during minima times within the scope of this study, Hα profiles of the components of AR Lac were too close to each other (see Figure 7). Therefore, the Hα profiles of the components could not be separated from each other. In addition, very few spectral Hα profiles of the components can be distinguished, so the equivalent width measurements for these Hα profiles were not made.

TABLE 4

ABSOLUTE AND ORBITAL PARAMETERS OF THE AR LAC SYSTEM

Parameters	*Primary Component*	*Secondary Component*	*Reference*
Spectral Type	G2IV	K0IV	Frasca et al. (2000)
Hα Amplitude of Radial Velocity Curve (km s^{-1})	119.43 ± 0.49	106.73 ± 0.29	Frasca et al. (2000)
M($M_\odot$)	1.17 ± 0.035	1.21 ± 0.077	Siviero et al. (2006)
R($R_\odot$)	1.51 ± 0.005	2.61 ± 0.009	Siviero et al. (2006)
log$g$ (cm s^{-2})	4.15 ± 0.021	3.69 ± 0.035	Siviero et al. (2006)
T (K)	5826 ± 5	5100 ± 100	Siviero et al. (2006)
$v \sin i$ (km s^{-1})	46	73	Frasca et al. (2001)
Inclination Angle i (degree)	90		Siviero et al. (2006)
Orbit eccentricity (e)	0		Siviero et al. (2006)
Space Velocity of the System's Center of Mass (km s^{-1})	-34.54 ± 0.50		Frasca et al. (2000)

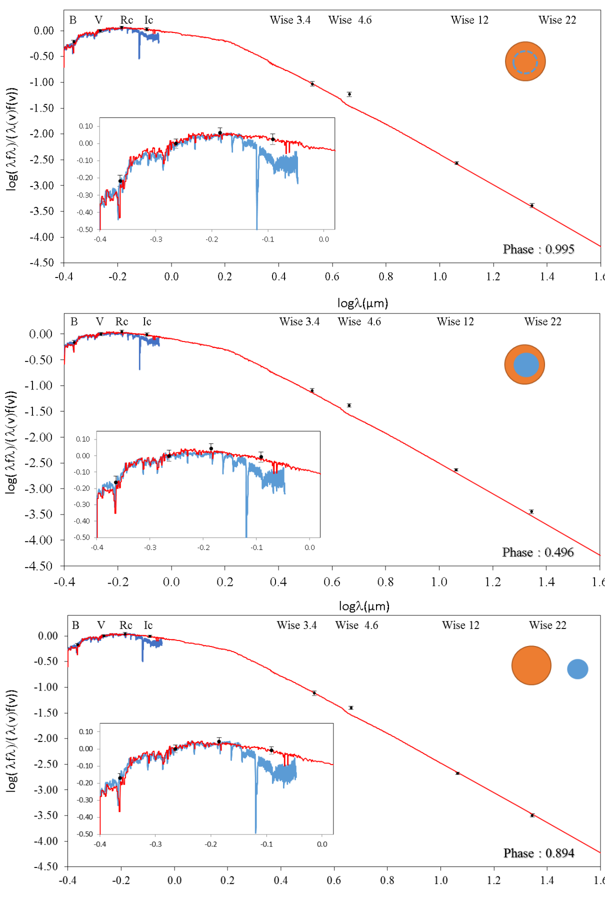

Fig. 3. Spectral energy distribution of AR Lac. The blue line shows the spectrum of TFOSC. The red line indicates the synthetic spectrum and black dots show photometric data. Blue and orange circles indicate the position of the components. The colour figure can be viewed online.

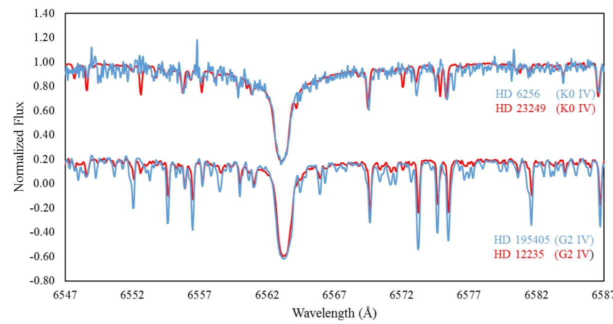

Fig. 4. Comparison of ELODIE (in red colour) and TUG (in blue colour) Hα spectra of reference stars HD 232249 and HR 6256 (upper) and HD 12235 and HD 195405 (lower). In the lower chart, the spectra are drawn by subtracting 0.8 from the flux of 1.0. The colour figure can be viewed online.

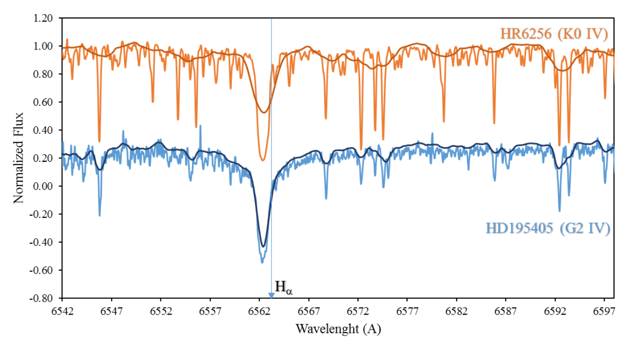

Fig. 5. Normalized Hα spectra of reference stars HD 195405 and HR6256. Straight lines are at 30 km s^{-1} for HD 195405 (G2IV) and 70 km s^{-1} for HR6256 (K0IV), and refer to the synthetic spectra obtained for the rotation speed. In the lower chart, the spectrum of HD 195405 was drawn by subtracting 0.7 from the flux of 1.0. The colour figure can be viewed online.

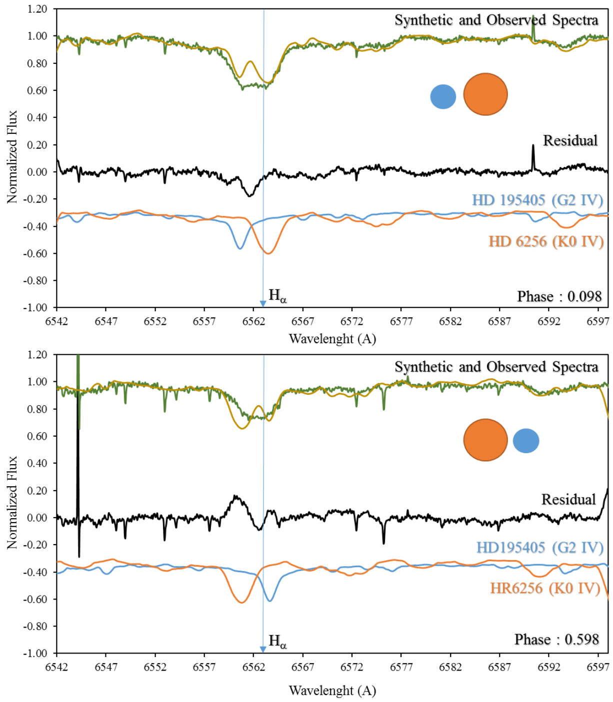

Fig. 6. The model spectral solution of high resolution Hα of AR Lac. The green line represents the observed spectrum; the yellow line shows the model synthetic spectrum; the black line shows the residual spectrum; the blue and orange lines represent the spectra of reference `G2 IV` and `K0 IV` stars, respectively. The colour figure can be viewed online.

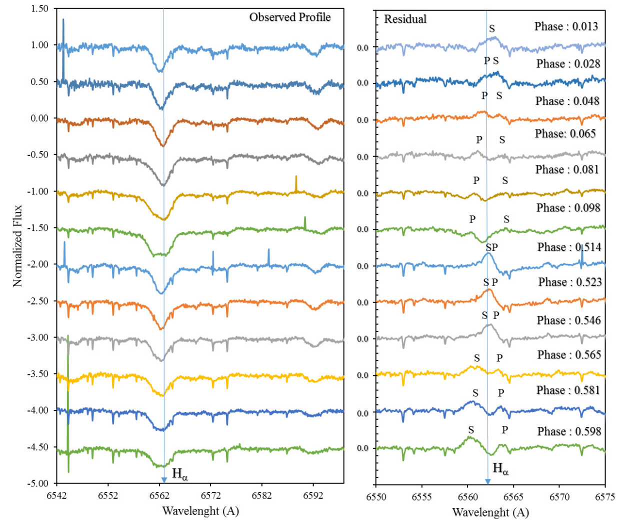

Fig. 7. High resolution normalized Hα line profiles of AR Lac (left panel, consecutive profiles are drawn with a difference of 0.5 in normalized flux values). The corresponding residual Hα line profiles of AR Lac (right panel; P and S, indicate the positions of the primary/hotter and secondary/cooler components, respectively). The colour figure can be viewed online.

TABLE 5

RADIAL VELOCITIES FROM OUR RESIDUAL Hα PROFILES OF AR LAC

Phase	`G2 IV`		`K0 IV`	
	Type	RV (km s^{-1})	Type	RV (km s^{-1})
0.013	-	-	Emission	-28.8
0.028	Emission	-47.5	Emission	-4.6
0.048	Emission	-66.7	Emission	-7.3
0.065	Emission	-81.3	Absorption	-16.9
0.081	Emission	-95.5	Absorption	-47.5
0.098	Emission	-116.9	Absorption	-59.8
0.514	Emission	-26.0	-	-
0.565	Emission	23.8	Emission	-93.2
0.581	Emission	38.4	Emission	-100.0
0.598	Emission	47.5	Emission	-109.6

2.3. *Photometric CCD and Infrared Observations*

In order to evaluate the spectral results of this study within the scope of extended matter research, together with the results of photometric `CCD` and Infrared observations, we constructed the B, V, R_c, I$_c$, `W1, W2, W3` and `W4 (WISE)`[4] (see Wright et al. 2010) band light curves and some characteristics of the AR Lac active binary system based on related observational data of Karakuş & Ekmekçi (2020). These BVR_cI_c observational data were obtained during the period 2012-2013, while the *WISE* data were obtained in 2010. Light curves obtained in normalized luminosity for each band are shown in Figures 9 and 10. The results of colour excess `(CE)` measurements for different photometric bands are shown in Figure 11.

By taking advantage of the geometric configuration of the components of an active and total eclipsing binary system, the presence of an excess radiation of the active component can easily be detected during the primary minimum, at which the occultation of the hotter component by the cooler and active one occurs (e.g. Hall & Ramsey 1994; Karakuş & Ekmekçi 2020). This configuration, during the primary minimum of a total eclipsing and active binary system, could also give an advantage to search for the interaction between the activity/spots phenomena and the extended/circumstellar matter which may exist in the system. Therefore, it is important and useful to examine the structural changes of the photospheric/chromospheric spectral line profiles and to reveal the structure of the spectral energy distribu-

[4]http://irsa.ipac.caltech.edu/Missions/wise.html.

TABLE 6

THE FLUX RATIOS OF THE COMPONENTS OF AR LAC IN ALL PHOTOMETRIC BANDS USED IN THIS STUDY

Band	$\lambda_{(pivot)}$(Å)	Bandwidth (Å)	Depth of Min. I (Err)	Depth of Min. II (Err)	F_{K0IV}/F_{G2IV} (Err)
B	4326	1816	0.491 (0.013)	0.281 (0.014)	1.751 (0.057)
V	5445	1129	0.429 (0.011)	0.275 (0.012)	1.562 (0.051)
R_c	6529	1877	0.433 (0.012)	0.311 (0.013)	1.395 (0.050)
I_c	8104	1604	0.399 (0.011)	0.287 (0.011)	1.388 (0.046)
W1	33526	6625.6	0.347 (0.033)	0.291 (0.046)	1.195 (0.184)
W2	46028	10423	0.335 (0.032)	0.409 (0.023)	0.821 (0.109)
W3	115608	55069	0.318 (0.008)	0.276 (0.007)	1.151 (0.036)
W4	220883	41013	0.356 (0.013)	0.255 (0.011)	1.399 (0.059)

tion (SED), during primary minimum. In this context, active and eclipsing binaries are important in extended/circumstellar matter's studies.

As can be seen from Figures 9 and 10, in the light curves of AR Lac the depths of the primary and secondary minima vary depending on colour (i.e the photometric band). Using the correlation below for the ratio of the minima depth of a light curve (see Kopal & Demircan 1978), in the case of $\sin i = 1$, we can estimate the flux ratio of the component stars as:

$$\frac{F_{K0IV}}{F_{G2IV}} = \frac{\text{Depth of Min. I}}{\text{Depth of Min. II}}. \tag{1}$$

Using all these light curves, the results for the flux ratios are given in Table 6.

As can be seen from these observational results, the observed flux ratios decrease gradually by about 10% towards the longer wavelength (W1), and in the infrared wavelengths of WISE the flux of components are approximately equal, except for the W3 and W4 bands (see Table 6). This decrease in flux ratios towards the longer wavelengths and the equality of fluxes in the W1 and W2 bands suggest that possible extended/circumstellar matter may exist in the AR Lac active binary system.

3. RESULTS

The flux values of SED obtained from photometric CCD data are well compatible with the spectral model results of AR Lac (see Figure 2). From a comparative analysis of the data in Figure 2, it was found that during the primary minimum of AR Lac, there was an excess radiation of $\simeq 0.143 \pm 0.043$ in the W2 band compared to the HD 56168 reference star. It is clear that this excess radiation at primary minimum can be attributed to the cooler component (K0 IV) of AR Lac.

As can be seen from Table 1, the low resolution TFOSC spectra of AR Lac were obtained on Oct. 12, 2015 and June 5, 2016 (at times corresponding to minima), and on Sept. 5, 2016 at times corresponding to outside eclipses. The times which correspond to minima and outside eclipses are determined within the scope of this study. The analysis results of our TFOSC observations were found as given in Figure 3, along with the synthetic spectrum comparison. In addition, visual and infrared photometric results were added to the evaluation of these low resolution spectral results in Figure 3.

From the patterns given in Figure 3, it is seen that the results of low resolution spectra of AR Lac, taken in both minima and outside eclipse phases, are compatible with the results of synthetic spectra. In addition, photometric flux measurements are also found to be compatible, except for the W2 band ($\lambda = 46028$ Å, $\Delta\lambda = 10423$ Å). The photometric flux measurements in the W2 band clearly show that there is an excess radiation in this band in AR Lac. Excess radiation rates in f(W2)/f(V) have been found as follows:

At $0.995P$ the excess radiation rate is about 0.227 ± 0.047.

At $0.496P$ the excess radiation rate is about 0.176 ± 0.031.

At $0.894P$ the excess radiation rate is about 0.136 ± 0.028.

Based on the model spectral solutions of high resolution Hα line profiles (see Figure 6) the variations of Hα and their residual profiles depending on orbital phases were obtained as given in Figure 7.

Using our synthetic model spectrum solutions, the radial velocities obtained from the residual Hα profiles of AR Lac are given in Table 5. These radial velocity measurements were also compared with the radial velocity curve by Frasca et al. (2000), as given

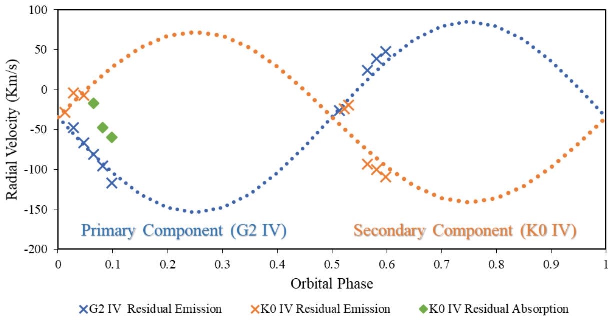

Fig. 8. A comparison of the radial velocities obtained from our residual Hα profiles of AR Lac binary system with the velocity curve by Frasca et al. (2000). The radial velocities of residual Hα profiles are denoted with cross signs, and the velocities obtained from the absorption structures appeared in residual Hα profiles are also denoted with green squares. The colour figure can be viewed online.

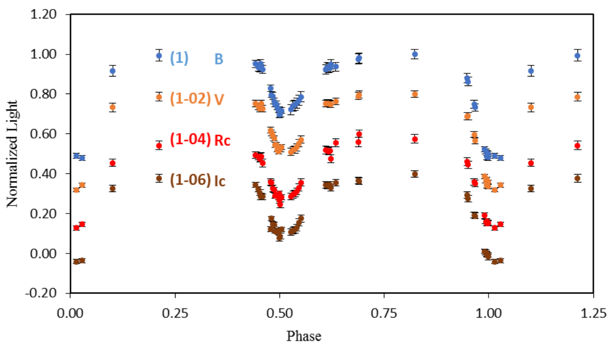

Fig. 9. Normalized Light curves of AR Lac in B, V, R_c, I$_c$ bands. The colour figure can be viewed online.

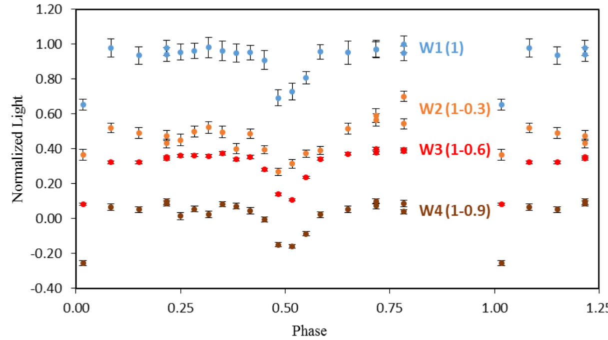

Fig. 10. Normalized Light curves of AR Lac in WISE bands. The colour figure can be viewed online.

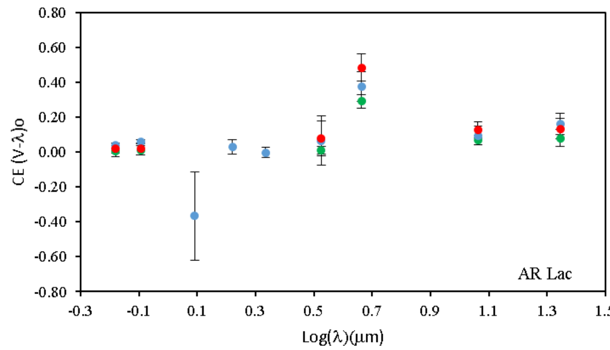

Fig. 11. As a function of wavelength, the colour excesses of AR Lac in all bands during minima and outside eclipses (0.0P are indicated as red colour, 0.5P as blue, and the outside phases as green points). CE values are in magnitudes (from Karakuş & Ekmekçi 2020). The colour figure can be viewed online.

in Figure 8. The discussion of these results is given in the following § 4.

From our analysis of the minimum depth ratios of the light curves of AR Lac (see Table 6 and Figures 9 and 10), obtained in this study, it was seen that the flux values of the components of this active binary system tend to be equal, towards the longer wavelengths. These results are also discussed in § 4 in the context of existence of an extended/circumstellar matter in the system.

4. DISCUSSION AND CONCLUSIONS

Although recently observational evidence of the presence of extended /circumstellar matter has not been found, except in the W2 band, by Karakuş & Ekmekçi (2020), in the AR Lac active binary system, based on the IR excess measurement results, this issue has been re-evaluated with the results of the spectral analyses of this study. Our analysis results for low and high resolution spectra of AR Lac were evaluated within the scope of extended/circumstellar matter, together with our previous photometric results. A discussion on these results can be summarized as follows:

(i) During the 0.0P orbital phase of the AR Lac binary system, the hotter component (G2 IV) is totally eclipsed and therefore only the radiation from the cooler component (K0 IV) of the system can be observed. In Figure 2, SED measurement results during the 0.0P orbital phase of AR Lac and the results of HD 56168 [$(B-V)_\circ = 0.90 \pm 0.01$, as an inactive reference star] were compared with the SED of a black body radiation of an effective temperature of 5100 K. From this comparison, it was seen that AR Lac has an excess radiation in the W2 band. We were unable to compare our SED results with those of Busso et al. (1988) for the AR Lac system because their evaluations did not depend on orbital phase and the components of AR Lac were taken into consideration as `G5 V+G8 IV` (see their Table 5b and Figure 4). However, roughly, our `SED` results for outside eclipse phases (see the bottom pattern of Figure 3 of this study) appear to be consistent with their results.

(ii) In addition to our `SED` evaluations made at the primary minimum for AR Lac in Figure 2, our `SED` results, together with our `TFOSC` spectral data, in the secondary minimum and outside eclipse phases were obtained as given in Figure 3. From all patterns given in Figure 3, it clearly appears that AR Lac has a significant excess radiation in the `W2` band at all orbital phases. The relative value of this excess radiation in the `W2` band was at highest level during primary minimum and at lowest level around outside of eclipse phases, with an average value of $\approx 0.18 \pm 0.03$. This result is also compatible with the results of photometric colour excess `(CE)` measurements obtained by Karakuş & Ekmekçi (2020) for AR Lac (see Figure 11). Therefore, these characteristics of excess radiation depending on orbital phase show that the source of excess radiation in AR Lac is mainly due to the cooler component `(K0 IV)` of the system. Using the `Spitzer Space Telescope` data, obtained during the observing period November 2005-January 2007, Matranga et al. (2010) reported that there was no significant warm dust in the AR Lac binary system, but they gave photometric `IR` measurements that were partially compatible with our findings. Unfortunately, our survey of data sources found no information about which element or molecule is emitting/absorbing radiation in the 4.6 micron region, and related atomic terms.

(iii) Within the scope of this study, the high resolution Hα profile observations of AR Lac were made especially at/near minima times. The *Spectral Extraction Method* was used to model spectral Hα profiles. The residual Hα profiles of AR Lac have been obtained in the form of emission and absorption profiles, which are compatible with the radial velocities of the components of the system (see Figures 6 and 7). These residual Hα profiles are clearly seen as emissions for both components, especially at the $0.013P$, $0.028P$, $0.514P$, $0.546P$, $0.565P$, and $0.581P$ orbital phases. However, the central depths of the Hα absorption profiles of AR Lac at the $0.048P$, $0.065P$, $0.081P$, and $0.098P$ orbital phases were less deep than the depths of synthetic profiles (see Figure 6). The absorption feature in the residual Hα profiles of AR Lac could be seen at these orbital phases. This excess absorption structure in the residual Hα profiles of AR Lac observed at/near primary minimum phases is compatible with the results of Zboril et al. (2004) and Frasca et al. (2000). These residual Hα profiles (see Figure 7) provide information about the level and the variation of stellar activity in the AR Lac binary system. In addition, the residual Hα profiles of the cooler component of AR Lac appear to be wider and more intense than the profiles of the hotter component. That is, from these residual Hα profiles, given in Figure 7, we see that the stellar activity in AR Lac comes mainly from the secondary/cooler component and that this cooler component rotates faster than the primary/hotter component. These are the characteristics related to the expected results of chromospherically active stars.

(iv) Using synthetic spectra constructed for high resolution Coude Echelle spectra for AR Lac, the radial velocity measurements of the component stars were made from the residual Hα profiles. All these radial velocity measurement results are shown in Figure 8 together with the radial velocity curves based on the radial velocity measurement results obtained by Frasca et al. (2000) for the AR Lac. As can be seen from Figure 8, the differences between these radial velocities (*RVs*) and the photospheric *RVs* give us observational evidence about the *RVs* which correspond to active regions in the chromosphere, which lie at higher layers of the stellar atmosphere. Frasca et al. (2000), based on their study of Hα spectroscopy of AR Lac, had reported an extra absorption during primary eclipse (at $0.99P$), which extends toward the blue side producing an asymmetric emission of the cool star, with a center position shifted to the red by $68\,\mathrm{km\,s^{-1}}$ (i.e. equal to the $v \sin i$ of the `K0 IV` component). A similar result of this extra absorption was determined by using the residual Hα absorption structure with the *RVs* of about $-47.5\,\mathrm{km\,s^{-1}}$ and $-59.8\,\mathrm{km\,s^{-1}}$, at $0.081P$ and $0.098P$, respectively (see Table 5 and green squares in Figure 8). It seems that this extra absorption is most likely due to a prominence on the `K0 IV` component of AR Lac. In summary, based on this observational evidence, it appears that a prominence-like extended/circumstellar matter most likely exists around the cooler component of AR Lac. Therefore, it can be suggested that such a low-density extended/circumstellar matter causes a colour excess or a residual emission/absorption in the AR Lac binary system.

(v) Our evaluations of the flux ratios of the component stars of AR Lac from the minima depth ratios of the light curves of the system (see Table 6 and Figures 9 and 10), show that the fluxes of the component stars are equal or almost equal to each other in the W1, W2, and W3 band light curves. As can be seen from Table 6, the flux ratio of the components of AR Lac in the W2 band is smaller than 1. This is because the depth of the primary minimum (Min. I) of the light curve is less than that of the secondary minimum (Min. II), that is, when the hotter component(G2 IV) is behind the cooler component (K0 IV). In other words, in the W2 band the system is brighter during primary minimum than during the secondary minimum phases. On the other hand, it was found that the W2 band is additionally sensitive to hot dust(see Cluver et al. 2014). Therefore, the fact that the W2 flux ratio for the components of AR Lac binary system is smaller than 1, suggests that the extended/circumstellar matter around K0 IV component could likely be heated by the hotter component during the orbital phase $0.0P$. In addition, the equality in fluxes, for the remaining bands could be the result of an extended/circumstellar matter/material that can be detected in the wavelengths of these bands. The colour excess(CE) measurement results in these bands by Karakuş & Ekmekçi (2020) also support this suggestion: *CE* values in these bands were obtained as $\mathrm{CE}(V - \mathrm{W1}) \simeq \mathrm{CE}(V - \mathrm{W3}) \simeq 0.1$ and $\mathrm{CE}(V - \mathrm{W2}) \simeq 0.4$ (see Figure 11).

The results of radio and polarization observations of the AR Lac binary system, published in the period 1977-2007 (see Owen & Spangler 1977; Brown et al. 1979; Walter et al. 1983; Doiron & Mutel 1984; Walter et al. 1987; Trigilio et al. 2001; Koch 2007), are in agreement with the results of this study. Based on the spectroscopic and photometric findings obtained in this study, it can be concluded that in AR Lac, there are not only evidences/contributions of excess radiation caused by stellar activity, but also caused by the presence of extended/circumstellar matter. In other words, the results obtained in this study, together with the radio and polarization observation results of AR Lac, were evaluated as follows: We made an investigation to find evidence as to whether the effect of the extended/circumstellar matter(thought to exists) or the extended corona of the K0 IV component of the system contributes more to the emergence of these observational findings.

It can be clearly seen that these results are in agreement with the conclusion of this study that an extended/circumstellar matter could, most likely, exist in the AR Lac active binary system.

However, it should also be noted that although the mass-loss rate obtained by using the long-term secular period decrease due to stellar magnetic activity is very small (see Lu et al. 2012), we see that the stellar activity of this binary system is sufficient to affect the coronal structure (see Walter et al. 1983) and the minima depth ratios of the light curves (see Table 6, Figures 9 and 10). This suggests the presence of a common envelope such as in β Lyr or W UMa type binary systems; the residual Hα emissions (see Figure 7) gave some important observational evidences for extended/circumstellar matter. Therefore, it is useful to have some more sensitive observational studies and continue these researches.

We thank TÜBİTAK National Observatory for partial support in using RTT150 telescopes with project numbers 13ARTT150-406 (Coudé) and 14BRTT150-664 (TFOSC). We would like to thank Prof. Dr. İlbeyi Ağabeyoğlu for checking our English text. And finally, we would like to thank the referee for his/her directions to improve the comments of some results of this study. This research has made use of the Simbad Database operated at CDS, Starsbourg, France and of NASA's Astrophysics Data System Bibliographic Services. This work has also made use of data from European Space Agency (ESA) mission Gaia (https://www.cosmos.esa.int/gaia), produced by the *Gaia* Data Processing and Analysis Consortium (DPAC, https://www.cosmos.esa.int/web/).

REFERENCES

Barden, S. C. 1985, ApJ, 295, 162
Bopp, B. W., Dempsey, R. C., & Maniak, S. 1988, ApJS, 68, 803
Brown, R. L., Broderic, J. J., & Neff, S. G. 1979, BAAS, 11, 630
Busso, M., Scaltriti, F., Persi, P., Ferrari-Toniolo, M., & Origlia, L. 1988, MNRAS, 234, 445

Busso, M., Scaltriti, F., Ferrari-Toniolo, M., et al. 1990, MmSAI, 61, 77
Castelli, F., Gratton, R. G., & Kurucz, R. L. 1997, A&A, 318, 841
Cluver, M. E., Jarrett, T. H., Hopkins, A. M., et al. 2014, ApJ, 782, 90
Doiron, D. J. & Mutel, R. L. 1984, AJ, 89, 430
Fekel, F. C., Moffett, T. J., & Henry, G. W. 1986, ApJS, 60, 551
Fernandez-Figueroa, M. J., Montes, D., de Castro, E., & Cornide, M. 1994, ApJS, 90, 433
Frasca, A., Marino, G., Catalano, S., & Marilli, E. 2000, A&A, 358, 1007
Frasca, A., Catalano, S., Marilli, E., & Marino, G. 2001, Long Term Hα Spectroscopy of AR Lac (CD-ROM Directory: contribs/frasca2), 943
Hall, J. C. & Ramsey, L. W. 1994, AJ, 107, 1149
Karakuş, O. & Ekmekçi, F. 2020, PASA, 37, 11
Koch, R. H. 2007, Obs, 127, 22
Kopal, Z. & Demircan, O. 1978, Ap&SS, 55, 241
Lanza, A. F., Catalano, S., Cutispoto, G., Pagano, I., & Rodono, M. 1998, A&A, 332, 541
Lu, Y., Xiang, F.-Y., & Shi, X.-M. 2012, PASJ, 64, 84
Matranga, M., Drake, J. J., Kashyap, V. L., Marengo, M., & Kuchner, M. J. 2010, ApJ, 720, 164
Montes, D., Fernandez-Figueroa, M. J., Cornide, M., & de Castro, E. 1996, A&A, 312, 221
Montes, D., Martin, E. L., Fernandez-Figueroa, M. J., Cornide, M., & de Castro, E. 1997, A&AS, 123, 473
Montes, D., Fernandez-Figueroa, M. J., de Castro, E., et al. 2000, A&AS, 146, 103
Owen, F. N. & Spangler, S. A. 1977, ApJ, 217, 41
Rodono, M. 1980, MmSAI, 51, 623
Scaltriti, F., Busso, M., Ferrari-Toniolo, M., et al. 1993, MNRAS, 264, 5
Siviero, A., Dallaporta, S., & Munari, U. 2006, BaltA, 15, 387
Strassmeier, K. G., Fekel, F. C., Bopp, B. W., Dempsey, R. C., & Henry, G. W. 1990, ApJS, 72, 191
Şenavcı, H. V., Bahar, E., Montes, D., et al. 2018, MNRAS, 479, 875
Trigilio, C., Buemi, C. S., Umana, G., et al. 2001, A&A, 373, 181
Walter, F. M., Gibson, D. M., & Basri, G. S. 1983, ApJ, 267, 665
Walter, F. M., Neff, J. E., Gibson, D. M., et al. 1987, A&A, 186, 241
Wright, E. L., Eisenhardt, P. R. M., Mainzer, A. K., et al. 2010, AJ, 140, 1868
Zboril, M., Armado, P. J., Oliveira, J. M. & Moreno, C. 2004, ASPC 318, Spectroscopically and Spatially Resolving the Components of the Close Binary Stars, ed. R. W. Hilditch, H. Hensberge, and K. Pavlovski (San Francisco, CA: ASPC), 382

Fehmi Ekmekçi and Osman Karakuş: Ankara University, Faculty of Science, Department of Astronomy and Space Sciences, 06100 Tandoğan, Ankara, Turkey (fekmekci@science.ankara.edu.tr, o_karakus@yahoo.com).

Revista Mexicana de Astronomía y Astrofísica, **57**, 181–188 (2021)

https://doi.org/10.22201/ia.01851101p.2021.57.01.13

ANALYTIC SOLUTIONS FOR TRUNCATED PLASMONS

J. Cantó[1] and A. C. Raga[2,3]

Received July 23 2020; accepted November 19 2020

ABSTRACT

We present a new plasmon model for a cometary clump moving supersonically in an environment with a non-zero gas pressure. We find that the environmental pressure produces a cutoff in the wings of the cometary clump, therefore resulting in quite "stubby" plasmons for a large range of flow Mach numbers. We derive a relation between the length-to-width ratio of the plasmon and the Mach number M of the flow, which could be used to directly derive M from observations of (appropriate) cometary clumps.

RESUMEN

Presentamos un nuevo modelo de plasmón para un nudo cometario moviéndose supersónicamente respecto de un medio ambiente con presión finita. Encontramos que la presión del medio ambiente produce un corte en las alas del nudo cometario, dando como resultado nudos "rellenitos" para un gran intervalo de números de Mach del flujo. Derivamos una relación entre el cociente "largo a ancho" del plasmón y el número de Mach M del flujo, el cual podría ser usado para derivar directamente M de observaciones de nudos cometarios apropiados.

Key Words: HII regions — ISM: jets and outflows — ISM: kinematics and dynamics — planetary nebulae: general — shock waves

1. INTRODUCTION

De Young & Axford (1967) derived the so-called "plasmon" solution, which consists of the balance between the gas pressure within a decelerating (or accelerating) isothermal clump of gas and the ram-pressure of the environment into which it is travelling. This simple solution still continues to be used to model the dynamics of different astrophysical flows involving cometary clumps (see, e.g., Rivera-Oríz et al. 2019a, b; Veilleux et al. 1999; De Young 1997).

Modified versions of the plasmon solution of De Young & Axford (1967) have been obtained including the effects of:

- the centrifugal pressure of the shocked environment (Cantó et al. 1998),
- the self-gravity of the clump (Lora et al. 2015),
- a clump with a polytropic equation of state (Cantó & Raga 1995),
- entrainment of clump material by the streaming environment (Rivera-Ortíz et al. 2019a, b).

The formation of "tails" by wind/clump interactions was explored analytically by Dyson, Hartquist & Biro (1993).

Numerical simulations show that plasmon-style "interstellar bullet" flows are highly unstable, with rather intense fragmentation of the plasmon configuration (see, e.g., Klein et al. 2003; Raga et al. 2007). It can be argued that if a high speed flow rapidly disrupts a liquid droplet (see, e.g., Nicholls & Ranger 1969), a gas cloud would be disrupted with even greater ease.

On the other hand, it is clear that some astrophysical flows (e.g., the Orion "fingers" around the BN-KL object, see Rivera-Ortíz et al. 2019a) do show the characteristics predicted by the "braking plasmon" analytic model. In a recent series of papers, Pittard et al. (2009, 2010) and Goldsmith & Pittard (2017, 2019) show that clumps with high clump to environment density ratios can be substantially braked (or accelerated, depending on the reference system) before fragmenting and mixing with the environment. This "dense clump regime" was

[1]Instituto de Astronomía, UNAM, México.
[2]Instituto de Ciencias Nucleares, UNAM, México.
[3]Inst. de Investigación en Ciencias Físicas y Matemáticas, USAC, Guatemala.

also explored by Rivera et al. (2019b), who carried out a comparison between an analytic plasmon model and numerical simulations. At least for such dense gas clumps, it appears that the plasmon model of De Young & Axford (1967) is still relevant.

In the present paper we consider the effect of the environmental gas pressure on the structure of a plasmon. This pressure will of course have an important effect for a plasmon moving at a relatively low Mach number (with respect to the environmental sound speed). Also, even in the case of a high Mach number plasmon, the environmental pressure will have an important effect in the plasmon "wings", where the bow shock becomes highly oblique.

The paper is organized as follows. In § 2, we present the new plasmon model, and derive a full analytic solution for the shape of the plasmon. In § 3 we derive the equation of motion for the modified plasmon, and integrate it numerically to determine the velocity and position of the plasmon as a function of time. Finally, we present a discussion of the results in § 4.

2. THE PLASMON MODEL

We consider the situation shown in the schematic diagram of Figure 1. In a cylindrical reference frame moving with the plasmon, the surrounding environment (of density ρ_a, pressure P_a and isothermal sound speed $c_a = \sqrt{P_a/\rho_a}$) impinges on the plasmon with a velocity v_a (this is the relative velocity between the environment and the plasmon).

In our model, we assume that the environment is isothermal, with a position-independent sound speed c_a. We also assume that the plasmon is isothermal, but allow it to have a different sound speed c_0. This choice is appropriate for a dense clump in an outflow from a young star, travelling within a higher temperature, neutral or partially ionized environment.

We assume that at any time in its evolution, the internal pressure stratification of the decelerating (or accelerating) plasmon instantaneously relaxes to the hydrostatic equilibrium, so that:

$$P(z) = P_0 e^{-z/H}\,, \tag{1}$$

for an isothermal gas, where

$$H \equiv \frac{c_0^2}{a}\,, \tag{2}$$

with c_0 being the isothermal sound speed and a the acceleration/deceleration of the plasmon. An exploration of the validity of equation 1 is presented in Appendix B.

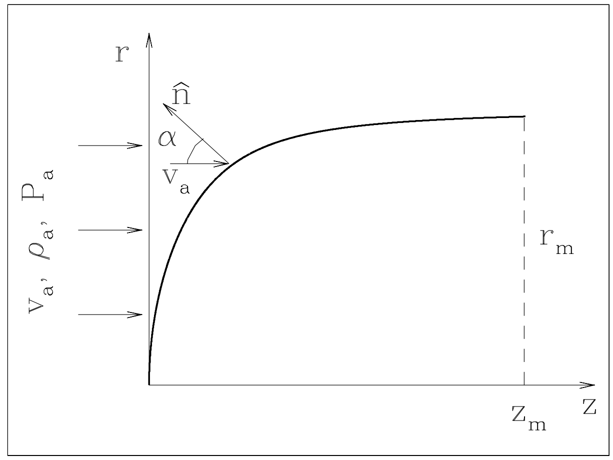

Fig. 1. Schematic diagram of a plasmon. In a frame of reference at rest with the plasmon, the environment (of density ρ_a and pressure P_a) impinges from the left, along the symmetry axis of the (z, r) cylindrical coordinate system. The thick curve represents the surface of the plasmon, which is truncated at the position (z_m, r_m). We show the angle α between the direction of the impinging flow and the local normal to the plasmon surface.

As discussed in Appendix A, the pressure of the shocked environment in contact with the plasmon is approximately given by:

$$P_s = P_a + \rho_a v_a^2 \cos^2\alpha\,, \tag{3}$$

where ρ_a, v_a and P_a are the ambient density, velocity and pressure (respectively) and $\alpha = \arctan(dz/dr)$ is the angle between the impinging flow and the normal to the surface of the plasmon (see Figure 1). Therefore, the pressure P_0 at the head of the plasmon (see equation 1) is:

$$P_0 = (1+\beta)\rho_a v_a^2\,, \tag{4}$$

with

$$\beta \equiv \frac{P_a}{\rho_a v_a^2} = \frac{1}{M^2}\,, \tag{5}$$

where M is the Mach number calculated with the velocity v_a of the plasmon and the isothermal sound speed c_a of the environment.

Now, setting $P(z) = P_s$ (equations 1 and 3) and considering that $dz/dr = \tan\alpha$ (see Figure 1), we obtain the differential equation

$$\frac{dz}{dr} = \tan\alpha = \sqrt{\frac{1}{(1+\beta)e^{-z/H} - \beta} - 1}\,, \tag{6}$$

with β given by equation (5).

From the second equality of equation (6) we obtain:

$$z = H \ln \left[\frac{(1+\beta)(1+\omega)}{1+\beta(1+\omega)} \right] , \tag{7}$$

with

$$\omega = \tan^2 \alpha \, . \tag{8}$$

It is clear that the plasmon solution ends at a finite z_m, for which $\alpha = \pi/2$ (so that also $\omega = \tan \alpha \to \infty$). From equation (7) we obtain:

$$z_m = H \ln \left(\frac{1+\beta}{\beta} \right) . \tag{9}$$

In order to obtain the $z(r)$ solution, we first consider the first equality of equation (6):

$$dr = \frac{dz}{\sqrt{\omega}} , \tag{10}$$

where ω is defined in equation (8). Also, from equation (7) we have:

$$dz = \frac{H}{(1+\omega)\,[1+\beta(1+\omega)]} d\omega \, . \tag{11}$$

Combining equations (10-11) we obtain the differential equation:

$$\frac{dr}{d\omega} = \frac{H}{(1+\omega)\,[1+\beta(1+\omega)]\,\sqrt{\omega}} , \tag{12}$$

which can be integrated to obtain:

$$r = 2H \left[\tan^{-1} \left(\sqrt{\omega} \right) - \sqrt{\frac{\beta}{1+\beta}} \tan^{-1} \left(\sqrt{\frac{\beta\omega}{1+\beta}} \right) \right] , \tag{13}$$

with ω given by equation (8). Equations (8) and (13) are then the solution for the shape of a plasmon interacting with an environment with a non-zero gas pressure.

This solution has the following limiting cases:

- $z \ll 1$:

$$r \approx 2 \sqrt{\frac{zH}{1+\beta}} , \tag{14}$$

- $z \to z_m$ (see equation 9):

$$r \to r_m = \pi H \left[1 - \sqrt{\frac{\beta}{1+\beta}} \right] , \tag{15}$$

- $\beta \to 0$:

$$r = 2H \tan^{-1} \left(\sqrt{e^{z/H} - 1} \right) . \tag{16}$$

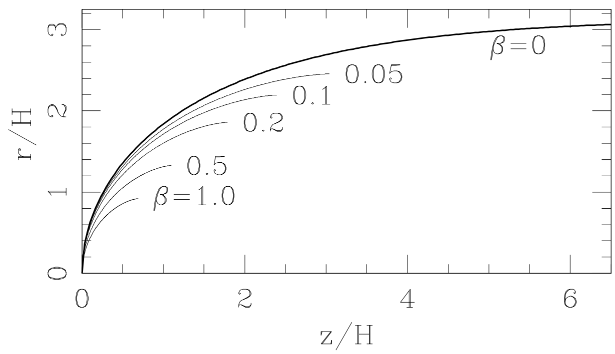

Fig. 2. The plasmon solution for different values of β. The curves are labeled with the corresponding β values.

Equation (16) is the plasmon solution of De Young & Axford (1967).

In Figure 2, we plot the $r(z)$ solutions (equations 8 and 13) for different values of β. It is clear that the length-to-width ratio of the plasmon grows as a function of decreasing β. This effect can be quantified by calculating the length-to-width ratio $L/W = z_m/(2r_m)$ from equations (9) and (15):

$$L/W = \frac{1}{2\pi} \frac{\ln\left(\frac{1+\beta}{\beta}\right)}{1-\sqrt{\frac{\beta}{1+\beta}}} = \frac{1}{2\pi} \frac{\ln\left(1+M^2\right)}{1-\frac{1}{\sqrt{1+M^2}}} , \tag{17}$$

where for the second equality, we have used the $M^2 = 1/\beta$ relation. This Mach number dependence of the length-to-width ratio of the plasmon is shown in Figure 3.

It is of interest to have an analytic expression for calculating the Mach number M of the plasmon flow as a function of the observed L/W length-to-width ratio. As equation (17) does not have an analytic inversion, we propose the fit:

$$M_a = \pi^{3/2} \left[\frac{e^{\pi(L/W)}}{(L/W)^{-1.5} + 5.18} - 0.16 \right] . \tag{18}$$

In Figure 3, we also show M_a vs. M/L solution, as well as its relative deviation $(M_a - M)/M$ (with M given by equation 17) with respect to the exact solution. In the bottom frame of Figure 3, we see that for the $M = 1 \to 100$ Mach number range, the relative error of the interpolation of equation (18) is smaller than 2%.

Finally, we calculate the mass of the plasmon. To do this, we combine equations (1), (4) and (8) to obtain

$$\rho(\omega) = \rho_0 \, \frac{1+\beta(1+\omega)}{(1+\beta)(1+\omega)} , \tag{19}$$

with $\rho_0 = P_0/c_0^2$ being the density at the head of the plasmon. Now, using equations (19), (11) and (13)

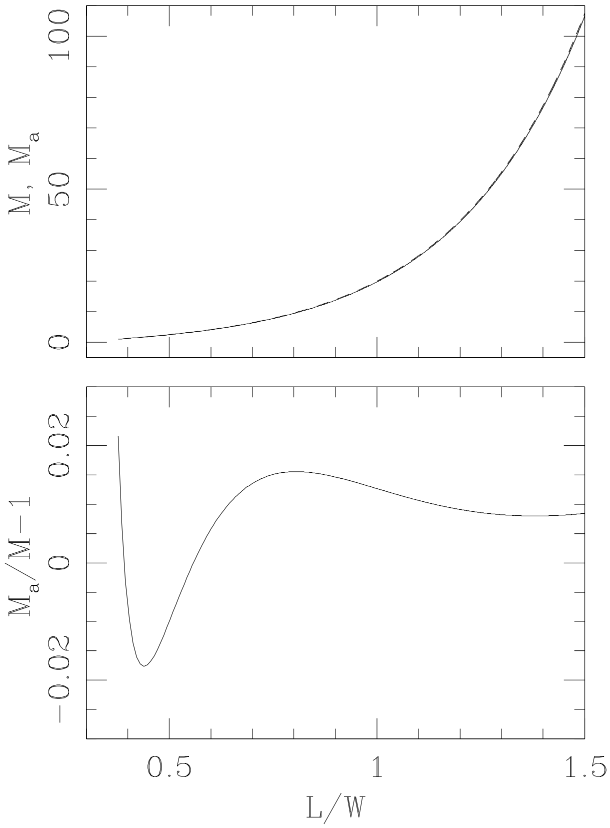

Fig. 3. Top plot: Mach numbers M (from the "exact" equation 17) and M_a (from the approximate inversion 18) as a function of the length-to-width ratio $L/W = z_m/(2r_m)$ of the plasmon. Bottom plot: relative error of the approximate inversion as a function of L/W.

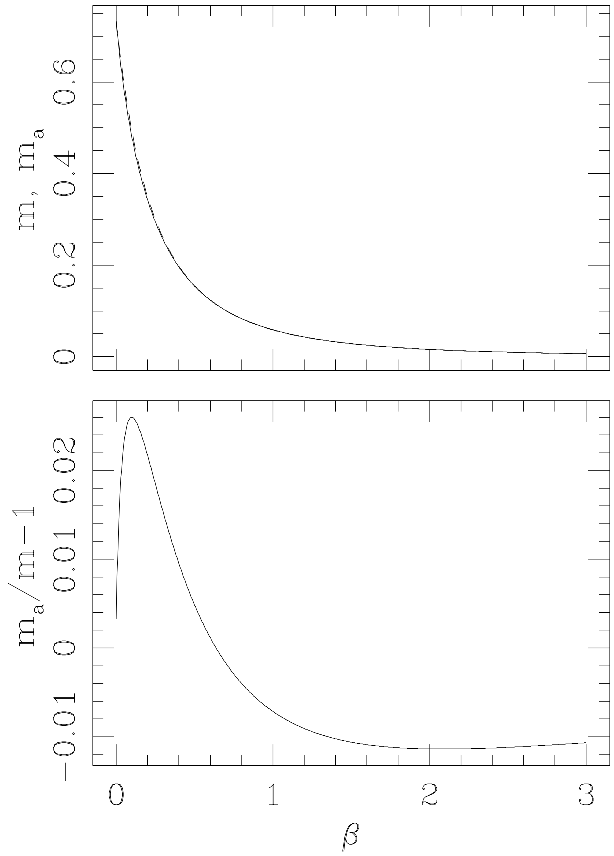

Fig. 4. Top plot: Dimensionless mass m (solid line, obtained from a numerical integration of equation 21) and the approximate solution m_a (dashed line, from equation 24) as a function of $\beta = 1/M^2$ (where M is the Mach number of the flow). Bottom plot: relative error of the approximate, analytic solution as a function of β.

we can calculate the mass M_p of the plasmon:

$$M_p = \pi \int_0^{z_m} \rho(z) r^2 dz = 4\pi\rho_0 H^3 m(\beta)\,, \tag{20}$$

with

$$m(\beta) = \int_0^\infty \frac{\left[\tan^{-1}\left(\sqrt{\omega}\right) - \sqrt{\frac{\beta}{1+\beta}}\tan^{-1}\left(\sqrt{\frac{\beta\omega}{1+\beta}}\right)\right]^2}{(1+\beta)(1+\omega)^2}\, d\omega\,. \tag{21}$$

We have not been able to carry out this integral analytically. However, in the limits of low and high β one obtains:

$$m(\beta) \approx \left(\frac{\pi^2-4}{8}\right) - \left(\frac{3\pi^2-4}{8}\right)\beta\,;\ \ \beta \ll 1\,, \tag{22}$$

$$m(\beta) = \left(\frac{9\pi^2-16}{192}\right)\frac{1}{\beta^3}\,;\ \ \beta \gg 1\,. \tag{23}$$

This latter, $\beta \gg 1$, limit corresponds to a highly subsonic flow, for which our model is probably not appropriate.

A good analytic approximation for β in the full $0 \to \infty$ range is:

$$m_a(\beta) = \frac{b_0}{1 + b_1\beta + b_2\beta^2 + b_3\beta^3}\,, \tag{24}$$

with

$$b_0 = \frac{\pi^2-4}{8}\,;\quad b_1 = \frac{3\pi^2-4}{\pi^2-4}\,;$$
$$b_2 = 5.25367\,;\quad b_3 = \frac{24(\pi^2-4)}{9\pi^2-16}\,. \tag{25}$$

Figure 4 (top) shows the dimensionless mass m obtained from a numerical integration of equation (21) as a function of β, as well as the analytic approximation m_a. The bottom plot shows the relative deviation between these two solutions, and we can see that the approximate analytic solution has deviations of less that 3% relative to the exact (i.e., numerical) solution.

3. THE EQUATION OF MOTION FOR THE PLASMON

The plasmon's equation of motion can be straightforwardly derived noting that the deceleration of the plasmon is $a = c_0^2/H$ (see equation 2), and then writing H in terms of the plasmon mass using equation (20). We then obtain:

$$a = \frac{dv_a}{dt} = -\left[\frac{4\pi\rho_a c_0^4(1+\beta)v_a^2 m(\beta)}{M_p}\right]^{1/3}, \quad (26)$$

where we have also used equation (4). We note that in this equation, $\beta = c_a^2/v_a^2$.

Equation (26) was derived assuming that the plasmon has a time-independent mass. This is of course not necessarily true, since

1. the plasmon could evaporate from the back side (which is probably not an important effect in the pressure confined plasmon tail that we are modelling here),

2. the flow around the plasmon head could entrain a substantial amount of plasmon material.

A parametrization of the "detrainment" of material from a plasmon has been obtained by Rivera-Ortíz et al. (2019b) by comparing a mass-losing plasmon analytic model with numerical simulations. Through their combined analytic and numerical aproach, these authors estimate a characteristic timescale

$$t_m = 10.45\frac{H}{c_0} \quad (27)$$

for substantial mass loss from the plasmon. A mass conserving plasmon model is therefore appropriate only for evolutionary times $< t_m$.

We first define dimensionless variables:

$$x' = \frac{x}{l_0}\,;\;\; v' = \frac{v_a}{c_a}\,;\;\; t' = \frac{tc_a}{l_0}\,, \quad (28)$$

where x is the position of the plasmon, and

$$l_0 \equiv \left(\frac{M_p}{4\pi\rho_a}\right)^{1/3}\left(\frac{c_a}{c_0}\right)^{4/3}. \quad (29)$$

In terms of these dimensionless variables, equation (26) takes the form:

$$\frac{d^2x'}{dt'^2} = \frac{dv'}{dt'} = -\left[\left(1+v'^2\right)m\left(\frac{1}{v'^2}\right)\right]^{1/3}. \quad (30)$$

This is the equation of motion for the plasmon, and a numerical integration is presented in § 3.

For $v' \gg 1$, we can set $1 + v'^2 \approx v'^2$, and

$$m(1/v') \approx b_0 = \frac{\pi^2-4}{8}\,, \quad (31)$$

(see equation 22 and 25) in the second equality of equation (30). With an initial condition $v'(t=0) = M_0$ (the initial Mach number of the plasmon), we integrate this equation to obtain:

$$v'(t') = \left(M_0^{1/3} - \frac{b_0^{1/3}t'}{3}\right)^3. \quad (32)$$

It is clear that $v' \to 0$ as $t' \to t'_0$, with

$$t'_0 \equiv 3\left(\frac{M_0}{b_0}\right)^{1/3}. \quad (33)$$

We can integrate again to obtain the dimensionless position of the plasmon as a function of time:

$$x'(t') = \frac{3M_0}{4b_0^{1/3}}\left[1-\left(1-\frac{b_0^{1/3}t'}{3M_0^{1/3}}\right)^4\right], \quad (34)$$

where we have assumed that $x'(t'=0)=0$. This solution has been previously derived, e.g., by Cabrit & Raga (2000).

In Figure 5 we present a comparison of the "large Mach number" analytical solution (equations 32 and 34) with a full, numerical integration of equation (30) for a plasmon with a $v'(t'=0) = M_0 = 10$ initial Mach number. It is clear that initially the two solutions are most similar, and that they start diverging when the plasmon slows down to $v' \approx 1$. While the analytic, high Mach number solution (which is really not applicable in this low v' regime) shows a plasmon which stops at a time t_0 (see equation 33), the full solution gives a plasmon that gradually slows down but does not stop at a finite distance.

Figure 5 also shows the axial extent z_m (equation 9) and the length-to-width ratio (L/W, given by equation 17) of the plasmon as a function of time. The length z_m initially grows with time, reaches a peak (of $\approx 1.42\,l_0$) and then slowly decreases for times $t > 4l_0/c_a$. The length-to-width ratio decreases monotonically from a $L/W \approx 0.8$ down to an asymptotic value of ≈ 0.32.

4. DISCUSSION

We have derived an analytic solution for the problem of an isothermal plasmon travelling supersonicaly within an environment with a non-zero pressure.

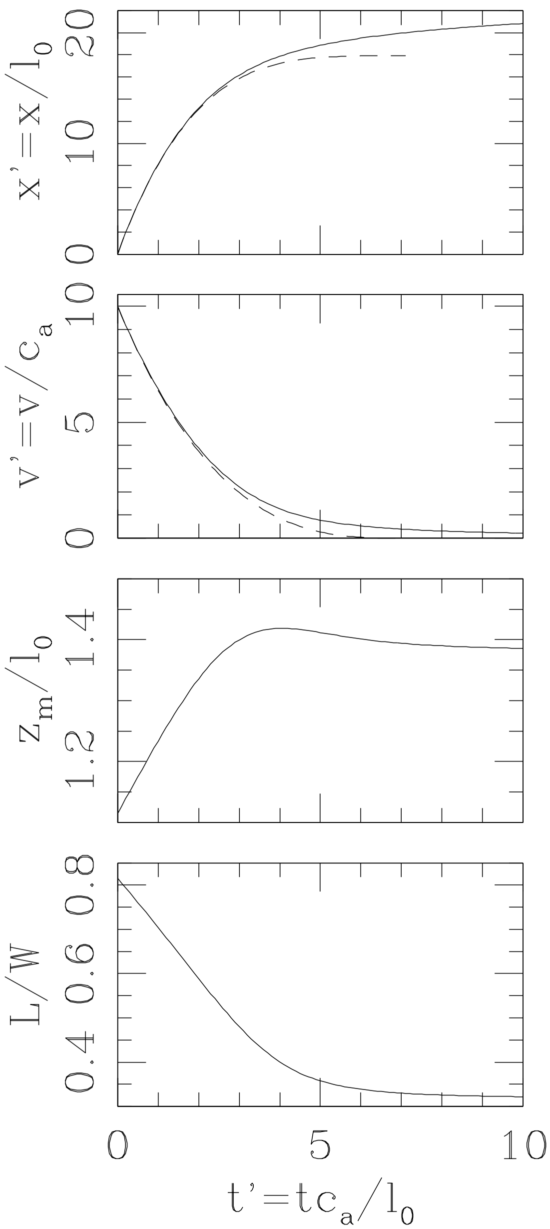

Fig. 5. Dimensionless position (top) and velocity (second from top) as a function of time. The solid curves correspond to the full (numerical solution of equation (30), and the dashed curves to the "high Mach number" analytic solution (equations 32 and 34). The two bottom frames show the dimensionless axial extent z_m/l_0 and the length-to-width ratio L/W of the plasmon as a function of time.

For a hypersonic flow with $M \gg 1$, our model coincides with the De Young & Axford (1967) plasmon solution.

Interestingly, we find that even for large values of M the non-zero environmental pressure produces a cut-off for the plasmon, which is terminated at the distance z_m and cylindrical radius r_m from the plasmon head given by equations (9) and (15). Thus cut-off results in rather stubby plasmons (see Figure 2), unless one goes to very high Mach number flows.

We find that the length-to-width ratio $L/W = z_m/(2r_m)$ of the plasmon solution (equations 17 and 18) has values ranging from ≈ 0.4 to ≈ 1.5 for Mach numbers $M = 1 \to 100$ (see Figure 3). Therefore, the extended wings of the De Young & Axford (1967) solution will basically never be formed in a real astrophysical flow, unless it has an extremely high Mach number. We find an analytical expression (equation 18) that can be used to derive an estimate for the flow Mach number from the observed length-to-width ratio of a cometary clump.

We also integrated the equation of motion for the new plasmon solution, and for high Mach numbers we find (not surprisingly) a time-dependent position and velocity which are similar to the ones found from the De Young & Axford (1967) plasmon solution. When the flow reaches a Mach number of ≈ 3, the new solution starts to separate from the De Young & Axford model, with the plasmon slowing down more slowly, and never stopping completely (while the De Young & Axford plasmon stops at a finite distance along its direction of motion).

Finally, we would like to point out an important qualitative result obtained from our new model. The ratio between the extent along the symmetry axis of the plasmon z_m and the scale-height H (equation 9) only has a logarithmic dependence on $\beta = 1/M^2$ (see equation 5). Therefore, for a wide range of possible values of M_a, we will have $H \approx z_m$, so that the gas within the plasmon will not be strongly stratified (as for this, one would need many pressure scale heights fitting within the length of the plasmon). This is a feature that is found when one tries to fit clumps obtained in numerical simulations with an analytic plasmon solution (see, e.g., Raga et al. 1998).

This work was supported by the DGAPA (UNAM) grant IG100218. We acknowledge an anonymous referee for helpful comments which (among other things) lead to the discussion in Appendix B.

APPENDICES

A. THE PRESSURE ON THE SURFACE OF THE PLASMON

In § 2, we have assumed that the pressure of the shocked environment at the surface of the plasmon is

$$P_s = P_a + \rho_a v^2 \,, \tag{A35}$$

where ρ_a and P_a are the pre-shock density and pressure (respectively) and v is the component of the pre-shock flow normal to the shock surface, see equation (3). This equation can be written as:

$$\frac{P_s}{\rho_a c_a^2} = M^2 + 1 \,, \tag{A36}$$

where $M = v/c_a$ is the Mach number calculated with the normal velocity and the isothermal sound speed.

This form for the pressure on the plasmon has the desired behaviour so that when the surface of the plasmon becomes parallel to the direction of the impinging flow (and therefore the normal velocity is $v \to 0$), the pressure on the plasmon is equal to the environmental gas pressure P_a. It is not clear whether or not equation (A35) gives the correct pressure for other orientations of the flow relative to the impinging flow.

To illustrate the kind of accuracy we obtain when using equation (A35), let us consider the stagnation region, where the environment flows normal to the plasmom surface (see Figure 1). For an isothermal shock, the postshock velocity v_p and the density ρ_p are given by:

$$v_p = \frac{c_a^2}{v_a} \;;\;\; \rho_p = \left(\frac{v_a}{c_a}\right)\rho \,, \tag{A37}$$

where c_a is the isothermal sound speed of the flow, and v_a and ρ_a are the preshock velocity and density (respectively). After going through the shock, the material slows down, until it is at rest at the stagnation point in contact with the head of the plasmon. The conditions at the stagnation region can be calculated with the isothermal Bernoulli theorem, giving the relation

$$\frac{v_p^2}{2} + c_a^2 \ln \rho_p = c_a^2 \ln \rho_{stag} \,, \tag{A38}$$

where ρ_{stag} is the density at the stagnation point. Using equations (A37-A38) we can calculate the stagnation pressure

$$\frac{P_{stag}}{\rho_a c_a^2} = M^2 \, e^{1/(2M^2)} \,, \tag{A39}$$

with $M = v_a/c_a$.

The value of P_{stag} obtained from equation (A39) clearly does not coincide with the pressure on the head of the plasmon calculated with equation (A35) or (A36). In order to show the differences between these two pressure values, we plot the two of them (as well as their relative difference) as a function of Mach number M in Figure 6. We see that the pressure obtained from equation (A36) differs from the correct stagnation pressure (given by equation A39) by $\approx 22\%$ for $M = 1$, and that it has smaller deviations for increasing values of M.

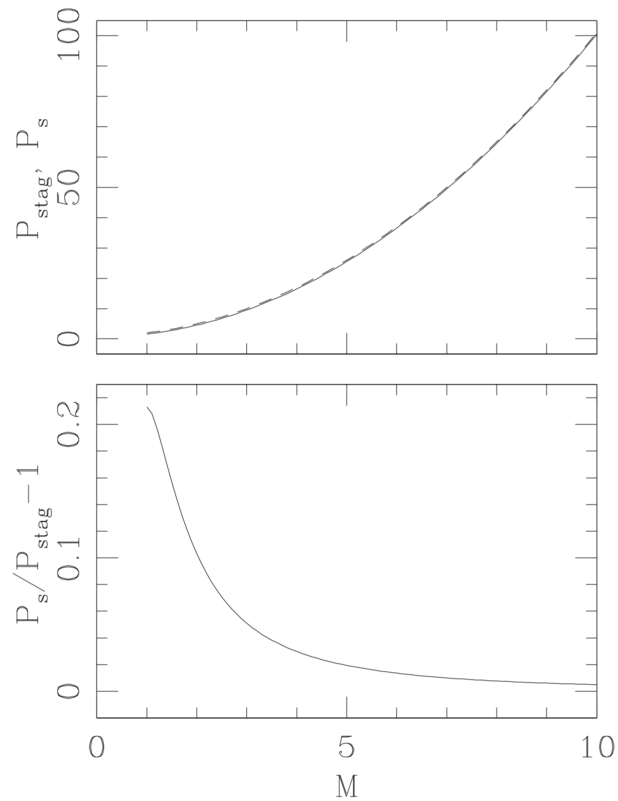

Fig. 6. Top frame: the P_s (dashed curve) and P_{stag} (solid curve) pressures (obtained from equations A36 and A39, respectively) as a function of pre-shock Mach number M. Bottom frame: the relative deviation $(P_s - P_{stah})/P_{stag}$ between the two pressures as a function of M.

From this, we conclude that the pressure on the plasmon surface given by equation (A35) has an accuracy that is appropriate for the simple, analytic plasmon model derived in our paper.

B. THE ASSUMPTION OF A HYDROSTATIC STRATIFICATION

Following De Young & Axford (1967), we have assumed that the plasmon has a hydrostatic equilibrium internal pressure distribution (see equation 1). This assumption is valid provided that the timescale τ_a for changes in the acceleration (or deceleration) a is smaller than the sound crossing time of the plas-

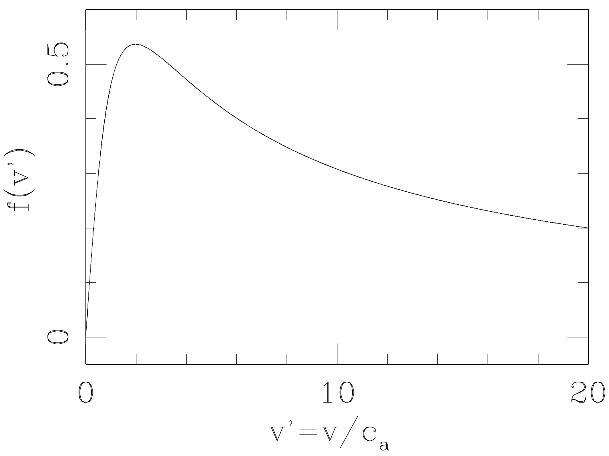

Fig. 7. The $f(v/c_a)$ function of the criterion for hydrostatic balance within the plasmon, see equations (B44-B45).

mon:

$$\tau_{hb} = \frac{z_m}{c_0} = \frac{c_0}{a} \ln\left(\frac{1+\beta}{\beta}\right) , \quad \text{(B40)}$$

where z_m is the axial extent, c_0 the sound speed and $\beta = (c_a/v)^2$ (see equations 2, 5 and 9).

In order to estimate the timescale

$$\tau_a = \left|\frac{a}{da/dt}\right| \quad \text{(B41)}$$

for substantial changes in the acceleration we first note that equation (30) can be written in an approximate way as:

$$a = \frac{dv}{dt} \approx A\, v^{2/3} , \quad \text{(B42)}$$

where A is a constant and we have assumed $m \approx const.$ and $v \gg c_a$. Taking the time derivative of this equation, we obtain:

$$\tau_a \approx \frac{3}{2}\tau_v ; \quad \text{with } \tau_v = \frac{v}{|dv/dt|} = \left|\frac{v}{a}\right| , \quad \text{(B43)}$$

where τ_v is the timescale for changes in the plasmon velocity v.

Finally. combining equations (B40) and (B43), we find that the condition for hydrostatic balance within the plasmon can be written as:

$$\frac{\tau_{hb}}{\tau_a} \approx \frac{c_0}{c_a} f(v') < 1 , \quad \text{(B44)}$$

wiht $v' = v/c_a$ and

$$f(v') = \frac{2}{3v'} \ln\left(1 + v'^2\right) . \quad \text{(B45)}$$

This function is shown in Figure 7, in which we see that it has a maximum value $f(v'_p) = 0.536$ at $v'_p = 1.981$. Therefore, the hydrostatic balance within the plasmon will be satisfied over all of its deceleration history for the case of a “cold plasmon” with $c_0 < 1.8c_a$ (where c_0 and c_a are the isothermal sound speeds of the plasmon and of the environment, respectively).

REFERENCES

Cabrit, S. & Raga, A. C. 2000, A&A, 354, 667
Cantó, J. & Raga, A. C. 1995, MNRAS, 277, 1120
Cantó, J., Espresate, J., Raga, A. C., & D’Alessio, P. 1998, MNRAS, 296, 1041
de Young, D. S. 1997, ApJ, 490, 55
de Young, D. S. & Axford, W. I. 1967, Natur, 216, 129
Dyson, J. E., Hartquist, T. W., & Biro, S. 1993, MNRAS, 261, 430
Goldsmith, K. J. A. & Pittard, J. M. 2017, MNRAS, 470, 2427
_________. 2018, MNRAS, 476, 2209
Klein, R. I., Budil, K. S., Perry, T. S., & Bach, D. R. 2003, ApJ, 583, 245
Lora, V., Raga, A. C., & Grebel, E. K. 2015, RMxAA, 51, 41
Nicholls, J. A. & Ranger, A. A. 1969, AIAAJ, 7, 285
Pittard, J. M., Falle, S. A. E. G., Hartquist, T. W., & Dyson, J. E. 2009, MNRAS, 394, 1351
Pittard, J. M., Hartquist, T. W., & Falle, S. A. E. G. 2010, MNRAS, 405, 821
Raga, A. C., Cantó, J., Curiel, S., & Taylor, S. 1998, MNRAS, 295, 738
Raga, A. C., Esquivel, A., Riera, A., & Velázquez, P. F. 2007, ApJ, 668, 310
Rivera-Ortíz, P. R., Rodríguez-González, A., Hernández-Martínez, L., Cantó, J., & Zapata, L. A. 2019a, ApJ, 885, 104R
Rivera-Ortíz, P. R., Rodríguez-González, A., Hernández-Martínez, L., & Cantó, J. 2019b, ApJ, 874, 38R
Veilleux, S., Bland-Hawthorn, J., Cecil, G., Tully, R. B., & Miller, S. T. 1999, ApJ, 520, 111

J. Cantó: Instituto Astronomía, Universidad Nacional Autónoma de México, Ap. 70-468, 04510 CDMX, México.
A. C. Raga: Instituto de Ciencias Nucleares, Universidad Nacional Autónoma de México, Ap. 70-543, 04510 CDMX, México, (raga@nucleares.unam.mx).
A. C. Raga: Instituto de Investigación en Ciencias Físicas y Matemáticas, USAC, Ciudad Universitaria, Zona 12, Guatemala, (raga@nucleares.unam.mx).

Revista Mexicana de Astronomía y Astrofísica, **57**, 189–198 (2021)

https://doi.org/10.22201/ia.01851101p.2021.57.01.14

ARTIFICIAL NEURAL NETWORK MODELING OF THE CONFORMABLE FRACTIONAL ISOTHERMAL GAS SPHERES

Yosry. A. Azzam[1], Emad A.-B. Abdel-Salam[2], and Mohamed I. Nouh[1]

Received October 22 2020; accepted January 7 2021

ABSTRACT

The isothermal gas sphere is a particular type of Lane–Emden equation and is used widely to model many problems in astrophysics, like the formation of stars, star clusters and galaxies. In this paper, we present a computational scheme to simulate the conformable fractional isothermal gas sphere using an artificial neural network (ANN) technique, and we compare the obtained results with the analytical solution deduced using the Taylor series. We performed our calculations, trained the ANN, and tested it using a wide range of the fractional parameter. Besides the Emden functions, we calculated the mass-radius relations and the density profiles of the fractional isothermal gas spheres. The results obtained show that the ANN could perfectly simulate the conformable fractional isothermal gas spheres.

RESUMEN

La esfera isotérmica de gas es un caso particular de la ecuación de Lane-Emden y se usa ampliamente para modelar problemas en astrofísica, como los relacionados con la formación estelar, los cúmulos estelares y las galaxias. Presentamos un esquema de cómputo para simular la esfera gaseosa fraccionalmente isotérmica utilizando una técnica de malla neuronal artificial (ANN) y comparamos los resultados con la solución analítica obtenida mediante series de Taylor. Realizamos los cálculos, entrenamos a la ANN y la probamos usando un gran intervalo del parámetro fraccional. Además de las funciones de Lane-Emden, calculamos las relaciones masa-radio y los perfiles de densidad de las esferas fraccionalmente isotérmicas. Los resultados muestran que la ANN fue capaz de simular perfectamente las esferas gaseosas fraccionalmente isotérmicas conformables.

Key Words: equation of state — methods: analytical — stars: interiors — stars: neutron

1. INTRODUCTION

In the last decade, fractional differential equations played a very important role in the advancement of science and engineering. One of the most interesting fractional differential equations, utilized in physics, astrophysics, engineering, and chemistry, is the Lane-Emden (and Emden-Fowler) equation. Many methods were proposed to solve these equations. The fractional polytropic models were investigated by El-Nabulsi (2011) for white dwarf stars, Bayin and Krisch (2015) for the incompressible gas sphere, Abdel-Salam and Nouh (2016) and Yousif et al. (2021) for the isothermal gas sphere. Analytical solutions to the fractional Lane-Emden equations using series expansion and Adomian decomposition methods were introduced by Nouh and Abdel-Salam (2018a), Abdel-Salam and Nouh (2020), Nouh and Abdel-Salam (2018b), and Abdel-Salam et al. (2020).

Artificial Neural Networks (ANNs) have proved to be a very promising tool that has been used in wide areas of scientific research and has found many applications to solve problems related to geophysics, engineering, environmental sciences, and astronomy [e.g., Weaver (2000), Tagliaferri et al. (1999), Tagliaferri and Longo (2003), Faris et al. (2014), Elminir et al. (2007), El-Mallawany et al. (2014), Leshno et al. (1993), Lippmann (1989), Zhang (2000)]. The great potential of ANNs is the high-speed processing provided by their massive parallel implementa-

[1]Astronomy Department, National Research Institute of Astronomy and Geophysics (NRIAG), Cairo, Egypt.

[2]Department of Mathematics, Faculty of Science, New Valley University, Egypt.

tions (Izeboudjen et al. 2014). Nowadays, ANNs are mostly used for universal function approximation in numerical paradigms because of their excellent properties of self-learning, adaptability, fault tolerance, nonlinearity, and advancement in input to output mapping (Wang et al. 2018). In addition, ANNs are effective, efficient and successful in providing a high level of capability to handle complex and noncomplex problems in many spheres of life. Besides, ANNs are appropriate for modeling many physical phenomena and have been used widely to solve fractional and integer differential equations problems with different patterns for the ANN architecture [Raja et al. (2010), Raja et al. (2011), Raja et al. (2015), Hadian-Rasanan et al. (2020), Pakdaman et al. (2017), Zuniga-Aguilar et al. (2017)]. In addition, Ahmad et al. (2017) used artificial neural networks (ANNs) to compute the solution of Lane-Emden type equations. Recently, Nouh et al. (2020) presented a solution to the fractional polytropic gas sphere (first kind of the Lane-Emden equation); the results indicated that the ANN method is precise when compared with other methods.

In the current work, we shall solve the fractional isothermal gas sphere equation using the Taylor series and train the ANN algorithm by using tables of the fractional Emden functions, mass-radius relations, and density profiles. For the sake of computational simulation, the normal feed-forward neural network is used to approximate the fractional Emden function solution, mass-radius relations, and density distributions which are in good agreement with other analytical schemes. The architecture used in this research is a feed-forward neural network that has three-layers and is trained using the back-propagation algorithm based on the gradient descent rule.

The rest of the paper is organized as follows: § 2 is devoted to the definition of the conformable fractional derivative. § 3 deals with the Taylor expansion solution of the fractional isothermal gas sphere equation. The mathematical modeling of the neural network is performed in § 4. In § 5, the results are introduced with discussions. The conclusion reached is given in § 5.

2. CONFORMABLE FRACTIONAL DERIVATIVE

Khalil et al. (2014) introduced the conformable fractional derivative using the limits in the form:

$$D^{\alpha} f(t) = \lim_{\varepsilon \to 0} \frac{f(t+\varepsilon\, t^{1-\alpha}) - f(t)}{\varepsilon}, \forall\, t > 0,\ \ \alpha\,\epsilon(0,1] \tag{1}$$

$$f^{\alpha}(0) = \lim_{t \to 0^{+}} f^{\alpha}(t). \tag{2}$$

Here$f^{\alpha}(0)$ is not defined. This fractional derivative reduces to the ordinary derivative when $\alpha = 1$. The following properties are found for the conformable fractional derivative:

$$D^{\alpha} t^{p} = p t^{p-\alpha}, \quad p\epsilon R, \quad D^{\alpha} c = 0, \quad \forall f(t) = c, \tag{3}$$

$$D^{\alpha}\,(a\,f + b\,g) \,=\, a\,D^{\alpha}\,f + b\,D^{\alpha}\,g, \qquad \forall\, a,\, b\,\epsilon\, R, \tag{4}$$

$$D^{\alpha}\,(f\,g) = \,f\,D^{\alpha}\,g \,+\, g\,D^{\alpha}\,f, \tag{5}$$

$$D^{\alpha}\,f(g) \,=\, \frac{df}{dg}\,D^{\alpha}\,g, \qquad D^{\alpha}\,f(t) \,=\, t^{1-\alpha}\,\frac{df}{dt}, \tag{6}$$

where f, g are two α-differentiable functions and c is an arbitrary constant. Equations (4) to (6) are demonstrated by (Khalil et al., 2014). The corresponding fractional derivative of certain functions could be given by:

$$D^{\alpha}\,(c\,e^{ct}) \,=\, c\,t^{1-\alpha}\,e^{t},\, D^{\alpha}\,\sin{(c\,t)} \,=\, c\,t^{1-\alpha}\,\cos{(c\,t)},$$
$$D^{\alpha}\,\cos{(c\,t)} \,=\, -\,c\,t^{1-\alpha}\,\sin{(c\,t)}, \tag{7}$$

$$D^{\alpha}\,e^{c\,t^{\alpha}} \,=\, \alpha\,c\,e^{c\,t^{\alpha}},\, D^{\alpha}\,\sin(c\,t^{\alpha}) \,=\, \alpha\,c\,\cos c\,t^{\alpha},$$
$$D^{\alpha}\,\cos(c\,t^{\alpha}) \,=\, -\,\alpha\,c\,\sin c\,t^{\alpha}. \tag{8}$$

3. TAYLOR EXPANSION OF THE FRACTIONAL ISOTHERMAL GAS SPHERE EQUATION

Let us consider the isothermal equation of state given by

$$P \,=\, K\,\rho$$

where K is the pressure constant. By implementing the principles of the conformable derivatives, Yousif et al. (2021) derived the conformable second-order nonlinear differential equation that describes the isothermal gas sphere as

$$\frac{1}{x^{2\alpha}}\,\frac{d^{\alpha}}{dx^{\alpha}}\,\left(x^{2\alpha}\frac{d^{\alpha}u}{dx^{\alpha}}\right) = e^{-u}. \tag{9}$$

The mass contained in the sphere is given by

$$M(x^{\alpha}) = 4\,\pi\left[\frac{K}{4\pi\,G}\right]^{\frac{3}{2}}\,\rho_c^{-\frac{3}{2}}\left(x^{2\alpha}\frac{d^{\alpha}u}{dx^{\alpha}}\right), \tag{10}$$

the radius is given by

$$R^{\alpha} = \left[\frac{K}{4\pi\,G}\right]^{\frac{1}{2}}\,\rho_c^{-\frac{1}{2}} x^{\alpha}, \tag{11}$$

and the density is given by

$$\rho = \rho_c e^{-u}, \tag{12}$$

where ρ_c is the central density.
Equation (9) can be written as

$$D_x^{\alpha\alpha} u + \frac{2\alpha}{x^\alpha} D_x^\alpha u - e^{-u} = 0,\ u(0) = 0,\ D_x^\alpha u(0) = 0. \tag{13}$$

The fractional Taylor series solution for any function $u(x)$ can be written as

$$u(x^\alpha) = u(0) + \frac{D_x^\alpha u(0)}{\alpha} x^\alpha + \frac{D_x^{\alpha\alpha} u(0)}{2!\alpha^2} x^{2\alpha} + \frac{D_x^{\alpha\alpha\alpha} u(0)}{3!\alpha^3} x^{3\alpha} + \frac{D_x^{\alpha\alpha\alpha\alpha} u(0)}{4!\alpha^4} x^{4\alpha} + \cdots .$$

Equation (13) can be written in the following form

$$x^\alpha D_x^{\alpha\alpha} u = -2\alpha D_x^\alpha u + x^\alpha e^{-u}. \tag{14}$$

Differentiating Equation (14) with respect to α, we get

$$\alpha D_x^{\alpha\alpha} u + x^\alpha D_x^{\alpha\alpha\alpha} u = -2\alpha D_x^{\alpha\alpha} u + \alpha e^{-u} - x^\alpha e^{-u} D_x^\alpha u,$$
$$\Rightarrow 3\alpha D_x^{\alpha\alpha} u + x^\alpha D_x^{\alpha\alpha\alpha} u = \alpha e^{-u} - x^\alpha e^{-u} D_x^\alpha. \tag{15}$$

Putting $x = 0$ in the last equation, we have

$$3\alpha D_x^{\alpha\alpha} u(0) = \alpha e^{-u(0)}, \quad \Rightarrow D_x^{\alpha\alpha} u(0) = \frac{1}{3}.$$

Differentiating equation (15) with respect to α, we get

$$4\alpha D_x^{\alpha\alpha\alpha} u + x^\alpha D_x^{\alpha\alpha\alpha\alpha} u = -2\alpha e^{-u} D_x^\alpha u + x^\alpha e^{-u} (D_x^\alpha u)^2 - x^\alpha e^{-u} D_x^{\alpha\alpha} u. \tag{16}$$

When $x = 0$,we have

$$4\alpha D_x^{\alpha\alpha\alpha} u(0) = 0, \qquad \Rightarrow D_x^{\alpha\alpha\alpha} u(0) = 0.$$

Differentiating Equation (16) with respect to α, we have

$$5\alpha D_x^{\alpha\alpha\alpha\alpha} u + x^\alpha D_x^{\alpha\alpha\alpha\alpha\alpha} u = 3\alpha e^{-u} (D_x^\alpha u)^2 - x^\alpha e^{-u} (D_x^\alpha u)^3 + 3x^\alpha e^{-u} D_x^\alpha u\, D_x^{\alpha\alpha} u - 3\alpha e^{-u} D_x^{\alpha\alpha} u - x^\alpha e^{-u} D_x^{\alpha\alpha\alpha} u. \tag{17}$$

When $x = 0$ we have

$$5\alpha D_x^{\alpha\alpha\alpha\alpha} u(0) = -3\alpha e^{-u(0)} D_x^{\alpha\alpha} u(0),$$
$$\Rightarrow D_x^{\alpha\alpha\alpha\alpha} u(0) = -\frac{3}{5} e^0 \frac{1}{3} = -\frac{1}{5},$$

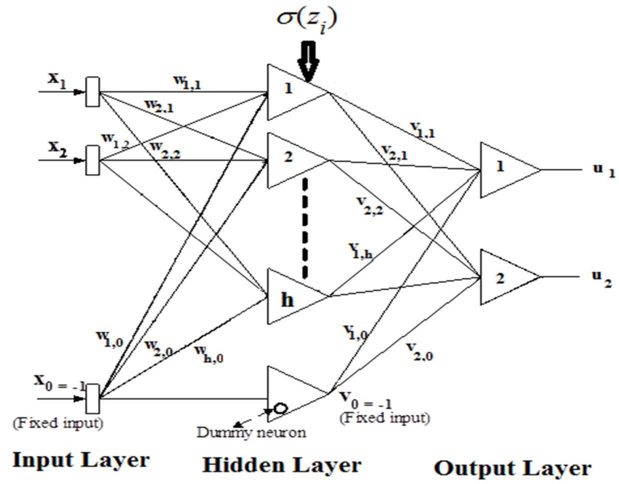

Fig. 1. ANN Architecture developed to simulate the fractional isothermal Emden function, mass-radius relation, and density profiles.

and so on. Finally, we have

$$u(x^\alpha) = u(0) + \frac{D_x^\alpha u(0)}{\alpha} x^\alpha + \frac{D_x^{\alpha\alpha} u(0)}{2!\alpha^2} x^{2\alpha} + \frac{D_x^{\alpha\alpha\alpha} u(0)}{3!\alpha^3} x^{3\alpha} + \frac{D_x^{\alpha\alpha\alpha\alpha} u(0)}{4!\alpha^4} x^{4\alpha} + \cdots .$$

Thus the solution of Equation (13) is given by

$$u(x^\alpha) = \frac{1}{6\alpha^2} x^{2\alpha} - \frac{1}{120\alpha^4} x^{4\alpha} + \cdots .$$

4. NEURAL NETWORK ALGORITHM

4.1. *Mathematical Modeling of the Problem*

The neural network architecture used to model the equation of conformal fractional isothermal gas spheres is shown in Figure 1. We write equation (9) as

$$D_x^{\alpha\alpha} u + \frac{1}{x^{2\alpha}} D_x^\alpha u = e^{-u}. \tag{18}$$

Along with the initial conditions $u(0) = 1$ and $D_x^\alpha u(0) = 0$, we generate a neural network solution, and we go through the following scheme: First, we suppose that the solution of Equation (18) is $u_t(x,p)$which can be approximated by

$$u_t(x,p) = A(x) + f(x, N(x,p)), \tag{19}$$

where $A(x)$ fulfills the initial conditions and $f(x, N(x,p))$ indicates the feed-forward neural network, and $N(x,p)$ is the output of the neural network. The vector x is the network input and p is the analogous vector of adaptable weight parameters. Then $N(x,p)$ can be written as

$$N(x,p) = \sum_{i=1}^{H} v_i \sigma(z_i), \tag{20}$$

where $z_j = \sum_{i=1}^{n} w_{ij} x_j + \beta_i$ and w_{ij} represents the weight from unit j in the input layer to unit i in the hidden layer, v_i symbolizes the weight from unit i in the hidden layer to the output, β_i is the bias value of the ith hidden unit and $\sigma(z_i)$ is the sigmoid activation function which has the form $\sigma(x) = \frac{1}{1+e^{-x}}$.

Taking the fractional derivative $N(x,p)$ for input vector, x_j gives

$$\begin{aligned} D_{x_j}^{\alpha} N(x,p) =& D_{x_j}^{\alpha} \left(\sum_{i=1}^{H} v_i \sigma \left(z_i = \sum_{i=1}^{n} w_{ij} x_j + \beta_i \right) \right) \\ =& \sum_{i=1}^{h} v_i w_{ij} \sigma^{(\alpha)}, \qquad \sigma^{(\alpha)} = D_x^{\alpha} \sigma(x), \end{aligned} \tag{21}$$

the n^{th} fractional derivative of $N(x,p)$ gives

$$\begin{aligned} D_{x_j}^{\overset{n\ times}{\alpha \dots \alpha}} N(x,p) = \sum_{i=1}^{n} v_i \; P_i \; \sigma_i^{(n\alpha)},\ P_i = \prod_{k=1}^{n} w_{ik}^{\alpha_k}, \\ \sigma_i = \sigma(z_i). \end{aligned} \tag{22}$$

Then, the approximate solution is given by

$$u_t(x,p) = x\, N(x,p). \tag{23}$$

This satisfies the initial conditions as:

$$u_t(0,p) = 0\,.N(0,p) = 0, \tag{24}$$

and

$$D_x^{\alpha} u_t(x,p) = x^{1-\alpha}\, N(x,p) + x\, D_x^{\alpha} N(x,p), \tag{25}$$

so that

$$D_x^{\alpha} u_t(0,p) = (0)^{1-\alpha}\, N(x,p) + 0.\, D_x^{\alpha} N(x,p) = 0. \tag{26}$$

4.2. *Gradient Computations and Parameter Updating*

Assuming that Equation (23) represents the approximate solution, the problem will be turned into an unconstrained optimization problem and the amount of error will be given by

$$\begin{aligned} E(x) =& \sum_i \Bigg\{ D_x^{\alpha\alpha} u_t(x_i,p) + \frac{2}{x^{\alpha}} D_x^{\alpha} u_t(x_i,p) - \\ & f(x_i,\ u_t(x_i,p)) \Bigg\}^2. \end{aligned} \tag{27}$$

Here:

$$\begin{aligned} f(x_i,\ u_t(x_i,p)) = e^{-u_t(x_i,p)}, \\ D_x^{\alpha} u_t(x,p) = x^{1-\alpha}\, N(x,p) + x\, D_x^{\alpha} N(x,p), \end{aligned} \tag{28}$$

and

$$\begin{aligned} D_x^{\alpha\alpha} u_t(x,p) =& (1-\alpha) x^{1-2\alpha}\, N(x,p) + \\ & 2x^{1-\alpha}\, D_x^{\alpha} N(x,p) + x\, D_x^{\alpha\alpha} N(x,p), \end{aligned} \tag{29}$$

where $D_x^{\alpha} N(x,p)$and $D_x^{\alpha\alpha} N(x,p)$ are given by equations (21, 22).

We computed the fractional derivative of the neural network input, as well as network parameters, to update the network parameters and use the optimized parameter values to train the neural network. We set up the network with the optimized network parameters after training of the network, and calculate $u_t(x,p)$ from $u_t(x,p) = x\, N(x,p)$.
The conformable fractional derivative is considered at par with a feed-forward neural network N with one hidden layer for each of its inputs, with the same weight values w and thresholds β_i with each weight v_i being exchanged with $v_i\ P_i$ where $P_i = \prod_{k=1}^{n} w_{ik}^{\alpha_k}$. Furthermore, the transfer function of each hidden unit is exchanged with the fractional derivative of the sigmoid function in the nth order. Consequently, with regard to the parameters of the original network, the conformable fractional gradient N of the original network is

$$\begin{aligned} D_{v_i}^{\alpha} N =& P_i\, \sigma_i^{(n\alpha)}, \\ D_{\beta_i}^{\alpha} N =& v_i P_i\ \sigma_i^{((n+1)\alpha)}, \\ D_{w_{ij}}^{\alpha} N =& x_i v_i P_i\ \sigma_i^{((n+1)\alpha)} + \\ & v_i \alpha_j w_{ij}^{1-\alpha_j} \left(\prod_{k=1,\, k\neq j} w_{ik}^{\alpha_k} \right) \sigma_i^{(n\alpha)}. \end{aligned} \tag{30}$$

The updating rule of the network parameters can be specified as

$$v_i(x+1) = v_i(x) + a\, D_{v_i}^{\alpha} N, \tag{31}$$

$$\beta_i(x+1) = \beta_i(x) + b\, D_{\beta_i}^{\alpha} N, \tag{32}$$

$$w_{ij}(x+1) = w_{ij}(x) + c\, D_{w_{ij}}^{\alpha} N, \tag{33}$$

where a, b, c are learning rates, $i = 1, 2, \dots, n$, and $j = 1, 2, \dots, h$.

4.3. *Back-Propagation Training Algorithm*

The back-propagation (BP) training algorithm is a gradient algorithm aimed to minimize the average square error between the desired output and the actual output of a feed-forward network. Continuously differentiable non-linearity is required for this algorithm. The gradient algorithm mathematics must assure that a specific node has to be adapted in a direct rate to the error in the units it is connected to. This algorithm has been described in detail in our previous paper (Nouh et al. 2020). Figure 2 shows a flow chart of an off-line back-propagation training algorithm, see Nouh et al. (2020), Yadav et al. (2015).

The back-propagation (BP) learning algorithm is a recursive algorithm starting at the output units and working back to the first hidden layer. A comparison of the desired output t_j with the actual output u_j at the output layer is executed using an error function which has the following form:

$$\delta_j = u_j(t_j - u_j)(1 - u_j). \tag{34}$$

The error function for the hidden layer takes the following form:

$$\delta_j = u_j(1 - u_j)\sum_k \delta_k w_k, \tag{35}$$

where δ_j is the error term of the output layer, and w_k is the weight between the output and hidden layers. The update of the weight of each connection is implemented by replicating the error in a backward direction from the output layer to the input layer as follows:

$$w_{ji}(t+1) = w_{ji}(t) + \eta\delta_j u_j + \gamma(w_{ji}(t) - w_{ji}(t-1)). \tag{36}$$

The learning rate η is chosen such that it is neither too large leading to overshooting nor very small leading to a slow convergence rate. The last part in Equation (36) is the momentum term which is affixed with a constant γ (momentum) to accelerate the error convergence of the back-propagation learning algorithm, and also to assist in pushing the changes of the energy function over local increases and boosting the weights in the direction of the overall downhill, Denz (1998). This part is used to add a portion of the most recent weight values to the current weight values. The values of the η and γ terms are set at the beginning of the training phase and determine the network speed and stability, see Basheer and Hajmeer (2000). The process is repeated for each input pattern until the output error of the network is decreased to a pre-specified threshold value.

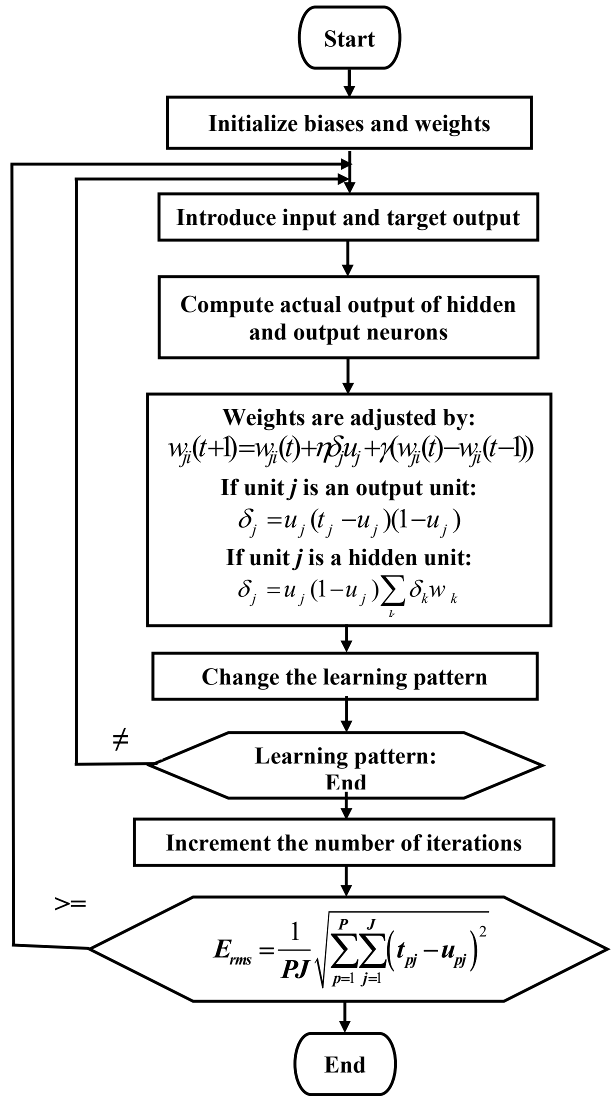

Fig. 2. Flowchart of an off-line back-propagation training algorithm.

The final weight values are frozen and utilized to get the precise values of the desired output during the test phase. The quality and success of training of ANN are assessed by calculating the error for the whole batch of training patterns using the normalized RMS error that is defined as:

$$E_{rms} = \frac{1}{PJ}\sqrt{\sum_{p=1}^{P}\sum_{j=1}^{J}(t_{pj} - u_{pj})^2}, \tag{37}$$

where J is the number of output units, P is the number of training patterns, t_{pj} is the desired output at unit j, and u_{pj} is the actual output at the same unit j. A zero error denotes that all the output patterns computed by the isothermal gas spheres ANN perfectly match the values expected, and that the isothermal gas spheres ANN is fully trained. Similarly, internal unit thresholds are adjusted by supposing that they are connection weights on links from the input with an auxiliary constant-value.

5. RESULTS AND DISCUSSIONS

5.1. *Data Preparation*

We developed a MATHEMATICA routine to calculate the fractional Emden function and the physical characteristics of the conformable isothermal gas spheres, like mass (equation 10), radius (equation 11), and density (equation 12). Equation (17) represents the series solution of fractional isothermal gas spheres, which is similar to the power series solution developed by Yousif et al. (2020), where we used only 10 series terms. As pointed out by Yousif et al. (2020), this series expansion (like equation 17) diverges for $x > 3.2$. We used the accelerated scheme developed by Nouh (2004) to accelerate the series. Our calculations are done for a range of fractional parameters ($0.75 \leq \alpha \leq 1$) with a step of 0.1. For the integer case ($\alpha = 1$), the Emden function computed according to the series solution, and the numerical one, are in good agreement, Yousif et al. (2021). Fractional models for the isothermal gas sphere can be computed using Equations (10) to (12) for the mass, radius, and density. So, we can investigate the mass-radius relations and density profiles at different fractional parameters.

In Table 1, we list the mass-radius relations for some fractional isothermal gas spheres models. The designations in the table are: R_* and M_* represent the radius and mass of the fractional star, R_0 and M_0 are the radius and mass of a typical neutron star with the physical parameters $M_0 = 1.4 M_\Theta$, central density $\rho_c = 5.75 \times 10^{14}\,\mathrm{g\,cm^{-3}}$, pressure $P = 2 \times 10^{33}$ par, and radius $R_0 = 1.4 \times 10^6\,\mathrm{cm}$. As seen in the table, as the value of the fractional parameter decreases the volume and mass of the star decreases.

TABLE 1

MASS-RADIUS RELATIONS FOR THE FRACTIONAL ISOTHERMAL GAS SPHERE.

α	R_*/R_0	M_*/M_0
1	1	1
0.99	0.956	0.915
0.98	0.915	0.838
0.97	0.875	0.768
0.96	0.838	0.703
0.95	0.802	0.644
0.94	0.767	0.591
0.93	0.735	0.514
0.92	0.703	0.495
0.91	0.673	0.464
0.9	0.644	0.415

TABLE 2

TRAINING, VALIDATION, AND TESTING DATA FOR THE FRACTIONAL ISOTHERMAL EMDEN FUNCTION.

Training phase	Validation phase	Testing phase
α	α	α
0.8, 0.85, 0.9, 0.95, 0.97, 0.98, 1	0.96, 0.99	0.91, 0.92, 0.93, 0.94

TABLE 3

TRAINING, VALIDATION, AND TESTING DATA FOR MASS-RADIUS RELATIONS AND DENSITY PROFILES.

Training phase	Validation phase	Testing phase
α	α	α
0.75, 0.90, 0.92, 0.93, 0.94, 0.96, 0.97, 0.99	0.95, 0.98	0.80, 0.85, 0.91

5.2. *Network Training*

To train the proposed neural network used to simulate the conformable fractional isothermal gas sphere equation, we used data calculated in the previous subsection. The data used for training of the ANN are shown in the first column of Tables (2-3). The architecture of the neural network (NN) we used in this paper for the isothermal gas sphere function is $2 - 120 - 1$, where the input layer has two inputs, which are the fractional parameter α and the dimensionless parameter x (x takes values from 0 to 80 in steps of 0.1), while the output layer has 1 node for the isothermal gas sphere function u computed for the same values of the dimensionless parameter x and input fractional parameter α. For the mass-radius relation, we used the architecture $2 - 120 - 2$, where the input layer has two individual inputs, which are the fractional parameter α and

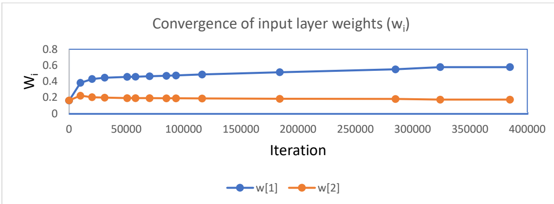

(a) The convergence of weights of the input layer (w_i)

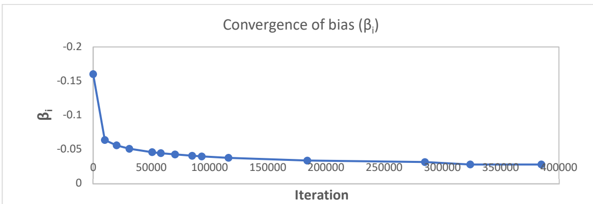

(b) The convergence of bias (β_i)

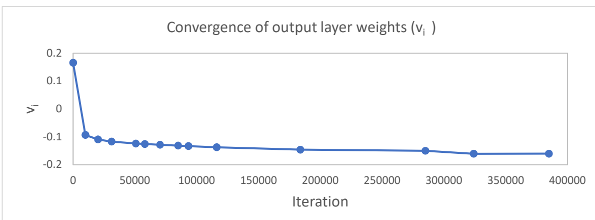

(c) The convergence of output layer weights (v_i)

Fig. 3. Convergence of input, bias, and output weights for the fractional isothermal Emden function. The color figure can be viewed online.

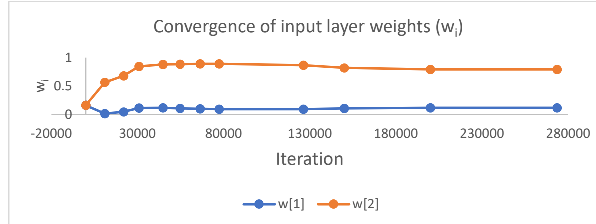

(a) The convergence of input layer weights (w_i)

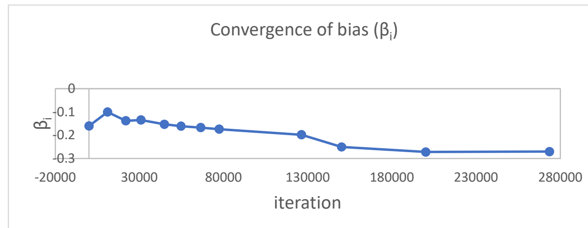

(b) The convergence of bias (β_i)

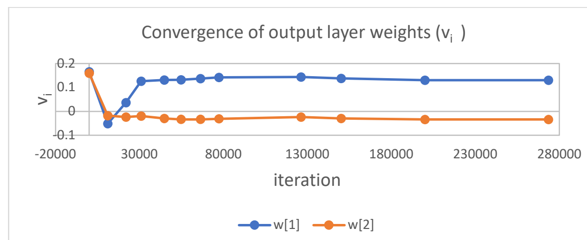

(c) Convergence of output layer weights (v_i)

Fig. 4. Convergence of the weights of input, bias, and output layers for the fractional mass-radius relation. The color figure can be viewed online.

the radius of the star R, while the output layer has 2 nodes, which are the mass and density at the same values of the input fractional parameters.

The choice of 120 neurons in the hidden layer of the NN was decided according to the findings we reached in our previous research (Nouh et al., 2020) after testing 80,120 and 200 neurons in one hidden layer of NN (shown in Figure 1), which gave the least RMS error and the best model for the network compared to the other two configurations for both the isothermal and mass-radius relation cases.

After multiple modifications and adjustments to the parameters of the NN, it converged to an RMS error value of 0.00002 for the training of the isothermal case, and to a value of 0.000025 for the training of the mass-radius relation and density profile case. During the raining of the NN, we used a value for the learning rate ($\alpha = 0.03$) and for the momentum ($\alpha = 0.5$). These values for the learning rate and momentum proved to quicken the convergence of the back-propagation training phase without exceeding the solution. In this research, we have programmed our algorithms using the C^{++} programming language running on Windows 7 of a CORE $i7$ PC. The network training typically took around 3 hrs. to converge for each case of the training previously mentioned. The trainings were implemented concurrently on different windows of the same machine. After network training, the frozen saved weights were utilized to get the values of the desired output during the validation and test phases in a very short time (about 1 second), as described in the next section.

For the demonstration of the convergence and stability of the values computed for the weight parameters of the network layers the behavior of the convergence of the input layer weights, bias and output layer weights (w_i , β_i and v_i) for the isothermal gas sphere case is as displayed in Figure 3. Moreover, the convergence behavior and stability of the values computed for the weight parameters of network layers (weights of the input layer, bias, and output layer) for the mass-radius relation case are shown in Figure 4. As these figures indicate, the values of the weights were initialized to random values and after many iterations they converged to stable values.

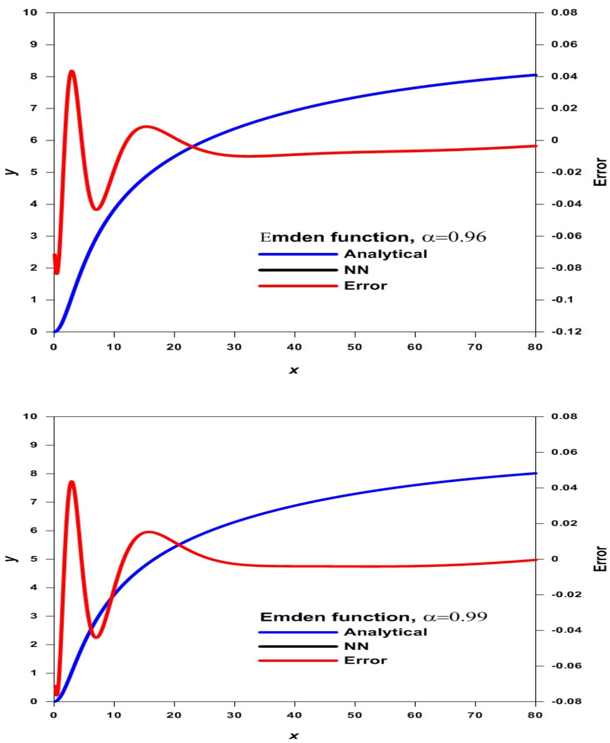

Fig. 5. The fractional Emden functions of the isothermal gas sphere obtained in the validation phase. The analytical and the ANN solutions are plotted with different colors. The maximum relative error is 1%. The color figure can be viewed online.

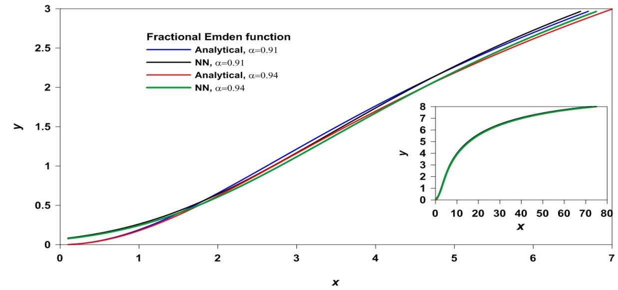

Fig. 6. The fractional Emden functions of the isothermal gas sphere obtained in the test phase. We plot the analytical and the corresponding ANN solutions with different colors to show the accuracy of the calculations. Also, the complete curve is included in the graph. The color figure can be viewed online.

5.3. *Validation and Test of the Training Phase*

To ensure the training of the NN, we used two values for the fractional parameter α, not being used in the training phase as a validation and verification of the goodness of that phase. These two values are shown in the middle column of Table 2 and Table 3 for the isothermal Emden function, and mass-radius relations and density profiles cases, respectively. The obtained results for those two validation values are as shown in Figure 5 for the isothermal Emden function, in Figure 7 for the fractional density profiles, and in Figure 9 for the fractional mass-radius relations. As shown in these figures, there is a very good coincidence between the NN prediction and the analytical results for the Emden function, mass-radius relations, and density profiles, where the maximum absolute error is $1\%, 2.5\%$, and 4%, respectively. We plotted the analytical solution and the NN prediction for the Emden function and the density profile with different colors, but due to the overlapping of the two curves, they appear as one. The big difference comes from the region near the center of the sphere, for $x \leq 10$. In the case of the mass-radius relation (Figure 9), the noticeable difference between the analytical solution and the NN is larger than that of the Emden function and density profiles due to the nature of the equation relating the mass to the radius (equation 10).

In Figures (6), (8), and (10), we plotted the predicted values of Emden functions, density profiles and mass-radius relations for some values of the fractional parameters listed in Tables 1 and 2. In these figures, due to the small change of the Emden function and density with the fractional parameter, and also the negligible difference between the analytical solution and the NN solution, we truncated the x-axis at a smaller value for more clarity. Again, there is a somewhat noticeable difference between the analytical solution and the predicted NN values in the case of the mass-radius relation (Figure 10) which is larger than the other two predicted NN values for the Emden functions and the density profiles (Figure 6 and Figure 8). This large difference may be attributed to the instability during performing and accelerating the series expansion of the fractional derivative of the Emden function (equation 10). It should be noted, here again, that the time taken to get the results of the validation and test phases, using the frozen saved values of the weights of the trained NN, is negligible (around 1 second). This proves the high efficiency and high-speed processing of the ANN when compared with the numerical and analytical methods.

6. CONCLUSION

The ANN modeling of the nonlinear differential equations shows a high efficiency when compared with the numerical and analytical methods. In the

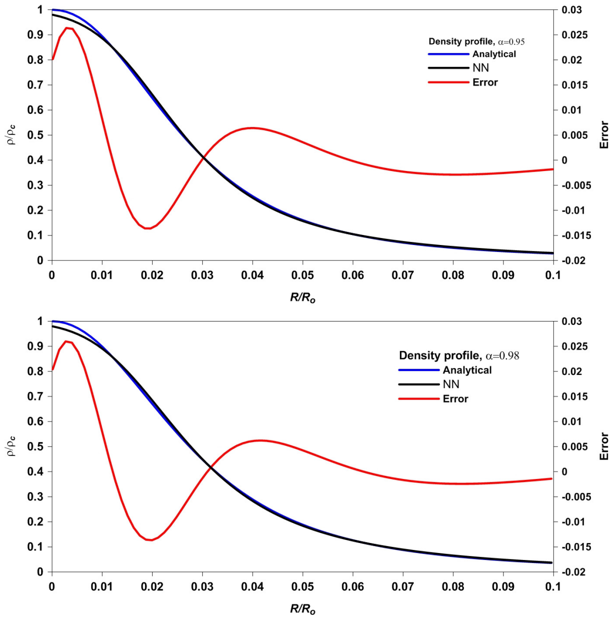

Fig. 7. The fractional density profiles obtained in the validation phase. There is a very low error except for the range of the radius ratio $R/R_0 \leq 0.015$. The maximum relative error is 2.5%. The color figure can be viewed online.

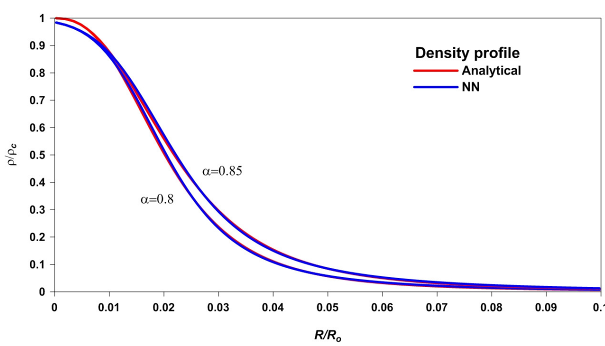

Fig. 8. The fractional density profiles obtained in the test phase for the fractional parameters $\alpha = 0.8, 0.85$. The color figure can be viewed online.

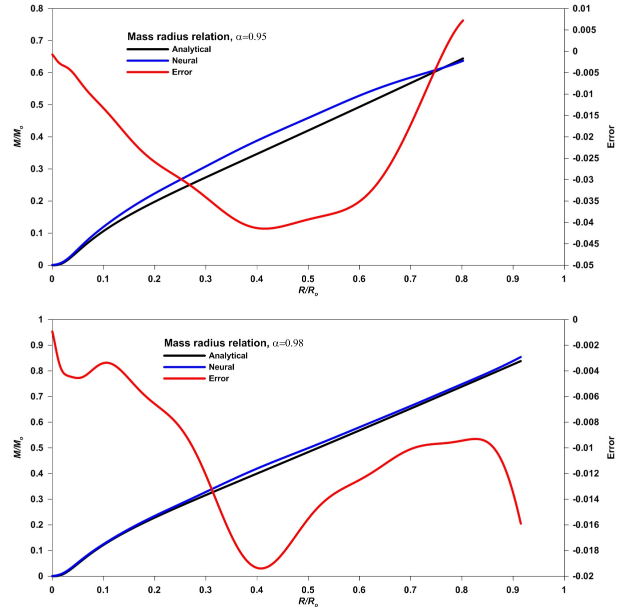

Fig. 9. The fractional mass-radius relations obtained in the validation phase. The maximum relative error is 4%. The color figure can be viewed online.

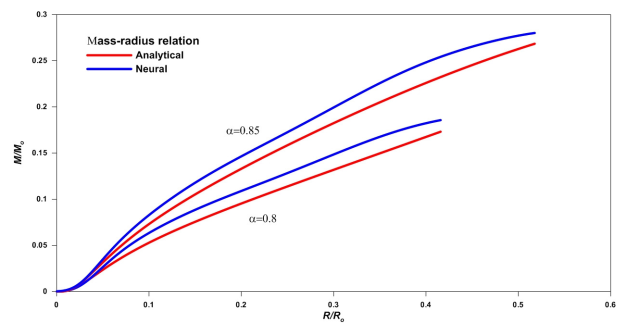

Fig. 10. The fractional mass-radius relations obtained in the test phase. The differences between the analytical and NN solutions are remarkable. The color figure can be viewed online.

present work, we aimed to introduce a computational approach to the fractional isothermal gas sphere via ANN. We solved the second type of Lane-Emden equation (the isothermal gas sphere) using the Taylor series, then we accelerated the resulting series to reach a good accuracy. The analytical calculations are performed for the Emden functions, mass-radius relations, and density profiles.

We obtained a good accuracy through the use of the ANN technique by using some calculated data to train the NN in the training phase, then validating the trained network by some other values, where we obtained maximum error values of 1%, 2.5%, and 4% for the isothermal fractional Emden function case, the density profile case, and the mass-radius relation case, respectively. To test the ANN technique in predicting unknown values, we used the trained network and ran the routine for the fractional test parameters listed in Tables 2 and 3. The comparison between the analytical and the ANN solution gives a very good agreement, as shown in Figures (6, 8, and 10) with a maximum error of 4%. The results obtained reflect the applicability and efficiency of using ANN to model stellar physical characteristics (i.e., radius, mass, and density) using the fractional isothermal gas sphere. In our opinion, the present results, besides the results obtained in Nouh et al. (2020), are an important step toward the composite modeling (e.g., isothermal core and polytropic envelope) of various stellar configurations using ANN.

We thank the referee for his/her valuable comments which improved the paper. The authors acknowledge the Academy of Scientific Research and Technology (ASRT), Egypt (Grant no. 6413), under the project Science Up. (ASRT) is the 2nd affiliation of this research.

REFERENCES

Abdel-Salam, E. A-B & Nouh, M. I. 2016, Ap, 2016, 59, 398

_________. 2020, NewA, 76, 101322

Abdel-Salam, E. A.-B, Nouh, M. I., & Elkholy, E. A. 2020, Scientific African, 8, 00386

Ahmad, I., Raja, M. A., Bilal, M., & Ashraf, F. 2017, Neural Comput & Applic, 28 (Suppl. 1): S929-S944

Basheer, I. A. & Hajmeer, M. 2000, Journal of Microbiological Methods, 43, 3

Bayin, S. S. & Krisch, J. P. 2015, Ap&SS, 359, 58

Denz, C. 1998, Optical Neural Networks, (Verlag: Springer)

El-Nabulsi, R. A. 2011, Applied Mathematics and Computation, 218, 2837

Elminir, H. K., Azzam, Y. A., Younes, F. I. 2007, Energy, 32, 1513

El-Mallawany, R., Gaafar, M. S., & Azzam, Y. A. 2014, Chalcogenide Letters, 11, 227

Faris, H., Alkasassbeh, M., & Rodan, A. 2014, Pol. J. Environ. Stud., 23, 341

Hadian-Rasanan, A. H., Rahmatic, D., Gorgind, S., & Parand, K. 2020, NewA, 75, 101307

Izeboudjen, N., Larbes, C., & Farah, A. A new classification approach for neural networks hardware: from standards chips to embedded systems on chip, Artificial Intelligence Review, 41, 491 (2014). https://doi.org/10.1007/s10462-012-9321-7

Khalil, R., Al-Horani, M., Yousef, A., & Sababheh, M. J. 2014, JCoAM, 264, 65

Leshno, M., Lin, V. Y., Pinkus, A., & Schocken, S., 1993, NN, 6, 861

Lippmann, R. P. 1989, IEEE Communications Magazine, 27, 11, 47

Nouh, M. I. 2004, NewA, 9, 467

Nouh, M. I. & Abdel-Salam, E. A-B. 2018, IrJST, 42, 2199

_________. 2018, EPJP, 133, 149

Nouh, M. I., Azzam, Y. A., & Abdel-Salam, E. A-B. 2020, Modeling fractional polytropic gas spheres using artificial neural network. *Neural Comput & Applic*, https://doi.org/10.1007/s00521-020-05277-9

Pakdaman, M., Ahmadian, A., Effati, S., Salahshour, S., & Baleanu, D. 2017, Applied Mathematics and Computation, 293, 81

Raja, M. A. Z., Khan, J. A., & Qureshi, I. M. 2010, A new stochastic approach for solution of Riccati diferential equation of fractional order. *Ann Math Artif Intell*, 60, 229 (2010). https://doi.org/10.1007/s10472-010-9222-x

Raja, M. A., Qureshi, J. M., & Khan, J. A. 2011, International Journal of Innovative Computing, Information and Control, 7, 6301

Raja, M. A., Manzar, M. A., & Samar, R. 2015, Applied Mathematical Modelling, 39, 3075

Tagliaferri, R., Ciaramella, A., Milano, L., Barone, F., & Longo, G. 1999, A&AS, 137, 391

Tagliaferri, R., Longo, G., Milano, L., et. al. 2003, NN, 16, 297

Wang, D., He, H., & Liu, D. 2018, IEEE Transactions on Industrial Informatics, 14, 2932, doi: 10.1109/TII.2017.2771256

Weaver, W. B. 2000, ApJ, 541, 298

Yadav, N., Yadav, A., & Kumar, M. 2015, An Introduction to Neural Network Methods for Differential Equations (Dordrecht: Springer)

Yousif, E. A., Adam, A. M. A., Hassaballa, A. A., & Nouh, M. I. 2021, NewA, 84, 101511

Zhang, G. P. 2000, "Neural networks for classification: a survey", in IEEE Transactions on Systems, Man and Cybernetics, Part C (Applications and Reviews), Vol. 30, No 4, pp. 451-462, Nov. 2020, doi: 10.1109/5326.897072

Zúñiga-Aguilar, C. J., Romero-Ugalde, H. M., Gómez-Aguilar, J. F., Escobar-Jiménez, R. F., & Valtierra-Rodríguez, M., 2017, CSF, 103, 382

Emad A.-B. Abdel-Salam: Department of Mathematics, Faculty of Science, New Valley University, El-Kharja 72511, Egypt.

Yosry. A. Azzam and Mohamed I. Nouh: Astronomy Department, National Research Institute of Astronomy and Geophysics(NRIAG), 11421 Helwan, Cairo, Egypt (abdo_nouh@hotmail.com).

Revista Mexicana de Astronomía y Astrofísica, **57**, 199–216 (2021)

https://doi.org/10.22201/ia.01851101p.2021.57.01.15

CONNECTING THE FORMATION OF STARS AND PLANETS. I – SPECTROSCOPIC CHARACTERIZATION OF HOST STARS WITH TIGRE

L. M. Flor-Torres[1], R. Coziol[1], K.-P. Schröder[1], D. Jack[1], J. H. M. M. Schmitt[2], and S. Blanco-Cuaresma[3]

Received February 6 2020; accepted January 7 2021

ABSTRACT

In search for a connection between the formation of stars and the formation of planets, a new semi-automatic spectral analysis method using iSpec was developed for the TIGRE telescope installed in Guanajuato, Mexico. TIGRE is a 1.2m robotic telescope, equipped with an Echelle spectrograph (HEROS), with a resolution R $\simeq$ 20000. iSpec is a synthetic spectral fitting program for stars that allows to determine in an homogeneous way their fundamental parameters: effective temperature, $T_{\rm eff}$, surface gravity, $\log g$, metallicities, $[M/H]$ and $[Fe/H]$, and rotational velocity, $V \sin i$. In this first article we test our method by analysing the spectra of 46 stars, hosts of exoplanets, obtained with the TIGRE.

RESUMEN

En la búsqueda de una conexión entre la formación estelar y planetaria, se desarrolló un nuevo método semiautomático de análisis espectral estelar usando iSpec, para el telescopio TIGRE, instalado en Guanajuato, México. El TIGRE es un telescopio robótico de 1.2m, el cuál está equipado con el espectrógrafo Echelle HEROS, que tiene una resolución R $\simeq 20,000$. iSpec es un programa de ajuste espectral sintético para estrellas que permite determinar de manera homogénea sus parámetros fundamentales: temperatura efectiva, $T_{\rm eff}$, gravedad superficial, $\log g$, metalicidades, $[M/H]$ y $[Fe/H]$, y velocidad de rotación, $V \sin i$. En este artículo, probamos nuestro método, analizando una muestra de 46 estrellas que albergan exoplanetas observadas por el TIGRE.

Key Words: planetary systems — stars: formation — stars: fundamental parameters — stars: rotation

1. INTRODUCTION

Since the discovery of the first planet orbiting another star in the 1990s, the number of confirmed exoplanets had steadily increased reaching in November of last year 4133.[4] The urgent tasks with which we are faced now are determining the compositions of these exoplanets and understanding how they formed. However, although that should have been straightforward (Seager 2010), the detection of new types of planets had complicated the matter, changing in a crucial way our understanding of the formation of planetary systems around stars like the Sun.

The first new type of planets to be discovered was the "hot Jupiters" (HJs; Mayor & Queloz 1995), which are gas giants like Jupiter and Saturn, but with extremely small periods, $P < 10$ days, consistent with semi-major axes smaller than $a_p = 0.05$ AU. The existence of HJs is problematic because, according to the model of formation of the solar system, they can only form in the protoplanetary disk (PPD) where it is cold enough for volatile compounds such as water, ammonia, methane, carbon dioxide and monoxide to condense into solid ice grains (Plummer et al. 2005). In the Solar System, this happens beyond the ice-line, which is located close to 3 AU (Martin & Livio 2012). This implies that HJs must have formed farther out in the cold regions of the PPD, then migrated close to their stars (Lin et al. 1996). Subsequent discoveries have then shown that far from being exceptional, artifacts of an observational bias, HJs turned out to be very

[1]Departamento de Astronomía, Universidad de Guanajuato, Guanajuato, Gto., México.

[2]Hamburger Sternwarte, Universität Hamburg, Hamburg, Germany.

[3]Harvard-Smithsonian Center for Astrophysics, Cambridge, MA, USA.

[4]http://exoplanet.eu/.

common around Sun-like stars, suggesting that large scale migration is a standard feature of the planet formation process (Butler et al. 2000; Udry & Santos 2007).

Two other new types of planets discovered are the "Super-Earths" (Leconte et al. 2009; Valencia et al. 2006; Martin & Livio 2015; Chabrier et al. 2009) and the "mini-Neptunes" (Gandolfi et al. 2017). These too were found to be common and very close to their stars, which, consequently, also makes them "hot". Their discoveries are important for two reasons. The first reason is that it makes the alternative "in situ" model for the formation of HJs (e.g., Boss 1997) a special model, since it cannot explain the large mass range and diversity of the "hot" exoplanets observed (Super-Earths and mini-Neptunes in situ models are discussed in Raymond et al. 2008; Chiang & Laughlin 2013). The second reason is that it was recently established by Lee et al. (2017) that their numbers around their host stars fall rapidly for periods $P < 10$ days (≈ 0.09 AU), which, assuming Keplerian orbits, clearly implies they all formed farther out (beyond 0.1 AU) and have migrated inward, but with a good many disappearing into their stars. This, once again, puts large scale migration at the front scene of the planet formation process.

This brings us to the present fundamental question in planet formation theory (McBride & Gilmour 2004): what explains the fact that large scale migration did not happen in the Solar System? Or, in other words, assuming all planets form in a PPD around a low mass star (Nomura et al. 2016; van der Marel et al. 2018; Pérez et al. 2019), what difference would make migration more important in one case and less important in another (see discussion in Walsh et al. 2011)?

Integrating the migration process into a consistent model of planet formation is an extremely active and fast evolving field of research (a recent review of this important subject can be found in Raymond & Morbidelli 2020). In the case of the HJs, two migration mechanisms are accepted now as most probable (Dawson & Johnson 2018):(1) disk migration, where the planet forms beyond the ice-line and then migrates inward by loosing its orbit angular momentum to the PPD (see thorough reviews in Baruteau et al. 2014; Armitage 2020), and (2) high-eccentricity migration, according to which the planet first gains a high eccentricity through interactions with other planets, which makes it to pass very close to its star, where it looses its orbit angular momentum by tidal interactions (this is a more complicated process, involving different mechanisms; e.g., Rasio & Ford 1996; Weidenschilling & Marzari 1996; Marzari & Weidenschilling 2002; Chatterjee et al. 2008; Nagasawa et al. 2008; Beaugé & Nesvorný 2012). However, what is not clear in these two models is, what importance must be put on the characteristics of the PPD, its mass, size, depth and composition?

According to PPD formation theory, there are two possible mass scenarios (Armitage 2020): the minimum mass model, between 0.01 to 0.02 $M_{\odot}$, which suggests that the PPD initial mass is only sufficient to explain the masses of the planets that formed within it, and the maximum mass model, which suggests the mass could have been much higher, close to 0.5 $M_{\odot}$. Consequently, more massive PPD (compared to the Solar System) might have either favored the formation of more massive planets (consistent with PPD observations, see Figure 2 and discussion in Raymond & Morbidelli 2020) or a larger number of planets. The problem is that this makes both migration mechanisms equally probable (also, the masses observed seem too low; also related to Figure 2 in Raymond & Morbidelli 2020). Another caveat is that the Solar System is a multiple planet system where migration on large scale did not happen.

In terms of angular momentum, the differences between the minimum and maximum mass model for the PPD might also be important. By definition, the angular momentum of a planet is given by the relation (e.g., Berget & Durrance 2010):

$$J_p = M_p \sqrt{G M_* a_p (1 - e_p^2)}, \qquad (1)$$

where M_p and M_* are the masses of the planet and its host star, a_p is the semi-major axis of the planet and e_p its eccentricity. This suggests that within the maximum mass model more massive planets would also be expected to have higher orbital angular momentum (through their PPD) and, consequently, to have lost a larger amount of their angular momentum during large scale migration ($a_p \to 0$). This implies that the efficiency of the migration mechanism must increase with the mass of the planet (or its PPD). In principle, such requirement might be one way to distinguish which migration process is more realistic. However, the problem is bound to be more complicated. First, stars rotate much more slowly than expected assuming conservation of angular momentum during their formation (McKee & Ostriker 2007). Second, defining the angular momentum of a planetary system as $J_{sys} = J_* + \Sigma J_p$ where ΣJ_p is the sum of the angular momentum of all the planets and J_* the angular momentum of the host star (cf. Berget

& Durrance 2010), the angular momentum of massive planets (even after migration, assuming $a_p \neq 0$) will always dominate over the angular momentum of its host stars. That is, $J_*/\Sigma J_p < 1$, and this is despite the enormous loss of angular momentum of the star during its formation. This implies that a sort of coupling must exist between the angular momentum of the stars and their planets through their PPDs. Understanding the nature of this coupling, therefore, is an important step in understanding how the PPD and the planets forming in it are connected to the formation of their stars. This, on the other hand, requires completing our information about the stars and the planets rotating around them.

In the case of the planets, the two most successful detection techniques, the radial velocity (RV) and transit (Tr) methods, yield estimates of the mass of a planet, M_p, and its radius, R_p, as well as the semi-major axis, a_p, and the eccentricity of its orbit, e_p. The first two parameters constrain their composition and formation process in the PPD, while the last two give information about their migration. By combining the four parameters we can also retrieve the angular momentum of the orbits of the planets (cf. equation 1). In the case of the stars the most important characteristics that can be derived from their spectra are the effective temperature, T_{eff}, the surface gravity, $\log g$, the metallicities, [M/H] or [Fe/H], and the rotational velocity, $V \sin i$. The first two can be used in combination with their magnitudes and distances (using GAIA parallaxes) to determine their radii and masses which, taken in combination with the rotational velocity, yield the angular momentum (or spin) of the star, J_*:

$$J_* = \gamma_* M_* R_* V_*^{rot}, \tag{2}$$

where M_*, R_* and γ_* are the star mass, radius and moment of inertia (which depends on the mass of the star; cf. Irwin 2015), and $V_*^{rot} = V \sin i / \sin i$ is the equatorial rotation velocity (where i is the inclination angle of the rotation axis relative to our line of sight).

To understand how the formation of planets is connected with the formation of their host stars, we must, consequently, make an effort to determine in parallel with the discovery of the former the physical characteristics of the latter. Present data banks for exoplanets (e.g., Kepler and now TESS, with 51 confirmed discoveries, and future surveys like PLATO)[5] require follow-up observations and analysis for the host stars, which are usually done with large diameter telescopes equipped with high resolution spectrographs. However, for the brightest stars (TESS targets, for example, being 30-100 times brighter than KEPLER stars), the use of smaller diameter telescopes equipped with lower resolution spectrographs might be more efficient in acquiring the information. Moreover, although high resolution spectra is justified when one uses the standard spectral analysis method, which is based on modeling the equivalent width (EW) of spectral lines, this might not be necessary when one uses the synthetic spectral analysis (e.g., Valenti & Debra 2005), which consists in fitting observed spectra to grids of synthetic spectra with well determined physical characteristics that can be produced at different spectral resolutions. Another problem in using large aperture telescopes for host stars follow-up is that, since these telescopes are in high demand (for faint objects), data are collected on short duration runs by different groups using different techniques and codes (although the same analysis method), which introduces discrepancies between the results (Hinkel et al. 2014, 2016; Blanco-Cuaresma 2014; Jófre et al. 2017). This suggests that a follow-up using a dedicated telescope and applying only one method of analysis could produce more homegeneous data (one effort to homogenize data is the Stars With ExoplanETs CATalog or SWEET-Cat for short; Sousa et al. 2008). For these reasons we developed a new method based on stellar spectral analysis for data obtained with the TIGRE telescope (Telescopio Internacional de Guanajuato Robótico Espectroscópico) that is installed at our institution in Guanajuato.

TIGRE is a 1.2 m fully robotic telescope located at the La Luz Observatory (in central Mexico) at an altitude of 2,400 m; a more detailed description can be found in Schmitt et al. (2014). Its principal instrument is the fibre-fed echelle spectrograph HEROS (Heidelberg Extended Range Optical Spectrograph), which yields a spectral resolution $R \approx 20,000$, covering a spectral range from 3800 Å to 8800 Å. The queue observing mode and automatic reduction pipeline already implemented for this telescope allow to optimize the observation and reduction process, producing highly homogeneous data rapidly and confidently. To optimize the analysis process, we developed a semi-automatic method that allows us to derive efficiently the most important physical characteristics of the stars: T_{eff}, $\log g$, [M/H], [Fe/H], and $V \sin i$. This was done by applying the synthetic spectral fitting technique as offered by the code iSpec (Blanco-Cuaresma 2014), which

[5]https://tess.mit.edu; about PLATO see https://platomission.com/about/.

was shown to yield results that are comparable to results in the literature obtained through different methods and codes (Blanco-Cuaresma 2019).

The goal of this first article is to explain our spectral analysis method based on iSpec and to compare results obtained by TIGRE with data taken from the literature. In an accompanying paper (Flor-Torres et al., hereinafter Paper II) we will present a preliminary study, based on our own observational results, about the coupling of the angular momentum of the exoplanets and their host stars.

2. SAMPLE OF HOST STARS WITH EXOPLANETS OBSERVED WITH TIGRE

Our initial target list for a pilot project was built from the revised compendium of confirmed exoplanets in the Exoplanet Orbit Database (hereinafter Exoplanets.org,[6]) selecting all stars with spectral types F, G or K, located on the main sequence (based on their luminosities and colors), and for which a confirmed planet with well determined mass, radius, and semi-major axis was reported. Note that we did not apply a restriction to single systems, since from the point of view of the angular momentum we verified that only the major planet of a system counts (like Jupiter in our solar system). To optimize our observation with TIGRE, we restricted further our target list by retaining only host stars that have a magnitude $V \leq 10.5$, obtaining a much shorter list of 65 targets.

Our observed sample consists of 46 stars, hosts of 59 exoplanets, which were observed by TIGRE in queue mode. In Table 1 the stars observed are given a running number (Column 1) which is used to identify them in the different graphics. The V magnitude of each star and its distance as calculated from Gaia parallaxes are listed in Columns 3 and 4 respectively. Also shown are the exposure times, in Column 5, and the signal to noise ratio (S/N) in Column 6, as measured in the red part of the spectrum. The last column lists the main references found in the literature with data about the host stars and their planetary systems.

The HEROS spectrograph on TIGRE is coupled to two ANDOR CCDs, cooled by thermocouple (Peltier cooling to -100 C): blue iKon-L camera DZ936N-BBB and red iKon-L camera DZ936N-BV. This yields for each star two spectra, one in the blue, covering a spectral range from 3800 Å to 5750 Å, and one in the red, covering a spectral range from 5850 Å to 8750 Å. All the data were automatically reduced

[6]http://exoplanets.org/.

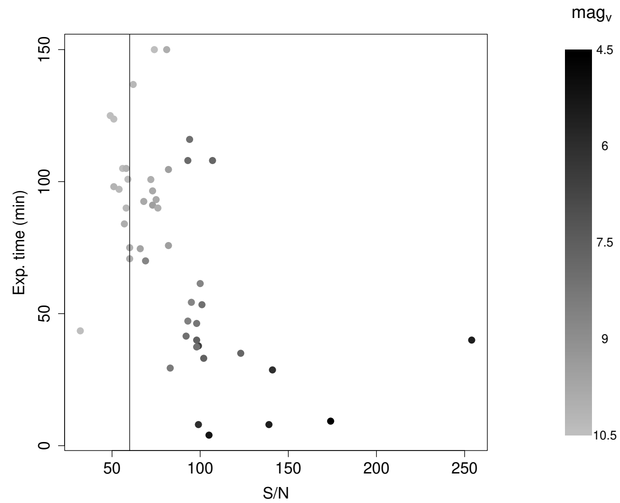

Fig. 1. S/N as a function of exposure time for our sample, limited to stars with magnitude limit $V \leq 10.5$. Note that the exposure time was adjusted to reach S/N $\geq$ 60 in less than two hours.

by the TIGRE/HEROS standard pipeline, which applies automatically all the necessary steps to extract Echelle spectra (Hempelmann et al. 2016; Mittag et al. 2016): bias subtraction, flat fielding, cosmic ray correction, order definition and extraction and wavelength calibration, which was carried out by means of Th-Ar lamp spectra taken at the beginning and end of each night. Finally, we applied a barycentric correction and as a final reduction step, corrected each spectrum for telluric lines using the code Molecfit developed by Smette et al. (2015). After verification of the results of the reduction process, we decided to concentrate our spectral analysis only on the red part of the spectra, where the S/N is higher.

In Figure 1 we show the S/N obtained as a function of the exposure time. For each star the total exposure time during observation was adjusted to reach S/N ≥ 60. Note that this result only depends on the telescope diameter, the fiber transmission, the spectrograph resolution (we used $R = 20,000$, but the resolution is adjustable in iSpec) and the photometric conditions (explaining most of the variance).The average exposure time was 74 s for an average S/N $\approx$ 87, which makes observation with TIGRE a very efficient process.

To determine how faint a follow-up with TIGRE could be done efficiently, we traced in Figure 2 an exponential growth curve based on our data, determining the S/N expected in one hour for stars with different magnitudes. One can see that a star with 10.5 mag in V would be expected to have a S/N near 30 (or 60 in 2 hours). The lowest we could go

TABLE 1

STARS OBSERVED WITH THE TIGRE

Id. #	Star	Magnitude (V)	Distance (pc)	Exp. time (min)	S/N	Ref. (as found in exoplanets.org)
1	*KELT-6	10.3	242.4	97.1	54	Damasso et al. (2015)
2	*HD 219134	5.6	6.5	8.0	139	Motalebi et al. (2015)
3	*KEPLER-37	9.8	64.0	93.2	75	Batalha et al. (2013)
4	HD 46375	7.8	29.6	108.0	107	Marcy et al. (2000)
5	HD 75289	6.4	29.1	37.8	99	Udry et al. (2000)
6	HD 88133	8.0	73.8	116.0	94	Fischer et al. (2005)
7	HD 149143	7.9	73.4	108.0	93	Fischer et al. (2006); da Silva et al. (2006)
8	HAT-P-30	10.4	215.3	100.9	59	Johnson et al. (2011)
9	KELT-3	9.8	211.3	92.5	68	Pepper et al. (2013)
10	KEPLER-21	8.3	108.9	29.4	83	Borucki et al. (2011)
11	KELT-2A	8.7	134.6	54.3	95	Beatty et al. (2012)
12	HD86081	8.7	104.2	61.4	100	Johnson et al. (2006)
13	WASP-74	9.8	149.8	96.5	73	Hellier et al. (2015)
14	HD 149026	8.1	76.0	37.4	98	Sato et al. (2005)
15	HD 209458	7.6	48.4	40.0	98	Henry et al. (2000); Charbonneau et al. (2000)
16	BD-10 3166	10.0	84.6	100.8	72	Butler et al. (2000)
17	HD 189733	7.6	19.8	33.1	102	Bouchy et al. (2005)
18	HD 97658	7.7	21.6	35.0	123	Howard et al. (2011)
19	HAT-P-7	10.5	344.5	43.5	32	Pál et al. (2008)
20	KELT-7	8.5	137.2	47.2	93	Bieryla et al. (2015)
21	HAT-P-14	10.0	224.1	84.0	57	Torres et al. (2010)
22	WASP-14	9.7	162.8	74.6	66	Joshi et al. (2009)
23	HAT-P-2	8.7	128.2	70.0	69	Bakos et al. (2007)
24	WASP-38	9.4	136.8	75.8	82	Barros et al. (2011)
25	HD 118203	8.1	92.5	41.5	92	da Silva et al. (2006)
26	HD 2638	9.4	55.0	104.6	82	Moutou et al. (2005)
27	WASP-13	10.4	229.0	123.7	51	Skillen et al. (2009)
28	WASP-34	10.3	132.6	136.8	62	Smalley et al. (2011)
29	WASP-82	10.1	277.8	98.1	51	West et al. (2016)
30	HD17156	8.2	78.3	46.3	98	Fischer et al. (2007)
31	XO-3	9.9	214.3	70.8	60	Johns-Krull et al. (2008)
32	HD 33283	8.0	90.1	53.4	101	Johnson et al. (2006)
33	HD 217014	5.5	15.5	40.0	254	Mayor & Queloz (1995)
34	HD 115383	5.2	17.5	4.0	105	Kuzuhara et al. (2013)
35	HAT-P-6	10.5	277.5	125.0	49	Noyes et al. (2008)
36	*HD 75732	6.0	12.6	28.7	141	Marcy et al. (2002)
37	HD 120136	4.5	15.7	9.3	174	Butler et al. (2000)
38	WASP-76	9.5	195.3	91.1	73	West et al. (2016)
39	Hn-Peg	6.0	18.1	8.0	99	Luhman et al. (2007)
40	WASP-8	9.9	90.2	150.0	81	Queloz et al. (2010)
41	WASP-69	9.9	50.0	90.0	76	Anderson et al. (2014)
42	HAT-P-34	10.4	251.1	105.0	56	Bakos et al. (2012)
43	HAT-P-1	9.9	159.7	75.0	60	Bakos et al. (2007)
44	WASP-94 A	10.1	212.5	105.0	58	Neveu-VanMalle et al. (2014)
45	WASP-111	10.3	300.5	90.0	58	Anderson et al. (2014)
46	HAT-P-8	10.4	212.8	150.0	74	Latham et al. (2009)

An * in front of the name of the star identifies multiple planetary systems.

would be S/N $\approx$ 10 which would be reached in one hour for a 12.5 mag star (or 2 hours for a 13 mag star). Since it is not clear how low the S/N of a star could be to be efficiently analysed using the synthetic-spectra method, we judged safer to adopt a limit S/N of 60, which can be reached within two hours using TIGRE. This justifies the magnitude limit, $V \leq 10.5$, adopted for this pilot project. Our observations suggest that a 1.2 m telescope could contribute significantly to the follow-up of exoplanet surveys like TESS, searching for small rocky planets around bright stars (stars much brighter than KEPLER stars), and in the near future PLATO, which will search for Earth-like planets in the habitable zones of one million nearby Solar type stars.

3. SPECTRAL ANALYSIS USING ISPEC

Our spectral analysis was developed using the synthetic spectral fitting technique offered by the code iSpec (version 2016.11.18; Blanco-Cuaresma 2014, 2019). In brief, this technique consists in compar-

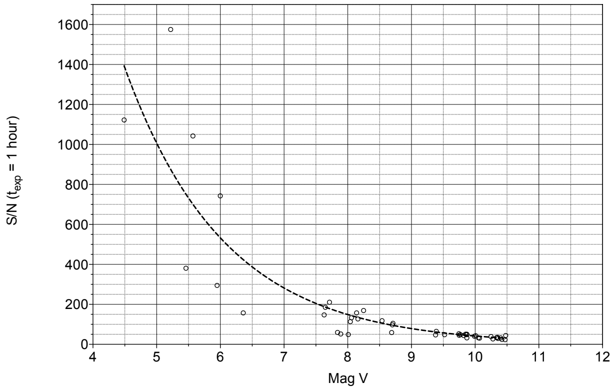

Fig. 2. Exponential growth curve giving the S/N expected after one hour exposure time for stars with different magnitudes.

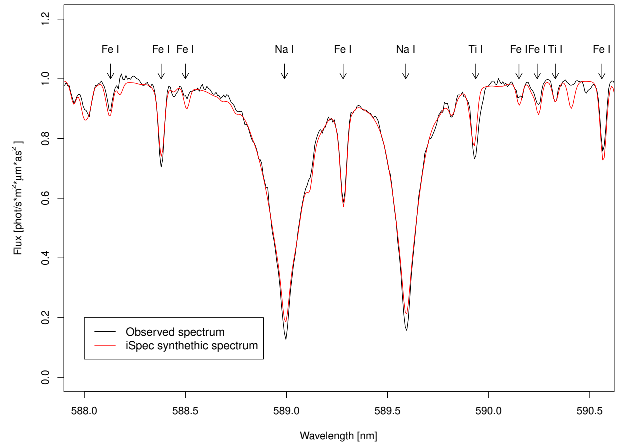

Fig. 3. Example of the result for the synthetic spectral fitting method in iSpec. The star is HD 46375, the observed spectrum is shown in blue and the fitted spectrum in red, with a rms of 0.0319. The color figure can be viewed online.

ing an observed spectrum with synthetic spectra interpolated from pre-computed grids, calculated using different radiative transfer codes, and applying a least-squares minimization algorithm to converge towards the closest approximation possible. In Figure 3 we show one example of a synthetic spectral fit for the star HD 46375. The fit has a rms 0.0319, which is relatively good considering HEROS intermediate resolution (Piskunov & Valenti 2017). Due to the low resolution of our spectra we can fit at the same time in a homogeneous manner the intensity and spectral profiles of more than 100 lines (compared to a few 10s at high resolution; e.g., Valenti & Debra 2005). The best fit then allows to determine five important atmospheric parameters: i.e., the effective temperature, T_{eff}, the surface gravity, $\log g$, two indexes of metallicities, $[M/H]$ and $[Fe/H]$, and the rotational velocity, $V \sin i$.

To optimize our analysis a crucial step of our method consisted in applying iSpec to a TIGRE spectrum from the Sun (as reflected by the Moon). Our main goal was to determine a subset of spectral lines and segments that best reproduced the physical characteristics of our star. Although this step is time consuming because each line and segment has to be tested incrementally by running iSpec, once these lines and segments are established, the analysis of stars becomes straightforward and efficient, the full process taking only a few minutes to converge on a modern desktop computer. Starting with the whole line-list available in the VALD database (Kupka et al. 1999, 2011), we kept only 122 lines in the red for which we defined specific segments in Table 6 of Appendix A. As we already verified in Eisner et al. (2020), these lines and segments can also be used in iSpec as a standard basis for observations obtained with different telescopes and (once adjusted for the resolution) other spectrographs.

Our initial analysis of the Sun also allowed us to decide which solar abundance, atmospheric model and radiative transfer code were optimal. We adopted the solar abundance of Asplund et al. (2009), the `ATLAS` atmospheric model of Kurucz (2005) and the radiative transfer code `SPECTRUM` of Gray & Corbally (1994). Another parameter that turned out to be important using iSpec is a correction for limb darkening, which we fixed to a value of 0.6 (Hestroffer & Magnan 1998; Blanco-Cuaresma 2019).

After working out the analysis of the Sun, we found an unexpected difficulty in obtaining the rotation velocity, $V \sin i$, for our stars. The problem comes from the fact that in low mass stars the turbulence velocity V_{mic} and V_{mac} have values comparable to $V \sin i$ (Doyle et al. 2014), and there is consequently no fail-proof recipe how to "constrain" these velocities using the synthetic method. One way to approach this problem (following different researchers in the field) is to adopt ad hoc values based on theory or observation (Gray 1984a,b; Fischer & Valenti 2005; Bruntt et al. 2010; Tsantaki et al. 2014; Doyle et al. 2014). For our analysis, we decided to adopt empirical values. For V_{mac} we used the relation (Doyle et al. 2014):

$$V_{mac} = a + b\Delta T + c\Delta T^2 - 2.00(\log g - 4.44), \quad (3)$$

where $\Delta T = (T_{eff} - 5777)$, $a = 3.21$, $b = 2.33 \times 10^{-3}$ and $c = 2.00 \times 10^{-6}$. For V_{mic} we used the relation

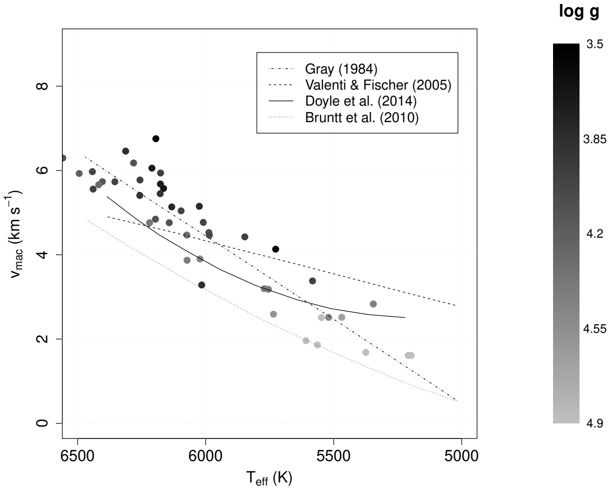

Fig. 4. Values of V_{mac} adopted for our analysis with iSpec as a function of our results for T_{eff}.

(Tsantaki et al. 2014):

$$V_{mic} = 6.932 \times 10^{-4} T_{eff} - 0.348 \log g - 1.437 \,. \quad (4)$$

Note that neither authors give uncertainties on these values. However, Doyle et al. (2014) suggest generic uncertainties of the order of ± 0.27 km/s and ± 0.15 for V_{mac} and V_{mic} respectively, which we adopted for our study.

In Figure 4 we show the final values of V_{mac} obtained in our analysis. Traced over the data, we draw the different relations proposed in the literature to fix this parameter. At high temperatures ($T_{eff} > 5800$ K), one can see that our values for V_{mac} are well above the upper limit determined by Valenti & Fischer (2005), while at low temperatures, the values are well above the lower limit determined by Bruntt et al. (2010). In general, our results for V_{mac} are consistent with the values expected based on the relation proposed by Gray (1984b).

Our final result for the Sun is shown in Table 2. These values were obtained after only ten iterations, using the parameters of the Sun as initial guess and fixing V_{mac} and V_{mic} using equation 3 and equation 4. For comparison, we also included in Table 2 the values adopted for the Gaia Benchmark stars. Although our best fit reproduces well the physical characteristics of the Sun, the uncertainty estimated by iSpec for $V \sin i$ is relatively high. But this, as we already explained, is expected considering the problem related to V_{mic} and V_{mac}. The different solutions (as shown in Figure 4) to this problem might explain, for example, why the macro turbulence we used for the Sun is lower than what was used by Gaia. In

TABLE 2

RESULTS FOR THE SOLAR SPECTRUM USING ISPEC

Char.	iSpec	Sun*
T_{eff}	5571 ± 30 K	5571 K
$\log g$	4.44 ± 0.04 dex	4.44 dex
$[M/H]$	0.00 ± 0.03	0
$[Fe/H]$	0.00 ± 0.03	0
$V \sin i$	1.60 ± 1.45 km/s	1.60 km/s
V_{mic}	1.02 km/s	1.07 km/s
V_{mac}	3.19 km/s	4.21 km/s
rms of fit	0.0289	

*Gaia benchmark Stars values(Blanco-Cuaresma 2019).

Doyle et al. (2014), the authors already noted a similar difference, by comparing the values they obtained by their relation with results reported by Fischer & Valenti (2005), where the V_{mac} were systematically higher by as much as 0.54 km s^{-1}. However, adding this difference (as a systematic correction) to bring our result for V_{mac} closer to the value proposed in the Gaia Benchmark, did not lower the uncertainties on $V \sin i$ obtained with iSpec. Therefore, considering that our method easily reproduces the value of $V \sin i$ for the Sun, we judged more realistic to keep a high uncertainty on this parameter. Besides, the question is possibly more complex, considering the uncertainty on the existence of a $J - M$ relation, $J_* \propto M^{\alpha}$, for low mass stars (Herbst et al. 2007) and taking into account that $V \sin i$ might also depend on the age of the star (that is, decreasing with the age; Kraft 1967; Wilson 1963; Skumanich 1972).

For the analysis of the stars, our semi-automatic method can be summarized in the following way. We first run iSpec using the parameters of the Sun as initial input. This implies calculating V_{mac} and V_{mic} using equation 3 and equation 4, keeping these values fixed and leaving all the other parameters free. The results of the first run give us new values of T_{eff} and $\log g$ based on which we calculate new initial values for V_{mac} and V_{mic} before running iSpec a second time.

To verify our solutions, for each star we use the final value of T_{eff} to calculate its mass and radius (first we get the mass, then the corresponding radius) using the mass-luminosity relation for stars with masses between 0.43 $M_\odot$ and 2 $M_\odot$ (Wang & Zhong 2018):

$$\frac{M}{M_\odot} = \left(\frac{L}{L_\odot}\right)^{1/4} = \frac{T_{eff}}{T_\odot}\left(\frac{R}{R_\odot}\right)^{1/2}, \quad (5)$$

where L is the bolometric luminosity as determined from its magnitude in V and its distance calculated from Gaia in Table 1. Then, we verify that the value of $\log g$ given by iSpec is consistent with the mass and radius obtained using the relation (equation 7 in Valenti & Debra 2005):

$$\log(M/M_\odot) = \log(g_*) + 2\log(R/R_\odot) - 4.437\,. \quad (6)$$

In general, we obtained consistent values for $\log g$, within the generic errors suggested by Doyle et al. (2014). However, for eight stars, we found discrepant masses, the masses obtained using equation 6 being higher than the masses using equation 5. To solve this problem we found it important to better constrain the initial value of $\log g$ before running iSpec a second time. The reason for this constraint is physically clear, since, as shown by equation 5 and equation 6, $\log g$ is coupled to T_{eff}. In Valenti & Debra (2005), for example, the authors took into account this coupling by first fixing the initial value of T_{eff} related to the $B - V$ color of the star, then used a generic $\log g$ consistent with this temperature. In our case we decided to use as initial parameters for the second run the value of T_{eff} obtained from the first run with iSpec (which uses the values of the Sun as first guesses) and to use as second guess the value of $\log g$ given by equation 6 that makes the two masses consistent. This also implies recalculating V_{mac} and V_{mic} for these new values, which, as before, are kept fixed running iSpec. The unique consequence of adding this constraint for the eight stars with discrepant masses was to lower the final values of their $\log(g)$, all the other parameters being equal. For each star, our method requires only two runs of ten iterations each, which amounts to about 30 minutes CPU time on a fast desktop computer. This makes our analysis process quite efficient.

4. RESULTS: CHARACTERIZATION OF THE HOST STARS OF EXOPLANETS OBSERVED WITH TIGRE

Our measurements for the physical parameters of the host stars as determined with our semi-automatic method are presented in Table 3. Note that for the metallicities, $[M/H]$ and $[Fe/H]$, an extra correction was needed following Valenti & Debra (2005), to eliminate spurious abundance trends (see their explanations in § 6.4). This correction is based on the assumption that the ratio of one elemental abundance to another must not vary systematically with the temperature. The correction then is simple: it consists in tracing the metallicities as a function of T_{eff}, fitting a second order relation, then subtracting this spurious relation from the data. All the uncertainties reported in Table 3 were calculated by iSpec, while the errors of the radii and masses are the quadratic sums of the uncertainties of the parameters used to calculate these values (see § 7.2 in Valenti & Debra 2005). As explained in Valenti & Debra (2005) and in Piskunov & Valenti (2017) the uncertainties estimated by the algorithms that produce the synthetic spectra and fit them to the observed spectra are usually undetermined, as compared to the random errors calculated from the measurements of multiple observations of the stars (§ 6.3 in Valenti & Debra 2005). Unfortunately, multiple observations were not programmed for our stars and we have only 4 stars in our study (17, 19, 23 and 46) that were observed more than once (four times for three and six times for the fourth one). This means that only a rough estimate of the random error can be obtained for our pilot-survey by calculating for each of these stars the standard deviations of the parameters measured applying the same spectral analysis as for the other stars. In table 4 we compare our mean uncertainties as obtained with iSpec with the mean of the standard deviations for the multiply observed stars in our sample. Except for $V \sin i$, the mean empirical errors are much larger than the iSpec values. In particular, our empirical errors are larger than the empirical uncertainties calculated by Valenti & Debra (Figure 9 in 2005), being comparable to their 2 sigma probabilities (the values in the table correspond to 1 sigma, the threshold that includes 68.3% of their error measurements).

Comparing with the Exoplanets.org and SWEET.cat mean uncertainties, our mean errors (standard deviations of multiple stars) are slightly larger, although still comparable to those reported in these studies. Although preliminary, this result is important as it suggests that our results based on iSpec analysis of low resolution spectra (R $\approx 20,000$) are in good agreement with results obtained using higher resolution spectra (R higher than 50,000).

Another way to verify the consistency of our data is to compare our results with those published in Exoplanets.org (on the left in Figure 5) and in SWEET-Cat (on the right). Taken as a whole, our results seem compatible with the data reported in these two catalogs (note that the uncertainties are those of iSpec), although there are also slight notable differences. In Figure 5a, our values for T_{eff} are slightly higher below 5800 K than the values reported by Exoplanets.org and SWEET-Cat. However, above 6000 K our temperatures are compa-

TABLE 3

PHYSICAL PARAMETERS OF THE HOST STARS OF EXOPLANETS IN OUR SAMPLE, AS DETERMINED WITH ISPEC

No.	Name of star	T_{eff} (K)	$\Delta T_{\rm eff}$ (K)	$\log g$	$\Delta \log g$	[M/H]	$\Delta[M/H]$	$[Fe/H]$	$\Delta[Fe/H]$	$V \sin i$ (km/s)	$\Delta V \sin i$ (km/s)	V_{mic} (km/s)	V_{mac} (km/s)	rms	R_* ($R_\odot$)	ΔR_* ($R_\odot$)	M_* ($M_\odot$)	ΔM_* ($M_\odot$)
1	KELT-6	6176	24	4.03	0.05	−0.38	0.02	−0.14	0.03	6.52	0.82	1.44	5.28	0.0292	1.71	0.20	1.22	0.20
2	HD 219134	5209	13	4.90	0.00	0.00	0.02	0.02	0.01	7.09	0.30	0.47	1.61	0.0318	0.54	0.09	0.77	0.09
3	KEPLER-37	5520	19	4.50	0.04	−0.40	0.02	−0.28	0.02	6.62	0.50	0.82	2.62	0.0317	0.71	0.15	0.88	0.15
4	HD 46375	5345	22	4.47	0.04	−0.05	0.01	0.11	0.01	2.01	0.73	0.71	2.52	0.0319	0.83	0.01	0.88	0.02
5	HD 75289	6196	23	4.16	0.06	0.16	0.02	0.42	0.02	4.11	0.56	1.41	5.10	0.0291	1.27	0.01	1.14	0.03
6	HD 88133	5582	16	4.05	0.03	0.15	0.01	0.34	0.01	1.98	0.76	1.02	3.61	0.0344	1.80	0.01	1.12	0.02
7	HD 149143	6067	20	4.36	0.04	0.17	0.02	0.48	0.02	3.53	0.61	1.25	4.22	0.0316	1.64	0.10	1.19	0.10
8	HAT-P-30	6177	30	3.81	0.08	0.06	0.04	0.15	0.03	8.88	0.60	1.52	5.72	0.0324	1.51	0.19	1.19	0.19
9	KELT-3	6404	26	4.20	0.05	0.02	0.03	0.24	0.02	8.51	0.57	1.54	5.93	0.0294	1.77	0.16	1.28	0.16
10	KEPLER-21	6256	31	4.02	0.06	−0.07	0.03	0.11	0.03	7.38	0.57	1.50	5.63	0.0317	1.96	0.10	1.28	0.10
11	KELT-2A	6164	22	3.74	0.05	−0.04	0.03	0.19	0.02	7.28	0.51	1.53	5.81	0.0315	2.01	0.10	1.27	0.10
12	HD86081	6015	19	3.94	0.06	0.14	0.02	0.38	0.02	4.01	0.57	1.36	4.88	0.0314	1.63	0.13	1.18	0.13
13	WASP-74	5727	14	3.70	0.03	0.14	0.02	0.22	0.02	8.24	0.38	1.25	4.58	0.0341	1.57	0.15	1.11	0.16
14	HD 149026	6096	14	4.06	0.02	0.25	0.02	0.38	0.02	5.28	0.49	1.38	4.92	0.0302	1.51	0.10	1.17	0.10
15	HD 209458	5988	17	4.17	0.06	−0.22	0.03	−0.01	0.02	2.96	0.86	1.26	4.33	0.0282	1.25	0.10	1.10	0.10
16	BD-10 3166	5578	23	4.64	0.04	0.22	0.01	0.39	0.02	6.88	0.38	0.82	2.43	0.0361	0.82	0.17	0.92	0.17
17	HD 189733	5374	18	4.89	0.04	−0.04	0.01	0.09	0.01	2.75	0.60	0.59	1.70	0.0287	0.60	0.01	0.82	0.02
18	HD 97658	5468	20	4.68	0.04	−0.39	0.01	−0.17	0.01	1.87	0.85	0.72	2.20	0.0320	0.62	0.01	0.84	0.02
19	HAT-P-7	6270	46	3.95	0.12	−0.01	0.07	0.43	0.05	5.70	1.44	1.53	5.82	0.0312	2.21	0.19	1.32	0.20
20	KELT-7	6508	38	3.95	0.13	−0.19	0.01	0.15	0.04	45.2	1.39	1.70	6.96	0.0269	2.01	0.15	1.34	0.17
21	HAT-P-14	6490	35	4.12	0.07	−0.11	0.04	0.09	0.03	8.86	0.65	1.63	6.53	0.0293	1.69	0.15	1.28	0.16
22	WASP-14	6195	24	3.60	0.04	−0.33	0.03	−0.23	0.03	1.47	2.11	1.60	6.21	0.0298	1.50	0.15	1.19	0.15
23	HAT-P-2	6439	24	4.05	0.05	0.15	0.03	0.29	0.03	20.66	0.58	1.62	6.41	0.0254	1.79	0.10	1.29	0.10
24	WASP-38	6178	18	3.95	0.04	−010	0.03	0.15	0.02	7.47	0.54	1.47	5.44	0.0301	1.49	0.13	1.18	0.13
25	HD 118203	5847	31	4.06	0.06	0.04	0.01	0.19	0.02	4.16	0.58	1.20	4.14	0.0321	2.04	0.10	1.21	0.10
26	HD 2638	5564	18	4.90	0.00	0.14	0.02	0.38	0.02	3.30	0.62	0.71	1.88	0.0355	0.72	0.13	0.89	0.13
27	WASP-13	6025	29	3.89	0.03	−0.01	0.03	0.12	0.03	2.35	1.30	1.39	5.01	0.0344	1.62	0.20	1.18	0.20
28	WASP-34	5771	27	4.44	0.04	−0.31	0.03	0.00	0.03	1.60	1.39	1.02	3.20	0.0326	1.08	0.20	1.02	0.20
29	WASP-82	6257	28	3.96	0.08	−0.05	0.04	0.22	0.03	2.86	1.23	1.52	5.75	0.0331	2.16	0.17	1.31	0.18
30	HD17156	5985	22	4.10	0.05	−0.06	0.01	0.09	0.02	3.02	0.78	1.29	4.46	0.0303	1.58	0.10	1.16	0.10
31	XO-3	6281	30	4.16	0.10	−0.12	0.04	−0.19	0.03	20.2	0.73	1.47	5.45	0.0270	1.83	0.16	1.27	0.16
32	HD 33283	5877	16	3.81	0.03	0.05	0.02	0.32	0.02	4.39	0.47	1.31	4.72	0.0320	1.99	0.09	1.21	0.09
33	HD 217014	5755	12	4.43	0.03	−0.30	0.01	−0.01	0.02	0.40	1.43	1.01	3.18	0.0312	1.16	0.19	1.04	0.19
34	HD 115383	5891	19	4.19	0.04	−0.16	0.02	0.22	0.02	8.11	0.40	1.19	4.00	0.0285	1.41	0.01	1.11	0.02
35	HAT-P-6	6442	34	4.05	0.05	0.04	0.02	−0.10	0.03	11.7	0.71	1.62	6.43	0.0440	1.70	0.17	1.28	0.18
36	HD 75732	5548	17	4.89	0.03	0.19	0.01	0.38	0.01	0.17	1.61	0.71	1.88	0.0338	0.80	0.19	0.91	0.19
37	HD 120136	6210	17	3.79	0.04	0.20	0.02	0.20	0.02	15.14	0.36	1.55	5.89	0.0292	1.61	0.19	1.21	0.19
38	WASP-76	6133	21	3.90	0.04	0.10	0.02	0.40	0.02	2.24	1.00	1.46	5.37	0.0301	2.03	0.16	1.27	0.16
39	HN-PEG	5853	18	4.41	0.04	−0.37	0.02	0.03	0.02	10.02	0.41	1.09	3.46	0.0337	1.03	0.01	1.02	0.02
40	WASP-8	5735	55	4.62	0.13	0.10	0.02	0.39	0.04	6.45	1.07	0.93	2.76	0.0308	0.89	0.19	0.97	0.20
41	WASP-69	5197	15	4.90	0.00	0.22	0.01	0.30	0.01	1.18	1.07	0.46	1.61	0.0360	0.58	0.15	0.78	0.15
42	HAT-P-34	6494	33	4.22	0.07	0.14	0.04	0.38	0.04	25.32	0.80	1.60	6.35	0.0287	1.57	0.19	1.26	0.19
43	HAT-P-1	6142	24	4.15	0.06	0.14	0.02	0.21	0.03	5.65	0.66	1.38	4.91	0.0330	1.41	0.10	1.16	0.10
44	WASP-94A	5988	23	3.76	0.04	0.17	0.03	0.38	0.02	5.55	0.60	1.41	5.15	0.0338	1.80	0.17	1.20	0.18
45	WASP-111	6312	32	3.94	0.08	0.05	0.04	0.30	0.03	11.57	0.54	1.57	6.03	0.0308	2.12	0.18	1.32	0.18
46	HAT-P-8	6009	60	4.06	0.09	0.15	0.05	−0.12	0.07	13.68	1.09	1.32	4.62	0.0365	1.55	0.16	1.16	0.16

rable with those in Exoplanets.org, while clearly lower compared to SWEET-Cat. The largest difference between our results and those of the two other surveys is for $\log g$. Compared with Exoplanets.org (Figure 5c), our values for $\log g$ are comparable within the range 4-4.7 dex, only slightly underestimated. Above 4.7 dex, our values tend to be overestimated while below 4 dex they are underestimated. These differences are amplified comparing with SWEET-Cat in Figure 5d. Once again, however, we must conclude that these differences already existed comparing Exoplanets.org

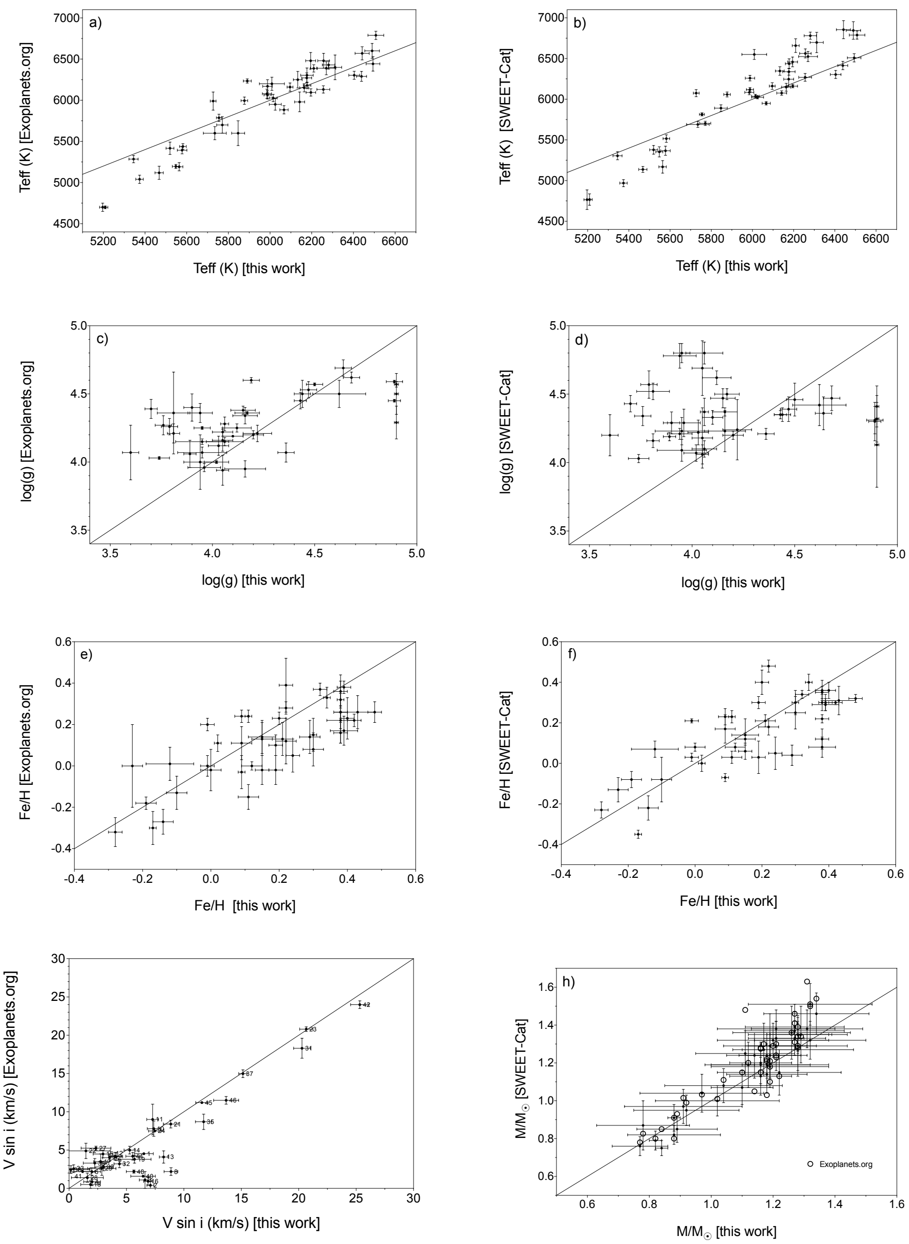

Fig. 5. Comparison of our results with those in Exoplanets.org (left) and SWEET-Cat (right): a) and b) T_{eff}; c) and d) $\log g$; e) and f) $[Fe/H]$; g) $V \sin i$; h) the mass of the stars, M_*, with data for Exoplanets.org included.

with SWEET-Cat. Despite the above differences, our metallicities in Figure 5e and Figure 5f are comparable with those published both by Exoplanets.org and SWEET-Cat. Once again, our results seem more similar to the former than to the latter.

The most important comparison for the purpose of our survey is for $V \sin i$ in Figure 5g. Unfortunately, we can only compare with Exoplanets.org, since SWEET-Cat did not publish their results. What we find is a very good agreement, with only a slight trend for our values to be higher. This trend is most probably due to our lower resolution and to the different way we determined V_{mic} and V_{mac} (more about that will be said later). In Figure 5h we compare the masses of the stars to those reported by SWEET-Cat. This time we observe a much better consistency. Note that we have also included the values given by Exoplanets.org (as open circles). In general, our masses show a weak trend to be smaller, although well within the uncertainties.

To quantify the differences between our values and those reported in Exoplanets.org and

TABLE 4

COMPARISON OF ERRORS

Errors	T_{eff} (K)	$\log g$ (dex)	$[Fe/H]$ (dex)	$V \sin i$ (km/s)
Standard deviations	73	0.14	0.08	0.8
iSpec	25	0.05	0.02	0.8
Valenti & Fischer	44	0.06	0.03	0.5
Exoplanets.org	66	0.06	0.07	0.7
SWEET-Cat	52	0.10	0.04	

SWEET-Cat we compare in Table 5 the medians and means (note that since the numbers of stars in the comparisons vary the means and medians are not the same). In both cases, we also determined if the differences were statistically significant, using non-parametric Mann-Whitney tests (Dalgaard 2008). The last two columns in Table 5 report the p-values of the tests and the level of significance of the differences (at a level of confidence of 95%). As one can see, the only parameter distributions that are significantly different are the surface gravity, which is slightly lower in our work than in Exoplanets.org and SWEET-Cat. The statistical test also confirms that the difference is more significant comparing our data with SWEET-Cat than with Exoplanets.org (p-value 0.0008 instead of 0.0195). Considered as a whole, therefore, these tests suggest that our results are quite comparable with those reported in the literature.

As we mentioned before, as the temperature of the stars goes down, V_{mic} and V_{mac} become comparable to $V \sin i$ and thus it is more complicated to separate one from the others. In the Valenti & Debra (2005) spectral synthesis analysis, the authors recognized this problem stating, in particular, that, "...adopting a global macroturbulence relationship should yield more accurate results than solving for V_{mac} in each individual spectrum." To determine such relation they fixed $V \sin i = 0$, obtaining the maximum values V_{mac} could have at different temperatures. Note that these authors did not report any dependence on the spectral resolution, although they used spectra with R between 50,000 and almost 100,000. The maximum relation they deduced can be seen in Figure 4. According to these authors, below $T_{eff} = 5800$ K $V \sin i$ becomes negligible, and what we measure then must be the "real" V_{mac}. However, this conclusion contradicts what was expected based on the semi-empirical relation established by Gray (1984b) and later the minimum relation for V_{mac} obtained by Bruntt et al. (2010) by line modeling (the

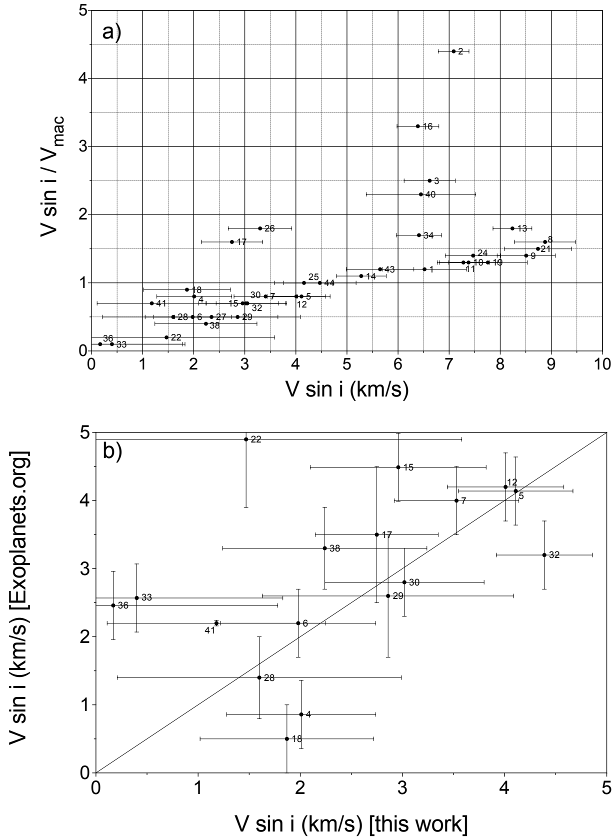

Fig. 6. a) The ratio $V \sin i/V_{mac}$ as a function of $V \sin i$. Below $V \sin i = 4$ the ratios are lower than 1. Three stars, 33, 36 and 22 have iSpec have values with uncertainties that include zero. b) Zoom of the region in Figure 5g with $V \sin i < 5$ km/s.

two relations can also be seen in Figure 4). These results suggest that applying the right macro (and micro) turbulence relationship one could obtain a value of $V \sin i \neq 0$ below $T_{eff} = 5800$ K. In fact, in our analysis of the Sun, we did reproduce the value of $V \sin i$, using the relations for V_{mic} obtained by Tsantaki et al. (2014) and V_{mac} determined by Doyle et al. (2014), both depending not only on T_{eff} but also on $\log g$, and where $V \sin i < V_{mac}$. The question then is how low can $V \sin i$ be compared to V_{mac} and still be distinguishable by iSpec?

In Figure 6a, we compare $V \sin i$ with the ratio $V \sin i/V_{mac}$. What we observe is that below $V \sin i = 4$ km/s the ratio is lower than one. As one can see in Figure 4, a value of $V_{mac} = 4$ km/s ($V \sin i/V_{mac} = 1$) corresponds to $T_{eff} \approx 5800$ K. Therefore, our results are at the same time consistent with the conclusion of Valenti & Debra (2005), since below $T_{eff} = 5800$ K $V \sin i$ is lower than V_{mac}, and consistent with Gray (1984a), Bruntt et

TABLE 5

COMPARISON WITH LITERATURE

Parameter	Units	TIGRE (45 stars) Median	TIGRE (45 stars) Mean	Exoplanets Median	Exoplanets Mean	p-value	s.l.
T_{eff}	(K)	6025	5975	6095	5952	0.7679	ns
$\log g$		4.06	4.18	4.26	4.28	0.0195	*
$[Fe/H]$		0.07	0.12	0.20	0.18	0.1638	ns
$V \sin i$	(km/s)	5.55	7.39	4.10	6.92	0.2732	ns
M_*	$(M_\odot)$	1.18	1.13	1.22	1.19	0.1010	ns
R_*	$(R_\odot)$	1.57	1.47	1.34	1.36	0.0868	ns
		TIGRE (44 stars)		SWEET-Cat		p-value	s.l.
Parameter	Units	Median	Mean	Median	Mean		
T_{eff}	(K)	6046	5977	6133	6036	0.2936	ns
$\log g$		4.06	4.18	4.33	4.34	0.0008	***
$[Fe/H]$		0.08	0.12	0.20	0.17	0.1973	ns
M_*	$(M_\odot)$	1.18	1.13	1.24	1.18	0.0700	ns

al. (2010) and Doyle et al. (2014), since $V \sin i \neq 0$. But how low could a value of $V \sin i$ below V_{mac} be? We already answered this question in Figure 5g where we compared our values of $V \sin i$ with the values reported by Exoplanets.org. To get a better view, in Figure 6b we zoom in on values of $V \sin i \leq 5$ km/s. Except for three stars, 22, 33 and 36, with $V \sin i / V_{mac} < 0.4$, all the other stars have $V \sin i$ comparable to the values reported in Exoplanets.org (in fact, two of the stars, 4 and 16, have higher values). In Figure 6a note that the iSpec uncertainty increases as $V \sin i$ goes down. As a consequence, the possible values for stars 22, 33 and 36 include zero. However, could stars with $V \sin i = 0$ exist physically? Considering that the loss of angular momentum plays an important role in the formation of stars, this would seem difficult to explain (note that we did obtained $V \sin i = 0$ for some stars in our initial list, but they were not included in our study). Since the Gray (1984b) study the problem seems clear: how can we measure the rotation of a star where V_{mac} is as high or even higher than $V \sin i$? It seems that the best approach is to assume an a priori global relation and to see what comes out from the residual (Gray 1984a,b; Fischer & Valenti 2005; Bruntt et al. 2010; Tsantaki et al. 2014; Doyle et al. 2014). However, to stay safe, due to their higher uncertainties we should not consider stars 22, 33 and 36 in our statistical analysis for $V \sin i$.

Considering the results above, one expects the rotation to decrease with the temperature, but still be above zero for cool stars. Moreover, since Tsantaki et al. (2014) and Doyle et al. (2014) have found relations for V_{mic} and V_{mac} that depend not only on T_{eff} but also on on $\log g$, we might expect a similar relation for $V \sin i$, T_{eff} and $\log g$. In Figure 7, we show the diagram of $V \sin i$ and T_{eff} for our stars. The dependence on $\log g$ is shown by the gray-scale bar. In Figure 7, we also traced over our data the bi-exponential relation we obtained, together with the interval of confidence (in gray) and the prediction in-

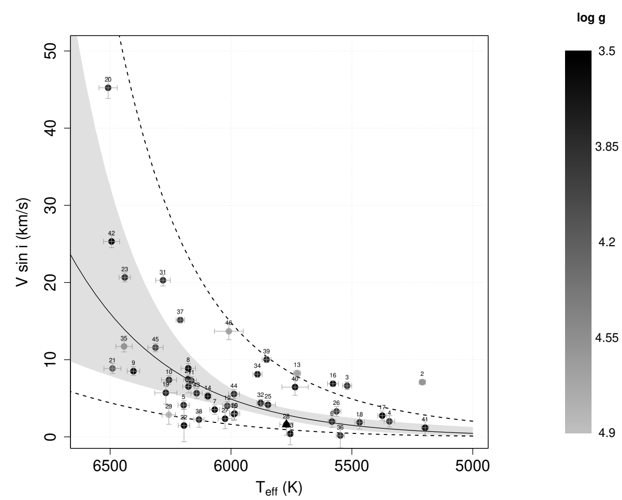

Fig. 7. Exponential relation between the rotational velocity, the temperature and the surface gravity for the 46 stars in our sample. The black triangle represents the Sun. The gray area corresponds to the interval of confidence and the dashed curves delimit the prediction interval.

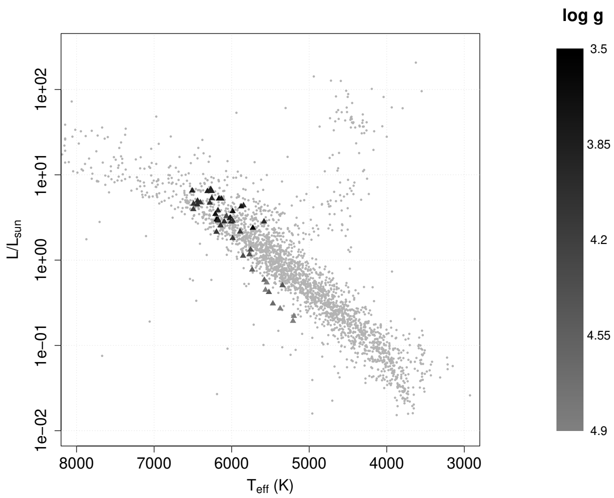

Fig. 8. HR diagram of our 46 stars, overlaid on the main sequence of Hipparchos stars.

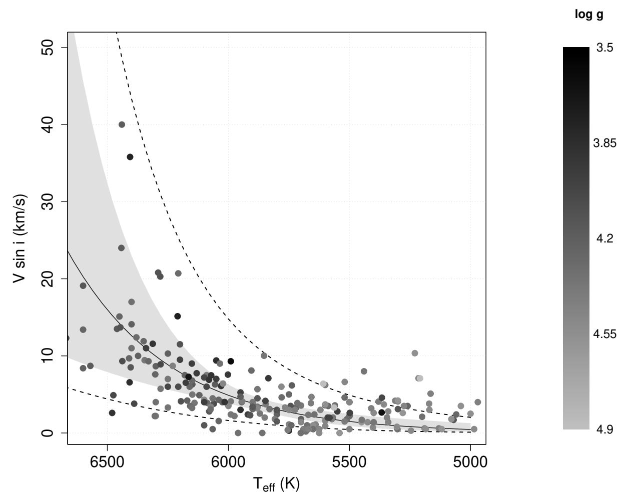

Fig. 9. Data as found in Exoplanets.org.

terval (dashed curves), which takes into account the uncertainty of each measurement. The final relation we obtained is the following:

$$\frac{V \sin i}{\mathrm{km/s}} = \exp \left[A \left(\frac{T_{eff}}{1000\mathrm{K}} \right) + B \log g - C \right], \quad (7)$$

where $A = 2.20 \pm 0.36$, $B = 0.30 \pm 0.46$ and $C = 12.91 \pm 3.59$, and which has a multiple correlation coefficient of $r^2 = 0.6329$. Except for stars 2, 3, 13 and 16, and the three stars with highest uncertainties (22, 33, and 36; not considered in this relation) all our data fit well inside the prediction interval.

Note that in order to obtain the highest correlation coefficient possible, 8 stars suspected to have peculiarly high rotation for their temperature were considered as outliers. They are, from right to left in Figure 7: 2, 3, 16, 13, 40, 39, 46 and 37. Different reasons were explored that could explain why these stars would be outliers. One is the age of the stars (e.g., Stauffer & Hartman 1986), younger stars rotating faster than older stars (see Figure 1.6 in Tassoul 2000). In Tassoul (2000) it was also shown that young stars trace the same relation of $V \sin i$ with T_{eff} as old stars, only with higher velocities, forming an upper sequence (or upper envelope). This could be what we see in Figure 7. However, in Figure 8 the HR diagram for our stars compared to Hipparchos stars suggests that, except for three stars with slightly higher luminosity for their temperature (6, 25 and 32; none of these stars forming the envelope) all of the stars more luminous than the Sun are clearly on the main sequence. This eliminates the young age hypothesis. Another explanation could be peculiar surface activity. Since more than one phenomenon can cause such activities, the expected effect would be pure random dispersion. Checking the literature for each of the stars in our sample we did find 8 stars with reported peculiarities: 2, 3, 17, 26, 33, 37, 39 and 46. The type of peculiarities encountered included, "Flare star", "Rotationally variable", "Variable BY DRa", and "Double or Multiple star". Of these "active" stars only five in Figure 7 have a higher $V \sin i$ for their temperature: 2, 3, 37, 39 and 46. This leaves three stars (13, 16 and 40) with unexplained, relatively high $V \sin i$ values. In fact, checking their V_{mac} we found these stars have lower values than stars with comparable temperatures. However, in our various attempts to get the higher highest correlation coefficient possible, we judged better to keep them as outliers.

To verify our relation, in Figure 9 we traced it over the distribution of the rotational velocities and temperatures of the stars that were in our initial sample based on Exoplanets.org. As one can see, except for a few stars below $T_{eff} = 5500$ K, with higher velocities, and stars below $T_{eff} = 5500$ K, with lower velocities (some with $V \sin i = 0$), the majority of the stars in this sample fall well between the prediction interval of our empirical relation. This result suggests that the decrease in angular momentum of low mass stars is a non-aleatory phenomenon, most probably reflecting the action of one specific mechanism, like, for example, magnetic braking or stellar wind (Wolff & Simon 1997; Tassoul 2000; Uzdensky et al. 2002). An exciting possibility, however, could be that this relation somehow is coupled to the formation of planets. Although this hypothesis proposed in the late 1960s was rapidly rejected, since no planet outside the Solar System was known at the time, the discovery of exoplanets allows us today to test this idea anew (e.g., Berget & Durrance 2010). This will be the subject of Paper II, in search of a connection between the formation of stars and planets.

5. CONCLUSIONS

In this study we have shown that our method of analysis developed for the TIGRE telescope using iSpec on intermediate Echelle resolution spectra yields results about the physical characteristics of stars hosting exoplanets that are comparable to those obtained using bigger telescopes and standard spectra analysis methods with high resolution spectra. Our results show that TIGRE can provide a helpful contribution in the follow-up of exoplanet surveys around bright stars, like TESS and PLATO. Such follow-up studies are essential in order to understand how the formation of planets is connected to the formation of their host stars (Eisner et al. 2020).

We like to thank an anonymous referee for a careful revision of our results and for comments and suggestions that helped us to improve our work. L. M. F. T. would like to thank the CONACyT for its support through grant CVU 555458. She also acknowledges CONACyT for travel support (bilateral Conacyt-DFG projects 192334, 207772, and 278156), as well as the Universidad de Guanajuato (Dirección de Apoyo a la Investigación y al Posgrado, DAIP, and Campus Guanajuato) for support given for conference participation and international collaborations. L. M. F. T. also thanks the time request committee of the TIGRE for granting her the observations and the whole observing team for their support in getting the data that were used in this study. More personally, she thanks Sebastian Kohl for his help with MOLECFIT. This research has made use of the Exoplanet Orbit Database, the Exoplanet Data Explorer at exoplanets.org (Han et al. 2014), the exoplanets.eu (Schneider et al. 2011) and the NASA's Astrophysics Data System.

APPENDIX

A. LIST OF SPECTRAL LINES AND SEGMENTS DEFINED FOR OUR ANALYSIS

TABLE 6

LINES AND SEGMENTS DEFINED IN THIS WORK

Line	Wave Peak	Wave Base	Wave Top	Segm. Wave base	Segm. Wave top
Na 1	588.9959	588.9422	589.0422	588.8922	589.0922
Na 1	589.5916	589.5411	589.6411	589.4911	589.6911
Fe 1	593.0186	592.9859	593.0539	592.9359	593.1039
Fe 1	593.4665	593.4289	593.5059	593.3789	593.5559
No ident.	595.6706	595.6206	595.7206	595.5706	595.7706
Fe 1	597.5341	597.4898	597.5898	597.4398	597.7729
Fe 1	597.6777	597.6299	597.7229	-	-
Fe 1	598.4831	598.4319	598.5689	598.3819	598.8099
Fe 1	598.7088	598.6449	598.7599	-	-
Fe 1	600.2986	600.2519	600.3509	600.2019	600.4009
Fe 1	600.8552	600.8249	600.8989	600.7749	600.9489
Mn 1	601.6628	601.6110	601.7110	601.5610	601.7610
Fe 1	602.0142	601.9637	602.0637	601.9137	602.1137
Fe 1	602.4066	602.3579	602.4639	602.3079	602.5139
Fe 1	605.6032	605.5599	605.6809	605.5099	605.7309
Fe 1	606.5494	606.5009	606.5919	606.4509	606.6419
Fe 1	607.8490	607.7729	607.8769	607.7229	607.9269
Fe 1	608.2757	608.2180	608.3180	608.1680	608.3680
Fe 1	608.5228	608.4775	608.5775	608.4275	608.6275
Ca 1	612.2225	612.1703	612.2703	612.1203	612.3203
No ident.	615.1608	615.1108	615.2108	615.0608	615.2608
Ca 1	616.2171	616.1690	616.2690	616.1190	616.3190
Fe 1	617.0503	617.0028	617.1168	616.9528	617.1668

TABLE 6. CONTINUED

Fe 1	617.3340	617.2828	617.3838	617.2328	617.4338
Fe 1	621.3421	621.2988	621.3958	621.2488	621.4458
Fe 1	621.9270	621.8418	621.9698	621.7918	622.0198
Fe 1	623.0722	623.0278	623.1868	622.9778	623.3578
Fe 1	623.2644	623.1868	623.3078	-	-
Fe 1	624.6326	624.5898	624.6868	624.5398	624.7368
Fe 1	625.2564	625.2108	625.3108	625.1608	625.7298
Fe 1	625.4240	625.3298	625.5098	-	-
Fe 1	625.6343	625.5628	625.6798	-	-
Fe 1	629.0951	629.0473	629.1473	628.9973	629.1973
Fe 1	629.7808	629.7138	629.8548	629.6638	629.9048
Fe 1	630.1508	630.0898	630.2028	630.0398	630.3528
Fe 1	630.2514	630.2028	630.3028	-	-
Fe 1	632.2710	632.2228	632.3128	632.1728	632.3628
Fe 1	633.5331	633.4658	633.5888	633.4158	633.7978
Fe 1	633.6827	633.6388	633.7478	-	-
Fe 1	635.5038	635.4468	635.5768	635.3968	635.6268
Fe 1	635.8671	635.8128	635.9258	635.7628	635.9758
Fe 1	638.0743	638.0264	638.1264	637.9764	638.1764
Fe 1	639.3612	639.2968	639.4278	639.2468	639.4778
Fe 1	640.8011	640.7578	640.9138	640.7078	640.9638
Fe 1	641.1646	641.0878	641.2198	641.0378	641.2698
Fe 2	641.6962	641.6449	641.7449	641.5949	641.7949
Fe 1	641.9949	641.9428	642.0408	641.8928	642.2598
Fe 1	642.1377	642.0758	642.2098	-	-
Fe 1	643.0851	643.0158	643.1528	642.9658	643.3681
Fe 2	643.2663	643.2181	643.3181	-	-
Ca 1	643.9063	643.8572	643.9572	643.8072	644.0072
Fe 2	645.6405	645.5866	645.6866	645.5366	645.7366
Ca 1	646.2606	646.2081	646.3081	646.1581	646.3581
Fe 1	646.9200	646.8711	646.9711	646.8211	647.0211
Fe 1	647.5657	647.5117	647.6117	647.4617	647.6617
Fe 1	648.1882	648.1362	648.2362	648.0862	648.2862
Fe 1	649.4989	649.4197	649.5437	649.3697	649.5937
Fe 2	651.6098	651.5587	651.6587	651.5087	651.7087
Fe 1	651.8385	651.7868	651.8868	651.7368	651.9368
Fe 1	654.6245	654.5757	654.6967	654.5257	654.7467
H 1	656.2808	655.5483	656.6832	655.1934	656.7340
Fe 1	657.5003	657.4507	657.5507	657.4007	657.6007
Fe 1	659.3887	659.3417	659.4537	659.2917	659.5037
Fe 1	659.7585	659.7073	659.8073	659.6573	659.8573
Fe 1	660.9067	660.8605	660.9605	660.8105	661.0105
Ni 1	664.3626	664.3139	664.4139	664.2639	664.4639
Fe 1	667.7983	667.7297	667.8707	667.6797	667.9207
Fe 1	670.5134	670.4570	670.5570	670.4070	670.6070
No ident.	671.3073	671.2573	671.3573	671.2073	671.4073
Ca 1	671.7701	671.7138	671.8138	671.6638	671.8638
Fe 1	672.6657	672.6178	672.7178	672.5678	672.7678
Fe 1	675.0182	674.9653	675.0653	674.9153	675.1153
Fe 1	680.6856	680.6358	680.7358	680.5858	680.7858
Fe 1	682.0359	681.9894	682.0894	681.9394	682.1394
Fe 1	682.8620	682.8085	682.9085	682.7585	682.9585
No ident.	683.9811	683.9311	684.0311	683.8811	684.0811
Fe 1	684.3658	684.3150	684.4150	684.2650	684.4650
Fe 1	691.6669	691.6218	691.7218	691.5718	691.7718
No ident.	693.3635	693.3135	693.4135	693.2635	693.4635

TABLE 6. CONTINUED

Fe 1	694.5196	694.4703	694.5703	694.4203	694.6203
-	-	-	-	694.6410	694.8410
Fe 1	695.1251	695.0721	695.1721	695.0221	695.2221
Fe 1	703.8209	703.7718	703.8718	703.7218	703.9218
Fe 1	706.8440	706.7918	706.8918	706.7418	706.9418
Fe 1	709.0378	708.9850	709.0850	708.9350	709.1350
Fe 1	713.0900	713.0451	713.1451	712.9951	713.1951
Fe 1	713.3001	713.2453	713.3453	713.1953	713.3953
CN 1	714.5241	714.4768	714.5768	714.4268	714.6268
Ca 1	714.8155	714.7666	714.8666	714.7166	714.9166
Fe 1	715.5670	715.5125	715.6125	715.4625	715.6625
No ident.	716.4473	716.3185	716.5085	716.2685	716.5585
Fe 1	717.5970	717.5403	717.6403	717.4903	717.6903
Fe 1	721.9712	721.9134	722.0134	721.8634	722.2190
CN 1	722.1100	722.0690	722.1690	-	-
No ident.	724.4812	724.4312	724.5312	724.3812	724.5812
Fe 1	732.0693	732.0178	732.1178	731.9678	732.1678
Fe 1	738.6353	738.5818	738.6818	738.5318	738.7318
Fe 1	738.9363	738.8454	738.9974	738.7954	739.0474
Fe 1	741.1151	741.0394	741.1764	740.9894	741.2264
Ni 1	742.2264	742.1770	742.2770	742.1270	742.3270
No ident.	744.0877	744.0377	744.1377	743.9877	744.1877
Fe 1	744.5740	744.5174	744.6654	744.4674	744.7154
Fe 1	749.5088	749.4484	749.5724	749.3984	749.6224
Fe 1	751.1024	751.0024	751.1854	750.9524	751.2354
Fe 1	771.0389	770.9827	771.0827	770.9327	771.1327
Fe 1	772.3237	772.2724	772.3724	772.2224	772.4224
Fe 1	774.8304	774.7653	774.8613	774.7153	774.9113
Ni 1	775.1163	775.0625	775.1625	775.0125	775.2125
Fe 1	778.0562	777.9613	778.1263	777.9113	778.1763
Fe 1	783.2221	783.1453	783.3183	783.0953	783.3683
Fe 1	793.7145	793.6112	793.7802	793.5612	793.8302
Fe 1	794.5839	794.5132	794.6502	794.4632	794.7002
Fe 1	799.8967	799.8112	799.9622	799.7612	800.0122
No ident.	804.6052	804.5282	804.7002	804.4782	804.7502
No ident.	808.5170	808.4442	808.6012	808.3942	808.6512
Fe 1	820.7791	820.7284	820.8284	820.6784	820.8784
Fe 1	832.7062	832.6341	832.7711	832.5841	832.8211
Fe 1	838.7760	838.7061	838.8521	838.6561	838.9021
Fe 1	846.8392	846.7820	846.8930	846.7320	846.9430
Fe 1	851.4073	851.3290	851.4650	851.2790	851.5150
Fe 1	868.8639	868.7760	868.9430	868.7260	868.9930
No ident.	871.0395	870.9895	871.0895	870.9395	871.1395

REFERENCES

Anderson, D. R., Collier Cameron, A., Delrez, L., et al. 2014, MNRAS, 445, 1114

Armitage, P. J. 2020, Astrophysics of Planet Formation (2nd ed.; Cambridge, UK: CUP)

Asplund, M., Grevesse, N., Sauval, A. J., & Scott, P. 2009, Annu. Rev. Astron. Astrophys., 47, 481

Bakos, G. Á., Kovács, G., Torres, G., et al. 2007, ApJ, 670, 826

Bakos, G. Á., Hartman, J. D., Torres, G., et al. 2012, AJ, 144, 19

Barros, S. C. C., Faedi, F., Collier Cameron, A., et al. 2011, A&A, 525, 54

Baruteau, C., Crida, A., Paardekooper, S.-J., et al. 2014, in Protostars and Planets VI, ed. H. Beuther, R. S. Klessen, C. P. Dullemond, and T. Henning (Tucson, AZ: UAP), 667

Batalha, N. M., Rowe, J. F., Bryson, S. T., et al. 2013, ApJS, 204, 24

Beatty, T. G., Pepper, J., Siverd, R. J., et al. 2012, ApJ, 756, 39
Beaugé, C. & Nesvorný, D. 2012, ApJ, 751, 119
Berget, D. J. & Durrance, S. T. 2010, Journal of the Southeastern Association for Research in Astronomy, 3, 32
Bieryla, A., Collins, K., Beatty, T. G., et al. 2015, AJ, 150, 12
Blanco-Cuaresma, S., Soubiran, C., Heiter, U., & Jofré, P. 2014, A&A, 569, 111
Blanco-Cuaresma, S. 2019, MNRAS, 486, 2075
Bland, A. P. & Schwenzer, S. P. 2004, in An Introduction to the Solar System, ed. D. A. Rothery, N. McBride, and I. Gilmour (New York, NY: CUP), 129
Borucki, W. J., Koch, D. G., Basri, G., et al. 2011, ApJ, 736, 19
Boss, A. P. 1997, Sci, 276, 1836
Bouchy, F., Udry, S., Mayor, M., et al. 2005, A&A, 444, 15
Bruntt, H., Bedding, T. R., Quirion, P.-O., et al. 2010, MNRAS, 405, 1907
Butler, R. P., Vogt, S. S., Marcy, G. W., et al. 2000, ApJ, 545, 504
Chabrier, G., Baraffe, I., Leconte, J., Gallardo, J., & Barman T. 2009, AIPC 1094, Cool Stars, Stellar Systems and the Sun, 1094, 12
Charbonneau, D. B., Brown, T. M., Latham, D. W., and Mayor, M. 2000, ApJ, 529, 45
Chatterjee, S., Ford, E. B., Matsumura, S., & Rasio, A. F. 2008, ApJ, 686, 580
Chiang, E. & Laughlin, G. 2013, MNRAS, 431, 3444
da Silva, R., Udry, S., Bouchy, F., et al. 2006, A&A, 446, 717
Dalgaard, P. 2008, Introductory statistics with R, (New York, NY: Springer) doi:10.1007/978-0-387-79054-1
Damasso, M., Esposito, M., Nascimbeni, V., et al. 2015, A&A, 581, 6
Dawson, R. I. & Johnson, J. A. 2018, ARA&A, 56, 175
Doyle, A. P., Davies, G. R., Smalley, B., Chaplin, W. J., & Elsworth, Y. 2014, MNRAS, 444, 3592
Eisner, N. L., Barragán, O., Aigrain, S., et al. 2020, MNRAS, 494, 750
Fischer, D. A., Laughlin, G., Butler, P., et al. 2005, ApJ, 620, 481
Fischer, D. A. & Valenti, J. 2005, ApJ, 622, 1102
Fischer, D. A., Laughlin, G., Marcy, G. W., et al. 2006, ApJ, 637, 1094
Fischer, D. A., Vogt, S. S., Marcy, G. W., et al. 2007, ApJ, 669, 1336
Gandolfi, D., Barragán, O., Hatzes, A. P., et al. 2017, AJ, 154, 123
Gray, D. F. 1984a, ApJ, 277, 640
_________. 1984b, ApJ, 281, 719
Gray, R. O., & Corbally, C. J. 1994, AJ, 107, 742
Grevesse, N., Asplund, M., Sauval, A. J., & Scott, P. 2010, Ap&SS, 328, 179
Han, E., Wang, S. X., Wright, J. T., et al. 2014, PASP, 126, 827
Hellier, C., Anderson, D. R., Collier Cameron, A., et al. 2015, AJ, 150, 18
Hempelmann A., Mittag M., Gonzalez-Perez J. N., et al. 2016, A&A, 586, 14
Henry, G. W., Marcy, G. W., Butler, R. P., & Vogt, S. S. 2000, ApJ, 529, 41
Herbst, W., Eislöeffel, J., Mundt, R., & Scholz, A. 2007, in Protostars and Planets V, ed. V. B. Reipurth, D. Jewitt, & K. Keil (Tuczon, AZ: UAP), 927
Hestroffer, D. & Magnan, C. 1998, A&A, 333, 338
Hinkel, N. R., Timmes, F. X., Young, P. A., et al. 2014, AJ, 148, 54
Hinkel, N. R., Young, P. A., Pagano, M. D., et al. 2016, ApJS, 226, 4
Howard, A. W., Johnson, J. A., Marcy, G. W., et al. 2011, ApJ, 730, 10
Irwin, S. A. 2015, Analysis of Angular Momentum in Planetary Systems and Host Stars, PhD Thesis, College of Science at Florida Institute of Technology
Jofré, P., Heiter, U., Soubiran, C., et al. 2014, A&A, 564, 133
Johns-Krull, C. M., McCullough, P. R., Burke, C. J., et al. 2008, ApJ, 677, 657
Johnson, J. A., Marcy, G. W., Fischer, D. A., et al. 2006, ApJ, 647, 600
Johnson, J. A., Winn, J. N., Bakos, G. Á., et al. 2011, ApJ, 735, 24
Joshi, Y. C., Pollacco, D., Collier Cameron, A., et al. 2009, MNRAS, 392, 1532
Kraft, R. P. 1967, ApJ, 150, 551
Kupka, F., Piskunov, N., Ryabchikova, T. A., Stempels, H. C., & Weiss, W. W. 1999, A&AS, 138, 119
Kupka, F. & Dubernet, M.-L. 2011, BaltA, 20, 503
Kurucz, R. L. 2005, MSAIS, 8, 14
Kuzuhara, M., Tamura, M., Kudo, T., et al. 2013, ApJ, 774, 11
Latham, D. W., Bakos, G. Á., Torres, G., et al. 2009, ApJ, 704, 1107
Leconte, J., Baraffe, I., Chabrier, G., Barman, T. S., & Levrard, B. 2009, A&A, 506, 385
Lee, E. J. & Chiang, E., 2017, ApJ, 842, 40
Lin, D. N. C., Bodenheimer, P., & Richardson, D. C. 1996, Natur, 380, 606
Luhman, K. L., Patten, B. M., Marengo, M., et al. 2007, ApJ, 654, 570
Marcy, G. W., Butler, R. P., & Vogt, S. S. 2000, ApJ, 536, 43
Marcy, G. W., Butler, R. P., Fischer, D. A., et al. 2002, ApJ, 581, 1375
Martin, R. G. & Livio, M. 2012, MNRAS, 425, 6
_________. 2015, ApJ, 810, 105
Marzari, F. & Weidenschilling, S. J. 2002, Icar, 156, 570
Mayor, M. & Queloz, D. 1995, Natur, 378, 355
McBride, N. & Gilmour, I. 2004, An Introduction to the Solar System, ed. N. McBride and I. Gilmour (Cambridge, UK: CUP)
McKee, C. F., & Ostriker, E. C. 2007, ARA&A, 45, 565
McNally, D. 1965, Obs, 85, 166

Mittag, M., Schröder, K.-P., Hempelmann, A., González-Pérez, J. N., & Schmitt, J. H. M. M. 2016, A&A, 591, 89
Motalebi, F., Udry, S., Gillon, M., et al. 2015, A&A, 584, 72
Nagasawa, M., Ida, S., & Bessho, T. 2008, ApJ, 678, 498
Neveu-VanMalle, M., Queloz, D., Anderson, D. R., et al. 2014, A&A, 572, 49
Nomura, H., Tsukagoshi, T., Kawabe, R., et al. 2016, ApJ, 819, 7
Noyes, R. W., Bakos, G. Á., Torres, G., et al. 2008, ApJ, 673, 79
Moutou, C., Mayor, M., Bouchy, F., et al. 2005, A&A, 439, 367
Pál, A., Bakos, G. Á., Torres, G., et al. 2008, ApJ, 680, 1450
Pepper, J., Siverd, R. J., Beatty, T. G., et al. 2013, ApJ, 773, 64
Pérez, S., Casassus, S., Baruteau, C., et al. 2019, AJ, 158, 15
Piskunov, N. & Valenti, J. A. 2017, A&A, 597, 16
Plummer, C. C., Carlson, D. H., & Hammersley, L. 2015, Physical Geology (New York, NY: McGraw-Hill Education)
Queloz, D., Anderson, D. R., Collier Cameron, A., et al. 2010, A&A, 517, 1
Radick, R. R., Thompson, D. T., Lockwood, G. W., Duncan, D. K., & Baggett, W. E. 1987, ApJ, 321, 459
Rasio, F. A. & Ford, E. B. 1996, Sci, 274, 954
Raymond, S. N., Barnes, R., & Mandell, A. M. 2008, MNRAS, 384, 663
Raymond, S. N. & Morbidelli, A. 2020, arXiv e-prints, arXiv:2002.05756
Sato, B., Fischer, D. A., Henry, G. W., et al. 2005, ApJ, 633, 465
Schmitt, J. H. M. M., Schröder, K.-P., Rauw, G., et al. 2014, AN, 335, 787
Schneider, J., Dedieu, C., Le Sidaner, P., Savalle, R. & Zolotukhin, I. 2011, A&A, 532, 79
Seager, S. 2010, Exoplanets (Tucson, AZ: UAP)
Skillen, I., Pollacco, D., Collier Cameron, A., et al. 2009, A&A, 502, 391
Skumanich, A. 1972, ApJ, 171, 565
Smalley, B., Anderson, D. R., Collier Cameron, A., et al. 2011, A&A, 526, 130
Smette, A., Sana, H., Noll, S., et al. 2015, A&A, 576, 77
Sousa, S. G., Adibekian, V., Delgado-Mena, E., et al. 2008, A&A, 620, 58
Stauffer, J. R. & Hartman, L. W. 1986, PASP, 98, 1233
Tassoul, J.-L. 2000, Stellar Rotation (New York, NY: CUP), doi:10.1017/CBO9780511546044
Torres, G., Bakos, G. Á., Hartman, J., et al. 2010, ApJ, 715, 458
Tsantaki, M., Sousa, S. G., Santos, N. C., et al. 2014, A&A, 570, 80
Udry, S., Mayor, M., Naef, D., et al. 2000, A&A, 356, 590
Udry, S. & Santos, N. C. 2007, ARA&A, 45, 397
Uzdensky, D. A., Königl, A., & Litwin, C. 2002, ApJ, 565, 1191
Valencia, D., O'Connell, R. J., & Sasselov, D. 2006, Icar, 181, 545
Valenti, J. A. & Debra, A. 2005, ApJS, 159, 141
van der Marel, N., Williams, J. P., & Bruderer, S. 2018, ApJL, 867, 14
Walsh, K. J., Morbidelli, A., Raymond, S. N., O'Brien, D. P., & Mandell, A. M. 2011, Natur, 475, 206
Wang, J. & Zhong, Z. 2018, A&A, 619, 1
Weidenschilling, S. J., & Marzari, F. 1996, Natur, 384, 619
West, R. G., Hellier, C., Almenara, J.-M., et al. 2016, A&A, 585, 126
Wilson, O. C. 1963, ApJ, 138, 832
Wolff, S. & Simon, T. 1997, PASP, 109, 759

S. Blanco-Cuaresma: Harvard-Smithsonian Center for Astrophysics, Cambridge, MA, USA.
R. Coziol, L. M. Flor-Torres, D. Jack, and K.-P. Schröder: Departamento de Astronomía, Universidad de Guanajuato, Guanajuato, Gto., México.
J. H. M. M. Schmitt: Hamburger Sternwarte, Universität Hamburg, Hamburg, Germany.

Revista Mexicana de Astronomía y Astrofísica, **57**, 217–231 (2021)

https://doi.org/10.22201/ia.01851101p.2021.57.01.16

CONNECTING THE FORMATION OF STARS AND PLANETS. II: COUPLING THE ANGULAR MOMENTUM OF STARS WITH THE ANGULAR MOMENTUM OF PLANETS

L. M. Flor-Torres[1], R. Coziol[1], K.-P. Schröder[1], D. Jack[1], and J. H. M. M. Schmitt[2]

Received February 6 2020; accepted January 7 2021

ABSTRACT

A sample of 46 stars, host of exoplanets, is used to search for a connection between their formation process and the formation of the planets rotating around them. Separating our sample into two, stars hosting high-mass exoplanets (HMEs) and low-mass exoplanets (LMEs), we found the former to be more massive and to rotate faster than the latter. We also found the HMEs to have higher orbital angular momentum than the LMEs and to have lost more angular momentum through migration. These results are consistent with the view that the more massive the star and the higher its rotation, the more massive was its protoplanetarys disk and rotation, and the more efficient was the extraction of angular momentum from the planets.

RESUMEN

Una muestra de 46 estrellas que albergan exoplanetas se usa para la búsqueda de una conexión entre su proceso de formación y el proceso de formación de los planetas que las orbitan. Separamos nuestra muestra en dos: estrellas que albergan exoplanetas de baja masa (LME) y de alta masa (HME); encontramos que las estrellas con HMEs rotan preferentemente alrededor de estrellas con alta masa y con mayor rotación que las estrellas con LMEs. También encontramos que las HMEs tienen un momento angular orbital más alto que las LMEs y que perdieron más momento angular durante su migración. Nuestros resultados son congruentes con un modelo en el cual las estrellas más masivas con alta rotación forman discos protoplanetarios más masivos que también rotan mas rápido, y que además son más eficientes en disipar el momento angular de sus planetas.

Key Words: planetary systems — stars: formation — stars: fundamental parameters — stars: rotation

1. INTRODUCTION

The discovery of gas giant planets rotating very close to their stars (hot Jupiter, or HJs) has forced us to reconsider our model for the formation of planets around low mass stars by including in an ad hoc way large scale migration. Since this did not happen in the Solar System, it raises the natural question of understanding under what conditions large scale migration could be triggered in a proto-planetary disk (PPD). By stating such a question, we adopt the simplest view that there is only one universal process for the formation of planets, following the collapse of dense regions in a molecular cloud (McKee & Ostriker 2007; Draine 2011; Champion 2019). This reduces the problem to a more specific one, which is: how do we include migration in a well developed model like the core collapse scenario (the standard model), which explains in details how the Solar System formed (Safronov 1969; Wetherill & W. 1989; Wurm & Blumm 1996; Poppe & Blum 1997; Klahr & Brandner 2006; Hilke & Sari 2011; de Pater & Lissauer 2015; Raymond & Morbidelli 2020)

In the literature, two migration mechanisms are favored for HJs (Dawson & Johnson 2018; Raymond & Morbidelli 2020). The first is disk migration (e.g., Baruteau et al. 2014; Armitage 2020, and references therein), which proposes that a planet loses its or-

[1]Departamento de Astronomía, Universidad de Guanajuato, Guanajuato, Gto., México.

[2]Hamburger Sternwarte, Universität Hamburg, Hamburg, Germany.

bit angular momentum by tidal interactions with the PPD, while the second, high-eccentricity migration (e.g., Rasio & Ford 1996; Weidenschilling & Marzari 1996; Marzari & Weidenschilling 2002; Chatterjee et al. 2008; Nagasawa et al. 2008; Beaugé & Nesvorný 2012), suggests that a planet interacting with other planets gains a higher eccentricity, which brings it close to its star where it reaches equilibrium by tidal interactions (a process know as circularization). In terms of migration, these two mechanisms might suggest that massive disks somehow amplified the level of migration compared to what happened in the Solar System, because more massive PPDs either increase the intensity of interactions of the planets with their disks or favor the formation of a higher number of planets. Within the standard model this would suggest that what counts is whether the PPD follows the minimum mass model, with a mass between 0.01 to 0.02 $M_{\odot}$, or the maximum mass model with a mass above 0.5 $M_{\odot}$ (Armitage 2010). There are few clues which could help us to determine which path the PPD of the Solar System followed (and strong difficulties compared to direct observations of PPD; see Figure 2 and discussion in Raymond & Morbidelli 2020). One is the total mass of the planets, which represents only 0.1% the mass of the Sun. This implies the Solar System PPD has lost an important amount of its mass after the formation of the planets. Another clue is that 99% of the angular momentum of the Solar System is located in the planets, suggesting that the initial angular momentum of the PPD might have been conserved in the planets. However, this is obviously not the case when large scale migration occurs, so what was the difference?

If the initial angular momentum of the PPD passes to the planets, then one could use the orbital rotation momentum in exoplanetary systems to test different scenarios connecting the formation of the planets to the formation of their stars. For example, how is the angular momentum of the PPD coupled to the angular momentum of the stars? Since large scale migration represents a loss of angular momentum of the planets (at least by a factor 10), what was the initial angular momentum of the PPD when it formed and how does this compared to the initial mass of the PPD? Does this influence the masses of the planets and their migration? The answers are not trivial, considering that the physics involved is still not fully understood.

In particular, we know that the angular momentum is not conserved during the formation of stars. This is obvious when one compares how fast the Sun rotates with how fast its rotation should have been assuming the angular momentum of the collapsing molecular cloud where it formed was conserved. Actually, working the math (a basic problem, but quite instructive; see course notes by Alexander 2017), the Sun effective angular momentum, $j_{\odot} = J_{\odot}/M_{\odot}$, is $\approx 10^6$ times lower than expected. Intriguingly, $j_{\odot}$ is also 10^3 lower than the angular momentum of its breaking point, j_b, the point where the centripetal force becomes stronger than gravity (McKee & Ostriker 2007). If that were not true, then no stars, whatever their mass, would be able to form. In fact, observations revealed that, in general, the angular momentum of stars with spectral type O5 to A5 traces a power law, $J \propto M^{\alpha}$, with $\alpha \approx 2$, with typical J_* values that are exactly ten times lower than their breaking point. However, how universal this "law" is and how stars with different masses get to it, is unexplained (Wesson 1979; Brosche 1980; Carrasco et al. 1982; Godłowski et al. 2003). To complicate the matter, it is clear now that lower mass stars, later than A5, do not follow this law, their spin going down exponentially (cf. Figure 6 in Paper I). For low-mass stars, McNally (1965), Kraft (1967) and Kawaler (1987) suggested a steeper power law, $J \propto M^{5.7}$, which implies that they lose an extra amount of angular momentum as their mass goes down. What is interesting is that low-mass stars are also those that form PPDs and planets, which led some researchers to speculate that there could be a link between the two.

To explain how low-mass stars lose their angular momentum, different mechanisms are considered. The most probable one is stellar wind (Schatzman 1962; Mestel 1968), which is related to the convective envelopes of these stars. This is how low-mass stars would differ from massive ones. However, whether this mechanism is sufficient to explain the break in the $J-M$ relation is not obvious, because it ignores the possible influence of the PPD (the formation of a PPD seems crucial; see de la Reza & Pinzón 2004). This is what the magnetic braking model takes into account (Wolff & Simon 1997; Tassoul 2000; Uzdensky et al. 2002). Being bombarded by cosmic rays and UV radiation from ambient stars, the matter in a molecular cloud is not neutral, and thus permeable to magnetic fields. This allows ambipolar diffusion (the separation of negative and positive charges) to reduce the magnetic flux, allowing the cloud to collapse. Consequently, a diluted field follows the matter through the accretion disk to the star forming its magnetic field (McKee & Ostriker 2007). This also implies that the accretion disk (or PPD) stays connected to the star through its magnetic field as long as it exists, that is, over a period that although brief includes the complete phase of planet formation and migration. According to the model of disk-locking, a gap opens between the star and the disk at a distance R_t from the star, and matter falling between R_t and the radius of corotation, R_{co} (where the Keplerian angular rotation rate of the PPD equals that of the star), follows the magnetic field to the poles of the star creating a jet that transports the angular momentum out. In particular, this mechanism was shown to explain why the classic T-Tauris rotate more slowly than the weak T-Tauris (Ray 2012). How this magnetic coupling could influence the planets and their migrations, on the other hand, is still an open question (Matt & Pudritz 2004; Fleck 2008; Champion 2019).

To investigate further these problems, we started a new project to observe host stars of exoplanets using the 1.2 m robotic telescope TIGRE, which is installed near our department at the La Luz Observatory (in central Mexico). In paper I we explained how we succeeded in determining in an effective and homogeneous manner the physical characteristics (T_{eff}, $\log g$, [M/H], [Fe/H], and $V \sin i$) of a initial sample of 46 bright stars using iSpec (Blanco-Cuaresma 2014, 2019). In this accompanying article, we now explore the possible links between the physical characteristics of these 46 stars and the physical characteristics of their planets, in order to gain new insight about a connection between the formation of stars and their planets.

2. SAMPLE OF EXOPLANETS

Our observed sample consists of 46 stars hosts of 59 exoplanets, which were selected from the revised compendium of confirmed exoplanets in the Exoplanet Orbit Database[3]. In Table 1 the dominant planet (Column 2) in each stellar system is identified by the same number (Column 1) which was used in Paper I to identify their stars. In Column 3 and 4 we repeat the magnitude and distance of the host stars as they appeared in Table 1 of Paper I. This is followed by the main properties of the planets as reported in the exoplanet Orbit Database: mass (Column 5), radius (Column 6), period (Column 7), major semi-axis (Column 8) and eccentricity (Column 9). Note that an eccentricity of zero could mean the actual eccentricity is not known. The last two columns identify the detection method and the distinction between high mass and low mass exoplanet (as explained below).

[3]http://exoplanets.org/.

Among our sample, one exoplanet, # 39 (Hn-Peg b), was found to have a mass above the brown dwarf (BD) lower limit of 13 M_{Jup} (Spiegel et al. 2011; Burgasser 2008). Note that Hn-Peg b was detected by imaging (identified as Im in Column 11), and its huge distance from its host star (Column 8) is more typical of BDs than of exoplanets (the other exoplanet detected by imaging is 34, HD 115383 b, at 43.5 AU from it stars, but with a mass of only 4 M_{Jup}). Another exoplanet whose mass is close to the lower mass limit for BDs is # 31 (XO-3 b), but since it is located very near its star, at 0.05 AU, there is no difficulty in accepting its classification as an exoplanet. Due to the small size of our sample, we cannot assess how the formation of exoplanets with masses above the BD limit can differ from the formation of the other exoplanets. Consequently, although we kept Hn-Peg in our sample of host stars we did not include its "exoplanet" in our statistical analysis.

Another point of importance that can be noted in Table 1 is the fact that we have only 14 exoplanets detected by RV. This is most probably due to the fact that we required the radius of the planets to be known, which is easier to determine by the Tr method. Curiously, only three of the 14 exoplanets detected by RV show the trend to be located farther from their stars than the Tr exoplanets, as observed in the literature (and as it is obvious in the Exoplanet Orbit Database). Two are close to the ice line and thus are rather warm than hot, and one with 3.86 M_{Jup} is at the same distance as Jupiter from the Sun. This implies that any bias introduced by the different detection methods, RV vs. Tr, cannot be explored thoroughly in our present analysis.

Although the variety of the characteristics of exoplanets cannot be addressed with our present sample, we can however separate our sample of exoplanets into two groups, based on their masses. For our analysis, this distinction is important in order to test how the mass of the exoplanet is related to the mass of its host star. To use a mass limit that has a physical meaning we choose 1.2 M_{Jup}, which is the mass above which self-gravity in a planet becomes stronger than the electromagnetic interactions (Padmanabhan 1993; Flor-Torres et al. 2016, see demonstration in Appendix A). Using this limit we separated our sample into 22 high mass exoplanets (HMEs) and 23 low mass exoplanets (LMEs). This classification is included in Table 1 in the last column.

According to Fortney et al. (2007) the mass-radius relation of exoplanets shows a trend for exoplanets above 1.0 M_{Jup} to have a constant radius

TABLE 1

PHYSICAL PARAMETERS THE PLANETS IN OUR SAMPLE

Id. #	Star and Planet	Magnitude (V)	Distance (pc)	M_p (M_{jup})	R_p (R_{jup})	Period (days)	a_p (AU)	e_p	Detection Method	Planetary type
1	*KELT-6 c	10.3	242.4	3.71	2.68	1276.0	2.39	0.21	RV	HME
2	*HD 219134 h	5.6	6.5	0.28	0.80	2198.0	3.06	0.37	RV	LME
3	*KEPLER-37 b	9.8	64.0	0.01	0.03	13.37	0.10	0	Tr	LME
4	HD 46375 b	7.8	29.6	0.23	1.02	3.02	0.04	0.05	RV	LME
5	HD 75289 b	6.4	29.1	0.47	1.03	3.51	0.05	0.02	RV	LME
6	HD 88133 b	8.0	73.8	0.30	1.00	3.42	0.05	0.08	RV	LME
7	HD 149143 b	7.9	73.4	1.33	1.05	4.07	0.05	0.01	RV	HME
8	HAT-P-30 b	10.4	215.3	0.71	1.34	2.81	0.04	0.04	Tr	LME
9	KELT-3 b	9.8	211.3	1.42	1.33	2.70	0.04	0	Tr	HME
10	KEPLER-21 b	8.3	108.9	0.02	0.15	2.79	0.04	0.02	Tr	LME
11	KELT-2A b	8.7	134.6	1.49	1.31	4.11	0.05	0.19	Tr	HME
12	HD86081 b	8.7	104.2	1.50	1.08	2.00	0.04	0.06	RV	HME
13	WASP-74 b	9.8	149.8	0.97	1.56	2.14	0.04	0	Tr	LME
14	HD 149026 b	8.1	76.0	0.36	0.72	2.88	0.04	0	Tr	LME
15	HD 209458 b	7.6	48.4	0.69	1.38	3.52	0.05	0.01	Tr	LME
16	BD-10 3166 b	10.0	84.6	0.46	1.03	3.49	0.05	0.01	RV	LME
17	HD 189733 b	7.6	19.8	1.14	1.14	2.22	0.03	0	Tr	LME
18	HD 97658 b	7.7	21.6	0.02	0.20	9.49	0.08	0.08	Tr	LME
19	HAT-P-7 b	10.5	344.5	1.74	1.43	2.20	0.04	0	Tr	HME
20	KELT-7 b	8.5	137.2	1.29	1.53	2.73	0.04	0	Tr	HME
21	HAT-P-14 b	10.0	224.1	2.20	1.20	4.63	0.06	0.10	Tr	HME
22	WASP-14 b	9.7	162.8	7.34	1.28	2.24	0.04	0.09	Tr	HME
23	HAT-P-2 b	8.7	128.2	8.74	0.95	5.63	0.07	0.52	Tr	HME
24	WASP-38 b	9.4	136.8	2.71	1.08	6.87	0.08	0.03	Tr	HME
25	HD 118203 b	8.1	92.5	2.14	1.05	6.13	0.07	0.29	RV	HME
26	HD 2638 b	9.4	55.0	0.48	1.04	3.44	0.04	0.04	RV	LME
27	WASP-13 b	10.4	229.0	0.49	1.37	4.35	0.05	0	Tr	LME
28	WASP-34 b	10.3	132.6	0.59	1.22	4.32	0.05	0.04	Tr	LME
29	WASP-82 b	10.1	277.8	1.24	1.67	2.71	0.04	0	Tr	HME
30	HD 17156 b	8.2	78.3	3.20	1.10	21.22	0.16	0.68	Tr	HME
31	XO-3 b	9.9	214.3	11.79	1.22	3.19	0.05	0.26	Tr	HME
32	HD 33283 b	8.0	90.1	0.33	0.99	18.18	0.17	0.46	RV	LME
33	HD 217014 b	5.5	15.5	0.47	1.90	4.23	0.05	0.01	RV	LME
34	HD 115383 b	5.2	17.5	4.00	0.96	–	43.5	0	Im	HME
35	HAT-P-6 b	10.5	277.5	1.06	1.33	3.85	0.05	0	Tr	LME
36	*HD 75732 d	6.0	12.6	3.86	2.74	4867.0	5.45	0.03	RV	HME
37	HD 120136 b	4.5	15.7	5.84	1.06	3.31	0.05	0.08	RV	HME
38	WASP-76 b	9.5	195.3	0.92	1.83	1.81	0.03	0	Tr	LME
39	Hn-Peg b	6.0	18.1	16.00	1.10	–	795	0	Im	BD
40	WASP-8 b	9.9	90.2	2.24	1.04	8.16	0.08	0.31	Tr	HME
41	WASP-69 b	9.9	50.0	0.26	1.06	3.87	0.05	0.00	Tr	LME
42	HAT-P-34 b	10.4	251.1	3.33	1.11	5.45	0.07	0.44	Tr	HME
43	HAT-P-1 b	9.9	159.7	0.53	1.32	4.47	0.06	0.00	Tr	LME
44	WASP-94 A b	10.1	212.5	0.45	1.72	3.95	0.06	0.00	Tr	LME
45	WASP-111 b	10.3	300.5	1.85	1.44	2.31	0.04	0.00	Tr	HME
46	HAT-P-8 b	10.4	212.8	1.34	1.50	3.08	0.04	0.00	Tr	HME

An * in front of the name of the planet identifies multiple planetary systems.

(see also Fortney et al. 2010). In fact, models of exoplanet structures (e.g., Baraffe et al. 1998, 2003, 2008) predict an inflection point in the mass-radius relation, where the radius starts to decrease instead of increasing as the mass increases. Actually, this is what we observe in brown dwarfs (BDs). Physically therefore, this inflection should be located near 1.2 M_{Jup}, where self-gravity becomes stronger than

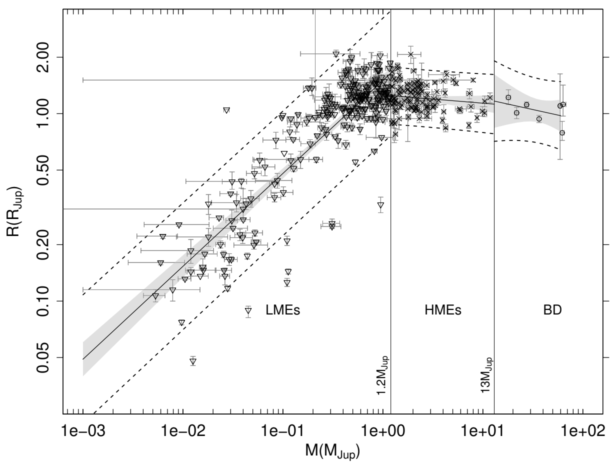

Fig. 1. The M-R diagram for exoplanets in the Exoplanet Orbit Database. The vertical line at 1.2 M_{Jup} corresponds to the mass criterion we used to separate the exoplanets in LMEs and HMEs. The other vertical lime is the lower mass limit for the BDs, 13 M_{Jup}.

the electromagnetic interaction and where the object starts to collapse (which is the case of BDs). However, if massive HJs have more massive envelopes of liquid metallic hydrogen (LMH) than observed in Jupiter (as suggested by JUNO; Guillot et al. 2018; Kaspi et al. 2018; Iess et al. 2018; Adriani et al. 2018), their structures might resist gravity (at least for a while), due to the liquid state being incompressible, pushing the collapse of the radius to slightly higher masses (models and observations verifying this prediction can be found in Hubbard et al. 1997; Dalladay-Simpson et al. 2016; Flor-Torres et al. 2016). This possibility, however, is still controversial, and we only use the mass limit in our analysis to separate our sample of exoplanets according to their masses. On the other hand, the possibility of massive LMH envelopes in the HMEs might have some importance, since these exoplanets would be expected to have higher magnetic fields than the LMEs , which, consequently, could affect their interactions with the PPD and nearby host stars (this fits the case of HD 80606 b, a HME studied by de Wit et al. 2016), leading possibly to different migration behaviors. Likewise, we might also consider the possibility of inflated radii in the LMEs, since they are so close to their stars, although less obvious is the effect of inflated radius on migration (one possibility is that they circularize more rapidly).

To test further our distinction in mass, we trace in Figure 1 the mass-radius relation of 346 exoplanets from the Exoplanet Orbit Database. Based on visual inspection it is not clear how to separate the HJs, due to inflated radii. One quantitative criterion is the mass-radius relation. In Figure 1, we traced three M-R relations, adopting 1.2 M_{Jup} to distinguish LMEs form HMEs. Below this limit we find the relation:

$$\ln R_{LME} = (0.496\pm0.018)\ln M_{\rm LME} + (0.407\pm0.034). \tag{1}$$

The slope is positive and the correlation coefficient is high, $r^2 = 0.75$, which implies that the radius within this range of masses continually increases with the mass. This relation is also fully consistent with what was previously reported by Valencia et al. (2006) and Chen & Kipping (2017). Above the lower mass limit for BDs we find the relation:

$$\ln R_{BD} = (-0.117\pm0.111)\ln M_{\rm BD} + (0.455\pm0.404), \tag{2}$$

with a negative slope and a weaker correlation coefficient of $r^2 = 0.18$, but sufficient to indicate that the trend is for the radius to decrease with the mass. This is as expected for objects where self-gravity is stronger than the electromagnetic repulsion (BDs not having enough mass to ignite fusion in their core cannot avoid the effect of gravitational collapse). Finally, in between these two mass limits defining the HMEs, we obtain the relation:

$$\ln R_{HME} = (-0.044\pm0.030)\ln M_{\rm HME} + (0.229\pm0.031), \tag{3}$$

which has an almost nil slope and a very weak coefficient of correlation, $r^2 = 0.02$, consistent with no correlation. This range of mass, therefore, is fully consistent with HJs near the inflection point, extending this region over a decade in mass (as previously noted by Hatzes & Rauer 2015). For our analysis, these different M-R relations are sufficient to justify our separation between LMEs and HMEs (note that this physical criterion has never been used in the literature; the only study which uses a limit close to ours is Sousa et al. 2011).

3. CONNECTING THE STARS TO THEIR PLANETS

In Paper I, we verified that the rotational velocity of a star, $V\sin i$, decreases with the temperature, T_{eff}. In Figure 2, we reproduce this graphic, but this time distinguishing between stars hosting LMEs and HMEs. We observe a clear trend for the HMEs to be found around hotter and faster rotator stars than the LMEs. Considering the small number of stars in our sample, we need to check whether this result is physical or due to an observational bias. For example, one could suggest that HMEs are easier to detect

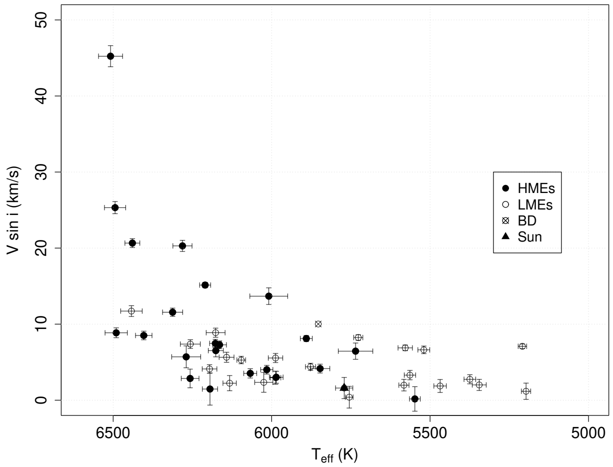

Fig. 2. Star rotational velocity vs. temperature, separating stars hosting HMEs and LMEs. The position of the Sun is included, as well as the star with a BD as companion.

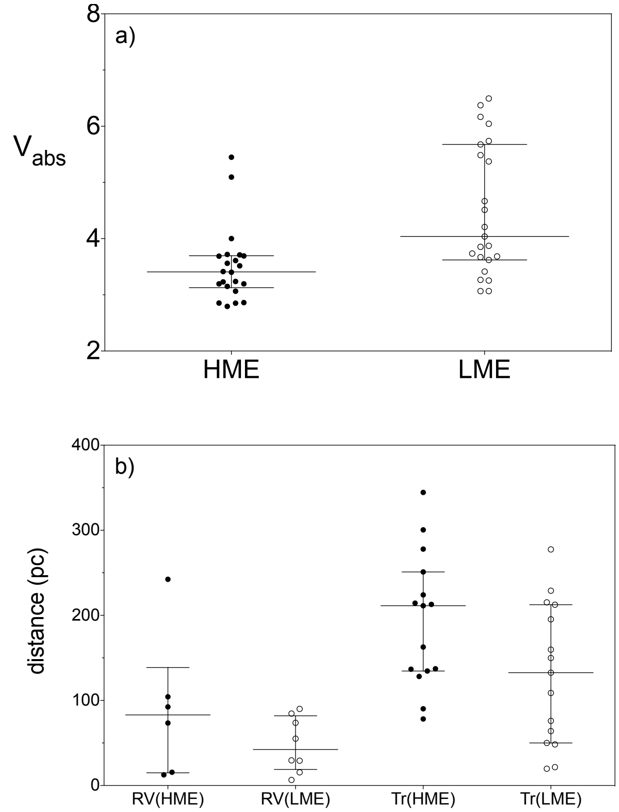

Fig. 3. a) Absolute magnitude in V separately for stars hosting HMEs and LMEs; b) Distance of the stars also separated by the detection method, radial velocity, RV, or transit, Tr. The bars correspond to the medians and interquartile ranges.

than LMEs through the RV than Tr method around hotter (more massive) and faster rotator stars. To check for observational biases, we trace first in Figure 3a the distributions of the absolute V magnitude for the stars hosting LMEs and HMEs. We do find a trend for the stars hosting HMEs to be more luminous than the stars hosting LMEs. This is confirmed by a non-parametric Mann-Whitney test with a p-value of 0.0007 (Dalgaard 2008). However, in Figure 3b we also show that the reason why the stars with HMEs are more luminous is because they are located farther out, and this is independent of the detection method. Consequently, the trend for the HMEs to be found around hotter and faster rotator stars than the LMEs does not depend on the method of detection, but is a real physical difference. Considering the mass-temperature relation on the main sequence, this suggests that the more massive exoplanets in our sample rotate around more massive stars.

In Figure 4 we compare the physical characteristics of the stars that host HMEs with those that host LMEs. Figure 4a shows a clear trend for the rotational velocity to be higher in the stars hosting HMEs than LMEs. In Table 2 we give the results of non-parametric, Mann-Whitney (MW) tests. The use of non-parametric tests is justified by the fact that we did not find normal distributions for our data (established by running 3 different normality tests). In Column 6 we give the p-values of the tests at a level of confidence of 95%, in Column 7, the significance levels (low, *, medium, ** and high, ***) and in Column 8 the acceptance or not of the differences observed. Note that a non-parametric test compares the ranks of the data around the medians, not the means. In the case of $V \sin i$, the MW test confirms the difference of medians at a relatively high level of confidence (stars 22, 33 and 36 were not considered due to their large uncertainties). In Figure 4b we see the same trend for T_{eff} on average, also with a significant difference in median in Table 2.

In Figure 4c the difference in mass is obvious, and confirmed by the MW test at the highest level of confidence. Stars with HMEs are more massive than stars with LMEs. On the other hand, we find no difference in the distribution of the metallicity. Although the medians and means reported in Table 2 look different, the p-value of the MW test is unequivocal, being much higher than 0.05. The median [Fe/H] for our sample is 0.07 dex and the mean is 0.12 dex, with a standard deviation of 0.24 dex. These values are comparable to those reported in the

TABLE 2

STATISTICAL TESTS

	HME		LME		MW	Sign.	Diff.
Parameter	Median	Mean	Median	Mean	p-value		
$V \sin i$	7.47	10.94	4.11	4.62	0.0048	**	yes
T_{eff}	6186	6158	5771	5800	< 0.0001	***	yes
M_*	1.22	1.21	1.11	1.05	< 0.0001	***	yes
$[Fe/H]$	0.21	0.19	0.15	0.16	0.6810	ns	no
J_*	8.83	14.3	4.17	7.33	0.0096	**	yes
J_p	4.17	4.93	1.04	1.09	< 0.0001	***	yes

The units and scale values for the medians and means are those of Figure 4.

literature for systems harboring massive HJ exoplanets (Sousa et al. 2011; Buchhave et al. 2012).

In Figures 4d and 4f, once again we distinguish obvious differences in the distributions, the stars with HMEs having higher angular momentum than the stars with LMEs, and the HMEs having also higher angular momentum than the LMEs. The MW tests in Table 2 confirmed these differences at a relatively high level of confidence (like for $V \sin i$). Considering Eq. 2 in Paper I for the angular momentum of the star, the statistical test confirms that the HMEs rotate around more massive and faster rotator stars than the LMEs. Considering the difference in angular momentum of the exoplanets, J_p, this result seems to support the hypothesis that more massive planets form in more massive PPDs with higher angular momentum. The question is, then, how does this difference affect the migration process of the different exoplanets?

In Figure 5a, following Berget & Durrance (2010), we trace the specific angular momentum of the stars, $j_* = J_*/M_*$, as a function of their masses, distinguishing between stars hosting HMEs and LMEs. The angular momenta of all the host stars in our sample fall well below the theoretical relation proposed by McNally (1965). There is a clear distinction between the LMEs and HMEs, except for the differences encountered in Figure 4 and confirmed in Table 2, and there is no evidence that the stars follow a $j - M$ relation.

On the other hand, when we compare in Figure 5b the angular momentum for the systems, $j_{sys} = j_* + j_p$, we do see a difference between systems with LMEs and HMEs. But this is expected since, by definition, the HMEs having higher masses naturally have a higher contribution to j_{sys}. However, and despite being more massive than Jupiter, very few of the HME systems have a value of j_{sys} comparable to the Solar System. Obviously, this is because of the large scale migration they suffered. To illustrate this point, we traced in Figure 5c the possible "initial" angular momentum the system could have had assuming the exoplanets formed at the same distance as Jupiter (5 AU). Comparing with the positions in Figure 5b, the HMEs would have lost on average 89% of their initial momentum, compared to 86% for the LMEs. Those losses are enormous. Considering the loss of angular momentum of the stars and planets, it might be difficult to expect a coupling between J_p and J_* or even a $j - M$ relation.

As a final test, we have calculated the Pearson correlation matrices (also explained in Dalgaard 2008) for the systems with HMEs and LMEs. The results can be found in Table 3 and Table 4. Since the correlation matrices are symmetrical we include only the lower diagonal of each, showing first the matrix with the p-values (with alpha ≈ 0.05), followed by the matrix for the Pearson correlation coefficient (keeping only the significant correlations, marked in bold in the matrix of the p-values).

Comparing the HMEs with LMEs, there are obvious correlations of the temperature with the mass and radius in both systems, which suggests that, in general, as the temperature increases, the mass and radius increase. This explains, therefore, the strong correlations in both systems of the temperature with the velocity of rotation and thus the angular momentum. Note that these results are consistent with the general relation we determined in Paper I between $V \sin i$, T_{eff} and $\log g$. This suggests that the more massive the star the faster its rotation.

One difference between the two systems is that, although there are no correlations of the temperature with the surface gravity in the HMEs, there is an an-

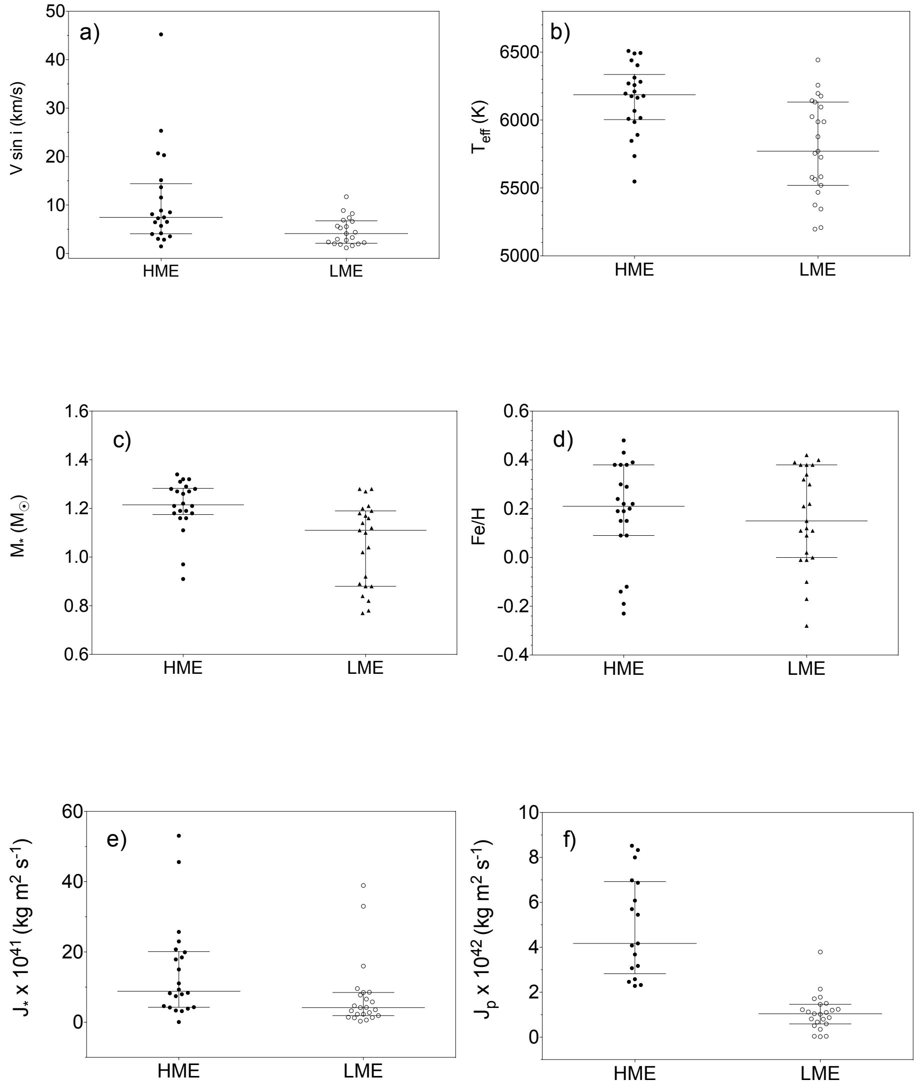

Fig. 4. Comparing the physical characteristics of the stars (and planet) hosting HMEs and LMEs. In each graph the medians and interquartile ranges are drawn over the data. a) rotational velocity, b) effective temperature, c) mass of the star, d) metallicity, e) the angular momentum of the star, f) the angular momentum of the orbit of the dominant planet.

ticorrelation in the LMEs. Due to the smallness of our samples, it is difficult to make sense of this difference physically. However, we note that $\log g$ in the LMEs is also well correlated with the radius, the mass and the angular momentum (but not $V \sin i$ itself), something not seen in the HMEs. In Figure 2 wee see that the dispersion of $V \sin i$ decreases at low temperatures, which implies that the bi-exponential relation of $V \sin i$ as a function of T_{eff} and $\log g$ becomes tighter, suggesting that the behavior of $\log g$ becomes more ordered, which could explain the anti correlations with T_{eff} and the correlations with M_* and R_* (and thus also with J_*).

It is remarkable that $[Fe/H]$ in both systems is not correlated with any of the other parameters, either related to the stars or the planets. For the stars, the most obvious correlations in both systems are between M_* and R_*, or $V \sin i$ and J_*. Note also that although $V \sin i$ shows no correlation with M_* and R_* in the HMEs it is correlated with M_* in the LMEs. This might also explain why R_* is not correlated with J_* in the HMEs, while it is in the LMEs.

In the case of the planets, the most important result of this analysis is the (almost complete) absence of correlations between the parameters of the planets and the parameters of the stars (most obvious in the

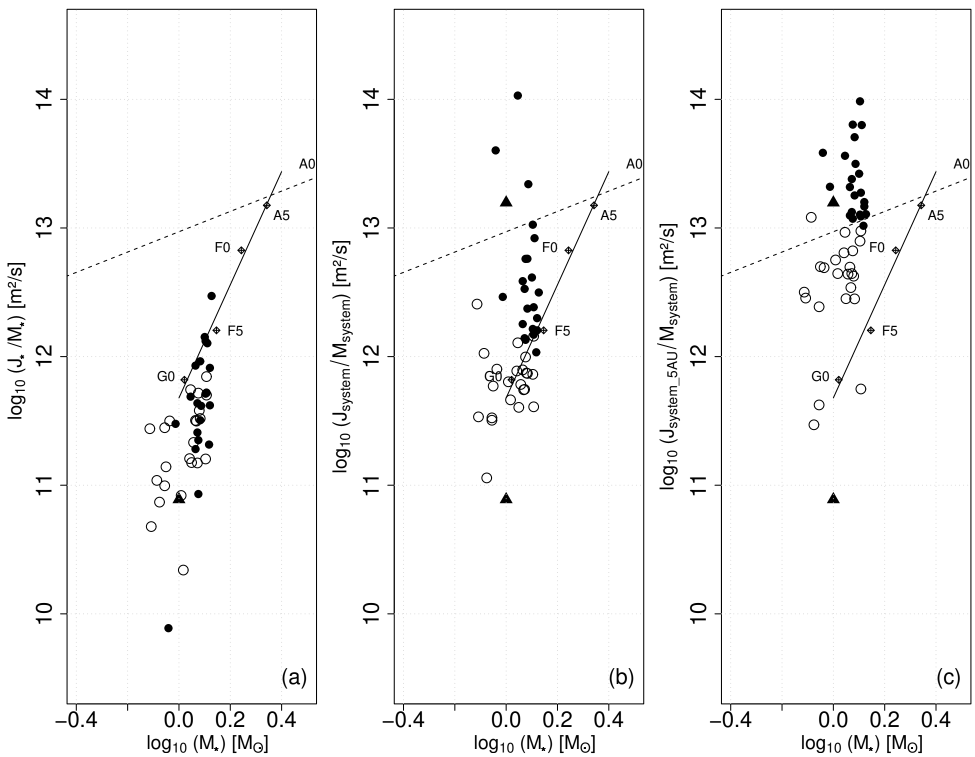

Fig. 5. In (a) Specific angular momentum of the host stars as function of their masses. The symbols are as in Figure 2. The solid black line is the relation proposed by McNally (1965) for low-mass stars (spectral types A5 to G0) and the dotted line is the extension of the relation suggested for massive stars. The black triangle represents the Sun; (b) specific angular momentum for the planetary systems, with the inverted black triangle representing the Solar system; (c) original angular momentum assuming the planets formed at 5 AU.

LMEs). The only parameter that shows some correlation with the star parameters is the semi-axis, a_p, of the orbit of the planets in the HMEs. This might suggests a difference in terms of circularization. Two results also seem important. The first is that R_p is only correlated to M_p in in the HMEs, which is consistent with the fact that the radius of the HMEs is constant. The second is that there is no correlation between J_p and J_*, which is consistent with the behavior observed in Figure 5, and which could suggest that there is no dynamical coupling between the two. This, probably, is due to important losses of angular momentum during the formation of the stars and to migrations of the planets.

4. DISCUSSION

Although our sample is small, we do find a connection between the exoplanets and their stars: massive exoplanets tend to form around more massive stars, these stars being hotter (thus brighter) and rotating faster than less massive stars. When we compare the spin of the stars with the angular momentum of the orbits of the exoplanets, we find that in the HME systems both the stars and planets rotate faster than in the LME systems. This is consistent with the idea that massive stars formed more massive PPDs, which rotate faster, explaining why the planets forming in these PPDs are found also to rotate faster.

When we compare the effective angular momenta of the stars (Figure 5a) we find no evidence that they follow a $j - M$ relation, in particular, like the one suggested by McNally (1965), or that the angular momentum of the systems (Figure 5b) follows such relation. Furthermore, there is a correlation between J_p and J_*, which suggests that there is no dynamical coupling between the two. This is probably due to the important losses of angular momentum of the stars during their formation (by a factor of 10^6) and of the planets during their migrations (higher than 80% of their possible initial values). For the planets, their final angular momenta depend on their masses when their migration ends, a_p. Assuming, consequently that they all form more or less at the same distance (farther than the ice line in their systems) and end their migration at the same distance from

TABLE 3

PEARSON CORRELATION MATRIX FOR THE HME SYSTEMS

HME	T_{eff}	$\log g$	$[Fe/H]$	$V \sin i$	R_*	M_*	J_*	M_p	R_p	a_p	e_p
$\log g$	0.2918										
$[Fe/H]$	0.6794	0.1519									
$V \sin i$	0.0048	0.6052	0.4121								
R_*	0.0199	0.0785	0.9143	0.8734							
M_*	<0.0001	0.0884	0.4889	0.1242	<0.0001						
J_*	0.0006	0.7412	0.1961	<0.0001	0.2345	0.0162					
M_p	0.8087	0.7356	0.3401	0.3785	0.0577	0.1892	0.7779				
R_p	0.3861	0.4608	0.2527	0.9065	0.2122	0.1460	0.8397	0.1323			
a_p	0.0339	0.0173	0.6018	0.9447	0.0118	0.0074	0.3824	0.0074	0.1050		
e_p	0.6455	0.4758	0.8288	0.9864	0.4266	0.1871	0.8931	0.0073	0.0418	0.0122	
J_p	0.4358	0.4193	0.4496	0.5536	0.0455	0.5697	0.7913	<0.0001	0.2679	<0.0001	0.0234
$\log g$											
$[Fe/H]$											
$V \sin i$	0.5909										
R_*	0.4925										
M_*	0.8402				0.8662						
J_*	0.6736			0.9857		0.5064					
M_p											
R_p											
a_p	-0.4539	0.5021			-0.5267	-0.5546		0.5544			
e_p								0.5550	-0.4373	0.5243	
J_p					-0.4305			0.9393		0.7272	0.4811

TABLE 4

PEARSON CORRELATION MATRIX FOR THE LME SYSTEMS

LME	T_{eff}	$\log g$	$[Fe/H]$	$V \sin i$	R_*	M_*	J_*	M_p	R_p	a_p	e_p
$\log g$	0.0002										
$[Fe/H]$	0.3461	0.2153									
$V \sin i$	0.0097	0.0389	0.0761								
R_*	<0.0001	<0.0001	0.2374	0.1499							
M_*	<0.0001	<0.0001	0.0618	0.0187	<0.0001						
J_*	0.0034	0.0012	0.1880	<0.0001	0.0077	0.0012					
M_p	0.0658	0.1672	0.5022	0.3259	0.3008	0.1802	0.3683				
R_p	0.1825	0.0681	0.5140	0.7583	0.1878	0.1902	0.9893	<0.0001			
a_p	0.4458	0.5652	0.5036	0.9258	0.4294	0.4570	0.8521	0.0303	0.2162		
e_p	0.2682	0.3735	0.3691	0.2266	0.5929	0.3681	0.3979	0.0645	0.0348	0.2426	
J_p	0.2301	0.1979	0.7299	0.2168	0.4060	0.3170	0.1022	<0.0001	0.0029	0.7167	0.4335
$\log g$	-0.6992										
$[Fe/H]$											
$V \sin i$	0.5506	-0.4537									
R_*	0.7509	-0.9084									
M_*	0.9036	-0.8577		0.5081	0.9407						
J_*	0.5840	-0.6319		0.9312	0.5408	0.6327					
M_p											
R_p								0.7468			
a_p								-0.4521			
e_p									-0.4418		
J_p								0.67921	0.5927		

their stars (which seems to be the case, as we show in Figure 6), the HMEs would have lost a slightly larger amount of angular momentum than the LMEs. Within the scenario suggested above, this might suggest that more massive PPDs are more efficient in dissipating the angular momentum of their planets.

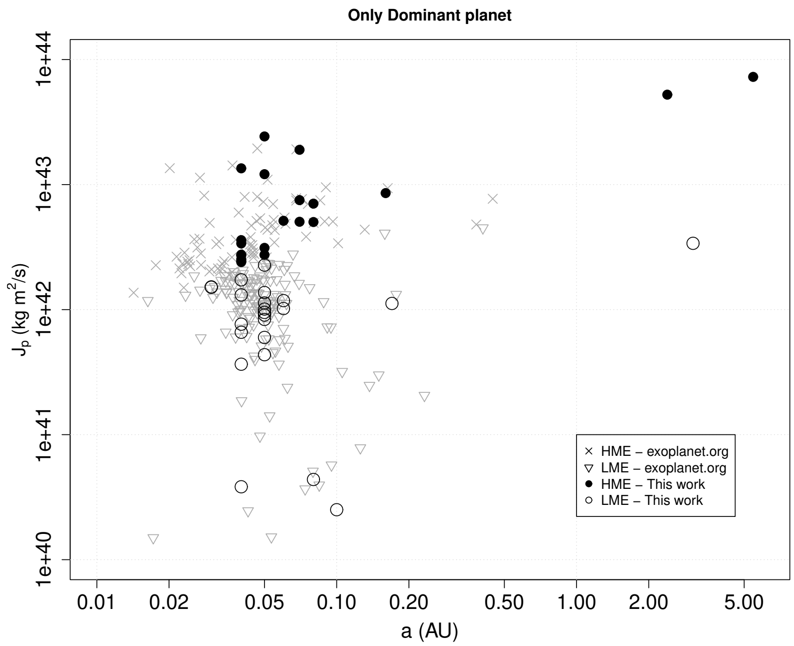

Fig. 6. Angular momentum of the exoplanets in our sample with respect to their distances from their stars. For comparison, the exoplanets in our initial sample are also shown as light gray signs.

One thing seems difficult to understand, however. Considering that HMEs are more massive and lost more angular momentum during their migration, why did they end their migration at almost exactly the same distance from their stars as the less massive LMEs?. In Figure 6 the accumulation we perceive between 0.04 and 0.05 AU is consistent with the well known phenomenon called the three-days pile-up (3 days is equivalent to slightly more than 0.04 AU, assuming Kepler orbits), which is supposed to be an artifact due to selection effects of ground-based transit surveys (Gaudi 2005). However, Dawson & Johnson (2018) in their review about migration suggested that this could be physical, and some authors did propose different physical explanations (see Fleck 2008, and references therein). The model of Fleck (2008) is particularly interesting because it tries to solve the problem using the same structure of the PPD that many authors believe explains how the stars lose their angular momentum during the T-Tauri phase, that is, by magnetic braking. In Appendix B we do some calculations which show that the radius where the planets in our sample end their migration could be close to the co-rotation radius, the region of the PPD where the disk rotates at the same velocity as the star. But does this imply that disk migration is more probable than high-eccentricity tidal migration?

According to the theory of high-eccentricity tidal migration, one expects a strong dependence of the tidal evolution timescale on the final location of the orbit of the planets, a_{final} (e.g., Eggleton 1998):

$$\dot{a} \propto a^8_{final}. \tag{4}$$

This implies that since the HMEs and LMEs have the same $a_{final} \approx 0.04$ AU they should also have the same tidal evolution timescale, and thus no difference would be expected comparing their eccentricities. What stops the planet migration in the high-eccentricity tidal migration model is the circularization of the orbit through tidal interactions with the central star. Therefore, assuming the same tidal evolution timescale, we would expect the eccentricities for the HMEs and LMEs to be all close to zero (Bolmont et al. 2011; Remus et al. 2014). Note that using our data to test whether the HMEs and LMEs have similar distributions in eccentricity is possibly difficult, because we are not certain if an eccentricity of zero is physical or not (meaning an absence of data). For the HME sample, on 22 exoplanets we count 7 (32%) with zero eccentricity, while in the LMEs out of 23, 10 (43%) have zero eccentricity. The difference seems marginal. For the remaining planets with non zero eccentricities (15 HMEs and 13 LMEs) we compare in Figure 7 their distributions. There is a weak difference, with a median (mean) of

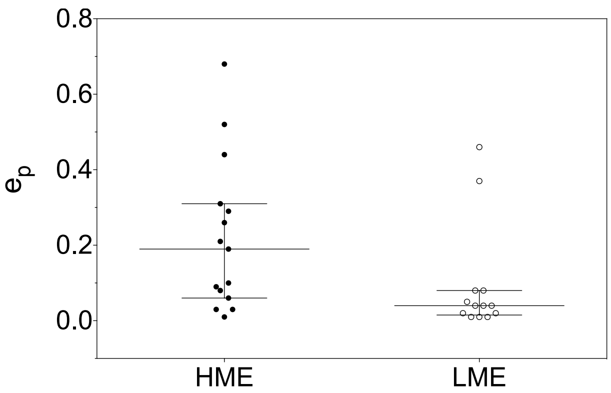

Fig. 7. Eccentricities of the exoplanets in our sample, distinguishing between HMEs and LMEs.

$e_p = 0.19$ ($e_p = 0.22$) for the HMEs compared, to $e_p = 0.04$ ($e_p = 0.10$) for the HMEs and LMEs. A MW test yields a p-value = 0.0257, which suggests a difference at the lowest significance level. Therefore, there seems to be a trend for the HMEs to have on average a higher eccentricity than the LMEs. The HMEs possibly reacted more slowly to circularization than the LMEs (de Wit et al. 2016), suggesting possibly different structures due to their larger masses (Flor-Torres et al. 2016).

5. CONCLUSIONS

Based on an homogeneous sample of 46 stars observed with TIGRE and analysed using iSpec we started a project to better understand the connection between the formation of the stars and their planets. Our main goal is to check whether there could be a coupling between the angular momentum of the planets and their host stars. Here are our conclusions.

There is a connection between the stars and their exoplanets, which passes by their PPDs. Massive stars rotating faster than low-mass stars had more massive PPDs with higher angular momentum, explaining why they formed more massive planets rotating faster around their stars. However, in terms of stellar spins and planet orbit angular momentum, we find that both the stars and their planets have lost a huge amount of angular momentum (by more than 80% in the case of the planets), a phenomenon which could have possibly erased any correlations expected between the two. The fact that all the planets in our sample stop their migration at the same distance from their stars, irrespective of their masses, might favor the views that the process of migration is due to the interactions of the planets with their PPDs, and that massive PPDs dissipate more angular momentum than lower mass PPDs. Consistent with this last conclusion, HMEs might have different structures than LMEs, which made them more resilient to circularization.

We would like to thank an anonymous referee for a careful revision of our results and for comments and suggestions that helped us to improve our work. L. M. F. T. thanks S. Blanco-Cuaresma for discussions and support with iSpec. She also thanks CONACyT for a scholar grant (CVU 555458) and travel support (bilateral Conacyt-DFG projects 192334, 207772, and 278156), as well as for support given by the University of Guanajuato for conference participation and international collaborations (DAIP, and Campus Guanajuato). This research has made use of the Exoplanet Orbit Database, the Exoplanet Data Explorer (exoplanets.org Han et al. 2014), exoplanets.eu (Schneider et al. 2011) and the NASA's Astro-physics Data System.

APPENDICES

A. CALCULATING THE SELF-GRAVITATING MASS LIMIT

According to Padmanabhan (1993) the formation of structures with different masses and sizes involves a balance between two forces, gravity, F_g and electromagnetic, F_e. For the interaction between two protons, we get:

$$\frac{F_e}{F_g} = \frac{\kappa_e e^2/r^2}{Gm_p^2/r^2} = \frac{\kappa_e e^2}{Gm_p^2} = \left(\frac{\kappa_e e^2}{\hbar c}\right)\left(\frac{\hbar c}{Gm_p^2}\right), \tag{A5}$$

where κ_e and G are the electromagnetic and gravitational constants, that fix the intensity of the forces, e and m_p the charges and masses interacting (m_p is the mass of a proton) and r the distance between the sources (the laws have exactly the same mathematical form). Introducing the reduced Plank constant $\hbar = h/2\pi$ and the velocity of light c (two important constant in physics), the first term on the right is the fine structure constant $\alpha \approx 7.29 \times 10^{-3}$, and the second term is the equivalent for gravity $\alpha_G \approx 5.88 \times 10^{-39}$. This implies that:

$$\frac{\alpha}{\alpha_G} \approx 1.24 \times 10^{36}. \tag{A6}$$

This results leads to the well-known hierarchical problem: there is no consensus in physics why the electromagnetic force should be stronger than the gravitational force in such extreme. The reason might have to do with the sources of the forces, in particular, the fact that in electromagnetic there are two types of charge interacting, while there is only one type of mass. The important consequence for the formation of large-scale structures is that while in the electromagnetic interaction the trend to minimize the potential energy reduces the total charge, massive object being neutral, the same trend in gravity is for the gravitational field to increase with the mass. Therefore, small structures tend to be dominated by the electromagnetic force, while large structures are dominated by gravity. Based on this physical fact, Padmanabhan calculated that there is a critical mass, M_c, above which the force of gravity becomes more important than the electromagnetic force. The point of importance for planet formation is that this critical mass turned out to be comparable to the mass of a gas giant planet.

To realize that, it suffices to compare the energy of ligation of a structure with its gravitational potential energy. Since the escape energy for an electron is:

$$E_0 \approx \alpha^2 m_e c^2 \simeq 4.35 \times 10^{-18}\mathrm{J}, \tag{A7}$$

a spherical body formed of N atoms would have an energy of ligation $E = N \times E_0$. On the other hand, its mass would be $M = N m_p$ and its volume would be $4/3\pi R^3 = N \times 4/3\pi a_0^3$, where $a_0 \simeq 5.30\times10^{-11}$ m, is the Bohr radius. From this we deduce that its radius woud be $R \approx N^{1/3} a_0$, and its gravitational potential:

$$E_G \simeq \frac{GM^2}{R} \simeq N^{5/3}\frac{Gm_p^2}{a_0} = N^{5/3}\alpha_G m_e \alpha c^2. \tag{A8}$$

Now, the condition for a stable object to form under gravity is $E \geq E_G$, while for $E < E_G$ the object would collapse under its own weight. In equilibrium we would thus have:

$$N^{5/3}\alpha_G m_e \alpha c^2 = N\alpha^2 m_e c^2. \tag{A9}$$

This yields to a maximum number of atoms, $N_{max} \approx (\alpha/\alpha_G)^{3/2} \approx 1.38 \times 10^{54}$, and a critical mass:

$$M_c = N_{max} \times m_p \approx 2.31 \times 10^{27}\mathrm{kg} \approx 1.2 M_J. \tag{A10}$$

This suggests that the inflection point we observe in the mass-radius relation of exoplanets could be the critical point where an object becomes unstable under self-gravity.

B. AT WHAT DISTANCE IS THE COROTATION RADIUS, R_{CO}

In their review about the migration of planets, Dawson & Johnson (2018) claimed that the distribution of exoplanets around their host stars is consistent with the co-rotation radius, R_{co}, which is part of the magnetic structure connecting the star to its PPD. In the model presented by Matt & Pudritz (2004), the authors discussed some specific aspects of this magnetic structure that could contribute in stopping planet migration (see their Figure 3 and explanations therein). Following this model, the star and disk rotate at different angular speeds except at R_{co}, where the magnetic field becomes twisted azimuthally by differential rotation, triggering magnetic forces. These forces would act to restore the dipole configuration conveying torques between the star and the disk. As a planet approaches R_{co}, therefore, these torques would transfer angular momentum from the star to the planet stopping its migration (Fleck 2008). One important aspect of this model is that the dumping would only work up to a distance $R_{out} \approx 1.6 R_{co}$, and thus one would expect the planets to pile-up over this region, that is, between R_{out} and R_{co}. The question then is what is the value of R_{co}?

One way to determine this value is to assume that when the wind of a newly formed star starts evaporating the PPD, $R_{out} \longrightarrow R_{co}$ and the magnetic pressure at R_{co} balances the gas pressure due to the wind, $P_B = P_g$. Assuming that the intensity of the magnetic field decreases as the cube of the distance, we get, $B \approx B_s R_*^3/r^3$, where B_s is the intensity of the magnetic field at the surface of the star, R_* is the radius of the star, and μ_0 is the permeability of the vacuum. This yields that:

$$P_B = \frac{B^2}{2\mu_0} = \frac{B_s^2 R_*^6}{2\mu_0 r^6}. \tag{B11}$$

For the gas pressure we used the expression for "Ram pressure":

$$P_g = nmv^2 \tag{B12}$$

where v is the velocity of the wind and nm is its load, that is, the amount of mass transported by the wind. This load then can be expressed in terms of the flux of matter, $\dot{M}$, as:

$$nm = \frac{\dot{M}}{4\pi r^2 v}. \tag{B13}$$

Assuming equality at $r = R_{co}$, we get:

$$R_{co}^4 = \frac{2\pi}{\mu_0}\frac{B_s^2 R_*^6}{\dot{M} v}, \tag{B14}$$

which for a star like the Sun ($B_s \approx 10^{-4}$ T, $\dot{M} \approx 2.00 \times 10^{-14} M_\odot$/yr and $v = 2.15 \times 10^{-3}$ m/s) yields $R_{co} \approx 6.77 \times 10^9$m or 0.045 AU. According to this model, therefore, we could expect to see a real pile up of exoplanets independent of their masses (and losses of angular momentum) between $0.04 - 0.07$ AU, which neatly fit the observations.

REFERENCES

Adriani, A., Mura, A., Orton, G., et al. 2018, Natur, 555, 216

Alexander R. 2017, Lecture 2 : Protoplanetary discs, https://www.astro.le.ac.uk/rda5/planets_2017.html

Armitage P. J. 2010, Astrophysics of Planet Formation (Cambridge, UK: CUP)

__________. 2020, Astrophysics of Planet Formation (2nd ed.; Cambridge, UK: CUP)

Asplund, M., Grevesse, N., Sauval, A.J., & Scott, P. 2009, ARA&A, 47, 481

Baraffe, I., Chabrier, G., Allard, F., & Hauschildt, P. H. 1998, A&A, 337, 403

Baraffe, I., Chabrier, G., Barman, T. S., Allard, F., & Hauschildt, P. H. 2003, A&A, 402, 701

Baraffe, I., Chabrier, G., & Barman, T. 2008, A&A, 482, 315

Baruteau, C., Crida, A., Paardekooper, S.-J., et al. 2014, Protostars and Planets VI, ed. H. Beuther, R. S. Klessen, C. P. Dullemond, & T. Henning (Tuczon, AZ: UAP), 667

Beaugé, C. & Nesvorný, D. 2012, ApJ, 751, 119

Berget, D. J. & Durrance, S. T. 2010, Journal of the Southeastern Association for Research in Astronomy, 3, 32

Blanco-Cuaresma, S., Soubiran, C., Heiter, U., & Jofré, P. 2014, A&A, 569, 111

Blanco-Cuaresma, S. 2019, MNRAS, 486, 2075

Bolmont, E., Raymond, S. N., & Leconte, J. 2011, A&A, 535, 1

Brosche, P. 1980, in Cosmology and Gravitation, ed. P. G. Bergmann & V. De Sabbata (Boston, MA: Springer), 375, doi:10.1007/978-1-4613-3123-0_17

Buchhave, L. A., Latham, D. W., Johansen, A., et al. 2012, Natur, 486, 375

Burgasser, A. J. 2008, PhT, 61, 70

Carrasco, L., Roth, M., & Serrano, A. 1982, A&A, 106, 89

Champion, J. 2019, PhD Thesis, Univertité de Toulouse

Chatterjee, S., Ford, E. B., Matsumura, S., & Rasio, F. A. 2008, ApJ, 686, 580

Chen, J. & Kipping, D. 2017, ApJ, 834, 17

Dalgaard, P. 2008, Introductory statistics with R (New York, NY: Springer) doi:10.1007/978-0-387-79054-1

Dalladay-Simpson, P., Howie, R. T., & Gregoryanz, E. 2016, Natur, 529, 63

Dawson, R. I. & Johnson, J. A., 2018, ARA&A, 56, 175

de la Reza, R. & Pinzón, G. 2004, AJ, 128, 1812

de Pater, I. & Lissauer, J. J. 2015, Planetary Sciences (2nd ed.; CUP)

de Wit, J., Lewis, N. K., Langton, J., et al. 2016, ApJ, 820, 33

Draine, B. T. 2011, Physics of the Interstellar and Intergalactic Medium (Princeton, MA: PUP)

Eggleton, P. P., Kiseleva, L. G., & Hut, P. 1998, ApJ, 499, 853

Fleck, R. C. 2008, Ap&SS, 313, 351

Flor Torres, L., Coziol, R., Schröeder, K.-P., Caretta, C. A., & Jack, D. 2016, pp 1-5 (arXiv:1607.07922), doi:10.5281/zenodo.58717, http://arxiv.org/abs/1607.07922

Flor-Torres, L., Coziol, R., Schröeder, K.-P., & Jack, D. 2020, in press

Fortney, J. J., Marley, M. S., & Barnes, J. W. 2007, ApJ, 659, 1661

Fortney, J. J., Baraffe, I., & Militzer, B. 2010, in Exoplanets, ed. S. Seager (Tuczon, AZ: UAP), 397

Gaudi, B. S. 2005, ApJ, 628, 73

Godłowski, W., Szydłowski, M., Flin, P., & Biernacka, M. 2003, GReGr, 35, 907

Guillot, T., Miguel, Y., Militzer, B., et al. 2018, Natur, 555, 227

Han, E., Wang, S. X., Wright, J. T., et al. 2014, PASP, 126, 827

Hatzes, A. P. & Rauer, H. 2015, ApJL, 810, 25

Hilke, E. S. & Sari, R. 2011, ApJ, 728, 68

Hubbard, W. B., Guillot, T., Lunine, J. I., et al. 1997, PhPl, 4, 2011

Iess, L., Folkner, W. M., Durante, D., et al. 2018, Natur, 555, 220

Kaspi, Y., Galanti, E., Hubbard, W. B., et al. 2018, Natur, 555, 223

Kawaler, S. D. 1987, PASP, 99, 1322

Klahr, H. & Brandner, W. 2006, Planet Formation: Theory, Observations and Experiments (Cambridge, UK: CUP)

Kraft, R. P. 1967, ApJ, 150, 551

Marzari, F. & Weidenschilling, S. J. 2002, Icar, 156, 570

Matt, S. & Pudritz, R. E. 2004, ApJ, 607, 43

McNally, D. 1965, Obs, 85, 166

McKee, C. F. & Ostriker, E. C. 2007, ARA&A, 45, 565

Mestel, L. 1968, MNRAS, 138, 359

Nagasawa, M., Ida, S., & Bessho, T. 2008, ApJ, 678, 498

Padmanabhan, T. 1993, Structure Formation in the Universe (New York, NY: CUP)

Poppe, T. & Blum, J. 1997, AdSpR, 20, 1595

Rasio, F. A. & Ford, E. B. 1996, Sci, 274, 954

Ray, T. 2012, A&G, 53, 19

Raymond, S. N. & Morbidelli, A. 2020, arXiv e-prints, arXiv:2002.05756

Remus, F., Mathis, S., Zahn, J.-P., & Lainey, V. 2014, IAUS 293, Formation, Detection, and Characterization of Extrasolar Habitable Planets, ed. N. Haghighipour (New York, NY: CUP), 362

Safronov, V. S. 1969, Ann. Astrophys., 23, 979

Schatzman, E. 1962, AnAp, 25, 18

Schneider, J., Dedieu, C., Le Sidaner, P., Savalle, R., & Zolotukhin, I. 2011, A&A, 532, 79

Sousa, S. G., Santos, N. C., Israelian, G., Mayor, M., & Udry, S. 2011, A&A, 533, 141

Spiegel, D. S., Burrows, A., & Milsom, J. A. 2011, ApJ, 727, 57
Tassoul, J.-L. 2000, Stellar Rotation, (New York, NY: CUP), doi:10.1017/CBO9780511546044
Uzdensky, D. A., Konigl, A., & Litwin, C. 2002, ApJ, 565, 1191
Valencia, D., O'Connell, R. J., & Sasselov, D. 2006, Icar, 181, 545
Weidenschilling, S. J. & Marzari, F. 1996, Natur, 384, 619
Wesson, P. S. 1979, A&A, 80, 296
Wetherill, G. W. 1989, in The formation and evolution of planetary systems, ed. H. A. Weaver & L. Danly, (Cambridge, UK: CUP), p. 1-24, Discussion, p. 24
Wolff, S. C. & Simon, T. 1997, PASP, 109, 759
Wurm, G. & Blum, J. 1996, AAS/Division for Planetary Meeting Abstracts, 28, p. 11.02

R. Coziol, L. M. Flor-Torres, D. Jack, and K.-P. Schröder: Departamento de Astronomía, Universidad de Guanajuato, Guanajuato, Gto., México.
J. H. M. M. Schmitt: Hamburger Sternwarte, Universität Hamburg, Hamburg, Germany.

Revista Mexicana de Astronomía y Astrofísica, **57**, 233–239 (2021)

https://doi.org/10.22201/ia.01851101p.2021.57.01.17

"HEAD/TAIL PLASMON" PRODUCED BY A GAUSSIAN EJECTION VELOCITY PULSE

A. C. Raga[1], J. Cantó[2], A. Castellanos-Ramírez[2], A. Rodríguez-González[1], and L. Hernández-Martínez[3]

Received October 5 2020; accepted January 26 2021

ABSTRACT

We present an analytic model of a collimated ejection with a "single pulse" Gaussian ejection velocity. This flow produces a dense "head" (the leading working surface) joined to the outflow source by a "tail" of lower velocity material. For times greater than the duration of the ejection pulse, this tail develops a linear radial velocity vs. position structure. This "head/tail plasmon" structure is interesting for modelling astrophysical "bullets" joined to their outflow sources by structures with "Hubble law" radial velocity dependencies. We study the case of a Gaussian ejection velocity law with a constant and a Gaussian ejection density history, We compare these two cases, and find that the main effect of the different ejection density histories is to change the mass and the density stratification of the plasmon tail.

RESUMEN

Presentamos un modelo analítico de una eyección colimada con una velocidad de eyección en forma de un único "pulso". Este flujo produce una "cabeza" densa (la superficie de trabajo) unida a la fuente por una "cola" de material de menor velocidad. Para tiempos mayores que la duración del pulso, esta cola desarrolla una dependencia lineal de velocidad radial vs. posición. Esta estructura de "plasmón cabeza/cola" es interesante para modelar "balas" astrofísicas unidas a su fuente por estructuras con velocidades radiales con forma de "ley de Hubble". Estudiamos el caso de una velocidad de eyección Gaussiana y con una historia de densidad de eyección constante o Gaussiana. Comparamos estos dos casos, y encontramos que el efecto más importante de las dos formas de la densidad de eyección es cambiar la masa y la estratificación de la densidad en la cola del plasmón.

Key Words: hydrodynamics — ISM: Herbig-Haro objects — ISM: jets and outflows — planetary nebulae: general — shock waves — stars: winds, outflows

1. INTRODUCTION

Collimated ejections from stars sometimes show high velocity clump structures which are joined to the source by a fainter emitting region with a "Hubble velocity law" of increasing radial velocities with distance. This type of structure is seen in some planetary nebulae; examples are described by Alcolea et al. (2001) and Dennis et al. (2008).

There is also the remarkable "Orion fingers" multiple outflow from the Orion BN-KL region (e.g, Allen & Burton 1983; Zapata et al. 2011; Bally et al. 2017). This outflow has ≈ 100 collimated features radiating away from the BN-KL multiple stellar system. These features have CO emission with Hubble law, linear radial velocity vs. position structures, ending in compact clumps (seen in H_2 and optical atomic/ionic lines). Rivera-Ortíz et al. (2019a, b) have modeled these structures as dense clumps travelling semi-ballistically away from the source region.

In a recent paper, Raga et al. (2020) have presented a model for a "single pulse ejection" jet, which results in the production of a dense "head" joined to the outflow source by a "tail" which develops a linear, Hubble law velocity structure for times greater than the duration of the pulse. This "head/tail plasmon" flow is clearly promising for modelling the objects described above.

[1]Instituto de Ciencias Nucleares, UNAM, México.
[2]Instituto de Astronomía, UNAM, México.
[3]Facultad de Ciencias, UNAM, México.

Raga et al, (2020) studied the problem of a collimated flow produced by a parabolic, single pulse ejection velocity variability. They also assumed the mass loss rate to be time-independent during the duration of the pulse (so that the ejection density is proportional to the inverse of the ejection velocity). With these assumptions, they obtained a fully analytic model, and also presented an axisymmetric numerical simulation of the flow.

In the present paper, we extend the work of Raga et al. (2020) to a different functional form for the ejection velocity pulse, which we now assume to have a Gaussian time-dependence. We also study two different forms for the ejection density history: a time-independent density, and a Gaussian density history (with the same time-width as the velocity pulse).

The paper is organized as follows. In § 2 we describe the time and position for the formation of the leading working surface of the flow. In § 3 we describe the method for determining the motion of the leading working surfaces, and apply it to the case of constant ejection density. The solutions obtained for different values of the environment to outflow density ratio are presented in § 4. Solutions for the case with a Gaussian ejection velocity variability are presented in § 5. The velocity and density structures of the tails (for the Gaussian plasmons with constant and with Gaussian ejection density histories) are modeled in § 6. Finally, the results are summarized in § 7.

2. THE FORMATION OF A WORKING SURFACE

In regions without shock waves, a 1D, hypersonic jet flow follows the free-streaming solution

$$u(x,t) = \frac{x}{t-\tau} = u_0(\tau)\,, \tag{1}$$

where $u(x,t)$ is the velocity (along the outflow axis) as a function of distance x from the source at an "evolutionary time" t, τ is the "ejection time" at which the fluid parcel at position x was ejected, and $u_o(\tau)$ is the velocity with which it was ejected.

From equation (1), one can straightforwardly derive the relation:

$$\frac{\partial u}{\partial x} = \frac{\dot{u}_0(\tau)}{(t-\tau)\dot{u}_0(\tau) - u_0(\tau)}\,. \tag{2}$$

where $\dot{u}_0 = du_0/d\tau$. The fluid parcels ejected close to a time τ will catch up with each other to form a discontinuity when $\partial u/\partial x \to \infty$. The condition for the formation of a discontinuity therefore is that the denominator of equation (2) becomes zero (of course provided that the ejection velocity is not constant, so that the numerator of equation 2 is non-zero). From this, we find that the time at which the flow ejected at a time τ forms a discontinuity is:

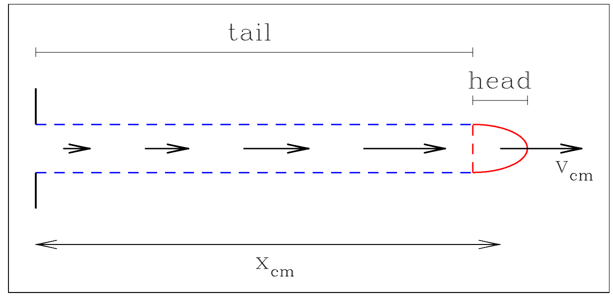

Fig. 1. Schematic diagram showing the structure of a "head/tail plasmon" produced by a single pulse ejection velocity variability. The rising velocity wing of the ejection pulse piles up into the leading head, and part of the decreasing velocity wing fills up the region between the head and the outflow source. The color figure can be viewed online.

$$t_{col} = \frac{u_0(\tau)}{\dot{u}_0(\tau)} + \tau\,. \tag{3}$$

We now propose a Gaussian form for the ejection velocity:

$$u_0(\tau) = v_0\, e^{-(\tau/\tau_0)^2}\,, \tag{4}$$

where τ_0 is the dispersion and v_0 the peak velocity, The time for the formation of a discontinuity (equation 3) is then:

$$t_{col} = -\frac{\tau_0^2}{2\tau} + \tau\,. \tag{5}$$

It is clear that for the flow ejected at large negative times the formation of a discontinuity occurs at a time $t_{col} = \tau$ (corresponding to the $\tau \to -\infty$ limit of equation 5). Therefore, the discontinuity is formed at the position of the outflow source ($x = 0$), and remains there until τ approaches τ_0 (see equation 4) and the ejection velocity begins to have significant values.

As discussed, e.g., by Raga et al. (1990), the discontinuities formed by an ejection velocity variability in a hypersonic jet correspond to two-shock "working surfaces". The motion of the "head" (leading working surface) of the flow produced by a Gaussian ejection velocity pulse is described in the following section. The region between the head and the outflow source is filled by material from part of the decreasing velocity wing of the ejection velocity pulse (see the schematic diagram of Figure 1).

3. THE MOTION OF THE PLASMON HEAD

Under the assumption of a cylindrical flow, the position x_{cm} of the center of mass of the material that has entered the working surface at the head of the plasmon (see equation 1 of Raga et al. 2020) is given by:

$$x_{cm} = \frac{\int_{-\infty}^{\tau} \rho_0 x_j u_0 d\tau' + \int_0^{x_{cm}} \rho_a x dx}{\int_{-\infty}^{\tau} \rho_0 u_0 d\tau' + \int_0^{x_{cm}} \rho_a dx}\,, \tag{6}$$

where ρ_a is the (possibly position-dependent) environmental density, $u_0(\tau')$ and $\rho_0(\tau')$ are the ejection velocity and density (respectively), x_j is given by:

$$x_j = (t-\tau')u_0(\tau')\,, \tag{7}$$

and the integration limit τ is the root of:

$$x_{cm} = (t-\tau)u_0(\tau)\,. \tag{8}$$

Following Cantó et al. (2000) and Raga et al. (2020), instead of inverting equation (8), we will use τ (i.e., the ejection time) as independent variable, and find x_{cm} (from equation 6) and the evolutionary time t (from equation 8) as a function of τ.

We now consider a Gaussian ejection velocity variability (see equation 4), a constant ejection density ρ_0 and a uniform ambient density ρ_a. Equation (6) then takes the form:

$$\frac{\rho_a x_{cm}^2}{2\rho_0} + x_{cm}\left[I_1 - \frac{1}{u_0(\tau)} I_2\right] = \tau\, I_2 - I_3\;, \tag{9}$$

where

$$I_1 = \int_{-\infty}^{\tau} u_0(\tau')d\tau' = \frac{\sqrt{\pi} v_0 \tau_0}{2}\left[1 + \mathrm{erf}\left(\frac{\tau}{\tau_0}\right)\right],$$
$$I_2 = \int_{-\infty}^{\tau} u_0^2(\tau')d\tau' = \sqrt{\frac{\pi}{2}}\frac{v_0^2\tau_0}{2}\left[1 + \mathrm{erf}\left(\frac{\sqrt{2}\tau}{\tau_0}\right)\right],$$
$$I_3 = \int_{-\infty}^{\tau} \tau' u_0^2(\tau')d\tau' = -\frac{v_0^2\tau_0^2}{4} e^{-2(\tau/\tau_0)^2}\,, \tag{10}$$

and

$$\mathrm{erf}\, x = \frac{2}{\sqrt{\pi}}\int_0^x e^{-x'^2}dx'\,, \tag{11}$$

is the error function.

From equations (9-10) we obtain the quadratic equation for x_{cm}:

$$\sigma\left(\frac{x_{cm}}{v_0\tau_0}\right)^2 + b\left(\frac{x_{cm}}{v_0\tau_0}\right) = c\,, \tag{12}$$

with

$$\sigma \equiv \sqrt{\frac{2}{\pi}}\frac{\rho_a}{\rho_0}\,, \tag{13}$$

$$b = \sqrt{2}\left[1 + \mathrm{erf}\left(\frac{\tau}{\tau_0}\right)\right] - e^{(\tau/\tau_0)^2}\left[1 + \mathrm{erf}\left(\frac{\sqrt{2}\tau}{\tau_0}\right)\right], \tag{14}$$

$$c = \left(\frac{\tau}{\tau_0}\right)\left[1 + \mathrm{erf}\left(\frac{\sqrt{2}\tau}{\tau_0}\right)\right] + \frac{e^{-2(\tau/\tau_0)^2}}{\sqrt{2\pi}}\,. \tag{15}$$

4. SOLUTIONS FOR DIFFERENT σ VALUES

4.1. *The $\sigma = 0$ "Free Plasmon"*

The σ parameter is the ratio between the environmental and ejection densities, multiplyed by a factor of order one (see equation 13). For the "free plasmon", $\sigma \to 0$ case, equation (12) has the solution:

$$\frac{x_{cm}}{v_0\tau_0} = \frac{\left(\frac{\tau}{\tau_0}\right)\left[1 + \mathrm{erf}\left(\frac{\sqrt{2}\tau}{\tau_0}\right)\right] + \frac{e^{-2(\tau/\tau_0)^2}}{\sqrt{2\pi}}}{\sqrt{2}\left[1 + \mathrm{erf}\left(\frac{\tau}{\tau_0}\right)\right] - e^{(\tau/\tau_0)^2}\left[1 + \mathrm{erf}\left(\frac{\sqrt{2}\tau}{\tau_0}\right)\right]}\,. \tag{16}$$

Numerically, we find that the denominator $\to 0$ as

$$\tau \to \tau_a = 0.4953\tau_0\,, \tag{17}$$

and then $x_{cm} \to \infty$ at $\tau = \tau_a$. This result implies that none of the material from the $\tau > \tau_c$ wing of the ejection pulse (see equation 4) ever reaches the working surface. Therefore, the leading head has to asymptotically approach a velocity

$$v_a = u_0(\tau_a) = 0.7825\, v_0\,. \tag{18}$$

Using the appropriate integrals from equation (10), we find that the mass of the plasmon as a function of τ is:

$$M_p(\tau) = \frac{M_0}{2}\left[1 + \mathrm{erf}\left(\frac{\tau}{\tau_0}\right)\right], \tag{19}$$

where M_0 is the mass of the ejection pulse. Evaluated at τ_a (see equation 17) we obtain an asymptotic mass $M_{asym} = 0.753 M_0$. In other words, $\approx 75\%$ of the mass of the pulse is incorporated into the head of the plasmon, and $\approx 25\%$ remains in the "tail" that joins the outflow source and the head.

4.2. *Solutions for $\sigma > 0$*

For $\sigma > 0$, the position x_{cm} of the head of the plasmon can be straightforwardly obtained by inverting equation (9), and evaluating the integrals (see equation 10) as a function of the ejection time τ. Also,

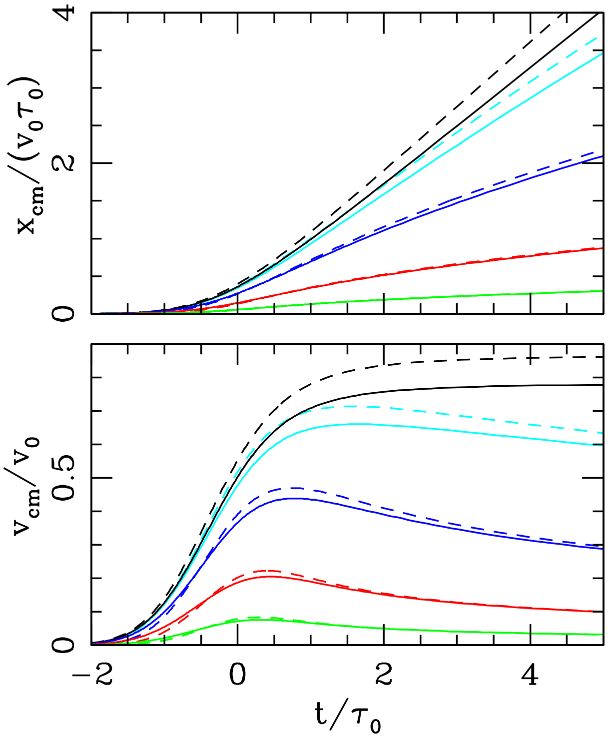

Fig. 2. Dimensionless position (top) and velocity (bottom) of the plasmon head as a function of evolutionary time for $\sigma = 0$ (black curve), 0.1 (cyan), 1.0 (blue), 10 (red) and 100 (green). The solid curves show the results for the constant ejection density problem, and the dashed curves show the Gaussian ejection density case (with σ_1 values equal to the σ values given above). The color figure can be viewed online.

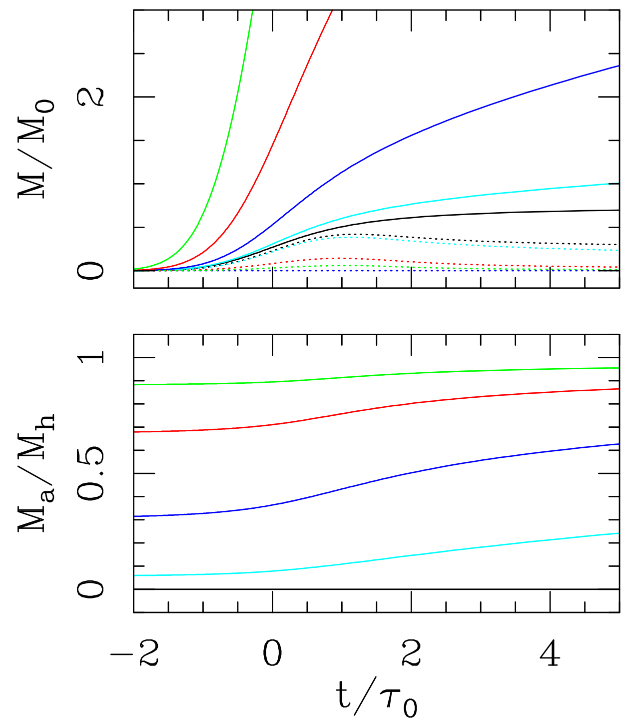

Fig. 3. Dimensionless mass (top) of the "constant density plasmon" head M_h (solid curves) and tail M_t (dashed lines), and fraction of environmental mass within the head (bottom). The results obtained for models with $\sigma = 0$ (black curves), 0.1 (cyan), 1.0 (blue), 10 (red) and 100 (green) are shown. The color figure can be viewed online.

calculating the evolutionary time t as a function of τ (see equation 8), we can obtain $x_{cm}(t)$. Doing the appropriate time derivatives (analytically or numerically), we can also obtain the velocity $v_{cm} = dx_{cm}/dt$ of the plasmon head.

The results obtained for different values of σ are shown in Figure 2. It is clear that for $\sigma = 0$ the plasmon reaches the asymptotic velocity v_a (see equation 18). For $\sigma > 0$, v_{cm} reaches a maximum value and then decreases as a funciton of time as the plasmon head incorporates more environmental material.

For $\sigma > 0$, the head of the plasmon has a mass given by the contribution from the ejection pulse (see equation 19) and also a contribution from the environment:

$$M_a(\tau) = M_0 \, \frac{\sigma}{\sqrt{2}} \frac{x_{cm}(\tau)}{v_0 \tau_0} \, , \tag{20}$$

where M_0 is the mass of the ejection pulse and σ is given by equation (13).

The mass in the tail (i.e., in the continuous beam segment between $x = 0$ and x_{cm}) is:

$$M_t(\tau) = \frac{M_0}{2} \left[\mathrm{erf}\left(\frac{t}{\tau_0}\right) - \mathrm{erf}\left(\frac{\tau}{\tau_0}\right) \right] \, , \tag{21}$$

In Figure 3 we plot the mass M_t of the tail, the total mass $M_h = M_p + M_a$ of the plasmon head and the fraction M_a/M_h of this mass that corresponds to the swept-up environment as a function of the evolutionary time t for models with different σ values.

5. THE CASE OF A GAUSSIAN EJECTION DENSITY VARIABILITY

Let us now consider an ejection with a Gaussian velocity variability (see equation 4) and also with a Gaussian density variability:

$$\boldsymbol{\rho_0}(\tau) = \rho_0 \, e^{-(\tau/\tau_0)^2} \, , \tag{22}$$

of the same shape. In this equation, $\boldsymbol{\rho_0}(\tau)$ (in boldface) is the time-dependent ejection density, and ρ_0 is the peak density.

Inserting the ejection velocity (equation 4) and density (equation 22) variabilities into equation (6), we obtain an equation of the same form as (9), but with

$$I_1 = \sqrt{\frac{\pi}{2}}\frac{v_0\tau_0}{2}\left[1+\mathrm{erf}\left(\frac{\sqrt{2}\tau}{\tau_0}\right)\right],$$
$$I_2 = \sqrt{\frac{\pi}{3}}\frac{v_0^2\tau_0}{2}\left[1+\mathrm{erf}\left(\frac{\sqrt{3}\tau}{\tau_0}\right)\right], \tag{23}$$
$$I_3 = -\frac{v_0^2\tau_0^2}{6}e^{-3(\tau/\tau_0)^2}.$$

Combining equations (9) and (23), we obtain the quadratic equation for x_{cm}:

$$\sigma_1\left(\frac{x_{cm}}{v_0\tau_0}\right)^2 + b_1\left(\frac{x_{cm}}{v_0\tau_0}\right) = c_1\,, \tag{24}$$

with

$$\sigma_1 \equiv \sqrt{\frac{3}{\pi}}\frac{\rho_a}{\rho_0}\,, \tag{25}$$

$$b_1 = \sqrt{\frac{3}{2}}\left[1+\mathrm{erf}\left(\frac{\sqrt{2}\tau}{\tau_0}\right)\right] - e^{(\tau/\tau_0)^2}\left[1+\mathrm{erf}\left(\frac{\sqrt{3}\tau}{\tau_0}\right)\right], \tag{26}$$

$$c_1 = \frac{\tau}{\tau_0}\left[1+\mathrm{erf}\left(\frac{\sqrt{3}\tau}{\tau_0}\right)\right] + \frac{e^{-3(\tau/\tau_0)^2}}{\sqrt{3\pi}}. \tag{27}$$

The position x_{cm} and velocity dx_{cm}/dt as a function of t obtained for different σ_1 values are shown in Figure 2. It is clear that for all σ_1 values, the plasmon head is faster than the "constant density plasmon" with $\sigma = \sigma_1$ (see equations 13 and 25). For $\sigma_1 = \sigma > 0$, the "Gaussian density" and "constant density" plasmons converge to the same velocity for $t \gg \tau_0$.

Also, using the appropriate integral from equation (23), we find that the contribution from the ejection pulse to the mass of the plasmon head as a function of τ is:

$$M_{p,1}(\tau) = \frac{M_0}{2}\left[1+\mathrm{erf}\left(\frac{\sqrt{2}\tau}{\tau_0}\right)\right], \tag{28}$$

where M_0 is the mass of the ejection pulse. The mass in the tail (i.e., in the continuous beam segment between $x = 0$ and x_{cm}) is:

$$M_{t,1}(\tau) = \frac{M_0}{2}\left[\mathrm{erf}\left(\frac{\sqrt{2}t}{\tau_0}\right) - \mathrm{erf}\left(\frac{\sqrt{2}\tau}{\tau_0}\right)\right], \tag{29}$$

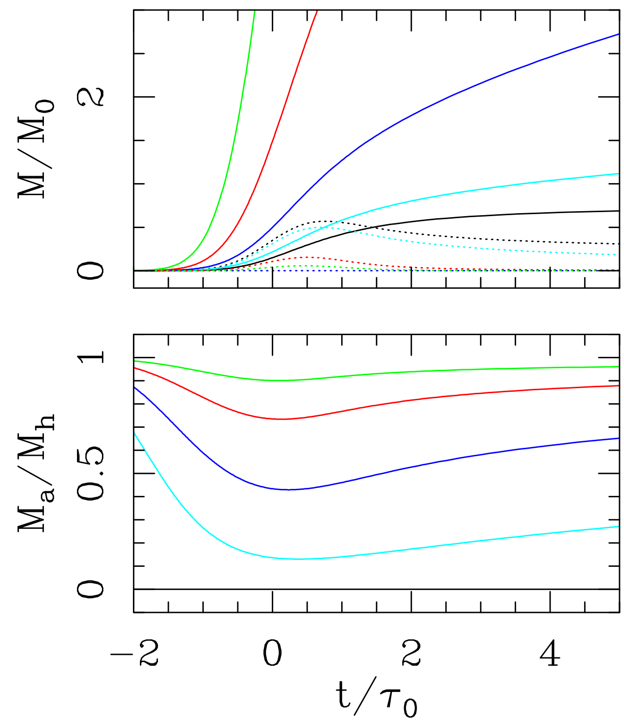

Fig. 4. Dimensionless mass (top) of the "Gaussian density plasmon" head M_h (solid curves) and tail M_t (dashed lines), and fraction of environmental mass within the head (bottom). The results obtained for models with $\sigma_1 = 0$ (black curves), 0.1 (cyan), 1.0 (blue), 10 (red) and 100 (green) are shown. The color figure can be viewed online.

The head of the plasmon has a mass given by the contribution from the ejection pulse (see equation 28) and a contribution from the environment:

$$M_{a,1}(\tau) = \sqrt{\frac{2}{3}}M_0\sigma_1\frac{x_{cm}(\tau)}{v_0\tau_0}\,, \tag{30}$$

where M_0 is the mass of the ejection pulse and σ_1 is given by equation (25).

In Figure 4 we plot the mass $M_{t,1}$ of the tail, the total mass $M_{h,1} = M_{p,1} + M_{a,1}$ of the plasmon head and the fraction $M_{a,1}/M_{h,1}$ of this mass that corresponds to the swept-up environment as a function of the evolutionary time t for models with different σ_1 values. The results are qualitatively similar to the ones obtained for the constant ejection density plasmon (see Figure 2).

6. THE VELOCITY AND DENSITY STRUCTURE OF THE TAIL

We now calculate the density along the plasmon tail. To this effect, we use the solution to the continuity

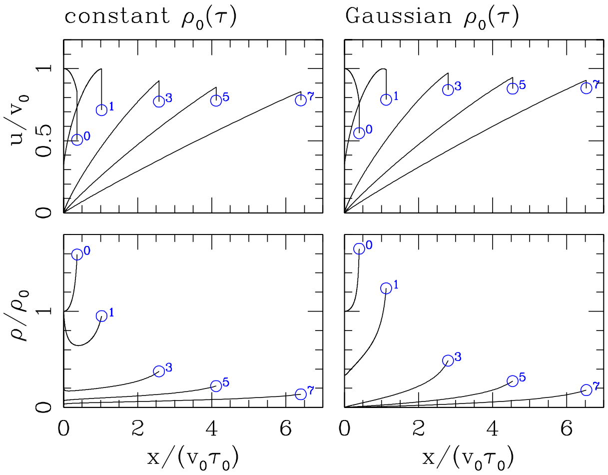

Fig. 5. Velocity (top) and density (bottom) vs. position along the plasmon tails, for evolutionary times $t/\tau_0 = 0$, 1, 3, 5 and 7 (the curves are labeled with these times). The curves end in an open circle, which indicates the position (and in the top diagrams, the velocity) of the plasmon head. The results obtained for the constant ejection density case are shown in the left frames, and the ones obtained for the Gaussian ejection density on the right. The color figure can be viewed online.

equation of a free-streaming, plane-parallel flow:

$$\rho = \frac{\rho_0(\tau)u_0(\tau)}{u_0(\tau) - (t-\tau)\dot{u}_0(\tau)}\,, \tag{31}$$

where $\dot{u}_0(\tau) = du_0/d\tau$ (see, e.g., Raga & Kofman 1992). For our Gaussian $u_0(\tau)$ (see equation 4) we then have:

$$\rho(x,t) = \frac{\rho_0(\tau)}{1 + 2(t-\tau)\tau/\tau_0^2}\,, \tag{32}$$

where x, t and τ are related to each other through the free-streaming condition (equation 1).

In Figure 5, we show the free streaming velocity and density along the tail of the constant ejection density (see § 4) and Gaussian ejection density (§ 5) free plasmons (i.e., with $\sigma = 0$) for different evolutionary times. As shown by Raga et al. (2020, who studied a plasmon with a parabolic ejection velocity), for $t > \tau_0$ the plasmon tail develops a "Hubble law" linear velocity vs. position dependence.

For both plasmon solutions, the density along the tail has its peak value approaching the position of the plasmon head (at all times shown in Figure 5). At $t = \tau_0$, the constant ejection density plasmon tail has a second peak at $x = 0$, and develops a flat density vs. position structure at larger evolutionary times. At $x = 0$, the Gaussian ejection density plasmon has a density that $\to 0$ at larger evolutionary times, leading to steeper density vs. position dependencies.

7. SUMMARY

As a follow up to the paper of Raga et al. (2020), who studied the flow resulting from an ejection velocity pulse with a parabolic time-dependence (and a time-independent mass loss rate), we consider ejection pulses with different time histories.

In particular, we study the flow resulting from a collimated ejection velocity pulse with a Gaussian time-dependence, considering the cases of a constant ejection density and a density with a Gaussian time-dependence (with the same width as the ejection velocity), moving into a uniform environment. Using the "center of mass formalism" of Cantó et al. (2000), we derive full analytic solutions (given in terms of the error function) for both cases.

We calculate the position and velocity of the plasmon head as a function of time, and obtain very similar results for the constant and Gaussian ejection densities (Figure 2). The two cases produce an initial acceleration of the plasmon head, followed by a convergence to a constant velocity (for the $\sigma = 0$, "free plasmon" case) or by a gradual velocity decrease for cases with substantial environmental braking (i.e., for $\sigma > 0$).

We also calculate the mass in the head and tail of the plasmon as a function of evolutionary time. We find that:

- for the constant ejection density plasmon: when $\sigma = 0$ the mass of the head is ≈ 3 times the tail mass for large evolutionary times. For $\sigma > 0$, the tail has less mass, and the head much larger masses (in part, due to the accumulation of environmental material in the head).

- for the Gaussian ejection density plasmon: the tail has somewhat larger masses. For times $t \approx \tau_0$, we find that the $\sigma = 0$ solution has tail masses ≈ 2 times the head mass, but for $t \gg t_0$ this proportion is reversed.

Finally, we calculate the velocity and mass as a function of position for the $\sigma = 0$ plasmons (see Figure 5). We recover the result of Raga et al. (2020) that for $t > \tau_0$ the tail has a velocity structure that approaches a linear "Hubble law" velocity vs. position. For the density structure, we see that there is a peak just before the head of the plasmon. In the rest of the tail, there are substantial differences between the constant and Gaussian ejection density cases, with the former case having zero density at

$x = 0$, and the latter case having a density ≈ 2 times lower than the peak density (at the position just before the head).

Therefore, we find that the assumption of a constant or a Gaussian time-dependent ejection density does not affect the dynamical characteristics of the "head/tail plasmon" in a substantial way. The main differences between these two cases are the mass and the density distribution within the plasmon tail.

We should note that the dynamical characteristics of the plasmons studied in this paper are also very similar to the ones of the "parabolic velocity pulse" plasmon studied by Raga et al. (2020). From this, we conclude that at least at large evolutionary times (i.e., for $t > \tau_0$) the dynamics of the head/tail plasmon are mostly independent of the details of the velocity and density ejection histories. The only important effect of different forms of the ejection is to change the mass content and density stratification of the material in the plasmon tail.

Now, the way forward to study the head/tail plasmon flow is with full axisymmetric or 3D numerical simulations of the flow. This will allow, among other things, an evaluation of the observational characteristics of the flow and of the stability of the plasmon head at large evolutionary times. Also, it would be interesting to extend the present work to the relativistic case, since it would have clear applications to microquasars and gamma-ray bursts.

This work was supported by the DGAPA (UNAM) grant IG100218. A.C.R. acknowledges support from a DGAPA-UNAM postdoctoral fellowship.

REFERENCES

Alcolea, J., Bujarrabal, V., Sánchez Contreras, C., Neri, R., & Zweigle, J. 2001, A&A, 373, 932

Allen, David A. & Burton, Michael G. 1993, Natur, 363, 54

Bally, J., Ginsburg, A., Arce, H., et al. 2017, ApJ, 837, 60

Cantó, J., Raga, A. C., & D'Alessio, P. 2000, MNRAS, 313, 656

De Young, D. S. & Axford, W. I. 1967, Natur, 216, 129

Dennis, T. J., Cunningham, A. J., Frank, A., et al. 2008, ApJ, 679, 1327

Raga, A. C., Rodríguez-González, A., Hernández-Martínez, L., Cantó, J., & Castellanos-Ramírez, A. 2020, MNRAS, in press

Raga, A. C. & Kofman, L. 1992, ApJ, 386, 222

Rivera-Ortíz, P. R., Rodríguez-González, A., Hernández-Martínez, L., Cantó, J., & Zapata, L. A. 2019a, ApJ, 885, 104

Rivera-Ortíz, P. R., Rodríguez-González, A., Hernández-Martínez, L., & Cantó, J. 2019b, ApJ, 874, 38

Zapata, L. A., Loinard, L., Schmid-Burgk, J., et al. 2011, ApJ, 726, 12

J. Cantó and A. Castellanos-Ramírez: Instituto Astronomía, Universidad Nacional Autónoma de México, Ap. 70-468, 04510 CDMX, México.

L. Hernández-Martínez: Facultad de Ciencias, Universidad Nacional Autónoma de México, Av. Universidad 3000, Circuito Exterior S/N, 04510 CDMX, México.

A. C. Raga and A. Rodríguez-González: Instituto de Ciencias Nucleares, Universidad Nacional Autónoma de México, Ap. 70-543, 04510 CDMX, México (raga@nucleares.unam.mx).

Revista Mexicana de Astronomía y Astrofísica, **57**, 241–246 (2021)

https://doi.org/10.22201/ia.01851101p.2021.57.01.18

RESULTS OF OBSERVATIONS OF MAXIMA OF PULSATING STARS[1]

J. H. Peña[2,3,4], H. Huepa[2], D. S. Piña[3,4], J. Guillén[4], A. Rentería[2], J. D. Paredes[5], R. Muñoz[6], J. Donaire[6], and T. Benadalid[6]

Received July 23 2020; accepted January 29 2021

ABSTRACT

The systematic study of some HADS stars, recognized as variables for decades, has allowed us to provide data on their secular variations through O-C analysis. However, some of the data have large gaps without observations. This is our motivation for continuously observing these stars as part of the research carried out by the "Grupo de Astronomía Observacional del Observatorio de Tonantzintla" (GAOOT). This article is our third compilation of times of maxima for pulsating stars. These observations have been carried out at the Observatorio Astronómico Nacional de Tonantzintla (TNT) and San Pedro Mártir (SPM), México and for the first time we also present data from the Complejo Astronómico de Cota Cota, Bolivia (Universidad Mayor de San Andrés) and the Observatorio Astronómico Centroamericano de Suyapa, Honduras (Universidad Nacional Autónoma de Honduras).

RESUMEN

El estudio sistemático de algunas estrellas pulsantes HADS ha permitido proporcionar datos sobre sus variaciones seculares mediante el analisis O-C. Sin embargo, en algunas de ellas los datos presentan grandes vacíos temporales sin observaciones. Esta es una motivación por la que hemos decidido observar continuamente estas estrellas como parte del trabajo que realiza el Grupo de Astronomía Observacional del Observatorio de Tonantzintla. Este grupo presenta esta tercera compilación de tiempos de máximo de estrellas pulsantes. Dichas observaciones se han llevado a cabo en los Observatorios Astronómicos Nacionales de Tonantzintla (TNT) y San Pedro Mártir (SPM), México a los que se han unido el Complejo Astronómico de Cota Cota, Bolivia (Universidad Mayor de San Andrés, Bolivia) y el Observatorio Astronómico Centroamericano de Suyapa (Universidad Nacional Autónoma de Honduras).

Key Words: ephemerides — stars: variables: Scuti

1. MOTIVATION

The study of δ Scuti stars has been carried out for many years since the pioneering works of Breger (1966) and Millis (1966). It was shortly after this that the monitoring of some of these stars was started in Mexico (Warman, Malacara and Breger, 1974, Warman, Peña and Arellano Ferro, 1979) and it has continued ever since.

More recently, with the acquisition of CCD detectors thirteen years ago, the observations of δ Scuti stars were retaken at the Observatorio Astronomico Nacional de Tonantzintla (TNT) with the participation of many students of the Observational Astronomy courses taught at the UNAM and later of the Escuela Latinoamericana de Astronomía Observacional (ESAOBELA). These students have provided us with motivation, and have supplied an eager workforce.

[1]Based on observations collected at the San Pedro Mártir and Tonantzintla Observatories, México, Tegucigalpa at Honduras and La Paz, Bolivia.

[2]Observatorio Astronómico Nacional de Tonantzintla, Universidad Nacional Autónoma de México, México.

[3]Instituto de Astronomía, Universidad Nacional Autónoma de México, México.

[4]Facultad de Ciencias, Universidad Nacional Autónoma de México, México.

[5]Facultad de Ciencias, Universidad Central de Venezuela, Venezuela.

[6]Planetario Max Schreier, Universidad Mayor de San Andrés, Bolivia.

TABLE 1

CHARACTERISTICS OF THE OBSERVED STARS

ID	RA	Dec	Magnitude	Spectral Type	Epoch (d)	P (d)
AD Ari	02 17 45	+18 27 18.00	7.43	F0	2453330.654	0.53972
RV Ari	02 15 07	+18 04 27.91	11.61	A0		0.09312808
BE Lyn	09 18 17	+46 09 11.31	8.80	A3		
BL Cam	03 47 19	+63 22 42.14	13.03			0.03909844
V367 Cam	04 40 55	+53 38 06.46	10.47			0.121596
KU Cen	11 51 51	-41 17 09.23	13.48			0.07996
AD Cmi	07 52 47	+01 35 50.47	9.38	F0IV/V	2453478.4714	0.1229746
AZ Cmi	07 44 07	+02 24 19.52	6.47	A5IV		0.095205
VZ Cnc	08 40 52	+09 49 27.15	7.18	A9III		0.178364
KZ Hya	10 50 54	-25 21 14.72	10.06	B9III/IV	2442516.15836	0.0595104212
AN Lyn	09 14 28	+42 46 38.36	10.64	A7IV/V		
BO Lyn	08 43 01	+40 59 51.77	11.49			
SZ Lyn	08 09 35	+44 28 17.61	9.08	F2	2438124.39824	0.120534920
TV Lyn	07 33 31	+47 48 09.83	11.54	A6	2440950.922	0.24065119
1 Mon	05 59 01	-09 22 56.00	6.16	F2/3IV	2441661.1668	0.13612600
V1162 Ori	05 32 01	-07 15 24.65	9.9			
RR Leo	10 07 43	+23 59 30.32	9.94	F0	2443295.402	0.4523933
V369 Sct	18 51 16	-06 21 11.16	9.35	F3/5II	2440393.709	0.223
AE Uma	09 36 53	+44 04 00.40	11.35	A9	2435604.338	0.086017055
EX Uma	08 45 12	+56 36 26.76	11.02			
GW Uma	10 44 11	+44 40 44.11	9.89	F3V		
YZ Boo	15 24 06	+36 52 00.60	10.36	F0	2448500.0030	0.1040920
EH Lib	14 58 55	-00 56 53.01	9.83	A5	2433438.6082	0.0884132445

TABLE 2

TIMES OF MAXIMUM LIGHT OF THE VARIABLE STARS CONSIDERED

ID	Date	N	Δt(d)	Nmax	Tmax +2450000	Telescope	Filters	Detector	Observatory	Observers/ Reducers
AD Ari	19120607	368	0.2119	1	8824.6543	Me	V	1001	TNT	JGT,HHC/JGT
RV Ari	19112930	81	0.1294	1	8817.7421	Me	V	1001	TNT	FS,DSP/DSP
	19113031	113	0.1841	2	8818.7621	Me	V	1001	TNT	FS,DSP/DSP
	19113031				8818.8606					
BE Lyn	17032223	420	0.1173	1	7835.6745	M8	G	402	OACS	AA/ARL,GIEP
BL Cam	20011112	122	0.0960	3	8860.7052	M2	wo	andor	TNT	E20/HHC
					8860.7448					
					8860.7842					
	20011213	162	0.1396	3	8861.7247	M2	wo	andor	TNT	E20/HHC
					8861.7641					
					8861.8022					
	20011314	116	0.0880	3	8862.7415	M2	wo	andor	TNT	E20/HHC
					8862.7804					
					8862.8204					
	20011415	151	0.1230	3	8863.7182	M2	wo	andor	TNT	E20/HHC
					8863.7599					
					8863.7959					
	20011617	117	0.0906	2	8865.7510	M2	wo	andor	TNT	E20/HHC
					8865.7905					
	20011718	146	0.1187	2	8866.7287	M2	wo	andor	TNT	E20/HHC
					8866.7684					
	20022425	40	0.0819	2	8904.6927	84	$uvby-\beta$	danish	SPM	DSP/DSP
					8904.7318					

TABLE 2. CONTINUED

ID	Date	N	Δt(d)	Nmax	Tmax +2450000	Telescope	Filters	Detector	Observatory	Observers/ Reducers
V367 Cam	20011314	91	0.1442	1	8862.8298	M1	V	ST-8300	TNT	E20/JGT
KU Cen	20011213	97	0.0818	1	8861.9195	M2	wo	andor	TNT	E20/HHC
	20011314	100	0.0724	1	8862.8795	M2	wo	andor	TNT	E20/HHC
	20011415	120	0.0934	1	8863.9195	M2	wo	andor	TNT	E20/HHC
	20011617	137	0.1232	2	8865.9165	M2	wo	andor	TNT	E20/HHC
					8865.9965					
AD CMi	16021112	130	0.1400	1	7430.7541	M2	V	1001	TNT	DSP/DSP
	16031112	167	0.1500	1	7459.6543	M1	V	1001	TNT	AOA16/DSP
	17011415	144	0.1200	1	7768.8131	M1	V	1001	TNT	E17/DSP
	17120607	40	0.1000	1	8095.0522	84	$uvby-\beta$	danish	SPM	JCC,DSP/DSP
	18030203	142	0.1600	1	8180.7831	M1	V	1001	TNT	AOA18/DSP
	18030304	157	0.1500	1	8181.7596	M1	V	1001	TNT	AOA18/DSP
	18031718	129	0.1300	1	8195.7759	M1	V	1001	TNT	AOA18/DSP
	19011415	84	0.1500	1	8498.8915	M2	G	ST-800	TNT	E19/HHC
	19011516	97	0.1500	1	8499.8951	M2	G	ST-800	TNT	E19/HHC
	19011819	205	0.1600	1	8502.8419	M2	G	ST-800	TNT	E19/HHC
	19012122	141	0.1900	1	8505.9170	M2	G	ST-800	TNT	E19/HHC
	19012223	186	0.2100	2	8506.7780	M2	G	ST-800	TNT	E19/HHC
					8506.9044					
	19020102	228	0.2700	2	8516.7387	M2	wo	ST-8300	TNT	JGT/JGT
					8516.8638					
	19031617	187	0.1400	1	8559.7805	Me	V	1001	TNT	AOA19/ARL
AZ CMi	20021920	51	0.1151	1	8899.8223	84	$uvby-\beta$	danish	SPM	DSP/DSP
VZ Cnc	18031718	267	0.2107	1	8195.7696	M1	G	ST-800	TNT	JGT,HHC/JGT
	19012122	211	0.1873	1	8505.9443	M1	G	ST-800	TNT	E19/JGT
	19012223	372	0.2447	1	8506.8515	M1	G	ST-800	TNT	E19/JGT
	19121011	383	0.1198	1	8828.9646	Me	V	ST-8300	TNT	JGT/JGT
	20022526	36	0.2352	1	8905.8573	84	$uvby-\beta$	danish	SPM	DSP/DSP
	20022627	49	0.0969	1	8906.9136	84	$uvby-\beta$	danish	SPM	DSP/DSP
	20032829	150	0.1304	1	8937.7654	M1	V	ST-8300	TNT	JGT/JGT
KZ Hya	17032223	270	0.7285	1	7835.7613	M8	G	402	OACS	AA/ARL,GIEP
	18021617	87	0.0919	2	8166.7547	Me	V	1001	TNT	SBJ,ALZ/HHC
					8166.8144					
	19020102	6	0.0678	1	8516.9686	M2	G	ST-800	TNT	Bo19/JGT
	19030102	50	0.0409	1	8544.8786	M1	V	1001	TNT	AOA19/HHC
	19040506	1393	0.2109	3	8579.6324	M8	G	402	OACS	Ho19/ARL,GIEP
					8579.6918					
					8579.7512					
	19042021	110	0.0930	2	8594.6884	Me	V	1001	TNT	DSP/DSP
					8594.7480					
	20012021	87	0.0892	1	8869.9210	Me	V	1001	TNT	E20/DSP,HHC
	20031314	64	0.0565	1	8922.8845	Me	V	1001	TNT	AOA20/HHC
	20031314	40	0.0309	1	8922.8847	M1	V	ST-8300	TNT	AOA20,JGT/HHC,JGT
AN Lyn	20010910	394	0.0966	1	8859.9659	M2	wo	andor	TNT	E20/HHC
BO Lyn	19011516	176	0.1419	2	8499.7999	Me	V	1001	TNT	E18/JGT
					8499.8890					
SZ Lyn	18011213	90	0.0702	1	8131.8979	M1	V	ST-8300	TNT	E18/HHC
	18011516	165	0.1672	1	8134.9104	M1	V	ST-8300	TNT	E18/HHC
	18011617	176	0.0873	2	8135.7517	M1	V	ST-8300	TNT	E18/HHC
					8135.8755					
	18012021	121	0.1053	1	8139.8537	M1	V	ST-8300	TNT	E18/HHC
	19020203	115	0.1106	1	8517.8584	M2	G	ST-800	TNT	Bo19/JGT
TV Lyn	19011617	300	0.0208	1	8135.8526	M2	G	ST-800	TNT	E18/HHC
	19020405	304	0.2884	1	8519.7864	M2	G	ST-800	TNT	Bo19/JGT

TABLE 2. CONTINUED

ID	Date	N	Δt(d)	Nmax	Tmax +2450000	Telescope	Filters	Detector	Observatory	Observers/ Reducers
	19020708	190	0.2903	1	8522.7723	M2	G	ST-800	TNT	Bo19/JGT
1 Mon	19020506	187	0.1481	1	8520.7220	M2	G	ST-800	TNT	Bo19/JGT
V1162 Ori	20011213	151	0.1118	1	8861.8051	Me	V	1001	TNT	E20/DSP
	20011718	185	0.1533	2	8866.7603	Me	V	1001	TNT	E20/DSP
					8866.8368					
	20022324	41	0.0940	1	8903.7422	84	$uvby-\beta$	danish	SPM	DSP/DSP
RR Leo	19011314	90	0.0881	1	8497.8039	Me	V	1001	TNT	Bo19/DSP
	19012122	260	0.2516	1	8505.9479	Me	V	1001	TNT	Bo19/DSP
	19012223	310	0.2804	1	8506.8542	Me	V	1001	TNT	Bo19/DSP
	19013101	390	0.3257	1	8515.9003	Me	V	1001	TNT	Bo19/DSP
	19020102	390	0.3589	1	8516.8054	Me	V	1001	TNT	Bo19/DSP
	19020203	363	0.3211	1	8517.7120	Me	V	1001	TNT	Bo19/DSP
	20022425	72	0.1883	1	8904.9676	84	$uvby-\beta$	danish	SMP	DSP/DSP
	20022526	36	0.2635	1	8905.8787	84	$uvby-\beta$	danish	SPM	DSP/DSP
	20033031	375	0.3155	1	8939.8071	M1	V	ST-8300	TNT	JGT/JGT
V369 Sct	19082930	471	0.1785	1	8817.7421	C16	v	1001	CotaCota	JMD/DSP
AE Uma	18011617	162	0.0545	2	8135.8224	Me	V	1001	TNT	E18
					8135.9041	Me	V	1001	TNT	
	18021617	90	0.0746	1	8166.8715	Me	V	1001	TNT	SBJ,ALZ/HHC
	18032526	100	0.0842	1	8203.8565	M1	G	ST-800	TNT	JGT/JGT
	19011415	69	0.1120	1	8498.8116	Me	V	1001	TNT	E19/JGT,DSP
	19020304	273	0.1925	2	8518.7688	Me	V	1001	TNT	Bo19/JGT
					8518.8482					
EX Uma	20011617	135	0.2232	1	8865.9608	M1	G	ST-8300	TNT	E20/JGT
GW Uma	19020102	218	0.1738	1	8516.9623	M1	V	1001	TNT	Bo19/JGT
	19020203	267	0.2392	1	8517.7795	M1	V	1001	TNT	Bo19/JGT
	19022122	220	0.1721	1	8536.8787	M1	G	ST-800	TNT	JGT
	19022324	124	0.1085	1	8538.9137	1M	V	ST-8300	TNT	JGT,APC/JGT
	20011415	101	0.1310	1	8864.0182	M1	G	ST-8300	TNT	E20/JGT
YZ Boo	18032829	120	0.1123	1	8206.8536	M1	G	ST-800	TNT	JGT,DSP/JGT
	18030304	90	0.0800	1	8181.8708	me	V	1001	TNT	AOA18/HHC
	18031617	76	0.8148	1	8194.8829	me	V	1001	TNT	AOA18/HHC
	19042021	130	0.1172	1	8594.8027	Me	V	1001	TNT	DSP/DSP
	20021920	30	0.0653	1	8899.9954	84	$uvby-\beta$	danish	SPM	DSP/DSP
	20022324	68	0.1622	2	8903.8477	84	$uvby-\beta$	danish	SPM	DSP/DSP
EH Lib	18031718	129	0.1114	2	8195.8240	me	V	1001	TNT	AOA18/HH
					8195.9122					

Remarks:

1. Telescope

1M - 1m telescope

ME - 10" Meade LX200 telescope Equatorial

M1 - 10" Meade LX200 telescope

M2 - 10" Meade LX200 telescope

C11 - 11" Celestron telescope

84 - 0.84m telescope

C16 - 16" Celestron Pacific telescope

M8 - Meade LX200 telescope

2. Detector

ST8 - CCD SBIG ST-8

1001 - CCD SBIG ST-1001

8300 - CCD SBIG ST-8300

danish - $uvby$-β Photometer

402 - CCD SBIG ST-402

3. Filter

V - V-filter in UBV system

G - Green in RGB set

V - y-filter in $uvby$ system

wo - Without filter

Remarks (Continued). Observers.: AA: A. Artola (UNAH); ALZ: A. L. Zuñiga; ARL: A. Rentería; DSP: D. S. Piña; FS: F. Saldaña; JCC: J. Calderón; JGT: J. Guillen; JHP: J. H. Peña; SBJ: S. B. Juárez.

E17 (ESAOBELA 2017): Ramirez, Vanesa; Rodríguez, Mariana; Vargas, Stephany; Castellón, Cindy; Salgado, Ricardo; Mata, Joaquin; Santa Cruz, Raúl; Chipana, Karol; Gonzales, Lisseth; Rodríguez, Reina; De la Fuente, Diana.

E18 (ESAOBELA 2018): Calle, Carla; Huanca, Ever; Uchima, Juan Pablo; Ramírez, Raquel; Funes, Ricardo; Martinez, Juan José; Sarmiento, Karina; Cruz, Mauricio; Meza, Enith; Alvarado, Mayubell; Huaman, Victor; Ochoa, Gerson; Matamoros, Andrea.

E19 (ESAOBELA 2019): Blanco, Agustina; Benadalid, Tania; Donaire, Johany; Salazar, Luis; Quirós-Rojas, Marianela; Portllo, Alejandro; Escobar, Pablo; Mejía, Raquel; Mireles, Monica; León, Antonis; Zelada, Cindy; Báez, Sol-haret; Ng,Jessica.

E20 (ESAOBELA 2020): Carrasco, Laura; Vargas, Camilo; Barba, Miguel; Martinez, Glenda; Castellanos, Mitsa; Mejia, Nicole; Buenfil, Guadalupe; Vásquez, Franklin; Martínez, Bexy; Beato, Manuel; Paredes, Jhonnayker; Muñoz, Fernanda; Salazar, Azalea.

AOA16: Juarez, Karen; Lozano, Karen; Padilla, Artemio; Velázquez, Roberto; Santillan, Priscila.

AOA18: Bustos, Sergio; Carrillo, José Luis; Chávez, Brian; Navez, David; Zuñiga, Ana.

AOA19: Briones, Joshua; Castro, Celeste; Martínez, Fernanda; Posadas, Hilde; Romero, Mitzi; Soberanes, Hilkar; Velasco, Alex.

AOA20: Blas, Karla; Madrigal, Norma; Perez, Alexis; Ramirez, José; Santiago, Beatríz.

Bo19 (Bolivia 19): Benadalid, Tania; Donaire, Johany; Muñoz, Ruber.

Ho19 (OACS Honduras 2019): Artola, Adán; Meza, Maria Renee; Mejia, Luis Fernando.

GIEP: Meza, María Renee; Argueta, Christian

HADS stars provided excellent targets since they have short periods of pulsation, large amplitudes and, most of them have been observed for large time spans providing a unique chance to study their secular variations. Surprisingly, most of the observed stars we studied show evidence of a light travel-time effect, suggesting the presence of another invisible companion star.

What we have found is that some of these stars have lacked continuous observations and that there are large gaps in which they were not observed. Conscious of the need for long continuous observations, we developed a systematic monitoring of HADS stars at Tonantzintla to pursue our study of HADS double systems.

Aware of this need we have previously presented two lists of times of maxima of pulsating stars (Peña et al. 2015 and Peña et al. 2017) and here we present the third list of results from our observations.

2. DATA COLLECTION

This is the third compilation of OAN results of 23 variable stars obtained from 2016 to March, 2020. These observations also include some maxima from the Observatorio Astronómico Centroamericano de Suyapa, Honduras and the Complejo Astronómico de Cota Cota, Bolivia. The results are presented for 23 stars, of which 114 maxima of pulsating stars were obtained.

The CCD reduction was done with AstroImageJ (Collins et al. 2017) whereas the photoelectric observations were reduced using a classical procedure (see Peña et al., 2016 for details). All times of maxima are heliocentric and were determined with a fifth grade polynomial fitting to the light curve.

The errors were determined from the RMS error of the residuals evaluated for the times of maxima, and are about 0.016 days. The accuracy of each point is given by the exposure time and varies between 3 min for the 1-meter telescope and 1 min for the smaller telescopes. It may seem contradictory to use a longer integration time for the larger aperture telescope. However, this is done because the mounting of the smaller telescopes is of an altazimuth type, which does not allow long integration times. For the 1-meter telescope there were around 40,000 counts, and for the 10-inch telescope there were 11,000 counts, enough to secure the high precision desired. The photoelectric measurements and all the light curves can be requested for inspection. The procedure followed to reduce $uvby-\beta$ of the San Pedro Martir Observatory is presented in Peña et al. (2021).

In Table 1 we present the characteristics of the observed stars; that is, their IDs, coordinates (epoch 20009), V magnitude, spectral types and the observational epoch and periods in days when available from the web site of the General Catalog of Variable Stars (http://www.sai.msu.su/gcvs/cgi-bin/search.htm GCVS) as they are reported in that source. No errors are provided. All information about telescopes, photometers and filters is specified in the remarks of the table. In Table 2 the following quantities are listed: Column 1 is the ID, Column 2, date of observation, Column 3, N gives the number of data points in each run, Column 4, Δt is the time span in days of the run, Column 5, the number of Tmax of the run, Column 6, the time of maxima in HJD, Column 7, the telescope, Column 8, the filter used, Column 9, the detector, Column 10 the observatory, and finally, Column 11 gives the observers and reducers. Observers and reducers are specified in the remarks at the end of the table.

REFERENCES

Breger, M. 1966, ApJ, 146, 958

Collins, K. A., Kielkopf, J. F., Stassun, K. G., & Hessman, F. V. 2017, AJ, 153, 77

Millis, R. L. 1966, IBVS, 137, 1

Peña, J. H., Villareal, C., Piña, D. S., et al. 2016, RMxAA, 52, 385

Peña, J. H., Renteria, A., Villareal, C. et al. 2015, IBVS, 6154, 1

Peña, J. H., Renteria, A., Piña, D., & Villareal, C. 2017, IBVS, 63, 6220

Samus, N. N., Kazarovets, E. V., Durlevich, O. V., Kireeva, N. N., & Pastukhova, E. N. 2017, ARep, 61, 80

Warman, J., Malacara, Z., & Breger, M. 1974, RMxAA, 1, 143

Warman, J., Peña, J. H., & Arellano Ferro, A. 1979, AJ, 84, 109

T. Benadalid, J. Donaire, and R. Muñoz: Planetario Max Schreier, Universidad Mayor de San Andrés, Bolivia.

J. Guillén, J. H. Peña, and D. S. Piña: Facultad de Ciencias, Universidad Nacional Autónoma de México, México.

H. Huepa, J. H. Peña, and A. Rentería: Observatorio Astronómico Nacional de Tonantzintla, Universidad Nacional Autónoma de México, México.

J. D. Paredes: Facultad de Ciencias, Universidad Central de Venezuela, Venezuela.

J. H. Peña and D. S. Piña: Universidad Nacional Autónoma de México, Instituto de Astronomía, AP 70-264, CDMX 04510, México (jhpena@astroscu.unam.mx).

La *Revista Mexicana de Astronomía y Astrofísica*, fundada en 1974, publica trabajos originales de investigación en todas las ramas de la astronomía, astrofísica y temas vinculados a éstas. Se editan dos números por año y su distribución es gratuita a todas las instituciones relacionadas con los campos cubiertos por esta revista.

La política editorial de la *RMxAA* consiste en enviar a arbitrar los artículos recibidos a especialistas en el campo. Los interesados en publicar en nuestra revista deberán enviar por correo electrónico, a la dirección rmaa@astro.unam.mx, la versión completa de su artículo en formato PostScript o PDF y el archivo LaTeX. Estos archivos deberán ir acompañados de una carta de presentación. Todos los trabajos deben ser preparados en inglés usando la versión más reciente del macro en LaTeX de la *RMxAA* "rmaa.cls" (disponible en https://www.irya.unam.mx/rmaa/). Se requiere un "Abstract" no mayor que 12 líneas, y un "Resumen" en español (este último podrá ser provisto por los editores de ser necesario); también se incluirán de 1 a 6 palabras clave ("Keywords") de la lista de las revistas astronómicas internacionales. Se requiere que cada tabla incluida en el texto esté numerada y con título; las figuras deberán estar en formato PostScript (.ps) o PostScript encapsulado (.eps), estar numeradas y con leyenda explicativa. Se requiere que cada tabla y figura estén mencionadas en el texto. El estilo de las referencias sigue las normas astronómicas internacionales recientes. Para mayor información sobre el estilo de la *RMxAA* se puede consultar el archivo de ejemplo que viene incluido en los macros. La publicación es gratuita para los autores.

En 1995 se inició la Serie de Conferencias de la *Revista Mexicana de Astronomía y Astrofísica*, dedicada a la publicación de las memorias de reuniones astrónomicas efectuadas en México y en otros países del continente. Hasta 1994 las memorias de reuniones astronómicas de la región se publicaron como volúmenes especiales de la *RMxAA*.

Las condiciones de publicación de cada volumen de las memorias de conferencias serán el resultado de un convenio establecido entre la *RMxAC* y los organizadores de cada evento. Los detalles de la publicación, que incluyen fechas y extensión de los textos, serán anunciados por los editores de cada conferencia. Las contribuciones extensas estarán en inglés con un resumen en español (o portugués en caso de las Reuniones regionales). Los resúmenes de las reuniones que no son temáticas tendrán una extensión máxima de 300 palabras incluyendo título, autores y afiliación; serán exclusivamente en inglés. Los macros LaTeX para las memorias se encuentran en http://www.astroscu.unam.mx/~rmaa. Todas las contribuciones y resúmenes deberán estar en estos formatos.

Se concede permiso a los autores de artículos y libros científi-cos para citar trabajos publicados en la *RMxAA* y en la *RMxAC* siempre y cuando se dé la referencia completa. También se permite la reproducción de figuras y tablas bajo las mismas condiciones.

La *RMxAA* aparece indexada en Current Contents, Science Citation Index, Astronomy and Astrophysics Abstracts, Physics Briefs, Publicaciones Científicas en América Latina, Astronomy and Astrophysics Monthly Index, PERIODICA, RedALyC, Latindex y SciELO.

The *Revista Mexicana de Astronomía y Astrofísica*, founded in 1974, publishes original research papers in all branches of astronomy, astrophysics and closely related fields. Two numbers per year are issued and are distributed free of charge to all institutions engaged in the fields covered by the *RMxAA*.

All papers received by the *RMxAA* are sent to a specialist in the field for refereeing. Authors interested in publishing in the *RMxAA* should send their papers to the e-mail address rmaa@astro.unam.mx, in PostScript or PDF format, along with the LaTeX file. A submission letter should also be sent. Papers should be prepared in English, using the most recent version of the *RMxAA* LaTeX document class "rmaa.cls" (available from https://www.irya.unam.mx/rmaa/). An "Abstract" of at most 12 lines is required, as well as a "Resumen" in Spanish. The latter can be provided by the Editors, if necessary. A total of six or fewer "Keywords", taken from the lists of international astronomical journals should be included. Tables should be numbered and include a title. Figures should be submitted in PostScript (.ps) or Encapsulated PostScript (.eps) format, should be numbered, and should include a caption. Both tables and figures should be mentioned in the text. The style of the references follows recent international astronomical usage. For more information about the style norms of *RMxAA* please consult the example included in the LaTeX package. Publication in *RMxAA* is free of charge to authors.

The Conference Series of *Revista Mexicana de Astronomía y Astrofísica* was founded in 1995 to publish the proceedings of astronomical meetings held in Mexico and other countries throughout the continent. Until 1994 such proceedings had been published as special issues of *Revista Mexicana de Astronomía y Astrofísica*.

Conditions of publication of proceedings of each conference will be the result of a mutual agreement between the *RMxAC* and the organizing committee. Details of publication, including length of papers, will be announced by the editors of each event. The extensive contributions should be in English, and should include an abstract in Spanish (or Portuguese for regional meetings). The abstracts of non-thematic meetings should not exceed 300 words including title, authors, and affiliation; they should be exclusively in English. The LaTeX templates specially prepared for proceedings can be obtained at http://www.astroscu.unam.mx/~rmaa; all papers should be submitted in this format.

Authors of scientific papers and books may quote articles published both in *RMxAA* and *RMxAC* provided that a complete reference to the source is given. Reproduction of figures and tables is also permitted on the same basis.

The *RMxAA* is indexed in Current Contents, Science Citation Index, Astronomy and Astrophysics Abstracts, Physics Briefs, Publicaciones Científicas en América Latina, Astronomy and Astrophysics Monthly Index, PERIODICA, RedALyC, Latindex, and SciELO.